Andreas Dietzel *Editor*

Microsystems for Pharmatechnology

Manipulation of Fluids, Particles, Droplets, and Cells

Springer

Microsystems for Pharmatechnology

Andreas Dietzel
Editor

Microsystems for Pharmatechnology

Manipulation of Fluids, Particles, Droplets, and Cells

Springer

Editor
Andreas Dietzel
Institute of Microtechnology
Technische Universität Braunschweig
Braunschweig, Germany

PVZ—Center of Pharmaceutical Engineering
Technische Universität Braunschweig
Braunschweig, Germany

ISBN 978-3-319-26918-4 ISBN 978-3-319-26920-7 (eBook)
DOI 10.1007/978-3-319-26920-7

Library of Congress Control Number: 2015958783

Springer Cham Heidelberg New York Dordrecht London

Printed on acid-free paper

Springer International Publishing AG Switzerland is part of Springer Science+Business Media (www.springer.com)

Preface

As the world becomes increasingly concerned about affordable health care, fast and effective screening methods for drugs in different formulations are required in the course of their development. Moreover, a more personalized medicine demands production of drugs in very small volumes. For both, the microfluidic approach seems ideally suited. With miniaturized systems that can be realized by microfabrication processes, new tools for research and development but also new products become available. New and better technologies for screening, for production by micro-reaction technology and micro-bioreactors, for small-scale processing of drug formulations, as well as for drug delivery are under development. Interdisciplinary research involving typical engineering disciplines and life science disciplines is the key for a further development of this field. This challenge has been accepted by the Center of Pharmaceutical Engineering (PVZ) of the TU Braunschweig established in 2012 where research groups from the pharmaceutical sciences, from biology, from process engineering, and from microtechnology intensively collaborate. Many but not all chapters of this book are written by authors active in this research center.

The book shall provide a comprehensive state-of-the-art review of microfluidic approaches and applications in pharma technology. It shall help students and postgraduate students with an interdisciplinary interest from both the pharmaceutical field and the engineering field but also process developers in the pharmaceutical industry and scientists with an overview of technologies and applications in this growing field of research.

I am grateful to all the authors for their excellent contributions to this book. I want to thank the management team of the PVZ, in particular Christel Müller-Goymann and Arno Kwade, the key persons to bring their vision and ideas into the reality of the new research center PVZ and Heike Bunjes, with whom I enjoy leading the postgraduate program “μ-Props” in which topics of this book continue in ongoing research. Special thanks go to Sabine Kral-Aulich who far in excess of what I could expect helped me in completing the book by keeping contact with the

authors and with the publisher and by working on all the details and adjustments necessary to bring the manuscripts and this book into a suitable format without losing her patience.

Braunschweig, Germany Andreas Dietzel
September 2015

Contents

Contributors

S. Beinert TU Braunschweig, Institut für Partikeltechnik, Braunschweig, Germany

N. Beißner Institut für Pharmazeutische Technologie, Technische Universität Braunschweig, Braunschweig, Germany

PVZ—Center of Pharmaceutical Engineering, Technische Universität Braunschweig, Braunschweig, Germany

H. Bunjes Institut für Pharmazeutische Technologie, Technische Universität Braunschweig, Braunschweig, Germany

PVZ—Center of Pharmaceutical Engineering, Technische Universität Braunschweig, Braunschweig, Germany

T.P. Burg Max Planck Institute for Biophysical Chemistry, Göttingen, Germany

S. Büttgenbach IMT—Institute of Microtechnology, Technische Universität Braunschweig, Braunschweig, Germany

S. Demming IMT—Institute of Microtechnology, Technische Universität Braunschweig, Braunschweig, Germany

Global Technology Chemical Intermediates, BASF SE, Ludwigshafen, Germany

A. Dietzel IMT—Institute of Microtechnology, Technische Universität Braunschweig, Braunschweig, Germany

PVZ—Center of Pharmaceutical Engineering, Technische Universität Braunschweig, Braunschweig, Germany

M. Eichler Fraunhofer IST—Institute for Surface Engineering and Thin Films, Braunschweig, Germany

T. Gothsch TU Braunschweig, Institut für Partikeltechnik, Braunschweig, Germany

F. Jürgens IMT—Institute of Microtechnology, Technische Universität Braunschweig, Braunschweig, Germany

C.-P. Klages IOT—Institute of Surface Technology, Technische Universität Braunschweig, Braunschweig, Germany

PVZ—Center of Pharmaceutical Engineering, Technische Universität Braunschweig, Braunschweig, Germany

R. Krull IBVT—Institute of Biochemical Engineering, Technische Universität Braunschweig, Braunschweig, Germany

A. Kwade TU Braunschweig, Institut für Partikeltechnik, Braunschweig, Germany

PVZ—Center of Pharmaceutical Engineering, Technische Universität Braunschweig, Braunschweig, Germany

K. Lachmann Fraunhofer IST—Institute for Surface Engineering and Thin Films, Braunschweig, Germany

M. Leester-Schädel IMT—Institute of Microtechnology, Technische Universität Braunschweig, Braunschweig, Germany

T. Lorenz IMT—Institute of Microtechnology, Technische Universität Braunschweig, Braunschweig, Germany

R. Luttge Department of Mechanical Engineering, Microsystems Group and ICMS Institute for Complex Molecular Systems, Eindhoven University of Technology, Eindhoven, The Netherlands

MESA+ Institute for Nanotechnology, University of Twente and MyLife Technologies BV, Enschede, The Netherlands

S. Lladó Maldonado IBVT—Institute of Biochemical Engineering, Technische Universität Braunschweig, Braunschweig, Germany

C.C. Müller-Goymann Institut für Pharmazeutische Technologie, Technische Universität Braunschweig, Braunschweig, Germany

PVZ—Center of Pharmaceutical Engineering, Technische Universität Braunschweig, Braunschweig, Germany

S. Reichl Institut für Pharmazeutische Technologie, Technische Universität Braunschweig, Braunschweig, Germany

PVZ—Center of Pharmaceutical Engineering, Technische Universität Braunschweig, Braunschweig, Germany

C. Richter IMT—Institute of Microtechnology, Technische Universität Braunschweig, Braunschweig, Germany

C. Schilde TU Braunschweig, Institut für Partikeltechnik, Braunschweig, Germany

H. Wachtel Boehringer Ingelheim Pharma GmbH & Co. KG, Ingelheim am Rhein, Germany

M. Windbergs Department for Biopharmaceutics and Pharmaceutical Technology, Saarland University, Saarbrücken, Germany

Helmholtz Centre for Infection Research (HZI), Helmholtz Institute for Pharmaceutical Research Saarland (HIPS), Saarbrücken, Germany

Chapter 1
A Brief Introduction to Microfluidics

A. Dietzel

1.1 Initial Remarks

With the enormous developments in micro- and nanofabrication, a new research field for scientists and engineers called micro- or nanofluidics was opened. While printer cartridges from which an ink-jet nozzle can shoot picoliter volume droplets of ink onto a sheet of paper are still one of the most prevalent microfluidic devices, this book focuses on the pharmaceutical and biochemical applications of microfluidics. Picoliter (10^{-12} L, equivalent to the volume within a cube of 10 μm edge length) droplets already appear very small, but are still large compared to functional entities in biology and chemistry. A picoliter water droplet consists of nearly 10^{13} molecules. In the same volume 10^4 bacteria and approximately ten red blood cells would only fit. To design, build, and operate devices that can manipulate drugs, particles, and biological materials like proteins and cells in miniaturized fluid volumes can be considered as a central theme of microfluidics. Such devices also known as Lab-on-a-chip systems (LOC), bio-microelectromechanical systems (BioMEMS) or miniaturized total analysis systems (μTAS) allow us bridging the gap between volumes which are familiar in classical laboratories or pilot factories and the microscale volumes common in biology. They can be the key to automated drug formulation, fast screening, protein crystallization, drug delivery, microbiorectors, organ-on-chip, and many other applications.

There are many books that describe the fundamentals and the theory of microfluidics in much more detail which will allow diving even deeper into the

A. Dietzel (✉)
IMT—Institute of Microtechnology, Technische Universität Braunschweig,
Alte Salzdahlumer Str. 203, Braunschweig 38124, Germany

PVZ—Center of Pharmaceutical Engineering, Technische Universität Braunschweig,
Franz-Liszt-Str. 35 A, Braunschweig 38106, Germany
e-mail: a.dietzel@tu-braunschweig.de

A. Dietzel (ed.), *Microsystems for Pharmatechnology*,
DOI 10.1007/978-3-319-26920-7_1

subject [2–4, 6, 7, 9]. In the following we will only briefly summarize what is important to understand some basic concepts of Labs-on-chip and the principles of fluid mechanics on which the other chapters of this book can build on.

1.2 Basic Concepts of Fluid Mechanics, Scaling

The basic concepts of pressure and buoyancy are assumed to be known. The concept of viscosity a special property however shall briefly be recapitulated. Fluids are much more deformable than solids. The force required to move two parallel plates as sketched in Fig. 1.1 separated by a liquid film of thickness Δy against each other with a velocity difference Δv depends on the plate's area and a quantity μ called the viscosity which is characteristic for a certain fluid:

$$F = \mu A \frac{\Delta v}{\Delta y} \tag{1.1}$$

The force to shear fluids is proportional to the rate of distortion (Δv in this case) which distinguishes them from solids, which are sheared by a force proportional to the distortion. For many fluids, which are called Newtonian, the viscosity can be assumed to be independent of velocity.

In general, forces acting on a surface can consist of components which are either normal or tangential to the surface. The tangential force per unit area also called shear stress will shear the fluid with a velocity as given in (1.1). The force per unit area normal to the surface will compress or dilate the fluid and is also called pressure. If we consider a volume element in a fluid not only forces localized to surfaces may act on it (as result from pressure or shear stress) but also volume forces like gravity or electromagnetic forces acting via fields from a distance influence the volume element.

As a consequence of volume and surface forces volume elements that move in a fluid stream, can be translated to a different position, can rotate and can be dilated or compressed. Flows can be visualized when tracers like bubbles, dyes, or small particles are added. To describe what is going on in a fluid one has two choices. One can pick a finite fluidic volume element and follow that element while it moves in the stream. To select a fixed location and study the fluid passing by is the other

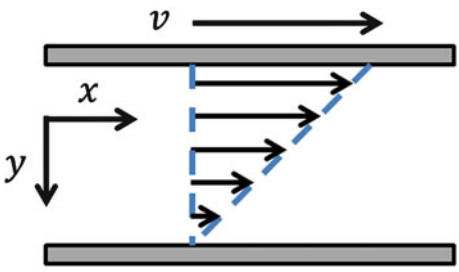

Fig. 1.1 Sketch illustrating the concept of viscosity

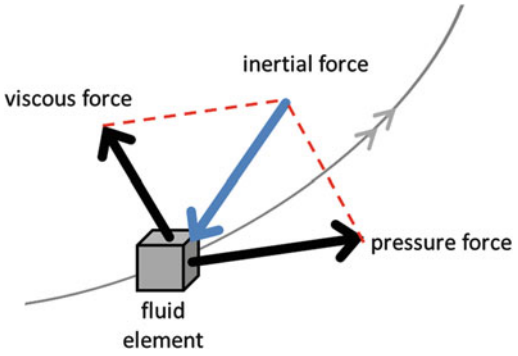

Fig. 1.2 Net forces acting on a fluid volume element

possibility. The first method is called the Lagrangian specification and the second is called Eulerian specification of the flow field.

If one looks at a fluid element with the Lagrangian view, in other words in a coordinate system that moves with the fluid element a mathematical description for the balance of net forces (as sketched in Fig. 1.2) can be easily formulated:

$$\overrightarrow{\text{inertial force}} = \overrightarrow{\text{pressure force}} + \overrightarrow{\text{viscous force}} \tag{1.2}$$

In a one-dimensional flow situation when an external force per volume f_x (for instance due to gravitation in flow direction) is encountered in addition we can formulate this momentum balance for the forces per volume [N m^{-3}] in Eulerian coordinates as

$$\rho \frac{\partial v}{\partial t} + \rho v \frac{\partial v}{\partial y} = -\frac{\partial P}{\partial x} + \mu \frac{\partial^2 v}{\partial x} + f_x \tag{1.3}$$

The left side of this equation resembles the inertial terms necessary for the description in Eulerian coordinates x, y. When the more general case of a three-dimensional flow is considered, the momentum balance in vector form (vectors are represented by bold characters) can be written using the Nabla Operator ∇ as follows

$$\rho\left(\frac{\partial \boldsymbol{v}}{\partial t} + \boldsymbol{v} \cdot \nabla \boldsymbol{v}\right) = -\nabla P + \mu \nabla^2 \boldsymbol{v} + \boldsymbol{f} \tag{1.4}$$

This is the basic Navier–Stokes-equation for the conservation of momentum describing non-compressible fluids in which the viscosity does not depend on position. In addition the conservation of mass for non-compressible fluids can be formulated as

$$\nabla \cdot \boldsymbol{v} = 0 \tag{1.5}$$

Also the conservation of energy can be used to formulate a governing equation. In practical situations the analysis may be simplified when some terms become negligible. In particular, the inertial terms become negligible in comparison to viscous forces for most microfluidic devices and (1.4) simplifies as

$$\nabla P = \mu \nabla^2 \boldsymbol{v} + \boldsymbol{f} \tag{1.6}$$

The fluidic regime in which (1.6) sufficiently describes fluidic behavior is called the Stokes-flow regime. Whether Stokes-flow approximation can be correctly applied can be decided by calculating the dimensionless Reynolds number Re which is the ratio of inertial forces over viscous forces

$$Re = \frac{\text{inertial force}}{\text{viscous force}} = \frac{\rho \cdot v \cdot L}{\mu} \tag{1.7}$$

where ρ is the fluid density and L the characteristic length of the system ($L{=}\Delta y$ in the case shown in Fig. 1.1). Only for small values of Re which is typical for many microfluidic systems (1.6) can be applied. Since no time dependency (unless for external boundary conditions) remains the system reacts instantaneous to external changes and all processes are reversible. In this regime the flow in pipes or microchannel produces a parabolic velocity profile. Further the flow rate $Q = \Delta V / \Delta t$ through a tube in contrast to high Reynolds number regimes is always a linear function of the pressure difference ΔP and in analogy to an electrical circuit, a constant flow resistance R_F of the tube can be defined as

$$Q = \Delta P \cdot R_\mathrm{F}, \qquad R_\mathrm{F} \propto \frac{L^4}{\mu \cdot D} \tag{1.8}$$

where R_F depends on the cross-sectional shape, the length L, and the diameter D of the tube. As a consequence most microfluidic networks can be handled like electrical circuits where the rules of Kirchhoff apply (Fig. 1.3). Microtubes or microchannels in series can be calculated like electrical resistors in series ($R_{\mathrm{F\ total}} = R_{\mathrm{F1}} + R_{\mathrm{F2}} + R_{\mathrm{F3}} + \ldots$) and microtubes or microchannels in parallel can be calculated like electrical resistors in parallel ($1/R_{\mathrm{F\ total}} = 1/R_{\mathrm{F1}} + 1/R_{\mathrm{F2}} + 1/R_{\mathrm{F3}} + \ldots$).

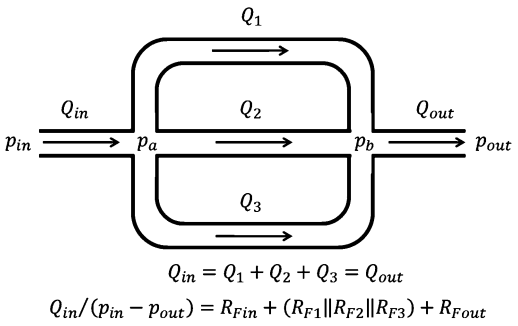

Fig. 1.3 Sketch illustrating the analogy of electric and microfluidic networks

Scaling laws are helpful to understand the consequences of decreasing dimensions of objects considered. Assuming a cube with an edge length L its volume is given by L^3 whereas the cubes surface area is given by $6L^2$. If the cube shrinks in every direction by one order of magnitude (by a factor of 10) the cube volume reduces by a factor of 1000 but the surface area only by a factor of 100. As a consequence, the surface-to-volume ratio increased by a factor of 10. This example illustrates how a body's surface area to volume ratio scales with its size. Similar considerations for other quantities can lead to different scaling laws which often provide arguments without going into a detailed analysis and are very helpful when discussing microfluidics. Navier–Stokes equations are often difficult to solve in practical situations but scaling can in such cases be used and the fluid mechanical behavior can be understood with the help of dimensionless numbers like the Reynolds number and more of those will be introduced in the following. These dimensionless numbers resemble ratios of two quantities that characterize the system and if such ratio in two experiments is the same both will show similar behavior.

1.3 Drag and Diffusion

While moving through a fluid a body experiences force acting in opposite direction to motion. This is a result of fluid friction and is called drag force. An example of drag force is already discussed with Fig. 1.1. In a more generalized description that holds also for other geometrical constellations than the one of two plates with contact surface and the drag force is given as:

$$\boldsymbol{F}_{\text{drag}} = C_{\text{d}} \boldsymbol{A} \frac{1}{2} \rho \boldsymbol{v}^2 \tag{1.9}$$

This force depends on the relative velocity v of the body with respect to the fluid, the effective drag surface A and the density of the fluid ρ. In different flow regimes, the drag coefficient C_{d} assumes different forms. C_{d} equals $\frac{24}{Re}$ for small Reynolds numbers (laminar regime) and assumes a constant value of ~0.44 at very high Reynolds numbers. The effective drag surface of a sphere of radius r is $=\pi r^2$. In laminar flows, the drag force is a linear function of relative velocity, size of the body, and viscosity, but does not depend on the fluid density and (1.9) takes the form of $\boldsymbol{F}_{\text{drag}} = \mu \cdot 6\pi r \cdot \boldsymbol{v}$ where r is the Stokes radius of an object which can deviate from the geometric radius to account for a non-spherical shape.

Diffusion is a random process leading to transport of mass. Brownian motion discovered in 1827 already gives an indication that small particles can be moved by this process. Diffusion transports molecules or very small particles from an area of higher concentration to one of lower concentration. The flux $\boldsymbol{j} = \Delta m/(\Delta t \cdot \boldsymbol{A})$

associated with diffusive transport of mass Δm of a substance through unit area A within a time interval $\Delta t = 1$ s depends on the gradient of concentration ∇c of the substance and stops as equilibrium is reached. It is described by Fick's first law:

$$\boldsymbol{j}_{\text{diff}} = -D \cdot \nabla c \tag{1.10}$$

where the diffusion constant D in [m^2 s^{-1}] describes the diffusive mobility of the substance particles or molecules. From that first law, Fick's second law can be derived from this first law when the conservation of mass (the sum of diffusive transports out/in a volume element is equal to a change in time if particle concentration in that volume) is also assumed:

$$\frac{\partial c}{\partial t} = -D \cdot \nabla^2 c \tag{1.11}$$

Equation (1.11) can be solved when boundary and initial conditions are set to get the time-dependent concentration profiles. For the one-dimensional example of an initially sharp interface at $x = 0$ separating two areas of constant but different concentrations of a molecule species at both sides (concentration step profile) the distribution will smear out over time and assume an S-shaped profile (mathematically described as $c = \text{erf}(x)$). Around $x = 0$, the curve is approximately linear and practically linear gradients can be generated. In addition to the diffusional transport, the transport due to fluid convection also leads to flux of species:

$$\boldsymbol{j}_{\text{conv}} = \boldsymbol{v} \cdot c \tag{1.12}$$

In the presence of both, diffusive and convective fluxes the Einstein–Stokes equation describes the change of concentration in a differential control volume as

$$\frac{\partial c}{\partial t} + \boldsymbol{v} \cdot \nabla c = -D \cdot \nabla^2 c \tag{1.13}$$

While both Fick's laws describe the phenomenon of diffusion in a mathematical form which is in agreement with experiments, the interpretation of diffusion as a result of random motion of particles was given first by Einstein in 1905 where he related diffusion to viscosity and temperature as follows

$$D = \frac{k_{\text{B}} T}{6\pi r \mu} \tag{1.14}$$

The product of k_{B} the Boltzmann constant and temperature T describes the average kinetic energy of a molecule and $6\pi\mu r$ already appeared in (1.9) as the friction resistance of a particle with stokes radius r. Einstein also showed that in time t a particle would move by diffusion an average distance L_{diff},

$$L_{\text{diff}} = \sqrt{2Dt} \tag{1.15}$$

The most important consequence of this equation is that time scales with the length squared. Assuming a saline solution ($D = 10^{-5}$ cm^2 s^{-1}) in a cubic container of edge length $L = 10$ cm containing a volume of 1 L, it would take 60 days to allow saline molecules to fully travel through the volume by diffusion, in other words to almost equilibrate their concentration. However, if the cubic container would be shrunk by a factor of 1000 to have an edge length of 100 µm and a volume of 1 nL equilibrium would be reached by diffusion already in about 5 s. In microfluidic devices, convectional flow and diffusion both being mass transport processes are in competition. While diffusional transport equalizes concentration gradients, convection moves matter in a flow direction. The dimensionless Peclet number Pe compares t_{diff}, the typical time for diffusive transport with the typical time for convective transport t_{conv}.

$$Pe = \frac{1}{2}\frac{t_{\text{diff}}}{t_{\text{conv}}} = \frac{vL}{D} \tag{1.16}$$

With v being the flow velocity and L the characteristic length as in (1.7) where the Re was defined. Gradients can exist if Pe is large, otherwise diffusion will equalize any gradient. Diffusive effects are brought in relation to the physical dimensions of an environment directly using the Fourier number which is defined as follows

$$Fo = \frac{1}{2}\frac{L_{\text{diff}}^2}{L^2} = \frac{Dt}{L^2} \tag{1.17}$$

If a bolus of an analyte is injected into a stream of fluid it will become dispersed as it travels through a microchannel. A pressure-driven laminar axial convection in the channel can be described by solving (1.6) with suitable boundary conditions. It is named Hagen–Poiseuille flow and is characterized by a parabolic velocity profile in absence of external forces. In this case, the diffusion occurring in axial and transverse directions combine and control the transport of the analyte. In certain flow regimes, an increased apparent diffusion constant D_{eff} is observed reflecting faster analyte dispersion. This phenomenon was discovered by Taylor and Aris [1, 14] and therefore named Taylor–Aris dispersion. It is illustrated in Fig. 1.4 for a microchannel of radius r.

Three stages of dispersion can be distinguished

1. $L_{\text{diff}} \ll r \Leftrightarrow t \ll r^2/D$

   This regime is uncommon in microfluidics and characterized by dominance of convection and therefore a dispersion according to parabolic velocity profile is observed in which $v = ½v_{\max}$ is the mean velocity in the tube. The bolus continues to stick at the channel walls where flow velocity remains zero. With

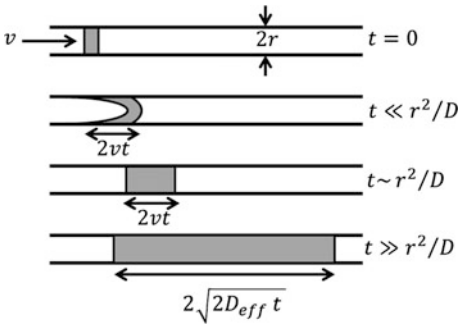

Fig. 1.4 Schematic illustration of Taylor–Aris dispersion from *top* to *bottom* with progressing time *t*: initial bolus at the *top*, *second*: bolus after elapsed time when the effect of diffusion is minor in comparison with dispersive effect of the flow, *third*: at a time where a finite radial/transverse diffusion has already occurred, bottom: at a time where diffusion already strongly influences dispersion and interplays with convective transport

starting influence of diffusion the concentration profile may be slightly broadened in axial direction.

2. $L_{\text{diff}} \sim r \quad \Leftrightarrow \quad t \sim r^2/D$

   This regime is characterized by concentration equilibration in radial direction by diffusion. Radial exchange will allow the bolus to detach from the tube walls and to start travelling with the flow. The bolus width is given by $w_{\text{bolus}} = 2vt$.

3. $L_{\text{diff}} \gg r \Leftrightarrow t \gg r^2/D$

   This regime is characterized by strong diffusion effects but the dispersion is stronger than expected when only considering diffusion. Such Taylor–Aris dispersion can be described introducing an apparent diffusion coefficient D_{eff} which equals D only for zero flow velocity ($Pe = 0$):

$$D_{\text{eff}} = D\left(1 + \frac{Pe^2}{48}\right) \tag{1.18}$$

   D_{eff} includes a diffusive component, and a dispersive component which allows describing dispersion analogous to (1.15):

$$w_{\text{bolus}} = 2\sqrt{2D_{\text{eff}}t} \tag{1.19}$$

   By radial diffusion the analyte molecules will visit both fast-moving and slow-moving parts of the Poiseuille flow, so each molecule sees an average velocity rather than the widely varying radially dependent x-velocities. The axial diffusion induces broadening of the concentration profile while radial diffusion

reduces the dispersive effects by diffusive exchange between slow- and fast-flowing regions. In contrast to the other regimes, dispersion proceeds proportional to $t^{1/2}$ rather than t. It is further important to notice that transition to regime 3 can be reached by allowing longer travelling time/distance but also by reducing the tube diameter.

1.4 Mixing

Like under macrofluidic conditions it is often desired to mix or sort ingredients for efficient chemical or biochemical processes or for analyzing components in a fluid. However, microfluidic systems allow some different forms of manipulating the distribution of substances and ingredients. A broad overview of microfluidic mixing can be found in [8]. Sometimes it is desired to physically separate components of a mixture in order to analyze each component or to concentrate or purify certain species. In other cases, such as biochemical assays the reagent has to get into intense contact with a functionalized surface, meaning that the reagents in the system have to become well mixed. If kinetics shall be studied a system has to become mixed much faster than the time scale of reaction kinetics. The Einstein–Stokes equation (1.13) describes the transport of a chemical concentration (or other conserved properties such as temperature) that moves with the fluid and does not affect fluid flow. Many microfluidic systems are characterized by low Reynolds number (laminar) but still high Peclet number (minimal diffusion). This regime allows to easily isolate chemical species in microdevices. However, the same situation also leads to challenges when species must be mixed. The challenge is to achieve a thorough mixing of multiple samples in a short time in the absence of turbulence. In a typical water-based microfluidic system ($Re < 1$) turbulent mixing does not occur. However, diffusive species mixing is often still too slow and needs to be intensified. In this regime, the so-called laminar flow patterning manipulates the spatial distribution of chemical species. In a microchannel system (which can be interpreted as a resistor network as described in Chap. 1) with one inlet of solution with species A at a flowrate Q_1 and with a second inlet of a solution of species B with a flowrate Q_2 a clear interface between the two streams will continue if the mixing between these two species is slow. The fraction of the microchannel filled with species A after the junction is given by Q_1 ($Q_1 + Q_2$). The interface location can be predicted and if the channel depth is small compared to its width it appears as sketched in Fig. 1.5 (left hand side).

Similar considerations can be made also for a system with more inlet flows and species. The Peclet number for this system is given by $Pe = v \cdot d/D$ and the system is mixed after fluid has passed a channel length of $l > d \cdot Pe$ which exceeds in most practical cases the dimensions of a microfluidic chip. In the case illustrated on the right hand side of Fig. 1.5 where the inflow of species B is symmetrically split into two inlet channels, flow focusing for the A species in the middle of the channel occurs if the channel after the junction is not too wide. Here, additional diffusion can occur through a second contact area.

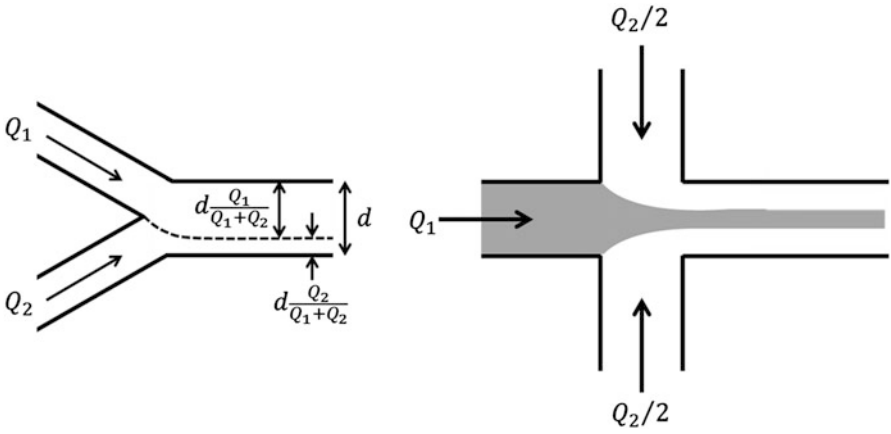

Fig. 1.5 *Left hand side*: interface location in a microchannel of width d as determined by inlet flow rates Q_1 and Q_2. *Right hand side*: flow focusing occurs if Q_1 is split into two inlets as sketched and if the channel after the junction is not too wide

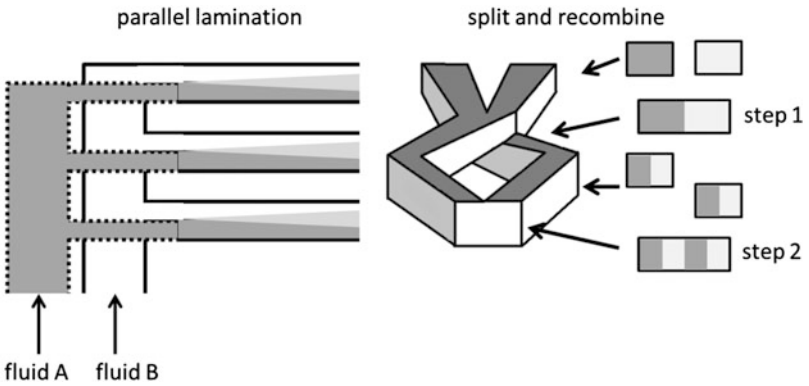

Fig. 1.6 *Left hand side*: schematic diagram illustrating parallel lamination of two fluids (A and B colored with different greyscales) for passive mixing in microchannels. The *dotted lines* represent sidewalls of microchannels which are at a different height than the other. *Right hand side*: illustration of sequential lamination. The channel cross-sections (two fluids at different greyscales) at each split and at each rejoin location are also illustrated (*right hand* part of the figure is adapted from [8])

To speed up the inherently slow process of sample mixing by diffusion between the different species flows, the contact area and contact time of the species samples can even be further increased. This can be achieved by either "active" schemes, requiring external energy to perturb the sample species, or by "passive" schemes through specially designed microchannel configurations. Examples for such configurations are parallel and sequential lamination schemes as sketched in Fig. 1.6.

In the parallel lamination approach, each inlet stream is split into n channels which can reduce the distance, diffusion needs to overcome by a factor of n. According to (1.15) the time required for mixing across the fluidic interfaces is even reduced by a factor of n^2. In sequential lamination each stage reduces the diffusion distance to half the value before and thereby reduces the time required for mixing by a factor of 4. For a flow that has passed n stages of split and rejoin (only two steps are shown in Fig. 1.6 but more stages of identical shape can be easily added) the mixing time is reduced by a factor of $4^{(n-1)}$.

If microchannels are curved centrifugal forces (which originate from inertia) can manipulate the fluid if they are of similar order or even higher than the viscous forces [5]. In this case the Stokes-flow conditions are strictly speaking no longer fully satisfied. However in typical microfluidic curved channels equation (1.6) can still be used if the centrifugal forces are handled as an additional external volume force. The dimensionless Dean number De can be used to characterize the flow in curved pipes and channels. De is given by the ratio of viscous forces and centrifugal forces and depends on the radius of curvature of the channel R and v the speed of flow:

$$De = \frac{F_{\text{viscous}}}{F_{\text{centrifugal}}} = \frac{\rho \cdot v \cdot d}{\mu} \left(\frac{d}{2R}\right)^{1/2} \tag{1.20}$$

Figure 1.7 illustrates how additional convection in the form of the so-called Dean vortices is induced when the flow is directed through a channel for the case of $De > 0$. The fluid moving down the channel center (fastest stream in a Hagen–Poiseuille parabolic flow velocity profile) experiences a higher centrifugal force than the surrounding liquid. As a result, a pair of counter-rotating vortices forms

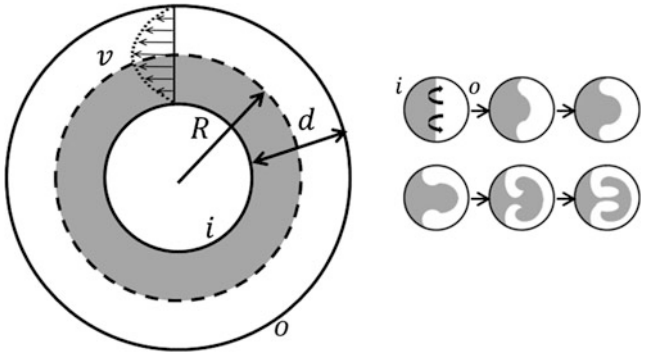

Fig. 1.7 Sketch illustration of the generation of Dean vortices in curved channels. *Left hand side*: interface of two liquids (at different greyscales) is assumed in the middle between inner (i) and outer (o) channel sidewall. The parabolic flow velocity profile leads to a maximum of axial velocity at the liquids interface. *Right hand side*: Microchannel cross-sectional views illustrate how fluidic volumes experiencing higher centrifugal forces and displace other volumes on their way outwards leading to Dean vortices

that ejects fluid from this high-speed core toward the outer wall as sketched on the right hand side of Fig. 1.7.

At even higher values of De additional vortices and oscillations in time can form depending on the form of the channel cross-section. Thereby, the distances which diffusion has to overcome is reduced and consequently mixing is accelerated in curved microchannels with $De > 0$.

1.5 Surface Tension, Two-Phase Flows, Droplets

A molecule of a fluid feels attractive forces in all directions from other molecules in proximity as long as it is located within the volume of the fluid. However, as sketched in Fig. 1.8 a molecule that has moved to the surface feels that half of its neighbors are now missing and it has assumed an energetically less favorable state. Creating a surface therefore requires energy. Surface tension γ is defined as the energy W required per additionally created surface area ΔA.

$$\gamma = \frac{W}{\Delta A} = \frac{F}{\Delta L} \tag{1.21}$$

In most practical cases, the liquid surface is created not against vacuum but as an interface between two phases. Therefore, interfacial tension γ_{SL} would be used instead for the case of a solid/liquid (SL) interface. Besides this thermodynamic definition also a mechanical definition as force per length (right hand side of (1.21)) which is consistent with the first one can be used. Here, F is a force that acts on the fluid and works against surface tension and ΔL is additional perimeter of the increased surface area. Surface tension force scales only linearly with length dimension and therefore becomes the largest force at very small length scales. In addition to the forces accounted for in the Navier–Stokes momentum equation this force has to be considered when a second phase (another liquid or a gas) is also present in the microgeometries or in cases where the walls of microchannels are facing changing wetting situations.

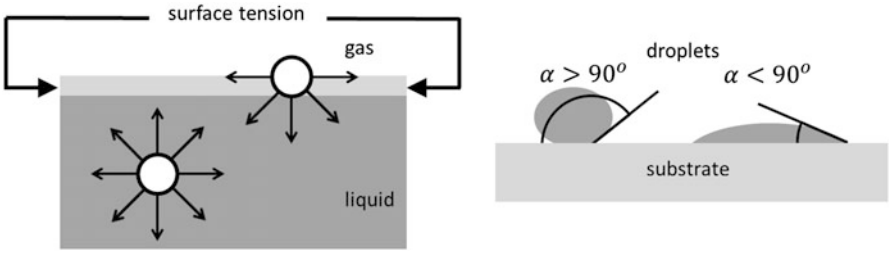

Fig. 1.8 *Left hand side*: Sketch of the molecular interactions leading to surface tension. *Right hand side*: contact angles for wetting ($\alpha < 90°$) and non-wetting ($\alpha < 90°$) conditions

Fluid surfaces becoming curved experience an increased surface area compared to the planar shape when still connecting the same ends. This results in a pressure drop across the surface balancing out the forces. This pressure drop ΔP is given by the Young–Laplace equation:

$$\gamma = \frac{\Delta P}{R} \tag{1.22}$$

For a cylindrical surface R is the radius. If the surface has curvature not only in one direction but in two directions R^{-1} has to be replaced by ${R_1}^{-1} + {R_2}^{-2}$. Here R_1 and R_2 are the radii of curvature in orthogonal directions which are equal in case of a spherical surface. If two phases (being solid, liquid, or gaseous) meet on the surface at a third phase (for instance a substrate) they create an interface at an energetically favorable angle as illustrated at the right hand side of Fig. 1.8. The contact angle α of a droplet of fluid in contact with a planar solid surface in a gaseous environment as sketched in Fig. 1.8 is given by

$$\cos\alpha = \frac{\gamma_{\mathrm{SG}} - \gamma_{\mathrm{SL}}}{\gamma_{\mathrm{LG}}} \tag{1.23}$$

Contact angle measurements offer a practical method to determine interfacial tension values. $\alpha > 90°$ characterizes a non-wetting situation whereas for $\alpha < 90°$ a wetting situation is given. It can be derived from (1.22) that as a consequence of interfacial tensions a pressure occurs in a capillary of radius r in which fluids/gases form an interface. In the case of a solid/gas (SG) interface within a capillary the pressure drop across this interface is given by

$$\Delta p = \frac{2\gamma_{\mathrm{SG}}\cos\alpha}{r} \tag{1.24}$$

where α is the contact angle measured on the material of the tube walls. Also liquid/liquid interfaces such as oil/water systems can be described using (1.24) if respective interfacial tensions are known. For miniaturized channels or tubes in microfluidics (very small r), these capillary pressure drops can play a very significant role. The behavior of systems in which surface tension is involved is characterized by the dimensionless capillary number Ca given by:

$$Ca = \frac{F_{\mathrm{viscous}}}{F_{\mathrm{surf.\ tension}}} = \frac{\mu \boldsymbol{v}}{\gamma} \tag{1.25}$$

Ca compares viscous to surface tension forces. Viscous forces dominate for $Ca \gg 1$ and vice-versa. The capillary number can also be used to characterize multiphase microfluidic flow phenomena involving bubbles, droplets, and emulsions. Adding an extra phase which does not mix with the other will add extra complexity to a microfluidic device but also offers new concepts. Droplets can for

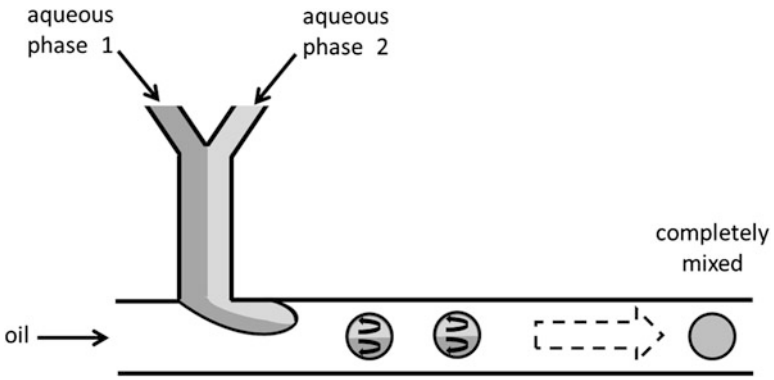

Fig. 1.9 Sketch illustrating a droplet-based microfluidic chemical reaction approach. Two reacting fluids are merged directly before they are injected into the oil stream in which they form small droplets isolated from each other and from the channel walls. Diffusion and convection within the droplet lead to fast mixing

instance act as independent compartments in which chemical processes can proceed. One can also use a gas as the continuous phase to separate plugs of liquids. As sketched in Fig. 1.9 water droplets can be created within a microfluidic oil stream [12] and used as tiny reaction chambers in which the time required for diffusion (according to (1.13)) becomes extremely short. In a droplet with a diameter of 1 µm containing approximately a femtoliter volume (10^{-15} L), the diffusion of saline molecules would typically take only about 500 µs. In addition to diffusion also convection as indicated by arrows in Fig. 1.9 resulting from friction between the droplet and the microchannel wall can promote fast mixing within the droplet. With decreasing thickness of the fluid layer of the continuous oil phase between droplet and channel wall, the friction and the convection within the droplet increase. Also the temperature would equalize very fast in these droplet compartments. The oil phase for most cases should be chosen to resemble an inert environment as much as possible. Also the precipitation of nanoparticles can occur within such droplet compartments in absence of strong local gradients and therefore with much narrower size distribution.

The physical process of microfluidic droplet formation and the resulting sizes of the dispensed droplets are determined by two parameters: the capillary number Ca as defined in (1.25) and the ratio $\alpha \ll 1$ between sample flow Q_i and carrier flow Q_c. The process can be understood when the forces acting on an emerging droplet are considered. If inertia and buoyancy can be neglected, the drag force (1.9) is smaller than the interfacial tension force (1.21) as long as a droplet cannot separate from the sample flow stream. The detachment of the droplet starts at the moment both forces are equal. At this moment the volume of the droplet is determined. The balance of the two forces defines the effective drag surface and thereby the radius r_d of the droplets as they separate:

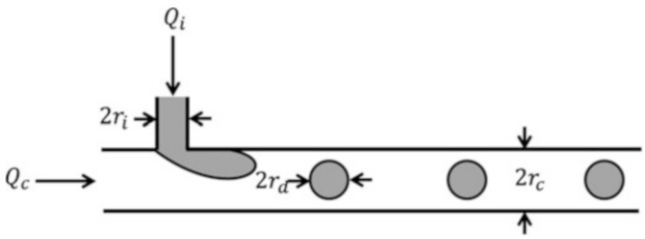

Fig. 1.10 Sketch illustrating the microfluidics droplet formation process

$$C_{\mathrm{d}} A \frac{1}{2} \rho \, \boldsymbol{v}^2 \; = \; \gamma \cdot 4\pi r_{\mathrm{i}} \; \Rightarrow r_{\mathrm{d}} = \sqrt{\frac{4A}{\pi}} = \; 2\sqrt{\frac{r_{\mathrm{i}}}{C_{\mathrm{d}}} \frac{\gamma}{\rho \, v^2}} \tag{1.26}$$

where r_{i} is the radius of the sample stream inlet channel, γ the interfacial tension between the two fluids and A the cross-sectional area of the droplet. Based on (1.26) r_{d} and from that also the droplet formation frequency f and can be calculated in dependence of α and Ca. The drag coefficient C_{d} equals $\frac{24}{Re}$ for very small Reynolds numbers and the droplet size can be calculated as

$$r_{\mathrm{d}} = Ca \cdot \frac{2}{3} (r_{\mathrm{i}} - \alpha \cdot r_{\mathrm{c}}) \tag{1.27}$$

where r_{c} is the radius of the main channel as sketched in Fig. 1.10.

Sometimes it is also important to have a measure for the importance of surface tension forces compared to body forces when the shape of bubbles or drops moving in a surrounding fluid needs to be characterized. The Bond number Bo gives the ratio of gravitational forces to surface tension forces as

$$Bo = \frac{F_{\mathrm{grav.}}}{F_{\mathrm{surf.\ tension}}} = \frac{\Delta\rho \cdot g \cdot (2r_{\mathrm{d}})^2}{\gamma} \tag{1.28}$$

where $\Delta\rho$ is the difference in density of the two phases, g the gravitational acceleration. Sometimes Bo is also calculated with other volume forces acting on the droplet or bubble instead of gravitation.

1.6 Cells in Microdevices

Traditional cell culturing as for instance in Petri dishes can often only poorly resemble in vivo conditions. Further, studies on larger scales involving large numbers of parallel experiments under different conditions are often not feasible. Microfluidics offers new perspectives for the manipulation and analysis of cultured

cells enabling large-scale parallelization and high throughput experiments but also integration of more functionality. Fluidic elements for medium exchange, patterned substrates, and elements for stimuli and for measurements, which can be of different physical nature such as mechanical, optical, or electrical can be integrated in microfabricated fluidic devices. Not only single cells but also larger populations and even intact tissues can be cultivated. This offers new approaches to quantitative and systems biology, to screening of pharmaceutical materials and to bioprocessing at small scales. With nanoliter-sized assay chambers very precisely defined experiments can be made while consumption of expensive reagents becomes very low. The intensified transport of heat and mass in small volumes allows dynamic control of conditions in which cells are cultivated and therefore new types of experiments in which also transient states can be investigated. Furthermore, not only chemical but also mechanical, electrical, or optical signals can be transferred to the cells, providing additional control parameters. Mammalian cells demand controlling the gas concentrations and surface chemistry very precisely and their cultivation in microfluidic chips is therefore more demanding than cultivation of bacterial cells. The microenvironment is given by the local chemical, thermal, and mechanical parameters in the direct surrounding of the cell. The cell medium is characterized by its temperature and by dissolved molecules and possibly by suspended (nano-) particles. The mechanical environment is defined by influences from the culture substrate but also from shear forces exerted by the surrounding flow. Many of the environmental parameters are easily controlled for a population of cells, but difficult to be addressed locally at the scale of the cell. But microfluidic devices render possible not only locally addressing parameters of the cell microenvironment, but also changing these parameters dynamically. Microscale gradient generators (μGGs) are devices that can create multiple biochemical gradients with spatiotemporal distribution controllable at subcellular resolution [15].

μGGs are operated under laminar flow conditions and concentration gradients are established by the diffusive mixing between two (or more) adjacent laminar streams of different composition as sketched in Fig. 1.11. The concentration gradient $\frac{dc}{dx}$ can be controlled through the flow rates of the two liquids and is sustained when these rates are constant. The required constant perfusion also permanently refreshes the medium and thereby enables cell culturing for longer times. Depending on the flow rate cells are exposed to shear stresses. By the addition of further fluid inlets, complex flow and concentration profiles can be realized.

With the ability to control microenvironments, to manipulate small volumes and to localize single cells the monitoring of single cells becomes possible in which the statistical noise originating from population heterogeneity is suppressed. Adherent cells can be studied using patterned adhesive patches to localize them on the walls of the microfluidic chambers. For the case of nonadherent cells, localizing by hydrodynamic traps can be applied to isolate single cells and perform experiments. Arrays of traps even allow studying cell-to-cell interactions. Further, cells can be

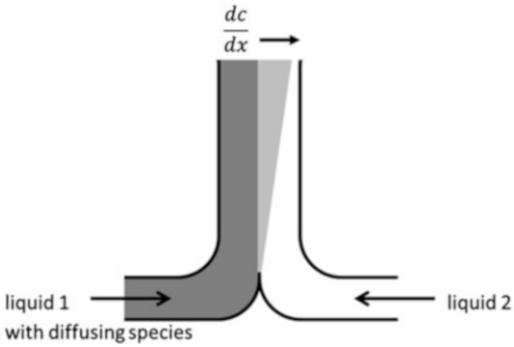

Fig. 1.11 Sketch illustrating the principle of a microfluidic gradient generator

trapped in microdroplets. With approaches similar to those in the previously discussed microfluidic droplet devices also cells can be completely separated but exchange of cell media inside the droplet is not possible.

1.7 Separation and Sorting

Separation or sorting of suspended particles, cell droplets, and molecules is very important in chemical or biological analysis and processing. Dead end and cross flow filtration techniques using porous structures can easily be adapted and the required structures be integrated in microfabricated systems. Moreover, the unique characteristics of microscale flow also led to the development of new separation techniques many of them with the benefit of continuous operation. Recently, there has been increasing interest in microfluidic separation processes for various particles including active techniques such as magnetic separation, optical tweezers, and electrophoresis. Passive techniques make use of interactions of particles with flow fields or with microchannel walls without requiring external fields. In active techniques employing external force fields the sorting efficiency may be higher but the systems become more complex. Acoustic, electrical optical and in particular also magnetic fields have already been successfully used to separate particles or cells in microfluidic devices [16]. An overview of microfluidic particle separation and sorting techniques can be found in [10] and [11].

Particles reaching a microfluidic bifurcation region as sketched in Fig. 1.12 have the tendency to follow the high flow rate branch. This phenomenon is known as Zweifach–Fung effect and was observed first with erythrocytes in branching blood vessels [13, 17]. Reasons for this behavior are that the differential pressure drop at the high flow rate branch is higher than the one in the low flow rate branch and that the shear forces along the high flow rate direction is larger than the one in low flow rate direction which results in a momentum by which the particle can roll into the high flow rate branch. The particle position in front of the bifurcation point relative to the critical streamline separating the two laminar flow streams going into the

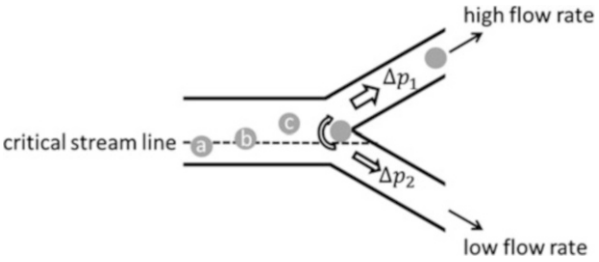

Fig. 1.12 Sketch illustrating the microfluidic particle separation by Zweifach–Fung effect. The particles center of mass position relative to the critical streamline determines whether the particle will follow the low flow rate branch (**a**) or the high flow rate branch (**b**, **c**)

daughter branches is determining which outlet branch the particle will follow. The critical streamline will shift further away from the central axis of the inlet channel when the flow rates difference between the outlet branches increases.

Particles dispersed in a moving fluid can also be seen as a form of a two phase flow (solid/liquid). Whether these particles will follow the fluid flow or will tend to collide with obstacles can be decided with the help of another dimensionless number *Stk* called Stokes number. *Stk* characterizes the balance between t_{relax}, a particle relaxation time and t_{conv}, the characteristic time of the flow (convective transport).

$$Stk = \frac{t_{\text{relax}} \cdot v}{L} \tag{1.29}$$

where v is the fluids velocity at far distance from the obstacle and L is the characteristic size of the obstacle. The particle relaxation time t_{relax} is the time constant in the exponential decay of the particle velocity relative to the fluid due to drag. Particles with a low Stokes number ($Stk \ll 1$) are dominated by drag and follow the fluid streamlines, while particles with a large Stokes number ($Stk \gg 1$) are dominated by inertia and continue to follow their initial trajectory, even when the streamlines turn to circumvent the obstacle. As discussed in a previous section the particle drag coefficient C_{d} equals $\frac{24}{Re}$ under Stokes-flow conditions and the characteristic time t_{relax} of the particle can be defined as

$$t_{\text{relax}} = \frac{\rho d^2}{18\mu} \tag{1.30}$$

where d is the particle diameter, ρ the particle density, and μ the dynamic viscosity of the fluid. Based on this principle particles that irreversibly interact with obstacles can be separated from smaller particles when obstacles are of suited form and dimension. Deterministic lateral displacement (DLD) as sketched in Fig. 1.3 is a method allowing continuous separation of particles in a laminar flow passing a regular arrangement of obstacles [11]. The gaps between the obstacles are larger

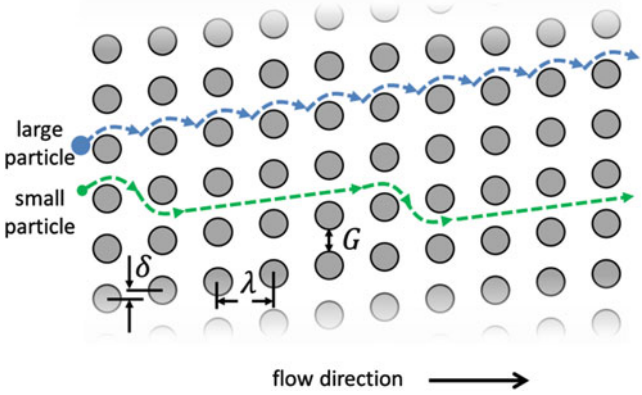

Fig. 1.13 Sketch illustrating deterministic lateral displacement particle sorting within a flow through a regular set of posts arranged at an angle

than the particle diameter ($G > d$) and the particles deterministically select a path on the basis of their size. Successive rows of obstacles are placed with a center-to-center distance λ between each other and with a lateral shift δ in a direction perpendicular to the flow. Thereby the array obstacles are oriented at an angle $\theta = \arctan\delta/\lambda$ with respect to the flow which is also called migration angle. Obstacles at row n are in line with obstacles at row $n+N$, defining N as the periodicity of the array ($N=5$ in the example of Fig. 1.13). The flow between adjacent obstacles splits into N streams which follow different routes through the array. The width of the stream in direct contact with the obstacle wall is approximately given by $(D/N)\sqrt{(N/3)}$ where D is the obstacle diameter. If the radius of a colliding particle is below this critical value the particles center of mass remains within this stream and the particle will follow this stream in a zig zag line through the array as shown for the green particle in Fig. 1.13. If however the particle is larger than the critical size and the center of mass shifts to the next stream it will be displaced and follow that stream up to the next post where this stream will be the one in contact with the obstacle and the displacement will occur again. A particle larger than the critical size (blue particle in Fig. 1.13) will be in a displacement mode, in other words will be sorted out.

The DLD method can also be used to separate deformable particles from more rigid ones and to separate droplets of different sizes. Lateral displacement arrays can also be used to separate much smaller particles and even molecules subjected to Brownian motion. If molecules have sufficient mobility to diffuse while passing the rows of obstacles they are more likely to be subjected to lateral displacement than molecules which are larger and therefore diffuse slower [10].

Table 1.1 Dimensionless scaling numbers used in this chapter

	Definition	Interpretation as ratio of two quantities	Meaning
Reynolds number	$Re = \frac{\rho \cdot v \cdot L}{\mu}$	$\frac{F_{\text{inertial}}}{F_{\text{viscous}}}$	Indicates the regimes of turbulent, laminar, and Stokes flow
Peclet number	$Pe = \frac{v \cdot L}{D}$	$\frac{t_{\text{diff.}}}{t_{\text{conv.}}}$	Indicates the balance between diffusive and convective transport
Fourier number	$Fo = \frac{D \cdot t}{L^2}$	$\frac{L^2_{\text{diff}}}{L^2}$	Indicates the balance between diffusive and convective transport
Dean number	$De = \frac{\rho \cdot v \cdot d}{\mu} \sqrt{\frac{d}{2R}}$	$\frac{F_{\text{viscous}}}{F_{\text{centrifug.}}}$	Indicates the appearance of Dean vortices in curved channels
Capillary number	$Ca = \frac{\mu \cdot v}{\gamma}$	$\frac{F_{\text{viscous}}}{F_{\text{surf. tension}}}$	Indicates the balance between viscous drag and surface tension in two-phase flows
Bond number	$Bo = \frac{\Delta\rho \cdot g \cdot (2r_{\text{d}})^2}{\gamma}$	$\frac{F_{\text{grav.}}}{F_{\text{surf. tension}}}$	Indicates the balance between gravity surface tension in two-phase flows
Stokes number	$Stk = \frac{\tau \cdot v}{L}$	$\frac{t_{\text{relax.}}}{t_{\text{conv.}}}$	Indicates how much a particle can follow changing stream

1.8 Overview of Important Dimensionless Numbers

As a quick reference a list of dimensionless numbers used in this chapter is given below (see Table 1.1).

1.9 Conclusion

This chapter is intended to provide a simplified introduction to microfluidics as a starting point for the following chapters, which concentrate on specific topics relevant to pharmaceutical technology. It should give the reader a first idea of the many opportunities of this extremely fast developing and fascinating technology but there are certainly many aspects of microfluidics which could not be covered in this chapter and will not be covered by this book. The list of references includes books and review articles which are very suitable for deeper studies.

References

1. Aris R (1956) On the dispersion of a solute in a fluid flowing through a tube. Proc R Soc A Math Phys Eng Sci 235:67–77
2. Bruus H (2007) Theoretical microfluidics (Oxford master series in physics). State University of New York Press, New York
3. Geschke O, Klank H, Telleman P (eds) (2004) Microsystem engineering of lab-on-a-chip devices. Wiley-VCH, Weinheim

4. Ghallab YH, Badawy W (2010) Lab-on-a-chip: techniques, circuits, and biomedical applications. Artech House, London
5. Jiang F, Dree KS, Hardt S, Küppers M, Schönfeld F (2004) Helical flows and chaotic mixing in curved microchannel. AIChE J 50:2297–2305
6. Kleinstreuer C (2014) Microfluidics and nanofluidics: theory and selected applications. Wiley, New York
7. Li D (ed) (2008) Encyclopedia of microfluidics and nanofluidics. Springer, Heidelberg
8. Nguyen N-T (2007) Micromixers: fundamentals, design and fabrication. William Andrew Publishing, Norwich
9. Nguyen N-T, Wereley ST (2006) Fundamentals and applications of microfluidics, 2nd edn. Artech House, London
10. Pamme N (2007) Continuous flow separations in microfluidic devices. Lab Chip 7:1644–1659
11. Sajeesh P, Sen AK (2014) Particle separation and sorting in microfluidic devices: a review. Microfluid Nanofluid 17(1):1–52
12. Seemann R, Brinkmann M, Pfohl T, Herminghaus S (2012) Droplet based microfluidics. Rep Prog Phys 75:016601 (41pp)
13. Svanes K, Zweifach BW (1968) Variations in small blood vessel hematocrits produced in hypothermic rats by micro-occlusion. Microvasc Res 1:210–220
14. Taylor GI (1935) Dispersion of soluble matter in solvent flowing slowly through a tube. Proc R Soc A Math Phys Eng Sci 219:186–203
15. Toh AGG, Wang ZP, Yang C, Nguyen N-T (2014) Engineering microfluidic concentration gradient generators for biological applications. Microfluid Nanofluid 16:1–18
16. van Pelt S, Derks RJS, Matteucci M, Hansen MF, Dietzel A (2011) Flow-orthogonal bead oscillation with a magnetic anisotropic flux-guide array. Biomed Microdevices 13(2):353–359
17. Yen RT, Fung YC (1978) Effect of velocity distribution on red cell distribution in capillary blood vessels. Am J Physiol (Heart Circ Physiol 4) 235:H251–H257

Chapter 2
Fabrication of Microfluidic Devices

M. Leester-Schädel, T. Lorenz, F. Jürgens, and C. Richter

Abstract Microfluidics could not be thought about without advances in micro- and nanofabrication. Following an approach that has been adapted from microelectronics fabrication is carried out in a cleanroom environment using monocrystalline silicon as base material. It typically involves mask-based photolithography, dry and wet etching and thin film deposition. Glass can be used as an alternative or in combination with silicon and allows optical access to the fluid in the microdevices. A different approach using the so-called soft lithography and PDMS (polydimethylsiloxane) material has found widespread applications because it is relatively cheap and easy to use. In most cases the manipulation of fluids at microscales takes place in closed volumes or channels. Several bonding techniques have been developed allowing closure by a lid which in many cases can be transparent. Recently, maskless techniques like inkjet- or 3D-printing, laser micromachining, and microelectrical discharge machining get more and more attention.

2.1 Introduction

Over the past several years there has been an increased interest in micromachining technologies. Today, microelectromechanical systems (MEMS), microoptoelectromechanical systems (MOEMS), and microfluidic systems can be found in nearly every manufacturing and industry segment (aerospace, medical appliance, automotive, communication technology, and safety engineering). Biotechnology and pharmaceutical process engineering are just joining the user group of mainly microfluidic systems. Innovative BioMEMS, Lab-on-Chip and Organ-on-Chip systems are being created.

The term “microsystem” has a variety of definitions. Usually, the sizes of functional microsystem parts are in the range of 10 nm and 100 μm. Depending on the application, a complete microsystem has dimensions of up to some 10 mm.

M. Leester-Schädel (✉) • T. Lorenz • F. Jürgens • C. Richter
IMT—Institute of Microtechnology, Technische Universität Braunschweig,
Alte Salzdahlumer Str. 203, Braunschweig 38124, Germany
e-mail: m.leester@tu-braunschweig.de

A. Dietzel (ed.), *Microsystems for Pharmatechnology*,
DOI 10.1007/978-3-319-26920-7_2

The fabrication of microsystems began in 1968 with semiconductor devices like diodes, transistors, integrated circuits, and later more complex electronic components. Especially communication and information technologies have profited significantly from these challenging advancements. Due to the excellent mechanical properties of silicon, which was and still is the most widely used semiconductor material, the semiconductor fabrication technologies have been further developed since the 1980s to build up 3D micromechanical systems. Today many different deposition, etching, second cast, bonding and as a newer achievement maskless patterning techniques are available to micromachine materials like polymers, silicon, glass, and metals. The key fabrication process is still the photolithography, based on a light-sensitive material (photoresist), in which the microstructures are transferred by exposing and developing.

Usually, the source material is a circular thin wafer with a diameter of 25 mm ($\approx 1''$) to 300 mm ($\approx 12''$). This wafer is machined as a whole (batch or wafer-level fabrication) as long as possible. The single microsystems are separated only in one of the last process steps. The main advantage of wafer-level micromachining is cost reduction for the single microsystem, because a few hundred devices can be fabricated at once, depending on the size of the micro device and the wafer. Industrial microfabrication is even specified for the simultaneous machining of up to 25 wafers.

2.2 Cleanroom

A low-particle environment is essential to manufacture semiconductor components and microsystems, as well as pharmaceutical products, medical and life science devices. Therefore, it is essential to minimize the level of contamination by dust, airborne particles, aerosol particles, and chemical vapors, which leads to degradation of product performance on the one hand, and cross-infection between medical staff and patients in the healthcare industry on the other hand.

2.2.1 Classification

A cleanroom is an environment with a controlled level of pollutants, temperature, humidity, and pressure. The contamination level of particulate matter is graded by the maximum allowable number of particles per unit volume (usually cubic meters) at a specified particle size. A discrete-particle-counting, light-scattering instrument is used to determine the concentration of airborne particles, equal to and larger than the specified sizes, at designated sampling spots [12]. Designation ISO 1 to ISO 9 refers to ISO 14644-1 standards, which specify the decimal logarithm of the number of particles with a size of 0.1 μm or larger permitted per cubic meter of air. For example, the ambient air outside in a typical urban environment contains one

billion (10^9) particles per cubic meter in the size range 0.1 µm and larger in diameter, corresponding to an ISO 9 cleanroom. An ISO 5 cleanroom has at most 10,000 particles/m^3 and an ISO 1 cleanroom allows ten particles in that size range and no particles above 0.2 µm. For pharmaceutical und biotechnological use, the number of maximum non-particulate contaminants such as microbes or germs must be monitored and limited according to the guidelines of good manufacturing practice [11].

To ensure a defined cleanroom class first the air entering from outside is filtered to exclude dust. Second the air inside is constantly recirculated through high-efficiency particulate air (HEPA) and/or ultra-low particulate air (ULPA) filters to remove internally generated contaminants. By applying either laminar air flow or turbulent air flow techniques to the environment air, any pollution is directed away from the workspace. Cleanroom architecture and equipment that promotes uncontrolled turbulence is to be avoided.

Personnel working in cleanrooms are another main particle source. To minimize the emission of contaminants naturally generated by skin, body, and garments the cleanroom staff has to wear special clothing (Fig. 2.1). The clothing itself is made of synthetics to be abrasion-resistant, lint-free, and impermeable to fibers and particles emitted of the undergarments. Furthermore, the cleanroom staff has to enter and exit the cleanroom through airlocks or air showers.

Fig. 2.1 Cleanroom garments for ISO 5: (**a**) head cover, beard cover, coverall, overshoes, latex disposable gloves and (**b**) hairnet, coverall, shoes, nitrile disposable gloves

2.2.2 *Cleanroom Concepts*

There are different concepts to build up a cleanroom, which vary by size, acquisition costs, and modularity or rather modifiability. A complete room with individual size and design, which fulfills the requirements of the intended ISO class, is a cleanroom in the proper meaning of the word (conventional cleanroom). This is the largest but the most expensive and the fewest modifiable concept. Today, many different wall, ceiling, and floor systems are available. Their surfaces have to be easily cleanable, resistant against solvents and other chemicals and abrasion-free. In addition cleanroom systems have to fulfill high demands concerning lighting, vibration damping, electrostatic charge, and noise level. Changing rooms, airlock/air shower systems, integrated air guidance, and integrated media supply are also part of modern cleanroom systems. As an example, the cleanroom at the Institute of Microtechnology, TU Braunschweig, has 300 m^2 working space, divided into three ISO 5-6 corridors (Fig. 2.2). Behind and between these so-called white aisles are service ("gray") aisles with a lower ISO class. This design has the advantage to get a large wall surface where process facilities and equipment can be integrated and installed.

A minienvironment (local cleanroom) is a high ISO class area within a lower ISO class laboratory. The high ISO class area is separated by PVC-strip or -film curtains and provided with filtered laminar airflow by an external laminar flow unit. The advantages are significant lower acquisition and operating costs, which are in contrast to the strongly limited space. A cleanroom cabin contains process facilities and working space as well as a laminar flow unit and can be integrated in laboratories or workshops without any complex external supply technology. This makes cleanroom cabins very flexible and consumer-adaptable. The most cost-saving and modifiable cleanroom concept is a tent, which is comparable to a cleanroom cabin but with PVC-film curtains instead of massive walls. This is the easiest way to realize a high ISO class in the direct surrounding of a process facility, for example a laser machine, but it cannot be used to install a fully equipped workplace with secure cleanroom conditions.

Fig. 2.2 The three "white" cleanroom corridors in the Institute of Microtechnology at TU Braunschweig: (**a**) process unit aisle; (**b**) area of chemical processing and (**c**) yellow-light aisle for photolithography

2.2.3 Cleanroom Equipment

The above-mentioned properties are largely valid for semiconductor/microsystem as well as for pharmaceutical/biological/medical cleanrooms. The laminar flow in semiconductor/microsystem cleanrooms used for particle reduction requires the surfaces of workbenches, tables, etc. to be perforated. Polymers like melamine resin, polypropylene (PP), and polyvinylidene fluoride (PVDF) are popular materials for semiconductor cleanroom equipment. In contrast, the equipment surfaces of pharmaceutical cleanrooms have to be closed and sealed and are normally made of stainless steel as an easy-to-sterilize material.

2.3 Materials

2.3.1 Polydimethylsiloxane

In the field of microfluidics and microoptics polydimethylsiloxane (PDMS) has gained increasing interest in the last two decades. The main reasons are the fast, easy, and cost-effective fabrication process of PDMS using softlithography.

PDMS has a unique combination of properties resulting from the presence of an inorganic siloxane backbone and organic methyl groups attached to silicon [7]. Therefore it belongs to a group of polymeric organosilicon compounds that are commonly referred to as silicones [17]. The chemical formula for PDMS is $CH_3[Si(CH_3)_2O]_nSi(CH_3)_3$. PDMS provides a good chemical stability and is not hydroscopic. Furthermore, it is inert, nontoxic, biocompatible, nonflammable, optically transparent down to $\lambda = 300$ nm and permeable to nonpolar gases like oxygen. PDMS is durable and has good thermal stability (up to 186 °C in air), a dielectric strength of 21 kV/mm and a dielectric constant of 2.7 stable over a wide frequency range [15], is isotropic and homogeneous, commercial available (e.g., Sylgard 184 by Dow Corning Inc.), and inexpensive [35]. It provides easy handling and can be bonded to itself and a series of other materials after oxygen or air plasma treatment [20]. However, there are some disadvantages accompanying these benefits: (a) PDMS shrinks by about 1 % upon curing; and the cured PDMS can be readily swelled by a number of nonpolar organic solvents such as toluene and hexane, (b) the elasticity and thermal expansion of PDMS may limit its utility in multilayer fabrication and/or nanofabrication, (c) its softness limits the aspect ratio of microstructures in PDMS, and (d) it can absorb drugs, proteins, and small hydrophobic molecules [33].

At room temperature PDMS is liquid and can be converted into solid elastomers by cross-linking. The polymerization is described by the example of the elastomer kit sylgard 184 from Dow Corning Inc.: The two components, siloxane oligomer and curing agent, are mixed in a mixing ratio depending on the intended Young's modulus of the elastomer (usually 10:1; if this ratio is increased, the Young's

Fig. 2.3 Micro bioreactor made of PDMS. Further details about the system will be given in Sect. 5.4.2

modulus decreases). The polymerization proceeds by a hydrosilylation reaction, where the vinyl groups (CH_2=CH^-) of the siloxane oligomers form covalent bonds with the hydrosilane (SiH) groups of the curing agent. The cross-linking reaction is catalyzed by a platinum-catalyst contained in the curing agent and takes place at room temperature but can be accelerated by enhancing the temperature [19] (Fig. 2.3).

2.3.2 SU-8

SU-8 is a UV-sensitive, high-contrast, epoxy-based negative tone photoresist designed for the lithography of ultra-thick resists. It is ideally suited for imaging permanent microstructures with high-aspect ratios and near vertical sidewalls [24]. There are already many examples of its use as material for micromolds, packaging, and devices [18]. SU-8 is based on the epon SU-8 epoxy resin, which is a multifunctional glycidyl ether derivative of bisphenol-A novolac, providing an epoxy group functionality of 8 (hence the "8" in SU-8). The epoxy resin is dissolved in an organic solvent (cyclopentanone C_5H_8O) with the addition of triarylsulfonium hexafluoroantimonate salt as photoinitiator. Depending on the quantity of solvent, SU-8 is available in different viscosities resulting in different layer thicknesses (e.g., SU-8 2005, SU-8 2025, and SU-8 2050 from MicroChem Corporation, which cover the thickness range from 1–2 to 250 µm per layer). Higher thicknesses can be achieved in a multilayer process.

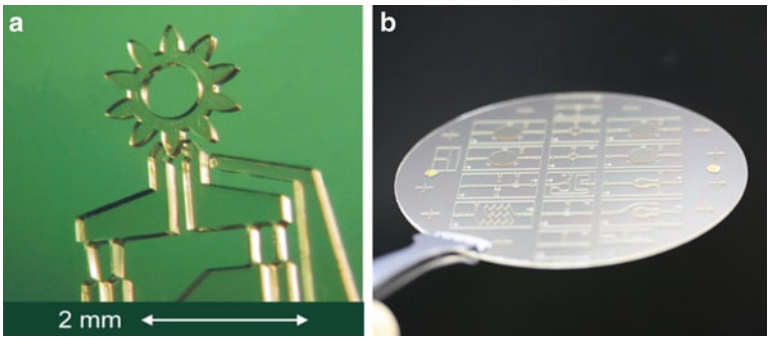

Fig. 2.4 *Left*: Microgripper and microgear made of SU-8, *right*: fluidic SU-8 structures on a carrier wafer

The exposure at conventional near UV radiation (350–400 nm; i-line (365 nm) is recommended) transforms the triarylsulfonium hexafluoroantimonate salt into a photoacid (H^+ SbF_6^-). The photoacid acts as a catalyst in the subsequent cross-linking reaction, whereby the H^+ ions attack the cyclic bonds of the epoxy groups so that they open up and, as an avalanche effect, deliver another H^+ ion. The open bonds cross-link to each other, so that the exposed areas become insoluble to liquid developers. The cross-linking process has to be enhanced by heat, requiring a post-exposure bake (PEB) at temperatures between 60 and 100 °C. The complete photolithography sequence is described in Sect. 2.5 (Fig. 2.4).

2.3.3 Silicon

The triumphal procession of single-crystalline silicon as substrate and polycrystalline silicon as thin film material has started in the semiconductor technology. Its excellent mechanical properties and the feasibility of integrating sensing and electronics on the same substrate have enabled the progression to MEMS. To fabricate functional silicon structures, many different techniques are available and well established. A distinction is made between surface micromachining, where the substrate stays unmachined and movable parts are fabricated by thin film deposition and subsequent removing of an underlying sacrificial layer, and bulk micromachining, where the microstructure is made by etching the substrate. The most popular etching techniques are described in Sect. 2.6.

Silicon is a semiconductor material, which means, that it is an insulator at low temperatures and a conductor at higher temperatures. Furthermore, the electrical conductivity can be enlarged, when foreign atoms (e.g., phosphor, brome) are added and integrated into the silicon lattice (doping [22]). However, for pure microfluidic components like channels, nozzles, and passive valves, mainly the mechanical properties of silicon and the suitability for etching and structuring are

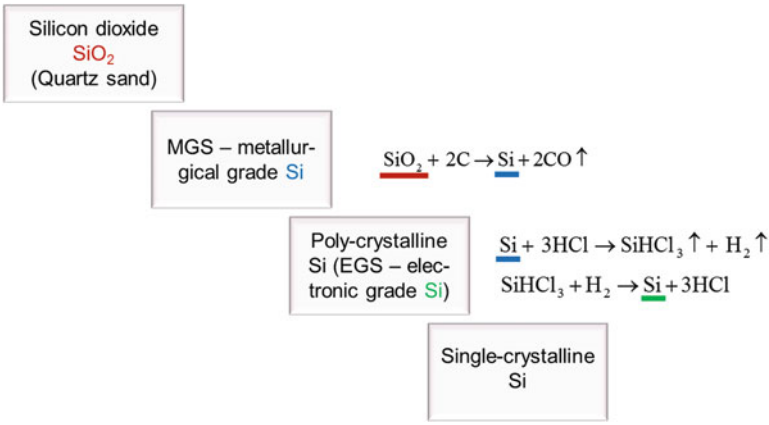

Fig. 2.5 Fabrication steps of single-crystalline silicon

relevant. As well silicon is a favorite material for medical technologies and chemical engineering, because it is medical compatible and chemically stable. The semiconductor characteristics become important, when sensor functions shall be integrated into the microfluidic chip.

Single-crystalline silicon substrates are available as circular wafers of 25 mm (≈1″) to 300 mm (≈12″). They are polished either on one or on both sides, and can be doped differently. The fabrication of high-purity single-crystalline silicon consists of several steps (Fig. 2.5). The basic material is natural silicon dioxide SiO_2 (quartz sand), which is reduced with carbon plus mild steel at a temperature of 1400 °C to elemental metallurgical grade silicon (MGS) with a purity of 96–98 %. In the next step the MGS reacts with hydrochloric acid to trichlorsilane, which is then cooled down and slowly heated up again to remove most of the impurities. The back reaction to silicon takes place in a cold wall reactor with high-purity silicon cores. The result is polycrystalline electronic grade silicon (EGS) with a purity of 99.99999 %. The last step is the transformation to single-crystalline silicon in a Czochralski crystal growing furnace or by using float-zone pulling technology. Both methods base on a silicon seed crystal, which defines the crystal orientation. By pulling the seed crystal very slowly out of melted EGS, a single-crystalline silicon ingot arises (Czochralski method). With the float-zone pulling technology an EGS ingot is melted zonewise, beginning at the seed crystal. The latter method achieves the highest purity resulting in an electric resistivity of nearly 2000 Ω cm, but is more expensive than the Czochralski method (<50 Ω cm). Afterwards the ingot is labeled with grinded flats and notches to indicate the crystal orientation and finally sawed into disks (wafers) with typical thicknesses of 50–5000 µm [30].

The crystal structure of silicon is cubic face-centered (Fig. 2.6). Planes and directions are identified by Miller indices. To determine the Miller indices of a plane, one takes the intercept of that plane with the axes of an orthogonal coordinate system. Then, the reciprocal of the axis sections is taken and multiplied by the

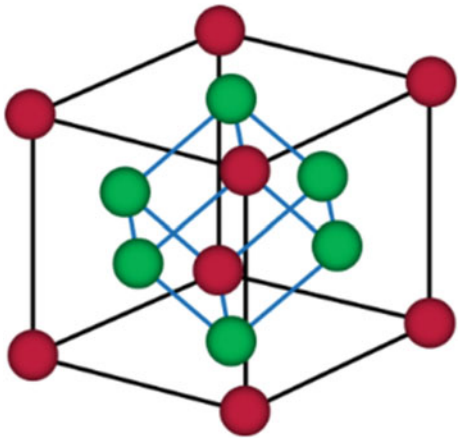

Fig. 2.6 Cubic face-centered crystal lattice (*red dots*) with primitive unit cell (*green dots*)

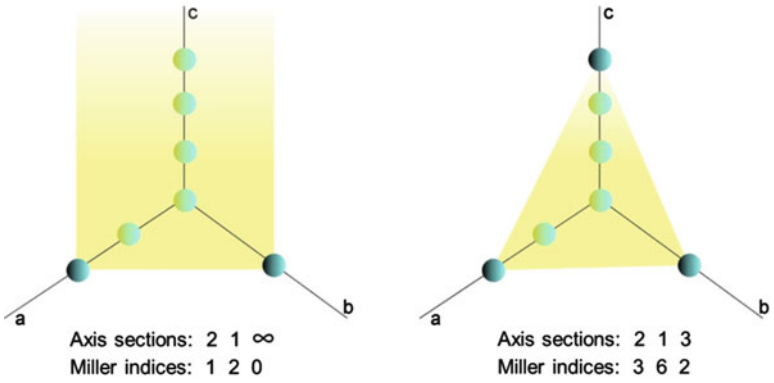

Fig. 2.7 Examples of crystal planes—points of intersection with the crystal axes plus Miller indices

smallest common denominator. The ensuring numerators are the Miller indices (*hkl*). Figure 2.7 shows two different crystal planes, their axis sections, and the related Miller indices.

Miller indices written in round brackets (*hkl*) describe one specific plane. Equivalent planes are written with closed brackets {*hkl*}. One specific direction, which is perpendicular to the plane, is defined with angle brackets ‹*h k l*›, equivalent directions with square brackets [*hkl*]. For a negative Miller index, the numeral is overlined ($h\,\overline{k}\,\overline{l}$). Figure 2.8 shows exemplary the position of the (1 0 0), the (1 1 0), and the (1 1 1) silicon crystal plane.

The silicon crystal planes are characterized by remarkable differences to each other concerning their mechanical properties as well as their etch behavior in specific wet chemical etch solutions. For example, in potassium hydroxide

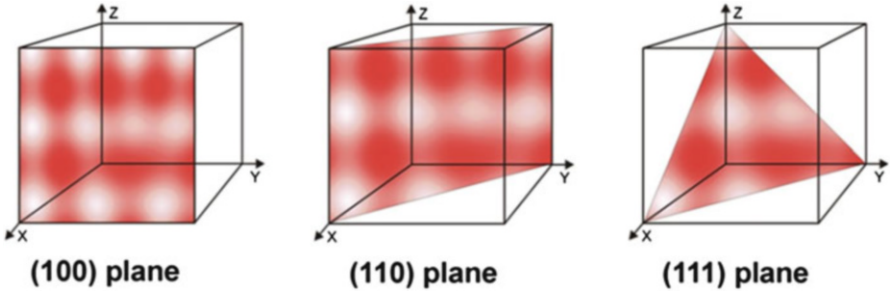

Fig. 2.8 Position of the (100), the (110), and the (111) silicon crystal plane

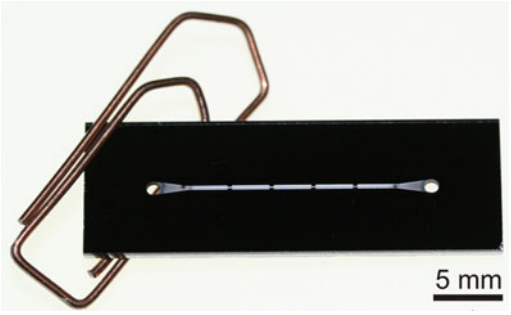

Fig. 2.9 Microfluidic system for the dispersion and emulsification of solid lipid nanoparticles made of silicon (channel bulk material) and glass (cover plate) [4]

(KOH) the etch rate of {1 1 1} planes is 40 times lower than that of {1 0 0} planes, so that the {1 1 1} planes can be conveniently used as etch stop. Silicon microstructures made by KOH etching therefore have always geometrics dominated by {1 1 1} planes (see Sect. 2.6) (Fig. 2.9).

2.3.4 Glass

The use of glass for microsystem components, especially for microfluidic parts, implies a low coefficient of thermal expansion α. Borosilicate glass with silica and boron trioxide fulfills this demand with an α of around 3×10^{-6}/°C at 20 °C and is therefore resistant to thermal shock and less subject to thermal stress. Another outstanding advantage is that borosilicate glass can be bonded to silicon by applying a voltage of 200–1000 V (anodic bonding, see Sect. 2.8.3). As well, it can be irreversibly bonded to PDMS after oxygen plasma treatment of the PDMS and glass surfaces. Not least, borosilicate glass can be bonded to itself. To do this, the bond surfaces have to be chemically activated, aligned to each other and then exposed to mechanical load and heat. (The bonding techniques are described in detail in

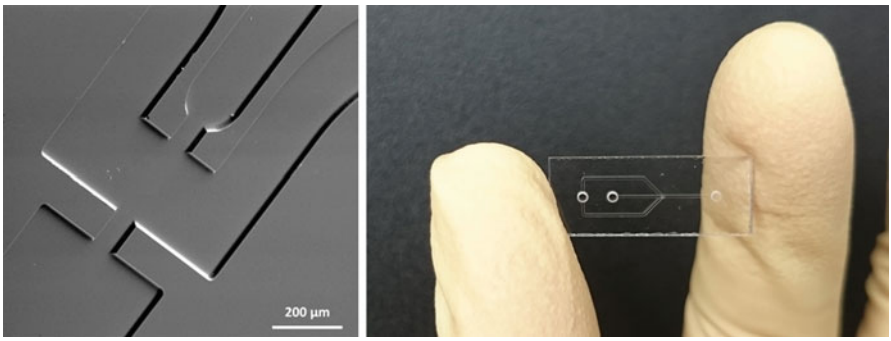

Fig. 2.10 Microfluidic system made of glass, *left*: detail, *right*: whole system

Sect. 2.8.) Furthermore, glass can be patterned by wet chemical and dry etching techniques as well as laser ablation, so that microchannels, through-holes, cavities, etc. can be easily fabricated.

Borosilicate glass was developed by the German glassmaker Otto Schott in the late nineteenth century. In 1915 Corning Glass Works introduced Pyrex, which became a synonym for borosilicate glass in the English-speaking world [34]. In the 1990s Schott set up the first microfloat production line for the manufacture of what would soon become one of the most influential specialty glass materials. The result was a floated borosilicate glass called borofloat. Over the years borofloat has made possible a multitude of innovative products across a broad spectrum of applications in research and industry [28].

The main advantage of glass compared to other materials is its optical transparency. Moreover, it has a high Young's modulus (64 kN/mm^2 [23]), a high resistance against many acids and base and it is biocompatible and low-priced (Fig. 2.10).

Another, very interesting material for microfluidics, MEMS, and MOEMS is the photosensitive glass called Foturan manufactured by Schott AG as well. Foturan is a lithium–potassium glass dotted with small amounts of silver and cerium oxides. This material combines the unique glass properties like transparency, hardness, chemical, and thermal resistance with the opportunity to achieve very fine structures with tight tolerances and high-aspect ratio. Smallest structures of 25 µm are possible with a roughness of 1 µm [6]. The microstructures are transferred by UV light at a wavelength between 290 and 330 nm, whereby the exposed regions become crystalline. The exposure can either be done by a direct laser writing process or a mask-based exposure method. Afterwards, Foturan is etched with a 10 % solution of hydrofluoric acid at room temperature. The etching is anisotropic (see Sect. 2.6), however, the crystallized regions have an etching rate up to 20 times higher than the vitreous regions. To enlarge the aspect ratio, the etch process can be supported by ultrasound. Either structured or unstructured individual parts of Foturan may be connected without any intermediate layer by thermal diffusion bonding.

2.3.5 Non-metal Thin Films

Silicon bulk micromachining is closely linked with thin silicon oxide (SiO_2) and silicon nitride (Si_3N_4) layers. Thin means in the range of a few hundred nanometers. Both of them are excellent insulating materials, often used in connection with semiconductor devices like resistors, capacitors, transistors, etc. On the other hand, both materials can be used as masking layers for silicon etching. They can be patterned photolithographically and etched in buffered hydrofluoric acid solution (SiO_2) and in phosphoric acid at 180 °C (Si_3N_4). The deposition of SiO_2 and Si_3N_4 is addressed in Sect. 2.4.1.

2.3.6 Metals

Metals are another important material group for the development of MEMS and MOEMS including microfluidic systems. Metallic conductor lines as well as masking and adhesion layers are thin-film deposited (see Sect. 2.4.2) and photolithographically patterned (gold, copper, aluminum, chrome, titanium). Thicker metallic components like electromagnetic coils (copper), magnetic field conducting structures (nickel iron), and microstamps (copper, Fig. 2.11) are usually electroplated (see Sect. 2.4.3). In microfluidic applications with high working pressures bulk stainless steel is a better choice than silicon or glass. In principle, stainless steel can be wet chemically etched, but the etch rate is rather low. However, a challenging processing method is microelectrical discharge machining (µEDM, see Sect. 2.9.5), which makes it possible to fabricate wear-resistant emulsifying and dispersing systems (Fig. 2.12).

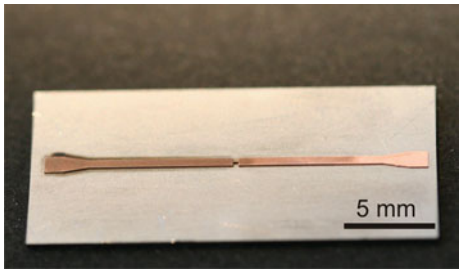

Fig. 2.11 Copper stamp for die-sinking µEDM

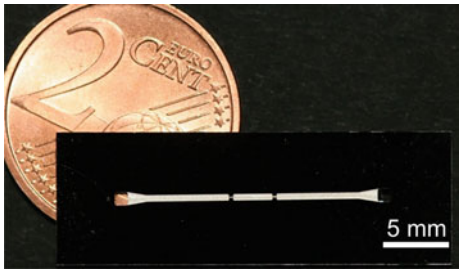

Fig. 2.12 Microfluidic system made of stainless steel by the use of µEDM

2.4 Deposition Techniques

2.4.1 Deposition Techniques for SiO_2 and Si_3N_4

Silicon oxide (SiO_2) can be deposited with mainly two different methods, resulting in different layer properties. One method is thermal oxidation, requiring a pure silicon substrate. SiO_2 growth involves the heating of the silicon wafer to temperatures between 1000 and 1250 °C and a stream of gaseous oxygen or steam. The silicon reacts with oxygen, so that the resulting SiO_2 layer grows both into the substrate surface (45 %) and upwards (55 %) (Fig. 2.13). If the oxidation takes place under pure oxygen atmosphere, it is called a "dry" oxidation.

$$Si + O_2 \rightarrow SiO_2 \tag{2.1}$$

The oxidation is called "wet", if the silicon reacts with water:

$$Si + 2H_2O \rightarrow SiO_2 + 2H_2 \tag{2.2}$$

The deposition rate of the wet oxidation is higher than that of the dry one, but the quality concerning density and dielectric strength is lower. (For example, the oxide thickness of a wet process is 420 nm after 30 min at 1100 °C and 600 nm after 30 min at 1200 °C. A dry oxidation process at 1100 °C results after 30 min in a thickness of 100 nm.) At the beginning of the oxidation process, the oxide thickness is determined by the reaction rate and is linearly dependent on the oxidation time. With the passing of process time, the oxide growth is limited by the diffusion of oxygen atoms through the already existing SiO_2 layer and is proportional to the square root of the oxidation time.

An alternative process to create thin SiO_2films but at significant lower temperatures and on nearly arbitrary substrates is the plasma-enhanced chemical vapor deposition (PE CVD). CVD processes are characterized by constituents of a vapor phase, often diluted with an inert carrier gas, reacting at a hot surface to deposit a solid film [16]. The reaction mechanism consists of several steps:

1. Gas phase reaction of reactants
2. Transport of the reaction products to the substrate surface
3. Surface reaction after adsorption of the reaction products
4. Desorption and mass transport of by-products

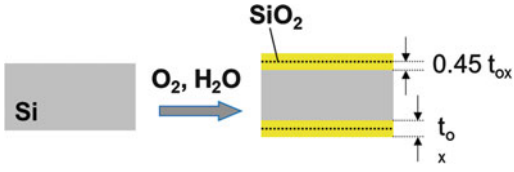

Fig. 2.13 Oxide growth at thermal oxidation

Energy to drive the surface reaction can be thermal and/or be supplied by photons, electrons, or ions. In case of the PE CVD process, the plasma (an ionized gas) is the main energy provider. The process temperature can therefore be rather low. To deposit SiO_2 the reactants are silane (SiH_4) and nitrous oxide (N_2O). The basic differences between the thermal and the plasma-enhanced oxidation are concluded in Table 2.1.

$$SiH_4 + 2N_2O \rightarrow SiO_2 + \text{Gases} \tag{2.3}$$

Silicon nitride Si_3N_4 can be deposited by two different CVD processes: Using a low pressure and, like SiO_2, a plasma-enhanced CVD process (LP CVD and PE CVD; the main differences between them are listed in Table 2.2). The LP CVD process takes place in a vertical diffusion furnace (Fig. 2.15). The chemical reactions for both of them are as follows:

Table 2.1 Comparison of thermal SiO_2 and PE CVD SiO_2

Process conditions/ layer properties	Thermal SiO_2	PE CVD SiO_2
Process temperature	800–1200 °C	<300 °C
Deposition rate	3 nm/min (dry oxidation)–20 nm/ min (wet oxidation)	55 nm/min
Pressure	Atmospheric pressure	4×10^{-4} bar
Substrate material	Silicon	Every material withstanding the process temperature
Standard layer thickness	<1 µm	Some hundred nm
Defect density	Low	High
Dielectric strength	High	Lower
One-sided/double-sided deposition	Double-sided deposition	One-sided deposition

Table 2.2 Comparison of LP CVD and PE CVD Si_3N_4

Process conditions/ layer properties	LP CVD Si_3N_4	PE CVD Si_3N_4
Process temperature	770 °C	300 °C
Deposition rate	2 nm/min	100 nm/min
Pressure	3.7×10^{-5} bar	8.7×10^{-4} bar
Substrate material	Any material withstanding the process temperatures	Any material withstanding the process temperatures
Standard layer thickness	100 nm	300 nm
Defect density	Low	High
One-sided/double-sided deposition	Double-sided deposition	One-sided deposition

$$\text{LP CVD} \quad 3SiH_2Cl_2 + 4NH_3 \rightarrow Si_3N_4 + 6HCl + 6H_2 \tag{2.4}$$

$$\text{PE CVD} \quad 3SiH_4 + 4NH_3 \rightarrow Si_3N_4 + 12H_2 \tag{2.5}$$

2.4.2 Deposition Techniques for Thin Metal Layers

Thin metal layers are usually deposited with a physical vapor deposition (PVD) technique. The oldest PVD technique is the thermal evaporation. Evaporation is based on the boiling off or sublimating of a heated material and its subsequent condensation on a substrate. An evaporation unit consists of a vacuum chamber, an evaporation source, an aperture to control the particle stream and a substrate holder. The evaporation is a quite simple and cheap technique, but the generated thin films are inhomogeneous and the deposition rate varies considerably. Another disadvantage is that the material to be evaporated has to have a lower melting point than the crucible, limiting the range of film materials. To overcome these disadvantages, the material can alternatively be heated by electron beam or laser radiation. But these machines are more complex and therefore more expensive. Suitable metals to be evaporated are silver, aluminum, gold, chrome, nickel, titanium, and platinum. Alloys are less suitable, because their stoichiometry is difficult to control, particularly if the alloy components have different melting points and therefore different deposition rates.

Another popular PVD vacuum technique is the sputtering. The material to be deposited in the form of a target (some centimeter thick disk) is bombarded with positive argon ions. The ions are created in a plasma and accelerated to the target due to a high electric direct-current voltage (the target is on negative potential, the substrate and the vacuum chamber walls are on positive potential). The impulse of the ions is transferred to the target atoms (similar to the start of a billiard game, where a billiard ball is hit into the group of the other balls), and as a result, uncharged target atoms are released and accelerated. The direction of acceleration is more or less arbitrary, so that the atoms touch down not only on the opposite substrate but also on the walls of the recipient, where they condensate. Sputtering with alternating current voltage is usual as well, but not absolutely necessary with conducting materials like gold, copper, chrome, aluminum, tin, nickel, titanium, platinum, and even alloys. Compared with evaporation, sputtering has some obvious advantages due to a wider variety of thin film materials, a better step coverage, and a usually better adhesion to the substrate.

2.4.3 Deposition Techniques for Thick Metal Layers

In microfluidics, thick metal structures are not very widely used. One example is a microplasma reactor, developed and fabricated at the IMT (Fig. 2.14, [2, 29]). The reactor made of nickel can be used for the decomposition of waste gas. Another

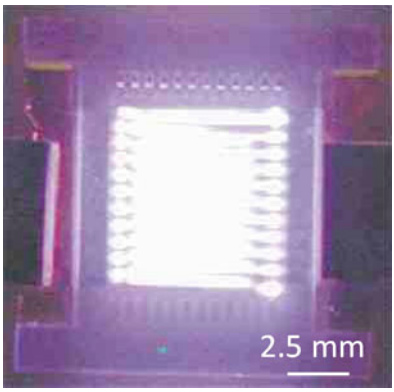

Fig. 2.14 Glowing microplasma reactor made at the IMT [29]

example is a copper die, which is used for die-sinking electrical discharge machining (see Sects. 2.3 and 2.9).

Microstructured thick metal layers are usually made by electroplating, that uses electric current to reduce dissolved metal cations by gaining electrons so that they generate a metal coating on an electrode (cathode). The substrate is first deposited (e.g., by sputtering) with a thin metal layer, the so-called seed layer. In a second step, an inverse mold of the metal structures is fabricated out of photoresist (SU-8 or AZ) using depth lithography (see Sect. 2.5). In the subsequent electroplating step, nickel, copper, or gold is plated upward from the seed layer into the voids left by the photoresist. Taking place in an electrolytic cell, the current density, temperature, and solution are carefully controlled to ensure proper plating. In the case of nickel deposition from $NiCl_2$ in a KCl solution, Ni is deposited on the cathode (metalized substrate) and Cl_2 evolves at the anode [12]. The resist either remains in the interstitials to isolate the metal structures from each other or it is stripped after electroplating.

2.5 Lithography

2.5.1 Photolithography

Photolithography has been employed for pattern generation in manufacturing of ICs, microchips, and MEMS devices. It is based on the exposure of light-sensitive polymers (photoresists), which are reactive to ultraviolet (UV) light with wavelengths in the range of 193–436 nm. The pattern transfer can be parallel through a mask that consists of opaque features on a transparent substrate or serially (direct writing) with a focused beam. The exposure causes the photoresist to be chemically modified, so that the exposed areas either become soluble in the subsequent developing step (positive tone photoresist) or becomes insoluble (negative tone resist) (Fig. 2.15). The patterned photoresist layer serves for example as masking

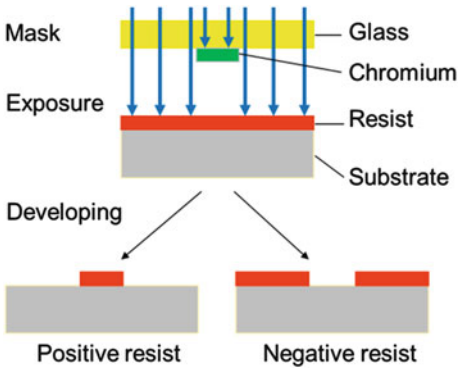

Fig. 2.15 Difference between positive and negative tone photoresist

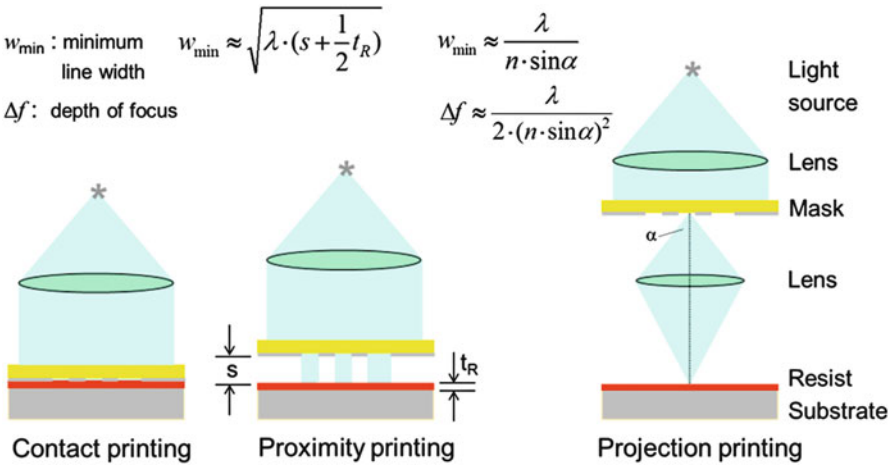

Fig. 2.16 Three methods of photolithography printing

layer in a following etch process. The resist protects the subjacent material against the etching, so that only the unprotected areas are etched. After the etch step the resist is usually removed. Another possible use for the patterned photoresist layer is a lift-off process. A thin metal layer is therefore deposited on the exposed and developed resist. Afterwards both layers are removed together. The metal remains in the resist openings.

The mask-based pattern transfer (the printing) can be performed in three different ways (Fig. 2.16): (1) the mask is in direct contact to the resist-deposited substrate (contact printing), (2) there is a small proximity distance s between resist surface and mask (proximity printing) and (3) the mask structures are projected onto the resist through an optical system (projection prining). Table 2.3 shows the main advantages and disadvantages of the three printing methods.

Table 2.3 Advantages and disadvantages of the three printing methods

	Contact printing	Proximity printing	Projection printing
Advantages	Very low minimum line width w_{min}	Mask and resist damage and contamination is avoided	Lowest minimum line width w_{min}
			Mask and resist damage and contamination is avoided
	No resolution reduction due to diffraction and refraction at slit		High throughput
	High throughput		
	Low cost		
Disadvantages	High risk of mask and resist damage and contamination	Larger minimum line width w_{min}	Equipment much more expensive
	Defects impact	Resolution is reduced due to diffraction and refraction at slit	
Examples of use	Very small or precise structures	Sensitive or sticky resists	Enlargement or reduction of the geometry

Mask aligner can be normally used for both, the contact and the proximity printing, and are used in most microfabrication research laboratories and many low-volume production facilities. The mask aligner is an alignment and exposure tool, adjusting the mask to a substrate (wafer) with submicron precision and providing the UV light source. Usually, only the upper side of the wafer is exposed. Therefore, mask and wafer are successively loaded into the mask aligner. Both are bearing alignment marks like register crosses, which are then precisely aligned to each other by means of a top side microscope. Some mask aligners are equipped as well with a backside microscope, which allows the alignment of the loaded mask to the already exposed and developed or even patterned back side of the wafer. Another feature of the backside microscope is the alignment of transparent substrates, if they have alignment marks on their back side. After exposure, the wafer is unloaded and developed. The complete photolithography process is shown in Fig. 2.17.

2.5.2 Depth Lithography

Depth lithography has its origin in LIGA technology (LIGA is a German acronym for Lithography, Galvanoformung, Abformung = Lithography, Electroplating, Molding). The LIGA starts in the early 1980s with X-rays, produced by a synchrotron to create high-aspect ratio structures. The X-rays made this

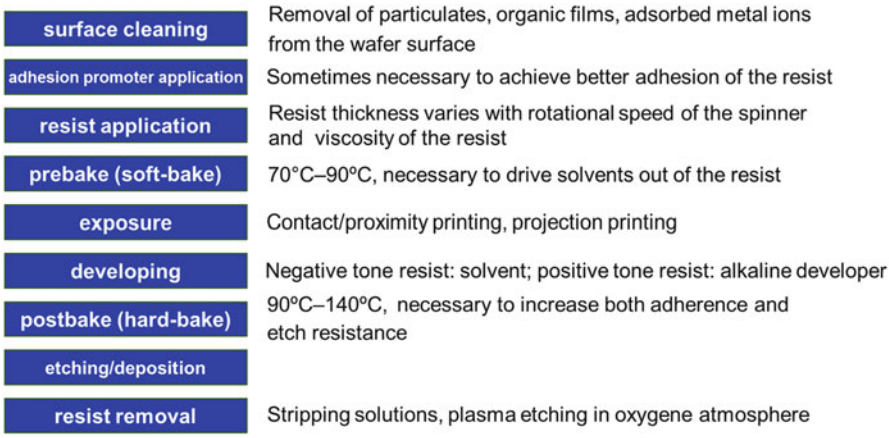

Fig. 2.17 Complete photolithography process flow

technology very equipment and cost intensive. Due to the development of special UV-sensitive polymer photoresists like SU-8 (see Sect. 2.3) the depth lithography becomes highly interesting for a broader user group. After substrate pretreatment (cleaning and drying) the so-called "Poor man's LIGA" starts with a two-step spin on process of the resist considering the recommended coating conditions [23]. The build-up of photoresist occurring at the edge of the substrate has to be removed or leveled after coating. This is done either by edge bead removal (EBR) or by leveling the wafer on a plane plate covered with a glass slid for up to half an hour. Then a pre-bake (also called soft-bake) is carried out. The next step is the exposure. The optimal exposure dose depends on the layer thickness and varies from 4 to 8 mJ/(cm^2 µm). The chemical transformation process of SU-8 to become insoluble is described in Sect. 2.3. To enhance the cross-linking process, a second thermal treatment, the PEB, has to take place directly after exposure. The PEB is followed by the developing under strong agitation. The last steps of photolithography are washing and drying. For washing fresh developer, 2-propanol is used. By contact with 2-propanol, undeveloped SU-8 will form a white haze. In this case, the development was not finished and needs to be continued. Afterwards the wafer is rinsed with DI-water and dried in a spin drier or by nitrogen stream.

If the developed resist is to be left as part of the final device and if this device is to be subjected to thermal load, a hard bake has to be incorporated into the process. It is recommended to use a final bake temperature 10 °C higher than the maximum expected device-operating temperature. However, the removal of fully cross-linked resist is extremely difficult. Recommended removal methods are plasma stripping, etching with piranha etch, laser ablation, and pyrolysis (Fig. 2.18).

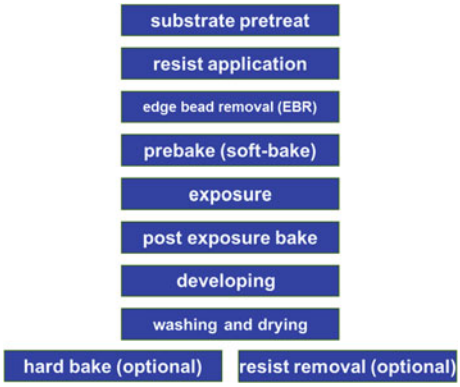

Fig. 2.18 Complete depth lithography process flow

2.6 Etching Techniques

2.6.1 Characteristics of Etching Processes

There are two main parameters to characterize etching processes: The selectivity S and the anisotropy A. The selectivity is the etch rate relation of different materials. A typical example of a treble etch system, shown in Fig. 2.23, is: (1) substrate, (2) layer to be etched, and (3) masking layer. The layer to be etched should have a high etch rate, whereas both the substrate and the mask layer should have a much lower etch rate. In other words, the selectivity should be as high as possible. Table 2.4 shows some exemplary double etch systems, common etch solutions, etch rates of both materials, and the resulting selectivity S [3].

The anisotropy A is the relation between the lateral and the vertical etch rate.

$$A = 1 - \frac{v_l}{v_v} \tag{2.6}$$

v_l: lateral etch rate
v_v: vertical etch rate

If $A = 0$ the etch process is fully isotropic (etch rates are equal in all directions). If $A = 1$ it is anisotropic (etch rate direction dependent) (Fig. 2.19).

2.6.2 Wet Chemical Etching of Thin Films

Most of the common thin film materials (SiO_2, Si_3N_4, and metals) can be etched by chemical solutions. Normally, the wet etching processes are isotropic. In case of thin films (<1 μm) the resulting undercutting of the mask layer reduces the

Table 2.4 Selectivity of some exemplary etch systems

Etch system	Etch solution	Average etch rate relation [nm/min]	Selectivity, *S*
SiO_2:Si	Buffered hydrofluoric acid $NH_4F + HF + H_2O$	200:2	ca. 100
Si_3N_4: SiO_2	Hot phosphoric acid H_3PO_4	10:1	ca. 10
Poly-Si:SiO_2	Nitric acid HNO_3 + hydrofluoric acid HF + acetic acid CH_3COOH	150:10	ca. 15
Al:SiO_2	Phosphoric acid H_3PO_4 + acetic acid CH_3COOH + nitric acid $HNO_3 + H_2O$	35:0.7	ca. 50

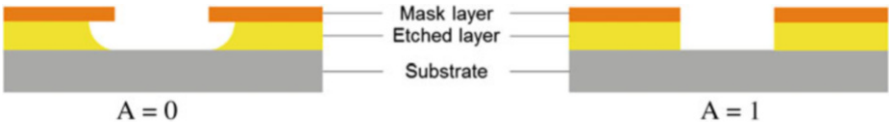

Fig. 2.19 Isotropic etching (*left*) and anisotropic etching (*right*)

resolution, but can be generally neglected (Fig. 2.19, left). To be wet chemically etched, the wafer is either dipped into an etch bath or sprayed with the etch solution.

2.6.3 Isotropic Wet Chemical Etching of Glass and Silicon

Solutions for isotropic wet etching of glass and silicon are usually hydrofluoric acid (HF) based. The glass etching solution contains varying hydrofluoric acid concentrations or solutions combining HF with other strong acids like HCL, HNO_3, H_2SO_4, or H_3PO_4 to enhance the etch rate [12]. The mask layer is usually a combination of chromium (to enhance the adhesion) and gold or alternatively photoresist, which saves some process steps but bears the risk of less reliable adhesion. For isotropic etching of silicon a solution consisting of HF, HNO_3, and NH_3COOH, called HNA (hydrofluoric, nitric, acetic) solution, in combination with a mask layer made of SiO_2 is used.

Both, the isotropic wet etching of silicon and glass are generally used to achieve large etching depths, so that the isotropic etch behavior has to be considered in determining the mask design.

2.6.4 Anisotropic Wet Chemical Etching of Silicon

As already mentioned in Sect. 2.3 single-crystalline silicon is characterized by its anisotropic (crystal plane dependent) behavior, also relating to the etch rates in specific etch solutions. The different etch rates of the crystal planes can be

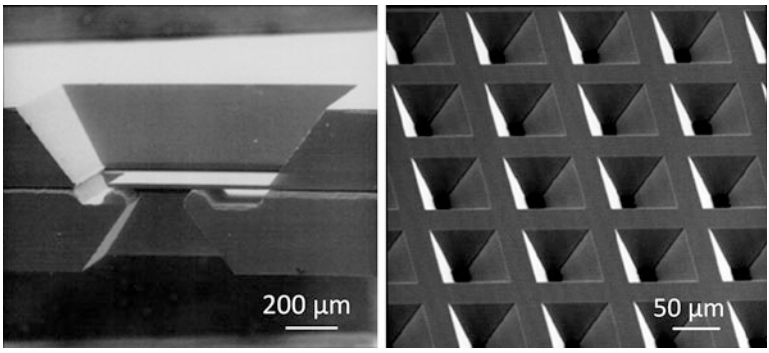

Fig. 2.20 Silicon bulk microfluidic devices: passive valve (*left*) and silicon grid (*right*)

Table 2.5 Etch rates of the {1 0 0}, {1 1 0}, and {1 1 1} planes of single crystal silicon in 40 % KOH solution at 80 °C

Crystallographic plane	Etch rate
{1 0 0}	1 µm/min
{1 1 0}	2 µm/min
{1 1 1}	0.03 µm/min

excellently used for building three-dimensional mechanical and fluidic microdevices (wet bulk micromachining). In Fig. 2.20, the left scanning electron microscope SEM picture shows a passive microvalve consisting of an upper and a lower part bonded together. The valve is normally closed. It opens, when the fluid pressure causes the beam to bend up and closes again, when the fluid pressure falls below a defined limit. The second exemplary silicon bulk device is a grid, which can be used as reactor unit (Fig. 2.21, right).

A well-known etch solution for anisotropic wet chemical etching of silicon is potassium hydroxide solution ($KOH + H_2O$) at a temperature of about 80 °C. In this case, anisotropy refers to the etch rate relation of different crystal planes, concretely those of the {1 0 0}, {1 1 0}, and {1 1 1} planes (Table 2.5). SiO_2 or Si_3N_4 are used as mask layers.

Thus, the anisotropy of {1 0 0}:{1 1 0}:{1 1 1} is about 40:80:1. In practice, the {1 1 1} planes are used as etch stop layers. Because of the angles between the (1 0 0) plane and the (1 1 0) respectively the (1 1 1) plane characteristic geometric structures are formed, as can be seen in Fig. 2.21a and b.

(1 0 0) wafers are used to etch indentations, cavities, and holes and to fabricate thin membranes. The sidewalls are always pyramid-shaped, the bases rectangular or square. With (1 1 0) wafers long, narrow channels with vertical sidewalls are fabricable. To conclude, the anisotropic wet chemical etching of silicon with, for example, KOH solution is very simple and cost saving concerning the process guiding and the equipment. But there are massive restrictions in terms of geometric forms impeding the design of microsystems.

Further solutions for anisotropic etching of silicon are tetramethylammoniumhydroxide (TMAH $C_4H_{13}NO$) and ethylenediaminpyrocatechol (EDP, $C_2H_8N_2 + C_6H_6O_2 + H_2O$). The anisotropy of both of them is lower than of KOH.

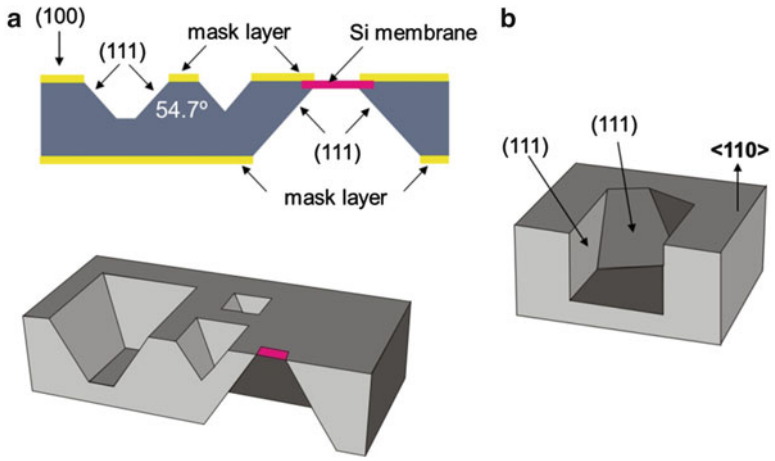

Fig. 2.21 (**a**) Silicon wafer with a (1 0 0) plane as surface etched in KOH solution. The (1 1 1) etch stop plane and the (1 0 0) plane stand at an angle of 54.7° to each other, resulting in pyramid-shaped holes (*above*: sectional view, *below*: 3D sketch). (**b**) Schematic 3D view of a (1 1 0) wafer etched in KOH solution. The angle between the (1 1 0) and the (1 1 1) plane is 90°, resulting in vertical side walls, and 35.26° as well

2.6.5 Dry Etching Techniques

If the etch process takes place in gaseous atmosphere, it is called "dry". There are pure chemical and pure physical mechanisms as well as combinations of both with different stakes (Table 2.6).

An alternative to KOH etching of silicon is the deep silicon reactive ion etching (Deep RIE or DRIE). It is based on an advanced silicon etching process, which has been originally developed and patented by the Robert Bosch GmbH in Stuttgart, Germany. This process alternates repeatedly between a nearly isotropic plasma etch step and the deposition of a chemically inert passivation layer. This etch technique provides nearly 90° sidewall profiles with any basic form. The etch rate is roughly the same as with KOH, and, as an advantage, photoresist is suitable as mask layer. If the energy to generate reactive ions is coupled inductively, it is also called ICP etch process.

The DRIE process can also be used for deep etching of glass. Fluidic channels and vias with high-aspect ratios as they are not practical in the more popular wet chemical etching process (Sect. 2.6.3) can be fabricated in the same devices like silicon dry etching. Here, gases like SF_6, C_4F_8, and CHF_3 are used for chemical etching. In the plasma the gas is ionized into fluorine and carbon radicals, which are accelerated towards the glass substrate. There fluorine radicals react with Si-atoms of the glass and carbon ions with the O_2 respectively to volatile compounds to be pumped out of the chamber. Additional gases like O_2, H_2, Ar, or He improve the stability and selectivity of the process, too [15]. Never the less, the selectivity is one

Table 2.6 Dry etching technologies

Techniques	Materials to be etched	Mechanism	Etch species	Etch profile	Selectivity
Barrel etching	Silicon, silicon nitride Si_3N_4	Chemical reaction	Reactive radicals diffuse to the substrate surface	Isotropic ($A = 0$)	High
Plasma etching (PE)	Semiconductor materials, metals, dielectrics, polymers	Combination of physical and chemical mechanisms; the physical stake increases top down	Reactive radicals with less ion bombardment	Rather isotropic	Lower
Reactive ion etching (RIE)	Silicon, glass, any organic matter		Reactive radicals and reactive ions	Rather anisotropic	Less
Reactive ion beam etching (RIBE)	Gallium arsenide, indium phosphide, cadmium mercury telluride		Reactive ions		
Ion beam etching (IBE), focused ion beam etching (FIB)	In general no restrictions (all metals, all semiconductor materials)	Physical bombardment	Non-reactive ions	Anisotropic ($A = 1$)	Low
Sputter etching	No restrictions; mainly used to clean the substrate surface before sputtering				

of the main issues and therefore a proper masking layer is important. Electroplated nickel, chrome, silicon, SU-8, and resist have been used as masking material [14].

2.7 Second Cast Techniques

2.7.1 Soft Lithography

To call this technique "soft lithography" is, however, misleading; it is in fact a non-photolithographic method for replicating a pattern. The result is a device made of PDMS (see Sect. 2.3) or other elastomeric (soft) materials. Rigid masters serve as pattern transfer agents. These masters can be made of a variety of materials. One of the most popular master materials is SU-8 (Sect. 2.3), which is photolithographically structured. To fabricate the PDMS replica, the siloxane oligomer and the

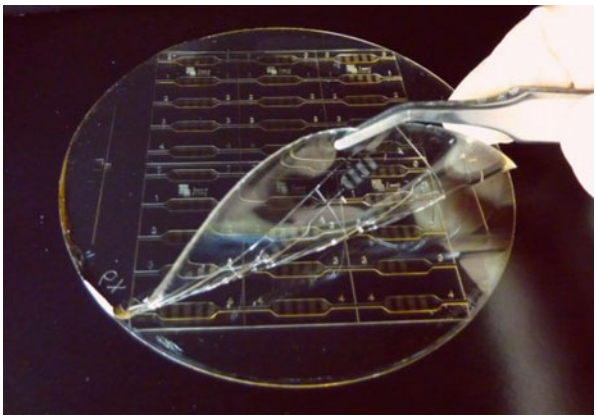

Fig. 2.22 Peeling off a PDMS layer. The master structure is made of SU-8 [5]

curing agent are mixed (usually in a ratio of 10:1) and afterwards degassed in a vacuum chamber. Then, the PDMS pre-polymer is poured over the master structure. The PDMS conforms to the shape of the master and replicates its features with high resolution. As already mentioned in Sect. 2.3 the cross-linking of PDMS can take place at room temperature, but is accelerated by enhancing the temperature (e.g., 70 °C for 60 min). The PDMS can then be peeled off the master structure (Fig. 2.22).

Soft lithography is a low-cost and effective method to fabricate PDMS micro- and nanostructures for microfluidic purposes.

2.7.2 Injection Molding

Macroscopic injection molding is a well-known technology, which enables a low-cost mass production of thermoplastic polymer devices. To fabricate micro-scale devices, a variotherm process has to be applied. Therefore, the two-part mold cavity with the micromold insert is closed, evacuated, and heated above the glass transition temperature of the polymer [13]. The polymer is heated as well to become viscous and is pressed into the mold. Both, the mold tool and the polymer are then cooled down below its glass transition temperature. Finally, the polymer workpiece is demoded and reworked if necessary. In general, cycle times are shortest when producing micro parts from polymers by injection molding. A disadvantage is the complex micromold insert, which can be fabricated for example by microelectrical discharge machining μEDM (see Sect. 2.9). A selection of thermoplastic polymers for injection molding is listed in Table 2.7.

Recent research activities include the development and design of micromold inserts, the fabrication, and processing of unfilled and magnetically soft ultrahigh-filled polymers, the characterization of the polymer's flow behavior, the investigation of weld lines, and the simulation of the melt distribution [36].

Table 2.7 Thermoplastic polymers for injection molding

Acronym	Full name
PMMA	Polymethylmethacrylate
PC	Polycarbonate
PS	Polystyrene
POM	Polyoxymethylene
PVC	Polyvinylchloride
PP	Polypropylene
PEEK	Polyetheretherketone
PA	Polyamide
PVDF	Polyvinylidenefluoride

2.8 Bonding Techniques

2.8.1 In General

Bonding of two or more microstructured components aims to create closed fluid channels, sealed cavities, and complex 3D structures. Furthermore, it can be used to strengthen the mechanical stability and to generate a thermal coupling or decoupling, an electrical contact, a galvanic separation, and the interface to the surrounding periphery.

Mainly, bonding takes place on wafer-level. Depending on the materials of the bond partner, commonly used techniques are the silicon direct bonding, the anodic bonding, the thermal bonding, the plasma-activated bonding, and the bonding with intermediate layers (solid–liquid interdiffusion bonding, adhesive bonding, glass frit bonding).

2.8.2 Silicon Direct Bonding

Two silicon wafers can be bonded by thermal treatment without any additional intermediate layers (Fig. 2.23). The so-called silicon direct bonding SDB is based on intermolecular interactions. Because of the necessary particle freedom of the bond surfaces, at first both wafers have to be cleaned very carefully. The RCA clean, which has been developed by Werner Kern at RCA laboratories, also creates hydrophilic surfaces with hydroxyl (OH^-) groups. After being cleaned, the silicon wafers are aligned and prebonded. The prebond, which is already quite stable but reversible, is induced by the bonding of the OH-groups and by Van der Waals forces. The wafers are then annealed in N_2 or O_2 atmosphere at a temperature above 800 °C. Thereby hydrogen H_2 is freed from the OH-groups and diffuses out leaving silicon–silicon and silicon–oxygen bonds.

Because of the compatibility of silicon to medical and chemical application areas, silicon direct bonding is mainly advantageous due to the absence of other materials. But the requirements concerning flatness and cleanliness of the bond surfaces in combination with high process temperatures make this bonding technique very demanding.

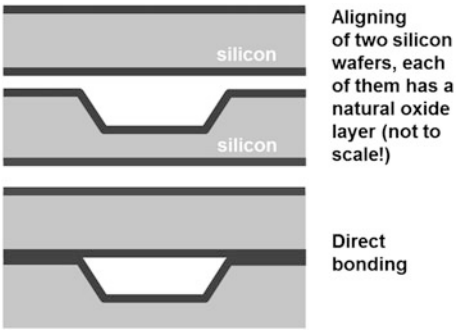

Fig. 2.23 Silicon direct bonding (sectional view of the two wafers)

2.8.3 Anodic Bonding

With the objective to provide a bond technique without any additional bond material but at considerably lower process temperatures the anodic bonding has been introduced. This technique is a type of field assisted or electrostatic bonding and demands borosilicate glass (pyrex or borofloat, see Sect. 2.3) and either silicon or metal as bond partners. Anodic bonding of two silicon wafers is only feasible if a glass layer is deposited on one of them. For medical or biological applications glass is suitable as well, so that the combination of glass and silicon is no general disadvantage; quite the contrary, glass is due to its transparency in many cases even more suitable. Furthermore, the above-mentioned glass types have a thermal expansion coefficient α quite similar to silicon, so that mechanical stress is avoided as far as possible.

For anodic bonding a process unit generating an electric field is necessary. Again, the silicon and the glass wafers are carefully cleaned and prebonded at first. Then they are placed on a heated bond chuck (350–450 °C) and a high negative voltage of 200–1000 V is applied to the glass side. Due to the heating, the positive sodium ions Na^+ (borosilicate glass contains app. 4 % by weight NaO_2) become mobile and drift towards the cathode. Therefore, a depletion region is formed at the Si/glass interface, resulting in a high electric field force generating stable intimate contact (Fig. 2.24). The oxygen ions O^{2-} bond to the silicon forming a hermetic seal.

2.8.4 Glass Bonding

Microfluidic channels fabricated from glass provide a transparent, chemical and temperature-stable system. Hence, the bonding has to keep these properties in the final fluidic chip. By thermal bonding of two glass wafers no additional material

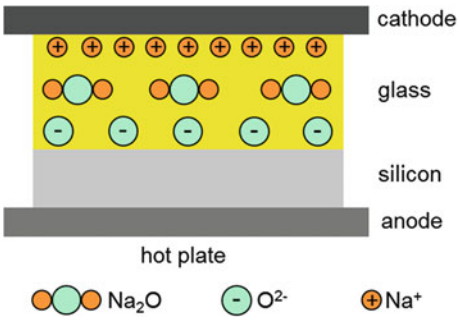

Fig. 2.24 Schematic of anodic bonding

like polymers, which are often opaque and not that chemical stable-like glass, is needed. Essential for a successful bond between two glass wafers is that both have the same thermal expansion coefficient and similar glass transition temperature [10]. Therefore bonding of identical glass type is preferred. Before bringing the surfaces in contact, each wafer has to be cleaned properly and activated by O_2-plasma or piranha treatment (peroxymonosulfuric acid H_2SO_5). This ensures the presence of sufficient OH-groups at the surface. Presence of Newton's rings after the prebond is an indicator for insufficient cleaning. In this case, the wafers have to be separated again and cleaning has to be repeated. The bonding itself takes place in a (vacuum) furnace at 500–650 °C for several hours. The result is a chemical and temperature stable bonding, which can withstand even high pressures [25, 32].

2.8.5 Plasma-Activated Bonding

Plasma activation of bond surfaces enables the direct bonding to be operated at lower temperatures. The plasma causes the removal of contaminants, the generation of Si–OH groups, and hence the hydrophilization of the surface, the enhancement of viscous flow of the surface layer, and the enhanced diffusivity of water at the interface. For microfluidic systems, the bonding of PDMS to itself or to other materials like glass, silicon, silicon oxide, silicon nitride, and SU-8 is a common task. The plasma treatment of the PDMS surface, which can for example take place in a barrel etcher, converts the methyl ($-OSi(CH_3)_2O-$) groups to silanol ($-O_n(Si(OH)_{4-n}$) groups, resulting in a hydrophilic surface with polar characteristics [8]. The hydrophilization of glass is equivalent. A condensation reaction, leading to the formation of covalent siloxane (Si–O–Si) bonds, leads to the irreversible bonding of two plasma-activated surfaces. In case of other bond partners the contamination removal (inorganic materials), and the introduction of polar functional groups (organic polymers) are the leading effects.

2.8.6 Bonding with Intermediate Layers

2.8.6.1 Solid–liquid Interdiffusion Bonding

The solid–liquid interdiffusion bonding (SLID) is based on rapid formation of intermetallic compounds (IMC) between two metal components: one low-temperature melting component (e.g., Sn) and one high-temperature melting component (e.g., Cu or Au). The bonding is typically carried out at moderate temperatures between 250 and 300 °C, which is above the melting point of Sn. When the Sn melts, the IMCs solidify isothermally. For correctly designed layer thicknesses, the resulting bond-line will only consist of Cu and the intermetallic phases (Cu_6Sn_5 and Cu_3Sn), with melting temperatures of 415 °C and 676 °C, respectively. The overall goal of the wafer-level bonding process is to achieve a $Cu/Cu_3Sn/Cu$ final bond-line, which is thermodynamically stable [21]. The advantages of SLID bonding are high temperature stability, oxidation resistance, relatively low-processing temperatures, and high mechanical robustness. Disadvantageous is that the technology is still relatively unexplored and in case of using gold quite expensive.

2.8.6.2 Adhesive Bonding

An appropriate method to bond devices of different materials, particularly new materials and new material combinations, is the adhesive bonding. This bonding technique involves glues, epoxies, or various plastic agents that bond by evaporation of a solvent or by curing a bonding agent with heat, pressure, or time [1]. The challenges of adhesive bonding are the necessary extensive knowledge of chemistry, physics, and engineering on the one hand, and the requirements to the application techniques on the other hand. The latter includes dosing and mixing techniques, the application methods themselves, and the determination of rheological properties. The main adhesives used for microsystems are epoxy resins (e.g., SU-8) and polymers (e.g., Benzocyclobutene BCB). Adverse properties of adhesive bonding are the low temperature and chemical stability as well as the medical and biological incompatibility. If the bond should be conductive, metal (nano) particles can be added to the adhesive, but the conductivity cannot be as high as in metallic connections.

2.8.6.3 Glass Frit Bonding

Low melting glass is deposited onto at least one of the bond surfaces by means of screen printing. Afterwards, the glass frit is heated to an intermediate temperature, where the glass does not yet fully melt, in order to degas the organic additives. Both wafers are then aligned and charged with heat and pressure, so that the glass frit

melts completely, wetting the surface of the second wafer and creating the bond interface. Finally, the stack is cooled down under pressure. Glass frit bonding has excellent sealing performances and a high bonding strength and does not need any voltage during bonding process. Disadvantages may be the relatively large final thickness of the glass frit (10 µm) and the large minimum line width of about 150 µm.

2.9 Maskless Patterning Techniques

2.9.1 In General

The photolithography technique as described in Sect. 2.5.1, which is highly developed and used in many areas, leaves the shortening of fabrication time to be desired. Maskless (="digital") techniques promise high-speed micromachining of different materials with micron resolution and are currently intensively advanced and optimized. The digital pattering techniques include laser micromachining, inkjet printing, 3D printing, microelectrical discharge machining, and machining techniques.

2.9.2 Laser Micromachining

Laser radiation has some outstanding properties for micromachining: Spatial coherence, which enables maximum focusing and the generation of very high energy densities, monochromaticity, and the creation of very short, exact laser pulses. The material is removed by laser ablation, which is usually based on the absorption of laser photons. The absorption again demands a material-specific wavelength. The absorbed energy causes the material to heat up and hence to melt, evaporate, or sublimate. In contrast, ultrafast lasers cause ablation as a result of multiphoton absorption at high peak intensities, so that even materials transparent to the laser wavelength can be machined.

Many types of lasers are supposed to be used for micromachining materials. These include microsecond carbon dioxide (CO_2) lasers at wavelengths between 9.3 and 11 µm, nanosecond and femtosecond solid-state lasers at wavelengths between 1030 and 1064 nm (e.g., Nd:YAG and Ti:Sapphire) with the possibility of higher harmonic generation in visible (515–535 nm) and ultraviolet (UV) spectrum (342–355 nm and 257–266 nm), then copper vapor lasers, diode lasers, and excimer lasers emitting at UV region (157–353 nm) [27].

Pulse duration, pulse energy, translation speed, and repetition rate are important process parameters. They influence the material removal rate and the size of the heat-affected zone and thus the quality of the microstructure. Ultra short pulse laser radiation (pulse duration in the range of pico- and femtoseconds) allows even

highly temperature-sensitive materials to be machined, because the heat input is almost nonexistent.

Moreover, glass can be patterned with high-intensity femtosecond laser pulses, which allows direct ablation of the material. Furthermore, fs-lasers can be used to modify the interior of glass in a selective manner. This is done by multiphoton absorption at the focal point of the laser beam. The chemical properties of the substrate get altered and allow selective etching in hydrofluoric acid (HF), as the etch rate of the laser-irradiated regions is several times higher than this of normal glass [31].

2.9.3 Inkjet Printing

Inkjet printing, a purely additive process, is commonly used to reproduce digital images in the form of depositing specially formulated ink onto paper or other substrates. More recently, researchers around the world are discovering innovative functional applications for inkjet printing in fields such as printed electronics, microfluidics, microoptics, life sciences, medicine, and security printing. Mainly, it has the potential to be a facile and rapid method to pattern conductive paths on rigid as well as flexible substrates or over prefabricated microstructures.

The majority of commercial inkjet printers have a piezoelectric printhead that jets an ink drop out of a nozzle, which has a diameter typically less than 40 μm. Printable materials are

- Conductive materials (nanoparticle/precursor inks)
- Polymers
- Dielectric powders
- Dopant
- Resists
- Silicon nanoparticles
- Enzymes
- Isolating materials

However, there is still a strong need for optimizing the printheads for particle-loaded inks with the goal to avoid irreversible blockages.

2.9.4 3D Printing

3D printing has started in the twenty-first century and is an additive process of fabricating three-dimensional solid objects from a digital file. Since then there has been an enormous development of printers, filament materials, and design software, and the complexity and resolution of printed devices have been already greatly increased. In parallel the price of 3D printers has dropped substantially.

The creation of a 3D printed object is achieved by laying down successive layers of material until the entire object is created. Each of these layers can be seen as a thinly sliced horizontal cross-section of the eventual object.

The technology currently receives a lot of attention both from industry and from private persons and the areas of use seem to be nearly unlimited: industrial design, architecture, engineering, and construction (AEC), automotive, aerospace, dental and medical industries, education, toy industry, geographic information systems, civil engineering, jewelry, footwear, and many others. Microfluidic systems benefit from the low cost and time-saving possibility of printing mainly housings with integrated fluidic interfaces. Nowadays, microsystems themselves are not fabricable, because the accuracy of 3D printed devices is still too low.

2.9.5 Microelectrical Discharge Machining

Microelectrical discharge machining (μEDM) is a promising method for the fabrication of 3D microdevices of unconventional and wear-resistant materials. It is a non-contact material removal without process forces, and a heat affected zone is not being expected. The EDM process is based on the thermoelectric energy generated between a workpiece and a tool electrode submerged in a dielectric fluid. Both are separated only by a small gap. An electric discharge (spark-over) causes material removal by melting and evaporation. The material removal always takes place on both sides: the workpiece and the tool electrode. According to the choice of adequate process parameters it is possible to minimize the tool wear and to maximize the material removal at the workpiece. Additionally the chosen process parameters determine the achievable removal rate, process time, and surface quality. The erosion parameters depend on the material combination of workpiece and tool electrode. They have to be proved and customized for every specific application. In general, four groups of μEDM types can be distinguished. In microwire electrical discharge machining (μWEDM), a wire with a diameter of about 200 μm is used to cut through a workpiece. The die-sinking EDM utilizes a die, which represents the negative geometry, to emboss the positive one into the workpiece. Both, μEDM-milling and μEDM-drilling use a rod electrode as tool [26].

2.9.6 Micromachining Techniques

There exists a wide variety of important applications for microsystems as well as for microfluidic devices (e.g., asymmetric high precision molds), which require high-strength materials and complex geometries that cannot be produced using current MEMS fabrication technologies. Micromachining has the potential to fill this void in MEMS technology by adding the capability of free form machining of

complex 3D shapes from a wide variety and combination of traditional and well-understood engineering materials (alloys, composites, polymers, glasses, and ceramics).

Micromachining techniques like microgrinding, microdrilling, and micromilling are downscaled from macroprocesses. Kinematically similar to conventional macromachining, micromachining is a mechanical material removal process using geometrically defined cutter edges. The size and geometry of microcutting tools determine the limit of the size and accuracy of micro devices.

Microgrinding is used to achieve high surface quality and shape accuracy of a workpiece. As an example, the usage of fine-grained diamond grinding wheels and adjusted process parameters enable to produce a surface roughness of about $R_a = 5$ nm. The grinding process can be assisted by ultrasound, reducing the process forces [9].

The manufacturing of bores is a challenging aspect within the production chain of micro devices. When scaling down twist drills, the ratio between core size and tool diameter increases to ensure a sufficient stability. This causes a more or less unsuitable drilling process, so that the parameters usually have to be determined only by experiments. Furthermore, the chip transportation from the bottom of the bore is more complicated [9].

Micromilling is much more flexible for machining three-dimensional microgeometries. Two-edged end mills are for example made of fine grain tungsten carbide, single-edged mills consist of monocrystalline diamond. With the tungsten carbide mill microstructures with an aspect ratio of 1:24 could be realized. With monocrystalline diamond, an aspect ratio of 1:13 could be achieved anyway [8].

References

1. Adhesives.org (2015) http://www.adhesives.org. Accessed 3 Aug 2015
2. Baars-Hibbe L, Sichler P, Schrader C, Geßner C, Gericke KH, Büttgenbach S (2003) Microstructured electrode arrays: atmospheric plasma process and applications. Surf Coat Technol 174–175:519–523
3. Büttgenbach S (1994) Mikromechanik. Teubner Verlag, Stuttgart. ISBN 3-519-13071-8
4. Büttgenbach S, Balck A, Demming S, Lesche C, Michalzik M, Al-Halhouli AT (2009) Development of on chip devices for life science applications. Int J Eng 3(2):148–158
5. Büttgenbach S, Balck A, Demming S, Lucas N, Michalzik M (2009) Softlithografie—der schnelle Weg zum Lab on Chip. Mikroproduktion vol 05/09, special Mikrostrukturtechnik, Carl Hanser Verlag, München
6. Caltech Engineering Design Research Laboratory (2015) Foturan® processing and properties. www.design.caltech.edu/micro-propulsion/Foturane.html. Accessed 3 Aug 2015
7. Clarson SJ, Semlyen JA (eds) (1993) Siloxane polymers. Prentice Hall, Englewood Cliffs
8. Demming S (2011) Disposable Lab-on-Chip systems for biotechnological screening. PhD Thesis, Berichte aus der Mikro- und Feinwerktechnik, vol 30, Shaker Verlag, Aachen
9. Denkena B, Hoffmeister HW, Reichstein M, Illenseer S, Hlavac M (2006) Micro-machining processes for microsystem technology. Microsyst Technol 12:659–664

10. Ehrfeld W, Bähr J (2002) Handbuch Mikrotechnik: 47 Tabellen. Hanser Verlag, München Wien. ISBN 3446215069, 9783446215061
11. European Commission (2015) Eudra book V1, compendium of EU pharmaceutical law, Annex 1. ISBN 978-92-79-44435-7. doi:10.2772/288501
12. Ferret (2015) ISO 21501: particle counters from Kenelec Scientific. https://www.ferret.com.au. Accessed 17 Aug 2015
13. Heckele M, Schomburg WK (2004) Review on micro molding of thermoplastic polymers. J Micromech Microeng 14:R1–R14. doi:10.1088/0960-1317/14/3/R01
14. Henry MD (2010) ICP etching of silicon for micro and nanoscale devices. PhD Thesis, California Institute of Technology
15. Kalangutkar PK (2015) Advances in biomedical field using NEMS a fusion between MEMS and nanotechnology. Int J Adv Res Comput Sci Softw Eng 5(11):132–136. ISSN 2277 128X
16. Kolari K, Saarela V, Franssila S (2008) Deep plasma etching of glass for fluidic devices with different mask materials. J Micromech Microeng 18:064010. doi:10.1088/0960-1317/18/6/064010 (6pp)
17. Linear polydimethylsiloxanes. Joint Assessment of Commodity Chemicals (1994) Report no. 26. ISSN 0773-6339-26
18. Lorenz H et al (1998) Mechanical characterization of a new high-aspect-ratio near UV-photoresist. Microelectron Eng 41(42):371–374
19. Lucas N (2009) Microplasma stamps—an atmospheric-pressure plasma source for the area-selective modification of surfaces. PhD Thesis, Be-richte aus der Mikro- und Feinwerktechnik, vol 23, Shaker Verlag, Aachen
20. Lucas N, Demming S, Jordan A, Sichler P, Büttgenbach S (2008) An improved method for double-sided moulding of PDMS. J Micromech Microeng 18:075037 (5pp)
21. Luu TT, Duan A, Aasmundtveit KE, Hoivik N (2013) Optimized Cu-Sn Wafer-level bonding using intermetallic phase characterization. J Electron Mater 42(12):3582–3592
22. Madou MJ (2002) Fundamentals of microfabrication, 2nd edn. CRC Press, Boca Raton. ISBN 0-8493-0826-7
23. MicroChem (2015) SU-8 2000 features. Datasheet. http://www.microchem.com/pdf/SU-82000DataSheet2000_5thru2015Ver4.pdf. Accessed 3 Aug 2015
24. MicroChem Corporation (2015) NANO SU-8 negative tone photoresist formulations 2-25. https://www.microchem.com. Accessed 3 Aug 2015
25. Oosterbroek RE, Hermes DC, Kakuta M, Benito-López F, Gardeniers HJGE, Verboom W, Reinhoudt DN, van den Berg A (2006) Fabrication and mechanical testing of glass chips for high-pressure synthetic or analytical chemistry. Microsyst Technol 12:450–454. doi:10.1007/s00542-005-0043-5
26. Richter C, Krah T, Büttgenbach S (2012) Novel 3D manufacturing method combining microelectrical discharge machining and electrochemical polishing. Microsyst Technol 18:1109–1118
27. Rihakova L, Chmelickova H (2015) Laser micromachining of glass, silicon and ceramics. Adv Mater Sci Eng 2015, Article ID 584952, 6 pages
28. Schott (2015) Borofloat. Inspiration through quality. www.schott.com/borofloat. Accessed 3 Aug 2015
29. Sichler P (2006) Mikrostrukturierte Fingerelektroden als Plasmaquellen. PhD Thesis, Be-richte aus der Mikro- und Feinwerktechnik, vol 17, Shaker Verlag, Aachen
30. Si-Mat (2015) Silicon materials. http://si-mat.com/de/silizium-wafer.html. Accessed 13 Aug 2015
31. Sugioka K, Cheng Y (2011) Integrated microchips for biological analysis fabricated by femtosecond laser direct writing. MRS Bull 36(12):1020–1027. doi:10.1557/mrs.2011.274
32. Tiggelaar RM, Benito-López F, Hermes DC, Rathgen H, Egberink RJM, Mugele FG, Reinhoudt DN, van den Berg A, Verboom W, Gardeniers HJGE (2007) Fabrication, mechanical testing and application of high-pressure glass microreactor chips. Chem Eng J 131:163–170. doi:10.1016/j.cej.2006.12.036

33. Toepke MW, Beebe DJ (2006) PDMS absorption of small molecules and consequences in microfluidic applications. Lab Chip 6(12):1484–1486. doi:10.1039/b612140c
34. Wikipedia (2015) Borosilicate glass. http://www.wikipedia.org/wiki/Borosilicate_glass. Accessed 3 Aug 2015
35. Xia Y, Whitesides GM (1998) Soft lithography. Annu Rev Mater Sci 28:153–184
36. Xie L, Kirchberg S, Steuernagel L, Ziegmann G (2010) A mechanism influencing micro injection molded weld lines of hybrid nano filled polypropylene. Microsyst Technol 16 (11):1855–1859

Chapter 3
Surface Functionalization of Microfluidic Devices

M. Eichler, C.-P. Klages, and K. Lachmann

Abstract Internal surfaces of pharmatechnological or biomedical microfluidic components may be functionalized—i.e., tailored or adapted to fulfill one or more specific physicochemical functions within a lab-on-chip system—by surface-technological methods selected from a number of available coating or modification processes.

Among various potential functions of a surface, its wetting behavior is of particular importance if two different phases (e.g., water and air, water and oil) are involved during operation of the system. Adhesive properties of internal walls are of major relevance in applications where particulate matter (cells, micro- or nanoparticles) plays a role: It may be necessary to prevent the adhesion of such particles on the surfaces in order to prevent clogging; on the other hand, the adhesion of cells may be aspired on certain parts of the surface. Adhesion promotion may, however, not only be an issue for the operation of an MF device but also for its manufacturing, for example for sealing or bonding processes. Frequently an undesired wall deposition of proteins or other constituents of the fluid has to be prevented by an antifouling coating or a suitable pretreatment of the surface. Coatings or surface modifications generating chemically reactive groups may be utilized to bind small molecules, polymers, biomolecules, or nanoparticles covalently to a surface. Controlling the density of charged functional groups, the ζ potential of a surface can be adjusted in order to influence, e.g., the charge of droplets dispensed from a pipette.

While so far mentioned functions of the MF device walls largely depend on their chemical composition close to the interface, specific geometrical and physical characteristics of surfaces and surface coatings may also be desired. Examples are the role of topography and Young's modulus for the attachment of cells and

M. Eichler • K. Lachmann
Fraunhofer IST—Institute for Surface Engineering and Thin Films, Bienroder Weg 54 E, Braunschweig 38108, Germany

C.-P. Klages (✉)
IOT—Institute for Surface Technology, Technische Universität Braunschweig, Bienroder Weg 54 E, Braunschweig 38108, Germany

PVZ—Center of Pharmaceutical Engineering, Technische Universität Braunschweig, Franz-Liszt-Str. 35 A, Braunschweig 38106, Germany
e-mail: c-p.klages@tu-braunschweig.de

A. Dietzel (ed.), *Microsystems for Pharmatechnology*,
DOI 10.1007/978-3-319-26920-7_3

microorganisms, coatings with specific electrical or optical functions involved in sensing and detection, electrowetting, or electrophoresis, and, last but not least, permeation barriers preventing the leaching of polymer constituents into the fluid or controlling gas transport through a polymer.

The present article gives an introduction to surface modification and coating processes which are established or under development in order to attain the above-mentioned surface functions. An emphasis will be laid on special requirements of microfluidic devices to be used with two-phase fluids and particulate matter.

3.1 Wet-Chemical Methods

3.1.1 Adsorption of Surfactants, Polymers, and Polyelectrolytes

3.1.1.1 Dynamic Adsorption

Adsorption of charged or uncharged polymers or surfactants of relatively small molecular size on the capillary surface, usually made from fused quartz, has been in use since decades already for the so-called dynamic coating in capillary electrophoresis (CE) [48, 101]. Purposes of these modifications are to prevent the adsorption of proteins or to alter the magnitude or direction of electroosmotic flow (EOF). Dynamic coating is achieved by rinsing the capillary with a solution of the polymer or surfactant. Since the amount physisorbed to the wall is in equilibrium with the solution concentration, the modifying agent is either continuously added to the medium or it is at least regenerated occasionally. A few examples for a large range of materials used are morpholine, cetyltrimethylammonium bromide (CTAB), poly (vinyl alcohol) (PVA), and poly(ethyleneimine) (PEI) [22].

With the advent of polymeric CE capillaries in the 1990s, the principle of dynamic coating was also applied, for example, to the surface modification by PVA of capillaries made from ethylene–vinylacetate (EVA), by just adding 0.1 % PVA to the running buffer [9]. EOF measurements in poly(methyl methacrylate) (PMMA) microfluidic capillaries, using dynamic coatings of surfactants, were reported by Azadi and Tripathi [5]. Three surfactant systems are considered: anionic (sodium dodecyl sulfate, SDS), cationic (CTAB), and nonionic (polyoxyethylene lauryl ether, Brij® 35).

3.1.1.2 Quasi-Permanent Coating by Polymers

Large polymers can make a considerable number of contacts to a surface even at moderate adsorption strength per monomer (high-affinity character of the adsorption) [24] and, while it may take only minutes to adsorb most of the equilibrium

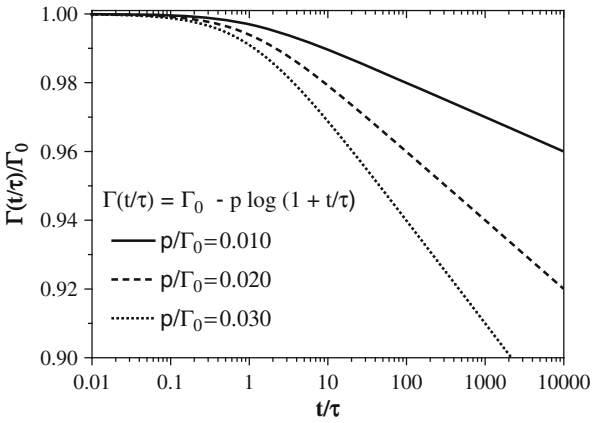

Fig. 3.1 Mass-transfer-controlled desorption kinetics for a polymer with a high-affinity adsorption isotherm according to an equation $\Gamma(t)$ derived by Dijt et al. [31], see *insert*

amount of such a polymer film from solution, the desorption is generally proceeding only very slowly, as explained in a paper by Dijt et al. [31]. Figure 3.1 shows three desorption curves calculated for different values of the parameter p (=slope of a theoretical adsorption isotherm, $p \equiv (\mathrm{d}(\Gamma)//\mathrm{d}(\log(c))$, typically a few % per decade; see the cited paper for the meaning of τ and more details.) The interesting point is that, after a short induction period, the desorbed amount, typically a few percent of the initial adsorbed quantity Γ_0 (mass/area), decreases with $\log(t)$; the time required for desorbing a given amount increases exponentially and the coating will practically never desorb completely.

Good examples for virtually permanent surface modifications obtainable by adsorption from aqueous solutions are amphiphilic triblock copolymers based on ethylene oxide and propylene oxide with the composition PEO_n–PPO_m–PEO_n, known under the trade name Pluronic® [1]. On a hydrophobic surface these block copolymers adsorb with their middle segment, the poly(propylene oxide) block, while the two poly(ethylene oxide) blocks will not be adsorbed due to a lack of affinity, resulting in a PEO brush conformation, completely preventing protein adsorption, while a flat, pancake-like configuration is formed on hydrophilic surfaces [111]. Owing to the high affinity of the hydrophobic PPO segment to hydrophobic surfaces the adsorption is practically irreversible [86].

Several uncharged or charged polymers have been shown to form quite stable coatings on silica surfaces used for CE, such as (pH dependent) PEO (MW = 8 MDa), poly(ethylene imines) (PEI) of various molecular weights, polyarginine, and poly (diallyldimethylammonium Chloride) (PDADMAC), see references 10 to 17 in the paper by Katayama et al. [54]. These authors themselves presented what they called a "successive multiple ionic-polymer layer (SMIL) coating" from a cationic and an anionic polyelectrolyte (polybrene and dextrane sulfate, respectively) which actually represents a layer-by-layer (LbL) deposition of a polyelectrolyte multilayer (PEM) introduced a few years before by Decher et al. [26].

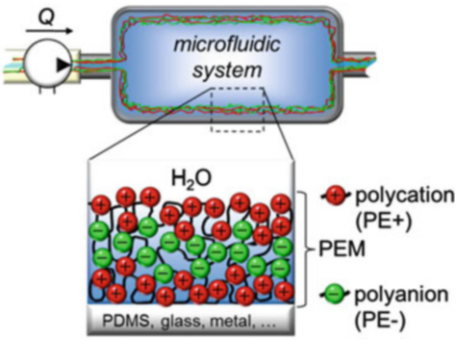

Fig. 3.2 Principle of flow-through layer-by-layer internal coating of a microfluidic device with a polyelectrolyte multilayer (PEM) (by courtesy of Hannah Schmolke, Technische Universität Braunschweig)

Using a flow-through layer-by-layer deposition process in a parallel-plate flow chamber, Schmolke et al. [107] prepared PEMs containing combinations of poly (diallyldimethylammonium chloride) (PDADMAC) or poly(allylamine hydrochloride) (PAH) with poly(acrylic acid) (PAA) on PDMS and tested the layers for nonspecific surface attachment of hydrophobic yeast cells, see Fig. 3.2.

The PDMS surface was pretreated wet-chemically in a mixture of H_2O_2 and HCl in order to generate silanol groups serving as anchors for the first PE layer [117]. A custom-made graft copolymer containing a PAA backbone with amide-bonded PEG side chains (PAA-g-PEG) was additionally adsorbed on some of the PEMs as a terminal layer. Interestingly the amount of adsorbed PAA-g-PEG increased considerably with the number of preadsorbed PE layers [108]. Irrespective of the PEM termination (anionic or cationic), the shear stress required to detach 50 % of preadsorbed hydrophobic yeast cells ($\equiv\tau_{w50\%}$) could be decreased by two orders of magnitude, compared with uncoated PDMS, if at least about ten PEM bilayers were deposited under suitable conditions. Capping the PEM with PAA-g-PEG, a further significant reduction of $\tau_{w50\%}$ was attained.

While these PEM coatings were originally designed to promote planktonic culturing of hydrophobic cells in hydrophobic PDMS microfluidic devices, their hydrophilic properties and stabilities turned out to be very useful to achieve proper functioning of a vertically arranged microfluidic system made from PDMS and glass, applied as a microbubble column (μBC) for biotechnological screening in suspension [28]. PDMS hydrophilization proved to be indispensable for reliable bubble generation and prevention of large bubbles sticking to the walls, see Fig. 3.3. Flow-through coating of the μBC with PEMs was found to be superior to an alternatively studied hydrophilization protocol based on silanization.

Detailed FTIR-ATR-based adsorption studies with solid lipid nanoparticles (SLNs) containing triglyceride/phospholipid or wax matrices by Finke et al. [36] showed that the PEMs prepared by Schmolke et al. [107, 108] could also be used to control the wall adhesion of SLNs: Again the PEMs PEGylated by a top layer of PAA-g-PEG showed the lowest adhesion of SLN, while largest amounts of adsorbed SLNs were measured on PEMs terminated by cationic polyelectrolytes, in accordance with expectations based on the negative ζ potentials of the SLNs.

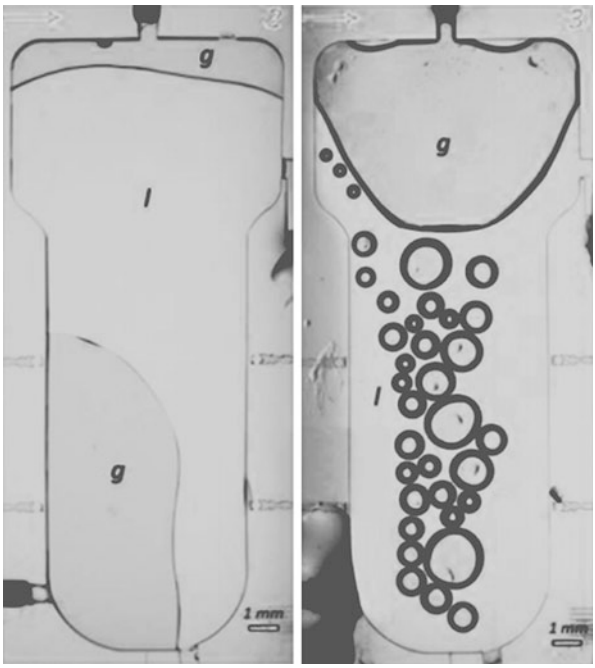

Fig. 3.3 Gas bubble formation in glass/PDMS microbubble columns without surface modification (*left*) and with a surface coating by a hydrophilizing PEM (PDADMAC/PAA, 6.5 bilayers) (*right*), respectively. Letters "l" and "g" indicate the liquid, aqueous phase, and the gas phase, respectively. Gas inlet is in the central region of the bottom. Without the hydrophilic surface modification a single large bubble is formed making a proper functioning of the bioreactor virtually impossible. Adapted from [106] (by courtesy of Hannah Schmolke and Gena Peterat, Technische Universität Braunschweig)

3.1.2 Sol–Gel Coatings

Sol–gel technologies are based on wet-chemical processes allowing the production of solid oxidic materials as fibers, monoliths, or coatings from solutions of low-molecular precursors [46]. Usually an organosilicate (i.e., an ester of orthosilicic acid $Si(OH)_4$ with an alcohol) such as the frequently applied tetraethyl orthosilicate ($(C_2H_5O)_4Si$) will be hydrolyzed by the addition of acidified water, immediately followed by a polycondensation via reactive Si–OH groups, forming an SiO_2 network of ≡Si–O–Si≡ linkages: The precursor solution is turned into a *sol*, i.e., a colloidal dispersion of solid, oxidic nanoparticles with typical sizes in the range from 1 to 100 nm. With time, due to condensation reactions between the nanosized polycondensates, the sol will turn into a *gel*, a three-dimensional interconnected rigid network with sub-micrometer-sized pores and polymer chain lengths beyond the μm range. When the pore liquid is removed by drying at or near ambient pressure at moderate temperatures (100–180 °C is required to remove

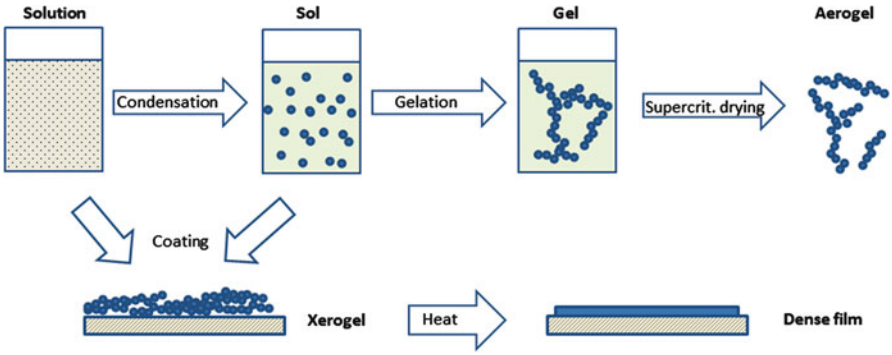

Fig. 3.4 Schematic of sol–gel coating processes

physisorbed water), a *xerogel* will be formed, accompanied by shrinking of the network and some collapsing of pores; nevertheless the internal surface is still very large, typically >400 m^2/g, with an average pore size below 10 nm, see Fig. 3.4. In order to arrive at a *dense solid* with a specific weight approaching that of fused quartz, sintering at very high temperatures, 1000 °C or more, will generally be necessary. On the other hand, solids of very low densities (below 0.1 g/cm^3) with pore fractions beyond 95 %, the so-called *aerogels*, can be achieved by supercritical drying of the gel [46].

A very wide range of interesting organic–inorganic composite materials, the so-called ormosils (*organically modified silicas* or *silicates*) or ormocers (*organically modified ceramics*) are accessible by substitution of an alkoxy substituent of the precursor by a nonhydrolyzable group R, for example an alkyl or aryl group or a moiety which is able to be cross-linked by radical polymerization [130]. Depending on the type and reactivity of R many different structures and functional properties of such materials may thus be obtained.

Sol–gel coatings derived from organosilicates, -titanates, -aluminates, -zincates, and many other precursors have found a plenty of applications as protective or optical (e.g., antireflective) coatings. Outside of the area of microfluidics, sol–gel coatings on polymeric substrates have been studied, for example, to impart scratch resistance to the surface of polypropylene [15]. Maximum applied processing temperature in that case was not more than 100 °C.

The porous nature of the SiO_2 gel obtained by the sol–gel route may be used as an attractive feature for immobilization of active enzymes in on-chip enzyme reactors, as shown, for example, in two papers by Sakai-Kato et al. [104, 105]: In the first paper, a fused-silica capillary was coated by a mixture of a trypsin solution with a hydrolyzed precursor solution prepared from tetramethyl orthosilicate (TMOS), water, and HCl. In the following publication, a similar process was applied to coat the sample reservoir of a microfabricated PMMA chip to obtain a gel containing 0.1 % (w/v) trypsin. Instead of a silica-based gel, titania- or alumina-derived gels where used by Wu et al. for online digestion of proteins, using trypsin-laden coating liquids based on titanium tetrabutoxide

($Ti(OBu)_4$) (TTIP), and aluminum isopropoxide ($Al(i\text{-}PrO)_3$), respectively. The microreactors were made by PDMS casting, using an O_2 plasma treatment to generate silanol surface groups serving as anchors for the sol–gel coating. The devices could repeatedly be used for more than 100 runnings in 1 week without noticeable activity loss [129].

Sol–gel-derived phases play an important role for isolation and purification of nucleic acids in microfluidic devices, see, e.g., review articles by Wen et al. [127] and, more recently, Reinholt and Baeumner [97]. Sol–gel techniques have also been used to immobilize fluorophores or indicators for chemical sensing [7]. Habouti et al. [43] used a special sol–gel coating variant to deposit a ZnO/PVA nanocomposite layers with optical transparency and very low water contact angle in a PDMS-based microfluidic chip for optical biosensing. The coating had a low affinity for irreversible adsorption of dye molecules.

An in situ sol–gel reaction was used by Ma and Zhang [75] to coat superhydrophilic TiO_2 in microchannels of a silicon wafer prior to covering with a glass lid. Deposition was achieved at 25 °C by adding TTIP in ethanol to a stirred mixture of ethanol and water in which the structured wafer was immersed. The authors point out that the method can also be applied to polymeric microsystems, thanks to the low temperature during the coating.

The term "sol–gel" is also applied to processes differing from the conventional approach using sols: A dispersion of SiO_2 nanoparticles with diameters around 10 nm in PDMS can be obtained by soaking the silicone in pure tetraethyl orthosilicate (TEOS) and subsequently exposing the polymer to an aqueous solution of methyl- or ethylamine, catalyzing the hydrolysis of TEOS under formation of silica nanoparticles within the polymeric matrix. Using this method prior to bonding the PDMS to a glass surface, Roman et al. [102] were able to achieve hydrophilic surfaces and a virtually complete suppression of the adsorption of a dye (Rhodamine B). Gomez-Sjoberg et al. [41] used a very similar method, however with an ethanol rinsing step between TEOS soaking and amine exposure in order to avoid nanoparticle formation on the PDMS surface. They achieved a very efficient reduction of the absorption of two anticancer drugs, camptothecin, and a kinase inhibitor, by the PDMS.

Even more remote from the classical sol–gel route is the method suggested by Zhang et al. [133] which they used for "sol–gel coating. . .a thin glass-like sol–gel layer . . . on PC." The authors utilized the carbonate functional groups at the surface of polycarbonate (PC) in order to achieve a reaction with the amino group of bis [3-(trimethoxysilyl)propyl]aminosilane (ABPTMS), bearing a secondary amino group and six hydrolyzable methoxy groups, dissolved in ethanol. The process does not just form a monolayer but, due to hydrolysis of the precursor and condensation of silanol groups, a "glass-like" coating which is simultaneously useful for bonding together two pieces of PC, and for purification of DNA by attachment to the silica-like surface and elution with subsequent on- or off-chip PCR amplification.

3.1.3 Silanization

A versatile, well-known, and proven method to achieve long-term stable surface modification on silicon, PDMS, and glass is surface silanization. The essential step to attach organosilanes to the surface is the generation of surface hydroxyl groups, which is very often associated with the cleaning procedure (Fig. 3.5). Pretreatment to generate such anchor groups is usually done by plasma treatment, UV-photon-based techniques, or wet-chemical processes (e.g., in RCA or "piranha" solution). Silanization is either performed from solution, using organic solvents or water-based systems, or from the vapor phase. The silanization process is finalized by removing the unbound reagents by rinsing and sonification. A terminating baking process may enhance stability of the thin layer and remove the excess of solvent when silanization is performed in solution. Glass et al. [38] summarized different silanization protocols to functionalize the surface in a desired way. Depending on the chemical compounds used, different surface properties are achieved, ranging from chemically reactive surfaces—with amino, thiol (mercapto), halogen, or epoxide groups obtainable from precursors such as 3-aminopropyl-trimethoxysilane (APTMS) or 3-aminopropyl-triethoxysilane (APTES), 3-mercaptopropyl-trimethoxysilane (MPTS), 11-bromoundecyl-trichlorosilane (BUTS), and 3-glycidyloxypropyl-trimethoxysilane (GPTS)—to surfaces with tailored surface wettability by using organofluorosilanes or PEG- and PEO-based compounds.

A notorious problem to be dealt with during plasma pretreatment of PDMS is the instability of the chemical activation, accompanied by a decay of the hydrophilicity obtained temporarily by plasma-chemical oxidation and silanol group generation ("hydrophobic recovery"). This effect may occur within hours after the treatment and is generally attributed to the migration of low-molecular weight polysiloxanes

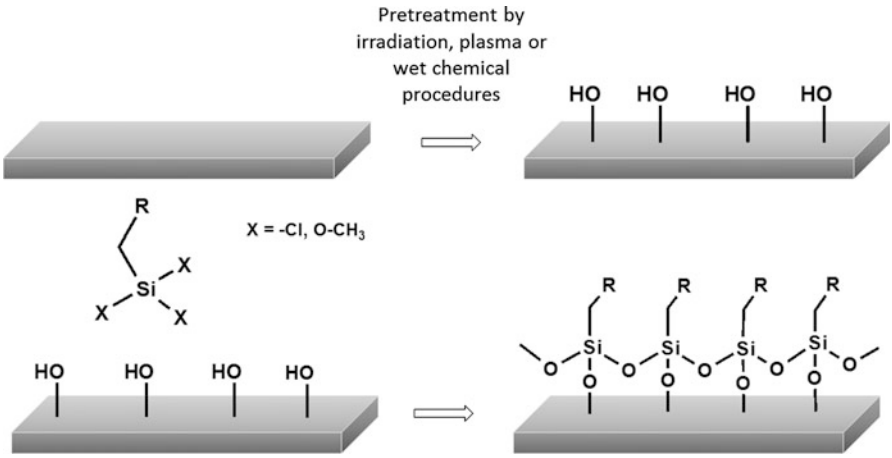

Fig. 3.5 Surface silanization with organosilanes after pretreatment

to the surface. To obtain a "shelfable" PDMS pretreatment Patrito et al. [90] developed a process consisting of an oxidizing plasma pretreatment with an immediate subsequent sputter deposition of a thin aluminum capping layer, able to preserve the surface activation for weeks. Before use of the surface, the metal film is removed by an aqueous etchant.

Seguin et al. [112] used this approach for a patterned surface silanization of PDMS: Using stencil masking by stainless steel meshes carrying an array of circular openings with diameters of 180 or 230 μm the PDMS surface was first plasma oxidized, then a thin (55 nm) Al coating was sputtered onto the oxidized spots. Etching with phosphoric acid was used to recover the oxidized surface for silanization with APTMS or 3-mercaptopropyl-trimethoxysilane (MPTMS) from methanol solution with small amounts of water and sulfuric acid, respectively. Successful patterned silanization was determined by fluorescence labeling of the amino and thiol groups, respectively. The surfaces were used to develop a protein assay on the one hand and to achieve an array for cellular capture and patterning on the other hand. Both applications were demonstrated successfully. Finally the patterned arrays were incorporated into microfluidic channels which were inscribed on PDMS.

An example to suppress nonspecific adsorption of serum albumin on PDMS by silanization is given in a paper by Hamada et al. [44]. VUV irradiation using a Xe excimer lamp (36 mW/cm^2, 30 s) under 100 Pa oxygen was applied as a pretreatment process to generate silanol groups on the surface of PDMS, serving as anchors for subsequent silanization with a copolymer obtained from [2-(methacryloyloxy)ethyl] phosphorylcholine (MPC) (Fig. 3.6) and [2-(methacryloyloxy)ethyl]triethoxysilane (MeTESi). The METESi units are used for coupling the copolymer to the surface, while the MPC units provide strong hydration due to its zwitterionic character [20], and reduces nonspecific protein adsorption to the surface [44]. The copolymer leads to a decrease in nonspecific adsorption of FITC-labelled BSA, whereas in the untreated regions of the surface, nonspecific adsorption occurred.

The authors did not compare their approach, using VUV, with other methods which could be used to prepare surface silanols on PDMS, such as a plasma treatment or wet-chemical hydrolysis or oxidation.

Pretreatment with acidic H_2O_2 was used by Sui et al. [117] to generate Si-OH in PDMS microchannels, followed by silanization with neat PEG-silane and APTMS, respectively, the former to prevent nonspecific adsorption of proteins and the latter for covalent attachment of biomolecules (Fig. 3.7). Protein-repelling properties of the PEG-grafted coatings remained stable for time periods beyond 2 months. Covalent attachment of three types of biomolecules (arginylglycylaspartic acid RGD, amino-terminated single-stranded DNA and a recombinant form of prostate

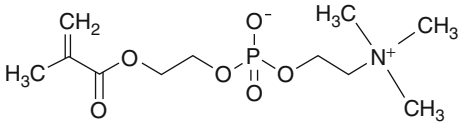

Fig. 3.6 Molecular structure of [2-(methacryloyloxy)ethyl] phosphorylcholine (MPC)

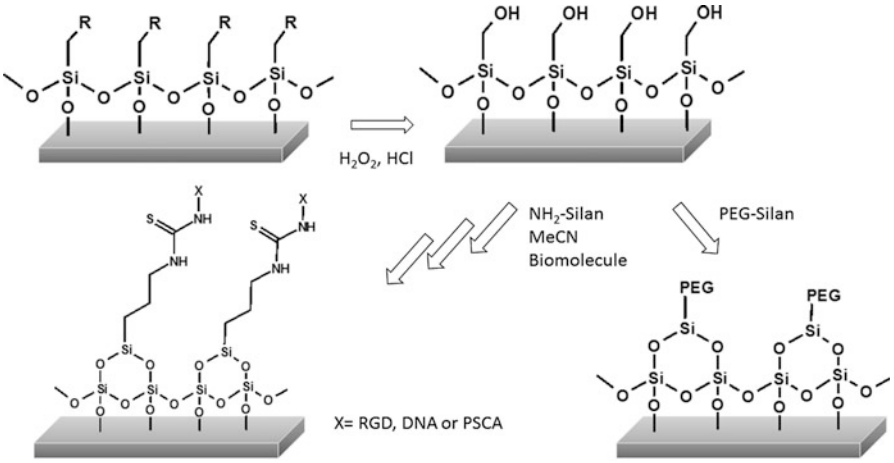

Fig. 3.7 Surface modification of PDMS microchannels for covalent attachment of biomolecules (adapted from Sui et al. [117])

stem cell antigen PSCA) was demonstrated successfully for the amine-terminated surfaces. Prior to the covalent attachment of these molecules the amino-functionalized PDMS surfaces were treated with thiophosgene solution to obtain isothiocyanate-grafted PDMS microchannels. Cell immobilization, semiquantitative DNA hybridization, and an immunoassay were demonstrated after covalent attachment of the biomolecules.

For the efficient synthesis of useful organic compounds and combinatorial libraries of molecules, a set of high-yield, wide-scope, easy-to-perform, and selective reactions has attracted much attention in the recent 15 years under the term "click chemistry" [62]. The 1,3-dipolar cycloaddition of organic azides R–N_3 to alkynes R′–C≡C–R″, resulting in the formation of 1,2,3-triazole heterocyclic rings, is of high interest under this aspect. Azide-functionalized surfaces were achieved by silanization of glass with BUTS followed by an immersion in a saturated solution of sodium azide in DMF to replace bromide -Br by azide -N_3. Afterwards, the azide-functionalized surfaces were soaked in solutions of propargyl amine (H–C≡C–CH_2–NH_2) or 1-octyne (H-C≡C–C_6H_{13}) to form amine- and methyl-terminated surfaces, respectively. Such modified samples were analyzed with regard to solvent stability and post-processing methods commonly used in microfabrication and operating. It was observed that click-modified surfaces were remarkably stable to different conditions, including UV light, thermal treatment up to 205 °C in air, different organic solvents and NaCl solutions with pH values ranging from 5 to 11. Strong oxidizing agents and HF lead to a degradation of the thin films [94].

Although silicon, glass, and PDMS are mostly used as substrates for silanization, other materials like polymers or paper also play an important role for this technique. A simple method to produce novel and low-cost paper-based analytical devices (μPAD) was established by Cai et al. [16]. Filter cellulose was silanized with

TMOS using a paper mask with a specific pattern. Silanization was achieved by the reaction of OH groups of cellulose and TMOS, where both reagents came in contact with each other. By this technique a pattern of hydrophilic and hydrophobic areas was achieved on filter paper. These μPADs were used as biosensors to determine glucose in human serum blood samples. The main advantage of this technique is that no expensive equipment is needed for sample preparation. Nevertheless, low resolution and reproducibility might be the main drawbacks so far.

Another example of paper-based microfluidics was given by Glavan et al. [39]. The authors describe vapor-phase silanization of Whatman chromatography paper with fluoroalkyl trichlorosilanes of different chain length and different degrees of fluorination. With a few exceptions the achieved hydrophobicity correlated with length and fluorine content of the silanes and with the roughness of the paper. As gas permeability and mechanical flexibility of the paper are retained after silanization, the modified paper can be used for the fabrication of channels and flow switches. Due to the highly water-repellent properties aqueous liquid droplets can be guided over the surface. Using similar compounds Lugli et al. [73] developed gradient surfaces on Si/SiO_2. A gradient in wettability was established by varying the amount of trichloro (1H,1H,2H,2H-perfluorooctyl)silane bound to the surface. Droplet motion on these gradient surfaces was demonstrated successfully.

Stojkovič et al. [116] used silanization with APTES of perfluoralkoxy alkane (PFA) microchannels followed by covalent attachment of glutardialdehyde to immobilize *S. cerivisiae*, *E. coli*, *Pseudomonas putida*, or *bacillus subtilis* in the microchannels. Different protocols were compared to identify the ideal experimental conditions for cell immobilization on PFA and on other materials, including glass, polystyrene, poly(methyl methacrylate), polycarbonate, Zeonor®, and Topas®, which are relevant for microfluidic applications. The authors assume that surface silanization on glass and polycarbonate occurs via covalently bonded ATPES, whereas hydrophobic interaction is proposed to be responsible for silanization of PFA, PS, as well as for Zeonor® and Topas® without pretreatment.

An example of vapor-based silanization of open microchannels is given in a paper by Chen et al. [19]. Formation of self-assembled organosilane monolayers was achieved at elevated temperature (50 °C) and low pressure (0.05 Torr) with the aid of vaporized deionized water. Afterwards, the thin films were annealed at 80 °C. Surface patterns of different organosilanes were generated with the aid of UV light using a photomask. The devices were used as micromixers for passive mixing of water and oil.

Shirai et al. [114] used vapor-based silanization to create a patterned APTES film to be used for covalent attachment of antibodies. The process was carried out at elevated temperature (120 °C, 2 h). Afterwards the substrate was covered with a photomask and irradiated with VUV light to remove APTES from defined regions of the substrate. After bonding the upper substrate, PEG-silane was attached to the bare silica and captured antibodies were immobilized on the patterned APTES. The procedure is schematically shown in Fig. 3.8.

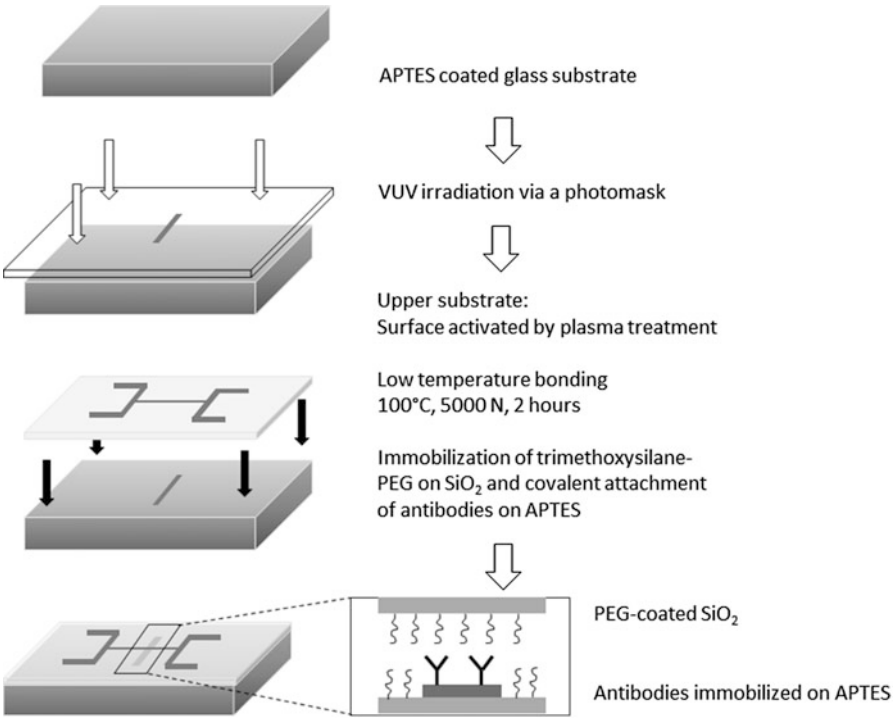

Fig. 3.8 Schematic illustration of the procedure for antibody pattering in nanochannels using VUV light and low-temperature bonding, adapted from Shirai et al. [114]. The APTES film on the glass slide is oxidatively decomposed by VUV irradiation, except of a masked part on the sample, so that the glass surface becomes superhydrophilic to be activated for glass–glass-bonding. After bonding the activated glass surface was coated with trimethoxysilane-poly(ethyleneglycol) (PEG) to prevent the channels from nonspecific adsorption of proteins. In a masked part of the substrate the APTES is used to immobilize antibodies on the surface

3.1.4 Grafting

Covalent attachment of polymers on different substrates can be realized by the so-called "surface grafting." Depending on the experimental conditions and the reagents used, one distinguishes "grafting to" and "grafting from." Both approaches are depicted schematically in Figs. 3.9 and 3.10.

Using "grafting to" preformed polymer chains are covalently attached to the surface. If this approach is taken chemically reactive groups are required both, on the surface and on the polymer. Such groups can be achieved on the substrate by pretreatment using, e.g., plasma processes or photon-based techniques, or by surface silanization. It may be a drawback of this approach in some situations, that the grafting density is limited due to sterical hindrance by already attached molecules.

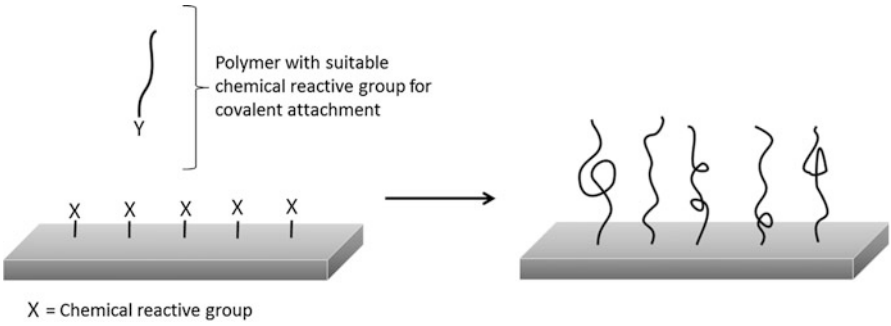

Fig. 3.9 Schematic depiction of the "grafting to" approach. Polymers are covalently attached to the surface by chemical coupling reaction

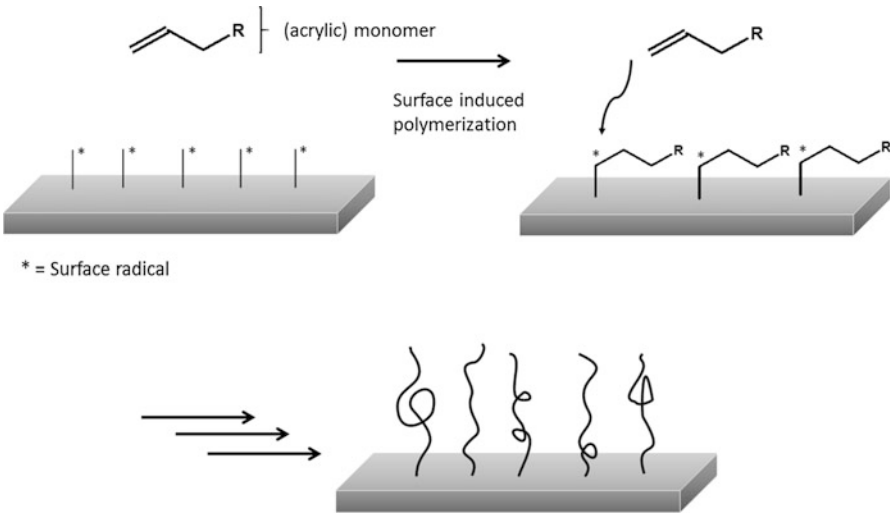

Fig. 3.10 Schematic depiction of the "grafting from" approach. Film deposition is performed via surface-induced radical polymerization

Higher grafting densities can be achieved using the "grafting from" approach, where a polymerization reaction is induced by surface radicals. These radicals are generated by different pretreatment methods like UV or electron beam irradiation, exposure to O_3, or by adding photoinitiators which diffuse into the bulk material. In contrast to "grafting to" higher polydispersity is observed, when polymers are bound to the surface via "grafting from," as molecular mass of the polymers is less controllable.

In the literature several examples are described, where grafting techniques are applied to modify microfluidic devices. Kovach et al. [63] investigated a surface coating which permits long-term hemocompatibility. High amount of fibrinogen was adsorbed on uncoated PDMS channels, so that platelet activation was initiated, causing increasing pressure loss along microchannels. Using plasma pretreatment

followed by covalent attachment of poly(ethylene glycol) long-term stable hydrophilic PDMS microchannels were achieved. PEG–silane was coupled inside the sealed channels. Fibrinogen adsorption under physical conditions and platelet adsorption from human blood was reduced significantly within a time period up to 28 days. Moreover, the hemocompatibility was improved, so that the lifetime of the device was increased 16× compared to the uncoated control sample.

A similar approach was applied by Demming et al. [27] to reduce the adsorption of hydrophobic yeast cells and to improve emulsification of oil in water. After plasma pretreatment of PDMS PEG–silane was grafted to the surface to achieve long-term hydrophilic microfluidic devices. Long-term stability in air and in different solvents, as well as the adhesion of hydrophobic yeast cells (*S. cerivisiae*) under defined wall shear stress was investigated. In contrast to a commercially available PEGylation kit, the method described in this paper needed less time and production steps, showed a better homogeneity of the deposited coating and better performance in bonding. The applicability of such modified microfluidic devices was proven by an anti-adhesive effect of hydrophobic yeast cells and successful emulsification of oil microdroplets in water. Later on, a flow-through coating of PDMS-based microfluidic devices by adsorption of PEMs was, however, found superior to silane grafting, see above [28].

An example for the "grafting from" approach to suppress nonspecific adsorption of proteins is given in a paper by Jena and Yue [51]. [2-(Methacryloyloxy)ethyl] phosphorylcholine (MPC) was photografted on COC to prevent protein adsorption and cell adhesion. It was observed, that hydrophilicity was increased with prolonged irradiation time. Using FTIR-ATR and XPS spectroscopy it was confirmed that the thickness of MPC rose with time until no significant changes in thickness were observed when the process exceeded 25 min. Longer treatment time resulted in significant changes in surface roughness. With regard to protein adsorption and cell adhesion the samples with higher amount of MPC showed better antifouling properties.

Another promising approach to reduce platelet adhesion on COC was investigated by Roy et al. [103]. The authors compared four different polymers (acrylic acid AAc, acryl amide AAm, hydroxyethyl methacrylate HEMA, *N*-vinylpyrrolidone NVP) photografted on COC with regard to hydrophilicity, transparency, platelet adhesion, and long-term stability after sealing. Photografted NVP showed the most promising results for all relevant parameters.

Fusion of microdroplets within surface-modified microfluidic devices was demonstrated be Fidalgo et al. [35]. The authors used the same chemical compounds which are described in the paper by Schneider et al. [109]. Hydrophilic poly(acrylic acid) was patterned on benzophenone-containing PDMS by photo-induced polymerization using a photomask. At a double T-junction channel, microdroplets of an aqueous solution in oil were formed. Due to the hydrophobic nature, the droplets remained stable until they were passing the hydrophilic PAA stripe. There the droplets were trapped and fused.

Patterned surfaces of thermoresponsive poly(*N*-isopropylacrylamide) (PNiPAAm) were described in a paper by Idota et al. [49]. In contrast to the

aforementioned pretreatments the authors used electron beam (EB) lithography to initiate grafting via radical polymerization of NiPAAm on poly(acrylamide)-coated glass. Using this method, no photomask was necessary to achieve stripe patterns with line width down to 200 nm. Thermoresponsive behavior and thermally controlled cell attachment and detachment were demonstrated successfully.

In a review by Deng et al. [29] different surface photografting techniques were summarized. Different initiation methods, effective controlling mechanisms, self-initiated grafting, grafting in liquid, vapor and bulk phase and grafting on different surfaces were described. Not only microfluidic applications were discussed, but application with regard to wettability, adhesion, responsive surfaces, photografting for lamination, membranes and biomedical-related applications. Regarding surface-initiated graft polymerization ("grafting from") effective control mechanisms are of great interest, as conventional techniques usually are accompanied by high amount of homopolymerization of the monomers or cross-linking. Yang and Rånby were the first who described the concept of "living" or "controllable" polymerization on polymeric surfaces [131]. Due to a dynamic equilibrium of active and inactive species, the polymerization is controllable so that chain length, composition, and distribution of the grafted chains can be tuned. A prominent example for a controlled polymerization is the so-called atom-transfer radical polymerization (ATRP) [70, 79, 80]. Another concept to achieve narrow polydispersity polymers is the reversible addition-fragmentation chain transfer (RAFT) reaction [83]. A different approach to achieve controllable surface polymerization is described by Matsuda et al. [78, 84, 85] with their concept of "photo-iniferters." A brief introduction of this concept is also given in the review by Deng et al. [29]. The concept of "controllable" polymerization is not widespread used for microfluidic devices yet.

3.1.5 Hydrogels

In contrast to the aforementioned techniques, deposition of hydrogels leads to the formation of cross-linked 3D polymeric structures. Hydrogels represent a three-dimensional, hydrophilic, porous network, capable of storing a significant amount of water or other small molecules, and proteins, making them interesting for drug-release applications [64, 87]. Due to their swelling properties, the integration of actuator functions is possible [132]. Depending on the nature of the monomer chosen even phase-changing properties are available. Phase-change can be introduced by an external stimulus, like temperature, pH, ionic strength, the electric or the magnetic field, light or radiation forces [6, 64, 119]. An overview on such "smart polymers" is given in a review by Kumar et al. One prominent example of a thermoresponsive polymer is PNiPAAm. Due to conformational changes at the so-called lower critical solution temperature (LCST), intermolecular bound water is released and the properties of the polymer change from hydrophilic to hydrophobic. The LCST of PNiPAAm around 32 °C makes it very attractive for biomedical applications.

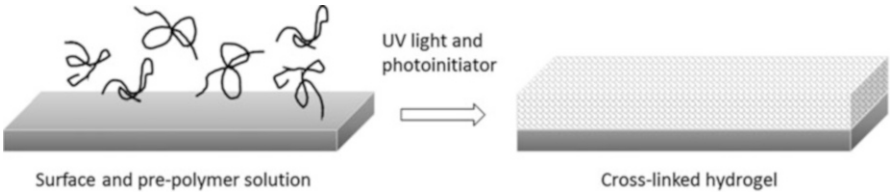

Fig. 3.11 Schematic depiction of hydrogel formation from prepolymer solutions on a flat surface

Synthetic polymers like PEG-diacrylate can easily cross-link with natural gels like chitosan, agarose, or alginate [61, 67, 89, 113]. Moreover, several examples of patterned deposition of hydrogels have been reported in the literature [45, 56, 121].

Mechanical properties of the hydrogel can be tuned by the monomer chosen and/or by the amount of cross-linking [3]. Regarding cellular applications this gives the opportunity to mimic extracellular matrix components (ECM) of different tissues. The properties of the hydrogel are determined by the prepolymer solutions used. Formation of hydrogels on different substrates or within microfluidic channels is mainly achieved by photopolymerization of prepolymer solutions (Fig. 3.11). Covalent attachment of the gels to microfluidic channel walls is essential for work under fluidic conditions [66, 67] to prevent that the gel is detached by the shear flow.

Photopolymerization of acrylamide-modified DNA probes in polycarbonate microchannels was investigated by Olsen et al. [88]. The reaction was induced by UV light leading to a cross-linked structure of acrylamide and single-stranded DNA-oligomer substituted acrylamide. These hydrogels were porous and allowed fluorescence-labelled DNA to hybridize with the complementary DNA strands within the gel. Even selective detection of multiple DNA targets was demonstrated successfully.

Photo-induced cross-linking of alginate and methacrylic groups in microchannels was described in a paper by Shah et al. [113] (Fig. 3.12). The hydrogel was loaded with antibody-captured cells. Controlled release of the cells was achieved by enzymatic degradation of the alginate by alginate lyase. Using this method a release efficiency of 99 ± 1 % with a cell viability of 98.9 ± 0.3 % was observed. Moreover, single-cell colony formation after 96 h was comparable to similar control cells. This example showed an interesting approach for an enzymatic driven release of biomolecules with high efficiency.

Patterned microchannels of hydrogels with different proteins exposed to the surface were investigated with regard to their capability to capture circulating tumor cells. Surface modification was achieved by photopolymerization of PAA via a photomask. Polymerization was induced by benzophenone which was adsorbed by the PDMS substrate. Areas without PAA were backfilled with MPTMS by surface silanization. Due to the different chemical nature of the patterned areas, protein immobilization was realized without mask alignment: Covalent attachment of the proteins was realized by a coupling reaction using EDC/NHS as active ester in the case of PAA. For MPTMS-functionalized surface

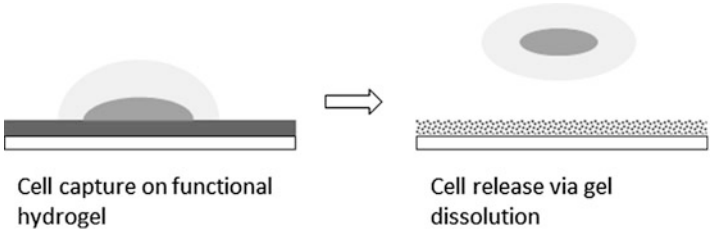

Fig. 3.12 Cell attachment on biotinylated cross-linked alginate hydrogel (*left*) and subsequent cell release by exposure to the bacterial enzyme alginate lyase (adapted from Shah et al. [113])

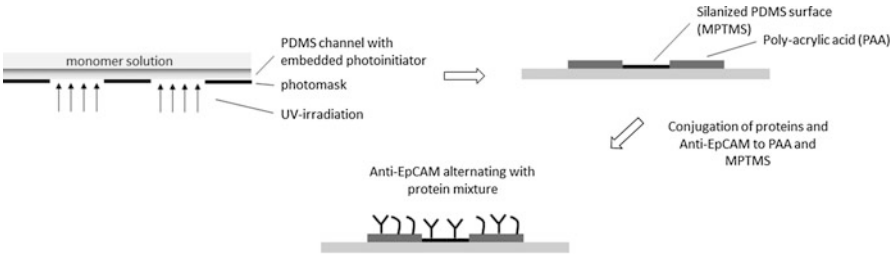

Fig. 3.13 Surface functionalization of PDMS microchannels to achieve a pattern of alternating anti-EpCAM and protein mixture (adapted from Launiere et al. [65])

areas, an amino-to-thiol cross-linking agent, 4-maleimidobutyric acid *N*-hydroxysuccinimide ester (GMBS) was used. Thus patterned microchannels were used to analyze circulation tumor cells (CTC) under flow conditions [65] (Fig. 3.13).

Annabi et al. [3] investigated photopolymerizable gelatin and tropoelastin hydrogel solutions which were deposited in the presence of a photoinitiator inside microfluidic channels under continuous flow. Various concentrations of the prepolymer solution were used. To determine the thickness of the hydrogel, FITC-conjugated dextran (10 kDa) was added. Assuming a parabolic flow profile at laminar flow it was assumed that residence time of the prepolymer solution is high enough for polymerization and film growth on the microchannel walls. It was observed that the residence time of the prepolymer solution is crucial for film homogeneity and film thickness. Primary cardiomyocytes were seeded on the maintained surfaces. A preferential attachment on the more elastic, soft tropoelastin surface was observed.

Gradient surfaces of PEG-RGD were deposited by photo-induced polymerization of PEG-diacrylate and acryloyl-PEG-RGD using a microfluidic gradient generator, which has two inlets to mix two different polymer solutions [72]. Glass slides were silanized with [3-(methacryloyloxy)propyl] trimethoxysilane (also known as 3-(trimethoxysilyl)propyl methacrylate, TPM) to guarantee covalent attachment of the PEG hydrogel. Gradient formation was modeled by computational fluid dynamics simulation to estimate the PEG-RGD

profiles formed in the microfluidic device. The experimental proof was given by fluorescence labeling of the RGD and by the distribution of bone-marrow-derived rat mesenchymal stem cells (MSCs) which adhered on the channel wall. Fluorescence intensity as well as number of spread cells increased with the density of bound RGD. In their review from 2013 Tehranirokh et al. [118] also mentioned gradients inside hydrogels which were suitable to study cell behavior at different concentrations of drugs or growth factors.

Piao et al. [92] developed a microfluidic device suitable to detect glucose. After plasma pretreatment of the PDMS substrate and silanization with TPM, poly (ethylene glycol) diacrylate (PEG-DA) was photopolymerized on the substrate. Before the polymerization was performed, glucose oxidase was added to the prepolymer solution. Patterning was achieved by a photomask. Glucose, even from urine samples, was detected successfully. Puchberger-Enengl et al. [96] also used photopolymerized PEG-DA as hydrogel for sensing applications within microfluidic channels. Sensing was tested by a colorimetric protein assay, due to a color shift of bromophenol blue which interacts with the protein in acidic environment.

Another example of biosensing is given in a paper by Tran et al. [123]. The authors integrated electrochemical impedance (ECIS) measurements for high-throughput cell-based biosensing on a hydrogel-based microfluidic device. Vessels which convey a flowing fluid were mimicked by the microchannel, the tissue structure was represented by the hydrogel made from agarose and enriched by a desired drug. Gradient amounts of the drug were released by the hydrogel. Cell attachment was promoted by L-cysteine which was adsorbed on the surface. The ECIS system was used to monitor cell viability under the drug gradient. Compared to other techniques ECIS allows real-time monitoring and noninvasive and a label-free detection.

Completely different reagents were investigated in a paper by Schröder et al. [110] (Fig. 3.14). Hydrogels with polyampholyte characteristics were deposited in order to achieve nonfouling properties. These hydrogels were composed of positively charged [2-(acryloyloxy)ethyl]trimethylammonium chloride (TMAC) and negatively charged 2-carboxyethyl acrylate (CAA) monomer subunits to

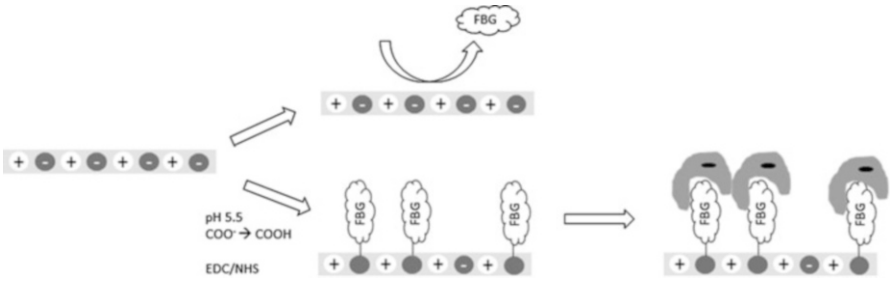

Fig. 3.14 Schematic depiction of a multifunctional polyampholyte hydrogel which shows fouling resistance and protein-conjugation capacity (adapted from Schröder et al. [110])

mimic zwitterionic behavior. Such films showed excellent nonfouling properties against fibrinogen and lysozyme. Depending on the amount of cross-linking different swelling behavior was demonstrated by the authors. Moreover, pH-depending protein-conjugation capabilities were observed without losing nonfouling properties. Nevertheless, covalent-attached fibrinogen still promotes cell attachment.

3.2 Gas-Phase Methods

3.2.1 CVD and ALD Coating

As alternatives to wet-chemical coating or modification processes for microfluidic device surfaces, chemical vapor deposition (CVD) methods have been described in more recent papers. Several different CVD methods are applicable to render a surface hydrophobic by deposition of highly fluorinated monolayers or polymers. In a paper by Lee et al. [68] two commercial fluoropolymer formulations, CYTOP™ (Asahi Glass) and Fluorinert™ (3 M), and a fluorosilane, pentafluorophenyltriethoxysilane (PFPTES), were compared as sources for the deposition of thin films of typically 5–10 nm thickness, and an ultrathin monolayer, respectively, on planar silicon wafers. Maximum water contact angles achieved were between 80° and 85° for the two fluoropolymers. The same authors later on compared four different fluorosilanes as CVD precursors to control hydrophobicity and protein adhesion behavior of silicon and PDMS surfaces, respectively [13], see also [12]. Besides the above-mentioned PFPTES with a pentafluorophenyl ring and three ethoxy groups (TES), three reactive silanes with linear fluorinated chains were applied: 1H,1H,2H,2H-perfluorooctyl-trichlorosilane (PFOTCS), 1H,1H,2H,2H-perfluorooctyl-dimethylchlorosilane (PFODCS) with only one -Cl group at the silicon, and 1H,1H,2H,2H-perfluorodecyltriethoxysilane (PFDTES) with a longer fluorinated chain. Deposition was done at pressures between 200 and 600 Torr at temperatures between 20 and 140 °C. A water contact (WCA) angle of 117° was achieved with PFDTES on PDMS which had undergone an oxygen-plasma treatment in order to generate silanol groups required as anchors for coupling of the fluorosilanes. On silicon substrates, cleaned by “piranha” treatment or by a plasma process, significantly smaller WCAs were obtained; with PFDTES 106° and 107°, respectively.

A vapor deposition technique which can be used to modify silicon microchannels with PEG in order to decrease the adsorption of proteins was reported by Popat et al. [93]. The authors use the polymerization of ethylene oxide, Lewis-acid-catalyzed by gaseous BF_3, to graft poly(ethylene glycol) chains on the surface. The process starts at amino groups attached to the silicon surface by gas-phase silanization with APTMS. Therefore the PEG chains are firmly bound to the surface; over a time period of 4 weeks in PBS (phosphate-buffered saline) solution, the carbon content of the PEG film is reduced by only 7 %. Protein

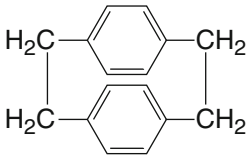

Fig. 3.15 Molecular structure of [2.2] paracyclophane, the precursor of parylene coatings

adsorption at the hydrophilized surfaces can be reduced by about 80 % using this method.

The function of the so far described coatings is predominantly physical. However, a rich variety of polymers with chemically reactive functional groups can also be deposited via the gas phase using an extension of the well-known deposition technology used for a long time to deposit protective poly(*p*-xylylene) "parylene" coatings from [2.2]paracyclophane (Fig. 3.15) or derivatives thereof obtained by substituting one or more hydrogen atoms at the benzene rings [30].

The precursor sublimes at low temperature and pressures in the range of 0.01–0.1 Torr and is carried into a pyrolysis zone (>500 °C) where it dissociates into reactive intermediate molecules (singlet or triplet diradicals) which, upon condensation on a cool surface, form a continuous polymer film $–(CH_2–CH_2–C_6H_4–)_n–$. Owing to the low temperature of the substrate the deposition can take place on virtually every material which can be brought into the vacuum chamber; the resulting coatings are usually of good conformality. The review article by Deng and Lahann gives an overview of the impressive richness of chemical functions which can be incorporated into the films by using substituted [2.2]paracyclophane carrying halogen, hydroxy, amino, or ester groups, to name just a few representatives from a large library of functional groups which have already been used [30].

Another low-pressure CVD technology with a considerable potential for—among other fields—applications in microfluidics are the iCVD and oCVD techniques developed in the group of K. K. Gleason at the MIT, MA, USA since nearly 20 years. Deposition of a large variety of polymers on virtually any substrate can be achieved at or near-room temperature from the vapor phase by delivering to the substrate either (1) a monomer vapor together with the vapor of a suitable oxidant such as Br_2, $FeCl_3$, $CuCl_2$, or $VOCl_3$ (oxidative CVD, oCVD) or (2) a monomer vapor containing organic radicals generated from an initiator such as an organic peroxide by thermal dissociation using an array of heated wires (initiated CVD, iCVD) [2, 4, 23].

oCVD is a powerful technique for CVD of conjugated polymers such as polythiophene or poly(3,4-ethylenedioxythiophene) (PEDOT). iCVD is an extension of the hot-filament CVD (HF-CVD, also hot-wire CVD, HW-CD) technique known since decades as an important method to deposit crystalline diamond thin films. While in diamond CVD the hot filaments with temperatures around 2000 °C or more are used to dissociate molecular hydrogen into atoms, in iCVD the hot wires are decomposing an initiator molecule R–R′ containing a labile bond such as –O–O– in peroxides, to generate radicals which initiate a free-radical polymerization of the adsorbed monomer M on the substrate surface. Much less wire

temperatures, a few 100 °C only, are generally sufficient to initiate the polymerization process consisting essentially from the following three steps ("gas" and "ads" denote gas phase and adsorbed species, respectively, radical character is indicated by a small empty circle):

$$\begin{aligned} &\mathrm{R-R'} \xrightarrow{T_{\mathrm{wire}}} \mathrm{R}\circ + \mathrm{R'}\circ \\ &\mathrm{R}\circ_{\mathrm{gas}} + \mathrm{M}_{\mathrm{ads}} \rightarrow \mathrm{R-M}\circ_{\mathrm{ads}} \\ &\mathrm{R-M}\circ_{\mathrm{ads}} + n\mathrm{M}_{\mathrm{ads}} \rightarrow \mathrm{R-M}_{n+1}\circ_{\mathrm{ads}} \end{aligned} \tag{3.1}$$

A large variety of functional polymers has been deposited by iCVD, several microfluidic applications are mentioned in the recent review article by Coclite et al. [23]. The organic functionality of the monomer is retained to a large extent by this method. Riche et al. used iCVD to deposit cross-linked fluoropolymer coatings on preassembled PDMS microfluidic devices to obtain barrier coatings increasing the chemical compatibility of the devices [99] and to control droplet formation and merger [100] in digital microfluidics. The authors applied di-tert butyl peroxide as an initiator molecule, 1H,1H,2H,2H-perfluorodecyl acrylate as a monomer and glycol diacrylate as a cross-linker at 0.1 Torr pressure, using stage and filament temperatures of only 35 °C and 200 °C, respectively (Fig. 3.16).

A gas-phase deposition method known since the early 1990s and still finding increasing interest for a wide range of applications, atomic layer deposition (ALD), has been applied for microfluidic applications only recently and so far only in a small number of reports. The principle of the method is schematically shown in Fig. 3.17, using as an example, the deposition of aluminum oxide, Al_2O_3, which is the most frequent material obtained by ALD, among several other oxides and other metal compounds or pure elemental metals [71].

The ALD process consists of a repetition of cycles made up of four steps in which the substrate is consecutively (1) exposed to the vapor of a precursor I, for alumina deposition usually trimethyl aluminum (TMA), (2) purged by an inert gas, (3) exposed to water, ozone, or an oxidizing plasma (plasma ALD, PALD) and (4) purged again by an inert gas.

In step 1 of Al_2O_3 ALD, the films surface is saturated with –O–Al$(CH_3)_2$ groups, this reaction comes to an end as far as a dense monolayer is obtained. In step 3, methyl

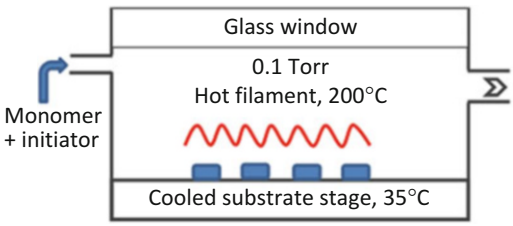

Fig. 3.16 Scheme of an iCVD reactor, parameters according to Riche et al. [100]

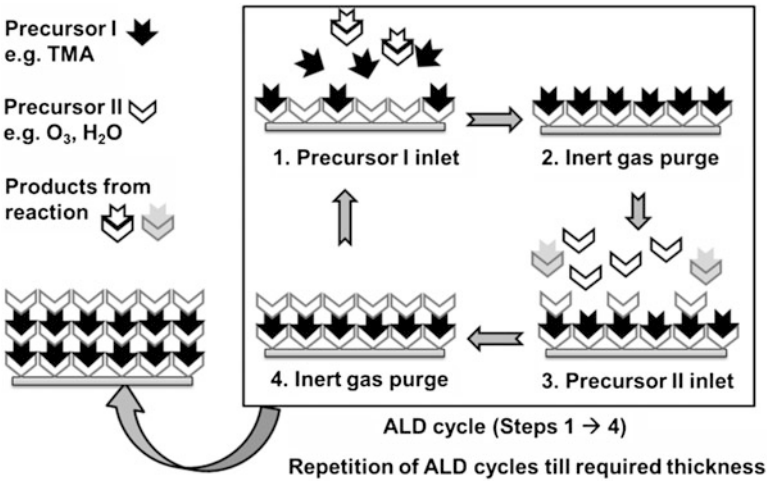

Fig. 3.17 Principle of ALD of aluminum oxide (by courtesy of Sanjeev Kumar Gurram, Fraunhofer IST)

groups are removed by hydrolysis or oxidation, and substituted by hydroxy groups, simplified:

$$-\mathrm{O}-\mathrm{Al}(\mathrm{CH_3})_2 \rightarrow -\mathrm{O}-\mathrm{Al}(\mathrm{OH})_2$$

In step 1 of the following cycle the –OH group will again react with TMA:

$$-\mathrm{O}-\mathrm{Al}(\mathrm{OH})_2 + 2\mathrm{Al}(\mathrm{CH_3})_3 \rightarrow -\mathrm{O}-\mathrm{Al}\left(\mathrm{OAl}(\mathrm{CH_3})_2\right)_2 + 2\mathrm{CH_4}$$

and so on. Inert gas purging in steps 2 and 4 is required in order to prevent contact of TMA with water which would result in the formation of alumina by CVD.

Major advantages of ALD-deposited oxides over CVD oxides are a very high degree of conformality with the substrate geometry and a superior film density, smoothness, and pinhole freeness. For this reason, ALD oxides are frequently applied or developed for applications requiring excellent permeation barrier layers and dielectrics.

Spagnola et al. [115] attempted to apply an Al_2O_3 coating deposited by ALD on PDMS to obtain a permanently hydrophilic surface. Like with several other approaches used to modify PDMS surfaces to increase the surface free energy and water wettability (plasma treatments, UV/ozone, etc.) the success was not lasting: Hydrophobic recovery was observed within hours of storage in air or an inert gas, very probably due to the diffusion of oligomer molecules through microcracks within the oxide coating. The limited success reported in this paper is not surprising, in view of the softness (low modulus of elasticity) of PDMS, making it a “difficult substrate” for depositing brittle ceramic layers. Nevertheless

ALD is thought to have some potential for microfluidics devices made from other polymers or from glass. It can be expected, for example, that the possibility to generate atmospheric-pressure microplasmas in selected regions of a microfluidic device (see Sect. 3.2.3 of this article) will enable localized surface modifications by "μPALD" which cannot easily be achieved by other techniques.

Chang et al. [18] used ALD to deposit 127 nm (1000 cycles) aluminum oxide as a high-dielectric-constant insulator ($\varepsilon_r \approx 10$) on a 100 nm Au film on glass serving as the electrode for an electrowetting-on-dielectric (EWOD) device for the manipulation of droplets in digital (droplet-based) microfluidics. Due to the small insulator thickness the driving voltage necessary to activate droplet movement could be reduced from several tens of volts to 3 V. Pei et al. [91] applied the same material (100 nm) on an a-Si:H film on glass for a light-actuated drop manipulation device and achieved lowering of required voltage and optical power by factors of 5 and 85, respectively.

3.2.2 *Photon-Based Technologies: UV, UVO, and VUV Treatment*

Absorption of UV radiation by a polymer under inert gas may result in photodegradation or photo-cross-linking (or both processes), depending on the type of the polymer and the irradiation conditions. In the presence of air or pure oxygen, a polymer can be photooxidized [17]. If a low-pressure mercury vapor lamp is used with a quartz bulb transmitting 184.9 nm radiation along with the dominating 253.7 nm line, the treatment is frequently called UV-ozone (UV/O_3, UVO) treatment because the low-wavelength component of the radiation is able to dissociate O_2 into ground state oxygen atoms $O(^3P)$ which will form ozone in situ by recombination with molecular oxygen:

$$O_2 + h\nu \rightarrow 2O\left(^3P\right)$$
$$O\left(^3P\right) + O_2 \rightarrow O_3$$

Wavelengths below 245.4 nm are required to dissociate O_2 [82]. O_3 and possibly $O(^3P)$ atoms may under these conditions become relevant as reactive species which play an important role in the modification mechanism.

The presence of ozone is, however, not always required: Using PMMA or PC substrates, surface carboxylic acid groups can be generated by relatively low-dose (<54 J cm^{-2}) UV irradiation excluding the high-energy line near 185 nm. Photocleavage of ester groups is assumed to play a role in the overall reaction scheme. The process leads to some roughening, however without major damage of the surface. The presence of the –COOH groups increases the surface free energy of the surface ("activation"), resulting in higher wettability. Irradiation through a mask, for example a simple metal mesh, leads to a patterned surface carboxylation.

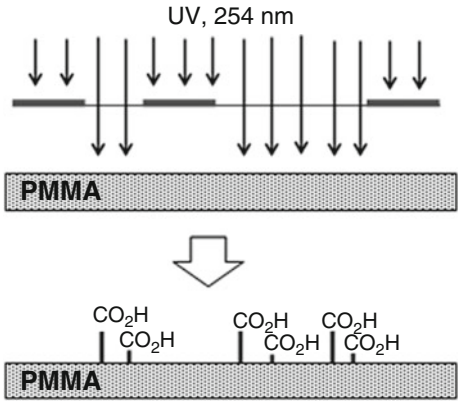

Fig. 3.18 Area-selective functionalization of PMMA surfaces by UV radiation through a metal mask (adapted from Wei et al. [126])

7.6 µm wide squares have, for example, been achieved by McCarley et al. [81] and by Wei et al. [126] (Fig. 3.18), see also references cited therein.

Applying the UV/O_3 technique to manufacture CTC microfluidic chips from PMMA and COC, respectively, Jackson et al. [50] found two previously unreported effects which have to be taken into account if polymer substrates containing microfluidic channels with relatively high aspect ratios have to be functionalized with carboxylic acid groups and if the substrates subsequently undergo heating during a thermal fusion bonding process (98–102 °C for PMMA; 132–134 °C for COC): The higher optical absorption of PMMA as compared to COC leads to a nonuniform functionalization along the depth of a microchannel and the higher propensity of PMMA to photodegradation results in a loss of functional groups from the surface upon heating.

A number of polymers (PDMS, PMMA, PS, PC, COC) were studied by Van Midwoud et al. [125] with respect to adsorption properties (reduction of adsorption of hydrophobic molecules such as 7-ethoxycoumarin or testosterone) and biocompatibility after an oxidizing treatment by UV/O_3 or an oxygen-plasma treatment. Only UV/O_3-treated PC and COC were found to satisfy both criteria. The surface hydrophilization after plasma treatment (30–120 s in a commercial low-pressure "plasma cleaner") was generally less efficient and less stable than after the UV irradiation (15–60 min, commercial low-pressure mercury UV lamp): After 1 week, contact angles of all plasma-treated polymers had risen beyond 40°, while for UV/O_3-treated PC, PC, and COC they had stayed below 20° even after 4 weeks (PMMA: 33°; PDMS: 85°).

UV irradiation in ambient atmosphere (400 W, 200–600 nm, several 10 min) was also used by Kano et al. [53] to turn a PDMS surface hydrophilic and water wettable. This effect is due to a change of the network structure $(–O–Si(CH_3)_2–)_n$ characteristic for PDMS into a glass-like network. In this case the surface stays hydrophilic for several weeks.

Spagnola et al. [115] compared UV/O_3 treatment (28 mW/cm^2, 60 min) with a plasma oxidation process (50 W, 20 s) as surface treatments of PDMS preceding an

Al_2O_3 coating using ALD and found the UV/O_3 process to produce a much smoother and uniform surface. Tsao et al. [124] used UV/O_3 treatment to achieve low-temperature bonding of PMMA and COC microfluidic substrates. For both polymers, bond strength improvements at low temperatures by one to two orders of magnitude were observed.

Higher photon energies are available in the vacuum-UV (VUV) region if a suitable excimer source is used for irradiating the polymer source. At wavelengths below 175.9 nm, O_2 may be dissociated according to the equation

$$O_2 + h\nu \rightarrow O\left(^1D\right) + O\left(^3P\right)$$

[82]; the excited metastable $O(^1D)$ atom is believed to have stronger oxidative reactivity than $O(^3P)$. Using a Xe excimer lamp to irradiate cyclo-olefin polymer (COP) in ambient air to improve the wettability and adhesion properties, oxygen functionalities such as ether, ketone, and carboxylic groups were found on the surface [57].

UV irradiation can be employed to "activate" a polymer surface for subsequently grafting a polymer from a monomer (solution). A more recent example was reported by Schneider et al. [109]; the principle is illustrated in Fig. 3.19. UV radiation was used to excite a photoinitiator (in this case benzophenone (BP)) which is cleaved by relatively low-energetic UV radiation band-pass-filtered from the spectrum of a 200 W mercury–xenon arc lamp. The resulting radicals start the polymerization of acrylic acid (AA) resulting in formation of a grafted layer of PAA.

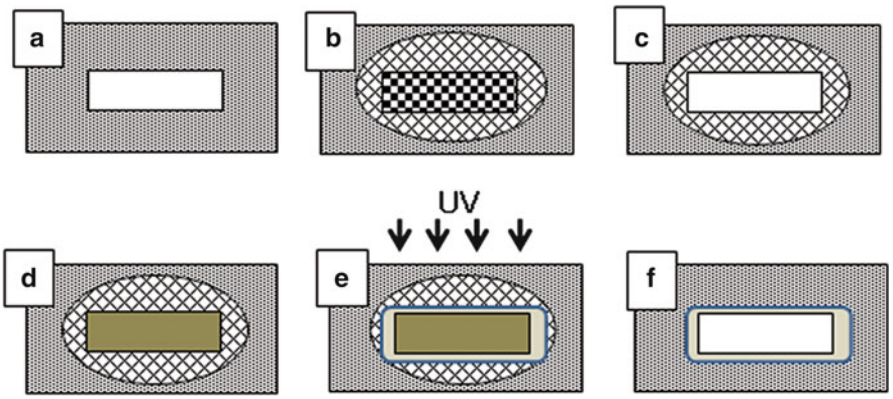

Fig. 3.19 Schematic of UV-induced grafting of poly(acrylic acid) in channels of PDMS microfluidic devices: (**a**) cross-section of channel in PDMS; (**b**) photoinitiator benzophenone (BP) diffuses (*crosshatched*) from a BP solution (*checkered*) flowed through the channel into the surrounding PDMS; (**c**) situation after removal of BP solution; (**d**) acrylic acid (AA) diffuses from a solution of AA (*dark gray*) flowed through the channel; (**e**) after establishment of a zone with diffused BP and AA the grafting is started by irradiation with UV; (**f**) after monomer removal a zone with grafted polymer (AA) has been formed (*light gray*) (adapted from Schneider et al. [109])

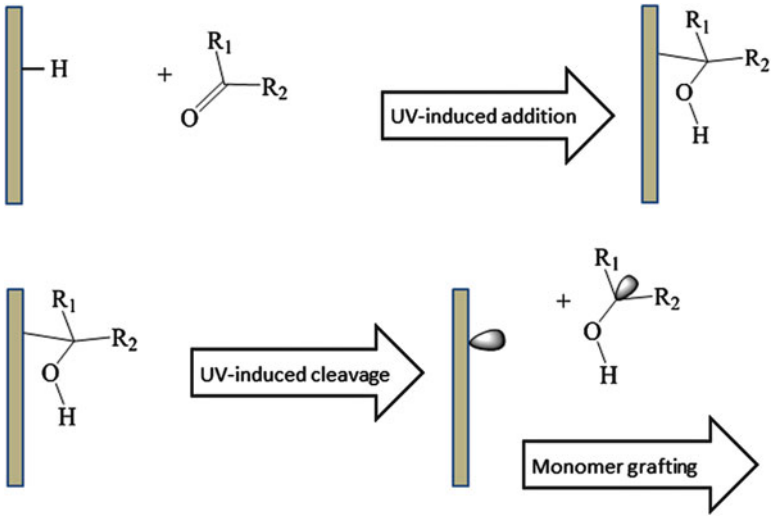

Fig. 3.20 Two-step procedure for UV-induced photografting on SU-8: The polymer is first irradiated in the presence of an aromatic ketone (HCPK, R_1 = phenyl, R_2 = 1-hydroxycyclohexyl; the cited article wrongly shows the 2-hydroxycyclohexyl isomer) in order to add a C–H bond of the substrate to the C=O bond. In a second step the modified surface is irradiated again in order to generate a radical site on the polymer surface to which the unsaturated monomers can graft (adapted from Gao et al. [37])

UV-induced photografting can also be used to enhance the wettability of other polymers such as SU-8 photoresists. In one example [37] UV irradiation of the polymer was done in two steps using a UV LED with 27 mW cm^{-2} at 375 nm emission (30 min): In the first step the sample was irradiated after soaking in a 5 % (w/w) solution of the photoinitiator 1-hydroxycyclohexyl phenyl ketone (HCPK) in ethanol in order to couple it to the surface; in the second step the such-modified surface was irradiated again in the presence of a mixture of monomers (HEMA, PEGMA) and/or cross-linkers (TEGDMA, PEGDMA) carrying hydrophilic OH groups (Fig. 3.20).

3.2.3 Plasma-Based Surface Functionalization

Plasma processes are widely used for the functionalization of surfaces [17, 21]. Some possibilities to use plasma processes as production step for the fabrication of microfluidic systems have already been mentioned in the preceding chapter as alternatives to photon-based technologies. For the following considerations a distinction between low- and atmospheric-pressure plasmas must be made. The mean free path (mfp) of plasma particles (such as atoms, molecules, ions, free electrons) is inversely proportional to the pressure of the process gas in which the

plasma is sustained. Order-of-magnitude-differences in mfps are responsible for largely different characteristics of low-pressure plasmas, typically run at pressures of a few Pascal, and atmospheric-pressure plasmas such as dielectric barrier discharges (DBD) in which mfps are a few hundred nanometers. Due to mfps in the centimeter range, ions in low-pressure plasmas may be accelerated in electric fields, e.g., in cathode falls, to energies in the 100 eV range or beyond, enabling the sputtering of solids and the deposition of hard coatings such as diamond-like carbon (DLC) or cubic boron nitride (cBN). On the other hand, however, low-pressure plasmas can hardly be ignited in small cavities with typical diameters of less than 1 mm, while atmospheric-pressure gas discharges such as DBDs can easily be sustained in cavities with diameters of 100 μm or less, and may easily be delimited to specific surface areas in order to achieve an area-selective functionalization [120].

3.2.3.1 Plasma-Chemical Modification

Exposure of a substrate to a gas discharge may induce physical processes and chemical reactions on the substrate surface and in its near-surface region. The resulting surface modification may be effected by photons from the plasma, by incident charged species, energetic metastables, atoms, or radicals. In low-pressure plasmas sputtering is often the most important physical effect, responsible for removal of impurities and major changes in surface morphology and structure, surface roughening or nanopatterning. Gogolides et al. [40], for example, describe the control of wettability, optical reflection and transmission, protein adsorption and cell growth by nanopatterning. Usually, individual plasma effects on the surface cannot be separated because various surface modifications take place at the same time. So, the kinetic energy of accelerated ions bombarding the substrate may not only break bonds, but also promote cross-linking in polymers [122]. For lab-scale microfluidics PDMS is a material of particular importance. By plasma oxidation the surface turns glass-like and the surface properties change in regard to wettability, chemical reactivity, and oxygen diffusion [74].

For chemical surface modifications low-pressure as well as atmospheric-pressure plasmas are suitable. Usually oxygen-containing process gases are used for an "activation" of the surface. The oxygen-plasma treatment introduces polar functional moieties such as hydroxyl, carbonyl, carboxyl groups (–OH, >C=O, –CO–OH) to polymer surfaces, increasing the free surface free energy and wettability. In case of oxidic inorganic materials such as silica or glass the treatment may result in a removal of thin organic contaminant films.

The activation effect achieved by plasma treatment of polymers is generally not long-term stable. In an extensive study Jokinen et al. investigated a range of polymers frequently used for microfluidic applications like PDMS, PMMA, PC, PE, PP, PS, SU-8, hybrid polymer ORMOCOMP, PCL, and P(CL/DLLA)) (polycaprolactone/D,L-lactide), regarding their wetting behavior after low-pressure microwave-plasma activation. In this study nitrogen and oxygen-plasma treatments

were compared and the long-term stability of the achieved effects was characterized. For each polymer the individual contact angle increase was determined over a time period of 100 days. The optimal process gas for activation was found to depend on the kind of polymer [52].

The hydrophilization of PMMA and PTFE by treatment in a diffuse coplanar surface barrier discharge (DCSBD) at atmospheric pressure was investigated by Hergelová et al. [47]. For activation the process gases oxygen, nitrogen, and water-vapor-enriched nitrogen were used. For both polymers the surface free energy could be increased by 50–60 %. The hydrophilization effect was stable during a period of 7 days [47].

For many microfluidic applications the control of protein immobilization is a crucial point. It can be realized by oxygen-plasma activation for various substrates. In addition oxygen-plasma is used as a pretreatment step for following coating processes in order to ensure defined surface properties. Kim and Herr gives an overview about different immobilization procedures and necessary surface modifications for silicon, metal, plastics, glass, and paper where oxygen-plasma treatments are often used as an intermediate step [55].

Examples of plasma pretreatments before wet-chemical coatings were already mentioned in preceding chapters. Thomas et al. [120] report a method using microplasmas at atmospheric pressure in nitrogen-containing gases as a pretreatment for the patterned metallization of polymers. This so-called plasma printing process is also suitable for the integration of metal electrodes in microfluidic systems.

In addition to modifying the surfaces coming into contact with liquids, the functionalization of seal surfaces plays an important role in the development of three-dimensional microfluidic components. In particular for plastics, temperature and pressure for the sealing process are limited. Pretreatments with oxygen-plasma help to increase the bond strength [11]. However, it must be assumed that the bond strength afterwards in aqueous environment decreases. Lee and Ram [69] report a pressure- and water-stable bond between plastic and PDMS, where after plasma treatment the faces were modified by bis-silanes with larger alkoxy end groups to promote organofunctional bond formation.

Plasma activation as a pretreatment for direct bonding is also known for inorganic materials like glass and silicon, which are used for wafer level production in microsystem technology. After an exposure to atmospheric-pressure or low-pressure plasmas the bond strength for pairs of silicon, fused-silica, and borosilicate glass wafers, respectively, can be increased many times at low temperatures, as reported by Eichler et al. [32].

3.2.3.2 Plasma-Activated Deposition

Diverse surface properties on a variety of materials can be realized by coatings deposited by a plasma process. Plasma-enhanced chemical vapor deposition (PECVD) allows to realize selected surface functionalities. For the plasma process

all kinds of plasma sources, gas pressures between a few Pascals and one bar and different excitation modes such as direct current, mid-frequency, radio frequency, and microwave may be used. The advantage of PECVD over many thermal CVD processes is the low substrate temperature which is generally sufficient to achieve a desired result; even polymeric substrate materials may remain unchanged in shape and properties and only its surface properties may be adapted to the application.

Unsaturated organic monomers with double or triple bonds may be plasma-deposited quite readily. However saturated compounds such as organosilanes, paraffin hydrocarbons, and saturated fluorocarbons are also widely used as precursors and the notion of "plasma polymerization" has been extended to this kind of PECVD [14]. PECVD of special unsaturated monomers in an inert gas atmosphere may lead to a high retention of the monomer structure. Monomers containing reactive groups thus can be used to deposit chemically reactive coatings. Epoxy-functionalized films, for example, may be obtained at ambient pressure from the precursor glycidyl methacrylate by plasma polymerization activated in a pulsed DBD [59].

Cordeiro et al. [25] report fluoropolymer coating in a downstream low-pressure reactor by the use of tetrafluoromethane. After the coating process, the fluorinated PDMS surface shows improved antifouling properties which were tested by two bacteria species. PDMS capillary electrophoresis microchips were coated by octafluoropropane and acryl acid, respectively, in order to modify the electroosmotic flow [76]. In order to improve adhesion of the fluorocarbon and acrylic acid films an Ar plasma pretreatment was applied. Interestingly this treatment was also found to decrease the absorption of a hydrophobic dye by the PDMS walls, indicating a cross-linking of surface-near regions of the polymer.

Plasma polymerization of diethylene glycol dimethyl ether ("diglyme") was successfully applied by Gross-Kosche et al. [42] in their study aiming at nonfouling surfaces, resisting protein adsorption and cell proliferation, of a thermoplastic elastomeric silicone copolymer, GENIOMER® 80 (G80).

3.2.3.3 Plasma Treatment and Film Deposition in Trenches, Microchannels, and Tubings

The integration of functionalized surfaces in microfluidic channels can be challenging, because of the different requirements for surface with liquid contact and sealing areas. But even if the requirements for the channels and the sealing areas are the same, the aspect ratio of the fluidic channels limits the homogeneous film thickness, see left side of Fig. 3.21. Besch et al. [10] studied the uniformity of film deposition on walls of trenches with aspect ratios from 2 to 10 and a trench depth of 3.5 mm. The allylamine coatings were characterized by XPS and FTIR spectroscopy. While the film compositions do not change significantly, the film thicknesses were reduced to 20 % at the bottom for an aspect ratio of 10. Riaz et al. [98] describe a low-pressure (40 Pa) PECVD method to deposit a glass-like SiO_x barrier film in long PDMS channels with rectangular cross-section

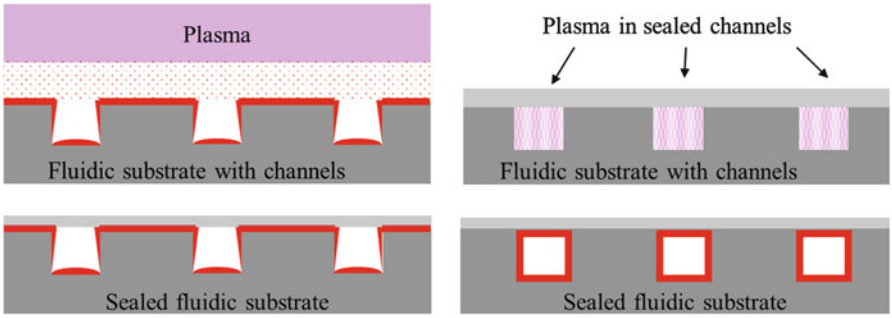

Fig. 3.21 *Left side*: plasma deposition (*red*) on a fluidic substrate with unsealed microfluidic channels. The coating is generally not uniform; at the side walls and bottoms of the trenches, the coating thicknesses are reduced. After sealing, the cap areas in the channels are uncoated. *Right side*: with a plasma in the sealed channel, all channel surfaces may be coated uniformly

(50 µm × 100 µm) using HMDSO and oxygen. Barrier properties were found for small molecules such as rhodamine B and biotin, and the films also resisted permeation of organic solvents such as toluene, preventing the PDMS microfluidic structures from swelling and deforming. The authors conclude that silicon radicals and elemental oxygen maintain sufficiently reactive for up to 7000 s and survive the random diffusion walk along the channel to form a film as much as 65 mm from the cavity entrance. This effect can be used to form thin barrier films of silicon oxide in commercially available plasma reactors.

Mascia and Zhang [77] investigated the hydrophilization of short fluoroelastomer tubings by plasma treatment. The water contact angle for the inner surfaces was measured with regard to the distance of the tube openings, treatment time, plasma power, process gas, and gas pressure. For the activated length in the tubings, an exponential relation with the treatment time was found.

Different requirements for the liquid contact areas and the sealing areas are also obvious for the cap of the channels, see left side Fig. 3.21. West et al. [128] describe a microplasma jet for surface-directed writing. Hydrophilic patterns were directly written to a hydrophobic glass substrate. This allows to turn the sealing areas hydrophilic while the channel areas remain untreated.

Evju et al. [34] reported an atmospheric-pressure plasma that is ignited in a sealed channel of a microfluidic device. Therefore two platinum electrodes were integrated opposite in the ends of the 6 mm long channel. The plasma ignition voltage was up to 15 kV DC and the current flow was limited by a 30 MΩ resistor. By using a C_2F_6/He process gas mixture hydrophobic surface properties were achieved in the channel after plasma treatment. With He/H_2O mixtures the surface turned hydrophilic.

Klages et al. [58, 60] presented a process for channel surface treatment in microfluidics based on a dielectric barrier discharge (DBD) at atmospheric pressure. The discharge is ignited between two electrodes, covered by dielectrics, see Fig. 3.22. Often the fluidic devices itself can act as this dielectric. At sufficiently

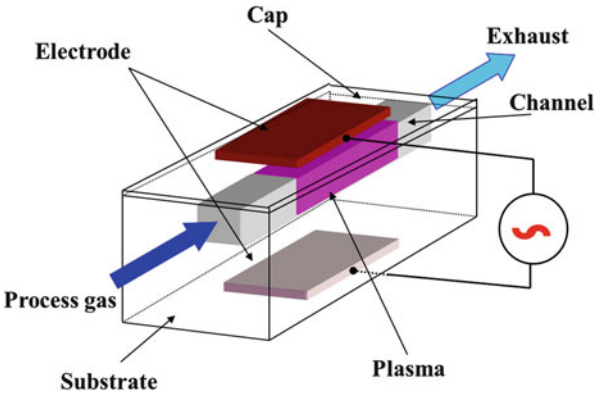

Fig. 3.22 Plasma treatment in a microfluidic channel

high electrode voltages, a plasma ignites in the channel. The ignition voltage is influenced by the choice of process gas. The length of the coated or treated area can be adjusted by the electrode dimensions. Localized surface modification in the channel has the potential to realize hydrophobic stops in hydrophilic channels or to immobilize biomolecules at certain areas.

Priest et al. [95] presented a patterned microplasma system using liquid gallium (melting point 29.8 °C) as electrodes injected into PDMS channels close to the microfluidic cannel to be treated. The injection of the gallium into the electrode channels was done by a syringe at 50 °C. The system was used to ignite localized plasmas and the plasma effect was characterized by a fluorescent dye.

Eichler et al. [33] presented a novel fluid-phase separator based on area-selective microplasma treatment. The separator consists of a Y-shaped channel which is coated in such a way that one branch is hydrophobic and the other hydrophilic. For the function of the separator it is important that the main channel close to the branch point has opposing hydrophilic and hydrophobic areas, see right side Fig. 3.23. This tailored coating was realized by using an individual gas stream for each branch flowing in the direction opposite to the intended liquid flows, see left side Fig. 3.23. The plasma was generated using an electrode configuration as shown in Fig. 3.22.

For hydrophobic coating precursors like tetramethylsilane (TMS) or octafluorocyclobutane ("Freon-C-318") can be used. Hydrophilic coatings can be realized e.g., by oxidizing silicon containing precursors like silane SiH_4 or TEOS. The laminar flow in the channels allows to apply the hydrophobic and the hydrophilic film at the same time. Otherwise one channel can be protected against coating by an inert gas without a precursor or by a quenching gas with a high ignition voltage in which no discharge is sustained under the applied conditions.

Bashir et al. [8] reported a novel coating technique using microplasma for sealed microchannels. They apply two different electrode configurations. The first configuration is related to the principle in Fig. 3.22 with an insulating barrier between the electrodes. One electrode is formed as a needle for the process gas inlet. The counter electrode is limited to the process gas outlet area, but not in electrical

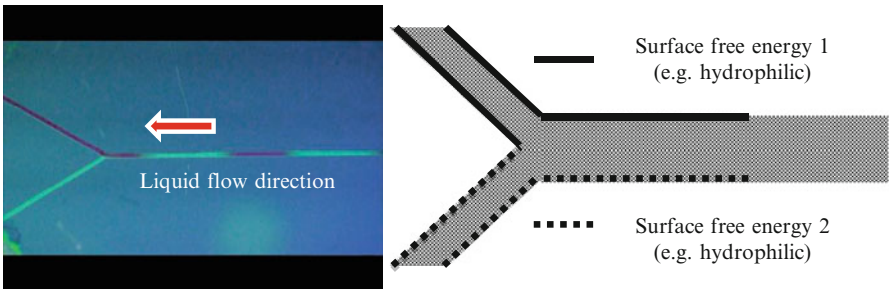

Fig. 3.23 *Left side*: Differences in surface-free energies lead to a phase separation of the segmented flow. All channels have a height of 300 µm. The widths of branches and main channel are 142 and 292 µm, resp. *Right side*: different surface-free energies on opposing surfaces are achieved in the main channel close to the branch point

contact with the process gas. The second configuration without dielectric barrier is similar to the set-up of Evju et al. [34] with the difference that both electrodes are needles for the process gas inlet and outlet. Coatings were applied from different monomers and characterized by FTIR and XPS. The authors achieved long-term stable hydrophilic coatings and deposited films containing amino functions.

References

1. Alexandridis P, Hatton TA (1995) Poly(ethylene oxide)-poly(propylene oxide)-poly(ethylene oxide) block copolymer surfactants in aqueous solutions and at interfaces: thermodynamics, structure, dynamics, and modeling. Colloids Surf A 96:1–46
2. Alf ME, Asatekin A, Barr MC, Baxamusa SH, Chelawat H, Ozaydin-Ince G, Petruczok CD, Sreenivasan R, Tenhaeff WE, Trujillo NJ, Vaddiraju S, Xu J, Gleason KK (2010) Chemical vapor deposition of conformal, functional, and responsive polymer films. Adv Mater 22:1993–2027
3. Annabi N, Selimović S, Acevedo Cox JP, Ribas J, Afshar Bakooshli M, Heintze D, Weiss AS, Cropek D, Khademhosseini A (2013) Hydrogel-coated microfluidic channels for cardiomyocyte culture. Lab Chip 13:3569–3577
4. Asatekin A, Barr MC, Baxamusa SH, Lau KKS, Tenhaeff W, Xu J, Gleason KK (2010) Designing polymer surfaces via vapor deposition. Mater Today 13:26–33
5. Azadi G, Tripathi A (2012) Surfactant-induced electroosmotic flow in microfluidic capillaries. Electrophoresis 33:2094–2101
6. Bäcker M, Raue M, Schusser S, Jeitner C, Breuer L, Wagner P, Poghossian A, Förster A, Mang T, Schöning MJ (2012) Microfluidic chip with integrated microvalves based on temperature and pH-responsive hydrogel thin films. Phys Status Solidi A 209:839–845
7. Basabe-Desmonts L, Reinhoudt DN, Crego-Calama M (2007) Design of fluorescent materials for chemical sensing. Chem Soc Rev 36:993–1017
8. Bashir M, Bashir S, Rees JM, Zimmerman WB (2014) Surface coating of bonded PDMS microchannels by atmospheric pressure microplasma. Plasma Process Polym 11:279–288
9. Bayer H, Engelhardt H (1996) Capillary electrophoresis in organic polymer capillaries. J Microcolumn Sep 8:479–484

10. Besch W, Foest R, Schröder K, Ohl A (2008) Allylamine plasma polymer coatings of interior surfaces in small trench structures. Plasma Process Polym 5:105–112
11. Bhattacharyya A, Klapperich M (2007) Mechanical and chemical analysis of plasma and ultraviolet-ozone surface treatments for thermal bonding of polymeric microfluidic devices. Lab Chip 7:876–882
12. Bhushan B, Cichomski M (2007) Nanotribological characterization of vapor phase deposited fluorosilane self-assembled monolayers deposited on polydimethylsiloxane surfaces for biomedical micro-/nanodevices. J Vac Sci Technol A 25:1285–1293
13. Bhushan B, Hansford D, Lee KK (2006) Surface modification of silicon and polydimethylsiloxane surfaces with vapor-phase-deposited ultrathin fluorosilane films for biomedical nanodevices. J Vac Sci Technol A 24:1197–1202
14. Biederman H (ed) (2004) Plasma polymer films. Imperial College Press, London
15. Blees MH, Winkelman GB, Balkenende AR, den Toonder JMJ (2000) The effect of friction on scratch adhesion testing: application to a sol-gel coating on polypropylene. Thin Solid Films 359:1–13
16. Cai L, Wang Y, Wu Y, Xu C, Zhong M, Lai H, Huang J (2014) Fabrication of a microfluidic paper-based analytical device by silanization of filter cellulose using a paper mask for glucose assay. Analyst 139:4593–4598
17. Chan CM, Ko TM, Hiraoka H (1996) Polymer surface modification by plasmas and photons. Surf Sci Rep 24:1–54
18. Chang JH, Choi DY, Han S, Pak JJ (2010) Driving characteristics of the electrowetting-on-dielectric device using atomic-layer-deposited aluminum oxide as the dielectric. Microfluid Nanofluid 8:269–273
19. Chen C, Xu P, Li X (2014) Regioselective patterning of multiple SAMs and applications in surface-guided smart microfluidics. Appl Mater Interfaces 6:21961–21969
20. Chen S, Li L, Zhao C, Zheng J (2010) Surface hydration: principles and applications toward low-fouling/nonfouling biomaterials. Polymer 51:5283–5293
21. Chu PK, Chen JY, Wang LP, Huang N (2002) Plasma-surface modification of biomaterials. Mater Sci Eng R 36:143–206
22. Cifuentes A, Rodríguez MA, García-Montelongo FJ (1996) Separation of basic proteins in free solution capillary electrophoresis: effect of additive, temperature and voltage. J Chromatogr A 742:257–266
23. Coclite AM, Howden RM, Borrelli DC, Petruczok CD, Yang R, Yagüe JL, Ugur A, Chen N, Lee S, Jo WJ, Liu A, Wang X, Gleason KK (2013) 25th Anniversary article: CVD polymers: a new paradigm for surface modification and device fabrication. Adv Mater 2013 (25):5392–5423
24. Cohen Stuart MA (2003) Macromolecular adsorption: a brief introduction. In: Malmsten M (ed) Biopolymers at interfaces, 2nd edn. Marcel Dekker, New York, pp 1–25
25. Cordeiro AL, Nitschke M, Janke A, Helbig R, D'Souza F, Donnelly GT, Willemsen PR, Werner C (2008) Fluorination of poly(dimethylsiloxane) surfaces by low pressure CF4 plasma—physicochemical and antifouling properties. eXPRESS Polym Lett 3:70–83
26. Decher G, Hong JD, Schmitt J (1992) Buildup of ultrathin multilayer films by a self-assembly process: III. Consecutively alternating adsorption of anionic and cationic polyelectrolytes on charged surfaces. Thin Solid Films 210(21):831–835
27. Demming S, Lesche C, Schmolke H, Klages CP, Büttgenbach S (2011) Characterization of long-term stability of hydrophilized PEG-grafted PDMS within different media for biotechnological and pharmaceutical applications. Phys Status Solidi A 208:1301–1307
28. Demming S, Peterat G, Llobera A, Schmolke H, Bruns A, Kohlstedt M, Al-Halhouli A, Klages CP, Krull R, Büttgenbach S (2012) Vertical microbubble column—a photonic lab-on-chip for cultivation and online analysis of yeast cell cultures. Biomicrofluidics 6:034106 (14 pp)
29. Deng J, Wang L, Liu L, Yang W (2009) Developments and new applications of UV-induced surface graft polymerizations. Prog Polym Sci 34:156–193

30. Deng X, Lahann J (2014) Orthogonal surface functionalization through bioactive vapor-based polymer coatings. J Appl Polym Sci 2014:40315 (9pp)
31. Dijt JC, Cohen Stuart MA, Fleer GJ (1992) Kinetics of polymer adsorption and desorption in capillary flow. Macromolecules 25:5416–5423
32. Eichler M, Hennecke P, Nagel K, Gabriel M, Klages CP (2013) Plasma activation as a pretreatment tool for low-temperature direct wafer bonding in microsystems technology. ECS Trans 50:265–276
33. Eichler M, Nagel K, Hennecke P, Klages CP (2012) Area-selective microplasma treatment in microfluidic channels for novel fluid phase separators. Plasma Process Polym 9:1160–1167
34. Evju JK, Howell PB, Locascio LE, Tarlov MJ, Hickman JJ (2004) Atmospheric pressure microplasmas for modifying sealed microfluidic devices. Appl Phys Lett 84:1668–1670
35. Fidalgo LM, Abell C, Huch WTS (2007) Surface-induced droplet fusion in microfluidic devices. Lab Chip 7:984–986
36. Finke JH, Schmolke H, Klages CP, Müller-Goymann CC (2013) Controlling solid lipid nanoparticle adhesion by polyelectrolyte multilayer surface modifications. Int J Pharm 449:59–71
37. Gao Z, Henthorn DB, Kim CS (2008) Enhanced wettability of an SU-8 photoresist through a photografting procedure for bioanalytical device applications. J Micromech Microeng 18:045013 (7 pp)
38. Glass NR, Tjeung R, Chan P, Yeo LY, Friend JR (2011) Organosilane deposition for microfluidic applications. Biomicrofluidics 5:036501–036507
39. Glavan AC, Martinez RV, Subramaniam AB, Yoon HJ, Nunes RMD, Lange H, Thuo MM, Whitesides GM (2014) Omniphobic "R^F Paper" produced by silanization of paper with fluoroalkyltrichlorsilanes. Adv Funct Mater 24:60–70
40. Gogolides E, Constantoudis V, Kokkoris G, Kontziampasis D, Tsougeni K, Boulousis G, Vlachopoulou M, Tserepi A (2011) Controlling roughness: from etching to nanotexturing and plasma-directed organization on organic and inorganic materials. J Phys D Appl Phys 44:174021
41. Gomez-Sjoberg R, Leyrat AA, Houseman BT, Shokat K, Quake SR (2010) Biocompatibility and reduced drug absorption of sol-gel-treated poly(dimethyl siloxane) for microfluidic cell culture applications. Anal Chem 82:8954–8960
42. Gross-Kosche P, Low SP, Guo R, Steele DA, Michelmore A (2014) Deposition of nonfouling plasma polymers to a thermoplastic silicone elastomer for microfluidic and biomedical applications. J. Appl Polym Sci 131. doi:10.1002/APP.40500
43. Habouti S, Kunstmann-Olsen C, Hoyland JD, Rubahn HG, Es-Souni M (2014) In situ ZnO–PVA nanocomposite coated microfluidic chips for biosensing. Appl Phys A 115:645–649
44. Hamada Y, Ono T, Akagi T, Ishihara K, Ichiki T (2007) Photochemical oxidation of poly (dimethylsiloxane) surface and subsequent coating with biomimetic phosphorylcholine polymer. J Photopolym Sci Technol 20:245–249
45. He M, Herr AE (2010) Polyacrylamide gel photopatterning enables automated protein immunoblotting in a two-dimensional microdevice. J Am Chem Soc 132:2512–2513
46. Hench LL, West JK (1990) The sol-gel process. Chem Rev 90:33–72
47. Hergelová B, Homola T, Zahoranová A, Plecenik T (2012) Plasma surface modification of biocompatible polymers using atmospheric pressure dielectric barrier discharge. In: WDS'12 proceedings of contributed papers, Part II, pp 128–133. ISBN 978-80-7378-225-2
48. Horvath J, Dolnik V (2001) Polymer wall coatings for capillary electrophoresis. Electrophoresis 22:644–655
49. Idota N, Tsukahara T, Sato K (2009) The use of electron beam lithographic graft-polymerization on thermoresponsive polymers for regulating the directionality of cell attachment and detachment. Biomaterials 30:2095–2101
50. Jackson JM, Witek MA, Hupert ML, Brady C, Pullagurla S, Kamande J, Aufforth RD, Tignanelli CJ, Torphy RJ, Yeh JJ, Soper SA (2014) UV activation of polymeric high aspect

ratio microstructures: ramifications in antibody surface loading for circulating tumor cell selection. Lab Chip 14:106–117
51. Jena RK, Yue CY (2012) Cyclic olefin copolymer based microfluidic devices for biochip applications: ultraviolet surface grafting using 2-methacryloyloxyethyl phosphorylcholine. Biomicrofluidics 6:012822 (12 pp)
52. Jokinen V, Suvanto P, Franssilab S (2012) Oxygen and nitrogen plasma hydrophilization and hydrophobic recovery of polymers. Biomicrofluidics 6:016501
53. Kano S, Matsumoto S, Ichikawa N (2009) Surface treated PDMS by UV-Vis light applied to micro-fluidic device. In: Vengallatore S, Bagdahn J, Sheppard NF, Spearing SM (eds) Microelectromechanical systems—materials and devices II book series: Materials Research Society symposium proceedings, vol 1139, pp 121–125
54. Katayama H, Ishihama Y, Asakawa N (1998) Stable capillary coating with successive multiple ionic polymer layers. Anal Chem 70:2254–2260
55. Kim D, Herr AE (2013) Protein immobilization techniques for microfluidic assays. Biomicrofluidics 7:041501
56. Kim D, Karns K, Tia SQ (2012) Electrostatic protein immobilization using charged polyacrylamide gels and cationic detergent microfluidic western blotting. Anal Chem 84:2533–2540
57. Kim YJ, Taniguchi Y, Murase K, Taguchi Y, Sugimura H (2009) Vacuum ultraviolet-induced surface modification of cyclo-olefin polymer substrates for photochemical activation bonding. Appl Surf Sci 255:3648–3654
58. Klages CP, Berger C, Eichler M, Thomas M (2007) Microplasma-based treatment of inner surfaces in microfluidic devices. Contrib Plasma Phys 47:1–8
59. Klages CP, Höpfner K, Kläke N, Thyen R (2000) Surface functionalization at atmospheric pressure by DBD-based pulsed plasma polymerization. Plasmas Polym 5:79–89
60. Klages CP, Thyen R (2000) German Patent DE 10035177 C 2
61. Koh WG, Pishko M (2005) Immobilization of multi-enzyme microreactors inside microfluidic devices. Sens Actuators B 106:335–342
62. Kolb HC, Finn MG, Sharpless KB (2001) Click chemistry: diverse chemical function from a few good reactions. Angew Chem Int Ed 40:2004–2021
63. Kovach KM, Capaona JR, Gupta AS, Potkay JA (2014) The effects of PEG-based surface modification of PDMS microchannels on long-term hemocompatibility. J Biomed Mater Res A 102A:4195–4205
64. Kumar A, Srivastava A, Galaev IY, Mattiasson B (2007) Smart polymers: physical forms and biomedical applications. Prog Polym Sci 32:1205–1237
65. Launiere C, Gaskill M, Czaplewski G (2012) Channel surface patterning of alternating biomimetic protein combinations for enhanced microfluidic tumor cell isolation. Anal Chem 84:4022–4028
66. Lee AG, Arena CP, Beebe DJ, Palecek SP (2010) Development of macroporous poly (ethylene glycol) hydrogels arrays within microfluidic channels. Biomacromolecules 11:3316–3324
67. Lee AG, Beebe DJ, Palecek SP (2012) Quantification of kinase activity in cell lysates via photopatterned macroporous poly(ethylene glycol) hydrogel arrays in microfluidic channels. Biomed Microdevices 14:247–257
68. Lee KK, Bhushan B, Hansford D (2005) Nanotribological characterization of fluoropolymer thin films for biomedical micro/nanoelectromechanical system applications. J Vac Sci Technol A 23:804–810
69. Lee KS, Ram RJ (2007) Plastic–PDMS bonding for high pressure hydrolytically stable active microfluidics. Lab Chip 9:1618–1624
70. Lee SB, Koepsel RR, Morley SW, Matyjaszewski K, Sun Y, Russell AJ (2004) Permanent, nonleaching antibacterial surfaces 1. Synthesis by atom transfer radical polymerization. Biomacromolecules 5:877–882

71. Leskelä M, Ritala M (2002) Atomic layer deposition (ALD): from precursors to thin film structures. Thin Solid Films 409:138–146
72. Liu Z, Xiao L, Xu B (2012) Covalently immobilized biomolecule gradient on hydrogel surface using a gradient generating microfluidic device for a quantitative mesenchymal stem cell study. Biomicrofluidics 6:024111–024111-12
73. Lugli F, Firavanti G, Pattani D, Pasquali L, Montecchi M, Gentili D, Murgia M, Hemmatian Z, Cavallini M, Zerbetto F (2013) And yet it moves! Microfluidics without channels and troughs. Adv Funct Mater 23:5543–5549
74. Lycans RM, Higgins CB, Tanner MS, Blough ER, Scott Day B (2014) Plasma treatment of PDMS for applications of in vitro motility assays. Colloids Surf B Biointerfaces 116:687–694
75. Ma H, Zhang M (2014) Superhydrophilic titania wall coating in microchannels by in situ sol–gel modification. J Mater Sci 49:8123–8126
76. Martin IT, Dressen B, Boggs M, Liu Y, Henry CS, Fisher ER (2007) Plasma modification of PDMS microfluidic devices for control of electroosmotic flow. Plasma Process Polym 4:414–424
77. Mascia L, Zhang Z (1996) Internal surface interactions in the plasma treatment of fine bore fluoropolymer tubings. Appl Surf Sci 93:1–7
78. Matsuda T, Ohya S (2005) Photoiniferter-based thermoresponsive graft architecture with albumin covalently fixed at growing graft chain end. Langmuir 21:9660–9665
79. Matyjaszewski K, Dong H, Jukabowski W, Pietrasik J, Kusomo A (2007) Grafting from surfaces for "Everyone": ARGET ATRP in the presence of air. Langmuir 23:4528–4531
80. Matyjaszewski K, Miller PJ, Shukla N, Immaraporn B, Gelman A, Luokala BB, Siclovan TM, Kickelbick G, Vallant T, Hoffmann H, Pakula T (1999) Polymers at interfaces: using atomic transfer radical polymerization in the controlled growth of homopolymers and block copolymers from silicon surfaces in the absence of untethered sacrificial initiator. Macromolecules 32:8716–8724
81. McCarley RL, Vaidya B, Wei S, Smith AF, Patel AB, Feng J, Murphy MC, Soper SA (2005) Resist-free patterning of surface architectures in polymer-based microanalytical devices. J Am Chem Soc 127:842–843
82. McNesby JR, Okabe H (1964) Vacuum ultraviolet photochemistry. In: Noyes Jr WA, Hammond GS, Pitts Jr JN (eds) Advances in photochemistry, vol 3. Interscience, New York
83. Moad G, Chong YK, Postma A, Rizzardo E, Thang SH (2005) Advances in RAFT polymerization: the synthesis of polymers with defined end-groups. Polymer 46:8458–8468
84. Nakayama Y, Matsuda T, Irie M (1993) A novel surface photograft polymerization method for fabricated devices. Trans Am Soc Artif Intern Org J 39:M545–M549
85. Nakayama Y, Matsuda T (1996) Surface macromolecular architectural designs using photograft copolymerization based on photo-chemistry of benzyl-N,N-diethyldithiocarbamate. Macromolecules 29:8622–8630
86. Nejadnik MR, Olsson ALJ, Sharma PK, van der Mei HC, Norde W, Busscher HJ (2009) Adsorption of Pluronic F-127 on surfaces with different hydrophobicities probed by quartz crystal microbalance with dissipation. Langmuir 25:6245–6249
87. Niedl RR, Beta C (2015) Hydrogel-driven paper-based microfluidics. Lab Chip 15:2452–2459
88. Olsen K, Ross DJ, Tarlov MJ (2002) Immobilization of DNA hydrogel plugs in microfluidic channels. Anal Chem 74:1436–1441
89. Park JJ, Luo X, Yi H, Valentine TM, Payne GF, Bentley WE, Ghodssi R, Rubloff GW (2006) Chitosan-mediated *in situ* biomolecule assembly in completely packaged microfluidic devices. Lab Chip 6:1315–1321
90. Patrito N, McLachlan JM, Faria SN, Chan J, Norton PR (2007) A novel metal-protected plasma treatment for the robust bonding of polydimethylsiloxane. Lab Chip 7:1813–1818
91. Pei SN, Valley JK, Neale SL, Jamshidi A, Hsu HY, Wu MC (2010) Light-actuated digital microfluidics for large-scale, parallel manipulation of arbitrarily sized droplets. In: Abstracts of the 23rd IEEE international conference on micro electro mechanical systems (MEMS),

Wanchai, Hong Kong, 24–28 January 2010, pp 252–255. INSPEc accession number: 11229702. doi:10.1109/MEMSYS.2010.5442519
92. Piao Y, Han DJ, Reza Azad M, Park M, Seo TS (2015) Enzyme incorporated microfluidic device for in-situ glucose detection in water-in-air microdroplets. Biosens Bioelectron 65:220–225
93. Popat KC, Johnson RW, Desai TA (2003) Characterization of vapor deposited poly ethylene glycol films on silicon surfaces for surface modification of microfluidic systems. J Vac Sci Technol B 22:645–654
94. Prakash S, Karacor MB (2011) Characterization stability of "click" modified glass surfaces to common microfabrication conditions and aqueous electrolyte solutions. Nanoscale 3:3309–3315
95. Priest C, Gruner PJ, Szili EJ, Al-Bataineh SA, Bradley JW, Ralston J, Steele DA, Short RD (2011) Microplasma patterning of bonded microchannels using high-precision "injected" electrodes. Lab Chip 11:541–544
96. Puchberger-Enengl D, Kruztler C, Keplinger F, Vellekoop MJ (2014) Single-step design of hydrogel based microfluidic assays for rapid diagnostics. Lab Chip 14:378–383
97. Reinholt SJ, Baeumner AJ (2014) Microfluidic isolation of nucleic acids. Angew Chem Int Ed 53:13988–14001
98. Riaz A, Gandhiraman RP, Dimov IK, Basabe-Desmonts L, Ducree J, Daniels S, Riccoa AJ, Lee LP (2012) Reactive deposition of nano-films in deep polymeric microcavities. Lab Chip 12:4877–4883
99. Riche CT, Marin BC, Malmstadt N, Gupta M (2011) Vapor deposition of crosslinked fluoropolymer barrier coatings onto pre-assembled microfluidic devices. Lab Chip 11:3049–3052
100. Riche CT, Zhang C, Gupta M, Malmstadt N (2014) Fluoropolymer surface coatings to control droplets in microfluidic devices. Lab Chip 14:1834–1841
101. Righetti PG, Gelfi C, Verzola B, Castelletti L (2001) The state of the art of dynamic coatings. Electrophoresis 22:603–611
102. Roman GT, Hlaus T, Bass KJ, Seelhammer TG, Culbertson CT (2005) Sol-gel modified poly (dimethylsiloxane) microfluidic devices with high electroosmotic mobilities and hydrophilic channel wall characteristics. Anal Chem 77:1414–1422
103. Roy S, Yue CY, Venkatraman SS (2013) Fabrication of smart COC chips: advantages of N-vinylpyrrolidone (NVP) monomer over other hydrophilic monomers. Sens Actuators B 178:86–95
104. Sakai-Kato K, Kato M, Toyo'oka T (2002) On-line trypsin-encapsulated enzyme reactor by the sol-gel method integrated into capillary electrophoresis. Anal Chem 74:2943–2949
105. Sakai-Kato K, Kato M, Toyo'oka T (2003) Creation of an on-chip enzyme reactor by encapsulating trypsin in sol-gel on a plastic microchip. Anal Chem 75:388–393
106. Schmolke H (2014) Funktionale Polyelektrolytschichten für mikrofluidische Systeme. In: Fraunhofer IST, Braunschweig (eds) Berichte aus Forschung und Entwicklung IST, Band 39, Fraunhofer Verlag
107. Schmolke H, Demming S, Edlich A, Magdanz V, Büttgenbach S, Franco-Lara E, Krull R, Klages CP (2010) Polyelectrolyte multilayer surface functionalization of poly(dimethyl-siloxane) (PDMS) for reduction of yeast cell adhesion in microfluidic devices. Biomicro-fluidics 4:044113
108. Schmolke H, Hartwig S, Klages CP (2011) Poly(acrylic acid)-graft-poly(ethylene glycol) preparation and adsorption on polyelectrolyte multilayers (PEMs) for custom-made antiadhesive surfaces. Phys Status Solidi A 208:1290–1300
109. Schneider MH, Willaime H, Tran Y, Rezgui F, Tabeling P (2010) Wettability patterning by UV-initiated graft polymerization of poly(acrylic acid) in closed microfluidic systems of complex geometry. Anal Chem 82:8848–8855

110. Schröder ME, Zurick KM, Mc Grath DE, Bernards MT (2013) Multifunctional polyampholyte hydrogels with fouling resistance and protein conjugation capacity. Biomacromolecules 14:3112–3122
111. Schröen CGPH, Cohen Stuart MA, van der Voort Maarschalk K K, van der Padt A, van't Riet K (1995) Influence of preadsorbed block copolymers on protein adsorption: surface properties, layer thickness, and surface coverage. Langmuir 11:3068–3074
112. Seguin C, McLachlan JM, Norton PR, Lagugné-Labarthet F (2010) Surface modification of poly(dimethylsiloxane) for microfluidic assay applications. Appl Surf Sci 256:2524–2531
113. Shah AM, Yu M, Nakamura Z, Ciciliano J, Ulman M, Kotz K, Stott SL, Maheswaran S, Haber DA, Toner M (2012) Biopolymer system for cell recovery from microfluidic cell capture devices. Anal Chem 84:3682–3688
114. Shirai K, Mawatari K, Kitamori T (2014) Extended nanofluidic immunochemical reaction with femtoliter sample volumes. Small 10:1514–1522
115. Spagnola JC, Gong B, Parsons GN (2010) Surface texture and wetting stability of polydimethylsiloxane coated with aluminum oxide at low temperature by atomic layer deposition. J Vac Sci Technol A 28:1330–1337
116. Stojkovič G, Krivec M, Vesel A, Marinšeka M, Žnidaršič-Plazla P (2014) Surface cell immobilization within perfluoralkoxy microchannels. Appl Surf Sci 320:810–817
117. Sui G, Wang J, Lee CC, Lu W, Lee SP, Leyton JV, Wu AM, Tseng HR (2006) Solution-phase surface modification in intact poly(dimethylsiloxane) microfluidic channels. Anal Chem 78:5543–5551
118. Tehranirokh M, Kouzani AZ, Francis PS (2013) Microfluidic devices for cell cultivation and proliferation. Biomicrofluidics 7:051502 (32pp)
119. Thévenot J, Oliveira H, Sandre O, Lecommandoux S (2013) Magnetic responsive polymer composite materials. Chem Soc Rev 42:7099–7116
120. Thomas M, Borris J, Dohse A, Eichler M, Hinze A, Lachmann K, Nagel K, Klages CP (2012) Plasma printing and related techniques - patterning of surfaces using microplasmas at atmospheric pressure. Plasma Process Polym 9:1086–1103
121. Tia SQ, He M, Kim D (2011) Multianalyte on-chip native western blotting. Anal Chem 83:3581–3588
122. Ting YK, Liu CC, Park SM, Jiang H, Nealey PF, Wendt AE (2010) Surface roughening of polystyrene and poly(methyl methacrylate) in Ar/O_2 plasma etching. Polymers 2:649–663
123. Tran TB, Cho S, Min J (2013) Hydrogel-based diffusion chip with electric cell-substrate impedance sensing (ECIS) integration for cell viability assay and drug toxicity screening. Biosens Bioelectron 50:453–459
124. Tsao CW, Hromada L, Liu J, Kumar P, DeVoe DL (2007) Low temperature bonding of PMMA and COC microfluidic substrates using UV/ozone surface treatment. Lab Chip 7:499–505
125. Van Midwoud PM, Janse A, Merema MT, Groothuis GMM, Verpoorte E (2012) Comparison of biocompatibility and adsorption properties of different plastics for advanced microfluidic cell and tissue culture models. Anal Chem 84:3938–3944
126. Wei S, Vaidya B, Patel AB, Soper SA, McCarley RL (2005) Photochemically patterned poly (methyl methacrylate) surfaces used in the fabrication of microanalytical devices. J Phys Chem B 109:16988–16996
127. Wen J, Legendre LA, Bienvenue JM, Landers JP (2008) Purification of nucleic acids in microfluidic devices. Anal Chem 80:6472–6479
128. West J, Michels A, Kittel S, Jacob P, Franzke J (2007) Microplasma writing for surface-directed millifluidics. Lab Chip 7:981–983
129. Wu H, Tian Y, Liu B, Lu H, Wang X, Zhai J, Jin H, Yang P, Xu Y, Wang H (2004) Titania and alumina sol-gel-derived microfluidics enzymatic-reactors for peptide mapping: design, characterization, and performance. J Proteome Res 3:1201–1209
130. Wright JD, Sommerdijk NAJM (2001) Sol-gel materials chemistry and applications. CRC Press, Boca Raton

131. Yang WT, Rånby B (1996) Radical living graft polymerization on the surface of polymeric material. Macromolecules 29:3308–3310
132. Ziółkowski B, Czugala M, Diamond D (2012) Integrating stimulus responsive materials and microfluidics: the key to next-generation chemical sensors. J Intel Mat Syst Str 24:2221–2238
133. Zhang Y, Trinh KTL, Yoo IS, Lee NY (2014) One-step glass-like coating of polycarbonate for seamless DNA purification and amplification on an integrated monolithic microdevice. Sens Actuat B 202:1281–1289

Chapter 4
Microbioreactors

R. Krull, S. Lladó-Maldonado, T. Lorenz, S. Demming, and S. Büttgenbach

Abstract In the last decade, microbioreactor (MBR) technology has allowed for rapid advances in biotechnology process development and the investigation of various biological systems from the industrial biotechnology and pharmaceutical biotechnology. Many of the devices that have been reported in the literature are being applied for early-stage bioprocess research. This research makes it possible to perform comprehensive experiments with very expensive substances that are only available in limited quantities.

Microtechnologically fabricated MBRs range in complexity from simple microtiter-based systems to complex automated parallel bioreactors designed to allow meaningful scaling up/scaling down of conventional pilot and large-scale bioprocesses. MBR technology and the capability to monitor cultivation process variables in situ, such as the optical density, dissolved oxygen, pH and fluorescent protein expression, provide real-time and quantitative data from a microliter cultivation broth. Currently, the majority of MBR systems have been designed for batch and fed-batch processing; there are a few efforts directed at developing MBRs for continuous chemostat mode operation.

This overview of microtechnologically fabricated MBRs, their design and application presents the advantages, different strategies for manufacturing and biotechnological applications of these tiny devices in different operation modes. The report discusses the possibility of design versatility and maintaining key aspects, for example, single-use and fluidic connections, as well as the application of MBRs in versatile and different biotechnological fields.

R. Krull (✉) • S. Lladó-Maldonado
IBVT—Institute of Biochemical Engineering, Technische Universität Braunschweig, Gaußstr. 17, Braunschweig 38106, Germany
e-mail: r.krull@tu-braunschweig.de

T. Lorenz • S. Büttgenbach
IMT—Institute of Microtechnology, Technische Universität Braunschweig, Alte Salzdahlumer Str. 203, Braunschweig 38124, Germany

S. Demming
IMT—Institute of Microtechnology, Technische Universität Braunschweig, Alte Salzdahlumer Str. 203, Braunschweig 38124, Germany

Global Technology Chemical Intermediates, BASF SE, Ludwigshafen, Germany

A. Dietzel (ed.), *Microsystems for Pharmatechnology*,
DOI 10.1007/978-3-319-26920-7_4

4.1 Introduction

Biotechnological process development includes the screening of microorganisms and the estimation of optimal process parameters for high-yield bioproduction. Biological reaction kinetics, growth behaviour and product formation are dependent on several physicochemical parameters, e.g., temperature, pH and nutrient availability. To minimise the uncertainty in these parameters, a homogeneous distribution of cells during the cultivation is indispensable for reproducible and reliable data. Due to the low solubility of oxygen in aqueous media, the characterisation of the oxygen transfer for aerobic cultivation processes represents the basis of all further biological studies. The generation of the information will provide comprehensive knowledge of the process and requires a variety of experiments that cover the proper range of process parameters.

Gathering this comprehensive process information requires several simultaneous experiments. Thus, there is a high demand for cost-effective, parallel, and multiparametric automated methods with high-throughput [158]. In particular, microprocess-engineered bioreactor systems are a focus of research [24, 123, 134]. These systems allow for online screening and monitoring of selected process conditions [18]. Furthermore, the microscale set-up ensures savings of high-cost substrates, including limited drug formulations. Currently, the screening set-up in microtiter plates, working in batch or fed-batch mode, allows for high-throughput experimentation. Unfortunately, there is a lack of information due to the time-dependent environmental conditions and limited process time as well as the lack of multiparametric online analysis. For cultivations, the simultaneous detection of several parameters is mandatory for holistic process information.

Due to novel manufacturing processes in microtechnology, various functional elements can be generated at the scale of a few micro- and even nanolitres [22, 23, 33, 40, 72, 108, 147] and merged into a complete analytical system, such as a micro total analysis system (μTAS) [87], also known as lab-on-a-chip (LoC). Microstructures are advantageous in terms of the effective heat and mass transfer due to their increased surface-to-volume ratio as well as the lower diffusion distances and increased laboratory safety [14, 131]. In addition to simple channel and reactor geometries, a LoC may include liquid-handling components (e.g., pumps, valves, and switches) and/or interrogation mechanisms for the online monitoring and control of physical, chemical, and biological process parameters [64].

Biotechnological process development requires a broad repertoire of methods to completely perform the required tasks. These tasks range from developing strains and screening microbial systems to improving productivity and determining the optimal cultivation parameters for production with high titres and yields up to obtaining kinetic parameters. Suitable methods make it possible to develop predictive models using this information to calculate and optimise biotechnological processes.

Process-relevant reaction kinetic data are usually determined in laboratory bioreactors with a reaction volume of 0.25–5 L. These reactors are versatile

experimental tools for the study of cultivation processes and enable operation in batch, fed-batch, and continuous modes. Here, in most cases, temperature, pH and aerobic cultivations, the dissolved oxygen concentration and the exhaust gas composition, in particular the O_2 and CO_2 contents are quantified and controlled online.

The rapid progress in molecular biotechnology and microtechnology, including the development of automated cultivation platforms, allows microbioprocess engineering to develop reliable methods and microbioreactors (MBR) for high-throughput processing (HTP) and improve these systems for daily laboratory use. The challenge is to develop HTP systems that allow for control of the dynamic interactions of complex biological systems and their defined microenvironment with simultaneous control of the mass transfer processes in multiphase cultivation systems.

For MBR systems with reaction volumes in the (sub) microlitre range, surface effects play an increasing role due to the high surface-to-volume ratio. Another challenge is the technical implementation of multiphase systems, where in addition to individual gas, liquid, and foam phases, immiscible liquid phases must also be considered. Energy dissipation and energy distribution change as a function of the size of the reactor chamber and the nature of the energy input (stirring and/or aeration). Cultivation media with high viscosity requires special demands on the homogenisation of the reactor content. The major process parameters of pH, the concentration of dissolved oxygen (DO), and the optical density (OD) in small reaction volumes must also be accurately measurable and as controllable as possible. For quantitative physiological studies of biological systems down to single-cell approaches, precise metrological detection of the microenvironment must be possible and non-invasive in-line, and at-line measurement techniques for minimal sample volumes must also be available to investigate microorganisms with high specific growth rates. In addition, at the microscale, batch, fed-batch, and continuous processes should be allowed. Overall, a very high demand for safe operation and administration exists for cheaper, parallel, and multi-automated culturing approaches with high-throughput to generate process-related data at high density to determine the optimal process parameters for product yield as well as for space–time yield [158].

These requirements show the great challenges in the development of MBRs. In Sect. 4.2, the developments of microbioprocess engineering will be discussed in recent years. Sect. 4.3 provides an overview of the existing MBR systems for the cultivation of microbial and animal/human systems, and further materials and microtechnical production technologies, including microfluidic components, will be discussed. In Sect. 4.4, two application examples of MBRs will be described. Sect. 4.5 summarises this part.

4.2 Development of Microbioprocess Engineering

To date, a variety of optimisations of biotechnological processes using HTP in simple microtiter plates (MTPs) and shake approaches at a scale of 0.1–50 mL have been conducted; this work was mainly conducted in batch mode to examine candidates for production by planktonic growth. Both macro- and MTP systems have their advantages and disadvantages, and their use must be carefully weighed against each other depending on the application. Bioreactor cultivation on the litre scale often has high operating costs due to the required substrates and media; in contrast, due to the lower reaction volume, cultivation in shake flasks or MTPs are more cost-effective, and a higher degree of parallelisation can be achieved [37].

A subsequent approach to facilitated handling and automation of MTP approaches is the integration of reliable pipetting features [143]. Huber et al. [50] first reported the successful integration of a pipetting robot (Hamilton Microlab Star pipettor) into an MTP BioLector system. Currently, this MTP system is advertised as an alternative to other pipetting robots (including Janus, Perkin Elmer, Freedom Evo, Tecan) for different applications. Thus, this commercialised system offers the possibility of fully automated MTP cultivation without manual assistance for the use of biotechnological process development [46].

To map conventional macroscale bioreactors (e.g., stirred tanks, bubble columns) to a comparable miniaturised scale, Kostov et al. [63] developed a miniaturised 2 mL cuvette reactor made of polystyrene with magnetic and optical sensors for pH, DO, and OD. The researchers mainly from the groups of Baganz and Weuster-Botz, simultaneously developed miniaturised bioreactors at the mL scale for different screening experiments and biotechnological process optimisation [9, 28, 29, 67, 114, 144].

In recent years, new microproduction techniques and developments in optosensor technology have led to the production of structures for reaction volumes on the order of a few micro- or nanolitres down to the single-cell level and to improved online measurement techniques [13, 33, 108, 147]. The microstructures gain their advantage from the fact that they allow more effective heat and mass transfer due to the increased surface-to-volume ratio and the lower diffusion distances compared with those of macrosystems [14, 131]. Mass and heat transfer are intensified, and thus the reaction rate, yield, and selectivity are increased [61].

MBR developments are strongly influenced by the increasing development of microtechnical production process since the 1970s; today, these advances have made it possible to integrate microfluidic functional elements that range from sampling, sample transport, preparation, and separation to the integration of chemical/biological sensor technology in μTAS or LoC [39, 87]. The first works on this integration were performed in the beginning of the 1990s, especially in the groups of Manz and Harrison [44, 87]. In addition to simple channel and reactor geometries at LoC systems, components for fluid handling (e.g., micropumps and microvalves, elements of mixing and reaction chambers, fries and flow resistances) and for signal detection for online monitoring and control of physical, chemical, and biological process parameters were also integrated [64].

The successful generation of the LoC concept in the 1990s was based on the parallel development of suitable gas-permeable polymeric materials, in particular polydimethylsiloxane (PDMS) and poly (methyl methacrylate) (PMMA) [30, 89, 90, 145]. These polymers are suitable materials for the production of microfluidic disposable reactors due to their low material cost, their biocompatibility, their chemical and biological inertness, their optical transmittance in the UV-NIR range, their permeability to non-polar gases, such as O_2, N_2, and CO_2, their impermeability to liquid water, the possibility of specific surface modification, and their applicability for mass production [64, 90, 99, 129, 145, 150, 160]. In particular, PDMS is suitable for production using soft lithography, a process that allows a cost-effective production of even the smallest structures [116, 151, 152].

MBRs with a reaction volume on the microlitre scale were first introduced in 2004 by the group of Jensen [158, 161]. The MBR application of LoC systems is certainly one of the most important milestones in the research and development activities of microprocess engineering [60, 123].

First, a whole series of horizontally arranged MBRs (hMBRs) with the main flow direction perpendicular to the lift force has been developed. In non-active stirred MBRs and in systems with a passive oxygen supply via the corresponding polymer membranes, the concentration gradients of the limiting substrate, metabolites, and products occur not only over the length of the reactor but also along the reactor height in terms of cell distribution and the oxygen supply. An alternative and improved operation of an MBR is an upright configuration that has a vertically arranged MBR (vMBR) with active gassing [22, 24, 111] (see Sect. 4.4.2); this configuration is commonly used in bubble column reactors on a macroscale.

4.3 Design and Manufacturing of Microbioreactors

4.3.1 Overview

For screening applications, e.g., pharmacokinetic studies, drug delivery experiments or metabolic flux analyses, where expensive and only limited amounts of presentable agents are used, reaction volumes in the millilitre range are still too large; thus, further miniaturisation down to the microlitre scale is necessary.

The small dimensions of MBR systems typically result in laminar fluid flow conditions of the fluid phase and the already mentioned high surface-to-volume ratios [8, 13, 135, 148, 157]. Thus, the flow characteristics in the MBR differ significantly from those on the laboratory scale [8, 135]. The Reynolds number in an MBR system is far below 1300 [39, 125, 140, 142]; in these systems, often a value as low as the order $Re \leq 1$ is assumed, which corresponds to creeping flow conditions [15]. With the lack of turbulence, convective mixing and multiphase flows are increasingly influential and limited by molecular phenomena, e.g., diffusion and the interactions among fluid, cells, and the reactor surface play a key role.

Due to the large surface-to-volume ratio of MBR systems, the specific interactions between cells and reactor materials must be considered. Depending on the desired application, it is possible to selectively influence the adhesion of cells [36, 96, 117]. Accordingly, suitable surface hydrophilisation is used to reduce non-specific cell and protein adhesion to the reactor wall material [7, 12, 20, 49, 85, 88, 128, 141, 150, 161, 162].

To achieve homogenous conditions within the MBR, magnetically driven elements [124, 134, 161] peristaltic mixers [70, 71] and pumps [106] have been integrated. In non-active stirred MBRs, the introduction and formation of gas bubbles by fresh media and during aerobic cultivation, respectively, have an adverse effect on the overall process. For this reason, the hMBRs are only passively supplied with (air) oxygen by membrane diffusion [11, 31, 32, 134, 158, 161]. Common methods of suppressing the formation of gas bubbles include the vacuum degassing of the cultivation medium [113], the wetting of the surface of the microstructures by means of ethanol or phosphate-buffered saline [51] or by suitable surface modification [127, 128] and the surface wetting with CO_2 or 3 wt.% Pluronic® before the MBR is filled with culture medium [134, 149].

Additionally, increasing the reactor internal pressure against the external environment or applying a vacuum from the outside of the MBR makes it possible to promote the passage of trapped air bubbles through the gas-permeable material from the cultivation media [55, 134, 136]. Furthermore, active bubble traps have been implemented [21, 130].

The generation of CO_2 due to metabolic cell activity or as a result of evaporation phenomena strongly influences the stable, uniform, and laminar flow in microstructures by completely clogging the microchannels. In such cases, cell viability also decreases due to the strongly reduced and irregular supply of nutrients. Bubbles that occur can remain in the system, thus displacing the liquid, influencing or completely blocking the liquid flow and disturbing optical measurements [157].

An alternative improvement can be achieved in vMBRs working in an upright arrangement, where active gassing is possible [24]. Bubbles formed at a micronozzle rise through the device and induce circular convection of the liquid, which reduces diffusion distances and prevents the sedimentation of cells. In brief, the hydrodynamic principle of a bubble column reactor, which is known from the macroscale, is scaled down to the microscale. Compared with currently published hMBRs based on mechanical or peristaltic active mixing, this three-phase microbubble column reactor (μBC) promotes mixing and oxygen transport due to air sparging and possesses the advantages of a simple construction, with no mechanical moving parts, and thus low manufacturing and operation costs. Depending on the gas flow rate, increased backmixing and thus a homogeneous cell and nutrient distribution can be achieved [110].

The scalability of the bioreactors from micro- to macroscale and vice versa is reproduced and validated in several cases [25, 46, 158, 161] showing the MBR's potential to provide much of the data and functionality that a large bioreactor system makes available while offering the advantages of HTP, in terms of costs, space, and time.

4.3.2 Application Examples of Microbioreactors

MBRs can be viewed as a special type of LoC system, which has been developed as a screening tool for bacterial or cell culturing systems, especially for biotechnological, pharmaceutical, and medical development and process optimisation; the uses of MBRs can be divided into two main applications. The first is the development of MBRs for HTP applications to screen bacterial cell cultures and to optimise their growth and production in planktonic suspension. The main focus lies on the feasibility of the integration of online analytics and the measurements of reaction kinetics parameters. For the second application field involving mammalian/human cells, MBRs have been developed to elucidate the interrelationship of intra- and intercellular processes and mechanisms. The challenge is to mimic in vivo environmental conditions within in vitro microfluidic elements. This application gives rise to new possibilities in the development of biological and pharmaceutical products. Furthermore, it offers future potential in the field of individual therapy, where the effect of active pharmaceutical ingredients on cells and on the formation of cellular tissue can be determined. Up to this point, several MBRs operating in batch, fed-batch, and continuous modes have been presented.

4.3.2.1 Bacterial Cell Cultures

Schäpper et al. [123], Hegab et al. [45], Kirk and Szita [60] and Lattermann and Büchs [69] reviewed the current MBR platforms used in biotechnological and process development. Some of the developed MBR have integrated elements for the online analysis of OD, DO, pH and temperature. In the following, some of the MBR concepts are described using examples.

An MBR system with a reaction volume of only 1 nL uses flow control for selective cell retention [108]. Due to the small dimensions of the reactor system, a stagnation zone (the so-called *zero speed point*) is formed, where an individual cell, in this case, *S. cerevisiae*, is retained in a laminar flow regime. Accordingly, microscopic single-cell studies can be conducted, and morphological constraints can be captured photographically. The volume flow in the flow channel above the stagnation point is approximately 6 μL h^{-1}, which corresponds to a fluid velocity of 200 μm s^{-1}.

Active mixing for isotropic conditions was achieved with the use of commercially available miniature stir bars [11, 122, 134, 163]. In another batch-operated MBR (250 μL), the cultivation medium of *E. coli* was also mixed with a steel ball (diameter 1.59 mm) on a pivot plate [84]. Aeration of the reaction mixture was achieved by using an electrolysis chamber under the cultivation chamber.

The basic materials include PMMA and PDMS. Around a PDMS membrane, the cultivation medium is passively supplied with oxygen. Online measurements within externally heated reactor chambers parameters, such as DO, pH (both via integrated sensor spots) and OD. The latter was measured with the use of LEDs and photodetectors located at the vertical axis of the reactor chamber. The MBR system (volume of 150 μL) was successfully used to cultivate *E. coli* and *S. cerevisiae* and tracked the active mixing of the reactor chamber with a magnetic stirring bar [11, 134]. Due to the good active mixing, it is possible to operate the MBR as a chemostat. For *E. coli*, flow rates between 30 and 120 μL h^{-1} are set, which corresponds to 0.2–0.8 volume changes per hour. For a continuous operation, the cultivation time was up to 7 days [161] and sometimes more than 21 days [6]. Park et al. [106] monitored a *S. cerevisiae* culture in continuous mode for 140 h. In a batch approach, *E. coli* was observed over a 20 h period [134] and *S. cerevisiae* was cultured for 30 h [164]. An example of fed-batch mode is given by Wilming et al. [146], where the glucose was released at different feed concentrations in cultures for up to 48 h. All recent advances in microscale continuous reactors have been aimed at developing chemostats, but there are other continuous modes, such as the turbidostat. Situations where cells need to be studied at steady state under very high cell densities, in non-nutrient limited environments, or under dynamically controllable environmental conditions are not possible with chemostat systems because they rely on a constant flow of media to gradually reach steady state. In contrast to chemostat operation, turbidostat operation allows one to study the metabolic behaviour of cells in washout conditions, such as during overflow metabolism and at the maximum growth rate in a steady state [71].

Different cell adhesion surface modifications of PDMS or PMMA were examined. Yamamoto et al. [153] coated the walls of flow channels and reaction chambers with a derivative of the phospholipid polymer, MPC-silane (poly (2-methacryloyloxyethyl-phosphorylcholine-co-3-methacryloyloxypropyl-trimethoxysilane)) to prevent protein adsorption and to ensure that the internal walls of the reaction chamber chip were hydrophilic for easy injection of reagents. Another example of coating to effectively reduce *E. coli* cell adhesion and cell wall-growth was presented by Zhang et al. [161]. In this case, the surfaces were coated with poly(ethylene glycol) (PEG)-grafted poly(acrylic acid) (PAA) copolymer films on PDMS and PMMA surfaces. Another approach consists of periodically flushing a lysis buffer to expel the cells it contains, including any wall-adhering cells [6].

Growth and reaction processes are measured using optical fibre OD and pH using a fluorescence-based measurement system. Lee et al. [70] developed a system of four parallel reactors (100 μL) based on peristaltic devices. Mixing was implemented via microtechnologically integrated peristaltic chambers made of PDMS that were continuously and alternatively activated by integrated injection valves. The process control was completed by online analytics for DO, pH, and OD. To control the pH in each reactor chamber, the LoC provided integrated reservoirs for the containment of acids and bases. The results of the cultivation of *E. coli* in the microchips were similar to those for 2 L stirred tank reactors. Another

example of a LoC system based on continuous absorbance measurements is presented by Demming et al. [26]. The chip has PDMS-segmented waveguides and microoptics for the local and continuous quantitative detection of biological samples.

A diffusion-based MBR (5–50 µL) was fabricated by Zanzotto et al. [158]; cultivation of *E. coli* was performed in circular PDMS chambers that were supplied with oxygen through the PDMS membrane, thus allowing stable chemostat operation. The principle of fluid perfusion was used for the cultivation of *S. cerevisiae* and *E. coli* by Groisman et al. [40]. In total, 340 parallel chambers with a volume between 0.05 and 0.1 nL were connected via capillaries with a central perfusion channel. Due to their small dimensions, the capillaries were impermeable for the cells. The chambers were loaded with cells by pressure, resulting in wide channels. Due to the small size of these channels, washout of cells was not possible; thus, the MBR behaved similarly to a chemostat with cell retention. The medium flowed through the channels for nutrient supply to the cells at a flow rate of 0.3 µL h^{-1}. Both the morphology and cell density and therefore the resulting specific growth rate could be determined from a time series of micrographs.

An important step is the disinfection or sterilisation of the MBR before cell inoculation and any possible re-use to ensure monoseptic operation without contamination. Common methods include disinfection with 70 % ethanol for 30 min, UV irradiation at a distance of 5 cm with a powerful mercury lamp for 10 min, the use of 70 % isopropanol and 10 % sodium hydrogen fluoride or the use of gamma-radiation [84, 104, 113]. Additionally, autoclaving the MBR at 121 °C is used for sterilisation of the cultivation approach [136, 149]. Another approach combines the sterilisation step with the manufacturing process and uses the sterilising properties of the used O_2 plasma; the reactor lid is combined with the base due to surface activation from the overall bond system [117]. Due to the implemented sensitive online analytics, such as the fluorescence-based pH spots, the current sterilisation method cannot be applied in some cases. Here, the addition of antibiotics to the growth medium of a suitably resistant strain ensures monoseptic culturing [158].

To ensure the reproducibility of the OD, the inoculation procedure must be standardised. In the previously mentioned 150 µL MBR [134, 158] 3 mL of inoculum ($OD_{600\ nm} = 0.05$) at homogeneous mixing was added continuously for 20 min with the aid of a magnetic stirrer. This strategy was followed for both *E. coli* as well as *S. cerevisiae*. An OD of 8 was achieved after 10–15 h at an initial substrate concentration of 8 g L^{-1}.

To accommodate biological reaction kinetics from stationary process data of a chemostat cultivation, a passive aerated hMBR system with integrated online measurement technology for OD and DO was developed. As a model organism, the hydrophobic *S. cerevisiae* DSM 2155 was used [32]. The hMBR was made of a glass bottom and a soft PDMS lid that was microstructured using UV depth lithography. The chamber height was 230 µm, resulting in a reactor volume of 10 µL. The hMBR was implemented in a suitable test system consisting of an incubation chamber with corresponding measurement and control components, a syringe pump system, an interface for data collection and a sampling system.

To perform HTP temperature profiling Kunze et al. [66] presented a system with a customised temperature control unit for 96-well MTPs. This system allows a rapid characterisation of temperature-dependent reaction processes.

Related to the position of the MBRs, several hMBRs operating in batch, fed-batch, and continuous modes have been reported during the 2000s. However, as mentioned previously, the disadvantage of the hMBR is that microbubbles can block the microfluidic devices. These bubbles destroy the stable laminar flow and cause channel obstruction and thus affect the cell viability. It is not easy to eliminate the bubbles, so an alternative for hMBRs is to generate vMBRs; in vMBRs, the flow goes in a vertical direction, and bubbles are inherently released by buoyancy and by hydrostatic forces (see Sect. 4.4.2) [23, 24, 111].

With the developments of MBR systems in the sub-microlitre range, it was possible to study cellular heterogeneity in populations; thus, in recent years, focus was drawn to single-cell analysis [80, 92]. The heterogeneity of populations is partly based on the stochastic nature of the response behaviour of individual cells as a reaction to changes in the microenvironment (e.g., nutrient limitations and concentration gradients [68] as well as the presence of toxic components or the induction of heterologous protein production [73]). This heterogeneity greatly affects the productivity of the overall process. With the development of powerful microfluidic tools, single-cell cultivation is now in a position to evaluate the distribution of a cellular response within a cell population using a large number of parallelised approaches. This type of evaluation can ensure that data are generated that provide a much more nuanced picture of a cell population, which is not yet possible using measurements of averaged process parameters for an entire cell suspension.

Exemplary publications of individual, single-cell cultivations besides those already mentioned above [40] include the work of the Kohlheyer group [41–43], who developed a bioreactor with a chamber volume in the picolitre range. Probst et al. [112] have shown the parallel operation of a reactor and described a simple, rapid, and reproducible method for microbial cell inoculation, in which the cultivation takes place only under diffusive culture conditions, while the supply in the adjacent supply routes—similar to Lee et al. [72] for human cancer cells (see Table 4.2)—is carried out by convective flow.

The previously discussed MBR devices for bacterial cultivation applications are summarised in Table 4.1.

4.3.2.2 Mammalian/Human Cell Cultures

Breslauer et al. [13] reviewed relevant microfluidic devices for performing single-cell studies to isolate individual cellular responses for mammalian and human cell cultivation. El-Ali et al. [33] provided an overview of MBRs, particularly highly integrated components, e.g., devices that included growth, treatment, selection, lysis, separation, and analysis in a single system.

Table 4.1 Overview of the developed MBR systems: bacterial cell cultivations

Reference	Type	Mode of operation	Volume	Organism	Application	Material	Mixing	Aeration	Implemented sensors
Yamamoto et al. [153]	Micro-reactor array	Batch	Eight chambers × 125 nL	*Escherichia coli*	HTP cell-free protein synthesis	PDMS and glass		Passive aeration via diffusion	T control chip, intensity of GFP and BFP fluorescence
Maharbiz et al. [84]	MBR array	Batch	250 µL	*Escherichia coli*	Electrolytic gas generation as a key component for aeration in a miniaturised bioreactor array	Plastic microplate strips, commercially fabricated printed circuit board, gold wire, and a silicone membrane	Mixed via external shaker	Passive aeration via diffusion	OD (array of 580 nm LEDs, AND, AND50A ultra-bright orange surface mount LED) and detectors (Silicon photodiodes, PDB-C154SM; Photonic Detectors, Simi Valley, USA), pH (ISFET sensor chip, Sentron Europe, The Netherlands), T control via buried thick film thermistors and heaters under each well
Peng and Li [108]	3D flow controlled microchip	Continuous fresh medium	15 µm deep channels with 15 µm radius of the arc slope	*Saccharomyces cerevisiae*	Cell scanning, and single-cell fluorescent measurement on a single yeast cell, but could also be applied to mammalian cells	Glass	3D flow (driven by electric potentials)		Flow field (optical microscopy, inverted microscope (Nikon TE 300) with a dual-image module (Nikon))
Zanzotto et al. [158]	Membrane-aerated MBR	Batch	5 and 50 µL	*Escherichia coli*	Reproduce growth kinetics, observed in bench-scale volumes, in MBR	PDMS and glass	Diffusion	Passive aeration via diffusion	DO (PSt3, PreSens, Germany), pH (HP2A, PreSens, Germany), OD (orange LED,

(continued)

Table 4.1 (continued)

Reference	Type	Mode of operation	Volume	Organism	Application	Material	Mixing	Aeration	Implemented sensors
									Epitex L600-10 V, 600 nm, Japan), LEDs and photo-detectors (PDA-55, Thorlabs, USA)
Balagaddé et al. [6]	Micro-chemostat	Continuous	6 × 16 nL	*Escherichia coli*	Monitor the programmed behaviour of bacterial populations during long cultivation time	PDMS	Diffusion	Passive aeration via diffusion and through the influx of fresh medium	Optical microscopy (Nikon TE 2000, Heinze, USA)
Groisman et al. [40]	Micro-chemostat in an array	Continuous	340 µL chambers (100 µm width × 70–200 µm length × 6 µm height)	*Candida albicans*, *Escherichia coli*, *Saccharomyces cerevisiae*, *Staphylococcus epidermidis*, *Pseudomonas aeruginosa*	Grow cell colonies to high density starting from as few as one cell, and monitor them for extended periods of time at a single-cell resolution	PDMS and glass	Through the influx of fresh medium	Passive aeration via diffusion	Colony growth (series of fluorescence images), T (infrared camera)
Szita et al. [134]	Multi plexed MBR	Batch	150 µL	*Escherichia coli*	Demonstrate the reproducible performance of the multiplexed system	PMMA and PDMS	Magnetic spin bar	Passive aeration via diffusion	Cell density and morphology with single-cell resolution (optical microscopy, Nikon TE 2000, Heinze, USA)
Zhang et al. [164]	MBR with integrated optical sensors	Batch	150 µL	*Escherichia coli*, *Saccharomyces cerevisiae*	Reproducible growth kinetics observed in conventional experiments	PMMA and PDMS	Ring-shaped magnetic stir bar	Passive aeration via diffusion	DO (PSt3, PreSens, Germany), pH (HP2A, PreSens, Germany), OD (orange LED, Epitex L600-10 V,

					in microbatch bioreactors				600 nm, Japan), LEDs and photodetectors (PDA-55, Thorlabs, USA)
Boccazzi et al. [11]	MBRs equipped with internal stirring	Batch	150 µL	*Saccharomyces cerevisiae*	Demonstrate the reproducible performance of differential gene expression analysis	PMMA and PDMS	Ring-shaped magnetic stir bar	Passive aeration via diffusion	DO (PSt3, PreSens, Germany), pH (HP2A, PreSens), OD (orange LED, Epitex L600-10 V, 600 nm, Japan), LEDs and photodetectors (PDA-55, Thorlabs, USA)
Lee et al. [70]	MBR array with integrated mixers	Batch	100 µL	*Escherichia coli*	Provide a platform for the study of the interaction of microbial populations with different environmental conditions	PDMS	Peristaltic oxygenating mixer	Peristaltic oxygenating mixer	pH control (injecting base or acid into the growth wells), DO control (varying the oxygen concentration of the peristaltic oxygenating mixer actuation gas), OD
Zhang et al. [161]	Microchemostat	Continuous	150 µL	*Escherichia coli*	Microchemostat as effective tool for investigations of cell physiology and metabolic rates	PMMA and PDMS	Ring-shaped magnetic stir bar	Membrane-aerated	DO (PSt3, PreSens, Germany), pH (HP2A, PreSens), Thermocouple (TP- 2444, TE Technology), T control (TC-24-10, TE Technology, USA), OD (orange LED, Epitex L600-10 V, 600 nm, Japan), LEDs and photodetectors (PDA-55, Thorlabs, USA)

(continued)

Table 4.1 (continued)

Reference	Type	Mode of operation	Volume	Organism	Application	Material	Mixing	Aeration	Implemented sensors
Zhang et al. [163]	MBRs integrated with automated sensors and actuators	Batch, fed-batch, continuous	150 µL	*Escherichia coli*	Demonstrate the feasibility of culturing microbial cells, in MBRs	PMMA and PDMS	Ring-shaped magnetic stir bar	Passive aeration via diffusion	DO (PSt3, PreSens, Germany), pH (HP2A, PreSens), LEDs and photodetectors (PDA-55, Thorlabs, USA)
Schäpper et al. [123] (review)	Review about suspension MBR	Batch, fed-batch, continuous	50–800 µL	*Escherichia coli*, *Saccharomyces cerevisiae*	Mimic typical bench-scale reactors	PMMA, PDMS, glass, silicon	Passive (molecular diffusion, chaotic advection), active (stirrer bar, steel beads, air cushions), recirculation, arranging inlet/outlet	Passive aeration via diffusion	Single sensor or combination of multiple sensors: T measure (RTD), T controller (Minco, Fridly, USA, CT325TF1A5), CO_2 in the off-gas (sensor spots, PreSens, Germany or sensor based on a fluorescent dye), pH (optical sensors based on fluorescence sensor spots), DO (optical sensors with the use of fluorescence sensor spots), OD (with LED), analyte concentration (through spectroscopy)
Edlich et al. [32]	Diffusion-based MBR	Continuous	8 µL	*Saccharomyces cerevisiae*	Work in parallel and continuous modes to study the growth kinetics of *S. cerevisiae*	PDMS and glass	Diffusion	Passive aeration via diffusion	DO (PreSens, Germany), OD (orange LED and a photosensor)

Schäpper et al. [122]	Aerated single-use MBR	Batch, continuous	100 µL	*Escherichia coli*, *Saccharomyces cerevisiae*	Research and development in a screening and in a production environment with a cheap, easy-to-use and disposable MBR	PDMS	Small magnetic stirrer bar	Diffusion	OD (yellow LED, L600-10 V, Epitex, Japan and NT45-317 Edmund Optics, UK), DO (sensor spot, SP-PSt3-NAU-D4-YOP, PreSens, Germany), pH (blue LED, 465 nm, NSPB500S, Nichia Corporation, Japan), T (Pt100 sensor, JUMO, Germany)
Demming et al. [25]	Parallel MBR with grid structure engraved on each chamber	Batch, continuous	5 chambers × 9 µL	*Aspergillus ochraceus*	Monitor the different germination behaviours of submerged cultivated spores	PDMS and glass		Passive aeration via diffusion	Temperature-controlled incubation chamber which is constructively adapted to microscope dimensions, T controller (KT4, Panasonic, Osaka, Japan), switch cabinet heating system (RO/SE, Bad Birnbach, Germany) and a Peltier element (Quick-Cool QC 127-1.4-8.SMD, Quick-Ohm Küpper, Wuppertal, Germany), MBR located under an optical microscope (Axioskop, Zeiss, Jena, Germany)

(continued)

Table 4.1 (continued)

Reference	Type	Mode of operation	Volume	Organism	Application	Material	Mixing	Aeration	Implemented sensors
Demming et al. [26]	MBRs with segmented waveguides	Continuous	11 µL	*Saccharomyces cerevisiae*	Local absorbance measurement and continuous cell monitoring. Study of either the spatial or the temporal evolution of a given analyte	PDMS and glass		Passive aeration via diffusion	Temperature (heating plate consisting of a foil heater (Minco Europe GmbH, Germany) and a Pt-100 thermo couple (Heraeus Sensor Technology, Germany), optical characterisation through the microspectrometer HR4000 (Ocean Optics, Dunedin, USA)
Lee et al. [71]	Microfluidic chemostat	Batch, continuous (chemostat and turbidostat)	1000 µL	*Escherichia coli*	Characterise production of different acids and/or products and determine yields. Characterisation of cell dynamics or induce chemically dependent responses	PDMS and plastic	Peristaltic mixer	Passive aeration via diffusion	pH sensor spots (Presens, Germany) Oxygen sensor, spots in the base of the growth chamber sections, T control (closed loop PID), OD (LEDs and fibres)
Demming et al. [24]	Vertical microbubble column (µBC)	Batch	70 µL	*Saccharomyces cerevisiae*	Validate the scalability from laboratory scale to microscale, and demonstrate the successful application of the µBC as a screening instrument	PDMS and glass	Mixing thanks to the generation of microbubbles	Rising microbubbles of air or oxygen	OD with integrated optical fibre sensors (Ocean Optics, Germany), bubble formation, T (integrated heating structures made of indium tin oxide (ITO))

Moffitt et al. [92]	Single-cell chemostat based in agarose	Continuous	1 µL	*Bacillus subtilis*, *Escherichia coli*, *Enterococcus faecalis*	Study the natural heterogeneity in growth and gene expression	PDMS	Diffusion	Passive aeration via diffusion	Bacterial growth (through optical microscopy with a home-built phase-contrast microscope and SEM, Supra55VP, Zeiss, Germany)
Grünberger et al. [41, 42]	Picolitre bioreactor for single-cell analysis	Continuous	1 pL	*Corynebacterium glutamicum*, *Escherichia coli*	Cultivation of bacteria on single-cell level to study population heterogeneity	PDMS	Diffusion	Passive aeration via diffusion	Number of cells and cells size (DIC microscopy images and fluorescence images, Nikon NIS Elements AR software package, Japan), production studies (FACS)
Hegab et al. [45] (review)	Review about suspension MBRs	Batch, continuous	1–1000 µL	*Aspergillus ochraceus*, *Candida utilis*, *Cyclotella cryptica*, *Escherichia coli*, *Methanosaeta concilii*, *Pichia stipites*, *Saccharomyces cerevisiae*, *Tetraselmis chuii*	Mimic typical bench-scale reactor, quorum sensing investigation	PMMA, PDMS, PC, glass, silicon	Small magnetic stir bar, pressure-based recycle flow, pressure-based oscillating driving force	Passive aeration via diffusion	Single sensor or combination of multiple sensors: T (electrochemical sensors), pH and DO measure (fluorescence lifetime-based sensors), OD, CO_2 in the off-gas, analyte concentration (through spectroscopy), pH control (addition of CO_2 and NH_3 gases)
Kirk and Szita [60] (review)	Review about passive aerated MBRs via PDMS membranes	Batch, fed-batch, continuous	5–1000 µL	*Escherichia coli*, *Saccharomyces cerevisiae*	Compare DO transport performance	PMMA, PDMS, glass base	Small magnetic stir bar, pneumatic peristaltic, shaken device, diffusion	Diffusion	Single sensor or combination of multiple sensors: DO and pH sensor spots (not specified), OD or

(continued)

Table 4.1 (continued)

Reference	Type	Mode of operation	Volume	Organism	Application	Material	Mixing	Aeration	Implemented sensors
									backscattered light (biomass)
Long et al. [80]	Micro-fluidic chemostat	Continuous	600 channels 13–20 µL (20 µm long × 0.6–0.9 µm wide × 1.1 µm deep)	*Escherichia coli*	Measure the bacterial growth dynamics, such as growth rate, cell sizes and GFP expression, at the single-cell level for a long time	PDMS	Diffusion	Passive aeration via diffusion	Growth rate and GFP expression (optical microscopy with inverted microscope, Leica DMI-4000B, Germany)
Park et al. [106]	Micro-chemostat array	Continuous perfusion	Array 8 × 250 nL	*Saccharomyces cerevisiae*	Study and monitor metabolic profiling/screening, drug response of microorganisms or conduct massive parallel testing of competing microbes	PDMS	Diffusion	Passive aeration via diffusion	Cell density (microscopic images, Nikon America, USA)
Grünberger et al. [43]	Micro-fluidic single-cell analysis systems	Batch	Picolitre scale	*Bacillus subtilis*, *Corynebacterium glutamicum*, *Enterococcus faecalis*, *Escherichia coli*, *Hansenula polymorpha Lactobacillus lactis*, *Pichia pastoris*, *Schizosaccharomyces pombe*	Collect information on industrially applicable production hosts with single-cell resolution	PDMS and glass	Diffusion	Passive aeration via diffusion	Population heterogeneity (fluorescence imaging)
Kunze et al. [66]	MTP for HTP temperature profiling	Batch	96 wells × 200 µL	*Escherichia coli*, *Kluyveromyces lactis*	Tool for rapid characterisation of temperature-	96-well lumox multiwell plates (Greiner Bio-One, Germany)	Mixed via external shaker	Aeration by pressurised air	Online monitoring with BioLector (m2p-labs, Germany), T (via fluorescent dyes

					dependent reaction processes				a mixture of Rhodamine B (RhB) and Rhodamine 110 (Rh110))
Peterat et al. [111]	Vertical micro-bubble column (μBC)	Batch	70 μL	*Saccharomyces cerevisiae*	Characterisation of mass transfer (k_La, OTR), submerged aerobic cultivation	PDMS and glass	Mixing thanks to the generation of microbubbles	Rising microbubbles of air and passive aeration via diffusion	OD (HL-2000-HP-FHSA, Ocean Optics, Germany), DO (NTH-PSt1-L2.5-TF-NS40/0.4-OIW, Presens, Germany), T (custom-made incubation chamber)
Probst et al. [112]	Parallel picolitre cultivation chambers	Continuous	1000 μL chambers (40–50 μm width × 60 μm long × 1 μm height)	*Corynebacterium glutamicum*	Fast and gentle cell transfer from pre-culture to the main microfluidic chip culture using an entrapped nanolitre-sized air bubble	PDMS	Diffusion	Passive aeration via diffusion	Particle trajectories and cell growth (inverted time-lapse microscope, Nikon TI-Eclipse, Nikon, Japan)
Wilming et al. [146]	Disposable MTP system	Fed-batch	44 wells × 40–200 μL	*Escherichia coli*, *Hansenula polymorpha*	Perform a primary screening of different strains, media, and process conditions at an early stage of process development	PMMA	Mixed via external shaker		Online monitoring with BioLector (m2p-labs, Germany)
Lattermann and Büchs [69] (review)	Review about MBRs and MTPs	Batch, fed-batch	<1000 μL	*Aspergillus terreus*, *Corynebacterium glutamicum*, *Escherichia coli*, *Hansenula polymorpha*, *Pichia pastoris*, *Rhizopus oryzae*,	Characterisation of mass transfer (k_La, OTR)	Elastomers, plastic or hydrogels	Mixed via external shaker	Different aeration strategies (not specified)	BioLector system with T controller (m2p-labs, Germany); MicroFlask system (Applikon, The Netherlands), pH, DO, CO_2 and product formation and biomass, (through

(continued)

Table 4.1 (continued)

Reference	Type	Mode of operation	Volume	Organism	Application	Material	Mixing	Aeration	Implemented sensors
				Schizosaccharomyces pombe, *Trichoderma reesei*					fluorescence and scattered light measurements), oxygen determination in the cytosol of living cells (sensor based on Förster resonance energy transfer)

The majority of the MBRs that are currently available for mammalian/human cell culture research are based on perfusion [72, 74, 136, 137]. The advantage of perfusion-based devices in contrast to (batch shaken) cell culture systems (microwell plate) is that they can continuously provide nutrient supply and waste removal and thus provide a more stable culture environment. In general, the morphological dependencies of cells were examined in different MBR geometries to screen the effect obtained after the addition of various toxins and active pharmaceutical ingredients.

The selective retention of cells and the generation of nutrient gradients were implemented in an MBR using microstructured reactor internals with animal cells (such as fibroblasts, epithelial cells, and hepatocytes) [113]. With this MBR, the possibility should be created to cultivate animal cell cultures under different environmental conditions and to investigate morphological parameters more accurately.

For monitoring animal cell cultures, the most common technique is image analysis; some approaches also monitor the metabolism and cell behaviour at different growth stages. Therefore, development phases can be investigated in situ and in real time [74, 121].

The MBR of Kim et al. [57] with a working volume of 100 μL is a further MBR development for mammalian cell cultures and is configured to mimic proposed large-scale operating conditions. Moreover; this MBR has the potential to support HTP studies.

To adjust the surface of MBRs for cell adhesion, Rhee et al. [117] developed a method that enables patterned cell culture inside microfluidic devices by allowing the patterning, fluidic bonding, and sterilisation steps to be performed in a single step. This method offers a convenient technique to micropattern biomaterials for selective attachment of cells on the substrates.

Apart from the particular situation where the adhesion of cells directly to the surfaces of the microfluidic system is desired [132], current research tends toward 3D microenvironments to mimic more precisely the in vivo conditions. For example, Wu et al. [147, 149] reported a 3D perfusion-based cell culture platform in which chondrocytes and cancer cells are incorporated in a 3D agarose matrix. The applications illustrated here, which describe microcell culture devices, only represent a selection. The fact that microfluidic cell culture systems are of high interest in drug research is clear from the recently published reviews [91, 148]. In these articles, cells tend to exhibit adherent growth on surfaces (2D) as well as in cell associations (3D). It is interesting to notice that online elements within these types of cell culture microenvironments have rarely been implemented. In most of the cases, the morphology and growth rates were quantified via microscopic determination.

Because animal cell cultures have special requirements for the homogenisation of the components due to their high shear sensitivity, attempts have been made to reproduce either the perfusion or tissue configuration characteristics of the bloodstream. The tested cell cultures tended to exhibit adherent growth both in fluidised cell agglomerates and on hard, flat reactor surfaces. The MBRs either retain cells

specifically by means of integrated microbarriers [113, 137] or by diffusion rings that are based on processes using two lithographic steps [70, 72]. Lee et al. [72] developed a culture chamber that was divided into two flow regions, a faster convective "blood" flow and a diffusion-dominated "interstitial" space for cell growth. Lee et al. [70] used the MBR for the cultivation of mammalian tumour cells consisted of 64 parallelised culture chambers (3 nL each) with an outer convective nutrition ring (flow rate of 12–24 μL h^{-1}) and an inner reaction compartment. Diffusion-controlled nutrient supply was attained by a 2 μm gap of the ring. The specific growth rates and the adhesion of different cell lines were determined using OD and microscopy, respectively.

A similar type of MBR system (reaction volume of 6 nL) consists of an array of 100 microfluidic chambers, which are radially surrounded by a variety of perfusion channels (smaller than the respective cell diameter) [51]. In this MBR, mammalian tumour cells were also cultured using a perfusion stream of 12 μL h^{-1}. Kinetic parameters, such as the specific growth rate depending on the perfusion rate, can be determined from the cell density by phase-contrast microscopy.

Ostrovidov et al. [104] developed a membrane-based MBR with a reaction volume of 10 μL. The reactor chamber was divided by a membrane into two compartments. In one compartment, the cultivation medium flowed convectively, and the second compartment served as a diffusion-controlled nutrient supply to hepatocytes. The kinetic parameters and the amount of different cell or medium components (including albumin and ammonium) were determined. Furthermore, morphological studies on cell adhesion could be performed on different surfaces with this system.

The previously discussed MBR devices for mammalian/human cell applications are summarised in Table 4.2.

4.3.3 Materials and Microfabrication Technologies

The fabrication of MBRs is essentially based on conventional micromachining technology. However, to meet the requirements for microbial cultivation at the microscale—such as optical transparency, biological and chemical compatibility, low production costs and fast prototyping—specific materials (glass and polymers) and processes adapted to these materials have to be applied. In fact, the two examples of MBRs described in detail in the following section consist of patterned PDMS layers bonded to a glass substrate. The PDMS elements are fabricated via replica moulding using negative master structures manufactured from the photoresist EPON SU-8. An advantage of PDMS is the fact that oxygen can be supplied to the cell cultures in the MBR by gas diffusion through the permeable material. In addition to these structural materials, a variety of functional structures can be used in MBRs, for example, gold electrodes for retention time measurements, indium tin oxide (ITO) thin film heaters for temperature control, optical filters or emitters based on dyed sol–gel glass and antiseptic PDMS composite elements based on

Table 4.2 Overview of the developed MBR systems: mammalian/human cell cultivation

Reference	Type	Mode of operation	Volume	Organism	Application	Material	Mixing	Aeration	Implemented sensors
Prokop et al. [113]	Nanolitre bioreactor	Batch, fed-batch, continuous	10–100 nL	CHO cells, fibroblast cell line, hepatocytes	Growth and maintenance of several hundred cultured mammalian cell populations in volumes three orders of magnitude smaller than those in standard multiwell screening plates	PDMS	Diffusion	Passive aeration via diffusion	pH, glucose and picocalorimetry (fabricated using an immobilised enzyme technology, Nafion coating, and electrochemical principles)
Hung et al. [51]	Micro-fluidic cell culture array	Continuous perfusion	10×10 array of microchambers (40 µm height $\times$ 1 mm diameter)	HeLa human cancer cells	HTP cell-based biological experiments integrating temperature control, fluid handling, and optical detection into a self-contained system	PDMS	Perfusion	Passive aeration via diffusion	
Ostrovidov et al. [104]	Membrane-MBR as a scaffold for the attachment of cells	Continuous	Chamber (10 mm $\times$ 10 mm $\times$ 100 µm)	Primary adult rat hepatocyte	MBR suitable for maintaining the structures and functionality of hepatocyte, properly mimicking the in vivo liver architecture	Commercially available polyester membrane, PDMS	Perfusion culture	Perfusion culture	
Lee et al. [72]	Nanolitre scale MBR array	Continuous perfusion	8×8 array of 3 nL	HeLa human cancer cells	Enable uniform cell loading, eliminating shear and pressure stresses on cultured cells, providing stable	PDMS	Perfusion	Passive aeration via diffusion	Reagent concentrations (determined by measuring the steady-state fluorescence intensity of a tracer dye (FITC))

(continued)

Table 4.2 (continued)

Reference	Type	Mode of operation	Volume	Organism	Application	Material	Mixing	Aeration	Implemented sensors
					control of fluidic addressing, and permitting continuous on-chip optical monitoring				
Thompson et al. [136]	Micro-channels and cell chambers as a living cell array	Continuous flow	Chamber (500 µm width × 50 µm height)	HeLa S3 cells	Control dynamic inputs and measure dynamic outputs from adherent mammalian cells in a high-throughput fashion	PDMS and glass	Diffusion	Perfusion culture	Fluorescent images (Metamorph V 6.0r4, Universal Imaging Corp., USA)
Rhee et al. [117]	Patterned microfluidic device	Batch (with exchange of nutrients and gas)	Three compartments <1 µL	Human umbilical vein endothelial cells (HUVEC), MDA-MB-231 breast cancer cells, NIH 3 T3 mouse fibroblasts, primary rat cortical neurons	Plasma-based dry etching approach that enables patterned cell culture inside microfluidic devices	PDMS	Exchange of nutrients and gas, diffusion	Exchange of gas	
Spence et al. [132]	Microchip channel for cell immobilisation	Batch	~370 nL	Bovine pulmonary artery endothelial cells	Help to define the exact roles of ATP and nitric oxide in the control of vascular calibre	PDMS		Passive aeration via diffusion	NO (detected amperometrically at a carbon-ink microelectrode that is modified with sulfonated Polytetrafluoroethylene (Nafion)
Breslauer et al. [13] (review)	Single-cell systems	Perfusion flow	Nanolitre scale	Bovine capillary endothelial (BCE), breast cancer cell chemotaxis, fibroblasts, HeLa cells, hepatocytes, rat	Review about microfluidic devices to perform single-cell studies to isolate individual cellular		Diffusive mixing		Single components or combination of multiple components: Filtration, electrophoresis, PCR, cell isolation, lysis, DNA/mRNA

				neural stem cells, etc.	responses for mammalian and human cell cultivations: single-cell studies, studies of intracellular systems, study of cell–cell communication, spatio-temporal characterisation of molecular and cellular events and HTP studies				purification, and recovery in a microfluidic platform
El-Ali et al. [33] (review)	Review of MBRs for human/mammalian cells	Perfusion flow	Nanolitre scale	Drosophila cells, hepatocytes, human neuronal stem cell, MDA231 cancer cells, osteoblasts, etc.	HTP combined with the integration of sample preparation and separation steps, resulting in applications for genomics and proteomics	PDMS and glass	Diffusive mixing	Passive aeration via diffusion	Single sensor or combination of multiple sensors: pH, DO and biomass, cell lysis, sample fraction, biosensors, drug screening, genetic analysis, single-cell analysis
Wu et al. [149]	MBR with a scaffold made of agarose gel	Continuous flow	Five cylindrical chambers (2 mm diameter × 200 μm height)	Chondrocytes	Provide a well-defined and homogenous culture environment to study the links between cell physiology and extracellular conditions	PDMS	Perfusion culture	Diffusion	pH, not on the chip → lactate production (Lactate Reagent Kit, Trinity Biotech Plc., Ireland), glycosaminoglycan production (colorimetric reaction), cell number (by DNA assay)
Wu et al. [147]	Micro-fluidic 3D cell (in agarose	Continuous perfusion	30 MBR (900 μm diameter × 220 μm in height)	Oral cancer cells	Create a more stable and uniform culture environment, enabling to	PDMS	Perfusion	Passive aeration via diffusion	

(continued)

Table 4.2 (continued)

Reference	Type	Mode of operation	Volume	Organism	Application	Material	Mixing	Aeration	Implemented sensors
	scaffold) culture platform				evaluate the links between the cellular responses to the culture conditions, cell viability (fluorescent dye kit and fluorescent microscopic images) (not on-chip)				
Meyvantsson and Beebe [91]	Micro-fluidic systems (cultures in suspension and in 3D)	Continuous		Cardiomyocytes, embryonic stem cells, endothelial cells, hepatic cells, human hepatocellular carcinoma cells, human neutrophils, mouse fibroblast neurons	Establish a complete microenvironment for human cells in culture to have in vitro models that would outperform both conventional cell culture models and animal models in predicting tissue-specific responses in humans	PDMS, PEG, glass, polycarbonate	Diffusive mixing	Perfusion of oxygenated media, passive aeration via diffusion	T, DO (oxygen-sensitive ruthenium dye), biosensors, amperometric sensors to detect quantal secretion of catecholamines, spectrometry for fluorescence analysis, microscopy
Satoh et al. [121]	Microchip	Batch	1 μL	Hepatocytes from rat	Cytofluorimetric assays and ammonia monitoring	PDMS and glass		Passive aeration via diffusion	Ammonia sensor commercial measurement kit (Ammonia-Test Wako, Wako Pure Chemical Industries, Japan), pH indicator
Toh et al. [137]	Micro-fluidic 3D hepatocyte chip	Perfusion culture	Eight parallel single-cell culture channels (1 μm length × 600 μm width × 100 μm height)	Hepatocytes from rats	Test in vitro drug toxicity to predict in vivo drug hepatotoxicity	PDMS	Perfusion	Passive aeration via diffusion	Reagent concentration, dead cells, albumin production (fluorescence images with a confocal microscope)

Wu et al. [148]	Micro-fluidic cell culture systems for drug research	Continuous	1 pL–1 µL	Human hepatocarcinoma cell, human liver microsome	Provide versatile approaches to regenerate more in vivo-like extracellular conditions, for more realistic cell-based drug research	PDMS	Perfusion	Passive aeration via diffusion	Effect of chemicals on the cell viability can be monitored via microscopic observation
Li et al. [74]	Micro-electrode array	Perfusion flow	Culture chamber (900 µm diameter × 150 µm height)	Human umbilical endothelial cell, neuronal differentiation of rat pheochromocytoma	HTP, labour-free, and automated or semiautomated technique for electrochemical detection on living cells	PDMS	Perfusion culture	Passive aeration via diffusion	Amperometric monitoring ∅of exocytosis from the cultured cells
Kim et al. [57]	MBR for animal cell culturing in suspension	Batch, fed-batch	100 µL	Chinese Hamster Ovary (CHO)	Mimic large-scale operating conditions for HTP studies	Polyacrylic acid housing and a polymethylpentene membrane	Pump cycles (the liquid receives a cyclic pressure signal so that it flows in the channels back and forth	Passive aeration via diffusion, aeration is also promoted by the pump cycles	DO (MI-730, Microelectrodes, USA) and a meter (OM-4), cell number through an hemocytometer (Bright-Line Hemocytometer, Hausser Scientific, USA)
Rodriguez-Rodriguez et al. [118]	Micro-fluidic device for antiproliferative drug screening	Perfusion flow	Five reactor chambers × 9 µL	Vascular smooth muscle cells from rat aorta	Evaluation of the anti-proliferative activity and cytotoxicity analysis of drugs in mammalian cell cultures	PDMS	Perfusion culture	Perfusion of oxygenated media, passive aeration via diffusion	Cell proliferation through image acquisition (CKX41 inverted microscope (Olympus, Japan) (×10 objective; NA 0.30) coupled to a SC30 digital camera (Olympus, Japan))
Muñoz-Berbel et al. [98]	Lab on a chip for cell culture	Perfusion flow	Incubation chamber: 0.42 cm diameter × 230 µm height,	Vascular smooth muscle cells from rat aorta	Cell proliferation and monitoring can be performed	PDMS and glass	Perfusion culture	Passive aeration via diffusion	pH indicator phenol red and absorbance through optical measurements

(continued)

Table 4.2 (continued)

Reference	Type	Mode of operation	Volume	Organism	Application	Material	Mixing	Aeration	Implemented sensors
			monitoring chamber: 0.5 cm diameter × 230 µm height		in separated chambers and secreted molecules could be measured in the monitoring chamber with highly energetic UV light sources without affecting cell proliferation				with a microspectrometer (USB2000, Ocean Optics, USA)

silver or copper nanoparticles. Additional functional materials, such as piezoelectric or magnetic components, are necessary to actuate peripheral microfluidic components, such as valves and pumps.

4.3.3.1 EPON SU-8 photoresist

The UV-sensitive epoxy-based negative-tone photoresist SU-8 has been specifically developed for high-aspect ratio lithography [81]. Cured SU-8 forms a highly cross-linked matrix of covalent bonds, resulting in glass-like mechanical properties and high chemical and thermal stability. Depending on the complexity of the three-dimensional PDMS structures to be replicated, the SU-8 masters are fabricated using single or double lithographic steps. Figure 4.1a outlines the double lithographic process [22]. First, a SU-8 adhesion layer is spun on a glass substrate, flood exposed to UV light and baked. Then, the first SU-8 structure layer is spun on the substrate, levelled, baked, and exposed to UV light while using a chromium mask containing the desired structures. The mask is aligned using metallic alignment structures on the bottom side of the substrate. After a post-exposure bake, the second SU-8 structure layer is spun on the substrate, levelled, baked, and exposed to UV light while using a second chromium mask, which is also adjusted using the

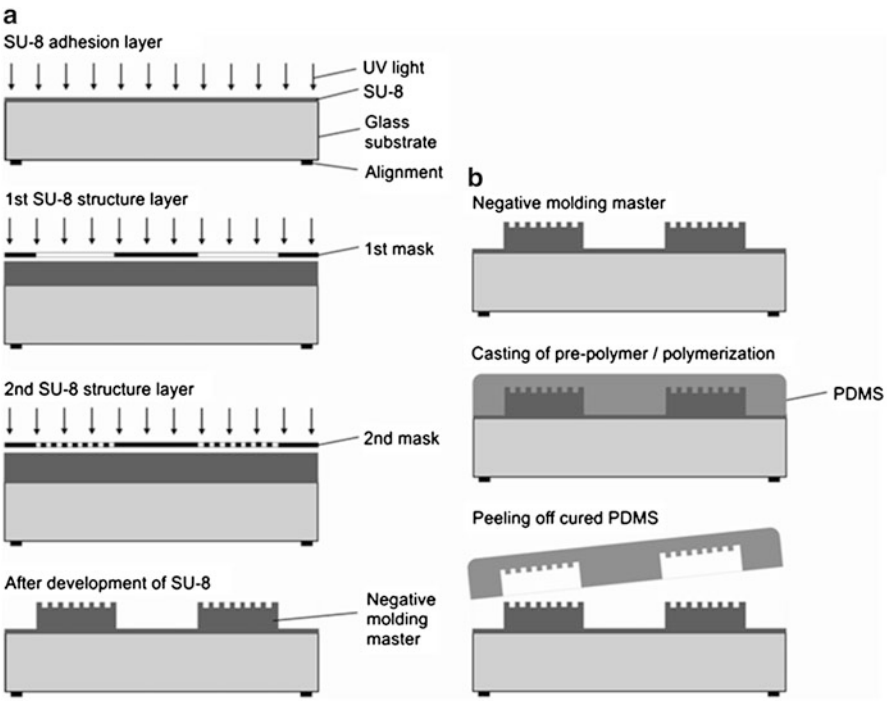

Fig. 4.1 (**a**) Fabrication process of a double structure generated using lithography and a negative SU-8 mould and (**b**) replica moulding process. Adapted from Demming [22]

alignment marks. After a post-exposure bake, the unexposed regions of the SU-8 are removed in propylene glycol methyl ether acetate.

4.3.3.2 Polydimethylsiloxane

PDMS is a flexible two-component polymer, which has many favourable properties, such as biocompatibility, chemical inertness, high optical transparency, thermal stability up to approximately 200 °C, and easy handling. PDMS elements are fabricated by replica moulding [151] using SU-8 master forms. The process is depicted in Fig. 4.1b. After the SU-8 mould is produced, the two components of the elastomer are mixed in an appropriate ratio. After degassing, the pre-polymer is poured onto the master form and cured at elevated temperature before it is peeled off from the master. For moulding of PDMS between two master structures, a double-sided moulding apparatus has been developed by Lucas et al. [83]. This technique allows, for example, for the fabrication of PDMS membranes with coplanar surfaces and defined thickness, which are frequently used in MBRs because they enable bubble-free oxygen transfer to the cultivation medium. The MBRs are assembled by combining one or more PDMS layers with each other and with a glass bottom via covalent bonding after surface activation in oxygen plasma. For a large degree of integration in MBR systems, the development of PDMS composites provides significant benefits. Optical filters based on ink-PDMS composites [77] and antiseptic surfaces based on silver and copper nanoparticle-PDMS composites [23] have been used. Further possibilities, particularly for microactuation, result from polymer magnets, in which microparticles of hard magnetic materials are suspended in a PDMS matrix [34].

4.3.3.3 Glass with Functional Structures

The glass substrate of the example MBRs allows for the integration of functional elements, such as metallic thin film structures, glass cavities for planar embedding of sensors or through holes for fluidic connections. Metallic thin film structures are fabricated by deposition of the material, typically by sputtering processes, and subsequent lithographic etching. In the case of ITO microheaters, an additional isolation layer, for example a silicon nitride layer, must be applied to prevent electrolysis. Glass cavities and through holes are conventionally manufactured by lithographic etching using a chromium-gold masking layer and a hydrofluoric etching solution. Alternatively, high-aspect ratio structures in glass can be fabricated by femtosecond laser radiation.

4.3.3.4 Sol–Gel Glass

Sol–gel glass, which is an organic–inorganic silicate-based glass featuring biocompatibility and chemical inertness, can serve as a rigid and compact matrix for the integration of nanoscale functional components, such as quantum dots as flexible emitters [22] or enzymes for application in biosensors [76]. In addition, sol–gel glass can be doped with polar dyes, which allow for the creation of optical filters and optical sensors, for example a phenol red-based pH sensor. The main steps of the sol–gel process are mixing, gelation and drying [47]. During the mixing step, the alkoxide precursor, for example tetramethyl-orthosilicate, is hydrolysed by mixing with water, and eventually—in a polycondensation reaction—sol particles are formed from the resulting hydrolysis products. During the gelation step, the sol particles link together to form a three-dimensional network (gel). During the drying step, the remaining liquid is removed, resulting in a solid xerogel. Sol–gel glass can also be used to fabricate optical structures, such as segmented waveguides. In this case, the sol–gel elements must be structured on the glass substrate of the MBR before the final bonding of the PDMS layer with the substrate. Different process technologies can be used to build the sol–gel components on the glass substrate, for example, the microtransfer moulding (μTM) technique [35], the micromoulding in capillaries (MIMIC) method [151] and a procedure using open fluidic-structured PDMS moulds [22].

4.3.3.5 Fluidic Interfaces

Apart from the standard electrical connections, fluidic interfaces are key components of MBR systems. Several requirements have to be met to guarantee the proper feeding of continuous, particle-laden fluids; these requirements include water tightness, small dead volume and stability under mechanical stress. Two basic geometrical designs can be used, a horizontal design with the inlet aligned with the flow direction and a vertical design with the inlet aligned at 90° to the flow direction. Vertical connections may be implemented, for example, by using O-rings [109], seal rings [62], miniaturised Luer-lock adapters [156] or magnet connectors [4]. Another method has been described by Chen et al. [19], who used needles glued to the inlet and outlet openings. A disadvantage of vertical connections is the dead volume in the 90° bends, which causes preferential particle settling when using particle-laden fluids. Horizontal connections can be achieved by press passings [115, 120], an integrated septum made of PDMS [79] and by the gluing of needles. The latter is a fast and reliable connection technology, especially for prototype disposables.

4.3.3.6 Microbioreactor System Platform

An MBR system comprises, aside from the actual MBR, peripheral microfluidic components (microvalves, micropumps, micromixers and microfilters, see

Sect. 4.3.3) and biosensors for the detection of educt and product concentrations. An MBR platform should allow for integration of all these single components. There are two ways of implementing such a system: modular or monolithic integration. A modular platform is composed of several components that each forms an individual functional system. As a result, the replacement of individual components and the integration of new components require a relatively minor expense. The main challenge of modular platforms is the fluidic connection between the single components. The fluidic interfaces must be optimised to avoid leakages and high dead volumes. The flexibility and performance of a modular platform can be considerably enhanced by the standardisation of chip and connection dimensions and the implementation of a plug-and-play concept [22, 156]. While the modular solution facilitates the development and prototyping of new systems, the more user-friendly monolithic platform is advantageous in the case of sufficiently mature systems. The monolithic platform integrates all necessary components on a single chip. The main advantages are the minimisation of chip space and the high performance due to direct fluidic connections featuring small dead volumes. The prerequisite is that the compatibility of different materials and process technologies must be taken into account even in the early design phase. Figure 4.2 shows an example of a monolithic chip [22] consisting of a glass bottom and two PDMS layers. The disadvantages of monolithic platforms are high production expenditure and the need to develop a completely new system if modifications shall be made.

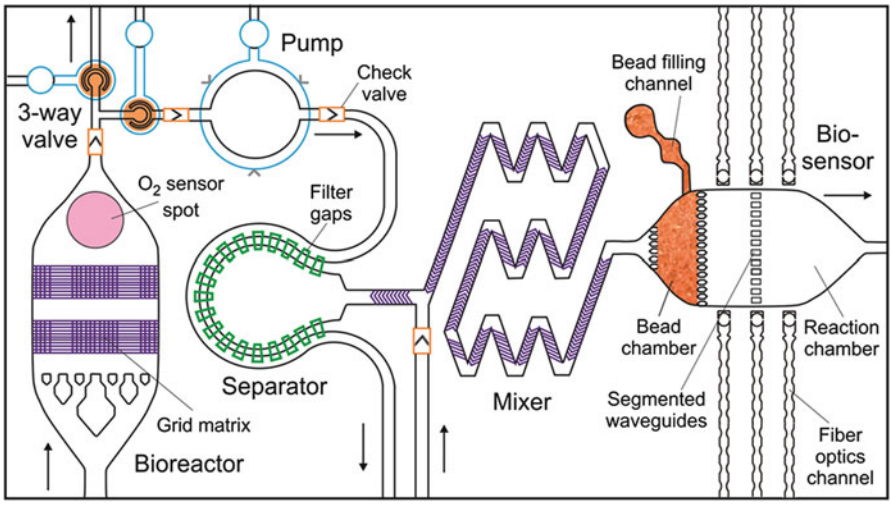

Fig. 4.2 Schematic of a monolithic microbioreactor system platform. The system consists of a structured glass chip, which is bonded to a PDMS sandwich composed of two layers. Each PDMS layer has up to three lithographic levels. The dimensions of the components are not drawn to scale. Adapted from Demming [22]

4.3.4 Peripheral Microfluidic Components

The MBR system, regardless of whether it is a modular or monolithic platform, requires several different peripheral microfluidic components for fluid guidance, preparation and processing. Sample preparation requires many different components between the MBR and the analysis sensor, as can be seen in the exemplary MBR system in Fig. 4.2. To analyse the products and educts of the bioprocess in the cultivation medium from the reactor, the sample must be collected. Therefore, the channel used for medium exchange needs to be closed by a microvalve, whereas a port or junction from the usual pathway needs to be opened by a second valve to allow sample collection. Then, a micropump is activated to generate a sample flow in the direction of the analysis section. Additionally, this pump must use two passive microvalves to define the direction of transport. Microorganisms that are cultivated inside the MBR can also be found in the collected sample. These microorganisms may alter the composition of the sample if they are still active or could hinder a precise measurement by the sensor. Thus, the microorganism must be separated from the sample using a filter or a different type of separator. In the example, a microseparator similar to a cross-flow filter is used. This separator consists of small microgrooves with a cross-section of only 2 μm × 5 μm, which allows fluid to pass through but retains the organisms. Afterwards, the retentate can be flushed out of the channel while the filtrate is further transported to the sensor. Depending on the type of sensor, additives must be added to the sample e.g., for an enzymatic reaction. In other cases, the sample needs to be diluted to reach the measuring range of the sensor. In the exemplary MBR system, an external port is connected to the fluid channel, which then leads to a mixing unit. While passing the mixer, the sample and additives become properly mixed to enter the sensor as a homogeneous fluid.

The design as well as the control of these peripheral devices should be kept as simple as possible to allow for proper and easy integration into a monolithic chip or a simple connection to a modular platform. This goal is particularly important if the MBR system incorporates many different functional devices or clusters of devices for diverse tasks. The four above-mentioned peripheral components (micropumps, microvalves, microseparators, and micromixers) will be discussed in more detail in the following.

4.3.4.1 Micropumps

Pumps ensure the fluid transport of the liquids (and gases) needed for the processes in the MBR system. The basic drive arrangement of micropumps differs enormously from that of macroscale pumps. At the microscale, surface effects dominate over volume effects due to the scaling law. Surface friction becomes a challenge for moving and rotating parts. The production of microscale bearings and gears is very complicated and very expensive. Therefore, different constructions need to be

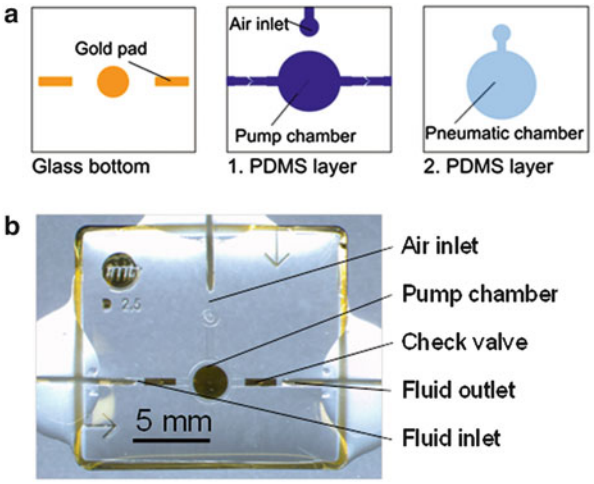

Fig. 4.3 (**a**) Schematic setup of a pneumatic micropump design consisting of a glass substrate and two PDMS layers and (**b**) image of the assembled micropump

considered in microtechnology. During the last years, several reviews on micropumps and valves in biological microelectromechanical systems (bioMEMS) have been published [3, 5, 101]. This section will illustrate and discuss one working principle as an example.

Most micropumps for bioMEMS use a membrane, which is deflected mechanically. This deflection leads to a volume displacement in a pumping chamber underneath the membrane and the expiration of fluid out of the chamber. Thereafter, the membrane is deflected in the opposite direction, whereby liquid is drawn into the pumping chamber. The displacement of this membrane can be generated by different types of actuators as pneumatics [52, 154], thermo-pneumatics [53, 59], hydraulics [75], piezoelectrics [38, 107], and electromagnetics [16].

Here, a pneumatically actuated pump shall be the reference system to explain the operation mode. The micropump shown in Fig. 4.3 is fabricated using two PDMS layers structured by soft lithography. Glass with a thickness of 700 µm is used as a substrate for the pump. Gold pads are structured by a photolithographic process on top of the glass. This process avoids bonding between PDMS and the substrate at specific regions. The first PDMS layer includes inlet and outlet channels for the fluid and also contains the pumping chamber. This layer is structured using a double-sided moulding apparatus [83] to obtain a 200 µm thick membrane and a flat surface for the bonding of the second layer. The second PDMS layer contains a pneumatic chamber, to which a positive or negative pressure (vacuum) is applied to achieve membrane displacement along the vertical axis. One check valve at the inlet and outlet channels of the fluid respectively defines the direction of flow and prevents backflow [22]. Alternatively, several pneumatic pumps are designed as peristaltic pumps using three-pump chambers, which are closed sequentially [147, 154]. This process prevents backflow, making the valves at the inlet and outlet unnecessary, and also allows for reversal of the pumping direction.

For most biological microfluidic systems, more than one pump is needed to transport several different fluids through the system. Wu et al. [147] presented a system containing 30 integrated micropumps on one chip. Important evaluation criteria for microfluidic pumps are a minimal and maximal flow rate, a counter pressure that can be overcome, the level of pulsation, and the dead volume.

4.3.4.2 Microvalves

Valves are necessary to guide the fluid, which is moved by pumps, through the microchannels of an MBR system. Several different designs of microvalves are described in the literature [103]. In general, these can be divided into two categories: active and passive. In the representative system in Fig. 4.2, sample collection is controlled by an active 3-way valve. The micropump in the systems defines the direction of liquid by passive check valves.

Many active valves for microfluidics have been constructed analogously to the micropump described above [70]. A peristaltic micropump with three-pump chambers transports liquid by closing each chamber sequentially and purges the liquid from one chamber to another. The first chamber remains closed while the second one becomes emptied, and this process prevents backward flow [154]. The first pumping unit acts as a closed valve for the second one, and the complete volume of the second chamber is pumped into the third chamber. Valves designed in this manner are classified as normally open valves because there is no blockage of the channel while the actuator is inactive.

In contrast, valves classified as normally closed valves block a path until they are opened by an actuating force. A very common design, which is very similar to the above described normally open valve, is the pneumatically actuated lifting gate valve [58, 93]. The channel flow is interrupted by a small blockade across the cross-section. A pneumatic chamber is situated above this blockage, similar to the situation for the pump in Fig. 4.3. The application of a vacuum to the chamber lifts the blockage and clears the channel for the fluid.

In contrast to active valves, passive microvalves function without any actuator, such as the situation for the well-known check valve [82]. These valves can easily be integrated into the same PDMS layer as the fluidic channels and therefore produce few additional expenses. Figure 4.4 shows the check valve from the pneumatic pump (Fig. 4.3) of the exemplary MBR system. This valve is designed with two convex lips, which have a width between 100 µm at the channel wall and 62.8 µm at the tip. Between both lips is a 10 µm wide gap to enable separation when liquid flows in the open direction (left to right). Due to the production process, the lips are connected to the ceiling of the wall. At the bottom, gold pads on the glass substrate prevent bonding and assure movability of the lips. When a liquid flows in the closing direction (right to left), the two lips become pressed against each other and block the pathway [22].

Special types of passive valves are nozzle/diffuser valves [38, 59] and tesla valves [97]. These valves function completely without moving parts. Special

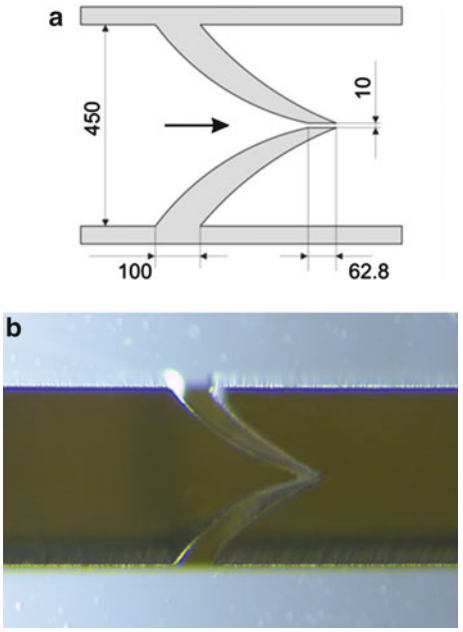

Fig. 4.4 (**a**) Schematic check valve with dimensions in µm and (**b**) image of the check valve fabricated in PDMS using soft lithography. Reproduced from Demming [22] with permission of Shaker-Verlag GmbH

channel geometries generate a higher fluidic resistance in one direction than in the opposite direction and lead to a predominant direction of flow. These valves are often used in micropumps to define a flow direction, but they are not able to completely block a channel.

Several other microvalves, such as the phase change [154] or burst valves [2], also exist. These lack different characteristics required for use in a MBR system, such as an appropriate switching speed or reversibility.

4.3.4.3 Microseparators

Microseparators, analogously to microvalves, can be separated into two categories: active separators requiring external energy or actuation versus passive separators. Most popular representatives of active separators use ultrasonics [105, 126] and dielectrophoresis [94, 95].

The exemplary MBR system (Fig. 4.2) uses a passive cross-flow filter to remove cells from the sample (Fig. 4.5). Filter channels with a cross-section (2 µm × 5 µm) that is smaller than the cell diameter (ca. 10 µm) allow the liquid to pass but retain the microorganisms. A filter cake forms while filtering. Because of the spherical shape of the cells that have a diameter of approximately 5–10 µm, the fluid can pass through the spaces between the contiguous cells and the channels do not become

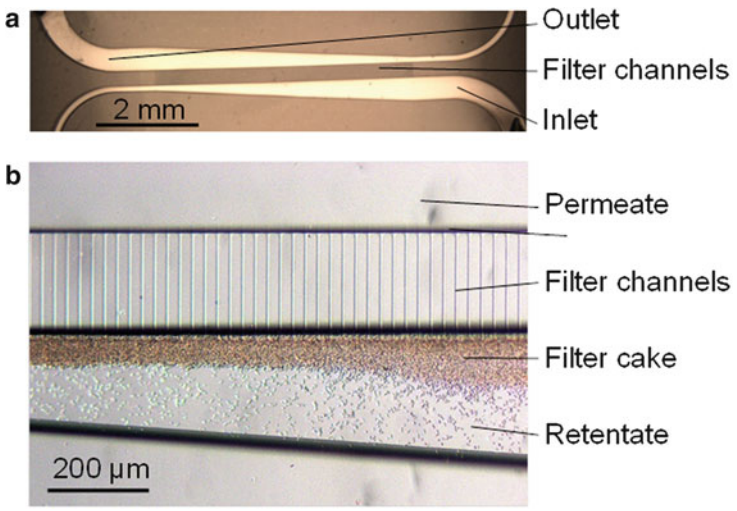

Fig. 4.5 (**a**) Image of a cross-flow filter system produced in PDMS and (**b**) magnification of the filter channels with dimensions of 2 µm × 5 µm × 300 µm

blocked. After removal of the permeate from the filter, the filter cake can be flushed out of the system using the outlet on the retentate side.

Another passive separation principle is based on inertial forces and dean vortices [10, 27]. Such a system is able to separate particles from the fluid but does also allow sorting of particles by their size. For proper function, the size of the particles must be known, and the separator must be adjusted appropriately. Furthermore, this type of separation only works for a limited size range due to the interactions of the different forces.

4.3.4.4 Micromixers

Microfluidic systems similar to an MBR have very low characteristic length and flow rates. This situation leads to Reynolds numbers below one and hence to laminar flow without turbulence. Two liquids flowing next to each other will only mix by diffusion at the fluid interface. According to Fick's law of diffusion, in the laminar regime, the mixing can only be accelerated by a longer time or a larger interface. Most passive micromixers use structures and geometries to bend the fluid interface and generate vortices. Another way to enlarge the interface is to split the flows and recombine them in parallel lamination. Because mixing is an important but complicated field in microfluidics, there have been many studies, and various different mixing principles were developed [48, 86, 100, 133].

Faster mixing can be obtained by the generation of turbulence in the fluid. Therefore, very fast fluid velocities must be induced locally. This condition can be obtained using active mixing principles, which come with the same problems of

moving parts as micropumps or valves. A well-known macroscopic mixing principle is using a stir bar. This bar was scaled down by Ryu et al. [119] and used an external magnetic field for actuation. Integration of electromagnetic motors in microfluidic systems for mixing and stirring has also been done. Al-Halhouli et al. [1] presented a MBR with an integrated micro stirrer which is driven by a synchronous micromotor. These mixers and stirrers showed very good mixing qualities but required a much more complex and expensive production process than that for passive mixers. Nevertheless, the microscale offers the opportunity to use completely new approaches for mixing compared with those for the macroscale. Some examples are acoustic mixing using low-frequency vibration [56], mixing by a focused surface acoustic wave [159] or using an electrorheological fluid [102].

4.4 Examples of Microbioreactor Applications

For the MBRs based on microtechnologies, as stated in Sect. 4.3.2, two main applications can be used. The first MBR application involves mammalian/human cell cultivation to elucidate the interrelationship of intra- and intercellular processes and mechanisms by mimicking environmental conditions within microfluidic elements. This gives rise to new possibilities in the development of biological and pharmaceutical products, drug screening, and diagnostics. Cell cultures require proliferation on surfaces, hMBRs are commonly used. Secondly, a vMBR can be used for throughput screening of microorganisms. The main focus here lies on the cultivation and the integration of online analytics to measure reaction kinetic parameters. For both applications, two examples are described in the following, including motivation, design, fabrication and experimental results.

4.4.1 Horizontal MBR for Screening of Cell Cultures with Simultaneous pH Monitoring

The following application describes a photonic hMBR for screening cell cultures with simultaneous pH monitoring. Although conventional cell culture formats (flasks, petridishes, 96-well plates) are extensively used world-wide, MBRs appear to be a good alternative as they provide additional capabilities, such as the possibility of performing microfluidic perfusion cultures and generating in vitro microenvironments that better mimic the in vivo situation while including a variety of online monitoring options. For the latter, integration of transduction and/or environmental control elements in the MBR is crucial. Most of these elements are based on electrochemical transduction.

The implementation of optical elements, as described in the following example, provides several advantages in comparison to electrochemical devices: (1) they are

non-invasive, do not alter the used cultivation medium or cells and do not compromise sterility; (2) they do not require metals or metal oxides and thus reduce fabrication costs; and (3) the integration of optical elements into the microfluidic chip may also require fewer fabrication steps.

4.4.1.1 Design

The monolithically integrated photonic hMBR contains two chambers with microfluidic and microoptical elements for cell retention/proliferation and real-time pH monitoring, respectively [98]. The pH monitoring without interference from cells in the supernatant is achieved by the implementation of two independent chambers connected via a microfluidic channel (Fig. 4.6a). The first incubation chamber (0.42 cm diameter, 230 μm high) consists of an integrated filter with 21 size-exclusion microchannels (3 μm deep) to trap the cells while allowing the passage of medium (Fig. 4.6b). The incubation chamber is connected to two inlets, one for cell inoculation and one for cultivation medium. At their widest end, the size-exclusion microchannels are connected by a fluidic channel that surrounds the incubation chamber and links it with the second, monitoring chamber (0.5 cm diameter, 230 μm high), which finally leads to the outlet.

For optical transduction, both chambers contain the following monolithically integrated micro-optical elements (Fig. 4.6c): (1) self-alignment elements for the clamping and precise alignment of the optical fibres, (2) biconvex microlenses for light collimation [78], (3) absorption filters that can be filled with dye-doped polymeric materials to selectively absorb excitation light during fluorescence measurements [17], and (4) two sets of air mirrors that surround the chambers to confine the light inside of the chamber.

4.4.1.2 Fabrication

The hMBR was fabricated by conventional soft lithography, as explained in Sect. 4.3.2. Briefly, a two-level master was fabricated using SU-8 polymer, whereas the size-exclusion channels were patterned in the first level of the master (total height of 3 μm), and the other elements (two chambers, microfluidic and microoptical elements) were patterned in a second layer (total height of 230 μm). After development and baking of the master, PDMS replicas of the master were moulded. The structured PDMS was then irreversibly bonded to a soda-lime glass wafer.

A photograph of the final hMBR filled with crystal violet (only for visualisation) is shown in Fig. 4.6d. It should be noted that the microoptical elements are exclusively composed of PDMS and air and therefore do not increase the technological complexity of the device, resulting in robustness combined with low fabrication costs.

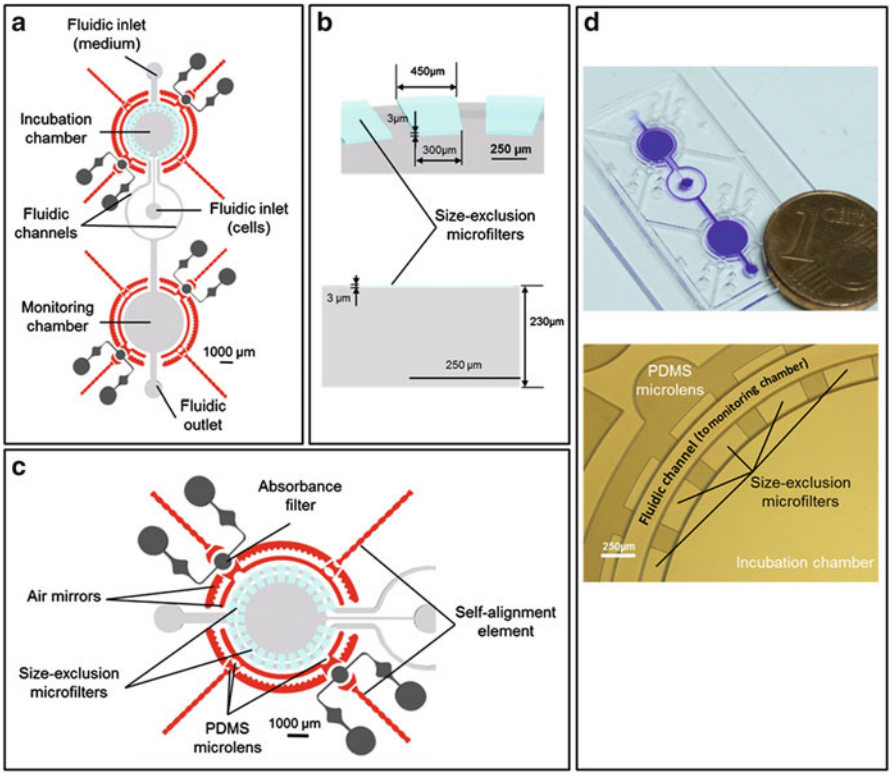

Fig. 4.6 (**a**) Schematics of the photonic hMBR with the fluidic elements (marked in *grey*), including the two fluidic inlets (one for cells and another one for cell culture medium), the fluidic outlet, the incubation chamber, the monitoring chamber and the fluidic channels connecting these chambers; (**b**) 3D representation and cross-section of the size-exclusion microchannels of the filter (marked in *blue*); (**c**) details of the optical elements integrated into each chamber, including self-alignment elements, PDMS microlenses and air mirrors (marked in *red*), and absorbance filters (marked in *dark grey*); (**d**) photograph of the hMBR filled with crystal violet dye (for validation purposes) with a magnification of the size-exclusion microfilters in the incubation chamber [98]. Reproduced from Muñoz-Berbel et al. [98] with permission of The Royal Society of Chemistry

4.4.1.3 Experimental Results and Discussion

Vascular smooth muscle cells obtained from a rat aorta, with sizes between 8 and 10 µm diameter, were applied as a mammalian cell model. These cells were efficiently trapped in the incubation chamber, where they proliferated under optimal experimental conditions (37 °C, 5 % CO_2 and a low continuous flow of culture medium containing phenol red as a pH indicator), resulting in a classical spindle-shaped morphology (80–100 µm wide, 2.5 µm high) and a traditional hill-and-valley phenotype [118].

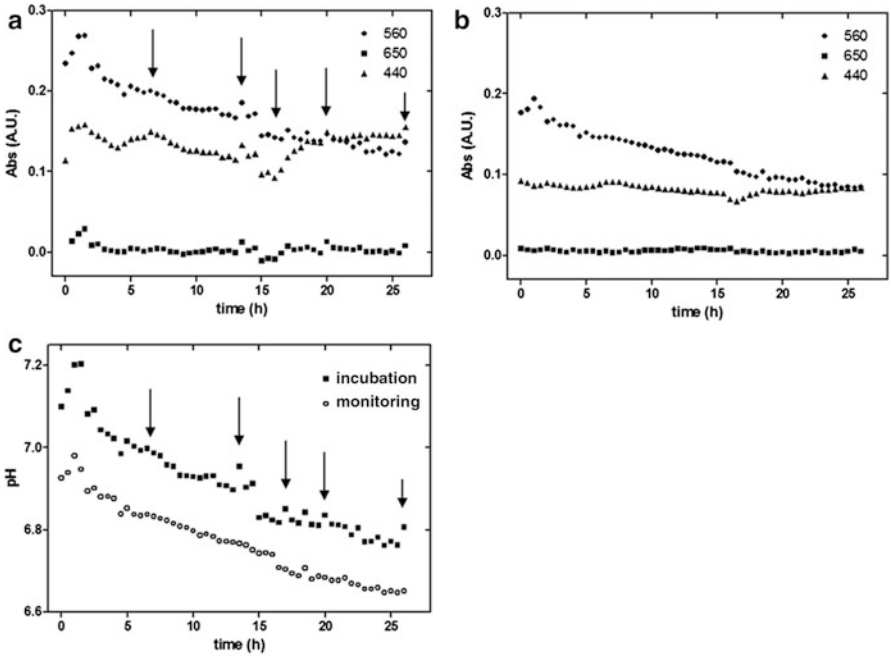

Fig. 4.7 Variation in the absorbance at wavelengths of 440, 560 and 650 nm with time during the proliferation in the (**a**) incubation and (**b**) monitoring chambers and (**c**) pH variation (at 560 nm wavelength) with time during proliferation in both the incubation and monitoring chambers. *Black arrows* indicate the areas where cell detachment influenced the absorbance measurements (Muñoz-Berbel et al. [98]). Reproduced from Muñoz-Berbel et al. [98] with permission of The Royal Society of Chemistry

The absorbance was monitored optically and simultaneously in both the incubation and monitoring chambers using the following setup: light from a broadband halogen lamp was coupled to the chamber through a multimode optical fibre (230 μm in diameter). Transmitted light was collected at the opposite side of each chamber using another identical optical fibre, which was then connected to a microspectrometer for direct read-out.

Figure 4.7a, b show the absorbance variations at wavelengths of 440 nm (protonated form of phenol red), 560 nm (deprotonated form of phenol red) and 650 nm (cell dispersion) for the two chambers. The cultivation medium contained phenol red as an indicator of the pH, which directly correlates to the cell metabolism. In both chambers, the absorbance at 560 nm decreased with time until stabilisation after approximately 22 h of cultivation, as expected due to the medium acidification induced by cell metabolism. In the incubation chamber, cell dispersion influenced the $Abs_{560\ nm}$ (Fig. 4.7c) because small increases in $Abs_{650\ nm}$—possibly due to detached cells—also induced an increase in $Abs_{560\ nm}$. However, in the monitoring chamber, $Abs_{650\ nm}$ constantly followed the expected profile. It has to be noted that

the 440 nm band is not suitable for monitoring pH during cell proliferation due to negative interference from foetal bovine serum.

To conclude, pH changes could be adequately analysed in the monitoring chamber by measuring the 560 nm band (corresponding to the deprotonated form of the pH indicator) in real-time and without the interference of cells. Thus, the suitability of the photonic hMBR for cell screening applications could be proven.

For future potential applications, the photonic hMBR might also be used to monitor small or large molecules that are secreted or assimilated by cells.

4.4.2 Vertical MBR as a Microbubble Column to Screen Microorganisms

The following application presents a vMBR, which can be applied as a microbubble column reactor (μBC) for biotechnological screening in suspension. The advantages of the μBC are (1) enhancement of submerged cultivation and aeration via an additional gaseous phase in the form of rising microbubbles and (2) circumvention of the blockage risk due to carbon dioxide produced by the microorganisms—a challenge predominant in common hMBRs—because the gas bubbles are released by buoyancy at the upper part of the reactor. This triphasic (air, cultivation medium and microorganisms) μBC provides several advantages in comparison to the currently reported hMBRs (based on mechanical or peristaltic active mixing); these benefits include robust and simple construction, a lack of mechanical moving parts, enhanced mass transfer properties and low construction costs.

4.4.2.1 Design

The μBC—illustrated in Fig. 4.8a—comprises a reaction chamber (70 μL in total volume) including two fluidic channels for in- and outlets of both the liquid and the gas phases [24]. The liquid cultivation medium is added via the upper inlet, whereas a complete discharge of the medium is feasible via the lower outlet. The gas phase enters the reactor via an integrated single nozzle consisting of a microchannel of 20–50 μm × 40 μm. Constant gas throughput provides a homogeneous suspension of biomass in the reaction chamber without needing additional mixing elements. The headspace above the liquid phase guarantees suitable gas liquid phase separation and does not require additional baffles.

In terms of online analytics, alignment channels for fibre optics were designed to lie in the horizontal direction on both sides of the reactor chamber. Stop structures and a clamp provide accurate positioning of the fibre optics, whereas biconvex PDMS lenses result in parallel beams that illuminate the reactor [78, 138] and allow for a sensitive analysis of the OD [24]. In addition, a guiding cannula is implemented in the reactor top to allow for the insertion of various objects,

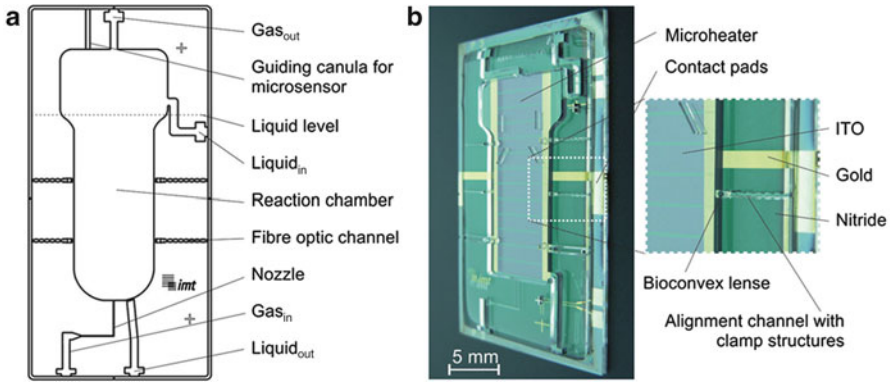

Fig. 4.8 Schematic of the microbubble column (μBC): (**a**) patterned PDMS layer including a reaction chamber, fluidic inlets and outlets, the gas nozzle, fibre optic channels with alignment and clamp structures and biconvex lenses, a guiding cannula for a needle-type sensor and (**b**) photograph of the μBC including a microheater arranged in parallel (structured with ITO, gold and nitride on the glass substrate). Adapted from Demming et al. [24]

e.g., the insertion of a needle-type sensor to monitor the DO during cultivation. Additional functional elements, such as an integrated microheater, can optionally be microstructured with e.g., ITO on the glass substrate, which allows for a defined constant temperature during cultivation (Fig. 4.8b). Furthermore, this system allows for quick response times and for quenching at high temperatures to rapidly deactivate biological material.

4.4.2.2 Fabrication

The μBC comprises two major parts: a patterned PDMS chip bonded to a glass substrate that might also be microstructured. The PDMS part is based on an optimised two-step lithographic process using replica moulding, as described in Sect. 4.3.2. The first layer has a height between 20 and 50 μm to provide structure for the nozzle, whereas the total height of the system (second layer) is 230 μm. The microheater is structured with ITO as described in Sect. 4.3.2. A subsequent chromium-gold layer results in electrical pads for contacting the periphery. To prevent electrolytic decomposition of the water and thus decomposition of the heating structures from erosion, a reliable isolation layer made of silicon nitride is deposited. Subsequently, the PDMS chip is covalently bonded to the glass substrate. Because the naturally hydrophobic PDMS causes problems, such as adherence and entrapment of cells and air bubbles on the unmodified reactor walls, the fabrication is finalised with a hydrophilisation step using PDADMAC-terminated PEM-surfaces [128].

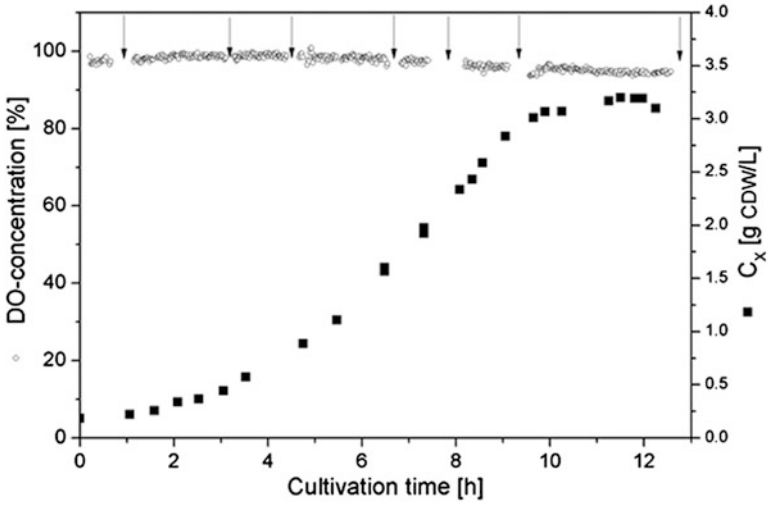

Fig. 4.9 Dissolved oxygen (DO) (*circle*) and biomass concentration (c_X) (*filled square*) during batch cultivation of *S. cerevisiae*. The DO data points represent the measured quasi-steady-state concentrations while gassing was applied. *Arrows* indicate the measurements via the dynamic method [111]. Copyright © 2014, Wiley Periodicals, Inc.

4.4.2.3 Experimental Results and Discussion

To prove the screening applicability of the μBC in aerobic biotechnological processes, cultivation experiments with the model organism *S. cerevisiae* strain CCOS 538 (ATCC 32167, Culture Collection of Switzerland) were performed. The time course of the measured biomass concentration (c_X) and DO during batch cultivation is depicted in Fig. 4.9 [111].

First, the gassing rate was adjusted arbitrarily until adequate gassing and degassing could be visually observed. This effect was achieved at a superficial gas velocity of 5×10^{-4} m/s (2.1 L L^{-1} min^{-1}). Under these conditions, the DO was permanently above 90 %, and no oxygen limitation occurred during aerated cultivation [111]. After a lag phase, the cells grew exponentially with a specific growth rate of 0.37 h^{-1} until approximately 9 h of cultivation time, after which there was a transition to the stationary phase. With an initial glucose concentration of 20 g L^{-1}, the yield coefficient ($Y_{X/S}$) could be estimated to be 0.148 g cell dry weight (CDW) g s^{-1}, which corresponds to previously reported data from macroscale experiments [139].

Several times during cultivation, the gassing of the μBC was stopped and restarted after an acceptable variation in DO, indicated by the arrows in Fig. 4.9. This recorded decrease and increase in profile (data not shown) allowed the calculation of the oxygen uptake rate (OUR) and the volumetric oxygen mass transfer coefficient ($k_L a$). Nevertheless, an adequate $k_L a$ could be achieved by active sparging with values up to 0.14 s^{-1}. Knowing the $k_L a$ during the aerated

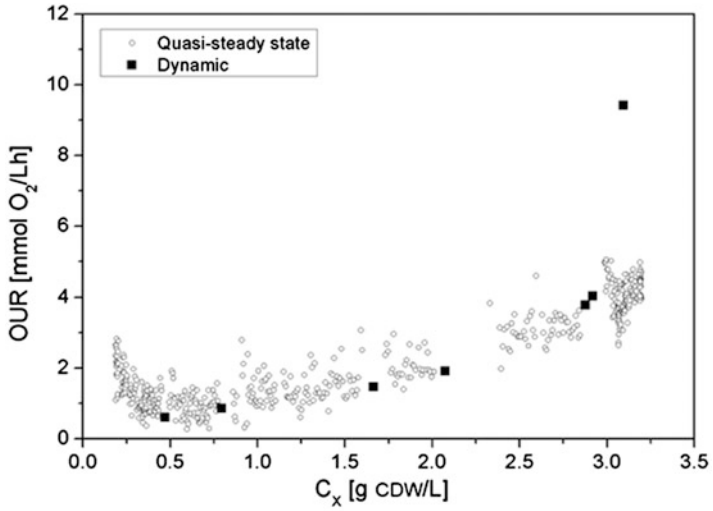

Fig. 4.10 Oxygen uptake rate (OUR) using dynamic (*filled square*) and quasi-steady-state (*circle*) methods during the cultivation of *S. cerevisiae* with respect to the biomass concentration (c_X) [111]. Copyright © 2014, Wiley Periodicals, Inc.

operation, the OUR could also be verified from the quasi-steady- state DO signal. The results are summarised in Fig. 4.10 with respect to c_X [111].

The OUR increased with c_X, and a specific OUR of 1.3–1.5 $mmol_{O2}\, g_{CDW}{}^{-1}\, h^{-1}$ can be calculated from the slope, which was on the same order of magnitude as the results reported by von Meyenburg [139] and Kuhlmann et al. [65] for this strain. The subsequent increase in OUR at $c_X \approx 3\ g\ L^{-1}$ indicated the end of the exponential growth phase, where a temporary change in metabolism occurs that causes a preference for the oxidative pathway [54, 111].

4.5 Conclusions

This article provides an overview of MBRs, the design and the benefits of various strategies of production and the biotechnological applications of these small devices in different operating modes for both bacterial and mammalian/human cell cultures. For these biological systems the discussed MBR devices ensure a broad range of biological screening applications, like cultivation optimisation, analysis of reaction kinetics, pharmacokinetic and drug delivery experiments or metabolic flux analyses; they allow high-throughput experimentation and reduce effectively the costs for expensive substrates, including limited drug formulations. The report discusses their design possibilities as well as the essential aspects of the use of disposable MBRs, fluid connections and the application of MBRs in diverse biotechnological fields.

For bioprocess development, there is a considerable need for efficient MBR systems that allow automated, highly parallelised operation with independent variation of individual process parameters. Equally important are the capability to control various processes, good scalability, and the generation of reliable and reproducible experimental data in real time over a long cultivation time. In recent years, microfabrication technology and microprocess engineering have met these challenges, different types of MBR systems have been developed and huge technological advances have been achieved.

It has been shown that the use of novel microfabrication techniques allows for unconstrained 3D structuring of microchannels, microreaction volumes and the microtechnical integration of additional sensors and elements for fluid manipulation (such as valves, pumps). These results suggest that MBR applications are capable of bridging the gap that exists between MTP-based high-throughput screening and laboratory/pilot reactors to obtain cultivation data that can be applied to larger bioreactors at production scale. For the near future, the challenge is to develop fully parallelised and automated MBR systems and to use these systems for daily laboratory operations.

Acknowledgments The authors gratefully acknowledge the financial support provided by the German Research Foundation (DFG) in the Research Unit 856 mikroPART—Microsystems for particulate Life-Science-Products at the Technische Universität Braunschweig, Germany. R. Krull has also received funding from the People Programme (Marie Curie Actions, Multi-ITN) of the European Union's Seventh Framework Programme for research, technological development and demonstration within the project EUROMBR—European network for innovative microbioreactor applications in bioprocess development (Project ID 608104). S. Büttgenbach gratefully acknowledges additional financial support from the Volkswagen Foundation.

References

1. Al-Halhouli A, Demming S, Waldschik A, Büttgenbach S (2014) Implementation of synchronous micromotor in developing integrated microfluidic systems. Micromachines 5:442–456
2. Allain M, Berthier J, Basrour S, Pouteau P (2010) Electrically actuated sacrificial membranes for valving in microsystems. J Micromech Microeng 20:035006
3. Amirouche F, Zhou Y, Johnson T (2009) Current micropump technologies and their biomedical applications. Microsyst Technol 15:647–666
4. Atencia J, Cooksey GA, Jahn A, Zook JM, Vreeland WN, Locascio LE (2010) Magnetic connectors for microfluidic applications. Lab Chip 10:246–249
5. Au AK, Lai H, Utela BR, Folch A (2011) Microvalves and micropumps for BioMEMS. Micromachines 2:179–220
6. Balagaddé FK, You L, Hansen CL, Arnold FH, Quake SR (2005) Long-term monitoring of bacteria undergoing programmed population control in a microchemostat. Science 309:137–140
7. Bechert T, Steinrücke P, Guggenbichler JP (2000) A new method for screening anti-infective biomaterials. Nat Med 6:1053–1056
8. Beebe DJ, Mensing GA, Walker GM (2002) Physics and applications of microfluidics in biology. Annu Rev Biomed Eng 4:261–286

9. Betts JI, Baganz F (2006) Miniature bioreactors: current practices and future opportunities. Microb Cell Fact 5:21
10. Bhagat AAS, Kuntaegowdanahalli SS, Papautsky I (2008) Continuous particle separation in spiral microchannels using dean flows and differential migration. Lab Chip 8:1906–1914
11. Boccazzi P, Zhang Z, Kurosawa K, Szita N, Bhattacharya S, Jensen KF, Sinskey AJ (2006) Differential gene expression profiles and real-time measurements of growth parameters in Saccharomyces cerevisiae grown in microliter-scale bioreactors equipped with internal stirring. Biotechnol Prog 22:710–717
12. Boxshall K, Wu M, Cui Z, Cui Z, Watts JF, Baker MA (2005) Simple surface treatments to modify protein adsorption and cell attachment properties within a poly(dimethylsiloxane) micro-bioreactor. Surf Interface Anal 38:198–201
13. Breslauer DN, Lee PJ, Lee LP (2006) Microfluidics-based systems biology. Mol Biosyst 2:97–112
14. Bridle H, Millingen M, Jesorka A (2008) On-chip fabrication to add temperature control to a microfluidic solution exchange system. Lab Chip 8:480–483
15. Brody JP, Yager P, Goldstein RE, Austin RH (1996) Biotechnology at low Reynolds numbers. Biophys J 71:3430–3441
16. Büttgenbach S (2014) Electromagnetic micromotors—design, fabrication and applications. Micromachines 5:929–942
17. Carregal-Romero E, Fernández-Sánchez C, Eguizabal A, Demming S, Büttgenbach S, Llobera A (2012) Development and integration of xerogel polymeric absorbance microfilters into lab-on-chip systems. Opt Express 20:23700–19
18. Chen A, Chitta R, Chang D, Amanullah A (2009) Twenty-four well plate miniature bioreactor system as a scale-down model for cell culture process development. Biotechnol Bioeng 102:148–160
19. Chen H, Acharya D, Gajraj A, Meiners J (2003) Robust interconnects and packaging for microfluidic elastomeric chips. Anal Chem 75:5287–5291
20. Choi H, Boccazzi P, Laibinis PE, Sinskey AJ, Jensen KF (2003) Poly(ethylene glycol) (PEG)-modified poly(dimethylsiloxane) (PDMS) for protein- and cell-resistant surfaces in microbioreactor. In: 7th International conference on miniaturized chemical and biochemical analysts systems, Squaw Valley, CA, USA, pp 1105–1108
21. Chung SK, Zhao Y, Cho SK (2008) On-chip creation and elimination of microbubbles for a micro-object manipulator. J Micromech Microeng 18:1–13
22. Demming S (2011) Disposable lab-on-chip systems for biotechnological screening. In: Büttgenbach S (ed) Berichte aus der Mikro- und Feinwerktechnik, vol 30. Ph.D. Thesis, Technische Universität Braunschweig, Shaker-Verlag, Aachen
23. Demming S, Hahn A, Edlich A, Franco-Lara E, Krull R, Barcikowski S, Büttgenbach S (2010) Softlithographic partial integration of surface-active nanoparticles in a PDMS matrix for microfluidic biodevices. Phys Status Solidi A Appl Mater Sci 207:898–903
24. Demming S, Peterat G, Llobera A, Schmolke H, Bruns A, Kohlstedt M, Al-Halhouli A, Klages C-P, Krull R, Büttgenbach S (2012) Vertical microbubble column-A photonic lab-on-chip for cultivation and online analysis of yeast cell cultures. Biomicrofluidics 6:34106
25. Demming S, Sommer B, Llobera A, Rasch D, Krull R, Büttgenbach S (2011) Disposable parallel poly(dimethylsiloxane) microbioreactor with integrated readout grid for germination screening of *Aspergillus ochraceus*. Biomicrofluidics 5:14104
26. Demming S, Vila-Planas J, Aliasghar Zadeh S, Edlich A, Franco-Lara E, Radespiel R, Büttgenbach S, Llobera A (2011) Poly(dimethylsiloxane) photonic microbioreactors based on segmented waveguides for local absorbance measurement. Electrophoresis 32:431–439
27. Di Carlo D, Irimia D, Tompkins RG, Toner M (2007) Continuous inertial focusing, ordering, and separation of particles in microchannels. Proc Natl Acad Sci U S A 104:18892–18897
28. Doig SD, Diep A, Baganz F (2005) Characterisation of a novel miniaturised bubble column bioreactor for high throughput cell cultivation. Biochem Eng J 23:97–105

29. Doig SD, Ortiz-Ochoa K, Ward JM, Baganz F (2005) Characterization of oxygen transfer in miniature and lab-scale bubble column bioreactors and comparison of microbial growth performance based on constant $k_L a$. Biotechnol Prog 21:1175–82
30. Duffy DC, McDonald JC, Schueller OJ, Whitesides GM (1998) Rapid prototyping of microfluidic systems in poly(dimethylsiloxane). Anal Chem 70:4974–4984
31. Edlich A (2010) Entwicklung eines Mikroreaktors als Screening-Instrument für biologische Prozesse. In: Wittmann C (ed) ibvt-Schriftenreihe, vol 51. Ph.D. Thesis, Technische Universität Braunschweig, Cuvillier-Verlag, Göttingen
32. Edlich A, Magdanz V, Rasch D, Demming S, Aliasghar Zadeh S, Segura R, Kähler C, Radespiel R, Büttgenbach S, Franco-Lara E, Krull R (2010) Microfluidic reactor for continuous cultivation of *Saccharomyces cerevisiae*. Biotechnol Prog 26:1259–1270
33. El-Ali J, Sorger PK, Jensen KF (2006) Cells on chips. Nature 442:403–411
34. Feldmann M, Buttgenbach S (2007) Novel microrobots and micromotors using Lorentz force driven linear microactuators based on polymer magnets. IEEE Trans Magn 43:3891–3895
35. Fernández-Sánchez C, Cadarso VJ, Darder M, Domínguez C, Llobera A (2008) Patterning high-aspect-ratio sol–gel structures by microtransfer molding. Chem Mater 20:2662–2668
36. Furno F, Morley KS, Wong B, Sharp BL, Arnold PL, Howdle SM, Bayston R, Brown PD, Winship PD, Reid HJ (2004) Silver nanoparticles and polymeric medical devices: a new approach to prevention of infection? J Antimicrob Chemother 54:1019–1024
37. Garcia-Ochoa F, Gomez E (2009) Bioreactor scale-up and oxygen transfer rate in microbial processes: an overview. Biotechnol Adv 27:153–176
38. Geng Z, Cui D, Wang H, Chen X (2006) Disposable PDMS diaphragm micropump actuated by PZT. In: 1st IEEE International conference on nano/micro engineered and molecular systems, IEEE, Zhuhai, China, pp 1436–1439
39. Gravesen P, Branebjerg J, Jensen OS (1993) Microfluidics—a review. J Micromech Microeng 3:168–182
40. Groisman A, Lobo C, Cho H, Campbell JK, Dufour YS, Stevens AM, Levchenko A (2005) A microfluidic chemostat for experiments with bacterial and yeast cells. Nat Methods 2:685–689
41. Gruenberger A, Probst C, Heyer A, Wiechert W, Frunzke J, Kohlheyer D (2013) Microfluidic picoliter bioreactor for microbial single-cell analysis: fabrication, system setup, and operation. J Vis Exp 82:50560
42. Grünberger A, Paczia N, Probst C, Schendzielorz G, Eggeling L, Noack S, Wiechert W, Kohlheyer D (2012) A disposable picolitre bioreactor for cultivation and investigation of industrially relevant bacteria on the single cell level. Lab Chip 12:2060–2068
43. Grünberger A, Wiechert W, Kohlheyer D (2014) Single-cell microfluidics: opportunity for bioprocess development. Curr Opin Biotechnol 29C:15–23
44. Harrison DJ, Manz A, Fan Z, Luedi H, Widmer HM (1992) Capillary electrophoresis and sample injection systems integrated on a planar glass chip. Anal Chem 64:1926–1932
45. Hegab HM, Elmekawy A, Stakenborg T (2013) Review of microfluidic microbioreactor technology for high-throughput submerged microbiological cultivation. Biomicrofluidics 7:21502
46. Hemmerich J, Adelantado N, Barrigón JM, Ponte X, Hörmann A, Ferrer P, Kensy F, Valero F (2014) Comprehensive clone screening and evaluation of fed-batch strategies in a microbioreactor and lab scale stirred tank bioreactor system: application on *Pichia pastoris* producing *Rhizopus oryzae* lipase. Microb Cell Fact 13:36
47. Hench LL, West JK (1990) The sol-gel process. Chem Rev 90:33–72
48. Hessel V, Löwe H, Schönfeld F (2005) Micromixers—a review on passive and active mixing principles. Chem Eng Sci 60:2479–2501
49. Hu S, Ren X, Bachman M, Sims CE, Li GP, Allbritton N (2002) Surface modification of poly (dimethylsiloxane) microfluidic devices by ultraviolet polymer grafting. Anal Chem 74:4117–4123

50. Huber R, Ritter D, Hering T, Hillmer A-K, Kensy F, Müller C, Wang L, Büchs J (2009) Robo-Lector—a novel platform for automated high-throughput cultivations in microtiter plates with high information content. Microb Cell Fact 8:42
51. Hung PJ, Lee PJ, Sabounchi P, Lin R, Lee LP (2004) Continuous perfusion microfluidic cell culture array for high-throughput cell-based assays. Biotechnol Bioeng 89:1–8
52. Inman W, Domansky K, Serdy J, Owens B, Trumper D, Griffith LG (2007) Design, modeling and fabrication of a constant flow pneumatic micropump. J Micromech Microeng 17:891–899
53. Jeong OC, Park SW, Yang SS, Pak JJ (2005) Fabrication of a peristaltic PDMS micropump. Sensors Actuators A Phys 123–124:453–458
54. Jones KD, Kompala DS (1999) Cybernetic model of the growth dynamics of *Saccharomyces cerevisiae* in batch and continuous cultures. J Biotechnol 71:105–131
55. Kang JH, Kim YC, Park JK (2007) Analysis of pressure-driven air bubble elimination in a microfluidic device. Lab Chip 8:176–178
56. Kardous F, Yahiaoui R, Aoubiza B, Manceau JF (2014) Acoustic mixer using low frequency vibration for biological and chemical applications. Sensors Actuators A Phys 211:19–26
57. Kim BJ, Zhao T, Young L, Zhou P, Shuler ML (2012) Batch, fed-batch, and microcarrier cultures with CHO cell lines in a pressure-cycle driven miniaturized bioreactor. Biotechnol Bioeng 109:137–45
58. Kim J, Kang M, Jensen EC, Mathies RA (2012) Lifting gate polydimethylsiloxane microvalves and pumps for microfluidic control. Anal Chem 84:2067–2071
59. Kim JH, Na KH, Kang CJ, Kim YS (2005) A disposable thermopneumatic-actuated micropump stacked with PDMS layers and ITO-coated glass. Sensors Actuators A Phys 120:365–369
60. Kirk TV, Szita N (2013) Oxygen transfer characteristics of miniaturized bioreactor systems. Biotechnol Bioeng 110:1005–1019
61. Kliche S, Räuchle K, Bertau M, Reschetilowski W (2009) Ganzzell-Biokatalyse mittels *Saccharomyces cerevisiae* im Mikroreaktor. Chem Ing Tech 81:343–347
62. Korivi NS, Jiang L (2007) A generic chip-to-world fluidic interconnect system for microfluidic devices. In: 39th Southeastern symposium on system theory, IEEE, Macon, GA, USA, pp 176–180
63. Kostov Y, Harms P, Randers-Eichhorn L, Rao G (2001) Low-cost microbioreactor for high-throughput bioprocessing. Biotechnol Bioeng 72:346–352
64. Kovarik ML, Gach PC, Ornoff DM, Wang Y, Balowski J, Farrag L, Allbritton NL (2012) Micro total analysis systems for cell biology and biochemical assays. Anal Chem 84:516–540
65. Kuhlmann W, Meyer H-D, Bellgardt KH, Schügerl K (1984) On-line analysis of yeast growth and alcohol production. J Biotechnol 1:171–185
66. Kunze M, Lattermann C, Diederichs S, Kroutil W, Büchs J (2014) Minireactor-based high-throughput temperature profiling for the optimization of microbial and enzymatic processes. J Biol Eng 8:22
67. Lamping SR, Zhang H, Allen B, Ayazi Shamlou P (2003) Design of a prototype miniature bioreactor for high throughput automated bioprocessing. Chem Eng Sci 58:747–758
68. Lara AR, Galindo E, Ramírez OT, Palomares LA (2006) Living with heterogeneities in bioreactors: understanding the effects of environmental gradients on cells. Mol Biotechnol 34:355–381
69. Lattermann C, Büchs J (2015) Microscale and miniscale fermentation and screening. Curr Opin Biotechnol 35:1–6
70. Lee HLT, Boccazzi P, Ram RJ, Sinskey AJ (2006) Microbioreactor arrays with integrated mixers and fluid injectors for high-throughput experimentation with pH and dissolved oxygen control. Lab Chip 6:1229–1235
71. Lee KS, Boccazzi P, Sinskey AJ, Ram RJ (2011) Microfluidic chemostat and turbidostat with flow rate, oxygen, and temperature control for dynamic continuous culture. Lab Chip 11:1730–1739

72. Lee PJ, Hung PJ, Rao VM, Lee LP (2005) Nanoliter scale microbioreactor array for quantitative cell biology. Biotechnol Bioeng 94:5–14
73. Lewis G, Taylor IW, Nienow AW, Hewitt CJ (2004) The application of multi-parameter flow cytometry to the study of recombinant *Escherichia coli* batch fermentation processes. J Ind Microbiol Biotechnol 31:311–322
74. Li L, Wang W, Zhang S, Chen S, Guo S, Français O, Cheng J-K, Huang W-H (2011) Integrated microdevice for long-term automated perfusion culture without shear stress and real-time electrochemical monitoring of cells. Anal Chem 83:9524–9530
75. Liu C-H, Lee G-B (2013) A micropump using amplified deformation of resilient membranes through oil hydraulics. Microfluid Nanofluid 17:393–400
76. Llobera A, Cadarso VJ, Darder M, Domínguez C, Fernández-Sánchez C (2008) Full-field photonic biosensors based on tunable bio-doped sol-gel glasses. Lab Chip 8:1185–1190
77. Llobera A, Demming S, Joensson HN, Vila-Planas J, Andersson-Svahn H, Büttgenbach S (2010) Monolithic PDMS passband filters for fluorescence detection. Lab Chip 10:1987–1992
78. Llobera A, Wilke R, Büttgenbach S (2004) Poly(dimethylsiloxane) hollow Abbe prism with microlenses for detection based on absorption and refractive index shift. Lab Chip 4:24–27
79. Lo R, Meng E (2008) Integrated and reusable in-plane microfluidic interconnects. Sensors Actuators B Chem 132:531–539
80. Long Z, Nugent E, Javer A, Cicuta P, Sclavi B, Cosentino Lagomarsino M, Dorfman KD (2013) Microfluidic chemostat for measuring single cell dynamics in bacteria. Lab Chip 13:947–954
81. Lorenz H, Despont M, Fahrni N, Brugger J, Vettiger P, Renaud P (1998) High-aspect-ratio, ultrathick, negative-tone near-UV photoresist and its applications for MEMS. Sensors Actuators A Phys 64:33–39
82. Loverich J, Kanno I, Kotera H (2006) Single-step replicable microfluidic check valve for rectifying and sensing low Reynolds number flow. Microfluid Nanofluid 3:427–435
83. Lucas N, Demming S, Jordan A, Sichler P, Büttgenbach S (2008) An improved method for double-sided moulding of PDMS. J Micromech Microeng 18:075037
84. Maharbiz MM, Holtz WJ, Howe RT, Keasling JD (2004) Microbioreactor arrays with parametric control for high-throughput experimentation. Biotechnol Bioeng 85:376–381
85. Mandal S, Rouillard JM, Srivannavit O, Gulari E (2007) Cytophobic surface modification of microfluidic arrays for in situ parallel peptide synthesis and cell adhesion assays. Biotechnol Prog 23:972–978
86. Mansur EA, Ye M, Wang Y, Dai Y (2008) A state-of-the-art review of mixing in microfluidic mixers. Chin J Chem Eng 16:503–516
87. Manz A, Graber N, Widmer HM (1990) Miniaturized total chemical analysis systems: a novel concept for chemical sensing. Sensors Actuators B Chem 1:244–248
88. Matsubara Y, Murakami Y, Kobayashi M, Morita Y, Tamiya E (2003) Application of on-chip cell cultures for the detection of allergic response. Biosens Bioelectron 19:741–747
89. McDonald JC, Duffy DC, Anderson JR, Chiu DT, Wu H, Schueller OJ, Whitesides GM (2000) Fabrication of microfluidic systems in poly(dimethylsiloxane). Electrophoresis 21:27–40
90. McDonald JC, Whitesides GM (2002) Poly(dimethylsiloxane) as a material for fabricating microfluidic devices. Acc Chem Res 35:491–499
91. Meyvantsson I, Beebe DJ (2008) Cell culture models in microfluidic systems. Annu Rev Anal Chem (Palo Alto CA, USA) 1:423–449
92. Moffitt JR, Lee JB, Cluzel P (2012) The single-cell chemostat: an agarose-based, microfluidic device for high-throughput, single-cell studies of bacteria and bacterial communities. Lab Chip 12:1487–1494
93. Mohan R, Schudel BR, Desai AV, Yearsley JD, Apblett CA, Kenis PJA (2011) Design considerations for elastomeric normally closed microfluidic valves. Sensors Actuators B Chem 160:1216–1223

94. Moncada-Hernández H, Lapizco-Encinas BH (2010) Simultaneous concentration and separation of microorganisms: insulator-based dielectrophoretic approach. Anal Bioanal Chem 396:1805–1816
95. Moon H, Nam Y, Jae CP, Jung H (2009) Dielectrophoretic separation of airborne microbes and dust particles using a microfluidic channel for real-time bioaerosol monitoring. Environ Sci Technol 43:5857–5863
96. Morones JR, Elechiguerra JL, Camacho A, Holt K, Kouri JB, Ramírez JT, Yacaman MJ (2005) The bactericidal effect of silver nanoparticles. Nanotechnology 16:2346–2353
97. Morris CJ, Forster FK (2003) Low-order modeling of resonance for fixed-valve micropumps based on first principles. J Microelectromech Syst 12:325–334
98. Muñoz-Berbel X, Rodríguez-Rodríguez R, Vigués N, Demming S, Mas J, Büttgenbach S, Verpoorte E, Ortiz P, Llobera A (2013) Monolithically integrated biophotonic lab-on-a-chip for cell culture and simultaneous pH monitoring. Lab Chip 13:4239–4247
99. Nazrul M, Zainal H, Gernaey KV (2012) Overview on design considerations for development of disposable microbiorector prototypes. J Teknol Sci Eng 59:53–60
100. Nguyen NT, Wu Z (2005) Micromixers—a review. J Micromech Microeng 15:R1–R16
101. Nisar A, Afzulpurkar N, Mahaisavariya B, Tuantranont A (2008) MEMS-based micropumps in drug delivery and biomedical applications. Sensors Actuators B Chem 130:917–942
102. Niu X, Liu L, Wen W, Sheng P (2007) Microfluidic manipulation in lab-chips using electrorheological fluid. J Intell Mater Syst Struct 18:1187–1190
103. Oh KW, Ahn CH (2006) A review of microvalves. J Micromech Microeng 16:R13–R39
104. Ostrovidov S, Jiang J, Sakai Y, Fujii T (2004) Membrane-based PDMS microbioreactor for perfused 3D primary rat hepatocyte cultures. Biomed Microdevices 6:279–287
105. Palme O, Comanescu G, Stoineva I, Radel S, Benes E, Develter D, Wray V, Lang S (2010) Sophorolipids from *Candida bombicola*: cell separation by ultrasonic particle manipulation. Eur J Lipid Sci Technol 112:663–673
106. Park J, Wu J, Polymenis M, Han A (2013) Microchemostat array with small-volume fraction replenishment for steady-state microbial culture. Lab Chip 13:4217
107. Pečar B, Križaj D, Vrtačnik D, Resnik D, Dolžan T, Možek M (2014) Piezoelectric peristaltic micropump with a single actuator. J Micromech Microeng 24:105010
108. Peng XY, Li PCH (2004) A three-dimensional flow control concept for single-cell experiments on a microchip. 1. Cell selection, cell retention, cell culture, cell balancing, and cell scanning. Anal Chem 76:5273–5281
109. Perozziello G, Bundgaard F, Geschke O (2008) Fluidic interconnections for microfluidic systems: a new integrated fluidic interconnection allowing plug“n”play functionality. Sensors Actuators B Chem 130:947–953
110. Peterat G (2014) Prozesstechnik und reaktionskinetische Analysen in einem mehrphasigen Mikrobioreaktorsystem. In: Krull R (ed) ibvt-Schriftenreihe, vol 75. Ph.D. Thesis, Technische Universität Braunschweig, Cuvillier-Verlag, Göttingen
111. Peterat G, Schmolke H, Lorenz T, Llobera A, Rasch D, Al-Halhouli AT, Dietzel A, Büttgenbach S, Klages C-P, Krull R (2014) Characterization of oxygen transfer in vertical microbubble columns for aerobic biotechnological processes. Biotechnol Bioeng 111:1809–1819
112. Probst C, Grünberger A, Braun N, Helfrich S, Nöh K, Wiechert W, Kohlheyer D (2014) Rapid inoculation of single bacteria into parallel picoliter fermentation chambers. Anal Methods 7:91–98
113. Prokop A, Prokop Z, Schaffer D, Kozlov E, Wikswo J, Cliffel D, Baudenbacher F (2004) NanoLiterBioReactor: long-term mammalian cell culture at nanofabricated scale. Biomed Microdevices 6:325–339
114. Puskeiler R, Kusterer A, John GT, Weuster-Botz D (2005) Miniature bioreactors for automated high-throughput bioprocess design (HTBD): reproducibility of parallel fed-batch cultivations with *Escherichia coli*. Biotechnol Appl Biochem 42:227–235

115. Quaglio M, Canavese G, Giuri E, Marasso SL, Perrone D, Cocuzza M, Pirri CF (2008) Evaluation of different PDMS interconnection solutions for silicon, Pyrex and COC microfluidic chips. J Micromech Microeng 18:055012
116. Quake SR (2000) From micro- to nanofabrication with soft materials. Science 290:1536–1540
117. Rhee SW, Taylor AM, Tu CH, Cribbs DH, Cotman CW, Jeon NL (2004) Patterned cell culture inside microfluidic devices. Lab Chip 5:102–7
118. Rodriguez-Rodriguez R, Muñoz-Berbel X, Demming S, Büttgenbach S, Herrera MD, Llobera A (2012) Cell-based microfluidic device for screening anti-proliferative activity of drugs in vascular smooth muscle cells. Biomed Microdevices 14:1129–1140
119. Ryu KS, Shaikh K, Goluch E, Fan Z, Liu C (2004) Micro magnetic stir-bar mixer integrated with parylene microfluidic channels. Lab Chip 4:608–613
120. Sabourin D, Snakenborg D, Dufva M (2009) Interconnection blocks: a method for providing reusable, rapid, multiple, aligned and planar microfluidic interconnections. J Micromech Microeng 19:035021
121. Satoh W, Takahashi S, Sassa F, Fukuda J, Suzuki H (2009) On-chip culturing of hepatocytes and monitoring their ammonia metabolism. Lab Chip 9:35–37
122. Schäpper D (2010) Continuous culture microbioreactors. Ph.D. Thesis, Technical University of Denmark (DTU)
123. Schäpper D, Alam MN, Szita N, Eliasson Lantz A, Gernaey KV (2009) Application of microbioreactors in fermentation process development: a review. Anal Bioanal Chem 395:679–695
124. Schäpper D, Stocks SM, Szita N, Lantz AE, Gernaey KV (2010) Development of a single-use microbioreactor for cultivation of microorganisms. Chem Eng J 160:891–898
125. Schlichting H, Gersten K (2006) Grenzschichttheorie, 10th edn. Springer, Berlin
126. Schmid L, Weitz DA, Franke T (2014) Sorting drops and cells with acoustics: acoustic microfluidic fluorescence-activated cell sorter. Lab Chip 14:3710–3718
127. Schmolke H (2013) Funktionale Polyelektrolytschichten für mikrofluidische Systeme. Ph.D. Thesis, Technische Universität Braunschweig
128. Schmolke H, Demming S, Edlich A, Magdanz V, Büttgenbach S, Franco-Lara E, Krull R, Klages CP (2010) Polyelectrolyte multilayer surface functionalization of poly(dimethylsiloxane) (PDMS) for reduction of yeast cell adhesion in microfluidic devices. Biomicrofluidics 4:44113
129. Sharma V, Dhayal M, Shivaprasad SM, Jain SC (2007) Surface characterization of plasma-treated and PEG-grafted PDMS for micro fluidic applications. Vacuum 81:1094–1100
130. Skelley AM, Voldman J (2008) An active, integrated bubble trap and debubbler for microfluidic applications. In: 12th International conference on miniaturized systems for chemistry and life sciences, San Diego, CA, USA, pp 1360–1362
131. Soares FO, Correia JH (2000) Bioreactor-on-a-chip: application to baker's yeast fermentation. In: 1st Annual international IEEE-EMBS special topic conference on microtechnologies in medicine and biology, IEEE, Lyon, pp 45–48
132. Spence DM, Torrence NJ, Kovarik ML, Martin RS (2004) Amperometric determination of nitric oxide derived from pulmonary artery endothelial cells immobilized in a microchip channel. Analyst 129:995–1000
133. Suh YK, Kang S (2010) A review on mixing in microfluidics. Micromachines 1:82–111
134. Szita N, Boccazzi P, Zhang Z, Boyle P, Sinskey AJ, Jensen KF (2005) Development of a multiplexed microbioreactor system for high-throughput bioprocessing. Lab Chip 5:819–826
135. Tehranirokh M, Kouzani AZ, Francis PS, Kanwar JR (2013) Microfluidic devices for cell cultivation and proliferation. Biomicrofluidics 7:51502
136. Thompson DM, King KR, Wieder KJ, Toner M, Yarmush ML, Jayaraman A (2004) Dynamic gene expression profiling using a microfabricated living cell array. Anal Chem 76:4098–4103
137. Toh YC, Lim TC, Tai D, Xiao G, van Noort D, Yu H (2009) A microfluidic 3D hepatocyte chip for drug toxicity testing. Lab Chip 9:2026–2035

138. Vila-Planas J, Fernández-Rosas E, Ibarlucea B, Demming S, Nogués C, Plaza JA, Domínguez C, Büttgenbach S, Llobera A (2011) Cell analysis using a multiple internal reflection photonic lab-on-a-chip. Nat Protoc 6:1642–1655
139. Von Meyenburg K (1969) Energetics of the budding cycle of *Saccharomyces cerevisiae* during glucose limited aerobic growth. Arch Mikrobiol 66:289–303
140. Walker GM, Zeringue HC, Beebe DJ (2004) Microenvironment design considerations for cellular scale studies. Lab Chip 4:91–97
141. Wang YC, Ho CC (2004) Micropatterning of proteins and mammalian cells on biomaterials. FASEB J 18:525–527
142. Weigl BH, Bardell RL, Cabrera CR (2003) Lab-on-a-chip for drug development. Adv Drug Deliv Rev 55:349–377
143. Wenk P, Hemmerich J, Müller C, Kensy F (2012) Hochparallele Bioprozessentwicklung in geschüttelten Mikrobioreaktoren. Chem Ing Tech 84:704–714
144. Weuster-Botz D, Altenbach-Rehm J, Hawrylenko A (2001) Process-engineering characterization of small-scale bubble columns for microbial process development. Bioprocess Biosyst Eng 24:3–11
145. Whitesides GM, Ostuni E, Takayama S, Jiang X, Ingber DE (2001) Soft lithography in biology and biochemistry. Annu Rev Biomed Eng 3:335–73
146. Wilming A, Bähr C, Kamerke C, Büchs J (2014) Fed-batch operation in special microtiter plates: a new method for screening under production conditions. J Ind Microbiol Biotechnol 41:513–525
147. Wu MH, Huang SB, Cui Z, Cui Z, Lee GB (2008) A high throughput perfusion-based microbioreactor platform integrated with pneumatic micropumps for three-dimensional cell culture. Biomed Microdevices 10:309–319
148. Wu MH, Huang SB, Lee GB (2010) Microfluidic cell culture systems for drug research. Lab Chip 10:939–956
149. Wu MH, Urban JPG, Cui Z, Cui ZF (2006) Development of PDMS microbioreactor with well-defined and homogenous culture environment for chondrocyte 3-D culture. Biomed Microdevices 8:331–340
150. Wu Z, Hjort K (2009) Surface modification of PDMS by gradient-induced migration of embedded Pluronic. Lab Chip 9:1500–1503
151. Xia Y, Whitesides GM (1998) Soft lithography. Annu Rev Mater Sci 28:153–184
152. Xia Y, Whitesides GM (1998) Soft lithography. Angew Chem Int Ed 37:550–575
153. Yamamoto T, Fujii T, Nojima T (2002) PDMS-glass hybrid microreactor array with embedded temperature control device. Application to cell-free protein synthesis. Lab Chip 2:197–202
154. Yang B, Lin Q (2009) A latchable phase-change microvalve with integrated heaters. J Microelectromech Syst 18:860–867
155. Yang YN, Hsiung SK, Lee GB (2008) A pneumatic micropump incorporated with a normally closed valve capable of generating a high pumping rate and a high back pressure. Microfluid Nanofluid 6:823–833
156. Yuen PK (2008) SmartBuild-a truly plug-n-play modular microfluidic system. Lab Chip 8:1374–1378
157. Zainal Alam MNH, Gernaey KV (2012) Overview on design considerations for development of disposable microbioreactor prototypes. J Teknol 59:53–60
158. Zanzotto A, Szita N, Boccazzi P, Lessard P, Sinskey AJ, Jensen KF (2004) Membrane-aerated microbioreactor for high-throughput bioprocessing. Biotechnol Bioeng 87:243–254
159. Zeng Q, Guo F, Yao L, Zhu HW, Zheng L, Guo ZX, Liu W, Chen Y, Guo SS, Zhao XZ (2011) Milliseconds mixing in microfluidic channel using focused surface acoustic wave. Sensors Actuators B Chem 160:1552–1556
160. Zhang W, Lin S, Wang C, Hu J, Li C, Zhuang Z, Zhou Y, Mathies R, Yang CJ (2009) PMMA/PDMS valves and pumps for disposable microfluidics. Lab Chip 9:3088–3094

161. Zhang Z, Boccazzi P, Choi H-G, Perozziello G, Sinskey AJ, Jensen KF (2006) Microchemostat-microbial continuous culture in a polymer-based, instrumented microbioreactor. Lab Chip 6:906–913
162. Zhang Z, Boccazzi P, Choi HG, Szita N, Sinskey AJ, Jensen KF (2004) A microchemostat-continuous cell culture in microbioreactors. In: 8th International conference on miniaturized systems for chemistry and life sciences, Royal Society of Chemistry, Malmo, Sweden, pp 231–233
163. Zhang Z, Perozziello G, Boccazzi P, Sinskey AJ, Geschke O, Jensen KF (2007) Microbioreactors for bioprocess development. J Assoc Lab Autom 12:143–151
164. Zhang Z, Szita N, Boccazzi P, Sinskey AJ, Jensen KF (2005) A well-mixed, polymer-based microbioreactor with integrated optical measurements. Biotechnol Bioeng 93:286–296

Chapter 5
Microsystems for Emulsification

H. Bunjes and C.C. Müller-Goymann

Abstract Emulsions are important pharmaceutical preparations that are traditionally prepared by techniques like high-shear mixing and high-pressure homogenization. In recent years, microstructured devices have attained increasing importance with regard to emulsion preparation. In particular, the possibility of preparing emulsions with very precisely controlled particle size distribution and/or of continuous manufacturing makes such devices interesting. This chapter introduces microsystem-based techniques operating at low to moderate pressure and high-pressure-based methods. The former comprise direct microchannel and membrane emulsification as well as premix membrane emulsification. The latter particularly focuses on emulsification in a customized microchannel system but also covers aspects of conventional high-pressure emulsification devices. Apart from explaining the respective principles and devices, their use for the preparation of pharmaceutical formulations is outlined.

5.1 Introduction

Emulsions are disperse systems of two immiscible liquids one of which usually is an oily substance (oil phase) whereas the other is water or an aqueous solution (aqueous phase). One of the liquids is distributed in the other in the form of droplets and thus forms the disperse phase (Fig. 5.1). The phase surrounding the droplets is called continuous phase and its nature (oily or aqueous) determines the overall appearance of the emulsion. Accordingly, emulsions can either have an oil-in-water (O/W) or water-in-oil (W/O) character. As the formation of a large interface between the two phases increases the energy of the system (interfacial energy) emulsions are thermodynamically unstable and the droplets tend to coalesce in

H. Bunjes (✉) • C.C. Müller-Goymann
Institut für Pharmazeutische Technologie, Technische Universität Braunschweig, Mendelssohnstr. 1, Braunschweig 38106, Germany

PVZ—Center of Pharmaceutical Engineering, Technische Universität Braunschweig, Franz-Liszt-Str. 35 A, Braunschweig 38106, Germany
e-mail: heike.bunjes@tu-braunschweig.de

A. Dietzel (ed.), *Microsystems for Pharmatechnology*,
DOI 10.1007/978-3-319-26920-7_5

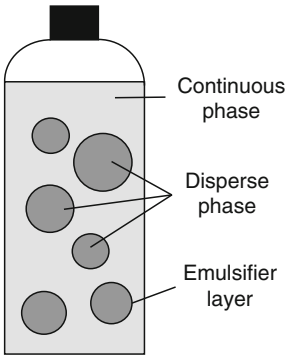

Fig. 5.1 Structure of an emulsion

order to decrease the interfacial area. Therefore, emulsifiers are usually added to the emulsion formulation to stabilize the system. Emulsifiers are surface-active agents that adsorb at the interface between disperse and continuous phase thereby lowering the interfacial tension. This makes the two phases much easier to disperse. Moreover, emulsifier molecules build energetic barriers around the droplets that counteract coalescence, often by electrostatic or steric interactions. Well-formulated emulsions thus can be kinetically stable over many years.

Emulsions are important pharmaceutical preparations, e.g., for administration of active agents to the skin or for the oral intake of drugs. There are also emulsions for intravenous injection in which tiny oil droplets act as carriers for water-insoluble drugs. In pharmaceutical emulsions, only ingredients of proven physiological compatibility can be used which limits the choice of components. Moreover, the particle size needs to be adapted to the site of administration. For example, the oil droplets in emulsions for intravenous injection must be of colloidal size (i.e., have diameters below around 500 nm) in order to avoid embolism by droplets getting stuck in the blood capillaries. Apart from being used as pharmaceutical formulations as such, emulsions are also used as intermediates in pharmaceutical processes. In particular, they are employed in the preparation of polymer or lipid micro-/nanoparticles that are formed by precipitation from an emulsified solution in an organic solvent (emulsification-solvent evaporation process) or by solidifying the melted disperse phase (melt-emulsification process). Such particles are often used in controlled release applications. Sometimes, "multiple emulsions" are created in such processes where the droplets of the disperse phase contain even smaller droplets of an immiscible liquid (e.g., water-in-oil-in-water emulsions). This way, active agents can effectively be encapsulated in a surrounding matrix.

Classically, emulsions are produced with high-shear mixers (in particular, rotor-stator devices) or by additional use of high-pressure homogenizers if very small

droplets need to be obtained. Such emulsification processes usually lead to emulsions with more or less broad droplet size distribution. More recently, microstructured devices have received increasing interest for the preparation of emulsions. They may allow the manufacturing of emulsions with lower energy input which can be relevant for the processing of sensitive materials. Moreover, it is often possible to produce emulsions of defined droplet size with very narrow size distribution. This chapter introduces the corresponding techniques with a major focus on techniques that easily allow the production of emulsion systems at pharmaceutically relevant scales such as membrane and high-pressure microchannel emulsification. Methods that can be used for the preparation of colloidal droplets are also of special interest.

5.2 Microsystems for Low-Pressure Emulsification

Conventional emulsification techniques relying on the breakup of a coarsely dispersed continuous phase, e.g., by using high-shear rotor-stator devices or high-pressure homogenizers, often lead to rather broad or even polydisperse particle size distributions. For many applications in the pharmaceutical and biomedical field it is, however, highly desirable to produce droplets with very uniform size. Thus, major efforts have been laid into the development of suitable manufacturing techniques and a variety of methods has become available during recent years. Most of them rely on direct emulsification, i.e., the direct preparation of the final emulsion droplets from the bulk phase upon contact with the continuous phase, and are typically carried out at low to moderate pressure.

5.2.1 Direct Emulsification

In direct emulsification, droplets are produced directly by injecting or extruding the disperse phase into the continuous phase. This can be accomplished by different microfluidic techniques, microchannel and membrane emulsification. Detailed overviews over the different techniques and devices used in direct emulsification can, for example, be found in [94, 95, 107]. As emulsification with microfluidic junctions (e.g., T-junctions, cross- and Y-shaped junctions) and flow-focusing devices is described in detail in Chap. 9 these techniques will not be treated here. Instead, this chapter focuses on microchannel and, in particular, membrane emulsification.

5.2.1.1 Direct Microchannel Emulsification

5.2.1.1.1 Principle

In microchannel emulsification, droplets are produced at the outlets of single microchannels etched in arrays into the surface of silicon wafers as grooves or straight-through holes. The technique can produce minimum droplet sizes down to around 1 μm with very narrow particle size distributions [95]. In grooved microchannel arrays the channel structure is usually fabricated onto a terrace and the process can be operated in dead-end or in cross-flow mode [33, 80]. At the end of the channels, the liquid to be dispersed first forms a flat disc between the terrace and the cover plate of the device; the disc is then transformed into a droplet by the surface tension upon leaving the terrace (Fig. 5.2). If operated below a critical flow rate, this method leads to monodisperse emulsion droplets [79]. As the number of microchannels is rather limited in dead-end emulsification modules, the flow rate is very low for typical applications (usually <0.1 mL/h). The throughput can be

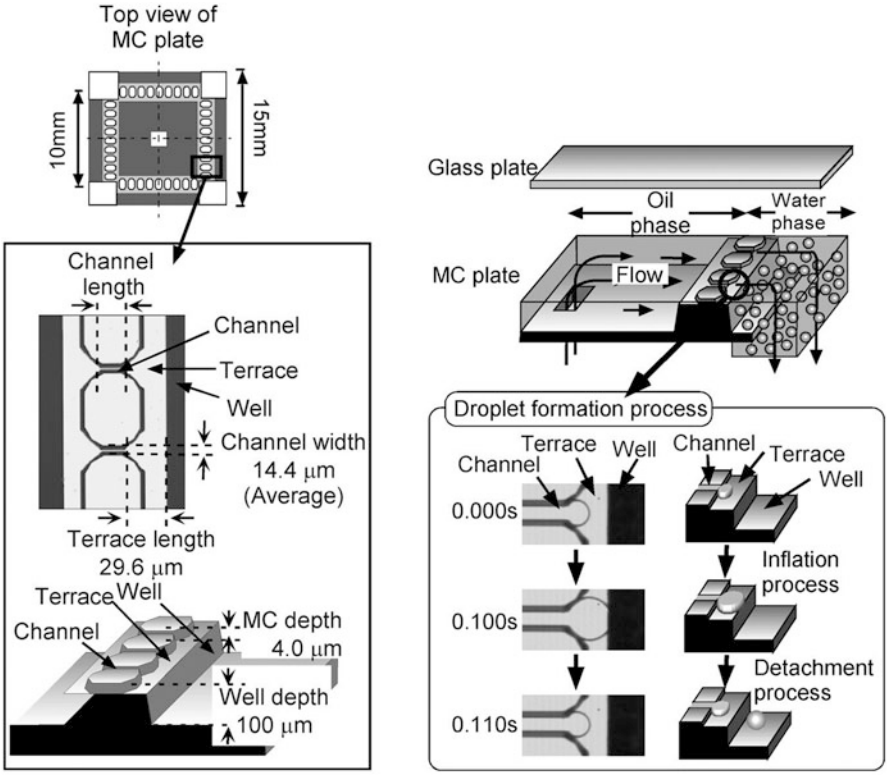

Fig. 5.2 Layout of a dead-end microchannel device (*left*) and corresponding droplet formation process (*right*). Reprinted from Sugiura et al. [80], Copyright (2003), with permission from Elsevier

increased to about 1.5 mL/h by using cross-flow devices which can accommodate a much higher number of channels [33, 34]. To further increase the flow rate to more application-oriented scales, straight-through microchannel arrays have been developed. Such arrangements can accommodate many more channels per wafer area as the channels are not etched in parallel to the surface of the substrate but vertically into the wafer (Fig. 5.3). A slit geometry of the channel openings has proven beneficial over circular pores with the aspect ratio of the pores preferably exceeding 3–3.5 for uniform droplet generation [30, 31]. With such devices, monodisperse emulsions (coefficients of variation below 10 %) with droplet sizes in the lower µm-region have been produced at a throughput of several tens of mL/h [32].

5.2.1.1.2 Applications

Microchannel emulsification is mainly applied for the preparation of precursor emulsions which are subsequently processed into microparticles with very uniform size [95]. For example, monodispersed solid lipid microspheres have been produced this way [81].

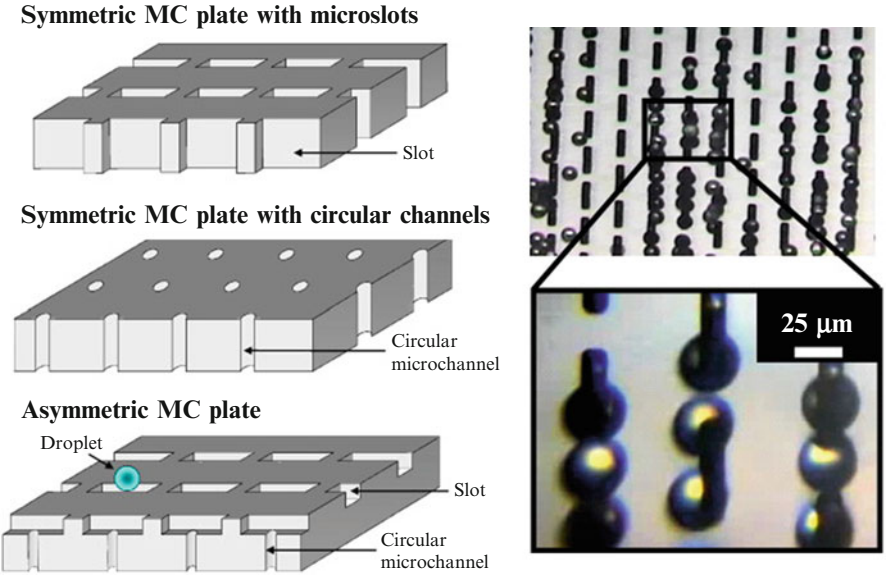

Fig. 5.3 Layout of symmetric and asymmetric microchannel plates (*left*) and droplet formation process at the channel outlets (*right*). Reprinted from Vladisavljević et al. [93], Copyright (2007), with permission from Elsevier

5.2.1.2 Direct Membrane Emulsification

5.2.1.2.1 Principle

In order to further increase the throughput, porous membranes or microsieves containing a large number of pores per unit area can be used for droplet generation. The pressurized disperse phase is forced through the pores of the membrane which is wetted with and in contact with the continuous phase. This way, single droplets are formed at the pore openings which are then detached from the membrane, usually by washing them away with a stream of the continuous phase [54] (Fig. 5.4). The relative movement between membrane and continuous phase is often generated by a pump or by stirring the continuous phase (in particular for small volume applications). However, rotating or vibrating membrane devices are also in use [71, 108]. The size of the resulting droplets is mainly determined by the pore size of the membrane: typically, the droplets formed are 2–10 times larger than the diameter of the pores [25]. In order to obtain a narrow particle size distribution, the forming droplets should not interact with each other. This can either be achieved by using membranes of low porosity or by operating porous membranes under conditions where only a small fraction of pores is active (i.e., at low emulsifying pressure) [2, 45].

The membrane emulsification process was originally developed as an application for Shirasu Porous Glass (SPG) membranes [54]. SPG is prepared from a primary glass based on a volcanic ash (Shirasu) rich in silica and alumina with addition of calcium carbonate and boric acid. The resulting $CaO–Al_2O_3–B_2O_3–SiO_2$ type glass is heat-treated for several hours leading to internal phase separation into an $Al_2O_3–SiO_2$ and a $CaO–B_2O_3$ phase. The latter is leached away by acid treatment leaving behind a continuous pore structure with narrow pore size distribution (Fig. 5.5). The mean pore size is determined by the course of the heat treatment process [95, 98]. Pore sizes between 0.1 and 20 µm are commercially available; the membranes are rather thick—0.4 to 1 mm [77]. The native SPG material is hydrophilic but the glass surface can be made hydrophobic, e.g., by chemical modification with organosilane compounds [41]. Surface hydrophilicity/hydrophobicity is highly important in membrane emulsification because usual

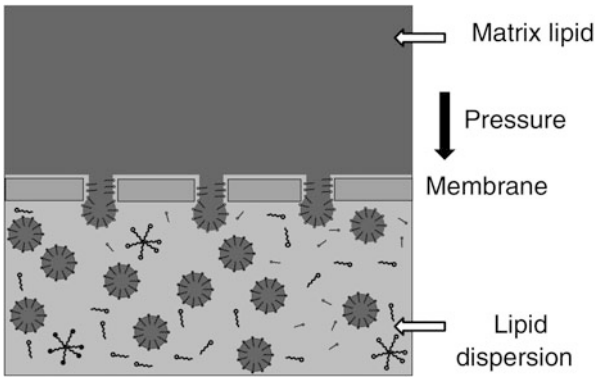

Fig. 5.4 Principle of direct membrane emulsification (not to scale). Modified from Joseph and Bunjes [28]

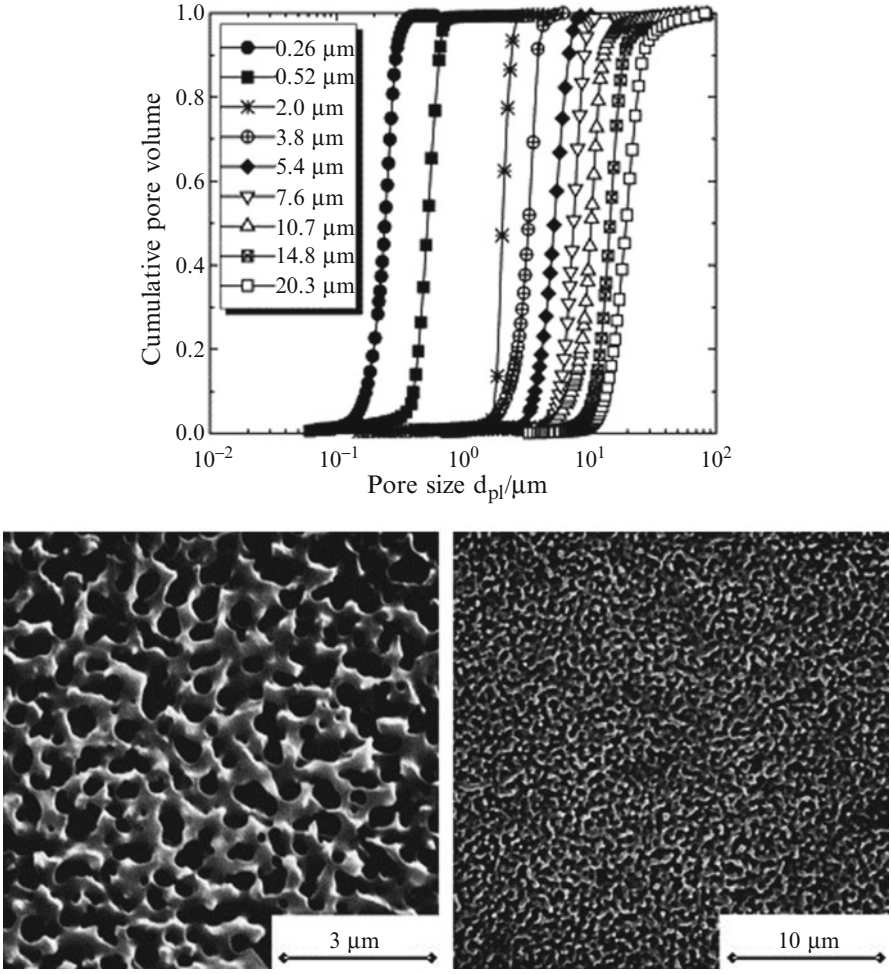

Fig. 5.5 Pore size distributions (mercury porosimetry) of different SPG membranes (*top*) and scanning electron micrographs of a membrane with 0.262 µm pore diameter (*bottom*). Reprinted from Vladisavljević et al. [98], Copyright (2004), with permission from Elsevier

applications require the membrane to be wetted by the continuous phase [1, 90]. Ceramic membranes have also been employed for membrane emulsification (e.g., [97]). As a further alternative to SPG membranes microsieves are increasingly being used (Fig. 5.6). Microsieves contain pores of controlled geometry and defined spatial arrangement. They can be prepared by semiconductor fabrication techniques, for example, from silicon nitride or nickel foils or by laser drilling of aluminum and steel foils [95, 100]. As they are much thinner than SPG membranes, higher fluxes can be achieved with microsieves [18, 99].

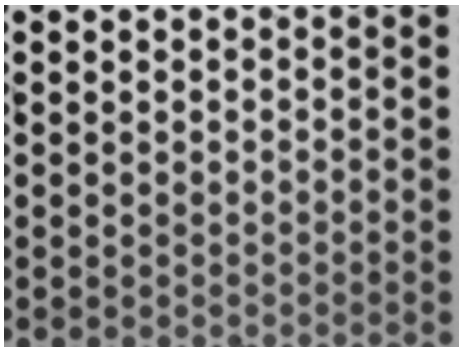

Fig. 5.6 Silicon nitride microsieve (pore size 5 µm) as used for membrane emulsification. Reprinted from Wagdare et al. [99], Copyright (2009), with permission from Elsevier

In direct membrane emulsification, a critical pressure has to be overcome before the to-be-dispersed phase can emerge from the membrane pores and form droplets at the membrane surface. Assuming the pores to be of ideally cylindrical shape, the minimum pressure can be estimated as the capillary pressure P_{cap} which is given by the Laplace equation ((5.1); γ: interfacial tension, θ: contact angle at the membrane, d_p: pore diameter):

$$P_{cap} = \frac{4\gamma \cos\theta}{d_p} \tag{5.1}$$

According to (5.1), the critical pressure increases steeply with decreasing pore size which complicates the preparation of droplets in the colloidal range with this technique [28]. With regard to a high production rate, it would be desirable to work at transmembrane pressures considerably above the critical pressure as a high transmembrane pressure increases the flux through the membrane. It is, however, advisable not to increase the pressure much above the critical pressure as—at a certain point—this leads to the transition from the "dripping" to a "jetting" regime. While dripping (release of single droplets) is considered to favor the formation of monodispersed size distributions, the formation of jets (which subsequently break up into droplets by interfacial instability) can lead to the formation of much more heterogeneous droplet size distributions [6, 39].

Membrane emulsification processes are usually performed under a cross-flow of the continuous phase over the membrane surface (Fig. 5.7). The wall shear stress exerted by this cross-flow influences the droplet formation process and the properties of the cross-flow, in particular its velocity has a major influence on the droplet size and size distribution. Increasing the cross-flow velocity usually leads to the formation of smaller droplets (as the droplets are more easily detached from the membrane) but at too high a cross-flow, the size distribution may become polydisperse [22, 35].

Upon droplet formation, the emulsifiers contained in the formulation adsorb to the evolving droplet surface at the pore opening. Surfactants that lead to a high decrease in interfacial tension are beneficial for the formation of homogeneous

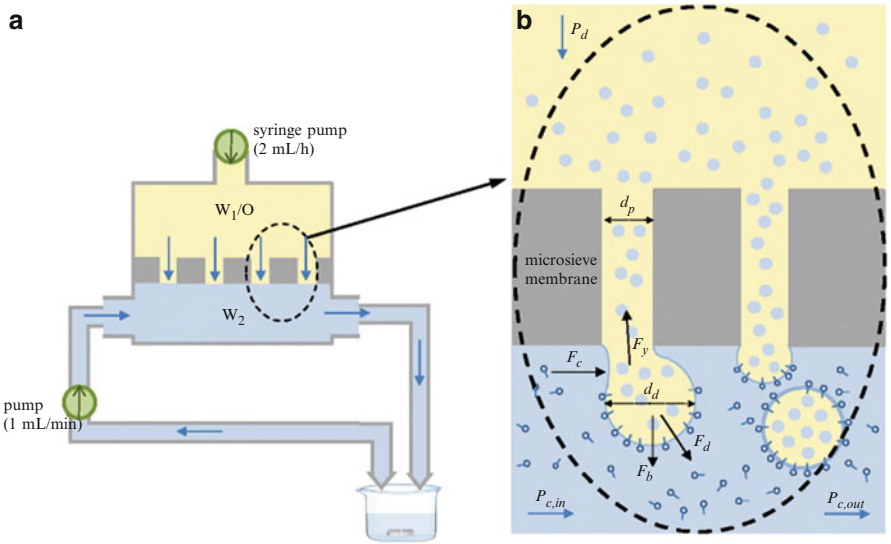

Fig. 5.7 Schematic diagram of the membrane emulsification method. (*Left*) Membrane module; (*right*) principle of particle preparation with microsieve membrane; W_1/O—dispersed phase (premix), W_2—external water phase, P_d—pressure applied on the dispersed phase, $P_{c,in}$ and $P_{c,out}$—pressure on the flowing continuous phase at both ends of the membrane modulus, d_p—diameter of the membrane pore, d_d—diameter of the droplet formed at the membrane pore, F_γ—the interfacial tension force, F_b—the buoyancy force, F_c—the drag force of the continuous phase flow, F_d—the inertial force caused by the flow of the dispersed phase. Reprinted from Kazazi-Hyseni et al. [29], Copyright (2014), with kind permission from Springer Science and Business Media

emulsions [22]. Moreover, quick adsorption usually favors the formation of smaller droplets and narrow size distributions [39, 89]. Care should be taken to avoid interaction of the surfactant with the membrane (e.g., due to opposite charge of surfactant and membrane) as this may lead to wetting of the membrane with the dispersed phase or to membrane fouling and blocking resulting in poor emulsion quality [54, 82]. On the other hand, surfactants that lead to a strong repulsion of the forming droplets from the membrane due to charge interactions favor the formation of smaller droplets [39].

5.2.1.2.2 Applications

Direct membrane emulsification has often been used to prepare micron-sized drug delivery systems such as simple o/w emulsions, w/o/w emulsions as well as lipid and polymer microspheres [23, 29, 40, 47, 54, 55]. In contrast, there are only few reports about attempts to create colloidal particles for pharmaceutical use with direct membrane emulsification. In principle, the preparation of colloidal dispersions should be possible when membranes with small pore diameters are used such

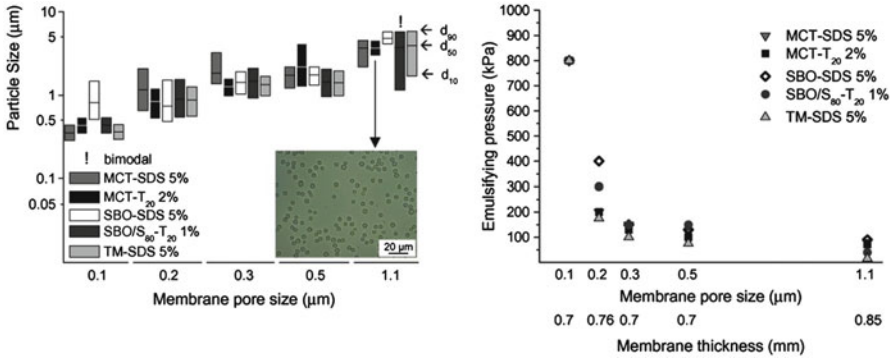

Fig. 5.8 Particle size distributions (*left*) and corresponding emulsifying pressures (*right*) observed in a formulation screening by direct SPG membrane emulsification with different membrane pore sizes. Lipid phase: *MCT* medium chain triglycerides, *SBO (/S$_{80}$)* soybean oil (/sorbitan oleate), *TM* trimyristin; Stabilizer: *SDS* sodium dodecyl sulfate, *T$_{20}$* polysorbate 20, concentrations refer to the stabilizer concentration in the aqueous phase. The concentration of the matrix lipid was 1–5 %. Reprinted from Joseph and Bunjes [28], Copyright (2013), with permission from Elsevier

as the commercially available 100 nm-SPG membranes. Emulsion particles with median particles down to below 500 nm and narrow size distribution could indeed be obtained with this process [28] (Fig. 5.8). Due to the typical particle to pore size ratio resulting from this technique the particle sizes obtained were, however, larger than usually desired for typical pharmaceutical colloidal emulsions. Moreover, in spite of the comparatively high required emulsifying pressure, the flux was very low resulting in long process times.

5.2.2 Premix Membrane Emulsification

5.2.2.1 Principle

The use of direct membrane emulsification still somewhat suffers from the fact that the throughput may be rather limited in particular with regard to the preparation of very small particles. Consequently, the resulting dispersed phase fraction is often low. Moreover, the preparation of emulsion droplets in the lower colloidal range is conceptually difficult as this would require the availability of suitable membranes with extremely small pore sizes. A variation of the direct emulsification process, premix membrane emulsification, may be used to overcome these limitations. This technique, developed by Suzuki in the 1990s [84], is fundamentally different from the direct emulsification techniques described above as it relies on the processing of a pre-formed coarse emulsion. By extruding the coarse emulsion droplets through the membrane pores, the droplets are disrupted into smaller ones (Fig. 5.9).

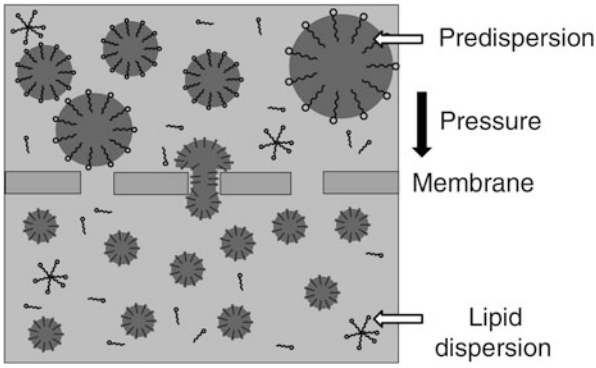

Fig. 5.9 Principle of premix membrane emulsification (not to scale). Modified from Joseph and Bunjes [28]

Repeated processing through the membrane can lead to a further decrease in droplet size and to a more uniform droplet-size distribution [27, 97]. The resulting particle size is mainly controlled by the pore size of the membrane and the number of extrusion cycles whereas the size and uniformity of the droplets in the premix do not have much effect on the emulsification results [96]. Typical ratios of average pore size to average particle size are in the range of 1:1 to 1:3 [38, 83]. The size ratio of the resulting droplets to the membrane pores is thus usually smaller than in direct membrane emulsification, whereas, however, the particle size distributions are usually slightly broader [97]. Typical membrane materials used for premix membrane emulsification are SPG [82, 97], polytetrafluoroethylene [83] and polycarbonate [26, 62] but other membrane materials can also be used [27]. Good wetting of the membrane with the continuous phase of the emulsion is considered essential to obtain good results [56]. Similar to direct membrane emulsification, the energy efficiency during premix membrane emulsification is much better than in traditional emulsification such as high-pressure homogenization [56].

It is not yet completely clear how the large droplets are broken up during premix membrane emulsification. Shear forces are assumed to play a major role during this process. Van der Zwan et al. visualized the droplet breakup during emulsification of an O/W premix in a model microfluidic device [91]. According to the results three factors have a major impact: (a) localized shear forces that occur at channel branchings may shear off small fractions of a larger droplet or a large droplet is split up due to divergent flows into two channels at a branching. (b) Droplets may be deformed (e.g., elongated into a cylindrical shape) upon passage of the narrow pores and be broken up by interfacial tension effects (e.g., Rayleigh instabilities). (c) Droplets accumulate before entering the membrane as well as within the membrane pores. At the corresponding places, the local droplet concentration is very high which may give rise to interactions between droplets that lead to droplet breakup, e.g., by droplet impact. This mechanism relies on a good stabilization of the droplets as otherwise coalescence may become predominant.

5.2.2.2 Applications

Besides simple emulsions [84], multiple emulsions [97], solid lipid microcapsules [38], and polymer microparticles [70, 103] can be prepared by premix membrane emulsification. With this technique, also the preparation of colloidal systems is feasible. For example, the technique has been used to prepare lipid emulsions and artificial low density lipoprotein (LDL) particles [3, 9, 58]. The concentration of the lipid to be emulsified was rather low in these early studies (≤8 %). Recently, this technique was also established for the preparation of nanoemulsions and solid lipid nanoparticles (prepared by melt-emulsification) at comparatively high lipid contents (up to 20 %), comparable to that used in conventional high-pressure homogenization [26]. The process could be performed at large scale with a pump-driven membrane extruder or in a small (≤1 mL) handheld extrusion device as it is often used to prepare liposomes at a small scale. The mean particle sizes of the lipid nanoparticle dispersions depended mainly on the membrane pore size and the number of extrusion cycles. Ratios of average pore size to average particle size in the range of 1:0.5–1:2.5 and narrow size distributions were obtained after repeated extrusion [26]. Apart from track-etched polycarbonate membranes other types of membrane filters as well as SPG membranes could be used [27, 28]. The use of SPG membranes led to small particles with narrow size distribution already after one passage of the membrane (Fig. 5.10). Investigations with a specially designed, instrumented small-scale extruder indicate that the combination of the type of membrane used for extrusion and the emulsion composition is of importance for the success of the process [16, 17].

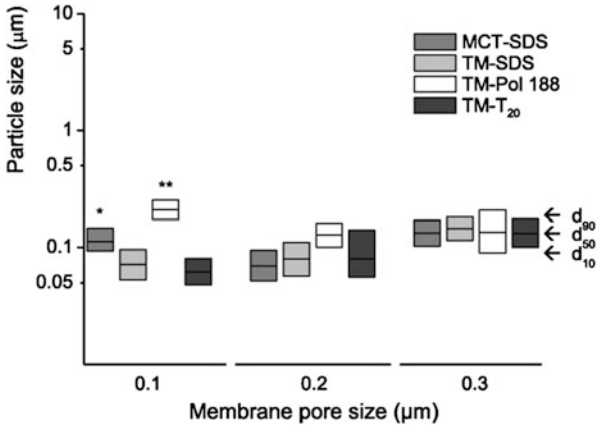

Fig. 5.10 Particle size distributions observed after one membrane passage in a formulation screening by premix SPG membrane emulsification with different membrane pore sizes. Lipid phase: *MCT* medium chain triglycerides, *TM* trimyristin; Stabilizer: *SDS* sodium dodecyl sulfate, *Pol 188* Poloxamer 188, T_{20} polysorbate 20. The predispersions usually contained 10 % matrix lipid stabilized with 7.5 % surfactant (*5 % matrix lipid, **2.5 % matrix lipid with correspondingly lower stabilizer content). Reprinted from Joseph and Bunjes [28], Copyright (2013), with permission from Elsevier

5.3 Microsystems for High-Pressure Emulsification

High-pressure emulsification at large scale is a well-known and industrially established process for the manufacturing of emulsions, i.e., dairy products such as homogenized milk. A sufficient kinetic stability of such emulsions along with small droplet size in submicron range and a narrow size distribution is achieved by this emulsification process. As for medicinal products, nanoemulsions are frequently used in parenteral nutrition [50] or as commercially available drug delivery systems for intravenous administration, e.g., for diazepam [46], vitamin K [74], and propofol [4].

In contrast to high-pressure emulsification at large scale, the manufacturing at small scale is required especially in the development of pharmaceutical emulsions and nanoscale lipid dispersions because only limited amount of the active pharmaceutical ingredient (API) is available for screening purposes of formulations in the early stages of the development. Therefore microsystems for high-pressure emulsification offer the advantage of low production volumes along with high performance of the resulting emulsions and dispersions with regard to nanoscale particle size, narrow particle size distribution, and high physicochemical stability. By customizing the design of a microsystem, a given surface to volume ratio and a well-defined residence time as well as input of stress to the product stream are achievable [15]. In this context a customized microchannel system was recently designed in a collaborative project of the German Research Foundation (DFG research group FG 856 mikroPART).

5.3.1 Customized Microchannel System (Disruption of Pre-formed Droplets)

5.3.1.1 Device

Stainless steel sheets were used as microsystem substrate and structured by a microelectrical discharge machining (μEDM) process in combination with a final electrochemical polishing process [68]. A variety of different microchannels were designed ranging from straight, z-shaped, y-shaped, and orifice channels as well as combinations thereof (Fig. 5.11). The microchannel-containing bottom plate was covered with an analogous, unstructured stainless steel plate and clamped together to obtain a leak-proof but reversible coverage [15]. Thus both the assembly and the disassembly for cleaning purposes are easily done and also fast, while leak tightness is guaranteed even at elevated temperature beyond the melting temperature of solid lipids and at high pressures above 2000 bar [20].

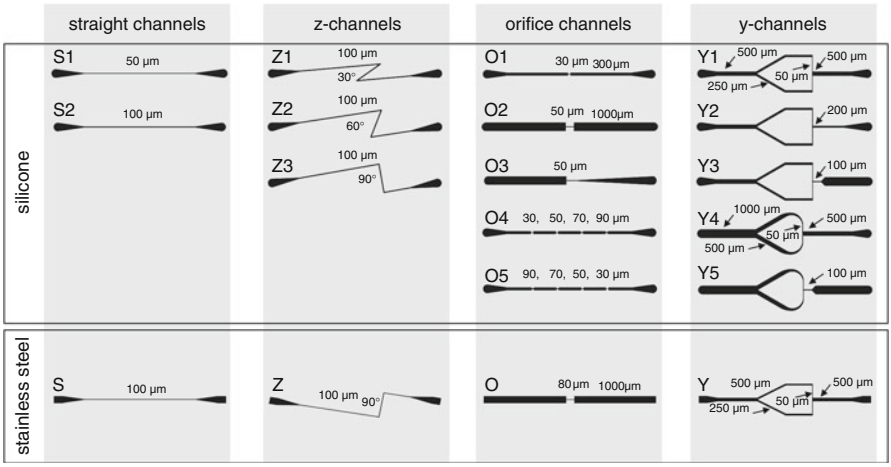

Fig. 5.11 Schematic representation of microsystems fabricated in either silicone (*top*) or stainless steel (*bottom*). Reprinted from Finke et al., [15] Copyright (2012), with permission from Elsevier

Further variations in orifice microchannel design include combinations of two or three orifices of the same width (80 µm) and of different widths (80 and 120 µm) as well as a variation in length between multiple orifices. For the triplicate-orifice microchannel the distance between each 80 µm wide orifice was 3000 µm, for the double-orifice microchannels the distances between 80 µm wide orifices were 300 µm, 3000 µm, and 5169 µm, respectively. The same distances between orifices were also applied for the combination of an 80 µm wide orifice with a 120 µm wide one. Whether the smaller orifice is passed first or the larger one was also of interest with regard to the emulsification efficiency. Furthermore the microchannel with a single orifice was run with varying counter pressures while passing a coarse pre-emulsion through it.

As the microchannels described above are not appropriate for the pre-emulsification step, i.e., the initial combination of the lipid and the aqueous phase by the formation of small lipid droplets with as homogeneous distribution as possible, an additional microcomponent has to be integrated for this initial emulsification step. Furthermore, commonly used unit operations such as the dispersion of solid particles into a suspension and the crystallization of liquid emulsion droplets to a solid nanoscale dispersion are also required. An overall microsystem was designed to combine all these unit operations of dispersion (e.g., a solid API powder), pre-emulsification, emulsification, and crystallization (cooling down) in a continuously operated process chain (Fig. 5.12). The aim of the implementation of multiple process steps in an integrated process chain is the reduction of losses due to sample handling between process steps as well as in tubing.

The challenge regarding the overall microsystem is to combine the particular microcomponents with regard to volume flow and pressure drop. The dispersion and the emulsification components require high pressure drops for the

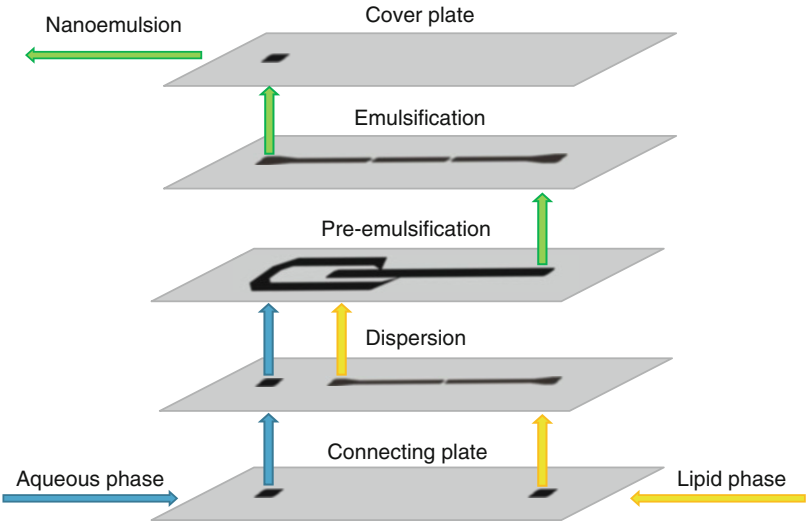

Fig. 5.12 Assembling principle and flow through the integrated overall microsystem. From Finke et al. [11]

disintegration process of agglomerates and droplets [69], respectively, whereas the pre-emulsification component has to work at relatively low pressure drops. Additionally, two fluids with different viscosities, i.e., aqueous solution and oil, have to be processed. In the pre-emulsification component, the ratio between the static pressures of the lipid and the aqueous phase has to be adjusted properly to prevent a backflow. Since the adaption of principles well known from emulsification approaches at low flow rates and low Reynolds numbers (e.g., flow focusing) is not possible at high pressure drops and accordingly high flow rates, an appropriate construction principle was designed for the injection of the water phase into the flow of the lipid phase via nozzles as depicted in Fig. 5.12.

5.3.1.2 Principle

The pre-emulsification micromodule is based on the formation of a high-velocity jet of an aqueous surfactant solution which splits the flow of the viscous oil into separate droplets of almost uniform size below 1 µm [67].

The subsequent microchannel emulsification works on the pre-formed droplets, i.e., a coarse emulsion with a not necessarily narrow size distribution flows through the microchannel. The droplets' velocity becomes increasingly high due to the high pressure and the narrowing of the channel according to its specific design. This forces the droplets to elongate and due to shear stress and turbulent flow characteristics tiny droplets of nanoscale dimensions rip off. The superposition of simultaneously prevailing shear, elongational, turbulent and cavitational stresses makes it difficult to identify the primary dispersion mechanism and the actual place of

droplet breakup [19]. The final droplet size inversely correlates with the driving pressure through the microchannel and thus the pressure loss versus ambient conditions, the shear rate, and also with the number of passes. The latter only plays a role, if the microchannel device is used separately for the disruption of pre-formed droplets and not as a modular overall microsystem designed for the emulsification of the original aqueous and oily phases in a single pass.

However, formulation-dependent parameters also affect the efficiency of dispersion. A large volume fraction of the phase to be dispersed is a challenge with regard to the emulsification efficiency whereas a high amount of an appropriate surfactant results in smaller particle sizes and narrower particle size distributions. Furthermore the droplet oil viscosity strongly influences the outcome of the high-pressure emulsification process [51]. The adjustment of the viscosities of both phases to similar values proved to be most efficient in terms of the emulsification efficiency [5, 106]. In this case, fluid dynamic stresses are better transferred from the continuous to the disperse phase [12]. In addition, due to an adjusted dynamic viscosity of the aqueous continuous phase the film drainage between two colliding droplets is slowed down which results in a hydrodynamic stabilization.

Comparing different designs of a microchannel applied for a given formulation at same pressure reveals highest droplet breakup efficiency for y-shaped and orifice channels while z-shaped and straight channels result in larger droplet sizes [15]. The pressure loss over the whole length of a straight channel is nearly constant, whereas orifice and y-shaped channels focus the main pressure loss on a small volume in the orifice or at the T-connection of the y-shaped microchannel towards the outlet [19]. This causes highest stress intensity and thus highest energy input per volume. Multiple orifices in a customized microchannel, i.e., a double-orifice channel proved superior to both a triplicate-orifice channel and a microchannel with only one orifice of the same width (80 μm) by reducing the coalescence of broken up droplets due to the establishment of a turbulent mixing zone [12]. In this zone, although the frequency of droplet collisions is high, the contact time is shorter than the time needed for coalescence. This fluid dynamical stabilization, however, requires a sufficient, yet not too long distance between the orifices within a given overall length of the microchannel. Furthermore, flow and cavitation measurements in high-pressure microfluidic systems made of silicon and covered with glass reveal a minor effect of the cavitation on the emulsification efficiency by applying an increasing counter pressure to a single orifice device and thus finally provoking a collapse of cavitation bubbles. Since in double-orifice systems, the second orifice also provides a counter pressure towards the first orifice, the minimization of cavitation is considered to coincide with higher emulsification efficiency. Therefore cavitation is not likely to be the dominating mechanism in droplet breakup [21].

5.3.1.3 Applications

A variety of different colloidal systems has been produced with the customized microchannel system so far. Apart from nanoemulsions made of medium chain triglycerides and stabilized with different emulsifiers such as sodium dodecyl sulfate or macrogol-15-hydroxystearate [12, 15, 20] solid lipid nanoparticle (SLN) dispersions have successfully been manufactured with this device while maintaining all the metal parts including the tubing at elevated temperature which guarantees the molten state of the lipid. A conventionally prepared (e.g., with an Ultraturrax®) hot pre-emulsion is passed through the temperature-controlled customized microchannel device at around 1250 bar (chosen for standardized production conditions) at least once or in some cases several times before being cooled down to room temperature to enable solidification of the molten lipid droplets to solid lipid nanoparticles (SLN) [14, 15, 69, 72]. The particle sizes and the particle size distributions are in the same range as with the conventional high-pressure emulsification at large scale even after a single passage whereas conventional processes at large scale require a rather high number of passages (up to 30) for the same outcome.

Different lipids may be used along with a variety of emulsifiers. The emulsification of 15 % (w/w) of a combination of melted waxes in an aqueous solution of 0.1 % (w/w) polysorbate 80 as emulsifier of the same temperature which is subsequently followed by a cooling down process at ambient temperature results in solidified wax nanoparticles of a mean particle size around 400 nm for a wax combination of carnauba wax (solid at ambient temperature) and decyl oleate as a liquid wax in a ratio 2:1 (solid:liquid) [14]. SLN from a standard formulation that is produced in the customized microchannel device are composed of a solid mixture of triglycerides from hydrogenated palm oil (Softisan®154) and phospholipids (Phospholipon®90G) in a ratio of 7:3 (T:P). A total of 5 % (w/w) of the melted lipid matrix is emulsified at 70 °C in an aqueous solution of 3 % (w/w) macrogol-15-hydroxystearate (Solutol®HS15) of the same temperature. After subsequent cooling the mean particle size of those SLN is around 120 nm [15].

SLN of the previously described composition have also been loaded with different APIs or model compounds thereof [13, 59, 61, 66]. Depending on the physicochemical characteristics of the API, the loading with the respective compound results in SLN modification or not with regard to particle size, particle size distribution, zeta potential, and thus agglomeration tendency. Rather lipophilic drug molecules with high affinity to the lipid matrix partition into the SLN core. At low concentrations, the particle size as well as the zeta potential remain unaffected [66]. Highly water-soluble drug molecules or their likewise soluble salts are mainly dissolved in the aqueous surrounding phase and to a minor part incorporated as particles inside the SLN where they are intended to serve as a depot for a modified release [60]. However, as the surface of nanoscale particles is extremely large, a prolonged release is not realistic but the release is rather fast. In addition, due to the dissolution of such molecules, the physicochemical characteristics of the aqueous

surrounding phase are modified which in turn change the SLN's zeta potential. The latter may also affect particle size and particle size distribution. In contrast, API molecules with a high affinity towards the stabilizing surface layer of the SLN, i.e., the phospholipid and the nonionic emulsifier, attach mainly to this surface layer.

With regard to the administration of sildenafil-loaded SLN dispersions via inhalation into the lungs, small-volume cell culture experiments for screening their toxicity on human alveolar epithelium and mouse heart endothelium demonstrate promising results [61]. Microfluidic cell culture experiments on human corneal epithelium prove a fast uptake of a lipophilic drug model into the cells from SLN dispersions [66]. The uptake mechanism is not particle-driven but diffusion-controlled.

5.3.2 Conventional High-Pressure Emulsification Systems

High-pressure homogenization of crude emulsions has a long tradition not only in food industry (i.e., high-pressure homogenization of milk) but, since 1950 onwards, also in the large-scale production of pharmaceutical o/w fat emulsions for parenteral nutrition. About 40 years later, research started on the high-pressure homogenization of hot pre-emulsions of melted lipids. Upon subsequent cooling down to ambient temperature the processed nanoscale emulsions transformed into solid lipid nanoparticle (SLN) dispersions appropriate for pharmaceutical applications [53, 75, 76, 105].

5.3.2.1 Devices and Principles

The high-pressure homogenizers used in these early publications were conventional homogenizers of the piston-gap type, i.e., APV Gaulin Micron Lab 40. Piston-gap type homogenizers such as equipment developed by manufacturers Avestin, APV, Niro, Stansted Fluid Power process a coarse pre-emulsion by bringing it to high pressure up to 1000 bar within a few seconds in the pressure intensifier and then forcing it through the valve gap of few micrometers in width. The processing performance importantly depends on the valve design (geometrical characteristics of the needle and seat, height and shape of the valve gap) apart from the physicochemical characteristics of the fluid (density, viscosity, flow rate) [10]. Intense mechanical forces and elongational stress in laminar flow at the valve entrance and in the valve gap occur, while due to the pressure drop at the gap outlet, turbulence, cavitation and impacts with solid surfaces contribute to the droplet breakup. The processing through the valve gap is accompanied by short-life heating phenomena that must be controlled if needed. Due to shear effects and partial conversion of mechanical energy into heat, a total jump in temperature by 17–21 °C per 100 MPa was therefore measured when processing whole milk or O/W emulsions processed at an initial temperature of 4–24 °C [8, 64, 88]. The development of heat especially

during several passages through the homogenizer is crucial for heat-sensitive APIs. With regard to SLN preparation, subsequent cooling devices such as heat exchangers result in the solidification of the dispersed lipid droplets.

Due to the dependency of the emulsification efficiency on the valve design many attempts have been made to improve droplet breakup and avoid re-coalescence. A new high-pressure dispersion chamber was introduced by Kolb et al. [37]. This new dispersion unit consists of three segments: an inlet nozzle with 0.2 mm orifice, a so-called turbulence chamber and an outlet nozzle, which has a wider orifice and is axially spaced apart relative to the inlet nozzle. The turbulence chamber is claimed to provide sufficient time for the stabilization of freshly broken-up droplets by the adsorption of emulsifier molecules. Therefore re-coalescence may be minimized and the authors report smallest particles sizes compared to a conventional nozzle with a single 0.2 mm orifice for a variety of different oil-in-water emulsions stabilized with different emulsifiers and at different oil contents up to 30 % (w/w). Tesch et al. [87] replaced a standard valve of a high-pressure homogenizer (APV Gaulin) by an orifice valve and a conical valve and compared the outcome of the emulsification efficiency for different oils (vegetable oil and paraffin oil) in aqueous fast-stabilizing surfactant solutions whose viscosities were adjusted with polyethylene glycol 20,000. They also varied the number of passages and found an improvement by using the dissipated energy more efficiently in the conical valve which in addition separates freshly disrupted droplets behind the narrowest cross section and thus helps to avoid coalescence.

Another type of conventional high-pressure homogenizers is designed with a microchannel architecture set in a fixed reaction chamber and operating quite differently (Microfluidics™) [92]. The microfluidizer technology was patented in 1985 [7] and was first reported in a scientific publication in 1987 [101]. Indeed, the microfluidizer technology has the pre-formed emulsion stream split into two jets at the inlet. The split fluid streams change their flow directions at the chamber outlet to interact with each other at ultrahigh velocities (>500 m/s) leading to enhanced particle collision and impingement on the chamber walls. The colliding fluid jets coming from two opposite microchannels lead to enhanced particle disruption. Such devices combine laminar extensional flow at the chamber inlet to highly turbulent flow with cavitation and impact in, and at the outlet of the chamber [63, 73, 78].

5.3.3 Applications

The conventional high-pressure homogenization has not only been used for the large-scale production of o/w and w/o emulsions but also for other colloidal systems such as liposomal dispersions [85], SLN dispersions [50], and polymeric nanoparticle dispersions [42].

For the production of liposomes containing hemoglobin, the microfluidizer technology proves all the energy remaining within a small area, resulting in the

production of liposomes with smaller size (micron or submicron liposomes), greater uniformity and better reproducibility than with other preparation methods such as sonication. Results of electronic microscopy, particle sizing, and protein measurement by Kjeldahl show that larger encapsulation efficiency is obtained (up to 18 % of the encapsulated hemoglobin and up to 90 % of the lipid included in the liposomal membrane). The use of a microfluidizer leads to a more homogeneous liposome size distribution and higher stability [92].

Soya oil/water emulsions using egg lecithin as emulsifier have been prepared with a microfluidizer and for comparative purposes also by ultrasonication on a small scale. The resultant emulsions have been compared with "Intralipid" 10 and 20 % as examples of commercially available products. The microfluidizer produces emulsions with droplet size and polydispersity similar to those of the commercial product "Intralipid," and with lower polydispersity and droplet size than those produced by ultrasonication. Emulsion droplet sizes are even smaller and distributions narrower when the apparatus is operated at a higher temperature. The microfluidizer also has several practical advantages over ultrasonication for the preparation of small quantities of emulsions for experimental purposes, and appears to be a useful technique for the preparation of intravenous fat emulsions [102].

The operating efficiency of a bench-top air-driven microfluidizer has been compared to that of a bench-top high power ultrasound horn in the production of pharmaceutical grade nanoemulsions using aspirin as a model drug. Both the emulsification methods produce very fine nanoemulsions with the minimum droplet size ranging from 150 to 170 nm. In the case of using the microfluidizer, the size of the emulsion droplets is almost independent of the applied microfluidization pressure (200–600 bar) and the number of passes (up to ten passes) while the pre-homogenization and drug loading has a marginal effect in increasing the droplet size [86]. In fact, it has been observed that microfluidization is superior as the droplet size distribution is narrower in microfluidized emulsions than those prepared using conventional emulsifying devices [65]. In some cases, however, an ultrasound probe sonicator has shown superior emulsification efficiency compared to microfluidization [24]. It is also shown that microfluidization is unfavorable in specific circumstances such as higher pressures and longer emulsification times, as it usually leads to "overprocessing", namely the re-coalescence of emulsion droplets and thereby an increase in the emulsion droplet size [48, 57].

A comparison of the emulsification performance of a high-pressure valve homogenizer (HPH) and a microfluidizer has been carried out for a range of different oil to aqueous phase viscosity ratios, emulsifier types, pressure drops, and number of passes through the chambers. Differences in droplet size have been demonstrated for the same pressure drop across the two chambers after a single pass, with the HPH producing larger droplets with a wider distribution of sizes. This difference can be attributed to the design of the homogenization chambers with the HPH producing a wide distribution of shearing forces. Thus all of the starting emulsion does not experience the maximum stress at each passage. After five passages, however, similar droplet sizes are produced. Droplet size has been shown to be independent of viscosity ratio (0.1–80) for both homogenizers

indicating that breakup is occurring in turbulent flow. No effect of emulsifier is observed in the microfluidizer with sodium dodecyl sulfate (SDS), polysorbate 20, and sodium caseinate. However, with the HPH, the droplet size reaches a limiting value after two passages with SDS while with polysorbate 20 and sodium caseinate five passages are required indicating that coalescence occurs in the HPH but this is more effectively eliminated by SDS [43, 44].

Vladisavljević et al. compared oil-in-water nanoemulsions consisting of rapeseed oil as the dispersed phase and 2 % (w/w) aqueous polysorbate 80 solution as the continuous phase. Different emulsification methods were used, such as membrane emulsification (ME) with Shirasu porous glass (SPG) and α-aluminum oxide (α-Al_2O_3) membranes, microfluidization (MF) and microchannel (MC) emulsification with regard to the operating conditions and the resultant emulsion properties. The microfluidization is a suitable method for producing o/w emulsions with a very small mean droplet sizes of 85–300 nm, that cannot be attained by membrane or microchannel emulsification, with the span of the droplet size distribution in the range between 0.91 and 2.7 [96].

Wengeler and Nirschl studied the dispersion efficiency of cylindrical orifices with a diameter of 125 μm along with a pressure difference of up to 1400 bar [104]. Another approach established by Köhler combines a homogenization valve and a subsequent T-shaped micromixer for the homogenization of dairy products with a fat content of up to 42 vol.% [36].

Three different emulsifying processes, i.e., a rotor-stator device (Silverson), a microfluidizer (Microfluidics) and a new patented high-pressure jet have been compared with regard to droplets' diameter reduction, emulsion stability, protein adsorption at the interface, and energy input in the process [63]. The droplets obtained with the two high-pressure devices are smaller than those from the rotor-stator process, in line with the difference in energy density input. The high-pressure jet, for low protein content, promotes the disruption of droplets into smaller ones (less than 90 nm) more than that of the microfluidizer. When protein content is increased up to 2 % w/w, the microfluidizer gives smaller average size and less polydispersed emulsion than the jet. The high-pressure jet allows direct emulsification by injecting the oily phase up to 30 % (w/w) into the continuous phase [49]. The dispersed phase is pressurized by a high-pressure pump (Resato, Netherland) up to 4000 bar. The dispersed phase is temperature-controlled while under pressure by using a tubular exchanger. When released through a sapphire nozzle (0.1 mm in diameter the dispersed phase was), the liquid forms a high-velocity jet (about 450 m s^{-1} at 2000 bar). The jet immerges into the dispersing phase. The high-shear stress resulting from the jet energy allows the emulsion formation.

The preparation of polymeric nanoparticles (NP) as potential drug carriers for proteins has successfully been demonstrated for the hydrophilic protein bovine serum albumin (BSA) as a model drug. Because of a high solubility of the protein in water, the double emulsion technique has been chosen using a microfluidizer. Two different biodegradable polymers, poly[D,L-lactic-co-glycolic acid] 50/50 (PLGA) and poly[ε-caprolactone] (PCL) have been used for the preparation of

the NP. The drug loading has been optimized by varying the concentration of the protein in the inner aqueous phase, the polymer in the organic phase, the surfactant in the external aqueous phase, as well as the volume of the external aqueous phase. The BSA encapsulation efficiency is high (>80 %) and release profiles are characterized by a substantial initial burst release for both PLGA and PCL NP. A higher release is obtained at the end of the dissolution study for PLGA NP (92 %) compared with PCL NP (72 %) [42].

Numerous references concern the production of SLN dispersions with conventional high-pressure homogenizers. For further reading, reviews are recommended [50, 52].

5.4 Conclusion

There is a broad variety of microsystem designs for emulsion preparation operating at low as well as high pressures. With such devices emulsions with different properties regarding particle size and particle size distribution can be manufactured at different scales. Small-scale preparation may be particularly interesting in screening studies as well as for the processing of precious ingredients. In contrast, many industrial processes rely on large-scale production. Recent developments offer the possibility of preparing well-defined emulsions and related products directly from the starting materials (i.e., the oil and the aqueous phase) in a single passage. The corresponding minimization of stress is highly advantageous for the processing of sensitive pharmaceutical ingredients.

References

1. Abrahamse A, van der Padt A, Boom R (2001) Process fundamentals of membrane emulsification: Simulation with CFD. AIChE J 47(6):1285–1291
2. Abrahamse A, van Lierop R, van der Sman R et al (2002) Analysis of droplet formation and interactions during cross-flow membrane emulsification. J Membr Sci 204:125–137
3. Baillie G, Owens M, Halbert G (2002) A synthetic low density lipoprotein particle capable of supporting U937 proliferation in vitro. J Lipid Res 43:69–73
4. Baker M, Naguib M (2005) Propofol: the challenges of formulation. Anesthesiology 103 (4):860–876
5. Braginsky L, Belevitskaja M (1994) Kinetics of drops breakup in agitated vessels. In: Kulov N (ed) Liquid-liquid systems. Nova Science, Commack
6. Christov NC, Danov KD, Danova DK et al (2008) The drop size in membrane emulsification determined from the balance of capillary and hydrodynamic forces. Langmuir 24:1397–1410
7. Cook E, Lagace A (1985) Apparatus for forming emulsions. US Patent 4,533,254
8. Cortés-Muñoz M, Chevalier-Lucia D, Dumay E (2009) Characteristics of submicron emulsions prepared by ultra-high pressure homogenisation: effect of chilled or frozen storage. Food Hydrocoll 23:640–654
9. Drew JLA, Chan R, Du H et al (1990) Preparation of lipid emulsions by pressure extrusion. Biochem Int 22:983–992

10. Dumay E, Chevalier-Lucia D, Picart-Palmade L et al (2013) Technological aspects and potential applications of (ultra) high-pressure homogenisation. Trends Food Sci 31:13–26
11. Finke et al (2014) Modular overall microsystem for the integrated production and loading of solid lipid nanoparticles. In: Kwade A, Kampen I, Finke JH (eds) Concluding results of the research group mikroPART. "Microsystems for particulate life science products" for 856, funded by the Deutsche Forschungsgemeinschaft (DFG), Braunschweig
12. Finke JH, Niemann S, Richter C et al (2014) Multiple orifices in customized microsystem high-pressure emulsification: the impact of design and counter pressure on homogenization efficiency. Chem Eng J 248:107–121
13. Finke JH, Richter C, Gothsch T et al (2014) Coumarin 6 as a fluorescent model drug: how to identify properties of lipid colloidal drug delivery systems via fluorescence spectroscopy? Eur J Lipid Sci Technol 116(9):1234–1246
14. Finke JH, Schmolke H, Klages C et al (2013) Controlling solid lipid nanoparticle adhesion by polyelectrolyte multilayer surface modifications. Int J Pharm 449(1–2):59–71
15. Finke J, Schur J, Richter C et al (2012) The influence of customized geometries and process parameters on nanoemulsion and solid lipid nanoparticle production in microsystems. Chem Eng J 209:126–137
16. Gehrmann S, Bunjes H (2016) Instrumented small scale extruder to investigate the influence of process parameters during premix membrane emulsification. Chem Eng J 284:716–723
17. Gehrmann S, Bunjes H (2015) Interaction of emulsifier and membrane material during the preparation of nanoemulsions by premix membrane emulsification. In: 1st European conference on pharmaceutics—drug delivery, Reims, France, 13/14 April 2015
18. Gijsbertsen-Abrahamse A, van der Padt A, Boom R (2004) Status of cross-flow membrane emulsification and outlook for industrial application. J Membr Sci 230(1–2):149–159
19. Gothsch T, Beinert S, Kampen I et al (2014) Investigation of high pressure dispersion in microsystems with experimental and numerical methods. In: Kwade A, Kampen I, Finke J (eds) Concluding results of the research group mikroPART. "Microsystems for particulate life science products" for 856, funded by the Deutsche Forschungsgemeinschaft (DFG), Braunschweig 2014
20. Gothsch T, Finke JH, Beinert S et al (2011) Effect of microchannel geometry on high-pressure dispersion and emulsification. Chem Eng Technol 34(3):335–343
21. Gothsch T, Schilcher C, Richter C et al (2015) High-pressure microfluidic systems (HPMS): flow and cavitation measurements in supported silicon microsystems. Microfluid Nanofluid 18:121–130
22. Hao D, Gong F, Hu G et al (2008) Controlling factors on droplets uniformity in membrane emulsification: experiment and modeling analysis. Ind Eng Chem Res 47(17):6418–6425
23. Higashi S, Shimizu M, Nakashima T et al (1995) Arterial-injection chemotherapy for hepatocellular carcinoma using monodispersed poppy-seed oil microdroplets containing fine aqueous vesicles of epirubicin: Initial medical application of a membrane-emulsification technique. Cancer 75:1245–1254
24. Jafari S, He Y, Bhandari B (2006) Nanoemulsion production by sonication and microfluidization—a comparison. Int J Food Prop 9:475–478
25. Joscelyne SM, Trägårdh G (2000) Membrane emulsification—a literature review. J Membr Sci 169:107–117
26. Joseph S, Bunjes H (2012) Preparation of nanoemulsions and solid lipid nanoparticles by premix membrane emulsification. J Pharm Sci 101(7):2479–2489
27. Joseph S, Bunjes H (2013) Influence of membrane structure on the preparation of colloidal lipid dispersions by premix membrane emulsification. Int J Pharm 446(1–2):59–62
28. Joseph S, Bunjes H (2014) Evaluation of Shirasu Porous Glass (SPG) membrane emulsification for the preparation of colloidal lipid drug carrier dispersions. Eur J Pharm Biopharm 87 (1):178–186

29. Kazazi-Hyseni F, Landin M, Lathuile A et al (2014) Computer modeling assisted design of monodisperse PLGA microspheres with controlled porosity affords zero order release of an encapsulated macromolecule for 3 months. Pharm Res 31(10):2844–2856
30. Kobayashi I, Mukataka S, Nakajima M (2004) CFD simulation and analysis of emulsion droplet formation from straight-through microchannels. Langmuir 20(22):9868–9877
31. Kobayashi I, Mukataka S, Nakajima M (2004) Effect of slot aspect ratio on droplet formation from silicon straight-through microchannels. J Colloid Interface Sci 279(1):277–280
32. Kobayashi I, Mukataka S, Nakajima M (2005) Production of monodisperse oil-in-water emulsions using a large silicon straight-through microchannel plate. Ind Eng Chem Res 44 (15):5852–5856
33. Kobayashi I, Uemura K, Nakajima M (2007) Formulation of monodisperse emulsions using submicron-channel arrays. Colloids Surf A Physicochem Eng Asp 296(1–3):285–289
34. Kobayashi I, Wada Y, Uemura K et al (2010) Microchannel emulsification for mass production of uniform fine droplets: integration of microchannel arrays on a chip. Microfluid Nanofluid 8(2):255–262
35. Kobayashi I, Yasuno M, Iwamoto S et al (2002) Microscopic observation of emulsion droplet formation from a polycarbonate membrane. Colloids Surf A Physicochem Eng Asp 207:185–196
36. Köhler K, Aguilar F, Hensel A et al (2007) Design of a microstructured system for homogenization of dairy products with high fat content. Chem Eng Technol 30:1590–1595
37. Kolb G, Viardot K, Wagner G et al (2001) Evaluation of a new high-pressure dispersion unit (HPN) for emulsification. Chem Eng Technol 24:293–296
38. Kukizaki M (2009) Preparation of solid lipid microcapsules via solid-in-oil-in-water dispersions by premix membrane emulsification. Chem Eng J 151(1–3):387–396
39. Kukizaki M (2009) Shirasu porous glass (SPG) membrane emulsification in the absence of shear flow at the membrane surface: Influence of surfactant type and concentration, viscosities of dispersed and continuous phases, and transmembrane pressure. J Membr Sci 327 (1–2):234–243
40. Kukizaki M, Goto M (2007) Preparation and evaluation of uniformly sized solid lipid microcapsules using membrane emulsification. Colloids Surf A Physicochem Eng Asp 293 (1–3):87–94
41. Kukizaki M, Wada T (2008) Effect of the membrane wettability on the size and size distribution of microbubbles formed from Shirasu-porous-glass (SPG) membranes. Colloids Surf A Physicochem Eng Asp 317(1–3):146–154
42. Lamprecht A, Ubrich N, Hombrero Perez N et al (1999) Biodegradable monodispersed nanoparticles prepared by pressure homogenization-emulsification. Int J Pharm 184 (1):97–105
43. Lee L, Hancocks R, Noble I et al (2014) Production of water-in-oil nanoemulsions using high pressure homogenisation: a study on droplet break-up. J Food Eng 131:33–37
44. Lee L, Norton I (2013) Comparing droplet breakup for a high-pressure valve homogeniser and a Microfluidizer for the potential production of food-grade nanoemulsions. J Food Eng 114(2):158–163
45. Lepercq-Bost É, Giorgi M, Isambert A et al (2010) Estimating the risk of coalescence in membrane emulsification. J Membr Sci 357(1–2):36–46
46. Levy M, Benita S (1989) Design and characterization of a submicronized o/w emulsion of diazepam for parenteral use. Int J Pharm 54:103–112
47. Liu W, Yang X, Winston Ho W (2011) Preparation of uniform-sized multiple emulsions and micro/nano particulates for drug delivery by membrane emulsification. J Pharm Sci 100 (1):75–93
48. Lobo L, Svereika A (2003) Coalescence during emulsification—2. Role of small molecule surfactants. J Colloid Interface Sci 261:498–507
49. Marie P, Perrier-Cornet J, Gervais P (2002) Influence of major parameters in emulsification mechanisms using a high-pressure jet. J Food Eng 53:43–51

50. Mehnert W, Mäder K (2012) Solid lipid nanoparticles: production, characterization and applications. Adv Drug Deliv Rev 64:83–101
51. Meleson K, Graves S, Mason TG (2004) Formation of concentrated nanoemulsions by extreme shear. Soft Mater 2(2–3):109–123
52. Muchow M, Maincent P, Müller R (2008) Lipid nanoparticles with a solid matrix (SLN, NLC, LDC) for oral drug delivery. Drug Dev Ind Pharm 34(12):1394–1405
53. Müller R, Mehnert W, Lucks J et al (1995) Solid lipid nanoparticles (SLN)—an alternative colloidal carrier system for controlled drug delivery. Eur J Pharm Biopharm 41(1):62–69
54. Nakashima T, Shimizu M, Kukizaki M (1991) Membrane emulsification by microporous glass. Key Eng Mater 61–62:513–516
55. Nakashima T, Shimizu M, Kukizaki M (2000) Particle control of emulsion by membrane emulsification and its applications. Adv Drug Deliv Rev 45:47–56
56. Nazir A, Schroën K, Boom R (2010) Premix emulsification: a review. J Membr Sci 362 (1–2):1–11
57. Olson D, White C, Richter R (2004) Effect of pressure and fat content on particle sizes in microfluidized milk. J Dairy Sci 87(10):3217–3223
58. Owens M, Halbert G (1995) Production and characterization of protein-free analogues of low density lipoprotein. Eur J Pharm Biopharm 41(2):120–126
59. Paranjpe M, Finke J, Richter C et al (2014) Physicochemical characterization of sildenafil-loaded solid lipid nanoparticle dispersions (SLN) for pulmonary application. Int J Pharm 476 (1–2):41–49
60. Paranjpe M, Müller-Goymann C (2014) Nanoparticle-mediated pulmonary drug delivery: a review. Int J Mol Sci 15(4):5852–5873
61. Paranjpe M, Neuhaus V, Finke JH et al (2013) In vitro and ex vivo toxicological testing of sildenafil-loaded solid lipid nanoparticles. Inhal Toxicol 25(9):536–543
62. Park S, Yamaguchi T, Nakao S (2001) Transport mechanism of deformable droplets in microfiltration of emulsions. Chem Eng Sci 56:3539–3548
63. Perrier-Cornet J, Marie P, Gervais P (2005) Comparison of emulsification efficiency of protein-stabilized oil-in-water emulsions using jet, high pressure and colloid mill homogenization. J Food Eng 66(2):211–217
64. Picart L, Thiebaud M, René M et al (2006) Effects of high pressure homogenisation of raw bovine milk on alkaline phosphatase and microbial inactivation. A comparison with continuous short-time thermal treatments. J Dairy Res 73:454–463
65. Pinnamaneni S, Das N, Das N (2003) Comparison of oil-in-water emulsions manufactured by microfluidization and homogenization. Pharm Unserer Zeit 58(8):554–558
66. Pretor S, Bartels J, Lorenz T et al (2015) Cellular uptake of coumarin-6 under microfluidic conditions into HCE-T cells from nanoscale formulations. Mol Pharm 12(1):34–45
67. Richter C, Demming S, Lorenz T et al (2014) Design and fabrication of micro systems for particulate life science products. In: Kwade A, Kampen I, Finke J (eds) Concluding results of the research group mikroPART. "Microsystems for particulate life science products" FOR 856, funded by the Deutsche Forschungsgemeinschaft (DFG), Braunschweig 2014
68. Richter C, Krah T, Büttgenbach S (2012) Novel 3D manufacturing method combining microelectrical discharge machining and electrochemical polishing. Microsyst Technol 18 (7–8):1109–1118
69. Richter C, Stegemann D, Vierheller A et al (2013) Innovative process chain for the development of wear resistant 3D metal microsystems. Microelectron Eng 110:392–397
70. Sawalha H, Purwanti N, Rinzema A et al (2008) Polylactide microspheres prepared by premix membrane emulsification—effects of solvent removal rate. J Membr Sci 310:484–493
71. Schadler V, Windhab E (2006) Continuous membrane emulsification by using a membrane system with controlled pore distance. Desalination 189(1–3):130–135
72. Schoenitz M, Finke JH, Melzig S et al (2014) Fouling in a micro heat exchanger during continuous crystallization of solid lipid nanoparticles. Heat Transfer Eng 36(7–8):731–740

73. Schultz S, Wagner G, Urban K et al (2004) High-pressure homogenization as a process for emulsion formation. Chem Eng Technol 27(4):361–368
74. Shearer MJ (2009) Vitamin K in parenteral nutrition. Gastroenterology 137(5 Suppl):S105–S118
75. Siekmann B, Westesen K (1992) Nanopartikuläre Trägersysteme auf Lipidbasis zur parenteralen Applikation schwer wasserlöslicher Arzneistoffe. Pharm Unserer Zeit 21:128–129
76. Siekmann B, Westesen K (1992) Submicron-sized parenteral carrier systems based on solid lipids. Pharm Pharmacol Lett 1:123–126
77. SPG Technology Co. L (2015) Introduction of product—SPG membrane. http://www.spg-techno.co.jp/english/product/spg_membrane.shtml. Accessed 18 July 2015
78. Stang M, Schuchmann H, Schubert H (2001) Emulsification in high-pressure homogenizers. Eng Life Sci 1(4):151–157
79. Sugiura S, Nakajima M, Kumazawa N et al (2002) Characterization of spontaneous transformation-based droplet formation during microchannel emulsification. J Phys Chem B 106(36):9405–9409
80. Sugiura S, Nakajima M, Oda T et al (2004) Effect of interfacial tension on the dynamic behavior of droplet formation during microchannel emulsification. J Colloid Interface Sci 269 (1):178–185
81. Sugiura S, Nakajima M, Tong J et al (2000) Preparation of monodispersed solid lipid microspheres using a microchannel emulsification technique. J Colloid Interface Sci 227 (1):95–103
82. Surh J, Jeong YG, Vladisavljević GT (2008) On the preparation of lecithin-stabilized oil-in-water emulsions by multi-stage premix membrane emulsification. J Food Eng 89(2):164–170
83. Suzuki K, Fujiki I, Hagura Y (1998) Preparation of corn oil/water and water/corn oil emulsions using PTFE membranes. Food Sci Technol Int Tokyo 4(2):164–167
84. Suzuki K, Shuto I, Hgura Y (1996) Characteristics of the membrane emulsification method combined with preliminary emulsification for preparing corn oil-in-water emulsions. Food Sci Technol Int Tokyo 2(1):43–47
85. Talsma H, Ozer A, van Bloois L et al (1989) The size reduction of liposomes with a high pressure homogenizer (Microfluidizer^{TM}). Characterization of prepared dispersions and comparison with conventional methods. Drug Dev Ind Pharm 15(2):197–202
86. Tang S, Shridharan P, Sivakumar M (2013) Impact of process parameters in the generation of novel aspirin nanoemulsions—comparative studies between ultrasound cavitation and microfluidizer. Ultrason Sonochem 20:485–497
87. Tesch S, Freudig B, Schubert H (2003) Production of emulsions in high pressure homogenizers—Part I: Disruption and stabilization of droplets. Chem Eng Technol 26:569–573
88. Thiebaud M, Dumay E, Picart L et al (2003) High pressure homogenisation of raw bovine milk. Effects on fat globule size distribution and microbial inactivation. Int Dairy J 13:427–439
89. van der Graaf S, Schroën C, van der Sman R et al (2004) Influence of dynamic interfacial tension on droplet formation during membrane emulsification. J Colloid Interface Sci 277 (2):456–463
90. van der Graaf S, Schroën K, Boom RM (2005) Preparation of double emulsions by membrane emulsification—a review. J Membr Sci 251(1–2):7–15
91. van der Zwan E, Schroën K, van Dijke K et al (2006) Visualization of droplet break-up in pre-mix membrane emulsification using microfluidic devices. Colloids Surf A Physicochem Eng Asp 277(1–3):223–229
92. Vivier A, Vuillemard J, St-Pierre S et al (1991) Large-scale blood substitute production using microfluidizer. Biomater Artif Cells Immobilization Biotechnol 19(2):499
93. Vladisavljević GT et al (2008) Generation of highly uniform droplets using asymmetric microchannels fabricated on a single crystal silicon plate: effect of emulsifier and oil types. Powder Technol 183:37–45

94. Vladisavljević GT, Khalid N, Neves MA et al (2013) Industrial lab-on-a-chip: design, applications and scale-up for drug discovery and delivery. Adv Drug Deliv Rev 65 (11–12):1626–1663
95. Vladisavljević GT, Kobayashi I, Nakajima M (2012) Production of uniform droplets using membrane, microchannel and microfluidic emulsification devices. Microfluid Nanofluid 13 (1):151–178
96. Vladisavljević GT, Lambrich U, Nakajima M et al (2004) Production of O/W emulsions using SPG membranes, ceramic α-aluminium oxide membranes, microfluidizer and a silicon microchannel plate—a comparative study. Colloids Surf A Physicochem Eng Asp 232 (2–3):199–207
97. Vladisavljević GT, Shimizu M, Nakashima T (2004) Preparation of monodisperse multiple emulsions at high production rates by multi-stage premix membrane emulsification. J Membr Sci 244(1–2):97–106
98. Vladisavljević GT, Shimizu M, Nakashima T (2005) Permeability of hydrophilic and hydrophobic Shirasu-porous-glass (SPG) membranes to pure liquids and its microstructure. J Membr Sci 250(1–2):69–77
99. Wagdare NA, Marcelis AT, Ho OB et al (2010) High throughput vegetable oil-in-water emulsification with a high porosity micro-engineered membrane. J Membr Sci 347(1–2):1–7
100. Warkiani ME, Bhagat AAS, Khoo BL et al (2013) Isoporous micro/nanoengineered membranes. ACS Nano 7(3):1882–1904
101. Washington C (1987) Emulsion production by microfluidizer. Lab Equip Dig 85:69–71
102. Washington C, Davis S (1988) The production of parenteral feeding emulsions by Microfluidizer. Int J Pharm 44(1–3):169–176
103. Wei Y, Wang Y, Kang A et al (2012) A novel sustained-release formulation of recombinant human growth hormone and its pharmacokinetic, pharmacodynamic and safety profiles. Mol Pharm 9(7):2039–2048
104. Wengeler R, Nirschl H (2007) Turbulent hydrodynamic stress induced dispersion and fragmentation of nanoscale agglomerates. J Colloid Interface Sci 306:262–273
105. Westesen K, Siekmann B, Koch M (1993) Investigations on the physical state of lipid nanoparticles by synchroton radiation X-ray diffraction. Int J Pharm 93:189–199
106. Wooster TJ, Golding M, Sanguansri P (2008) Impact of oil type on nanoemulsion formation and Ostwald ripening stability. Langmuir 24(22):12758–12765
107. Yuan Q, Williams RA (2014) Precision emulsification for droplet and capsule production. Adv Powder Technol 25(1):122–135
108. Zhu J, Barrow D (2005) Analysis of droplet size during crossflow membrane emulsification using stationary and vibrating micromachined silicon nitride membranes. J Membr Sci 261 (1–2):136–144

Chapter 6
On-Chip Fabrication of Drug Delivery Systems

M. Windbergs

Abstract The chapter provides an overview about the fabrication of drug delivery systems with microfluidic devices. Different microfluidic approaches are presented, describing the basic fabrication principles and highlighting representative examples. Diffusive mixing is preferentially used for controlled precipitation of small particles down to nanometer size. Particles can be collected in suspension or directly be spray dried with specific devices. Emulsion-based approaches are utilized for direct use of liquid emulsions and as templates for semisolid or solid systems ranging from polymer particles and hydrogels up to complex capsules and vesicles. In addition, scale-up approaches for microfluidic devices and recent development of delivery systems based on microfluidic devices for attachment to or implantation into the human body for controlled drug delivery over longer time intervals are presented. Finally, a future perspective is given discussing advantages and challenges of microfluidic approaches for safe and effective drug delivery.

6.1 Challenges for the Design of Drug Delivery Systems and the Potential of Microfluidic Techniques

Efficient therapy of diseased states within the human body relies on two basic elements-an effective drug and an adequate delivery system (carrier). The delivery system serves as a packing for the drug, ideally stabilizing and preserving the active form of the drug on its way through the human body as well as controlling its release for the desired therapeutic effect with respect to drug quantity and the duration of drug presence in the human body. Further, delivery systems may also selectively transport the drug to the site of action. Due to increasing complexity and

M. Windbergs (✉)
Department for Biopharmaceutics and Pharmaceutical Technology, Saarland University, Campus A 4.1, Saarbrücken 66123, Germany

Helmholtz Centre for Infection Research (HZI), Helmholtz Institute for Pharmaceutical Research Saarland (HIPS), Campus E 8.1, Saarbrücken 66123, Germany
e-mail: m.windbergs@mx.uni-saarland.de

A. Dietzel (ed.), *Microsystems for Pharmatechnology*,
DOI 10.1007/978-3-319-26920-7_6

at the same time decreasing stability of many novel drug molecules from the research pipeline (especially proteins and peptides), there is a strong need for advanced drug delivery systems capable of safely and efficiently delivering such compounds. In addition, current challenges in the field of drug delivery include targeted delivery to a specific body site or tissue as well as controlled and constant release over longer time intervals.

Against this background, there is a high demand to develop and establish techniques which allow for fabrication of tailor-made carrier systems for safe and effective drug delivery. In this context, microfluidic systems gain more and more attention as the accurate and individual control of different fluids within the channels of such "lab on a chip" devices provides the opportunity to generate a large variety of different structures for potential use as drug carriers. The design and fabrication of microfluidic devices including appropriate surface functionalization is highly diverse, as Chap. 2 (Leester-Schädel et al.) as well as Chap. 3 (Eichler et al.) in this book describe. For generation of drug delivery systems, mainly elastomers like polydimethylsiloxane (PDMS), glass, and metal are used as device materials. As the use of metal devices is extensively discussed in Chap. 5 (Bunjes et al.), this chapter will mainly focus on PDMS devices and systems based on assembled glass capillaries. For elastomers like PDMS, strong solvents like acetone might cause swelling of the device material [1], whereas the use of glass devices is potentially hampered by poor wetting properties of the channel walls. Thus, the choice of an appropriate device for each individual system is a mandatory prerequisite. However, as extensively described in Chap. 3 (Eichler et al.) in this book, material properties of devices might be modified in a specific post-fabrication procedure. The flow regimes which are used for the generation of drug delivery systems in the channels of a microfluidic chip can generally be subdivided into parallel multiphase flow and droplet based fluid regimes incorporating a droplet generation element within the channel structure.

The following parts of this chapter will give an overview about different drug delivery systems which can be generated in microfluidic devices and highlight representative examples. In addition, advantages and challenges of such approaches are discussed and a future perspective is given.

6.2 Drug Delivery Systems Based on Diffusive Mixing in Microfluidic Channels

6.2.1 Prerequisites for the Fabrication of Nanoparticles

In the last decade, nanosized structures have experienced considerable interest as carriers for drugs [2, 3]. Beneficial effects include the potential for enhancing the solubility of poorly soluble drugs in the human body, controlling release kinetics, and passive or active targeting of the drug. Despite of many achievements in this field, challenges for the fabrication of optimized drug-loaded nano systems still

remain [3]. Among them is the reproducible production of small nanoparticles (<100 nm) with high drug load and homogeneous size distribution. Established fabrication techniques generally result in a rather broad size distribution which consequently affects the release characteristics (kinetics) of the incorporated drug. Further, drug loading is conventionally performed in a second process step after nanoparticle formation based on a concentration gradient between immersion medium and particles. This procedure entails significant quantities of wasted excess material, which can be problematic in case of extremely potent actives or expensive materials. Recently, microfluidic approaches for fabrication of such particles gained considerable interest with the attempt to produce carriers with tunable characteristics (like size and drug loading) at the same time being homogeneous among each other to avoid post-processing procedures like size adjustments.

6.2.2 *Fabrication of Drug Delivery Systems by Precipitation in Microfluidic Channels*

In contrast to top-down approaches for which the bulk material is reduced in size with procedures like milling or high-pressure homogenization, bottom-up procedures involve the conversion of molecularly dispersed substances into small particles. With respect to microfluidic devices, most commonly diffusion-based mixing of two or more liquids is used as the fabrication process. For this purpose, the device generally consists of several inlets conveying different liquids which are consolidated in one single outlet channel. Besides the composition of the fluids, the system can be controlled via the design of the channels as well as via the flow rates of the liquids inside the device. Consequently, the fabricated drug delivery systems may vary in size, shape, and morphology depending on the concentration of the liquids, flow rates, and geometry of the device channels.

In general, the principle of hydrodynamic flow focusing (see Chap. 1 by Dietzel for details on flow regimes) can be applied to generate an interface of two individual liquids which are miscible with each other. As basic principle, one liquid is a good solvent for the carrier material (polymer etc.), whereas the material is less or not soluble in the other liquid. Upon co-flow within the channels of the device, the carrier material gets into contact with the "anti-solvent" and precipitation of particles can be achieved at the interface of the two liquids. The extent of contact and mixing of the two liquids can be influenced by the structure of the device and the flow conditions (e.g. by incorporating additional mixing elements). The size of the particles depends on the level of supersaturation of the solute in the liquid as well as on the duration of the process. An example for this principle is demonstrated in Fig. 6.1. Here, one solution contains the polymer dissolved in an adequate solvent. This solution is guided through the inner inlet of a flow focusing device, whereas the anti-solvent for the polymer as the second liquid is directed through two outer inlets arranged perpendicular to the inner inlet.

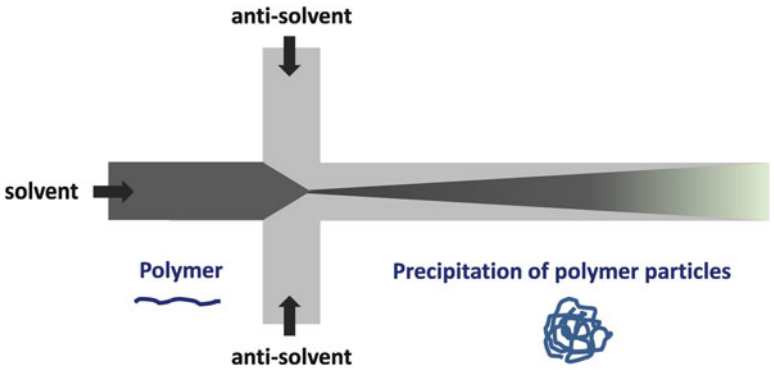

Fig. 6.1 Basic principle of particle fabrication in a flow focusing device based on a solvent-anti-solvent approach

After optimization of the flow rates, the aqueous phase flow-focuses the polymer solution into the straight outlet channel. The proceeding mixing of the two liquids at their interfaces initiates the formation of polymeric nanoparticles. This reaction can precisely be controlled by the flow rates, consequently also governing the degree and velocity of mixing. Such particles can also be based on block copolymers. For instance, the copolymer poly(ethylene glycol)-poly(lactic-co-glycolic acid) (PEG-PLGA) has successfully been used for the fabrication of particles loaded with docetaxel, an anticancer drug [4]. The authors of this study compared these drug-loaded carriers prepared with a microfluidic device with particles based on the same composition, but prepared by bulk fabrication, and could demonstrate superior characteristics as smaller size and higher drug encapsulation efficacy for the particles produced by microfluidic techniques.

Besides relatively simple co-flow systems, different other device geometries have been used. One more complex example is based on an impact-jet micromixer which consists of three inlets conveying mixed solutions containing two excipients (poly (methyl methacrylate) as a polymer and a PEG-substituted castor oil as a surfactant) and the drug ketoprofen dissolved in tetrahydrofuran. In addition, three inlets are used for water as the second liquid and anti-solvent (Fig. 6.2). All inlets are connected to one single outlet which allows for mixing the liquids resulting in the formation of nanoparticles loaded with ketoprofen [5]. By changing the process parameters, the size of the particles as well as the drug loading could be modified in a controlled manner. Modification of drug release kinetics could be achieved by exchanging the polymer by poly(lactic-co-glycolic acid), thereby demonstrating the versatility of such platform technologies.

Further, even in the field of gene therapy, different complex carrier systems for the delivery of plasmids and oligonucleotides have been generated by microfluidic techniques. For instance, polyethyleneimine (PEI) was successfully used to form polyplexes with DNA [6]. In a comparison to the same polyplex formulation fabricated by bulk mixing using a pipette, the microfluidic production resulted in polyplexes with a more uniform size distribution. In addition, lipid nanoparticles

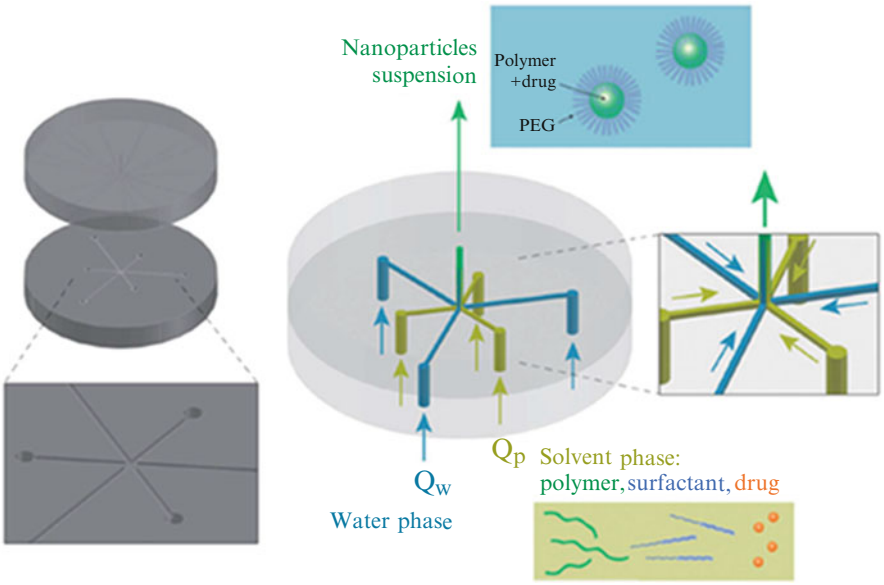

Fig. 6.2 Schematic of a microfluidic device for nanoparticle preparation and the principle of particle formation. Reproduced from [5] with permission from The Royal Society of Chemistry

have successfully been generated in a microfluidic device to form carriers incorporating siRNA [7]. These particles were superior in terms of reproducibility, monodispersity, and encapsulation efficacy for the siRNA molecules.

6.2.3 *Fabrication of Drug Delivery Systems by Spray Drying via Microfluidic Channels*

Spray drying is a common technique for the fabrication of drug-based or drug-loaded particles with favorable characteristics like increased surface and often also increased bioavailability in the human body. However, the technique implicates two major disadvantages. The production of particles with diameters below 100 nm is extremely challenging and a conventional spray drying setup requires a rather large amount of material due to dead volume within the apparatus as well as due to generation of wasted excess material. Especially in the early phase of formulation development for drugs coming from the research pipeline, the availability of material in large quantities is limited. In this context, microfluidic techniques can be applied to overcome such restrictions.

A simple PDMS flow focusing device can be converted into a miniaturized spray dryer. As described above, two liquids are applied, the inner one consisting of the drug dissolved in an appropriate solvent, the outer one is constituted by an

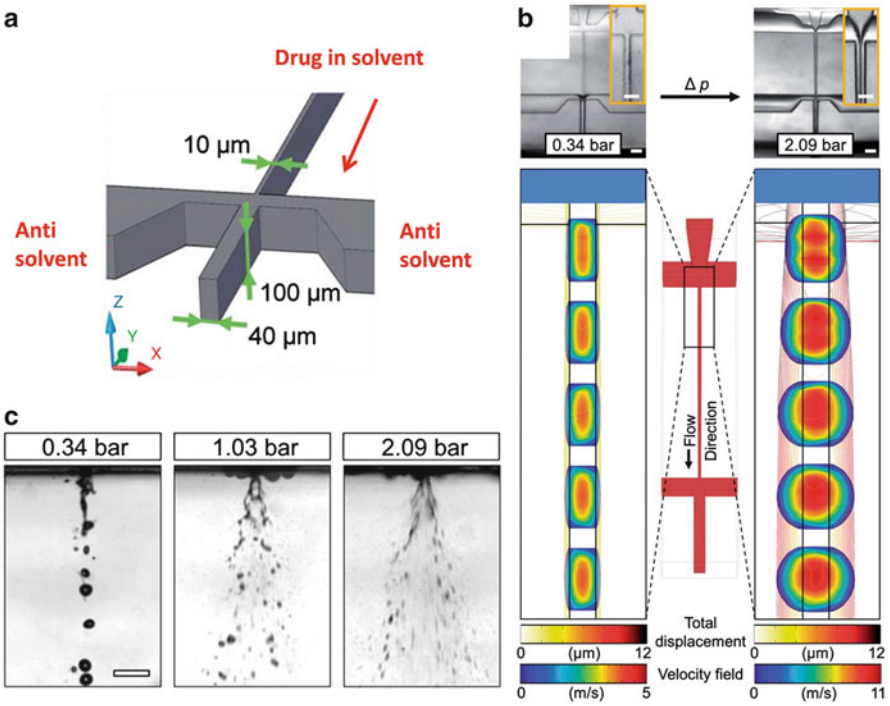

Fig. 6.3 Spray drying with a microfluidic chip: (**a**) Schematic of the flow focusing unit within the device; (**b**) pressure-induced deformation of the outlet channel with computational fluid dynamics simulations; (**c**) spray profiles at different air pressures. Adapted from [8] with permission from The Royal Society of Chemistry

anti-solvent for the drug (Fig. 6.3a). In addition, a third channel is implemented conveying pressurized air instead of a liquid which is forming the final spray of the two inner phase liquids (Fig. 6.3b). Depending on the applied pressure, the outlet channel deforms adapting a quasi-circular shape (Fig. 6.3b), allowing for generation of a sheath stream of air. The size of the sprayed droplets posing the templates for the particles which can be collected after spraying can be controlled by the pressure (Fig. 6.3c). Besides particles consisting of pure drug, coprecipitates of drug and excipients (e.g. crystallization inhibitors) have successfully been produced with such a device [8].

6.3 Drug Delivery Systems Based on Droplet Formation

6.3.1 Emulsification as the Basic Principle

A broad variety of different drug delivery systems can be generated based on emulsions comprising single emulsions as well as double (droplet in droplet) or even multiple emulsions. The emulsion can directly be used as a liquid-in-liquid system or be further processed (by cross-linking, solidification etc.) to form the final delivery system in a semisolid or solid state. In general, the formation of a suitable emulsion poses two major challenges-homogeneous size distribution of the droplets forming the inner phase and physical stability of the system over time. Both factors are closely linked with each other, as a narrow size distribution typically improves physical stability of emulsions over time.

As the use of microfluidic techniques allows for the fabrication of monodisperse emulsions, there is a multitude of studies demonstrating the versatility of applications for on-chip fabrication of drug delivery systems based on emulsions. A broad variety of different materials can be used for device generation; however, this chapter will mainly focus on devices based on elastomers like PDMS as well as based on assembled glass capillaries. In most cases, PDMS devices consist of a PDMS block in which the two-dimensional channel structure is generated by soft- and photolithography which is finally bonded by oxygen plasma activation (or any similar technique) to a glass slide [9]. In contrast, devices based on glass capillaries are less frequently used and are constructed from a coaxial assembly of tapered glass capillaries which is finally attached to a glass slide [10]. Here, the advantage is the three-dimensional geometry of the capillary lumen facilitating stable droplet generation processes (Fig. 6.4).

6.3.2 Solid Particles and Hydrogels

As already described above, initially formed emulsions can be converted into semisolid or solid particles with increased physical stability. Spontaneous particle formation can be initiated by processes like merging droplets with polymer and cross-linker [11] and self-assembly due to solvent evaporation [12]. In addition, external stimuli like temperature or UV light can be applied for solidification. In terms of temperature-dependent formation of particles, a common approach involves introducing molten or dissolved material into the microfluidic channels and subsequent cooling to solidify the final particles. This approach has been shown for gelatin [13], agarose [14] and different lipids [15].

Besides complete solidification of the droplets forming particles, emulsion droplets can also form a gel within the channel of microfluidic devices. For instance, covalent bonding of hydrazide functionalized cellulose and aldehyde functionalized dextran has successfully been achieved. Bupivacaine hydrochloride,

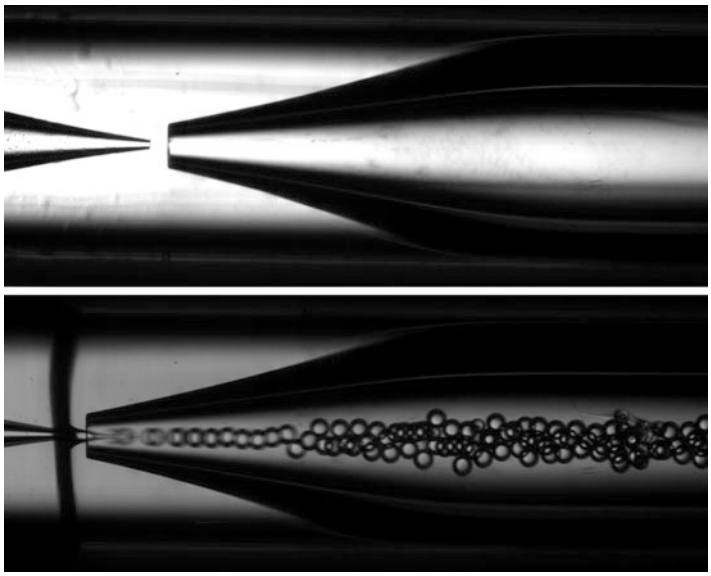

Fig. 6.4 Microscopic image of a microfluidic device based on assembled glass capillaries (*upper* image) and device producing a water/oil/water double emulsion (*bottom* image)

which has been incorporated as the active, was released in a controlled manner over 4 days from such hydrogel particles [16].

Polymer particles fabricated by a droplet-to-particle approach are commonly spherical in shape. However, non-spherical particles (in form of rods, disc etc.) can be created in microfluidic channels with confined geometries as Fig. 6.5 depicts [17]. Application of temperature changes or spatially defined cross-linking with UV light is used to preserve such unspherical morphology. In general, a broad variety of polymeric materials can be used for the fabrication of microgel particles ranging from synthetic polymers like polyethylene glycol and PLGA up to biopolymers including alginate [18], gelatin [13], chitosan [19], and pectin [20].

6.3.3 Capsules

In contrast to solid particles and hydrogels which generally consist of a coherent and homogeneous matrix structure, capsules are characterized by a core shell organization. The shell can provide additional stability and support for the core compartment. Further, drug release from the core can be controlled and additional drugs can exclusively be incorporated into the shell material. The release can be triggered by using shell material which is physically changing as a response to a stimulus like changes in temperature or pH.

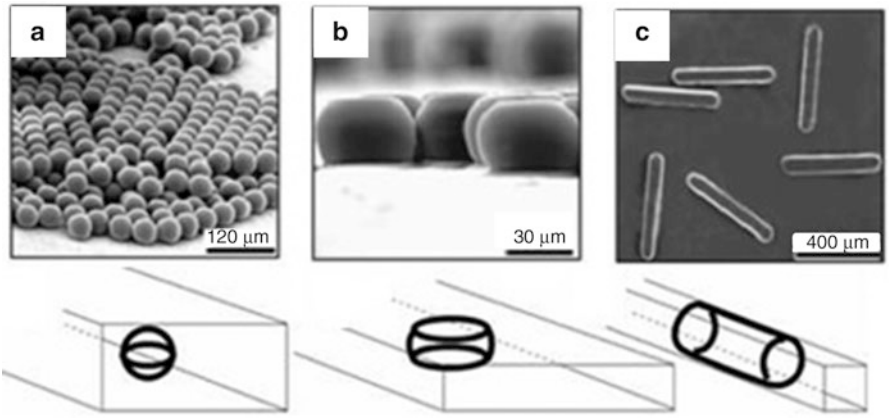

Fig. 6.5 Optical microscopy images of (**a**) microspheres, (**b**) discs, and (**c**) rods with the corresponding schematics of the respective shape of the initial droplets in the channels (*bottom row*). Adapted from [17] with permission from Wiley-VCH

Double emulsions formed within microfluidic devices constitute ideal templates for the conversion into capsules, the inner phase constituting the core and the middle phase forming the shell. After generating the double emulsion, the middle phase has to be solidified to form the capsule shell. Again, the emulsion can be formed in a hydrodynamic flow focusing device, either with lateral liquid streams for two-dimensional devices or with coaxial streams in three-dimensional devices, the latter one facilitating stable emulsion formation due to the continuous sheath flow completely surrounding the inner phase. Thus, unfavorable interactions of inner phase and channel walls can be avoided.

A variety of different materials has been used to form capsules in microfluidic devices ranging from synthetic polymers to lipids for the shell and from aqueous solution to oil for the core compartment. One example of a complex drug-loaded microcapsule is presented in Fig. 6.6. A glass capillary device was used to form a double emulsion with an aqueous solution containing the hydrophilic anticancer drug doxorubicin hydrochloride as inner phase and a molten glyceride containing paclitaxel, a hydrophobic anticancer drug, as the middle phase [21]. Both phases form water/oil/water double emulsion droplets upon flow focusing with an outer aqueous phase. The glyceride middle phase solidifies in room temperature creating a solid lipid shell incorporating the hydrophobic drug depicted in an electron micrograph in Fig. 6.6. Such core shell particles could successfully be dried forming a free flowing powder for storage. Simultaneous release of both actives can be achieved by temperature increase above the melting point of the lipid (in this case body temperature). Figure 6.6 depicts a time series of fluorescence-based microscopy images during release testing at 37 °C demonstrating simultaneous release of the synergistic actives from shell and core of the capsule.

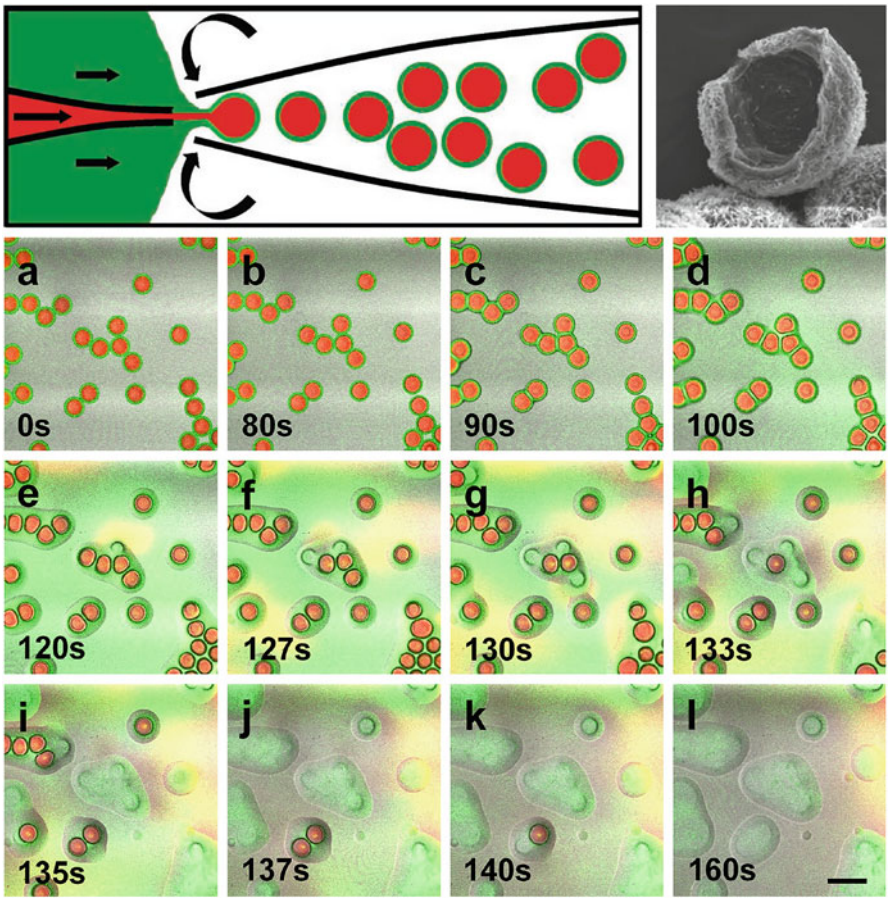

Fig. 6.6 Fabrication and drug release from core shell particles. The schematic depicts the formation of the drug delivery system in a microfluidic device based on a double emulsion incorporating a hydrophilic drug in the core (*red*) and a hydrophobic drug in the shell (*green*). The electron micrograph visualizes the solid shell which had been cracked for demonstration. Simultaneous release of both actives is depicted as a time series of fluorescence images (**a**–**l**). The scale bar denotes 200 μm. Reprinted and adapted with permission from [21]. Copyright 2013, American Chemical Society

6.3.4 Vesicles Based on Amphiphilic Molecules

Vesicles are spherical structures formed via self-assembly of amphiphilic molecules in a specific concentration range. In the vesicle, an organized layer of the amphiphilic molecules is separating the inner part from the surroundings. Similar to capsules, drugs can be encapsulated into the core as well as into the membrane layer. In addition, the outer part of vesicles can be decorated with molecules either avoiding recognition and elimination by the immune system in the human body or

for active targeting to specific cells, body sites etc. Vesicles can be formed based on lipids (called liposomes) as well as on synthetic, nonionic surfactants (called niosomes) and on polymers (called polymersomes).

In contrast to non-amphiphilic substances, for which the process of particle formation can simply be controlled by the flow rates, the extent of electrostatic and steric interactions is governing the size of the assemblies formed by amphiphilic molecules. Hence, during bulk production vesicles broadly vary in terms of size and lamellarity due to poor control of mechanical agitation, etc. necessitating post-processing like extrusion to improve homogeneity of the vesicles.

For nanosized vesicles, laminar co-flow systems as already described for precipitation of drug delivery systems can be applied [22]. In addition, polymeric micelles and liposomes can be produced with this strategy [23]. Further, water/oil/water double emulsion templates can be used for fabrication of vesicles after solvent evaporation. For instance, polymersomes can be produced from amphiphilic block copolymers. In comparison to liposomes, the membrane composition and thickness can accurately be adjusted by choice of the monomers (chemical nature and length) used for generation of the block copolymers. Hydrophilic substances can be incorporated into the core, whereas hydrophobic molecules can be embedded into the membrane. The composition of the membrane can also potentially be used to control the release of incorporated actives.

For instance, Amstad et al. prepared polymersomes based on a combination of the diblock copolymers poly(ethylene glycol)-b-poly(lactic acid) (PEG-b-PLA) and poly(N-isopropylacrylamide)-b-poly(lactic-co-glycolic acid) (PNIPAM-b-PLGA) in a microfluidic device [24]. Depending on the ratio of the two copolymers, the time-dependent degradation of the polymersomes at increased temperature varied (Fig. 6.7a). With increasing amount of PNIPAM-b-PLGA, the membrane disrupted after shorter time intervals and to a greater extent. Thus, variation of the ratio of such copolymers can be used to create drug delivery systems with controlled release of actives encapsulated into the polymersomes. Figure 6.7b depicts optical microscopy images of the polymersomes loaded with a red dye to visualize the rupture of the membrane by release of the dye after incubation for 20 min. Depending on the amount of PNIPAM-b-PLGA (indicated in the right upper corner of the individual images), the extent of the dye release varied.

6.4 Scale-Up Approaches

The access of newly developed therapeutics to the patient does not only depend on the demonstration of safety and efficacy of such systems for the regulatory authorities. For successful market entry, a reliable approach for large-scale production is an inevitable prerequisite. However, microfluidic devices are in general rather intended for small-scale production. For the development of a novel carrier in the initial phase of drug formulation, this bares several advantages, as novel actives in this phase are limited to small quantities. For the latter stage of development, the

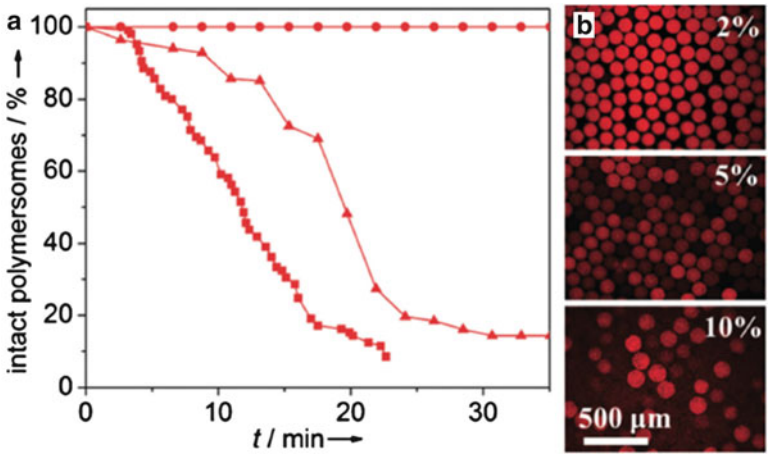

Fig. 6.7 Release of a fluorescent dye from polymersomes composed of PEG-b-PLA and varying quantities of PNIPAM-b-PLGA (2 wt% *circle*, 5 wt% *triangle*, and 10 % *square*) at 40 °C: (**a**) The fraction of intact polymersomes is strongly dependent on their individual membrane composition; (**b**) This effect can also be visualized by the extent of dye release from the respective polymersomes. Adapted from [24] with permission from Wiley-VCH

active is produced or isolated in large quantities, and consequently the scale of the production of the drug delivery system has to increase accordingly. Based on these circumstances, multiple research groups work on the scale-up of microfluidic devices. This is especially challenging for droplet-based microfluidics, as the frequency of droplet generation is approximated to be up to 1000 Hz for oil-in-water droplets and up to 12,000 Hz for water-in-oil droplets [25], resulting in a throughput capacity of a few to hundreds of microliters per minute depending on the droplet size.

From an industrial perspective, Holtze illustrated these facts with performing a theoretical calculation as follows: Theoretically, a flow focusing unit in a microfluidic device is able to produce up to 1 g of droplets per hour, depending on the size of the droplets and the viscosity of the liquid phase. Thus, if such a device is continuously operated for roughly 8000 h/year, it would produce less than 8 kg droplets per year. In comparison, industrial production of an emulsion requires an estimation of about 1000 t/year. Consequently, 125,000 flow focusing units with continuous perfect performance are required to match this productivity. However, simple multiplication of individual devices is hampered by the requirement of individual pumps or pressure tanks for operating each device [26].

To circumvent this obstacle, research projects were directed towards implementing multiple droplet generation units on one single device. However, as one critical incidence like channel blockage would stop the whole device, integration of several devices with multiple parallelized droplet generators is desirable. Successful approaches have been performed by Nisisako and Torii implementing 256 droplet generators radially arranged on a device with the

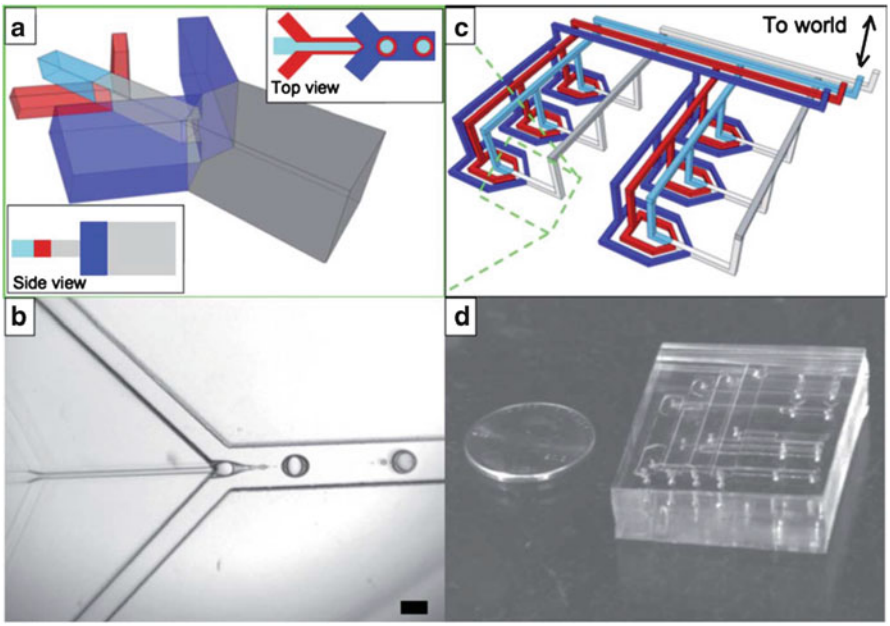

Fig. 6.8 Three-dimensional microfluidic arrays for high-throughput fabrication of double emulsions: (**a**) Schematic of one emulsification unit; (**b**) optical microscopy image of one emulsification unit; (**c**) schematic of two rows of emulsification units; and (**d**) photograph of one array. The scale bar denotes 100 μm. Adapted from [29] with permission from The Royal Society of Chemistry

dimensions of 42×42 mm with a throughput of 320 mL droplets per hour [27]. Another approach involved the splitting of droplets into equal daughter droplets for single as well as for double emulsions [28]. By three splitting steps, the throughput can be increased by factor 5. In addition, three-dimensional arrays were successfully developed and functionally subdivided into distribution and collection channels for high-throughput generation of double emulsions as depicted in Fig. 6.8 [29].

6.5 Microfluidic Systems as Drug Delivery Devices

Besides the use of microneedles which are extensively described in Chap. 9 (Luttke et al.), it is worth mentioning that several research projects have been performed on the development of small (mostly implantable) microfluidic devices for convective transport of the drug to a specific target or body site in the human body. Diffusion-based drug transport from conventional controlled release systems delivers the drug in a rather slow manner over extended time intervals (apart from rapid initial burst release).

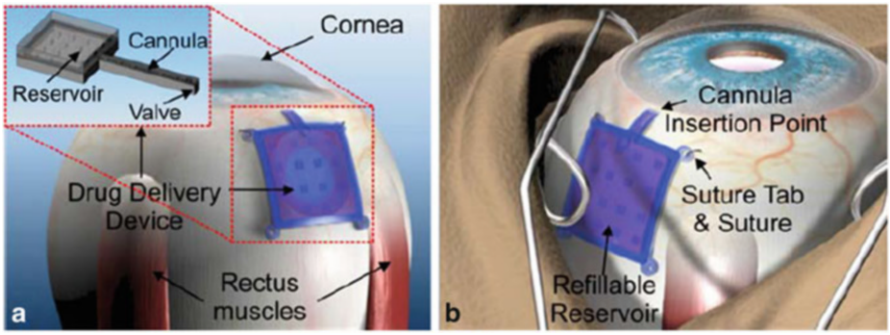

Fig. 6.9 Microfluidic device for application of drugs to the eye. Reproduced with kind permission from Springer Science + Business Media from [30]

Actuation for active drug transport through such implanted devices is generally relying on a power source, either with manual pressure, voltage or a magnetic field. As an example, for treatment of chronic ocular diseases, an implantable system consisting of a drug reservoir, a cannula, and avalve has been studied driven by manual actuation [30]. The device is depicted in Fig. 6.9. In addition, with the intention to treat diabetic retinopathy, a system with a magnetic PDMS membrane was invented [31]. When applying an external magnetic field, this membrane deforms, thereby releasing drug from a reservoir.

6.6 Outlook and Perspective

Current developments in microfluidic technologies have resulted in significant contributions to the field of drug delivery systems. Due to the flexibility of microfluidic devices paired with an unprecedented level of control over fluids, powerful platform technologies for reproducible fabrication of drug delivery systems with precise control of size, shape, and composition have been developed. However, despite these achievements, the translation from a research-based drug delivery system to a market product for patients is still challenging.

Major obstacles which are still to be addressed include the development of large-scale production approaches for continuous use. For this purpose, simple and versatile microfluidic platform devices have to be established.

One further challenge is constituted by the solvents used for the fabrication of drug delivery systems in microfluidic devices. Besides suitable solvation capacity for the material which is finally forming the drug delivery system, toxicity aspects are a major concern in the development of novel drug delivery systems. There are strict limitations for residual solvent content in drug carriers, which are regulated by law for the market entry of novel therapeutics. Unfortunately, physiologically toxic

solvents are often favorable with respect to their performance properties in microfluidic devices (e.g., fast evaporation, solvation capacity).

Last but not least, the development of novel microfluidic application systems for direct delivery of drugs and drug-loaded delivery systems to the human body is rapidly proceeding. The unique combination of accurate control of liquids and small size allows for implantation or attachment of such systems to the human body with a tremendous potential for future applications allowing self-determined therapy for patients (e.g. for chronic diseases).

References

1. Lee JN, Park C, Whitesides GM (2003) Solvent compatibility of poly(dimethylsiloxane)-based microfluidic devices. Anal Chem 75(23):6544–6554
2. Wagner V, Dullaart A, Bock A, Zweck A (2006) The emerging nanomedicine landscape. Nat Biotechnol 24:1211–1218
3. Couvreur P (2013) Nanoparticles in drug delivery: past, present and future. Adv Drug Deliv Rev 65(1):21–23
4. Karnik R, Gu F, Basto P, Cannizzaro C, Dean L, Kyei-Manu W, Langer R, Farokhzad OC (2008) Microfluidic platform for controlled synthesis of polymeric nanoparticles. Nano Lett 8 (9):2906–2912
5. Anton N, Bally F, Serra CA, Ali A, Arntz Y, Mely Y, Zhao M, Marchioni E, Jakhmola A, Vandamme TF (2012) A new microfluidic setup for precise control of the polymer nanoprecipitation process and lipophilic drug encapsulation. Soft Matter 8:10628–10635
6. Koh CG, Kang X, Xie Y, Fei Z, Guan J, Yu B, Zhang X, Lee LJ (2009) Delivery of polyethylenimine/DNA complexes assembled in a microfluidics device. Mol Pharm 6 (5):1333–1342
7. Chen D, Love KT, Chen Y, Eltoukhy AA, Kastrup C, Sahay G, Jeon A, Dong Y, Whitehead KA, Anderson DG (2012) Rapid discovery of potent siRNA-containing lipid nanoparticles enabled by controlled microfluidic formulation. J Am Chem Soc 134(16):6948–6951
8. Thiele J, Windbergs M, Abate AR, Trebbin M, Shum HC, Förster S, Weitz DA (2011) Early development drug formulation on a chip: Fabrication of nanoparticles using a microfluidic spray dryer. Lab Chip 11(14):2362–2368
9. Whitesides GM (2006) The origins and the future of microfluidics. Nature 442:368–373
10. Utada AS, Lorenceau E, Link D, Kaplan P, Stone HW, Weitz DA (2005) Monodisperse double emulsions generated from a microcapillary device. Science 308:537–541
11. Choi CH, Jung JH, Rhee YW, Kim DP, Shim SE, Lee CS (2007) Generation of monodisperse alginate microbeads and in situ encapsulation of cell in microfluidic device. Biomed Microdevices 9(6):855–862
12. Yi GR, Thorsen T, Manoharan VN, Hwang MJ, Jeon SJ, Pine DJ, Quake SR, Yang SM (2003) Generation of uniform colloidal assemblies in soft microfluidic devices. Adv Mater 15:1300–1304
13. Yeh CH, Chen KR, Lin YC (2013) Developing heatable microfluidic chip to generate gelatin emulsions and microcapsules. Microfluid Nanofluid 15:775–784
14. Eun YJ, Utada AS, Copeland MF, Takeuchi S, Weibel DB (2010) Encapsulating bacteria in agarose microparticles using microfluidics for high-throughput cell analysis and isolation. ACS Chem Biol 6(3):260–266
15. Capretto L, Mazzitelli S, Nastruzzi C (2012) Design, production and optimization of solid lipid microparticles (SLM) by a coaxial microfluidic device. J Control Release 160(3):409–417

16. Kesselman LR, Shinwary S, Selvaganapathy PR, Hoare T (2012) Synthesis of monodisperse, covalently cross-linked, degradable "smart" microgels using microfluidics. Small 8 (7):1092–1098
17. Xu S, Nie Z, Seo M, Lewis P, Kumacheva E, Stone HA, Garstecki P, Weibel DB, Gitlin I, Whitesides GM (2005) Generation of monodisperse particles by using microfluidics: control over size, shape, and composition. Angew Chem Int Ed Engl 44(5):724–728
18. Huang KS, Lai TH, Lin CY (2006) Manipulating the generation of Ca-alginate microspheres using microfluidic channels as a carrier of gold nanoparticles. Lab Chip 6(7):954–957
19. Yang CH, Huang KS, Chang JY (2007) Manufacturing monodisperse chitosan microparticles containing ampicillin using a microchannel chip. Biomed Microdevices 9(2):253–259
20. Ogonczyk D, Siek M, Garstecki P (2011) Microfluidic formulation of pectin microbeads for encapsulation and controlled release of nanoparticles. Biomicrofluidics 5:013405–013412
21. Windbergs M, Zhao Y, Heyman J, Weitz DA (2013) Biodegradable core-shell carriers for simultaneous encapsulation of synergistic actives. J Am Chem Soc 135:7933–7937
22. Jahn A, Stavis SM, Hong JS, Vreeland WN, DeVoe DL, Gaitan M (2010) Microfluidic mixing and the formation of nanoscale lipid vesicles. ACS Nano 4(4):2077–2087
23. Hood RR, Shao C, Omiatek DM, Vreeland WN, DeVoe DL (2013) Microfluidic synthesis of PEG and folate-conjugated liposomes for one-step formation of targeted stealth nanocarriers. Pharm Res 30(6):1597–1607
24. Amstad E, Kim SH, Weitz DA (2012) Photo- and thermoresponsive polymersomes for triggered release. Angew Chem Int Ed 51(50):12499–12503
25. Yobas L, Martens S, Ong WL, Ranganathan N (2006) High-performance flow-focusing geometry for spontaneous generation of monodispersed droplets. Lab Chip 6(8):1073–1079
26. Holtze C (2013) Large-scale droplet production in microfluidic devices—an industrial perspective. J Phys D Appl Phys 46:114008
27. Nisisako T, Torii T (2008) Microfluidic large-scale integration on a chip for mass production of monodisperse droplets and particles. Lab Chip 8(2):287–293
28. Abate AR, Weitz DA (2011) Faster multiple emulsification with drop splitting. Lab Chip 11 (11):1911–1915
29. Romanowsky MB, Abate AR, Rotem A, Holtze C, Weitz DA (2012) High throughput production of single core double emulsions in a parallelized microfluidic device. Lab Chip 12(4):802–807
30. Lo R, Li PY, Saati S, Agrawal RN, Humayun MS, Meng E (2009) A passive MEMS drug delivery pump for treatment of ocular diseases. Biomed Microdevices 11(5):959–970
31. Pirmoradi FN, Jackson JK, Burt HM, Chiao M (2011) On-demand controlled release of docetaxel from a battery-less MEMS drug delivery device. Lab Chip 11(16):2744–2752

Chapter 7
Microsystems for Dispersing Nanoparticles

C. Schilde, T. Gothsch, S. Beinert, and A. Kwade

Abstract Typically in the production of nanoparticles via bottom-up syntheses, agglomerates or even strong aggregates are formed which have to be redispersed in a subsequent dispersion process. Especially for the processing and screening of aggregated highly potential and cost-intensive biotechnological or pharmaceutical products, microsystems are advantageous due to high stress intensities, narrow residence time distributions, and high reproducibility as well as low volume flow. Depending on the geometry and the operating conditions of dispersing units within microsystems, various stress mechanisms have an effect on the dispersion process. However, in contrast to emulsification processes, the effect of cavitation is disadvantageous for high-pressure dispersion processes and can be avoided by applying backpressure. For the characterization and optimization of the stress intensity distribution and stressing probability in microchannels at various operating conditions, microparticle image velocimetry (μPIV) as well as single- and two-phase CFD simulations are well suited.

7.1 Introduction

Since several years, the importance of nanoparticles as high potential additives increases continuously in numerous branches of industry, e.g., chemical, pharmaceutical, extractive, food, and dye industry. Due to their size of 1–100 nm in at least one direction in space [13], the large specific surface area and the high amount of reactive surface molecules nanoparticles are attributed by extraordinary properties

C. Schilde • T. Gothsch • S. Beinert
TU Braunschweig, Institut für Partikeltechnik, Volkmaroder Str. 5, Braunschweig 38104, Germany

A. Kwade (✉)
TU Braunschweig, Institut für Partikeltechnik, Volkmaroder Str. 5, Braunschweig 38104, Germany

PVZ—Center of Pharmaceutical Engineering, Technische Universität Braunschweig, Franz-Liszt-Str. 35 A, Braunschweig 38106, Germany
e-mail: a.kwade@tu-braunschweig.de

A. Dietzel (ed.), *Microsystems for Pharmatechnology*,
DOI 10.1007/978-3-319-26920-7_7

[77]. These properties are considerably different from the well-known macroscopic material properties. For this reason, using nanoparticles as additives in a process chain can be advantageous to enhance existing product properties or to generate completely new product properties, e.g., photocatalytic activity, catalytic activity, abrasion resistance, thermal and electrical conductivity, tensile strength, hardness, hydrophobicity, easy-to-clean effect, viscosity, and color strength. Apart from the traditional top-down processing of particles down to the nanoscale via stirred media milling [11, 27, 51, 52], chemical bottom-up processes such as crystallization, precipitation, or pyrolysis are typically used in industry because of economic reasons. Despite significant process optimization, the resultant particle characteristics are related in a complex way to the chemical and physical processes of the particle synthesis [53]. Hence, in most bottom-up production processes, agglomerates or even strong aggregates [13] are formed which have to be redispersed in a subsequent more or less intense dispersion process. With respect to the required particle or aggregate fineness rotor-stator systems, high-pressure or ultrasonic homogenizers, dissolvers, kneaders, stirred media mills, and other dispersing machines are suitable for this dispersion step [55, 56]. Hereby, high-pressure systems are typically characterized by a narrow residence time distribution, a relative accurate adjustment of the induced stress intensities and frequencies as well as a good reproducibility [48]. For microsystems, the high stress intensities, narrow residence time distribution, and high reproducibility as well as low volume flow could be advantageous, e.g., for processing of highly potential and cost-intensive biotechnological or pharmaceutical products [6, 17].

7.2 Dispersing of Nanoparticles

Typically in industrial mass production of nanoparticles via chemical synthesis, agglomerate or even strong aggregate clusters of primary particles are produced, which have to be redispersed in order to obtain the desired product fineness and properties. A classification of agglomerates, aggregates, and flocculates depending on the interaction forces between the primary particles and specific surfaces is summarized by Schilde et al. [52]. Depending on the aggregate/agglomerate structure, size, primary interaction, and stability, the resistance against fragmentation and the efficiency of the dispersion process differs strongly [8, 50]. The influencing factors on the dispersion process can be classified into the aggregate/agglomerate properties, the properties of the continuous phase, and the characteristics and operating parameters of the dispersing device (see Fig. 7.1 [59]):

- Aggregate/agglomerate properties: The strength of a particulate structure depends basically on the material, the structure, and the type and strength of particle–particle interactions [32, 54, 57–60]. Hence, the dispersion process is strongly affected by the material, size, and structure of the aggregate/agglomerate. Especially, nanoparticulate aggregates have a high strength due to the number and strength of solid bridges between the primary particles.

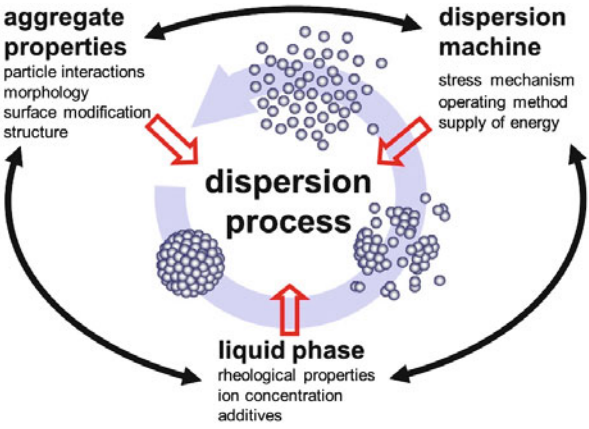

Fig. 7.1 Influencing parameters in a dispersion process (aggregate properties, dispersing machine, liquid phase) (original graphic by Schilde [59])

- Liquid phase: The properties of the continuous phase have an effect on the transferred stress frequencies and intensities by the dispersion machine [62] as well as on the suspension stability [37, 51, 78] concerning reagglomeration (rheological properties, ion concentration, additives, etc.).
- Dispersion machine: The stress mechanisms, intensities, and frequencies acting on aggregate/agglomerate surfaces depend considerably on the type, geometry, and operating conditions of the dispersing machine. In practice, dissolvers, high-pressure and ultrasonic homogenizers, kneaders, three roller mills as well as stirred media mills are used as dispersion devices [56].

7.3 Stress Mechanisms in Microsystems

A first principal classification of different stress mechanisms predominating the dispersion and comminution of particles in different dispersing machines was postulated by Rumpf [43, 52, 59]. The stress mechanisms were differentiated by the type of force transmission, e.g., compression or impact, stress by the surrounding fluid phase or thermal, chemical or electrical stresses. Apart from that the direction of energy initiation can be differentiated, e.g., normal or shear stress on a surface as well as shear or turbulent flow due to the fluid. A summary of different stress mechanism acting in different dispersing machines is given by Schilde et al. [52, 55]. For emulsification and dispersing in high-pressure systems, the hydrodynamic stresses acting on the particle and droplet surface due to pressure and velocity gradients are of major importance. Apart from particle–particle and particle–geometry interactions, the dispersion relevant stress mechanisms can be focused on stress via laminar and turbulent shear flow and stress via cavitation. The significance of these three stress mechanisms, especially the role of cavitation, on the emulsification result in high-pressure systems is not fully clarified and discussed controversially by different authors [18]. There are a large number of authors who

predict a positive effect of cavitation on the emulsification result [3, 15, 21, 31, 70, 71]. However, a large number of authors postulated a contrary minor or negative influence of cavitation on the emulsification result compared to laminar or turbulent shear flow [40–42, 67]. A few authors conclude that both turbulent shear flow and cavitation are the reasons for a successful breakup of droplets [24, 25].

While emulsification processes are intensely investigated regarding the effect of different mechanisms on the resultant product droplet size, only little literature exists on dispersing processes using high-pressure homogenizer or microsystems. However, similar to emulsification processes, it can be assumed that areas of high energy dissipation are responsible for a sufficient dispersion process. Sauter et al. identified hydrodynamic, cavitation, and impact stresses as effective stress mechanisms for dispersing pyrogenic nanoparticles [48, 49]. Anyway, cavitation leads to abrasion and damage and a reduced lifetime of the high-pressure systems. Thus, wear of the high-pressure homogenizer or microsystem has to be considered for dispersing in microsystems. Moreover, the dominant stress mechanisms in dispersing and emulsification processes differ considerably.

7.3.1 Stress via Laminar Fluid Flow

For Reynolds numbers below a critical value, laminar flow with only a marginal transverse flow can be observed [61]. This laminar flow can be differentiated into laminar shear flow [44] and laminar elongation flow [9, 20, 69] with different shear stresses acting on the particle surface. In general, both laminar shear and elongation flow occur simultaneously in a microsystem. Figure 7.2 shows the dominating stress mechanisms during dispersing of nanoparticulate suspensions in high-pressure and microsystems. Usually, in microsystems, these laminar shear and elongation stresses occur simultaneously but with various frequencies and intensities. For spherical particles in laminar shear flow of a Newtonian fluid, the shear stress and stress frequency acting on the particle surface can be calculated according to the following equation [44]:

$$\tau_{\mathrm{l,P,s}} = 2.5 \cdot \dot{\gamma} \cdot \eta_{\mathrm{f}} \tag{7.1}$$

$\tau_{\mathrm{l,P,s}}$	$\mathrm{N/m^2}$	Shear stress acting on the particle surface in laminar shear flow
$\dot{\gamma}$	1/s	Shear rate
η_{f}	$\mathrm{Pa \cdot s}$	Dynamic viscosity of the Newtonian fluid phase

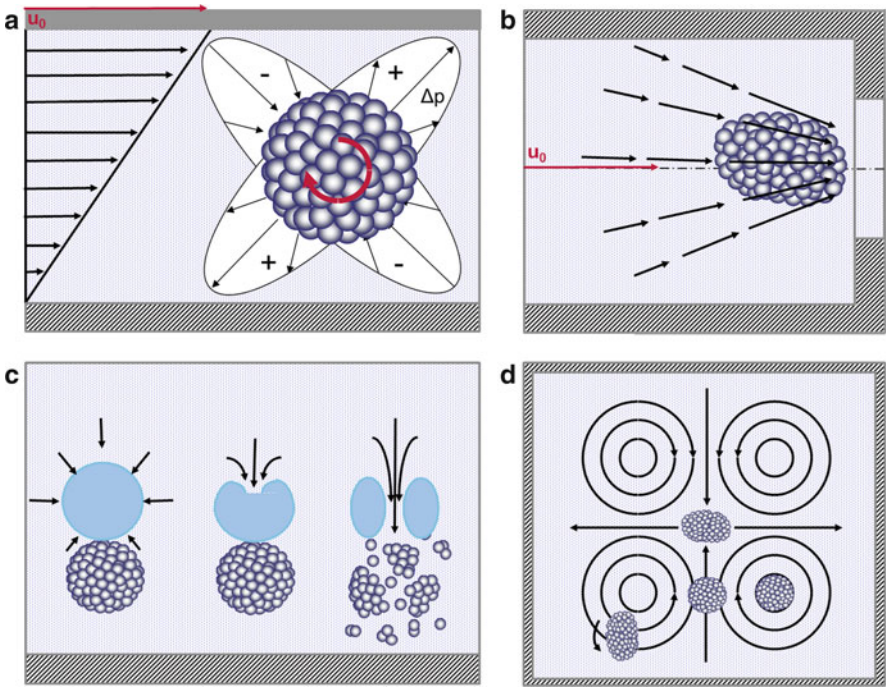

Fig. 7.2 Main stress mechanisms during high-pressure dispersing in microsystems: (**a**) laminar shear flow according to Rumpf [44]; (**b**) laminar elongation flow according to Stang [66]; (**c**) Cavitation; (**d**) turbulent shear flow according to the theory of Kolmogorov [12]

The stress frequency is proportional to the rotational angular velocity of the particle/aggregate within a stationary laminar shear flow:

$$\omega = \frac{\dot{\gamma}}{2} \tag{7.2}$$

ω	1/s	Angular velocity

Besides the shear stress acting on the particle surface, additionally centrifugal forces appear due to the rotation of the particle/aggregate within the stationary laminar fluid flow. However, the centrifugal forces are proportional to the square of the particle radius [44] and, thus, insignificant for dispersing small particles in the nanometer size range within microsystems. The elongation stress in laminar elongation flow is defined according to the following equation [33]:

$$\tau_{\mathrm{l,P,e}} = \dot{\varepsilon} \cdot \eta_{\mathrm{f}} \tag{7.3}$$

$\tau_{l,P,e}$	N/m^2	Elongation stress acting on the particle surface in laminar flow
$\dot{\varepsilon}$	1/s	Elongation rate

7.3.2 Stress via Turbulent Fluid Flow

In most cases, an accurate characterization of the three-dimensional flow and stress pattern is hardly available. Hence, computational fluid dynamics or mean field theories are suitable to describe the shear stress acting on the particle surface in turbulent shear flow. Turbulent shear flow is highly irregular, characterized by apparently random and chaotic three-dimensional eddies [16]. The energy is transferred by an eddy cascade and dissipated into energy of the smallest eddies with the Kolmogorov length scale due to dominating viscosity effects. In principle, the acting stresses can be classified using the ratio of the particle/aggregate and the Kolmogorov microscale into three to four classes [26, 29, 30, 38]:

- The inertial subrange, where the particles are stressed due to the relative velocities between vortices:

$$\tau_{t,P,isr} \sim \rho_f \cdot (\varepsilon \cdot d_P)^{2/3} \quad 25 \geq \frac{d_P}{\lambda_K} \geq 12 \tag{7.4}$$

$\tau_{t,P,isr}$	N/m^2	Turbulent stress in inertial subrange
ε	m^2/s^3	Energy dissipation rate
d_P	m	Particle/aggregate size
ρ_f	kg/m^3	Fluid density
υ_f	m^2/s	Kinematic fluid viscosity
$\lambda_K = \left(\frac{\upsilon_f^3}{\varepsilon}\right)^{1/4}$		Kolmogorov microscale

- The upper dissipation region, where the particles are stressed due to the relative velocities between vortices, but particle/aggregate diameter and kinematic viscosity have a higher influence on the acting stresses:

$$\tau_{t,P,uD} \sim \rho_f \cdot d_p^2 \cdot \frac{\varepsilon}{\upsilon_f} \quad 12 \geq \frac{d_P}{\lambda_K} \geq 3 \tag{7.5}$$

$\tau_{t,P,uD}$	N/m^2	Turbulent stress in the upper dissipation region

- The lower dissipation region, where the particles are stressed via rotation within the center of an eddy. The shear stress is independent on the particle/aggregate size. Typically, the ratio of the particle size and the Kolmogorov microscale for dispersing nanoparticle reaches values below 3 [55]:

$$\tau_{\mathrm{t,P,lD}} \sim \rho_{\mathrm{f}} \cdot (\varepsilon \cdot \upsilon_{\mathrm{f}})^{1/2} \quad \frac{d_{\mathrm{P}}}{\lambda_{\mathrm{K}}} \leq 3 \tag{7.6}$$

$\tau_{\mathrm{t,P,lD}}$	$\mathrm{N/m^2}$	Turbulent stress in the lower dissipation region

Bache postulated an extended function for the lower dissipation region [2]:

$$\tau_{\mathrm{t,P,lD,\ Bache}} \sim \frac{1}{15} \rho_{\mathrm{f}} \cdot (\varepsilon \cdot \upsilon_{\mathrm{f}})^{\frac{1}{2}} \cdot \left(\frac{d_{\mathrm{P}}}{\lambda_{\mathrm{K}}}\right)^2 \quad \frac{d_{\mathrm{P}}}{\lambda_{\mathrm{K}}} \leq 3.5 \tag{7.7}$$

7.3.3 Stress via Hydrodynamic Cavitation

Typically, in literature, cavitation is discussed as a main stress mechanism during dispersion or emulsification processes using high-pressure or ultrasonic homogenizers [3, 5, 14, 21, 31, 35, 47, 63, 71]. Cavitation describes the spontaneous formation, growth, and subsequent collapse of cavities in a liquid phase. The previous nucleation process of cavities can be differed in homogeneous and heterogeneous nucleation. Due to thermal motion of liquid molecules, temporary, microscopic cavities arise which represent weak spots within the fluid and grow up, forming macroscopic cavities. This type of nucleation is called homogeneous nucleation. If the nucleation starts induced to already existing small gas bubbles or particles within the fluid phase, heterogeneous cavitation nucleation takes place. The implosion time and resultant velocities of the resultant cavities can be approximated according to Baldyga et al. [3]. The stress intensity of the microjet after implosion of the cavity can be described by the following equation [4]:

$$\tau_{\mathrm{j}} = \alpha \cdot \rho_{\mathrm{f}} \cdot c_{\mathrm{sw}} \cdot u_{\mathrm{j}} \tag{7.8}$$

τ_{j}	$\mathrm{N/m^2}$	Stress intensity of the microjet
c_{sw}	m/s	Speed of shock wave
u_{j}	m/s	Speed of microjet
α	–	Empirical constant

In high-pressure systems, the hydrodynamic cavitation is generated due to high pressure gradients caused by high velocity gradients within the fluid flow. This cavitation can be differentiated into (1) travelling cavitation, (2) fixed cavitation,

(3) vortex cavitation, and (4) vibratory cavitation [64]. Furthermore, in microsystems which are based on orifice geometries, the cavitation regimes can be characterized similar to a quasi-stationary fluid flow:

- Beginning of the cavitation (cavitation inception).
- The steam fills the flow separation region (sub-cavitation stage).
- Expanding cavitation downstream (transitional cavitation) [46].

The amount of vapor-filled areas within the microsystem can be described using the cavitation number, e.g., [36]:

$$\mathrm{CN} = \frac{p_1 - p_3}{p_3 - p_\mathrm{v}} \tag{7.9}$$

CN	–	Cavitation number
p_1	$\mathrm{N/m^2}$	Pressure upstream the orifice
p_3	$\mathrm{N/m^2}$	Pressure downstream the orifice
p_v	$\mathrm{N/m^2}$	Vapor pressure

As described before, the significance of laminar and turbulent shear flow and stress via cavitation is not fully clarified and discussed controversially by different authors. Typically, the presence of cavitation can be characterized using photo-optical measurement methods, e.g., for diesel injection nozzles [10, 45, 65, 68]. Figure 7.3 (left) shows exemplarily the visualization of cavitation in a rectangular silicon orifice [34] using a fluorescent dye with ambient pressure at the outlet of the microsystem [18, 19]. A dark blue color represents a low fluorescent intensity and, thus, cavities. The method is described in detail by Gothsch et al. [19]. The flow

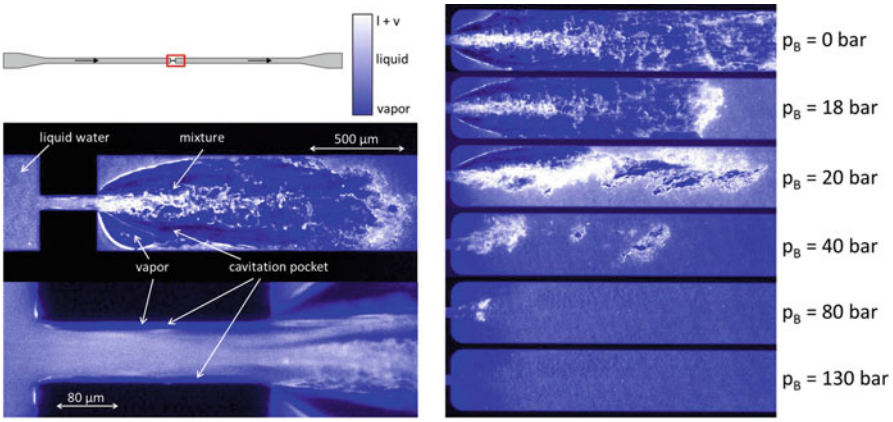

Fig. 7.3 *Left*: Cavitation images of a rectangular silicon orifice geometry ($\Delta p = 100$ bar; backpressure $p_\mathrm{B} = 0$ bar (ambient pressure); channel height $h_\mathrm{mc} = 53$ µm). *Right*: Cavitation downstream of the orifice at a pressure difference of 300 bar and increasing backpressure (original graphic by Gothsch et al. [19])

separation in the Vena Contracta as well as the detachment of the flow from the side walls forming cavitation pockets which propagate downstream can be described qualitatively. The fluid leaves the orifice as a jet with two fixed cavitation pockets next to it. In Fig. 7.3 (right), the effect of a backpressure on the reduction of downstream cavitation within the microsystem can be illustrated. In a first step, the fixed cavitation pockets collapse and small cavities can be observed in the region of the jet [1, 36]. Above a critical backpressure (130 bar at a pressure difference of 300 bar), cavitation is eliminated downstream of the orifice. The effect of cavitation on the product fineness dispersing pyrogenic alumina nanoparticles is discussed in Sect. 7.5.

7.4 Characterization of Fluid Flow in Microsystems

In principle, computational fluid dynamics as well as visual observations are well suited for the characterization of the fluid flow for dispersing nanoparticles at high pressures and small channel geometries of several tens of microns. However, high pressures and fluid velocities are a major challenge for the establishment of an experimental setup for visual observations of the fluid flow. Often sensors are integrated in the walls of the microchannels as an alternative experimental method [41]. However, the effect of these sensors on the fluid flow is unpredictable compared to the favored visual observations. As a result of the challenges associated with an experimental setup for visual observations, most investigations on dispersing particles/aggregates and formation of cavities within microsystems were conducted at larger channel geometry scales [1, 36, 39, 46, 63] or strongly reduced pressure gradients [22]. For this reason, the resultant observations regarding cavitation and dispersing phenomena differ strongly from those obtained at high pressures and small channel geometries. An opportunity to measure the velocity flow field within a microsystem at comparatively high pressures and small channel geometries is the usage of Microparticle Image Velocimetry (μPIV). Due to the high fluid velocities, small interframing times are necessary. In order to reduce the interframing time below the interframing time of a single CCD camera, the installation of two CCD cameras with matched internal shutters is necessary for the visual observations in microsystems with high fluid velocities. Figure 7.4 shows exemplarily the experimental setup of the μPIV for the characterization of fluid flow and cavitation within microsystems for high fluid velocities. Figure 7.5 shows exemplarily a cavitation image of a T-microchannel geometry at the conjunction without backpressure and a pressure difference of 200 bar (top) as well as the resultant flow field at a pressure difference of 500 bar and an additional backpressure of 60 bar to eliminate cavitation (bottom) [18, 19]. Fluid velocities of about 185 m/s were measured directly in the conjunction.

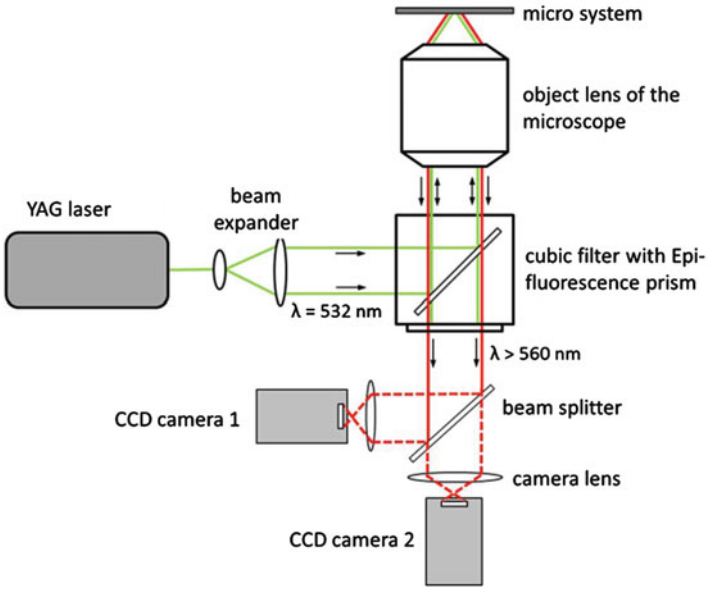

Fig. 7.4 Experimental setup of the μPIV for the characterization of fluid flow and cavitation within microsystems

7.5 High Pressure Dispersing in Microsystems

High-pressure systems are composed of a high-pressure device (e.g., pump) for pressure generation and a dispersing unit which expands the fluid to ambient pressure. Depending on the application, pressure differences between 20 and 4000 bar are realized [28]. Classically, radial diffusors consisting of valve seat and valve plunger are used as dispersing unit [63].

High-pressure homogenizers are predominantly used for emulsification processes, since dispersion of nanoparticulate suspensions demands higher stress intensities and frequencies for a successful reduction of the aggregate size as well as a higher abrasion resistance of the dispersion device. Figure 7.6 shows exemplarily the damage of an orifice dispersing unit due to cavitation and an abrasive nanoparticulate alumina suspension. Typically, the pressurized suspension is expanded abruptly to ambient pressure using a dispersing unit with a cross-sectional tapering. In front of the cross-sectional tapering, the fluid flow is characterized by a laminar elongation flow with superimposed laminar shear flow which changes to turbulent shear flow subsequent to the smallest cross-sectional area [28]. Furthermore, cavitation may occur due to abrupt changes in the microchannel geometry. Thus, several stress mechanisms for aggregate breakup described in detail in Sect. 7.3, i.e., stress via laminar shear and elongation and turbulent flow as well as stress via cavitation, take place simultaneously within or subsequent to the dispersion unit. Apart from other influencing factors (see Fig. 7.1), the dominating

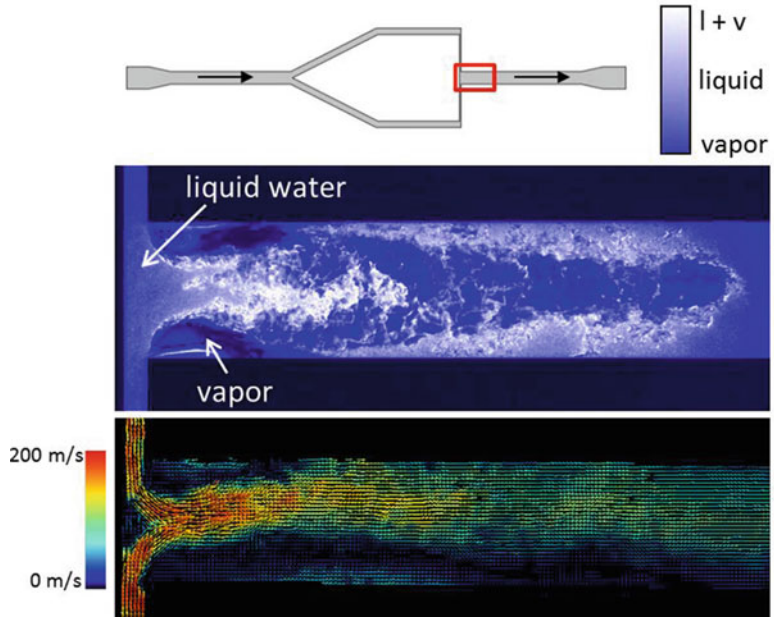

Fig. 7.5 *Top*: Cavitation images of the T-geometry at the conjunction ($\Delta p = 200$ bar; without backpressure $p_B = 0$ bar (ambient pressure); channel height of $h_{mc} = 53$ µm). *Bottom*: Flow measurement at a pressure difference of 500 bar and a backpressure of 60 bar using the µPIV setup shown in Fig. 7.4 (original graphic by Gothsch et al. [19])

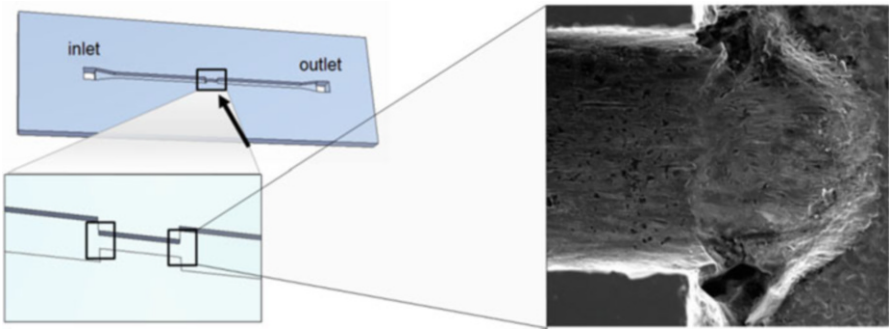

Fig. 7.6 Damage of a silicon orifice dispersing unit due to cavitation and an abrasive nanoparticulate alumina suspension

stress mechanisms as well as the product fineness of the dispersion process depend on the geometry of the dispersion unit, the suspension viscosity, the pressure difference, backpressure, and specific energy input. General statements regarding the dominating stress mechanisms are hardly possible. However, the effect of various process and formulation parameters on the product fineness can be identified, which are discussed in the following.

In general, only little literature exists on dispersing nanoparticles using high-pressure homogenizers or microsystems. Wengler et al. investigated the dispersion of nanoparticulate suspensions experimentally and via computational fluid dynamics using an orifice as dispersing unit [73–76]. According to Wengler et al. [72], elongation stresses exceed the stresses induced by turbulent shear flow. Moreover, laminar shear flow is negligible. The crucial stress mechanisms according to Sauter et al. are cavitation, impact, and hydrodynamic stresses [48, 49]. For an effective dispersion process, a high energy dissipation density is necessary. Moreover, according to Sauter et al., applying backpressure or a post-feeding of the nanoparticulate suspension directly behind the orifice is advantageous for the dispersion process.

7.5.1 Effect of the Microsystem Geometry

For cylindrical orifice dispersion units with orifice diameters between 80 and 300 µm, Sauter et al. [48] investigated the effect of impinging jets with different angles of the boreholes and an orifice with a subsequent impinging plate compared to a standard orifice configuration. The volume specific energy input to reach a certain product particle size was strongly decreased by using impinging orifice geometries. Moreover, the product fineness was increased using the impinging jet geometry and further increased by dispersing within impinging plate geometry. An increasing angle of the boreholes of the impinging jet geometry leads to increasing product fineness and energetic efficiency of the dispersion process. Apart from those crucial findings, these orifice dispersion units differ from classical microsystems.

Figure 7.7 shows exemplarily the effect of different dispersion geometries on the resultant median aggregate size of pyrogenic alumina as function of the number of passes through the microchannels (channel height of 26.6 µm and pressure difference of 500 bar) according to Gothsch et al. [19]. Although the differences in the resultant aggregate sizes are small, a clear trend of the dispersion efficiencies and maximum stresses between the different geometries can be derived. The highest dispersion efficiencies and stresses are provided by orifice geometries followed by the T-geometries, whereas straight and Z-channels lead to coarser particle sizes. Furthermore, significant differences within the same geometry type cannot be identified except for the orifice geometries.

The relative velocities of particle and fluid as well as the acting stresses within different microsystem geometries can be calculated from tracking the path of

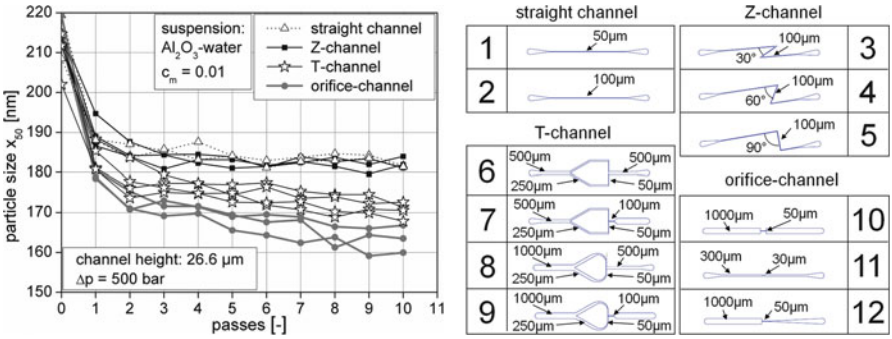

Fig. 7.7 Effect of the microsystem geometry on the dispersion result for rectangular microsystems with a channel height of 26.6 µm at a pressure difference of 500 bar and no backpressure (ambient pressure) (original graphic by Gothsch et al. [17])

particles with a certain diameter (230 nm) along the microsystem in a two-phase (liquid and gas) CFD simulation [7]. Figure 7.8 shows the maximum relative particle velocities for the abovementioned microchannel geometries at a pressure difference of 500 bar. Moreover, the velocity distribution within these geometries is shown. The relative velocities are an indicator for the stresses acting on the particle surface. The z- and straight channel geometries show a similar dispersion efficiency in the experiments (Fig. 7.7) which corresponds to the similar relative velocity distributions. The highest relative velocity distribution in the CFD simulation as well as the best dispersion efficiency is obtained for the orifice dispersion geometry. The T-channel (similar to the y-channel geometry) lays in-between (Figs. 7.7 and 7.8).

7.5.2 *Effect of the Microsystem Height and Orifice diameter*

The channel height of rectangular microsystems and the orifice width or diameter have a considerable effect on the dispersion process. Sauter et al. [48] investigated the effect of the orifice diameter on the resultant product fineness of dispersing nanoparticulate silica suspensions. As a result, the volume specific energy input for a certain product particle size increases strongly with decreasing orifice diameter. The dispersing unit with the smallest orifice diameter provides maximum product fineness.

Comparing the dispersion results of Figs. 7.7 and 7.9 with different channel heights, an increasing channel height leads to higher product fineness of all geometry types, except the orifice type. This corresponds to the results obtained by Sauter et al. [48] where a decreasing orifice diameter leads to an increasing product fineness. Main reason for the different effect of the channel height on the dispersing efficiency is the varying effect of the change in the cross-sectional areas on one hand and the change in the flow rate at a certain pressure drop on the other hand. A smaller channel height results in a higher fluid velocity if the volume flow rate stays

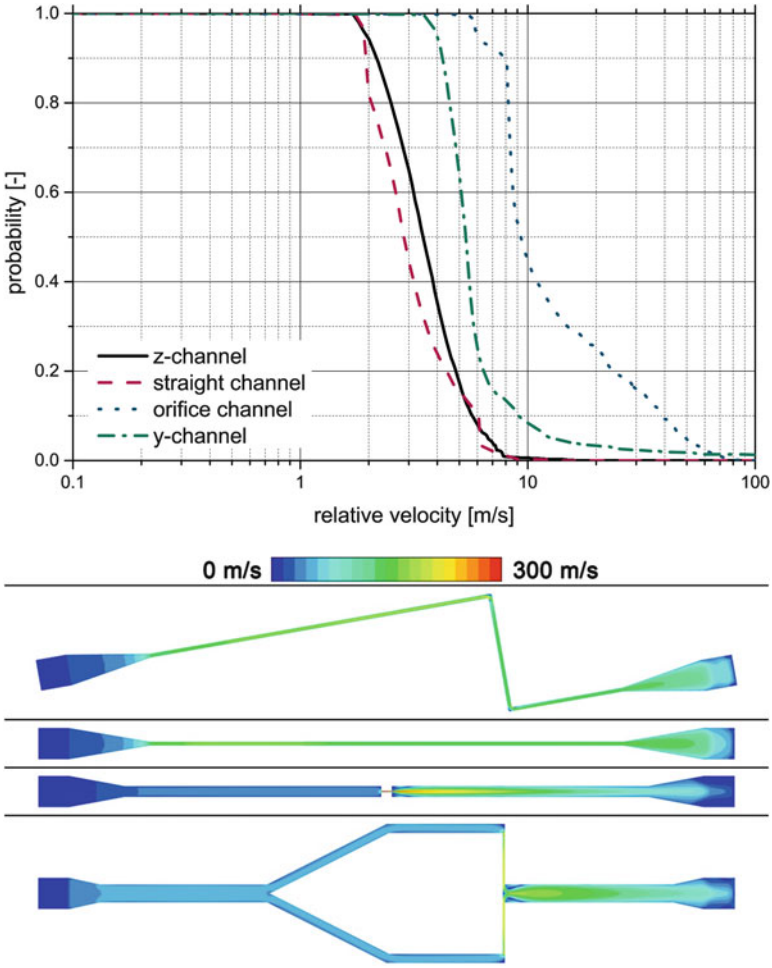

Fig. 7.8 Velocity distribution in the four different rectangular microsystem geometry types at a pressure difference of 500 bar obtained from two-phase CFD simulations (original graphic by Beinert et al. [7])

constant. However, the volume flow rate decreases due to a higher flow resistance at a constant pressure drop. A quantitative evaluation of the differences in the dispersion efficiencies, which are caused by various stress mechanisms, relative velocities, and stress distributions along the microchannels, can only be determined by Computational Fluid Dynamics (CFD) (e.g., by Beinert et al. [6, 7]).

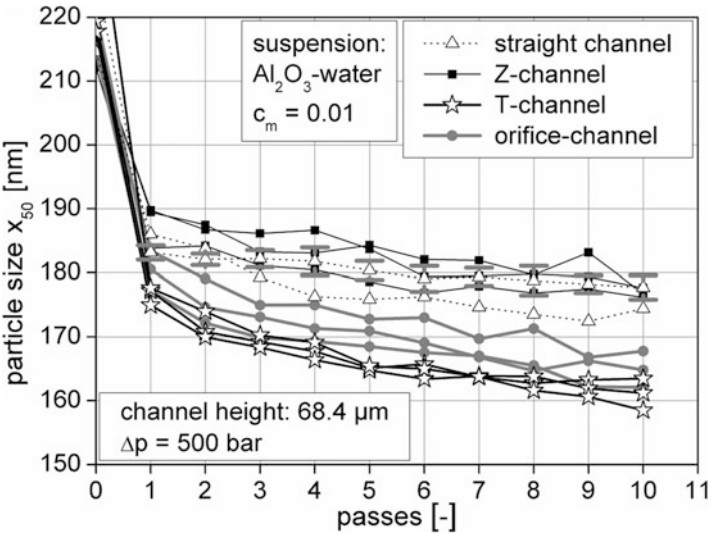

Fig. 7.9 Effect of microsystem geometry at a channel height of 68.4 µm on the dispersion result for rectangular microsystems at a pressure difference of 500 bar and no backpressure (ambient pressure) (original graphic by Gothsch et al. [17])

7.5.3 Effect of Cavitation

As mentioned before, the significance of the different stress mechanisms in microsystems, i.e., laminar and elongation shear flow, turbulent shear flow, and cavitation, especially the role of cavitation, on the dispersion is not fully clarified and discussed controversially by different authors. However, the importance of cavitation is solely discussed in context to emulsification processes or damage of microsystems. In emulsification processes a large number of authors predicted a positive effect of cavitation on the emulsification result [3, 15, 21, 31, 70, 71], a contrary minor or negative influence [23, 40–42, 67] or that both, turbulent shear flow and cavitation are the reasons for a successful breakup of droplets [24, 25]. The presence of cavitation can be characterized using photo-optical measurement methods shown in Fig. 7.3 and reduced or prevented by applying increasing backpressure [18].

The effect of cavitation on the dispersion efficiency was not clear and, thus, was investigated using an orifice geometry with different backpressures for dispersing pyrogenic alumina nanoparticles by Gothsch et al. (see Fig. 7.10). The cavitation was characterized via photo-optical measurements and visible at ambient pressure. Above 170 bar backpressure, no cavitation can be observed which is in good agreement with the results of a CFD simulation by Beinert et al. [7] which revealed the absence of cavitation at a backpressure of 170 bar. The dispersion efficiency of the orifice geometry increases by applying backpressure and, thus, by reducing and finally eliminating cavitation. Thus, cavitation does not contribute to the dispersion

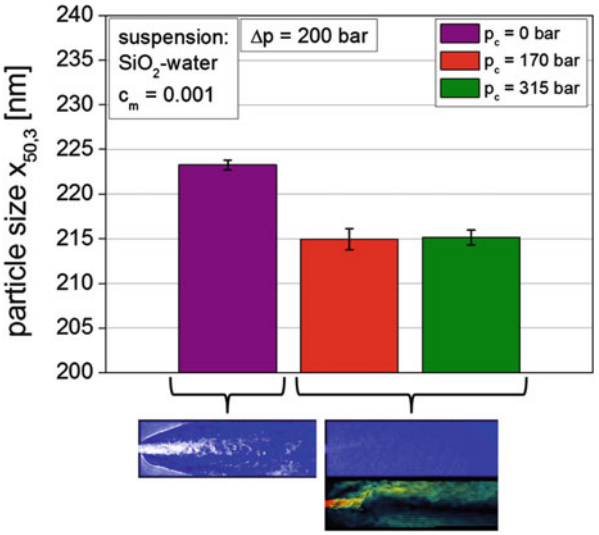

Fig. 7.10 Effect of cavitation on the dispersion efficiency at different backpressures for dispersing pyrogenic alumina nanoparticles (one pass at a pressure difference of 500 bar). Photo-optical measurements with visible cavitation at ambient pressure and photo-optical and μPIV measurements without cavitation above 170 bar backpressure

process but rather decreases dispersion efficiency in planar orifices. The effect of a backpressure on the volume flow rate as well as the dispersion efficiency is discussed in more detail at Gothsch et al. [18].

Highest shear stresses for dispersing within orifice channel geometries are just before and in the vena contracta. According to Beinert et al. [7], as long as the cavitation pockets in the orifice channel extend beyond the vena contracta, the volume flow rate should be reduced. Similar results are obtained by Gothsch et al. [18, 19] by investigating the effect of backpressure on cavitation and the volume flow. As mentioned before, the fluid volume flow stays constant independent of an increasing backpressure if cavitation is restricted to the area of flow detachment in the vena contracta. Figure 7.11 shows the experimentally measured and computed mass flow of an orifice microchannel geometry with and without backpressure. By applying backpressure and, thus, preventing cavitation the experimental mass flow data is in good agreement to the single-phase CFD simulations. Without backpressure and in the presence of cavitation, a two-phase CFD simulation is necessary to match the experimental measured and computed mass flow. Hence, CFD simulations can reproduce and predict cavitation and steam effects in microchannels. Figure 7.12 shows exemplarily the steam distribution in the different microchannel geometries without backpressure at a pressure difference of 500 bar.

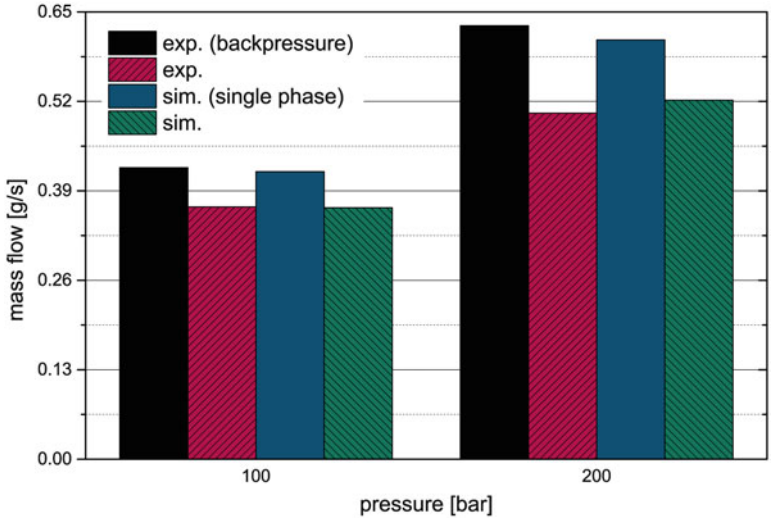

Fig. 7.11 Experimentally measured and computed (CFD simulations) mass flow for an orifice microchannel geometry with and without backpressure at two different pressure differences (original graphic by Beinert et al. [7])

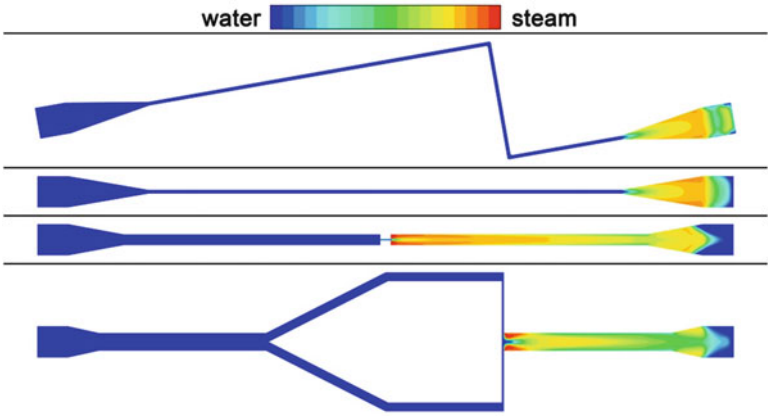

Fig. 7.12 Computed steam distribution in different microchannel geometries without backpressure at pressure difference of 500 bar (original graphic by Beinert et al. [7])

7.5.4 Effect of Number of Passes

For the breakage of aggregates and agglomerates within microsystems, the provided stress intensity of the dispersing unit has to be greater than the aggregate/agglomerate strength [6, 55]. Thus, the increase in product fineness depends on the maximum stress intensity, the stress intensity distribution as well as the stress frequency

or probability. Due to the fact that the aggregate strength typically increases with decreasing aggregate size and the maximum stress intensity provided by the dispersion unit of the microsystem is constant at constant operating conditions, a minimum aggregate/agglomerate size is obtained for infinite passes. Depending on the stress intensity distribution and stress frequency, the probability for each particle being stressed with the maximum stress intensity varies for each microchannel geometry. As an example, the maximum stress intensity within the straight and Z-channel geometry in Figs. 7.7 and 7.9 is comparatively low and greater particle sizes were reached. However, the probability that a particle experiences highest stress intensities is high and the maximum product fineness is reached after a few passes. In contrast, a further decrease of the particle size with increasing number of passes can be observed for the T- and the orifice channel due to a broad stress intensity distribution with small local areas of high maximum stresses.

To compare the dispersion efficiency of a dispersion process with a high number of passes with a single pass at much higher pressure differences, Fig. 7.13 shows a comparison of the dispersion via multiple passes and a single pass at various pressure differences as function of the volume specific energy input (according to Gothsch et al. [17]). Although the maximum stress intensity at a constant pressure difference stays constant and the probability that each particle is at least one time stressed by the maximum stress intensity increases with increasing number of passes, the dispersion efficiency via multiple passes at a lower pressure difference is limited by the maximum stress intensities. For increasing pressure differences, the stress intensity increases and a higher product fineness can be obtained. Hence,

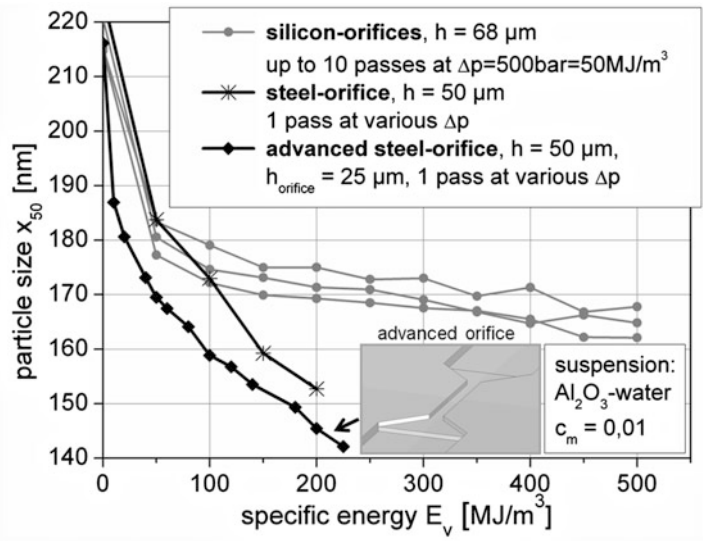

Fig. 7.13 Comparison of the dispersion process of multiple passes and a single pass at various pressure differences as function of the volume specific energy input (original graphic by Gothsch et al. [17])

higher pressure differences in a single pass are much more relevant for the dispersion of nanoparticles than multiple passes at a constant pressure difference. Moreover, Figure 7.13 shows the positive effect of an optimized orifice geometry with higher stress intensities on the dispersion efficiency.

7.6 Conclusion

Depending on the geometry and the operating conditions of dispersing units within microsystems, various stress mechanisms have got an effect on the dispersion process. In contrast to emulsification processes, the effect of cavitation is less important for high-pressure dispersion processes. Indeed, cavitation leads to damage of the dispersing units, reduces the volume flow, and leads to a less efficient dispersion of nanoparticulate suspensions. By applying backpressure, cavitation can be reduced and, thus, the volume flow increased and the dispersion efficiency of the dispersing unit increased. Furthermore, the usage of T-channels and especially orifice geometries as dispersing unit leads to high stress intensities and an increased dispersion efficiency. As a result depending on the target product fineness for application, the channel height or diameter has to be optimized. Moreover, in dispersion processes, a single pass at higher pressure difference is more efficient than dispersing multiple passes at a constant pressure difference. In summary, solid particles have a higher strength compared to droplets and are slightly deformable. Hence, emulsification and dispersing processes are hard to compare. Besides microparticle image velocimetry (μPIV), single- and two-phase CFD simulations (without and with cavitation) are well suited to characterize and optimize the stress intensity, stress distribution, and probability in microchannels. Moreover, the presence and effect of cavitation can be studied.

Acknowledgments The authors gratefully acknowledge the DFG for financial support within the DFG research group 856 “Mikrosysteme für partikuläre Life-Science-Produkte” (mikroPART).

References

1. Arai M, Shimizu M, Hiroyasu H (1985) Breakup length and spray angle of high speed jet. In: 3rd international conference on liquid atomization and spray systems (ICLASS), London
2. Bache DH (2004) Floc rupture and turbulence: a framework for analysis. Chem Eng Sci 59:2521–2534
3. Baldyga J, Makowski L, Orciuch W, Sauter C, Schuchmann HP (2008) Deagglomeration processes in high-shear devices. Chem Eng Res Des 86:1369–1381
4. Baldyga J, Orciuch W, Makowski L, Malski-Brodzicki M, Malik K (2007) Break up of nanoparticle clusters in high-shear devices. Chem Eng Proc 46:851–861
5. Behrend O, Schubert H (2001) Influence of hydrostatic pressure and gas content on continuous ultrasound emulsification. Ultrason Sonochem 8:271–276

6. Beinert S, Gothsch T, Kwade A (2012) Numerical evaluation of flow fields and stresses acting on agglomerates dispersed in high-pressure microsystems. Chem Eng Technol 35:1922–1930
7. Beinert S, Gothsch T, Kwade A (2015) Numerical evaluation of stresses acting on particles in high-pressure microsystems using a Reynolds stress model. Chem Eng Sci 123:197–206
8. Beinert S, Schilde C, Gronau G, Kwade A (2014) CFD-Discrete element method simulations combined with compression experiments to characterize stirred-media mills. Chem Eng Technol 37:770–778
9. Bentley BJ, Leal LG (1986) An experimental investigation of drop deformation and breakup in steady, two-dimensional linear flows. J Fluid Mech 167:241–283
10. Bergwerk W (1959) Flow pattern in diesel nozzle spray holes. Proc Inst Mech Eng 173:655–660
11. Breitung-Faes S, Kwade A (2008) Nano particle production in high-power-density mills. Chem Eng Res Des 86:390–394
12. Diekmann H, Metz H (1991) Grundlagen und Praxis der Biotechnologie: eine Einführung für Naturwissenschaftler und Ingenieure. G.Fischer, Stuttgart
13. DIN ISO/TS 27687:2010–02 (2010) Nanotechnologie—Terminologie und Begriffe für Nanoobjekte. Deutsches Institut für Normung e. V. (DIN)
14. Freudig B, Tesch S, Schubert H (2002) Herstellen von Emulsionen in Hochdruckhomogenisatoren—Teil 2: Bedeutung der Kavitation für die Tropfenzerkleinerung. Chemie Ingenieur Technik 74:880–884
15. Freudig B, Tesch S, Schubert H (2003) Production of emulsions in high-pressure homogenizers—Part II: influence of cavitation on droplet breakup. Eng Life Sci 3:266–270
16. George WK (2013) Lectures in turbulence for the 21st century. Chalmers University of Technology, Gothenburg
17. Gothsch T, Finke JH, Beinert S, Lesche C, Schur J, Büttgenbach S, Müller-Goymann C, Kwade A (2011) Effect of microchannel geometry on high-pressure dispersion and emulsification. Chem Eng Technol 34:335–343
18. Gothsch T, Richter C, Beinert S, Schilcher C, Schilde, Büttgenbach S, Kwade A (2016) Effect of Cavitation on Dispersion and Emulsification Process in High-pressure Microsystems (HPMS). Chemical Engineering Science (in press)
19. Gothsch T, Schilcher C, Richter C, Beinert S, Dietzel A, Büttgenbach S, Kwade A (2014) High-pressure microfluidic systems (HPMS): flow and cavitation measurements in supported silicon microsystems. Microfluidics Nanofluidics 18:121–130
20. Grace HP (1982) Dispersion phenomena in high viscosity immiscible fluid systems and application of static mixers as dispersion devices in such systems. Chem Eng Commun 14:225–277
21. Grob M (1951) Homogenisation von Milch und Milchkonzentraten mit einer Lavaldüse. Doctor PhD thesis, ETH Zürich, Zürich
22. Hakansson A, Fuchs L, Innings F, Revstedt J, Bergenstahl B, Trägardh C (2010) Visual observations and acoustic measurements of cavitation in an experimental model of a high-pressure homogenizer. J Food Eng 100:504–513
23. Mohr K-H (1980) Mechanismen der Hochdruckhomogenisierung, 1. Mitteilung: Turbulenz oder Kavitation als Zerkleinerungsmechanismen. Lebensmittelindustrie 27:399–403
24. Karbstein H (1994) Untersuchungen zum Herstellen und Stabilisieren von Öl-in-Wasser-Emulsionen. Dissertation, TH Karlsruhe, Karlsruhe
25. Karbstein H, Schubert H (1995) Developments in the continuous mechanical production of oil-in-water macro-emulsions. Chem Eng Proc 34:205–211
26. Kelly S (1999) Fluiddynamischer Einfluss auf die Morphogenese von Biopellets filamentöser Pilze. Institute of Biochemical Engineering, TU Braunschweig, Braunschweig
27. Knieke C, Steinborn C, Romeis S, Peukert W, Breitung-Faes S, Kwade A (2010) Nanoparticle production with stirred-media mills: opportunities and limits. Chem Eng Technol 33:1401–1411
28. Köhler K, Tesch S, Freudig B, Schuchmann HP (2012) Emulgiertechnik: Emulgieren in Hochdruckhomogenisatoren. Behrs Verlag, Hamburg

29. Kolmogorov AN (1958) Die lokale Struktur der Turbulenz in einer inkompressiblen zähen Flüssigkeit bei sehr großen Reynoldsschen Zahlen. Akademie Verlag, Berlin
30. Kolmogorov AN (1991) The local structure of turbulence in incompressible viscous fluid for very large Reynolds numbers. Proc Roy Soc Lond A 434:9–13
31. Kurzhals H-A, Reuter H (1979) Untersuchungen über die physikalisch-technischen Vorgänge beim Homogenisieren von Milch in Hochdruck-Homogenisiermaschinen. Chemie Ingenieur Technik 51:325
32. Kwade A, Schilde C, Burmeister CF, Roth M, Lellig P, Auerhammer GK (2013) Micromechanical properties of colloidal structures. Powders Grains 1542:939–942
33. Langer G, Deppe A (2000) Zum Verständnis der hydrodynamischen Beanspruchung von Partikeln in turbulenten Rührerströmungen. Chemie Ingenieur Technik 72:31–41
34. Lesche C, Gothsch T, Kwade A, Büttgenbach S (2011) Development of a dispersion micro-element for pharmaceutical screening applications: material and fabrication. In: Proceedings of MST Kongress 2011, Darmstadt, Germany, pp 642–645
35. Loo CC, Carleton WM (1953) Further studies of cavitation in the homogenization of milk products. J Dairy Sci 36:64–75
36. Martynov S (2005) Numerical simulation of the cavitation process in diesel fuel injectors. Doctor of Philosophy PhD thesis, University of Brighton, Brighton
37. Mende S, Stenger F, Peukert W, Schwedes J (2003) Mechanical production and stabilization of submicron particles in stirred media mills. Powder Technol 132:64–73
38. Niedballa S (1999) Dispergierung von feinen Partikelfraktionen in Gasströmungen—Einfluss von Dispergierbeanspruchung und oberflächenmodifizierenden Zusätzen. Faculty of Mechanical, Process and Energy Engineering, Technische Universität Bergakademie Freiberg, Freiberg
39. Payri R, Salvador FJ, Gimeno J, Venegas O (2013) Study of cavitation phenomenon using different fuels in a transparent nozzle by hydraulic characterization and visualization. Exp Therm Fluid Sci 44:235–244
40. Phipps LW (1971) Mechanism of oil droplet fragmentation in high-pressure homogenizers. Nature 233:617
41. Phipps LW (1974) Cavitation and separated flow in a simple homogenizing valve and their influence on the break-up of fat globules in milk. J Dairy Res 41:1–8
42. Phipps LW (1975) The fragmentation of oil drops in emulsions by a high-pressure homogenizer. J Phys D 8:448–462
43. Rumpf H (1959) Beanspruchungstheorie der Prallzerkleinerung. Chemie Ingenieur Technik 31:323–337
44. Rumpf H, Raasch J (1962) Desagglomeration in Strömungen. Symposium Zerkleinern, Weinheim
45. Salvador FJ, Martínez-López J, Caballer M, De Alfonso C (2013) Study of the influence of the needle lift on the internal flow and cavitation phenomenon in diesel injector nozzles by CFD using RANS methods. Energy Conv Manag 66:246–256
46. Sato K, Saito Y (2001) Unstable cavitation behavior in a circular-cylindrical orifice flow. In: Fourth international symposium on cavitation: CAV 2001, California Institute of Technology, Pasadena
47. Sauter C, Emin MA, Schuchmann HP, Tavman S (2008) Influence of hydrostatic pressure and sound amplitude on the ultrasound induced dispersion and de-agglomeration of nanoparticles. Ultrason Sonochem 15:517–523
48. Sauter C, Schuchmann HP (2007) High pressure for dispersing and deagglomerating nanoparticles in aqueous solutions. Chem Eng Technol 30:1401–1405
49. Sauter C, Schuchmann HP (2008) Materialschonendes Hochdruckdispergieren mit dem high pressure post feeding (HPPF)-system. Chemie Ingenieur Technik 80:365–372
50. Schilde C, Beinert S, Kwade A (2011) Comparison of the micromechanical aggregate properties of nanostructured aggregates with the stress conditions during stirred media milling. Chem Eng Sci 66:4943–4952

51. Schilde C, Breitung-Faes S, Kampen I, Kwade A (2013) Grinding kinetics of nano-sized particles for different electrostatic stabilizing acids in a stirred media mill. Powder Technol 235:1008–1016
52. Schilde C, Breitung-Faes S, Kwade A (2007) Dispersing and grinding of alumina nano particles by different stress mechanisms. Ceramic Forum Int 84:12–17
53. Schilde C, Gothsch T, Quarch K, Kind M, Kwade A (2009) Effect of important process parameters on the redispersion process and the micromechanical properties of precipitated silica. Chem Eng Technol 32:1078–1087
54. Schilde C, Burmeister C, Kwade A (2014) Measurement and simulation of micromechanical properties of nanostructured aggregates via nanoindentation and DEM-simulation. Powder Technol 259:1–13
55. Schilde C, Kampen I, Kwade A (2010) Dispersion kinetics of nano-sized particles for different dispersing machines. Chem Eng Sci 65:3518–3527
56. Schilde C, Mages-Sauter C, Kwade A, Schuchmann HP (2011) Efficiency of different dispersing devices for dispersing nanosized silica and alumina. Powder Technol 207:353–361
57. Schilde C, Westphal B, Kwade A (2012) Effect of primary particle morphology on the micromechanical properties of nanostructured alumina agglomerates. J Nanopart Res 14 (3):1–11
58. Schilde C, Kwade A (2015) Synthesis, structure and mechanics of nano-particulate aggregates. Springer, Switzerland
59. Schilde C (2012) Structure, mechanics and fracture of nanoparticulate aggregates. Institute of Particle Technology, TU Braunschweig, Braunschweig
60. Schilde C, Kwade A (2012) Measurement of the micromechanical properties of nanostructured aggregates via nanoindentation. J Mater Res 27:672–684
61. Schlichting H, Gersten K (2006) Grenzschichttheorie. Verlag G. Braun, Karlsruhe
62. Schröder C (2012) Rheologie- und Stabilitätseffekte bei der Nanozerkleinerung anorganischer Materialien. Institute of Particle Technology, TU Braunschweig, Braunschweig
63. Schuchmann HP, Danner T (2004) Emulgieren: Mehr als nur Zerkleinern. Chemie Ingenieur Technik 76:364–375
64. Shah YT, Pandit AB, Moholkar VS (1999) Cavitation reaction engineering. Kluwer Academic Plenum Publishers, New York
65. Sou A, Hosokawa S, Tomiyama A (2007) Effects of cavitation in a nozzle on liquid jet atomization. Int J Heat Mass Transf 50:3575–3582
66. Stang M (1998) Zerkleinern und Stabilisieren von Tropfen beim mechanischen Emulgieren. VDI-Verlag, Düsseldorf
67. Stang M, Schuchmann H, Schubert H (2001) Emulsification in high-pressure homogenizers. Eng Life Sci 1:151–157
68. Suh HK, Lee CS (2008) Effect of cavitation in nozzle orifice on the diesel fuel atomization characteristics. Int J Heat Fluid Flow 29:1001–1009
69. Taylor GI (1934) The formation of emulsions in definable fields of flow. Proc Roy Soc 29:501–523
70. Treiber A (1979) Zum Einfluss der Kavitation bei der Hochdruckhomogenisation von Öl-in-Wasser-Emulsionen. Dissertation, TH Karlsruhe, Karlsruhe
71. Treiber A, Kiefer P (1976) Kavitation und Turbulenz als Zerkleinerungsmechanismen bei der Homogenisation von O/W-Emulsionen. Chemie Ingenieur Technik 48:259
72. Wengeler R (2006) Hydrodynamic stress induced dispersion of nanoscale agglomerates by a high pressure process. PhD thesis, TH Karlsruhe, Karlsruhe
73. Wengeler R, Nirschl H (2004) Dispergierung nanoskaliger Agglomerate mittels Hochdruckver-fahren. Chemie Ingenieur Technik 76:1387–1388
74. Wengeler R, Nirschl H (2007) Turbulent hydrodynamic stress induced dispersion and fragmentation of nanoscale agglomerates. J Colloid Interface Sci 306:262–273
75. Wengeler R, Ruslim F, Nirschl H, Merkel T (2004) Dispergierung feindisperser Agglomerate mit Mikro-Dispergierelementen. Chemie Ingenieur Technik 76:659–662

76. Wengeler R, Teleki A, Vetter M, Pratsinis SE, Nirschl H (2006) High-pressure liquid dispersion and fragmentation of flame-made silica agglomerates. Langmuir 22:4928–4935
77. Yokoyama T (2007) Basic properties and measuring methods of nanoparticles: size effect and properties of nanoparticles, 1st edn. Elsevier, Amsterdam
78. Zellmer S, Grote C, Cheema T, Garnweitner G (2015) Colloid process engineering: small-molecule stabilization mechanisms of metal oxide nanoparticles. Springer, Switzerland, pp 73–91

Chapter 8
Particles in Microfluidic Systems: Handling, Characterization, and Applications

T.P. Burg

Abstract This chapter gives a tour of the fascinating opportunities for handling and characterizing solid particles by microfluidic methods. First, attention will be given to the hydrodynamic, electrical, and magnetic forces which may be used to manipulate suspended particles at small scales. Second, important methods for the detection and characterization that have been proposed in the literature are illustrated and discussed. The third and last part of the chapter will give the reader a sense of the exciting applications of these methods in different fields, in particular flow cytometry, particle synthesis, and bioanalytical measurement. These applications exemplify the subtle invasion of particle-based microfluidics into many areas of the life sciences, pharmaceutical technology, chemistry, and materials science. In the future, the trend towards miniaturization will continue, and we are likely to see an increasing number of technologies and products using some of the principles reviewed here.

8.1 Introduction

Microfluidic systems provide exquisite control over the distribution and transport of solutes from the molecular scale to micrometer-size particles. This precision is mainly a result of laminar flow and short diffusional time scales.

The first part of this chapter will review important phenomena that can be exploited for handling solid particles at the microscale. These include hydrodynamic forces, electric and dielectrophoretic forces, and the forces on paramagnetic particles in external magnetic fields. Together, these three form the mainstay of directed particle manipulation methods commonly employed in microfluidic systems. There also are several other, less frequently encountered techniques, such as the use of optical fields, thermal gradients, or surface tension, which are not contained in this chapter, but can be found in the specialized literature.

T.P. Burg (✉)
Max Planck Institute for Biophysical Chemistry, Am Fassberg 11, Göttingen 37077, Germany
e-mail: tburg@mpibpc.mpg.de

A. Dietzel (ed.), *Microsystems for Pharmatechnology*,
DOI 10.1007/978-3-319-26920-7_8

The second part will provide an overview of characterization techniques for micro- and nanoparticles in microfluidic systems. Some of the methods, such as mass and impedance measurements, benefit specifically from miniaturization. Others perform equally well in macroscale and microscale systems, and their combination with microfluidics is interesting predominantly for the ability to handle minute volumes and provide gentle sorting, for example to maintain the viability of cells.

In the last part on applications, we examine some of the opportunities that emerge from the combination of micro- and nanoparticles with microfluidic systems. The methods described in the first two parts of the chapter are quite universal to applications dealing with synthetic or biological particles from the nanoscopic to the micrometer scale. Most current applications of these methods fall in one of the three major groups shown in Fig. 8.1. The first group is centered about the production, handling, and characterization of functional nanoparticles, such as crystallized drugs or drug delivery particles. The second group comprises applications that involve living cells in suspension. Finally, a third set of applications that are increasingly raising interest are uses of microparticles as mobile solid phases for separation or for multiplexed affinity assays in microfluidic systems. We will highlight devices that exemplify some of these applications and demonstrate the numerous opportunities that lie in the combination of microfluidics and particle technology.

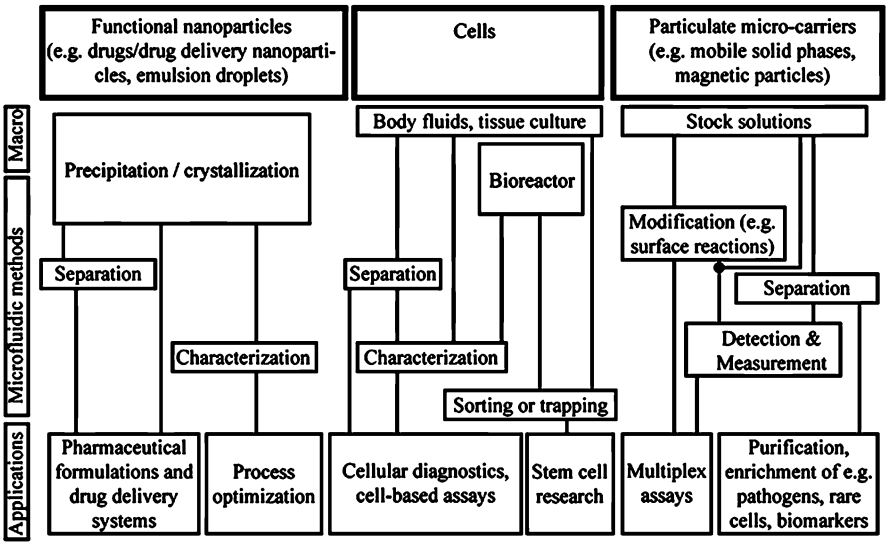

Fig. 8.1 Microfluidic technologies for the production, handling, and characterization of micro- and nanoparticles are beginning to play an important role in several fields. Most of the applications today belong to one of the groups of functional nanoparticles, cells, or analytical methods based on particulate micro-carriers. Microfluidics for characterization, separation, and sorting often use samples produced at the macroscale or are themselves a source for particles of interest (e.g. microbioreactors, microscale precipitation). A small number of example applications that appear to dominate the current literature are listed at the bottom

8.2 Particle Handling

8.2.1 Hydrodynamic Forces

The movement of solid particles suspended in a flowing stream is tightly coupled to the dynamics of the liquid. This is quite intuitive from everyday experience. However, in carrying our intuition from the macroscopic world over to suspensions in microfluidic systems, the importance of viscous drag, inertia, and gravity needs to be reconsidered. Gravity is a body force, and its magnitude scales with the weight of an object ($\sim r^3$, if the dimension r describes the size). A microparticle of, for example, 10 μm diameter experiences a gravitational settling force one billion (10^9) times smaller than a 1 cm diameter object of the same density. Analogous to gravity is the scaling of inertia. In order to stop a particle moving at velocity v, the time-integral of the decelerating force must match the momentum $\left(m_\mathrm{p} \cdot v\right)$, where the particle mass m_p again scales as $\sim r^3$. However, in viscous fluids, the drag force on a moving particle scales only as $\sim r$. For example, for a sphere moving at velocity $\vec{v}$, the Stokes drag is given by $\vec{F}_\mathrm{Stokes} = -6\pi\eta r\,\vec{v}$, where η is the viscosity. This strong difference in scaling causes small particles to follow the streamlines almost exactly, and if the flow were to suddenly stop, particles would come to a seemingly instantaneous halt.

It becomes clear from the scaling of the different forces that the movement of particles at low Reynolds numbers, much like the flow of the fluid, is dictated by the effects of viscosity. Inertia and gravity play almost no role. In an idealized description, one could thus identify the trajectories of particles simply with the streamlines on which their center of mass is located. But this is an oversimplification when the size of the channel itself is on the same order of magnitude as the diameter of the particles. As finite size particles can only approach the channel walls to within one radius, perhaps the most obvious consequence of the narrow confinement is that a significant fraction of the flow profile is not accessible. Therefore, the velocity distribution of the suspension does not follow the same parabolic profile as the laminar fluid flow. Staben et al. described the velocity distribution of particles in Poiseuille flow for diameters that are on the same order as the channel height, as shown in Fig. 8.2 [51, 52].

Second, the shear flow leads to a migration of particles due to the so-called "tubular pinch effect," which occurs whenever particles are large enough so that their motion relative to the fluid is not negligible. The tubular pinch effect was first discovered in studies of blood flow through small capillaries, when it was observed that the effective hematocrit, i.e., the volume fraction of red blood cells, differed unexpectedly between small and large capillaries. In the context of physiology, this phenomenon is today called the Fahraeus effect, and we now know that it is caused by the fact that cells in small blood vessels tend to avoid the vessel walls by some

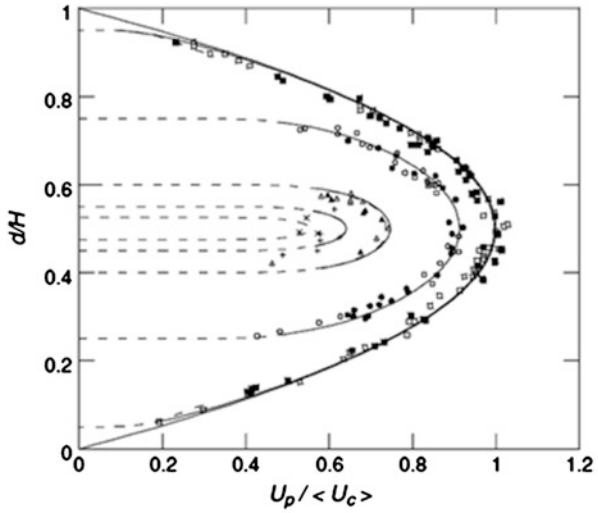

Fig. 8.2 The velocity of particles travelling through a microfluidic channel depends on the particle diameter and the position in the channel. Particles that are large compared to the channel size remain near the center and move approximately at the average velocity of the fluid. Particles that are small compared to the channel closely follow the unperturbed parabolic velocity profile. Shown here are simulations and measurements by Staben et al., which illustrate this effect for particles of 0.1, 0.5, 0.8, and 0.9 times the height (H) of a much wider channel. The vertical axis is the position of particles in the channel, and the horizontal axis gives the velocity normalized to the maximum velocity of the unperturbed fluid flow. Reprinted from [51], copyright (2005), with permission from Elsevier

margin. This discovery spawned a vivid research field investigating the radial forces that act on particles carried by viscous flows in channels and tubes.

It turns out that radial forces can only arise when the Reynolds number is sufficiently large or when the flowing particles are deformable (or both). At Reynolds numbers (Re) on the order ~1, inertia starts to influence the particle trajectory. It should be stressed, however, that this does not necessarily entail turbulence, and all the results described here in fact assume that flow is still laminar. To see how $Re \rightarrow 0$ forbids lateral migration, one first notes that the Stokes equation is linear. Therefore, if a particle had migrated towards the center while flowing in one direction, it would be required to migrate away from the center again when the direction of flow is reversed. However, this is not possible, as the radial direction of migration is independent of the flow direction in the tube. Therefore, for very low Reynolds number and stiff particles, the lateral force must be zero, and the tubular pinch effect only plays a role in high Reynolds number flows [13]. A formal proof can be found in [5].

The first systematic experimental measurements of the lateral migration of particles in tube flow were carried out by Segre and Silberberg in the early 1960s [48]. Although the migration of red blood cells in narrow capillaries had been described long before, the effect had never been characterized quantitatively.

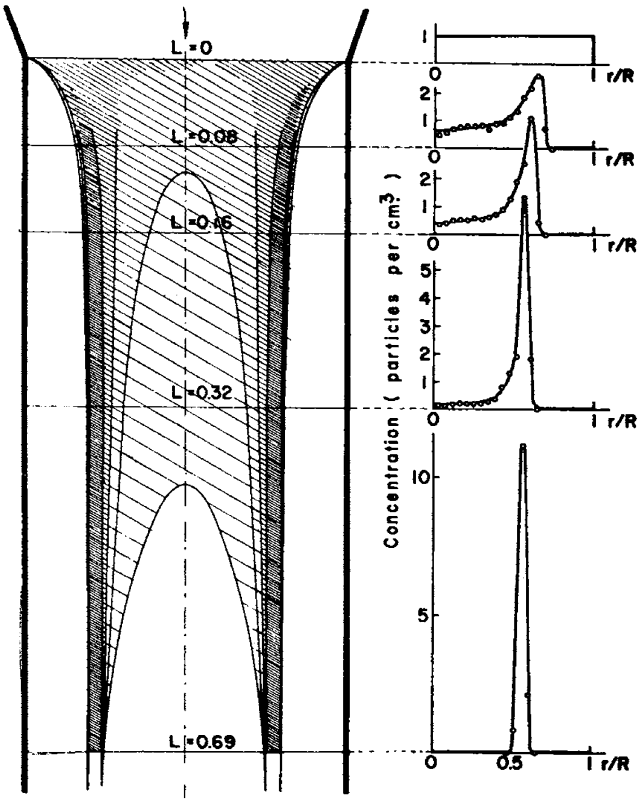

Fig. 8.3 The original observation of the tubular pinch effect by Segre and Silberberg [48] showing lateral migration of particles in laminar flow. The image shows the concentration of particles, indicated by the shading, along the tube. Note that the length has been normalized according to the flow conditions. Under all conditions, the initially uniformly dispersed particles migrate to a stable annulus with a radius of approximately 0.6 times the radius of the tube. Reprinted by permission from Macmillan Publishers Ltd: [48], copyright (1961)

Segre's and Silberberg's results were quite surprising. All particles regardless of their starting position seemed to be drawn towards an annulus having a radius of ~0.6 times the tube diameter (Fig. 8.3). Although this migration of particles in the parabolic flow profile within a tube is reminiscent of the Magnus effect, which causes a ball thrown with a spin to follow a curved trajectory, the analogy is incomplete. For example, it fails to explain why particles collect at an intermediate stationary position of nonzero shear flow rather than be driven towards the channel center or collect at the walls. A more complete explanation emerged when Ho and Leal accurately predicted the experimental observations using the method of matched asymptotic expansions [25]. Lateral migration was seen to result from the combination of two counteracting forces: An outward force acting in the direction of increasing shear, and an inward force pointing away from the walls. The latter is a common phenomenon for particles travelling in fluid in close

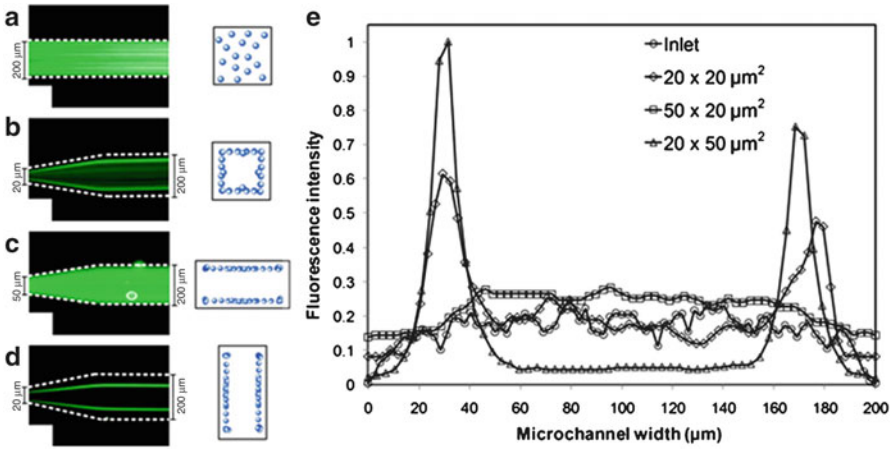

Fig. 8.4 Lateral migration of 1.9 µm particles in microfluidic channels of different aspect ratios. Particles were uniformly distributed in the 200 µm wide inlet sections of all three channels (*top* fluorescence image shows a representative inlet). When the channels constricted to the sizes shown in the legend on the *right*, the particles migrated to stable positions that were delocalized along the long dimension of the channel cross section (E). Reprinted with permission from [4]. Copyright [2008], AIP Publishing LLC

proximity to a solid wall. Further development of the theory revealed that the radius of the annulus to which particles were focused increases monotonically with the Reynolds number. This has also been confirmed experimentally.

Microfluidic systems differ in some ways from the circular tubes that were the subject of most studies on lateral migration at the end of the twentieth century. Most important is the lack of a circular symmetry. Microfluidic channels generally have a rectangular shape, which leads to a collapse of the annulus observed by Segre and Silberberg into discrete equilibrium positions [4, 12, 16]. For square channels, there are eight stable positions at $Re < 100$, and when the Reynolds number increases above 500, only the four corner positions remain stable. In rectangular channels, focusing is dominated by the large shear along the narrow channel dimension. In this case, particles all eventually migrate towards two narrow stripes parallel to the wide sidewalls, but they always remain at some distance from the wall (Fig. 8.4).

The magnitude of the lift force was calculated by Asmolov [1] and is given by

$$F_L = \rho \left(\frac{2\overline{u_f}}{H} \right)^2 C_L d^4 \tag{8.1}$$

where ρ is the fluid density, $\overline{u_f}$ is the mean fluid velocity, H is the short dimension of the channel cross section, d the particle diameter, and C_L is the lift coefficient, which depends on the position in the channel and on the Reynolds number. For $Re < 100$, however, $C_L \approx 0.5$ is a good approximation. By balancing the lift force with the Stokes drag, a guideline for designing the channel length so that the

majority of particles are focused into one narrow stream can be given. For particles to migrate by a distance L_p, a channel of at least a length

$$L = \frac{3\pi\mu H^2 L_p}{2\rho\overline{u_f}d^3 C_L} \tag{8.2}$$

is required [4]. Note that an underlying assumption in this formula is that the particles being focused are neutrally buoyant and that the channel is straight. Many interesting phenomena arise in more general cases, and the reader is referred to the excellent review of the topic by Di Carlo et al. for an in-depth treatment [17].

8.2.2 External Fields

8.2.2.1 Electrophoresis and Dielectrophoresis

There is a multitude of fascinating phenomena that arise from the interaction of charged and uncharged particles in fluids with applied electric fields. Of these, electrophoresis and dielectrophoresis have emerged to be exceptionally useful for the targeted manipulation of particles in microfluidic systems. We will therefore briefly review the physical basis of these effects. Electrophoresis is the movement of a charged particle in an electrolyte when an electric field is applied. Dielectrophoresis, on the other hand, is not dependent on a net charge but only requires a difference in electrical permittivity between the particle and the surrounding solution; movement is driven by an electric field gradient and not by a uniform field.

Electrophoresis. Charged particles in an electric field experience a force directed parallel to the field lines. Net movement is only observed in non-alternating, or DC, fields. Intimately linked to the electrophoresis of particles in microfluidic systems is the phenomenon of electroosmotic flow (EOF), which can accelerate, decelerate, or even reverse the velocity vector of charged particles due to electrophoresis alone. We first introduce some important concepts of charged interfaces in electrolyte solutions that will prove useful for understanding both phenomena.

Solid–liquid interfaces often possess a nonzero charge due to the adsorption of ions or the decomposition of surface groups. Oxide surfaces, such as SiO_2 or TiO_2, for example, generally acquire a negative charge in aqueous solution due to the decomposition of hydroxyl groups ($OH \rightarrow O^- + H^+$). The charge of the surface is screened by counterions, which are attracted from the solution to the charged interface. At the same time, co-ions are repelled by the interface (Fig. 8.5). The packing of counterions close to the surface depends on the charge density, the ionic strength, and also on the nature of the ions in solution. Helmholtz first introduced a model that assumed all counterions were adsorbed within a thin layer termed the electrical double layer. However, this model proved to be insufficient to explain, for example, the capacitance curves of metal electrodes in electrolyte solutions. As an alternative to the Helmholtz model, the model of the diffuse double layer was

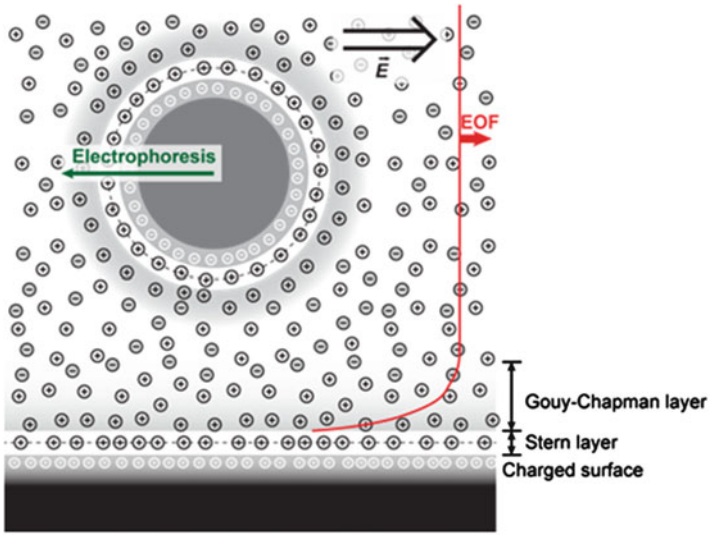

Fig. 8.5 Electrophoresis and electroosmotic flow (EOF) are frequently used to control the movement of particles in microfluidic devices. Shown here is the structure of the charged interfaces according to the Stern model. Directly attached to the charged interface is a layer of tightly bound counterions (Stern layer). Further away from the interface, a diffuse cloud of counterions forms the Gouy–Chapman layer. Movement of mobile charges in the Gouy–Chapman layer in response to a field that is tangential to the surface results in electroosmotic flow of the bulk liquid. EOF exhibits a plug-flow profile

proposed independently by Gouy and Chapman at the beginning of the twentieth century [9, 21]. In this model, the counterions are allowed to roam about freely near the charged interface, bound only by the requirement that they satisfy the Poisson–Boltzmann equation with a potential approaching zero far away from the interface. The Poisson–Boltzmann equation relates the electrical potential to the charge distribution:

$$\epsilon \nabla^2 \Psi = -z q_e (n_+ - n_-) \tag{8.3}$$

Here, Ψ is the electrical potential, ϵ the permittivity of water, q_e the elementary charge, and $n_\pm$ the concentration of positive and negative ions, respectively. We assume a symmetric electrolyte of valency number z. The ion concentration follows a Boltzmann distribution:

$$n_\pm = n_0 e^{\mp \frac{z q_e \Psi}{k_B T}} \tag{8.4}$$

Equations (8.3) and (8.4) can be combined to yield

$$\epsilon \nabla^2 \Psi = 2zq_e n_0 \sinh\left(\frac{zq_e \Psi}{k_B T}\right) \tag{8.5}$$

For small values of the potential Ψ, the right-hand side of (8.5) can be linearized using $\sinh(x) \approx x + O(x^2)$ to yield:

$$\nabla^2 \Psi \approx \frac{2z^2 q_e^2 n_0}{\epsilon k_B T} \Psi \tag{8.6}$$

This is the Debye–Hückel approximation, and the solution for a planar charged interface decays exponentially with the distance from the interface. The length scale $\lambda_D = \left(\frac{\epsilon k_B T}{2z^2 q_e^2 n_0}\right)^{\frac{1}{2}}$, which appears on the right-hand side of (8.6) in the form of its inverse square, is called the *Debye length*. One can also find the exact solution to (8.3) by a separation of variables, but a comparison with the Debye–Hückel approximation shows surprisingly little discrepancy up to a surface potential of 50–80 mV.

Although more realistic than the Helmholtz model, the diffuse double layer of Gouy and Chapman still has some shortcomings. In particular, ions are assumed to be point charges, neglecting the fact that they are normally surrounded by a more or less strongly bound hydration shell. In reality, there is often not enough space near the surface to accommodate the density of ions predicted by the diffuse double layer model. In addition, many ions, primarily anions such as Cl^-, Br^-, I^-, or $PO_4{}^{3-}$shed their hydration shell with relative ease and can adsorb strongly to some solid surfaces. As a result, there generally is a tightly packed immobile layer of counterions directly at the surface, and the diffuse cloud of the Gouy–Chapman layer only becomes an adequate model at some distance from the surface.

German physicist Otto Stern (1888–1969) is credited with the synthesis of the Helmholtz and the Gouy–Chapman model to a unified, more realistic description, the *Stern model*. Here, a fixed layer of counterions is densely packed on the surface, extending to approximately a distance of one hydrated ion diameter from the interface. This first layer is called the Stern layer. Ions directly adjacent to the Stern layer are not strongly bound. Yet, depending on the nature of the interface, their mobility parallel to the surface may be restricted. In practice, such restrictions in mobility can, for example, arise due to surface roughness or if macromolecules are adsorbed to the interface and reach out into the solution. The so-called *shear plane* delineates the transition between the region of restricted lateral ion mobility and the portion of the diffuse layer that is free to slide parallel to the surface. The shear plane may be close to, but is not necessarily coincident with the boundary of the Stern layer. The value of the electrical potential at the shear plane is commonly referred to in the literature as *Zeta potential* (ζ).

When an axial electric field is applied to an electrolyte in a capillary or a microfluidic channel, the phenomenon of electroosmosis causes the fluid to move. Using the Stern model, the flow velocity can be seen to scale linearly with the Zeta

potential and the electric field strength. To be specific in the illustration, we shall assume the surface to carry a net negative charge, which is common for glass capillaries and microchannels made of glass, silicon, or oxygen plasma-treated polymers in the vicinity of neutral pH. Positive charges in the mobile portion of the diffuse double layer then move in the direction of the axial electric field, dragging the fluid along with them. Positive counterions dominate the drag compared to the negative co-ions, which are in the minority in the double layer. Outside the double layer, positive and negative ions are in balance, and the electric field exerts no net force on the solution. To calculate the resulting fluid velocity, we designate the axial direction by x and the direction perpendicular to the wall by y ($y = 0$ at the wall); the Reynolds number is assumed to be small. The velocity component in the x-direction (v_x) then satisfies the Stokes equation with an added electric body force:

$$\rho \frac{\partial v_x}{\partial t} = -\frac{\partial P}{\partial x} + \eta \frac{\partial^2 v_x}{\partial y^2} + z q_e (n_+ - n_-) E_x \tag{8.7}$$

The electric field in the axial direction (x) is denoted E_x. Assuming steady state and no externally applied pressure, (8.5) becomes

$$\eta \frac{\partial^2 v_x}{\partial y^2} = -z q_e (n_+ - n_-) E_x \tag{8.8}$$

Using the Poisson–Boltzmann equation for the net charge density on the right-hand side gives

$$\eta \frac{\partial^2 v_x}{\partial y^2} = \epsilon \frac{\partial^2 \Psi}{\partial y^2} E_x \tag{8.9}$$

Integrating (8.9) over the interval (y_1, y_2), where $y_2 \gg \lambda_D$, yields $\eta \frac{\partial v_x}{\partial y}\big|_{y_1} = \epsilon \frac{\partial \Psi}{\partial y}\big|_{y_1} E_x$, and one more integration from the shear plane, where $v_x = 0$ and $\Psi = \zeta$, to any location outside the diffuse layer leads to the position-independent electroosmotic flow velocity

$$v_x = -\frac{\epsilon \zeta E_x}{\eta}. \tag{8.10}$$

Electrophoresis of charged particles whose diameter is much larger than the Debye length is mathematically quite analogous to electroosmotic flow. In the large diameter approximation, the effect of curvature can be neglected. The particle and the immobile counterions possess a net charge Q. The electrostatic force is balanced by the Stokes drag, so we can write

$$E_x Q = 6\pi\eta d \ \Delta v_x, \tag{8.11}$$

where Δv_x is the relative velocity of the particle to the fluid. Fortunately, it is not necessary to calculate the charge Q to find Δv_x. Instead, we can for a moment look at the system in the reference frame of the moving particle. Here, the surface with its attached charge is, by definition, immobile. Since the magnitude of the electric field is not altered in the new reference frame, the electroosmotic flow velocity corresponds to the velocity difference between the particle and the fluid. Therefore, if the walls are uncharged and there is no external pressure applied, the particle must move with the electrophoretic velocity

$$v_{EP} = \frac{\epsilon \zeta_p E_x}{\eta}, \tag{8.12}$$

where ζ_p denotes the Zeta potential of the particle. In reality, however, the channel walls typically do carry some charge of their own, and the resulting electroosmotic flow counteracts the electrophoretic motion of the particle. The net velocity is then the difference between the electroosmotic flow velocity, calculated from (8.10) with the Zeta potential of the walls, and v_{EP}.

Electrophoresis of particles or molecules whose diameter is on the same scale as the Debye length cannot be described by the above model. Equation 8.12 is the well-known Helmholtz–Smoluchowski solution for electrophoretic movement of large particles. The opposite extreme, in which the Debye length is significantly larger than the particle diameter, is described by the Hückel equation of electrophoresis, which differs from the Helmholtz–Smoluchowski equation only in that the former velocity is lower by a factor 2/3. In the intermediate regime, a numerical factor can be found, as described initially by Henry in 1931 [24]; an excellent treatment of this and other corrections is given in the book by Probstein [44]. The relative simplicity of the above description should also not obscure the fact that electrophoretic movement of particles in microfluidic channels can become quite complex when the particle size is comparable to the size of the channel, or when particles are in close proximity to the walls. Such cases generally require numerical methods.

Dielectrophoresis, DEP for short, is the second electrostatic effect that is very well suited for manipulating solid particles in microfluidic systems. The first reference to the term goes back to the work of H. A. Pohl [43]. In contrast to electrophoresis, particles do not need to carry a net charge for dielectrophoresis to work. The principle is based on the attraction or repulsion of a dielectric particle by an electric field gradient when the permittivity of the particle differs from the surrounding medium. Importantly, the direction of the force in dielectrophoresis is independent of the field polarity, so that DC and AC fields are equally effective.

To first order the strength of the dielectrophoretic force can be obtained as follows [31]. A spherical, nonconducting particle of permittivity ϵ_p in a medium

of permittivity ϵ_m, in which there is a DC electric field $\vec{E}$, acquires an effective dipole moment given by

$$\vec{P}_{DC} = 4\pi\epsilon_m K_{CM} r^3 \vec{E}. \tag{8.13}$$

In (8.13), r denotes the radius of the particle, and $K_{CM} = (\epsilon_p - \epsilon_m)/(\epsilon_p + 2\epsilon_m)$ is the Clausius–Mosotti factor derived in many classical texts on electrodynamics [27]. The force on this dipole in an electric field is given by $\vec{F}_{DC} = \left(\vec{p}_{DC} \cdot \vec{\nabla}\right)\vec{E}$. Inserting (8.13) and recalling that, because $\vec{E} = \vec{\nabla}\phi$ one may substitute $\left(\vec{E} \cdot \vec{\nabla}\right)\vec{E} = \frac{1}{2}\ \vec{\nabla}\ \vec{E}^2$, we get

$$\vec{F}_{DC} = 2\pi\epsilon_m \frac{\epsilon_p - \epsilon_m}{\epsilon_p + 2\epsilon_m} r^3 \vec{\nabla}\ \vec{E}^2. \tag{8.14}$$

In AC dielectrophoresis, $\vec{E}$, $\vec{p}_{DC}$, and $\vec{F}_{DC}$ are time dependent. Equation 8.13 tacitly assumes that the polarization of the particle follows the field instantaneously, so that there is no phase delay between the electric field and the induced dipole moment. Therefore, the force scales directly with the square of the field strength in (8.14), and the direction of the force is independent of the field polarity. Important to note is that the dielectrophoretic force also scales with the particle volume. As holding a particle in position in a laminar stream of velocity v requires a force equal to the Stokes drag $F_{Stokes} \sim vr$, much steeper field gradients are required as the particle size gets smaller. This can be accomplished by scaling down the dimensions of the electrodes and their spacing.

When the dielectric constant of the particle is smaller than that of the medium ($\epsilon_p < \epsilon_m$), then the DEP force is acting to push the particle away from locations of high field strength. The effect is then called *negative DEP*. When $\epsilon_p > \epsilon_m$, the particle is attracted by regions of high field strength, and the effect is termed *positive DEP*.

So far, we have assumed that the electric field varies very slowly on the size scale of the particle. If this is not the case, then the spatial extent of the particle cannot be neglected, and the induced field due to polarization is more complex than that of a simple dipole. A powerful technique to deal with such effects is to use multipole expansions, which are explained nicely in the body of work by Jones on the subject [30–32]. In many cases of practical interest, terms higher than the dipole contribute only a small correction and are not essential for a qualitative understanding and for initial system design. Yet, some effects can be explained only by considering at least the next order, the quadrupole term. For example, if four planar electrodes are positioned in the corners of a square such that diagonally opposed corners have the same polarity, the field strength at the center must vanish due to symmetry. Therefore, there is no DEP force due to an induced dipole. However, continuing the calculation to the quadrupole term reveals a dielectrophoretic lift force away from the surface. This is a magnificent feature that can be used for

holding cells and particles in place against gravity so as to prevent interactions with the surface.

Most applications of DEP in microfluidics are done in aqueous electrolytes. AC dielectrophoresis then is the method of choice for several reasons. First, using AC current avoids electrochemical reactions at the metal/electrolyte interface of microelectrodes, as the coupling across the double layer is almost purely capacitive at high frequency. This prevents gas evolution and degradation of the electrodes. Second, electroosmotic flow and electrophoresis play no role, as their time-average is zero.

When the solutions and particles to be manipulated are not ideal dielectrics, but have a finite conductivity, the force calculation becomes slightly more complex. In return, however, one is rewarded with a rich and often unique response profile, which depends sensitively on the internal composition and structure of different particles. To incorporate the frequency dependence and finite conductivity into the calculation of the DEP force, the complex dielectric constants $\hat{\epsilon}_{p,m}(\omega) = \epsilon_{p,m} + \sigma_{p,m}/(i\ \omega)$ of the particle and medium, respectively, are employed. Here ω denotes the angular frequency of the applied field in radians per second, $\sigma_{p,m}$ is the conductivity, and $i = \sqrt{-1}$. An equation analogous to (8.13) results from the substitution $\epsilon_{p,m} \rightarrow \hat{\epsilon}_{p,m}(\omega)$, and with the understanding that going back from the mathematically convenient, but somewhat unintuitive, complex-valued formulation to a real-valued formulation can be done simply by a projection onto the real axis. After some algebraic manipulations, the complex-valued Clausius–Mosotti factor for a conducting particle in a conducting fluid is [31]

$$\hat{K}_{CM}(\omega) = K_{hf} + \frac{K_{lf} - K_{hf}}{i\omega\tau_{MW} + 1} \tag{8.15}$$

with

$$\begin{aligned} K_{hf} &= (\epsilon_p - \epsilon_m)/(\epsilon_p + 2\epsilon_m) \\ K_{lf} &= (\sigma_p - \sigma_m)/(\sigma_p + 2\sigma_m) \\ \tau_{MW} &= (\epsilon_p + 2\epsilon_m)/(\sigma_p + 2\sigma_m). \end{aligned} \tag{8.16}$$

The subscripts indicate the asymptotic behavior $\hat{K}_{CM} \approx K_{hf}$ at *high frequencies*, and $\hat{K}_{CM} \approx K_{lf}$ at *low frequencies*, with the cutoff frequency $f_c = 1/(2\pi\tau_{MW})$ given by the inverse Maxwell–Wagner time constant, τ_{MW}. The time-dependent force is $\vec{F}_{AC}(t) = \left(Re\ [\vec{p}_{AC}(t)] \cdot \vec{\nabla}\right) \mathrm{Re}\left[\vec{E}\ e^{i\omega t}\right]$ with $\vec{E}$ real and

$$\vec{p}_{AC}(t) = 4\pi\epsilon_m \hat{K}_{CM}(\omega)\, r^3\ \ \vec{E}\ e^{i\omega t}.$$

The corresponding time-varying force is

$$\vec{F}_{\mathrm{AC}}(t) = 2\pi\epsilon_{\mathrm{m}}\, Re\left[\hat{K}_{\mathrm{CM}}(\omega)e^{\mathrm{i}\omega t}\right] r^3\ \vec{\nabla}\ \vec{E}^2 \cos\left(\omega t\right)$$

At low frequency, the conductivity difference dominates, while at high frequency, the permittivity is more important. The transition between these regimes is typically in the range between 10 and 100 MHz for aqueous solutions commonly used in cell and particle handling.

An important assumption in the above theory was that the particles are homogeneous. However, this is often too simplistic. Cells, for example, have a relatively complex internal structure with numerous compartments isolated by lipid bilayers that are only a few nanometers thick. Fortunately, much of this complexity can be accounted for by the introduction of an effective permeability and conductivity such that a homogeneous particle with these characteristics would display the same DEP characteristics as the complex multilayered particle. This method was first introduced by Irimajir and colleagues [26] and has been further developed by many authors since.

8.2.2.2 Magnetic Forces

The magnetic force on solid particles in an external field is, by nature, a dipole interaction. Therefore, there are many phenomenological similarities to dielectrophoresis. However, there also are some notable differences. One important difference is that some magnetic particles of practical relevance can possess a permanent dipole moment, while particles in DEP lose their polarization as soon as the external field is turned off. Particles smaller than 100–200 nm often comprise only a single magnetic domain, a property that endows them with the largest saturation magnetization attainable for a given material and size. In the case of spherical iron particles, the critical single-domain size can be estimated to be ~14 nm, for cobalt ~70 nm, and for iron oxides between 130 and 170 nm [22].

Whether magnetic particles can or cannot hold a permanent moment, i.e., whether they are ferromagnetic or paramagnetic, also depends strongly on size. Single-domain particles can retain a remnant magnetization for a time that scales as $\sim\exp((K_{\mathrm{eff}}V)/(k_{\mathrm{B}}T))$, where K_{eff} is the magnetic anisotropy constant (units J/m^3) and V is the volume of the particle. This is a very steep function of volume, and even more so of diameter. As the particle size approaches the 10 nm scale, the relaxation time at room temperature quickly drops to timescales that are so short, they may be considered instantaneous for all practical purposes [36]. Particles with these characteristics are called superparamagnetic.

For many applications, strongly paramagnetic particles of diameters in the range of several hundred nanometers or even many micrometers are desirable. These can be made by incorporating superparamagnetic particles as fillers in a polymer matrix.

Superparamagnetic particles are extraordinarily useful as mobile solid phases as they have a large surface area per mass, do not tend to aggregate in the absence of

an external field, and have a high magnetic permeability. Importantly, they enable highly specific separations, for there are no natural particles of such high permeability in typical biochemical samples.

Before describing the quantitative force experienced by paramagnetic particles, the following paragraph gives a brief summary of the equations and the units underlying the description of magnetism in this chapter. Magnetism has unfortunately never enjoyed a universally adopted system of units as the field of electrostatics has [47]. Here we will use the SI system with the magnetizing field $\vec{H}$ in units of A/m, the magnetic induction $\vec{B}$ in Tesla (T), and the magnetization per volume $\vec{M}$ in A/m. Inside a given material, magnetization and magnetic induction are connected through $\vec{B} = \mu_0 \mu \vec{H}$, where $\mu_0 = 4\pi \cdot 10^{-7} T\frac{m}{A}$ is the permeability of free space and the relative permeability of the material, $\mu = (1 + \chi)$, plays a role analogous to the relative permittivity ϵ/ϵ_0 in electrostatics. Magnetization density is given by $\vec{M} = \chi \vec{H}$ below saturation, and the numerical factor χ is called the susceptibility of the material.

A paramagnetic particle of susceptibility $\chi_\mathrm{p} > 0$ surrounded by a medium with $\chi_\mathrm{m} = 0$ experiences a force

$$\vec{F} = \left(\vec{m} \cdot \vec{\nabla}\right)\vec{B}, \tag{8.17}$$

where $\vec{m} = \chi_\mathrm{p}\left(\vec{B}/\mu_0\right)\ V$ is the magnetic moment of the particle, V its volume, and $\vec{B}$ is measured inside the surrounding medium, i.e., $\vec{B} = \mu_0 \vec{H}$.

In reality, paramagnetic micro- and nanoparticles often exhibit some nonzero remnant magnetization. This may be accounted for by inserting $\vec{m} = \vec{M}_0 V + \chi_\mathrm{p}\left(\vec{B}/\mu_0\right)V$ into (8.17) [49]:

$$\vec{F} = V\left(\vec{M}_0 \cdot \vec{\nabla}\right)\vec{B} + \frac{\chi_\mathrm{p} V}{\mu_0}\left(\vec{B} \cdot \vec{\nabla}\right)\vec{B}. \tag{8.18}$$

Typical parameters for microparticles are, for example, $d = 6\ \mu\mathrm{m}$, $\chi = 0.17$ in the range of $\left|\vec{B}\right| < 2.5\ \mathrm{mT}$, a saturation magnetization of 4500 A/m, and a remnant magnetization after saturation of $M_0 = 300\ \mathrm{A/m}$ [49].

Magnetic fields that are strong enough for the manipulation of particles in microfluidic systems are most easily generated by external permanent magnets. Powerful rare earth magnets of relatively small size (millimeter scale) are readily available and provide a magnetic induction on the scale of several hundred milli-Tesla. Alternating fields are of course not available in that case, but this is of no significant incommodity, as static magnetic fields easily penetrate common samples and the characteristics of alternating-field magnetophoresis are not as rich as the AC characteristics of DEP. Practical microfabricated electromagnets produce one to two orders of magnitude weaker fields (~10 mT) than permanent magnets, but the advantage is that they may be activated or deactivated to trap and release particles on demand.

8.3 Particle Detection and Characterization

Methods for the detection of micro- and nanoparticles in microfluidic systems can be classified as optical, electronic, and mechanical. Optical detection is perhaps the most common and versatile class. Light can be precisely focused to a tight spot for sensitive detection by scattering, absorbance, or fluorescence. Alternatively, information-rich images can be produced using a wide array of different contrast methods that can reveal, for example, local mass density or the concentration and state of specific molecules. Sophisticated detectors can be constructed entirely from macroscopic lenses and optoelectronic components, minimizing the complexity of microfabricated parts. At the same time, a number of optical elements, such as waveguides and simple focusing elements, may also be integrated on chip. In contrast, electrical detection generally requires electrodes to be integrated on chip. Direct electrical detection of particles relies on the measurement of conductivity or complex impedance changes. In addition, magnetic particles can be sensed by electronic transducers for magnetic fields that may be integrated with microfluidic systems. Finally, micromechanical sensors provide unique opportunities for the direct detection and characterization of micro- and nanoparticles in microfluidic systems. Table 8.1 provides an overview of important detection principles for suspended particles in microfluidic devices.

8.3.1 High-Speed Imaging

Conventional wide-field light microscopy is straightforward to combine with most microfluidic devices and allows real-time observation of particles inside channels with all routine contrast methods, such as bright field, dark field, Nomarski DIC (differential interference contrast), and fluorescence. An excellent overview of the principles and technology of light microscopy can be found on the Molecular Expressions website maintained by the National High Magnetic Field Laboratory of Florida State University (http://micro.magnet.fsu.edu).

Capturing images of moving particles and cells in microfluidic channels requires short shutter times. If, in addition, one requires imaging not only of a representative few, but of all particles passing through the detection zone in a given time, very high frame rates are also important. The first challenge of creating blur-free images of fast-moving objects has inspired inventors from the very beginning of photography in the mid-nineteenth century. At a fundamental level, the challenge lies in the finite detection sensitivity of the camera, as the shorter the shutter is open, the fewer photons strike the detector. Two approaches can solve this problem: First, one can increase the light intensity dramatically by using intense flashes of light that are synchronized with the shutter. Or one can work to improve the sensitivity of the detector. Credit for making the first method practical and demonstrating its potential on the

Table 8.1 Detection principles for suspended particles in microfluidic devices

Detection methods	Imaging	Scattering	Fluorescence	Impedance	Mass
Single particle	•	•	•	•	•
Ensemble average		•			•
Dynamic range	1–100 μm	1–100 μm (single)/ 1–100 nm (ensemble)	Single molecule at low throughput	(10 nm) 1–100 μm	50 nm–30 μm (single) <1 MDa ensemble
Throughput	10^4/s	10^2–10^4/s	10^4–10^5/s	10^4/s	10–100/s
Information content	Shape and internal structure	Size	Concentration of specific molecules and some information about their state	Size	Mass, density, size

Methods capable of characterizing single particles provide detailed information on the composition of heterogeneous populations. Ensemble average measurements are sometimes more sensitive, but are more limited in applications that involve mixed samples. The dynamic range is the range between the smallest detectable size and the largest size that can be characterized by a method. Throughput, i.e., the number of single particles that can be characterized in a given time, only applies to single-particle measurement

macroscopic scale goes to Harold Edgerton of M.I.T. (1903–1990). Edgerton used stroboscopic illumination extensively for taking images of fast-moving everyday objects. Today, LED light sources for microscopy can be switched on and off within microseconds and enable a convenient and inexpensive implementation of the stroboscope method for high-speed microphotography. To also achieve high frame rates, modern electronic high-speed cameras are needed. Instruments with exposure times on the scale of 1 μs and frame rates on the order of 100,000 frames per second are readily available and are often used to observe the dynamics of particles, cells, and droplets in microfluidic systems. A nice example of this is the work of Gossett et al., who used high-speed imaging of cell deformation at a four-way junction to indirectly measure cell stiffness with high throughput [20] (Fig. 8.6). An obvious challenge is the requirement for large storage space, high-bandwidth data transfer, and time-consuming image analysis. Real-time applications, for example for sorting of particles and droplets based on high-speed imaging, are therefore not easily possible with current technology. Another restriction is that the limited image intensity due to the short exposure time often allows only bright field imaging, which provides poor contrast when the refractive index of particles is similar to the medium. The situation may be improved through the use of image intensifier modules that can be inserted between the camera port of the microscope and the camera and work up to frame rates of ~30 kHz [53].

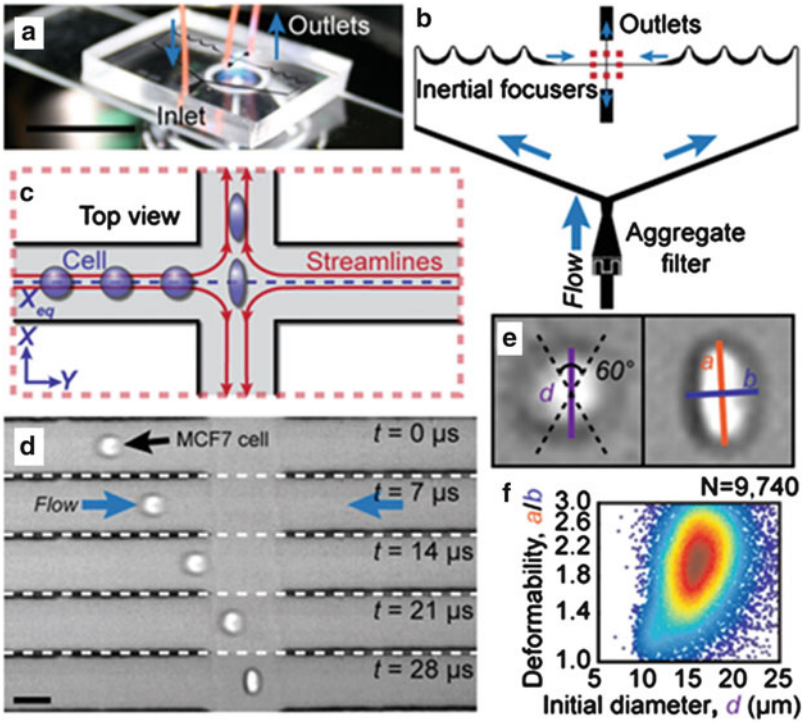

Fig. 8.6 High-speed imaging provides unique information about shape and inner structure of particles and cells in microfluidic systems. Shown here is a device of the DiCarlo laboratory for measuring deformability of cells in extensional flow at a four-way junction. Inertial focusing (**b**) is used to guide cells to the channel center, where they pass the junction at high speed. Image analysis (**e**, **f**) reveals the deformation as a function of the initial diameter (Reproduced with permission from [20])

8.3.2 Light and X-ray Scattering

Scattering techniques for the detection and characterization of colloidal particles are useful for many applications. Static light scattering patterns can be used to evaluate particle sizes and to extract coarse-grained information about the shape and inner structure of particles. This concept is equally applicable for the full spectrum of optical wavelengths and for X-rays with wavelengths on the order of 1 Å.

Common to all scattering-based methods is that the detected signal corresponds to a Fourier-space representation of some property of the particle, such as refractive index or density. What is attractive about this is that the signal at any point in the plane of the detector is formed by an average over the entire object. For example, the center location on the detector represents the static mean intensity value over the full illuminated field; a spatially localized disturbance in this field due to a

particle introduces higher spatial frequencies, diverting some of the power of the illuminating source into areas in the periphery of the detector. To differentiate between methods that primarily analyze the high spatial frequency information found at large scattering angles from the low spatial frequency information at small angles, a specific terminology has evolved. In visible light scattering, the latter (small angles) is often called "forward scattering," or SALS (small-angle light scattering) to contrast it from large-angle scattering. When using X-rays, the small-angle regime is known as SAXS (small-angle X-ray scattering), and the large-angle regime as WAXS (wide-angle X-ray scattering).

Static light scattering is directly compatible with microfluidic devices and allows high measurement rates if a simple analog pulse signal is collected. For example, Pamme et al. used a Helium–Neon laser (632.8 nm) to illuminate a detection spot of ~200 μm diameter and collected scattering signals at 15° and 45° from the incident axis by optical fibers coupled to photomultiplier tubes [40]. At 10 kHz acquisition rate, up to 150 particles per second could be counted, and by quantifying the scattering intensity it was possible to discriminate particle sizes between 2 and 9 μm. The scattering intensity at small angles was found to scale approximately linearly with particle volume, while the correlation with size at large scattering angles was weak, as expected. Several alternative implementations of static light scattering intensities for particle analysis and microfluidic flow cytometry have been devised by different groups. In most cases, light at one or a few positions is collected by optical fibers, which may be directly integrated on chip. One challenge with these systems, however, is the relatively large variability of the signal compared to conventional flow cytometers [42].

An approach towards higher precision and increased signal strength is to replace individual photomultipliers by a CCD or CMOS camera that records the entire scattering pattern for individual particles. In a system described by Dannhauser et al., the detection volume was illuminated by red light from a Helium–Neon laser concentrated by a gradient index (GRIN) lens to a 110 μm diameter beam with a low divergence (7 mrad divergence angle) [14] (Fig. 8.7). The scattered light was then relayed to a CMOS camera, which recorded the full small-angle scattering pattern between 2° and 30° at 20 frames per second. By fitting a theoretical model to the scattering pattern, it was possible to measure the size of particles with high accuracy in the range between 1 and 4 μm. There is great interest in similar combinations of microfluidics with X-ray scattering for the analysis of macromolecules and nanoparticles in solution. With wavelengths on the scale of Angstroms, the formation of nanoscopic clusters and particles can be detected, and it is possible to differentiate between amorphous and crystalline particles. This is of great value in screening protein crystallization conditions [23]. One challenge when using X-rays is the limited penetration depth through the millimeter-thick covers of conventional microfluidic devices [22]. This problem can be alleviated by using thin membranes, thin-walled capillaries, or polymers that have a high transparency to X-rays [2, 28, 54, 57]. Another interesting approach was described by Vig et al., who devised an entirely windowless method using microfluidic channels with a small hole in the top and bottom cover. With sufficiently hydrophobic outer

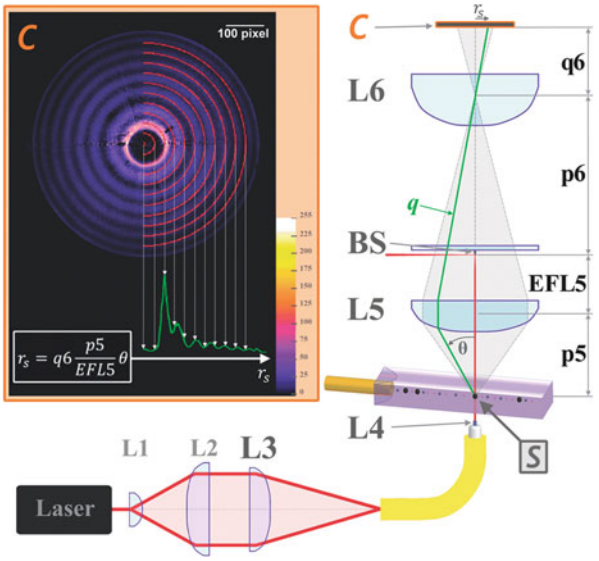

Fig. 8.7 Particle size measurement on a microfluidic chip by static light scattering. A laser is focused to a 110 µm spot by a GRIN lens (L4) and the scattering pattern is recorded by a CMOS camera (C). By fitting the radial ring pattern, particles in the size range of 1–4 µm could be characterized. Reproduced from [14] with permission of The Royal Society of Chemistry

surfaces, surface tension keeps the sample from leaking out and makes continuous measurements possible [55].

An alternative to particle sizing by static light scattering is dynamic light scattering (DLS). In this method, information is derived from fluctuations of the intensity pattern created by constructive and destructive interference of light scattered by particles smaller than the wavelength. The temporal correlation of the fluctuations reveals the diffusivity, which is inversely proportional to the hydrodynamic radius of the particles. DLS only provides accurate ensemble-averaged measurements, and the samples must be relatively clean, as the signal is easily overwhelmed by the strong scattering intensity of larger contaminants. With pure samples, DLS allows size determination from a few nanometers to several microns. However, the method is rarely used for in-line particle characterization in microfluidic systems because convection interferes with the measurement of diffusion. Destrenaut et al. suggest maintaining a shear rate below 10 s^{-1} to allow reliable measurements [15]. To fulfil this criterion, either slow flow rates or an expansion of the channel into a large detection chamber are required [10].

8.3.3 Laser-Induced Fluorescence (LIF)

Fluorescence is arguably the most sensitive technique known for the detection of specific molecules or particles in solution. Among the different light sources that can be used to excite fluorescence, lasers offer many advantages. First, the ability to focus laser light to a tight spot makes it easy to reach the maximum emission from a given fluorophore. Lasers also have a high spectral purity, which helps in the

reduction of background. Laser-induced fluorescence (LIF) has a long tradition in the field of capillary electrophoresis and flow cytometry, where the most sensitive systems with good fluorophores nearly attain single-molecule sensitivity [29]. What limits the sensitivity in well-designed LIF setups is often not the technology, but the physical constraints imposed by bleaching and the fluorescence lifetime of the fluorophore. Taking this into account, the emitted number of photons has to exceed the background. Among the most significant sources of background is residual excitation light reaching the detector combined with autofluorescence and Raman scattering of the solution and the optical elements on the illumination path. Important to note is that the problem is not directly the offset caused by a steady background intensity, as this could be measured and subtracted. More troublesome are intensity fluctuations due to noise in the laser combined with shot noise that is inherent to the quantum nature of light.

While ultra-sensitive LIF detection requires considerable expertise and attention to technical details, simple systems based on a conventional fluorescent microscope configuration are often adequate for the detection of particles and cells in microfluidic systems. Photomultiplier tubes (PMT) or avalanche photodiodes (APD) are preferred as detectors due to their large bandwidth and high sensitivity. Applications are mainly in the area of microfluidic cell counting and sorting, or in multiplexed bead assays, where specific labels may be attached to the particles of interest prior to analysis [42].

8.3.4 Conductivity Measurements and Impedance Spectroscopy

The gold standard in cell counting and cell size measurement today is the so-called Coulter counter, a method invented in the 1940s by Wallace Coulter. In essence, the idea is to detect the temporary blockage of a tiny aperture upon passage of particles by monitoring the change in electrical conductivity of the aperture. One limitation is that this method only works in conducting fluids, and that the size of the particles must be smaller than the aperture, but still within the same order of magnitude. However, these conditions can be easily satisfied for a wide range of applications involving cells in physiological buffers.

There are numerous adaptations of the Coulter principle to microfluidic systems. While macroscopic instruments generally rely on conventionally machined apertures in glass or sapphire diaphragms, most microfluidic implementations use a simple flow constriction of appropriate width and height built into the channel system. Particles are driven through this constriction at a low concentration by pressure-driven flow or by electrophoresis. To define the measurement channel, conventional optical lithography can be used down to dimensions of approximately 1 μm. To detect

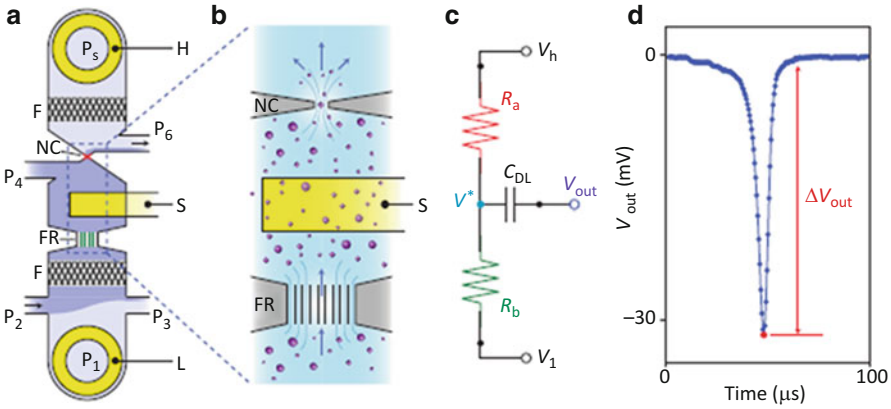

Fig. 8.8 Resistive pulse sensing with on-chip electrodes for the characterization of nanoparticles and viruses using the Coulter principle. At the heart of the system is a nanoconstriction (NC) through which particles are driven by controlling the pressures P1–P6. A prefilter (F) prevents large particles from clogging the constriction, and a fluid resistor (FR) serves as an electrical reference. A voltage is applied between electrodes H and L, and voltage spikes due to partial blockage of the constriction upon passage of particles are picked up through the electrode S. Reprinted by permission from Macmillan Publishers Ltd: [18], copyright 2011

even smaller particles, several groups have resorted to electron-beam lithography in order to fabricate apertures with sub-micrometer length, width, and height.

A challenge specific to microfluidic systems is the implementation of high-bandwidth, low-noise resistive pulse sensing. The millimeter- or even centimeter-long lead channels on chip have high electrical impedance and often dwarf the impedance of the small aperture. A solution to this problem is to integrate measurement electrodes directly into the channel. A beautiful example of this idea is the device by Fraikin et al. shown in Fig. 8.8 [18]. Here a three-electrode configuration is used to measure occlusion of a $250 \times 250 \times 290$ nm aperture at 650 kHz bandwidth for the sizing of nanoparticles with high throughput. Two electrodes are located in the buffer reservoirs P1 and P5; a constant voltage is applied between these electrodes, and the local potential close to the nano-constriction (NC) is recorded via a third electrode (S). Particles that pass through the constriction block the flow of current so that the potential of the sensing electrode shifts transiently towards the voltage at P1. This transient couples capacitively through the double layer (C_{DL}) at the sensing electrode and is recorded by a low-noise amplifier. Particles of ~40 nm diameter and single T7 bacteriophage viruses could be well resolved above the noise.

Essential to the sensitivity of the resistive pulse method is that particles fill an appreciable volume fraction of the aperture. Intricate nanofabrication methods are therefore required to analyze sub-micrometer particles. There also is a high probability of clogging unless the sample can be pre-filtered stringently. An elegant way to avoid these difficulties is to use hydrodynamic focusing with an insulating sheath flow to create an aperture defined by liquid–liquid interfaces rather than

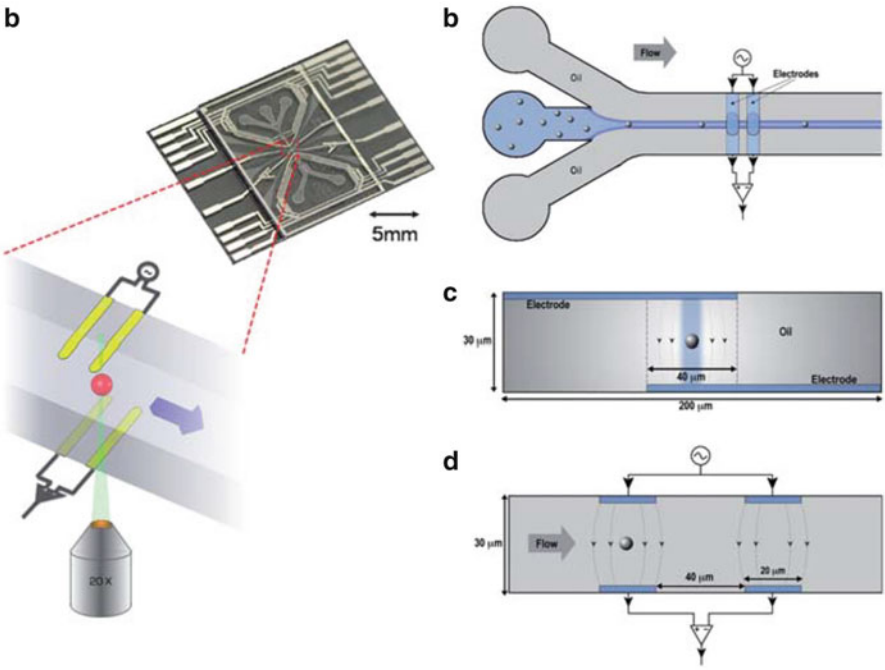

Fig. 8.9 Impedance-based flow cytometry provides information about the structure and internal composition of cells and particles: (**a**) In the device of Bernabini et al. shown here, hydrodynamic focusing in combination with a differential measurement is used to implement an aperture-free impedance measurement; (**b**) The conducting sample is focused by sheath flow of nonconducting oil; (**c**) Side view; (**d**) The cross section reveals the placement of upstream and downstream electrode pairs. Reproduced from [3] with permission of The Royal Society of Chemistry

liquid–solid interfaces. Figure 8.9 shows an example of such a system developed by the group of Hywel Morgan [3]. A pair of platinum electrodes at the top and bottom of the channel couples an AC current into the sample stream, which is focused in the lateral dimension by a sheath flow of nonconducting oil. Stabilizing the two-phase flow required the addition of a surfactant (1 % Tween 20). Due to the relatively high conductivity of the sample, the current is shunted through the narrow stream, the impedance of which is altered significantly by the presence of a particle. The hydrodynamic focusing method has been validated for the detection of single polymer microbeads and individual bacteria. A challenge with this scheme is that even minimal instabilities of the flow introduce fluctuations in the width of the focused stream and degrade the reliability of the measurement. In the work of Bernabini et al., this was elegantly addressed by measuring the relative difference in the signals from the upstream and downstream pairs of electrodes [3].

8.3.5 *Nanomechanical Sensing*

A complementary method to optical and electrical detection of particles in microfluidic systems is mass sensing with micro- and nanomechanical resonators. Due to their small size and low mass, these devices can be extraordinarily sensitive when operated in vacuum or air. However, a trick is required for precision high-throughput measurements in liquid. Resonance frequency-based measurements in viscous fluids are challenging due to the damping of the vibration, which degrades the quality factor (Q), i.e., the sharpness of the resonance. A second difficulty is that collecting statistics requires a large number of particles to interact sequentially with the resonator. Both challenges can be addressed by Suspended Microchannel Resonators (SMR), shown schematically in Fig. 8.10 [6]. A microcantilever is shown here as an example, but other designs are possible. Inside of the cantilever beam is an embedded U-shaped fluidic channel while the outside is under vacuum. In sufficiently dilute samples, only one or no particle is within the detector volume at any time.

While the fluid is flowing, the resonance frequency is measured continuously either by an optical lever system similar to the atomic force microscope or by integrated strain sensors [34]. A feedback circuit, e.g., a phase-locked loop or an oscillator circuit, allows very accurate real-time tracking of the resonance frequency. Electronic frequency measurements are among the most accurate signal transduction methods known, and noise levels on the order of 10 parts-per-billion have been achieved for SMR devices with quality factors in the range $Q \sim 10{,}000$–$20{,}000$ and 1 Hz measurement bandwidth. Frequency noise can be translated into mass resolution by the first-order approximation

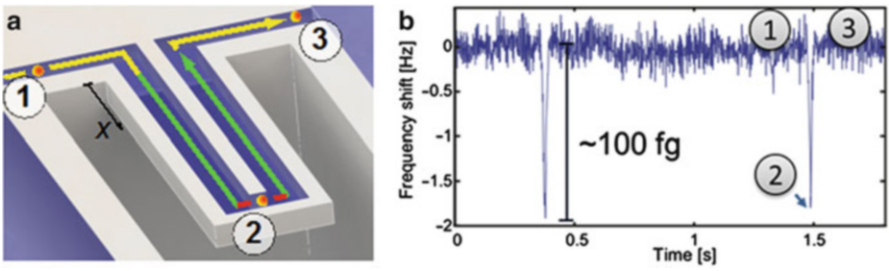

Fig. 8.10 Micromechanical resonators with embedded fluidic channels enable weighing of single nanoparticles: (**a**) Schematic of the operation principle. Typical dimensions are 200 μm length, 30 μm width, and 7 μm thickness with embedded channels of 3×8 μm cross section (height × width). The channel is normally closed and drawn open here only for illustration; (**b**) Particles entering the channel (1) do not affect the frequency while close to the base. The frequency shift reaches the maximum at the tip when the device vibrates in the first mode (2). As the particle leaves, the baseline is restored (3)

$$\frac{\Delta m_{\text{noise}}}{m^*} = 2\frac{\Delta f_{\text{noise}}}{f_0}, \tag{8.19}$$

where f_0 is the resonance frequency, Δf_{noise} denotes the frequency measurement noise in a given bandwidth, m^* is the effective mass of the resonator, and Δm_{noise} is the mass-equivalent noise level. An effective mass $m^* \approx 0.25 \cdot m$ is a good approximation for cantilever-type SMR sensors operating in the first mode. Devices as light as 400 pg have been fabricated to date, enabling single-particle mass resolution on the attogram scale (1 ag $= 10^{-18}$ g) [39].

As fluid flows through the device continuously, particles that are carried by the solution pass from the base of the cantilever to the tip and back to the base. Sensitivity varies continuously along this path and is to first order in Δm proportional to the square of the local amplitude of vibration $u(x_t)$, where the axial distance from the start of the path is parameterized by x_t:

$$\Delta f(t) = \Delta f_p \cdot \frac{u(x_t)^2}{u_p^2} \tag{8.20}$$

In (8.20), $\Delta f_p = f_0 \cdot \left(\Delta m_p / m^*\right)$ is the peak frequency shift induced by a particle of buoyant mass Δm_p, and u_p is the vibration amplitude at the corresponding position. Note that the buoyant mass of a particle is related to its dry mass (m_p) simply via the difference in density between the particle, ρ_p, and the carrier fluid, ρ_f, i.e., $\Delta m_p = m_p\left(1 - \frac{\rho_f}{\rho_p}\right)$. Mass and density can be extracted from two separate measurements in carrier fluids of different density [19].

An important limitation of embedded channel resonators is that their dynamic range is restricted by the size of the internal channel. To be able to use the method, the sample must always be filtered to ensure that it only contains particles that are small enough to pass through the channel without clogging it. This limit on size is in conflict with a desire to make the resonator as light and thin as possible in order to obtain a high mass sensitivity. Therefore, measuring the mass of eukaryotic cells [46] requires different devices than weighing bacteria or nanoparticles [7, 35, 39].

Some applications only require the characterization of particle mass or size averaged over a population. For example, the characterization of aggregation and polymerization processes, or measuring the growth and dissolution of coatings, can be done very well by looking at mean values. In such cases, correlation methods may be used to dramatically enhance the measurement sensitivity. By analyzing the auto-covariance of the frequency fluctuation signal, it is possible to separate white measurement noise from the time-correlated fluctuations that are induced by flowing particles. This is possible since suspended particles in laminar flow have a characteristic distribution of residence times, and the auto-covariance therefore has a predictable signature that extends to much greater lag times than uncorrelated noise. This technique, which is termed mass correlation spectroscopy, has enabled improvements of up to five orders of magnitude in sensitivity over single-particle measurements [37].

8.4 Applications

8.4.1 Microfluidic Flow Cytometry

Microfluidic flow cytometry is a prototypical application for single-particle handling and analysis requiring high fidelity and high throughput. Miniaturization opens up many exciting opportunities in this field. Besides the potential for a reduction in cost and complexity, perhaps the greatest value of microfluidic flow cytometers may lie in their ability to provide functions that go beyond what is possible with conventional technology, as shown in some of the examples below. Today, laboratory flow cytometers are indispensable in many areas of basic biological research and clinical diagnostics, for example in counting CD4+ T-lymphocytes for HIV diagnostics. Their utility is largely due to the ability to analyze individual cells and particles rather than population-averaged values and to isolate a selected few cells of interest from an enormous pool of other cells.

The development of conventional flow cytometers began in the 1970s, and since then the technology has evolved greatly. Despite numerous technical advances, however, the key principles developed in the early days still form the basis of modern instruments. High-end laboratory flow cytometers are complex and expensive, and they require highly-skilled personnel for operation and maintenance. Fortunately, significant efforts have been made in recent years to alleviate these shortcomings, and robust portable instruments now exist for HIV-screening, hematology, freshwater analysis, and cell culture applications (e.g., Partec GmbH, Germany; Merck Millipore, USA).

Microfluidic flow cytometers cannot yet fully compete with conventional systems in terms of sensitivity, speed, and number of simultaneously measured parameters, but the gap is narrowing steadily [56]. An important advantage of microfluidic chips over the expensive machined glass flow cells employed in macroscale systems is that they are disposable, so that no cleaning and decontamination is necessary, and no expensive maintenance is required. Due to the short length of the channels, experiments can be conducted at low pressure and with minute volumes.

Flow-focusing is one of the key technologies enabling precision measurements of single particles and cells in flow cytometry. In capillary-based systems, a sample stream emerging from a nozzle is focused by a concentric sheath flow such that suspended particles pass single file through a well-defined, narrow detection zone. An important advantage of the method is that no easy-to-clog tubes and nozzles with diameters comparable to the particle size are needed. On the downside, large amounts of fluid are consumed, and practical implementations require numerous discrete optical and fluidic components to be accurately aligned.

Among the first and most successful commercial systems to adopt microfluidic flow-focusing has been the Agilent 2100 Bioanalyzer (Agilent Technologies

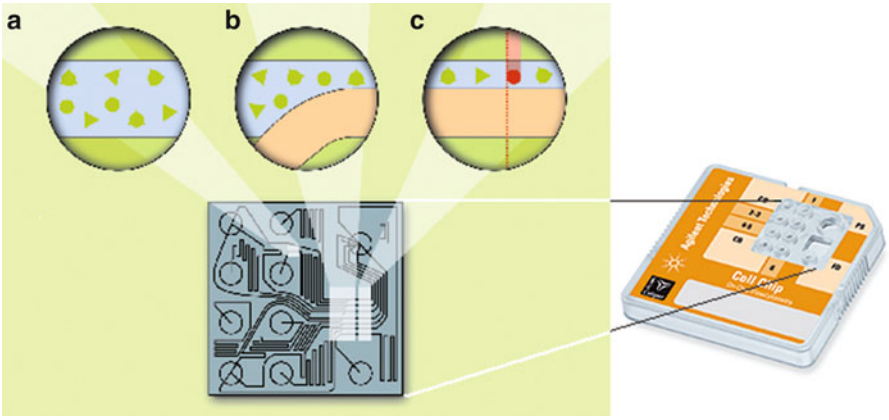

Fig. 8.11 Microfluidic flow cytometry chip design of the Agilent Bioanalyzer system. The sample channel (**a**) merges with a sheath flow (**b**) so that particles are hydrodynamically focused to a narrow stream at the channel wall (**c**). They are thereby forced to pass the detection spot single file. © Agilent Technologies, Inc. 2002. Reproduced with Permission, Courtesy of Agilent Technologies, Inc.

GmbH, Waldbronn, Germany). This system comprises a laboratory instrument, which contains a flow control unit and optical detectors, together with a range of dedicated microfluidic chips for flow cytometry as well as nucleic acid and protein analysis. As shown in Fig. 8.11, the flow cytometry chip uses hydrodynamic focusing, albeit in a slightly different configuration as its macroscopic counterparts. Instead of focusing cells to a central stream, the sheath flow pushes particles towards the wall where they pass the detector. Readout is done by fluorescence, which can be excited either by a red laser or a blue LED. Another commercial microfluidic-based flow cytometer is the Fishman-R of On-Chip Biotechnologies (Tokyo, Japan). This device features 2D flow-focusing, up to three laser excitation sources for fluorescence, a sensitivity equivalent to ~200 FITC molecules, and the ability to also collect scattering signals.

While well-implemented flow focusing has been shown to significantly enhance stability and precision in flow cytometry, several microfluidic systems have been proposed that work without it. An alternative to hydrodynamic focusing is the use of inertial effects to concentrate suspended particles into a narrow stream so that they pass through the detector one after another [16] (Fig. 8.12). This is particularly interesting as the hydrodynamic lift forces can be different for particles of different elasticity. Focusing by inertial microfluidics may thus provide an inherent sorting based on mechanical properties prior to detection by light scattering and fluorescence; this could, for example, facilitate the isolation of circulating tumor cells (CTCs), which are extremely rare and differ in their mechanical characteristics from red and white blood cells.

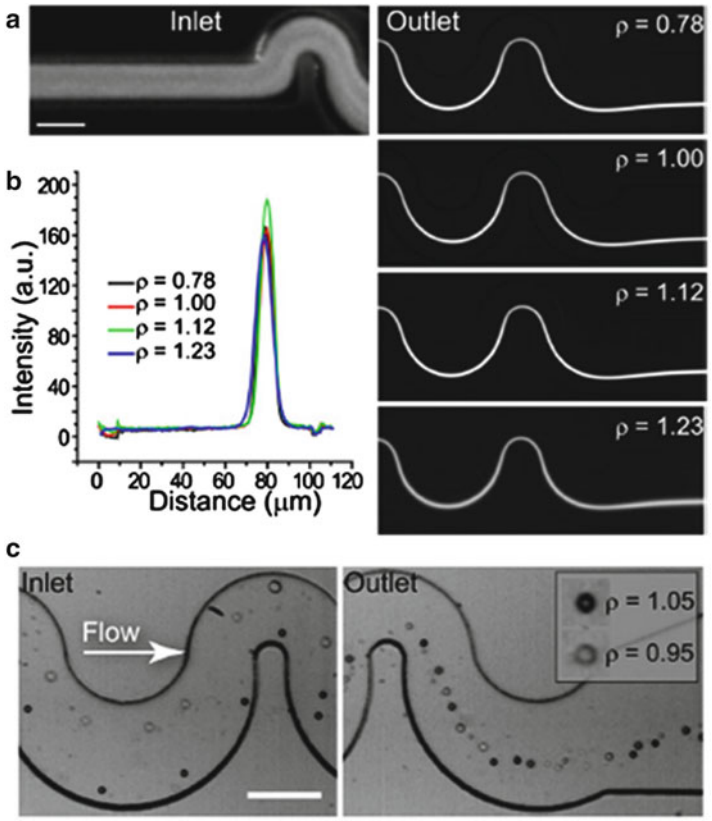

Fig. 8.12 Lateral migration at high Reynolds number can be used for microfluidic flow cytometry. DiCarlo et al. demonstrated this effect for different particles and cells. (**a**) A mixed sample of randomly distributed particles enters the device. (**b**) The particles were focused to the same streamline, independent of the density of the suspending solution. (**c**) Polystyrene particles and silicone oil droplets (density 1.05 g/cm^3 and 0.95 g/cm^3) also focused to the same streamline. (Reproduced with permission from [16])

The possibility of sorting based on stiffness is just one example of a number of fascinating possibilities opened up by non-optical microfluidic flow cytometry. Another physical property that may be used to distinguish different cells and particles is electrical impedance. Cheung et al. showed that on-chip impedance measurements conducted in flow-through revealed unique signatures for intact red blood cells, ghosts, and cells that had been fixed with glutaraldehyde [11].

By combining sophisticated micromechanical, optical, and electrical detectors, complex physical fingerprints of individual cells can be identified. Genetically engineered fluorescent proteins or staining with fluorescent antibodies can highlight specific cellular events or mark a subpopulation in a heterogeneous pool. Physical

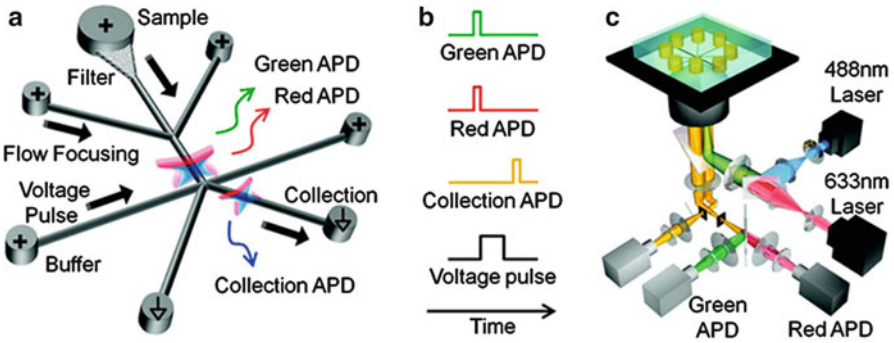

Fig. 8.13 Microfluidic system for fluorescence activated sorting of subcellular particles. Electrophoresis is used to drive the flow of the sample and to switch between two different collection channels. Reprinted with permission from [46]. Copyright 2012 American Chemical Society

properties, in contrast, provide information about structure, composition, or size. A nice example of the value of such combinations is the work of the Manalis-laboratory towards the integration of mass and fluorescence sensing in order to characterize cell growth [50]. By measuring mass using the suspended microchannel resonator (SMR) technology and also reading a fluorescence signal, Son et al. found that the G1-S transition in L1210 mouse lymphocytes is triggered when the cells achieve a critical growth rate rather than a critical size threshold.

Label-free cytometric measurements that indicate whether cells are viable may be of great value in cell-based assays for drug development. Flow-through impedance-based viability measurements have been demonstrated for a variety of cell types, including Yeast, Jurkat, MCF-7, and different types of bacteria [11, 41, 45].

Most subcellular particles are at or below the limit of detection for conventional flow cytometers and cannot easily be sorted. Microfluidic devices, by virtue of scaling, make this domain accessible. For example, the Chiu-laboratory has created a nanofluidic flow cytometer shown in Fig. 8.13 for sorting of synaptic vesicles [46]. The laser-induced fluorescence detection system has single molecule sensitivity, and switching rates up to 10 kHz have been achieved by driving the sample and sheath flow using electroosmosis. This system enabled the purification of a subpopulation of vesicles that simultaneously expressed the synaptic vesicle proteins SV2 and VAMP.

8.4.2 Production of Nanoparticles and Protein Crystallization

The precipitation of solid particles may, at first sight, not appear as a fitting application for microfluidic devices, as even a partial block due to a single particle

would disrupt or halt the smooth flow pattern and render the device unusable. Nonetheless, there are good reasons to venture into this field. We would like to illustrate this through two exemplary applications. The first one is protein crystallization, relevant mostly to basic science, and the second is the production of nanoparticles with well-controlled properties for drug delivery. In both areas, the benefits brought about by the microfluidic environment have the potential to significantly outweigh any challenges. With careful design and precise flow control, robust microfluidic particle generation is possible.

In protein crystallization, the goal is to find conditions that favor the formation of nuclei in supersaturated solutions and allow the subsequent growth of high-quality crystals. Exploring the enormous space of control parameters requires high throughput and low-volume methods using as little of the precious protein as possible per trial. Two-phase flows, in which plugs or droplets containing an aqueous phase are separated by an organic phase (often fluorinated oil), provide an excellent basis for setting up large numbers of crystallization trials using microfluidics. In the simplest implementation, the protein solution is mixed with precipitants and encapsulated in nanoliter-sized droplets. If the solution is supersaturated, nucleation and crystallization will eventually occur. This approach has been demonstrated, for example, by the group of Rustem Ismagilov who generated droplets using a PDMS microfluidic device and then stored these droplets in thin-walled glass capillaries for several days [57]. The quality of crystals that grew during maturation in the glass capillary could then be assessed directly by X-ray diffraction. High-quality crystals of lysozyme were obtained with this method, although the kinetics of the process was found to be significantly slower in nanoliter-sized droplets than in conventional microliter-scale batches. This is not surprising due to the relatively low probability of the presence of nuclei in a small volume. When the droplets are embedded in an oil phase that is impermeable to water and to the solutes in the aqueous phase, this technique belongs to the class of so-called microbatch methods. Alternatively, the initial condition can be set up so that the solution is not saturated at first. Gradual dehydration of the droplets in a water-permeable continuous phase then shifts the equilibrium to favor crystallization. This has been done in the droplet-loaded capillary system by alternating droplets containing the protein/precipitant mixture with droplets containing a highly concentrated salt solution. Choosing polytrifluoropropylmethylsiloxane (FMS-121) for the oil phase allowed the exchange of water between adjacent droplets until the osmotic pressures were balanced.

Protein crystallization is a slow process, with characteristic times on the scale of hours and days. Separating the long incubation step from the generation of the different trial batches is a good compromise to satisfy different requirements. In the first part of the system, a stable continuous flow can be maintained, while in the second part, the reaction progress can be monitored for extended times and independently for the different batches.

When the kinetics is sufficiently fast, particles can be formed in uninterrupted flow within microfluidic channels. A nice example is the work of Karnik et al. on generating nanoparticles for drug delivery by hydrodynamic focusing [33]. By rapidly diluting an

organic phase injected between two aqueous streams, polymeric drug-carrier nanoparticles 10–50 nm in diameter were formed as the mixed solution travelled down a 1 cm long aging channel. At a flow rate of 10 μL/min, the average residence time in the aging channel was ~70 ms. Such a fast completion of the precipitation reaction is the exception, rather than the rule, as is evident from the excellent review of different microfluidic approaches given by Moschou et al. [38]. More often, one sees the combination of mixing in microfluidic channels of 20–100 μm size combined with a much larger aging reactor in the form of a tube or capillary attached to the microfluidic device.

8.4.3 Microfluidic Particle-Based Assays

Microparticles employed as a "mobile surface" may greatly improve the throughput, sensitivity, and specificity of biochemical assays. Particle-based assays improve throughput over conventional microplate-based methods in two ways. First, the mobility of particles in the sample accelerates mass transport and shortens the required incubation times. Second, specially "barcoded" particles that are functionalized differently may be mixed with a single sample and allow a very high level of multiplexing when later read by flow cytometry. One of the first commercially available bead-based multiplex assays is the Luminex platform (Bio-Rad Inc.). Conventional sandwich assays with fluorescently labeled secondary antibodies are carried out on mixtures of different beads in micro-well plates. Each bead population is labeled with a unique fluorescent dye. After incubation and washing, the sample is analyzed in a benchtop flow cytometer. Because only a relatively small fraction of the beads in a micro-well is actually need to achieve statistical significance, and because the reagents are expensive, there is a motivation to reduce the volume using microfluidics.

The degree of multiplexing that can be attained using spectrally encoded beads is ultimately limited by the availability of distinct fluorophores and the number of parallel excitation and detection channels of the flow cytometer. An elegant method to circumvent this limitation was proposed by the group of Patrick Doyle (Fig. 8.14). Instead of using batch-produced microbeads, the group generated small hydrogel micro-carriers by photopolymerization in a multi-laminated stream [32]. A unique physical barcode was imprinted in each particle by structuring the UV illumination. Primary antibodies or DNA were immobilized in the gel phase, so that the entire volume was available for target capture. After collecting the particles in a microtube and incubating with the sample, the mixture was reinjected into a microfluidic flow-focusing device, where the gel particles aligned with the flow and could be read out using fluorescence.

Selectivity and/or specificity in biochemical assays can be improved to some level by particle-based purification schemes that effectively reduce the relative concentration of interfering species in complex samples. Functionalized particles employed as a dispersed solid phase can be easily separated from the mixture by

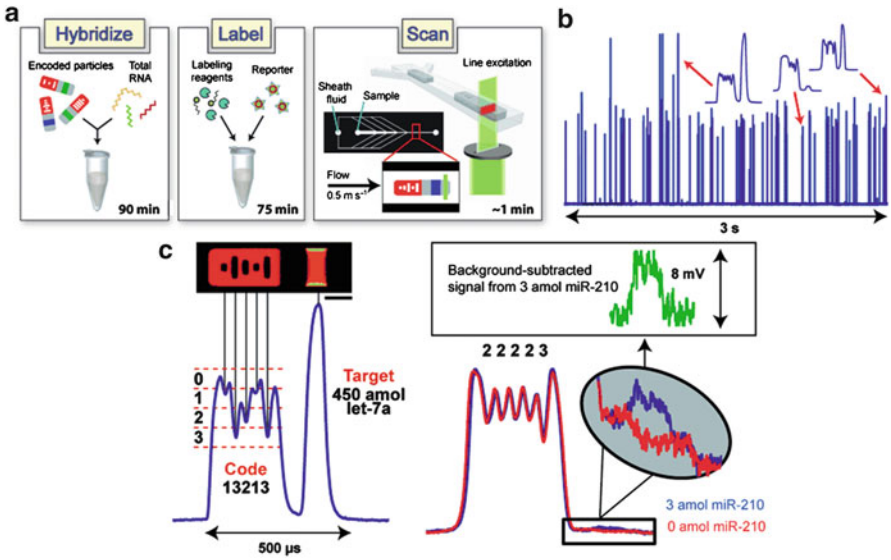

Fig. 8.14 Affinity-based microfluidic multiplex assay for DNA and protein detection using barcoded gel microparticles: (**a**) After production and simultaneous barcoding by in-channel polymerization, particles are collected in external vials and incubated with the sample. The particles are then reinjected into a microfluidic device for analysis; (**b**) Detection by fluorescence; (**c**) Each fluorescence peak contains a signature that corresponds to the unique barcode of each particle. The biochemical information is contained in a non-barcoded region, and the signal intensity of this region is translated into concentration based on a standard curve. (Reproduced with permission from [8]. Copyright © 2011 WILEY-VCH Verlag GmbH & Co. KGaA, Weinheim)

centrifugation or by magnetic separation. The latter, in particular, has the advantage of being applicable to complex samples, such as cell lysates or tissue homogenates, with minimal preprocessing. By purifying and concentrating bound ligands in this way, the detection problem is often simplified. Particles that were bound to the ligand of interest can be captured by immobilized secondary antibodies.

References

1. Asmolov ES (1999) The inertial lift on a spherical particle in a plane Poiseuille flow at large channel Reynolds number. J Fluid Mech 381:63–87
2. Barrett R, Faucon M, Lopez J, Cristobal G, Destremaut F, Dodge A, Guillot P, Laval P, Masselon C, Salmon JB (2006) X-ray microfocussing combined with microfluidics for on-chip X-ray scattering measurements. Lab Chip 6(4):494–499
3. Bernabini C, Holmes D, Morgan H (2011) Micro-impedance cytometry for detection and analysis of micron-sized particles and bacteria. Lab Chip 11(3):407–412
4. Bhagat AAS, Kuntaegowdanahalli SS, Papautsky I (2008) Enhanced particle filtration in straight microchannels using shear-modulated inertial migration. Phys Fluids 20(10)

5. Bretherton FP (1962) The motion of rigid particles in a shear flow at low Reynolds number. J Fluid Mech 14(2):284–304
6. Burg TP, Manalis SR (2003) Suspended microchannel resonators for biomolecular detection. Appl Phys Lett 83(13):2698–2700
7. Burg TP, Godin M, Knudsen SM, Shen W, Carlson G, Foster JS, Babcock K, Manalis SR (2007) Weighing of biomolecules, single cells and single nanoparticles in fluid. Nature 446 (7139):1066–1069
8. Chapin SC, Appleyard DC, Pregibon DC, Doyle PS (2011) Rapid microRNA profiling on encoded gel microparticles. Angew Chemie Int Ed 50(10):2289–2293
9. Chapman DL (1913) A contribution to the theory of electrocapillarity. Philos Mag 25 (148):475–481
10. Chastek TQ, Beers KL, Amis EJ (2007) Miniaturized dynamic light scattering instrumentation for use in microfluidic applications. Rev Sci Instr 78(7)
11. Cheung KC, Di Berardino M, Schade-Kampmann G, Hebeisen M, Pierzchalski A, Bocsi J, Mittag A, Tarnok A (2010) Microfluidic impedance-based flow cytometry. Cytometry A 77A (7):648–666
12. Chun B, Ladd AJC (2006) Inertial migration of neutrally buoyant particles in a square duct: an investigation of multiple equilibrium positions. Phys Fluids 18(3):031704
13. Cox RG, Mason SG (1971) Suspended particles in fluid flow through tubes. Annu Rev Fluid Mech 3:291–316
14. Dannhauser D, Romeo G, Causa F, De Santo I, Netti PA (2014) Multiplex single particle analysis in microfluidics. Analyst 139(20):5239–5246
15. Destremaut F, Salmon JB, Qi L, Chapel JP (2009) Microfluidics with on-line dynamic light scattering for size measurements. Lab Chip 9(22):3289–3296
16. Di Carlo D, Irimia D, Tompkins RG, Toner M (2007) Continuous inertial focusing, ordering, and separation of particles in microchannels. Proc Natl Acad Sci U S A 104(48):18892–18897
17. Di Carlo D (2009) Inertial microfluidics. Lab Chip 9(21):3038–3046
18. Fraikin JL, Teesalu T, McKenney CM, Ruoslahti E, Cleland AN (2011) A high-throughput label-free nanoparticle analyser. Nat Nanotechnol 6(5):308–313
19. Godin M, Bryan AK, Burg TP, Babcock K, Manalis SR (2007) Measuring the mass, density, and size of particles and cells using a suspended microchannel resonator. Appl Phys Lett 91 (12):123121
20. Gossett DR, Tse HTK, Lee SA, Ying Y, Lindgren AG, Yang OO, Rao JY, Clark AT, Di Carlo D (2012) Hydrodynamic stretching of single cells for large population mechanical phenotyping. Proc Natl Acad Sci U S A 109(20):7630–7635
21. Gouy M (1910) Sur la constitution de la charge électrique à la surface d'un électrolyte. J Phys Theor Appl 9(1):457–468
22. Greaves ED, Manz A (2005) Toward on-chip X-ray analysis. Lab Chip 5(4):382–391
23. Hansen CL, Classen S, Berger JM, Quake SR (2006) A microfluidic device for kinetic optimization of protein crystallization and in situ structure determination. J Am Chem Soc 128(10):3142–3143
24. Henry DC (1931) The cataphoresis of suspended particles Part I—the equation of cataphoresis. Proc R Soc Lond Contain Papers Math Phys Char 133(821):106–129
25. Ho BP, Leal LG (1974) Inertial migration of rigid spheres in 2-dimensional unidirectional flows. J Fluid Mech 65(2):365–400
26. Irimajir A, Hanai T, Inouye A (1979) Dielectric theory of multi-stratified shell-model with its application to a lymphoma cell. J Theor Biol 78(2):251–269
27. Jackson JD (1998) Classical electrodynamics. Wiley, New York
28. Jain R, Petri M, Kirschbaum S, Feindt H, Steltenkamp S, Sonnenkalb S, Becker S, Griesinger C, Menzel A, Burg TP, Techert S (2013) X-ray scattering experiments with high-flux X-ray source coupled rapid mixing microchannel device and their potential for high-flux neutron scattering investigations. Eur Phys J E 36(9):109

29. Johnson ME, Landers JP (2004) Fundamentals and practice for ultrasensitive laser-induced fluorescence detection in microanalytical systems. Electrophoresis 25(21–22):3513–3527
30. Jones TB, Washizu M (1996) Multipolar dielectrophoretic and electrorotation theory. J Electrostat 37(1–2):121–134
31. Jones TB (2003) Basic theory of dielectrophoresis and electrorotation. IEEE Eng Med Biol Mag 22(6):33–42
32. Jones TB (1995) Electromechanics of particles. Cambridge University Press, Cambridge
33. Karnik R, Gu F, Basto P, Cannizzaro C, Dean L, Kyei-Manu W, Langer R, Farokhzad OC (2008) Microfluidic platform for controlled synthesis of polymeric nanoparticles. Nano Lett 8 (9):2906–2912
34. Lee J, Chunara R, Shen W, Payer K, Babcock K, Burg TP, Manalis SR (2011) Suspended microchannel resonators with piezoresistive sensors. Lab Chip 11(4):645–651
35. Lee J, Shen WJ, Payer K, Burg TP, Manalis SR (2010) Toward attogram mass measurements in solution with suspended nanochannel resonators. Nano Lett 10(7):2537–2542
36. LesliePelecky DL, Rieke RD (1996) Magnetic properties of nanostructured materials. Chem Mater 8(8):1770–1783
37. Modena MM, Wang Y, Riedel D, Burg TP (2014) Resolution enhancement of suspended microchannel resonators for weighing of biomolecular complexes in solution. Lab Chip 14 (2):342–350
38. Moschou P, de Croon MHJM, van der Schaaf J, Schouten JC (2014) Advances in continuous crystallization: toward microfluidic systems. Rev Chem Eng 30(2):127–138
39. Olcum S, Cermak N, Wasserman SC, Christine KS, Atsumi H, Payer KR, Shen WJ, Lee JC, Belcher AM, Bhatia SN, Manalis SR (2014) Weighing nanoparticles in solution at the attogram scale. Proc Natl Acad Sci U S A 111(4):1310–1315
40. Pamme N, Koyama R, Manz A (2003) Counting and sizing of particles and particle agglomerates in a microfluidic device using laser light scattering: application to a particle-enhanced immunoassay. Lab Chip 3(3):187–192
41. Pierzchalski A, Hebeisen M, Mittag A, Di Berardino M, Tarnok A (2010) Label-free single cell analysis with a chip-based impedance flow cytometer. Imaging Manipulation Analys Biomol Cells Tissues VIII 7568
42. Piyasena ME, Graves SW (2014) The intersection of flow cytometry with microfluidics and microfabrication. Lab Chip 14(6):1044–1059
43. Pohl HA (1951) The motion and precipitation of suspensoids in divergent electric fields. J Appl Phys 22(7):869–871
44. Probstein RF (1989) Solutions of charged macromolecules and particles. In: Probstein RF (ed) Physicochemical hydrodynamics. Butterworth-Heinemann, Boston, pp 201–225
45. Schade-Kampmann G, Huwiler A, Hebeisen M, Hessler T, Di Berardino M (2008) On-chip non-invasive and label-free cell discrimination by impedance spectroscopy. Cell Prolif 41 (5):830–840
46. Schiro PG, Gadd JC, Yen GS, Chiu DT (2012) High-throughput fluorescence-activated nanoscale subcellular sorter with single-molecule sensitivity. J Phys Chem B 116 (35):10490–10495
47. Scholten PC (1995) Which Si. J Magn Magn Mater 149(1–2):57–59
48. Segre G, Silberberg A (1961) Radial particle displacements in Poiseuille flow of suspensions. Nature 189(476):209–210
49. Shevkoplyas SS, Siegel AC, Westervelt RM, Prentiss MG, Whitesides GM (2007) The force acting on a superparamagnetic bead due to an applied magnetic field. Lab Chip 7 (10):1294–1302
50. Son S, Tzur A, Weng Y, Jorgensen P, Kim J, Kirschner MW, Manalis SR (2012) Direct observation of mammalian cell growth and size regulation. Nat Meth 9(9):910–912
51. Staben ME, Davis RH (2005) Particle transport in Poiseuille flow in narrow channels. Int J Multiphase Flow 31(5):529–547

52. Staben ME, Zinchenko AZ, Davis RH (2003) Motion of a particle between two parallel plane walls in low-Reynolds-number Poiseuille flow. Phys Fluids 15(6):1711–1733
53. Thoroddsen ST, Etoh TG, Takehara K (2008) High-speed imaging of drops and bubbles. Annu Rev Fluid Mech 40:257–285
54. Toft KN, Vestergaard B, Nielsen SS, Snakenborg D, Jeppesen MG, Jacobsen JK, Arleth L, Kutter JP (2008) High-throughput Small Angle X-ray Scattering from proteins in solution using a microfluidic front-end. Anal Chem 80(10):3648–3654
55. Vig AL, Haldrup K, Enevoldsen N, Thilsted AH, Eriksen J, Kristensen A, Feidenhans'l R, Nielsen MM (2009) Windowless microfluidic platform based on capillary burst valves for high intensity X-ray measurements. Rev Sci Instr 80(11):115114-1–6
56. Wlodkowic D, Darzynkiewicz Z (2011) Rise of the micromachines: microfluidics and the future of cytometry. Recent Adv Cytom Part A 102:105–125
57. Zheng B, Tice JD, Roach LS, Ismagilov RF (2004) A droplet-based, composite PDMS/glass capillary microfluidic system for evaluating protein crystallization conditions by microbatch and vapor-diffusion methods with on-chip X-ray diffraction. Angew Chemie Int Ed 43 (19):2508–2511

Chapter 9
Respiratory Drug Delivery

H. Wachtel

Abstract The treatment of diseases by respiratory drug delivery offers a noninvasive route to deliver either topically active medications or systemic drugs. Nose and lung are target organs which provide opportunities for aerosol drug delivery by deposition on the right surface. However, filter and clearance mechanisms of the body must be overcome in order to achieve successful applications. Basic mechanisms of deposition and their interplay with the particle size (aerodynamic diameters, approx. 40–80 μm (nose) and 2–5 μm (lung)) and the patient's inhalation flow profile are discussed. The required particle size motivates the technological approaches for aerosol generation by different inhalers. Among them are nebulizers, dry powder inhalers (DPI), pressurized metered dose inhalers (p-MDI), and non-pressurized metered dose inhalers (np-MDI). Two recently designed examples of non-pressurized liquid inhalers are presented in more detail as they make direct use of microfluidic structures in their nozzle and filter designs.

9.1 Introduction

Historically, aerosol treatment of diseases reaches back in ancient times when the generation of aerosols was based on smoke [1] or water vapor containing ingredients displaying healthy effects when inhaled, e.g., in Roman baths [2].

To date, the airways can be understood as a series of filter stages starting at the nose with a relatively coarse filter characteristic and finally ending in the peripheral lung, where the terminal alveoli are reached through very thin air ducts, the terminal bronchioli [16]. The airways constitute a natural microfluidic system for aerosols, and it is the task of respiratory drug delivery to facilitate the transport of droplets or particles containing drug into the lung. Once delivered at their target region the particles face different clearing mechanisms or they dissolve and/or permeate into the tissue and finally the systemic circulation. This process is investigated by pharmacodynamic studies.

H. Wachtel (✉)
Boehringer Ingelheim Pharma GmbH & Co. KG, Binger Str. 173,
Ingelheim am Rhein 55216, Germany
e-mail: herbert.wachtel@boehringer-ingelheim.com

A. Dietzel (ed.), *Microsystems for Pharmatechnology*,
DOI 10.1007/978-3-319-26920-7_9

9.1.1 The Airways as Target for Deposition of Droplets and Particles

Nasal delivery relies on the relatively small surface area of the nasal mucosa for topical treatment or the transition into the blood circulation. As the nose acts as a filter for larger particles, the particle size for deposition in the nose is in the range from 40 to 80 μm [28]. However, recently the treatment of sinusitis was improved by smaller particles (MMAD 3.5 μm) in combination with artificially induced pressure oscillations in the nasal ducts [19].

9.1.1.1 The Lung as Target Organ

While most data on lung deposition mechanisms was originally derived from studies on healthy volunteers, both, the healthy and the diseased lung are treated using similar methods. On the one hand, the healthy lung is seen as entrance organ for the purpose of systemic delivery mainly because of the large surface (~120 m^2 in adults), e.g., for the delivery of insulin [25]. On the other hand, the organ of asthmatics or patients with chronic obstructive pulmonary disease (COPD) is the target of topical treatment. In order to reach the largest possible airway surface area, the regions deep in the lung must be treated. Typical applications are the deposition of bronchodilators and anti-inflammatory agents.

There are four major mechanisms of deposition:

1. Impaction
   Large particles are unable to follow the bent air flow
2. Sedimentation
   Gravity forces the particles down, where they deposit on the bottom part of the airway
3. Diffusion
   Very small particles are accelerated by impact of molecules (Brownian motion) and hit the wall
4. Anchoring of fibers
   The length of fibers is longer than the diameter of the airway. When the flow direction changes, the fibers get stuck.

These mechanisms have their competing clearance mechanisms, e.g., the mucociliary escalator which transports mucus upwards until it is swallowed. On the microscopic level, macrophages can catch foreign particles. Once the particles have landed, their fate is governed by surface forces (wetting behavior) which decide whether the particles will stay at the air–mucus interface or are drowned. Solubility and/or permeability and size of the remaining particles decide on their further way into the body. Because of this complex situation many models have been proposed to explain aspects of the entrance into the lung tissue; however, there is no general acceptance of such a model yet. A possible approach might be the

distinction and risk assessment according to solubility and permeability of the drug substance.

The geometry of the human respiratory tract as well as the breathing patterns of the individual subjects govern the transport regimes of aerosols in the lung. The particle properties, e.g., density, shape, surface roughness, and size can be summarized in an equivalent diameter, the aerodynamic diameter. The nose or the oral cavity represent a first coarse filter unit. Nose models [24] and mouth–throat models [12] have been created in order to investigate the deposition in these regions.

Figure 9.1 gives an insight of the complex geometry of the lung when following just one single path from the trachea to the most peripheral alveoli. Using the most advanced X-ray tomography, the 3D geometry can only be resolved with voxels in the 0.1 mm range in living subjects. In theory, this provides sufficient quality of the geometry representation up to the tenth generation (~10 subdivisions in the diameter of 1 mm). However, most segmentations of the human lung are limited to lower generations because of contrast issues. The aerosol transport can be checked by radiolabeling. Using a gamma camera, 2D projections of the aerosol deposition in the lung can be obtained. Also 3D techniques (e.g., Single Photon Emission Computer Tomography (SPECT)) are available. Their spatial resolution is currently limited to 6.4 mm (e.g., GE starcam 4000 [18]). Because of this restriction, SPECT data is often combined with high-resolution CT scans. If labeling of the active molecule is desired, Positron Emission Tomography (PET) techniques can be applied [10].

In order to simulate the aerosol transport and deposition, many models have been developed (e.g., [3, 9, 22]). A consensus-based mathematical model is explained in detail in the Publication 66 by the International Commission on Radiological Protection, ICRP [16]. As an example of more recent work, Fig. 9.2 displays a single path lung model [6]. Lengths and diameters were based on Finlay's findings

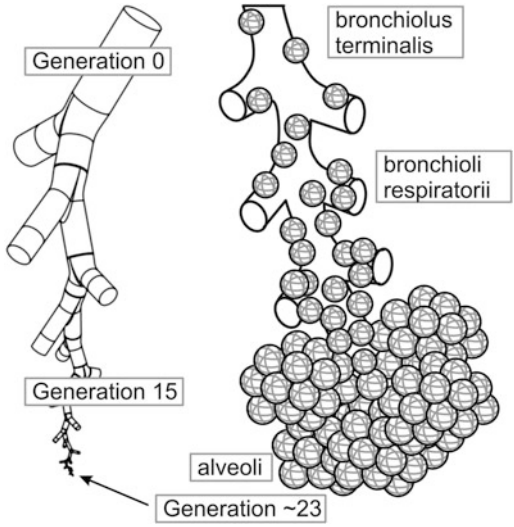

Fig. 9.1 Artist's view of the airway along one path from the trachea (generation 0) to the bronchi and finally to the alveoli (*left*) and magnified view of the terminal generation (approx. 23) with alveoli (*right*). Between generation 15 and 23 increasing numbers of alveoli are attached to the air ducts. For more details, refer to Netter [21]

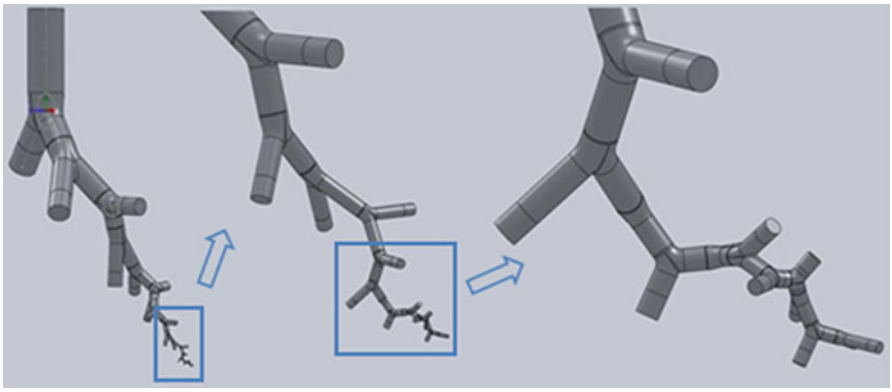

Fig. 9.2 Single path model of the respiratory tract from the trachea to the terminal generation 23 [5]

[9] who refers to Raabe et al. [23] and Haefeli-Bleuer [14]. Angles between the daughter and parent branches were taken from Raabe et al. [23]. In this model, the contribution of alveolar volume is considered by boundary conditions defining an appropriate air outflow for each individual generation. The comparison of Figs. 9.1 and 9.2 illustrates the complexity introduced by considering alveoli and explains why many models based on computational fluid dynamics (CFD) are limited to approximately generation 15.

9.1.2 Technical Requirements for Successful Drug Delivery

Key parameters of the aerosol are the aerodynamic diameter and the velocity of the particles as well as the velocity of the carrier gas. In practice, this translates into the need for the (aerodynamic) particle size distribution, the exit velocity at the inhaler outlet, and the air flow rate through the inhaler. In addition, the geometry of the air duct must be defined, hence the need for 3D CAD data of the inhaler and of typical patients.

In detail the aerodynamic diameter is an equivalent diameter defining the sphere of density 1000 kg/m^3 which acts with the surrounding air like the arbitrarily shaped particle. The velocity of the carrier gas is responsible for acceleration or slowing down the particles and for realistic evaluations its time dependence (flow profile) must be considered. This flow profile is controlled by the subject/patient using the inhaler, and it is highly variable (intra-patient and inter-patient). Therefore, patient training is required and in addition the inhaler must be robust with respect to variations in flow rate and duration of the inhalation process. The flow resistance R of the inhaler determines to some degree how fast a patient inhales through this device. Based on the turbulent flow regime present in almost all of the inhalers R is

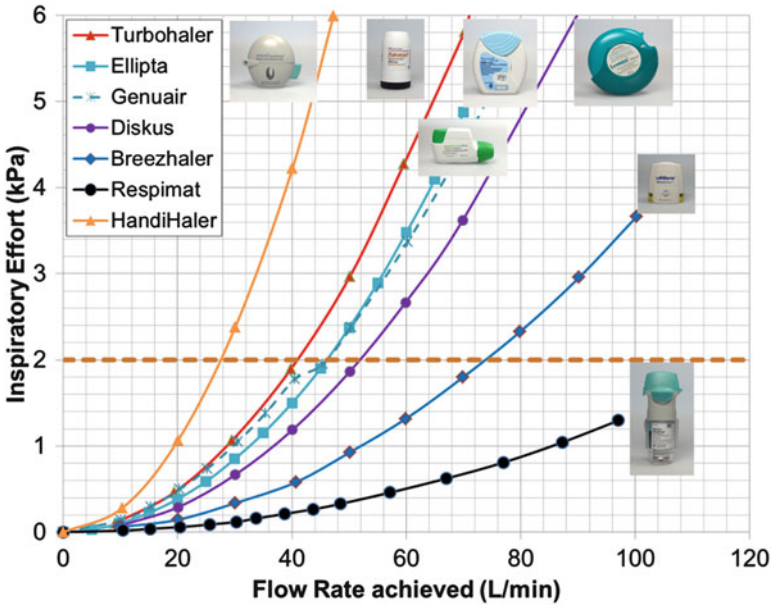

Fig. 9.3 Pressure drop in inhalers as function of the flow rate

in good approximation, the square root of the pressure drop (=inspiratory effort) at a given air flow rate divided by that flow rate (See Fig. 9.3 for examples of pressure-flow characteristics). The value of *R* characterizes the different inhalers.

9.2 Overview of Established Technologies for Delivery of Microparticles

In the following sections, the technical aspects of dosage forms for inhaled therapy will be discussed. It must be mentioned, however, that human factor engineering will become more and more important besides the purely technical facts. It must be ensured that the operation of inhalers is sufficiently simple and in the long run, standardization of the main operating steps should be envisaged.

9.2.1 Nebulizer

Preparations for nebulization can be administered by several stationary or handheld devices. Historically, the combination of drug formulation and device was not defined and open to recommendations by the health care professional. Future

drug applications will have to specify the nebulizer [10]. Conventional jet nebulizers use pressurized air for atomization of the liquid formulation which has a typical volume of 1–5 mL. Many jet nebulizers incorporate an impaction plate which captures too large droplets which are then recycled. Mesh nebulizer use the ultrasonic vibration of a metal foil which carries multiple orifices through which the liquid flows and then is broken up into single drops. Ultrasonic nebulizers create surface waves on the upper side of the liquid which then is disrupted and broken into small droplets. All nebulizers are active devices, i.e., they consume energy for the generation of small droplets. This energy is provided by gas pressure or mechanical vibrations. Advanced nebulizers contain electronic breath control, may be triggered by the inhalation, and can also register patient compliance data and permit dose calculations.

9.2.2 Pressurized Metered Dose Inhaler

The pressurized metered dose inhaler (pMDI) is still the most widely distributed aerosol source for respiratory drug delivery; however, environmental concerns and the limited availability of innovative drugs in this dosage form limit its application in the western countries. A metering valve is responsible for the name of this inhaler. The energy required for the generation of the aerosol is provided by a propellant made of a liquefied gas. The advent of the ozone hole resulted in a ban of the propellants consisting of CFCs and enforced the transition from CFC to HFA. This propellant, however, raises concerns with respect to the Green House Effect (global warming). Drugs are either solved in a solution of ethanol and propellant or they are suspended in the propellant. Therefore, they are called solution aerosols or suspension aerosols. The latter require shaking immediately before application.

The nozzle technology of pMDIs is challenging because typical channels have a diameter of 0.2 mm and are 0.5 mm long, and they are produced as injection-molded parts in large quantities (Fig. 9.4). The liquefied gas which is metered and released from the valve runs through the valve stem and the nozzle, thereby cavitating and generating bubbles. The exit velocity is high [15] and on their way to the patient the required small particles form by rapid evaporation of the propellant (flashing).

9.2.3 Non-pressurized Metered Dose Inhaler

Two examples of non-pressurized metered dose inhalers (npMDIs) will be discussed in detail in Sect. 9.3. The main feature of these devices is that they do not require any propellant.

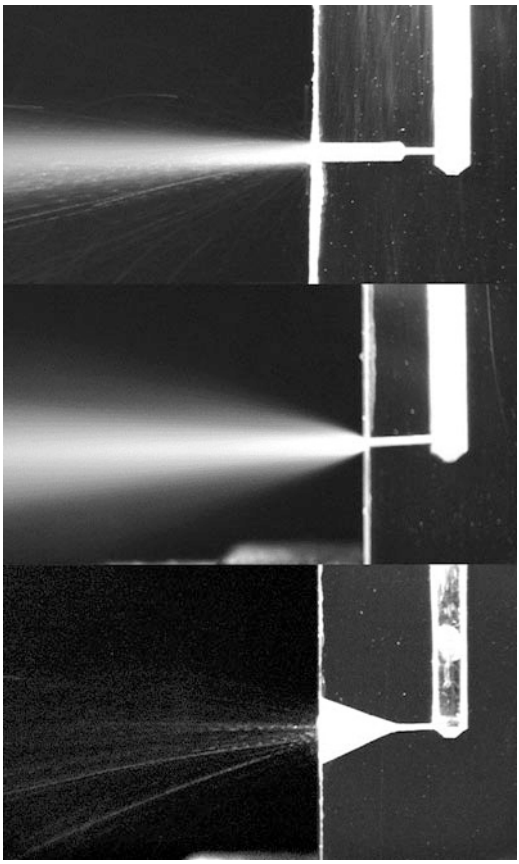

Fig. 9.4 pMDI nozzles drilled in PMMA. The outlet geometry significantly influences the spray properties

9.2.4 Dry Powder Inhaler

The currently marketed dry powder inhalers (DPIs) are passive devices, i.e., they rely on the inhalation airflow generated by the patients. The aerodynamic design of the air ducts inside the DPIs is critical to the robust delivery of drug containing aerosol. Using the energy provided by the inhalation air flow, the dry powder must be deagglomerated and the drug particles should be aerosolized providing an aerodynamic diameter of 2–5 μm. Many drugs used in respiratory therapy are cohesive, and this feature is worsened by the need for small particles which generate a large surface area. Two challenges arise: (a) high energy density (high local velocity) is required to break up cohesive powder beds, (b) the exit velocity of the aerosol should be low enough in order to avoid high deposition in the patient's mouth–throat region. The classical approach to solve this contradiction is to achieve flowability and to facilitate deagglomeration by creating powder blends. The primary task of blending is to separate the drug particles by adding large inert particles. Several alternative formulation approaches are known which overcome the cohesion by surface engineering.

Table 9.1 Widely used formulation options

Inhaler	Type	Description
pMDI	Solution	Solution of propellant, ethanol, and drug
	Suspension	Suspension of drug, stabilizer, other excipients in propellant
npMDI	Solution	Drug solved in water, if required: preservative, stabilizer
DPI	Blend	Drug blended with lactose or manitol, if required: Mg-stearate or others
	Spray-drying	Drug, drug/excipient mixture if required blended with excipients
	Soft pellets	Soft agglomerates of drug particles

Many premetered DPIs rely on capsules as primary package of the powder for inhalation (e.g., Aerolizer, Breezhaler (Novartis), TwinCaps (Hovione), HandiHaler (Boehringer Ingelheim), Revolizer (Cipla)) while others use blister cavities (Diskus, Ellipta (Glaxo), Discair (Neutech), Gyrohaler (Vectura)). In general, capsule-based systems take advantage of the capsule motion for shaking and breaking up the powder bed. Reservoir DPIs incorporate a metering function and expose a defined volume of well-flowing formulation to the inhaled air flow (TurboHaler(AstraZeneca), EasyHaler (Hexal)).

9.2.5 Formulation Development

All inhaled dosage forms require their specific know how on the formulation because of the required match of physical–chemical properties between formulation and inhaler. The degrees of freedom are uncounted for designing formulations; however, only a few technologies have reached the market. This is explained by the vulnerable nature of the lung and the extreme care taken in order to assess the possibly irritating or even toxic effects not only of new drugs but also of any excipient in the formulation, as well as extractables and leachables of the device and packaging materials in contact with the formulation. Table 9.1 gives an overview:

All formulations have in common that a reasonable shelf life should be guaranteed, approximately 2 years is accepted by many companies as the minimum specification in the final package.

9.3 Examples of Inhalers Using Microfluidic Technology

9.3.1 Medspray®

In order to obtain improved drug deposition in the lower airways, monodisperse droplets have been proposed by many authors. Using the mechanism of Rayleigh

break up, these droplets were generated by the novel Medspray Wet Aerosol Inhaler [20]. The result of a clinical study in mild asthmatics indicated that 6 µm large droplets generated the largest effect during and after a dose escalation series from 10 to 40 µg (total mass of salbutamol 80 µg). This dose is below the conventionally administered 200 µg using a pMDI.

In the handheld Medspray inhaler uniformly shaped droplets are generated by pumping the aqueous formulation through defined orifices. Small jets are formed which break up into the said droplets. Their diameter is theoretically 1.95 times that of the orifice diameter [8]. Therefore, a 2.5 µm nozzle theoretically delivers a ~5 µm droplet. Coalescence effects increase the mass median droplet size slightly. Figure 9.5 shows a linear array of nozzles which all generate well-separated droplets.

9.3.1.1 Technical Background of the Droplet Generation

The nozzle consists of an array of many orifices (Fig. 9.5 shows 30 orifices in a linear arrangement, as an example) with nominal diameters of 1.5–2.5 µm. Special attention was paid to the surface of the nozzle outlet. For example, superhydrophobic nanoparticle films on the nozzle surface may improve the cleaning properties and the onset of droplet generation by facilitating the removal of undesired large drops or other material [17].

In order to achieve reliable operation, the operating conditions of the nozzle must be carefully selected. Figure 9.6 gives the operating point with respect to orifice radius and average exit velocity.

The pump meters a volume of 30 µL liquid per actuation during the time of 1–2-s duration. Assuming the published data (e.g., 2.5 µm nozzle diameter) and a large number of nozzle orifices (~100 orifices in parallel), the area-weighted average of the exit velocity u of a single jet can be estimated. $u \sim 41$ m/s. This would result in a total

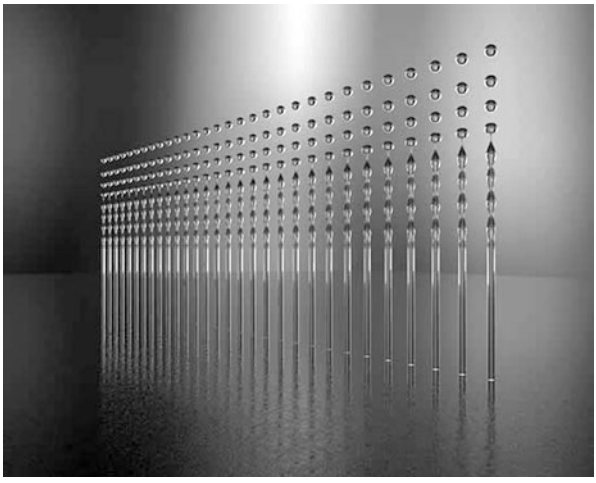

Fig. 9.5 Example of a nozzle arrangement for generation of liquid droplets. Image used with kind permission from Medspray

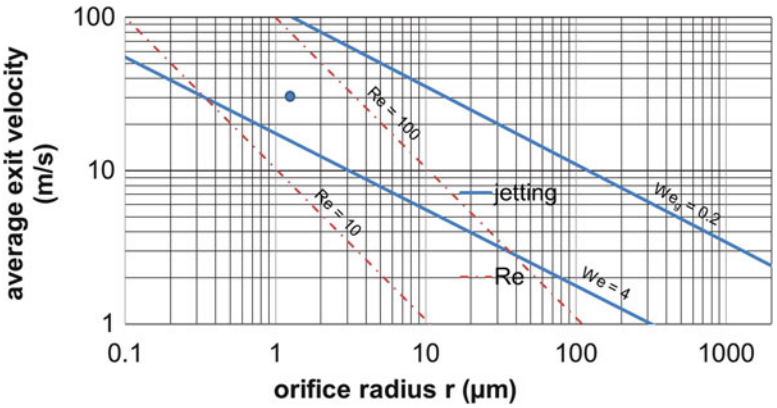

Fig. 9.6 Optimized operating point around 31 m/s exit velocity and 1.25 µm orifice radius. The jetting regime between $0.2 < We < 4$ is indicated

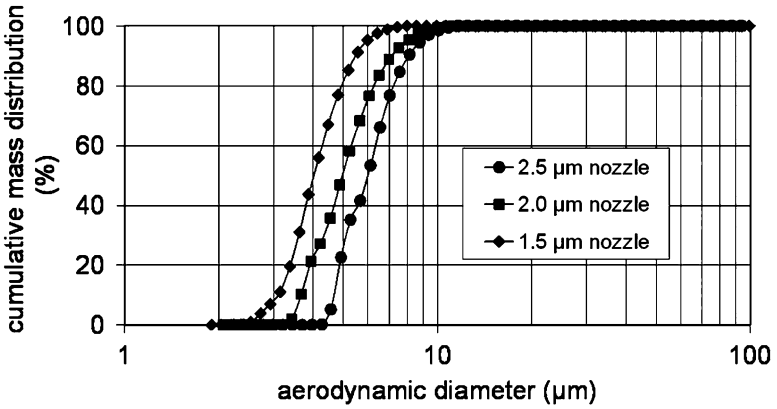

Fig. 9.7 Cumulative mass distribution curves versus aerodynamic diameter for aerosols from an aqueous 0.9 % sodium chloride solution delivered at an air flow rate of 60 L/min from the Medspray handheld inhaler using 1.5-, 2.0-, and 2.5-µm spray nozzles. Aerodynamic diameters were obtained via aerodynamic particle sizing. Curves corrected for evaporation effects [8]

flow of 1.2 mL/min. Velocity u and the orifice diameters are selected in a way that the operating regime is well within the jetting regime of the Rayleigh breakup mechanism (see Fig. 9.6). The combination of nozzle and pump therefore will support consistent operation of the delivery system (Fig. 9.7). For further details, refer to [27].

9.3.1.2 Device Properties

The device contains 200 doses which is comparable to classical pMDIs. The intended air flow rates for inhalation are between 30 and 60 L/min and are enforced

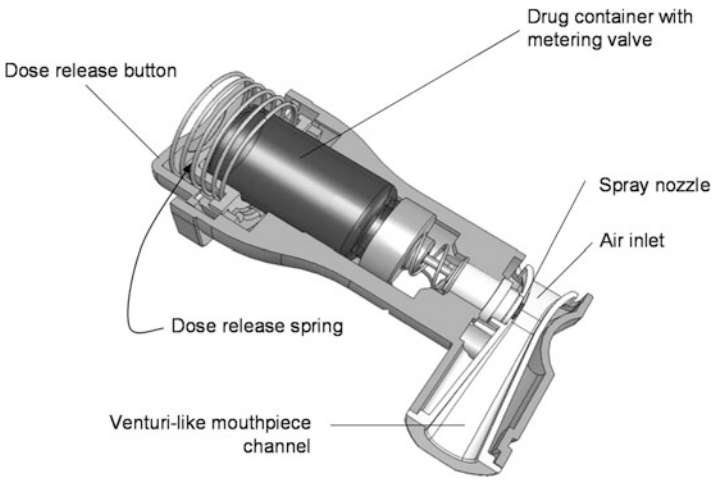

Fig. 9.8 Schematic view of a prototype of the Medspray inhaler demonstrating the similarity to pMDI designs [20]

by means of an air flow restrictor, which is present inside the inhalation air duct of the device. The intention of the restriction is to reduce the inter-/intrasubject inhalation flow variability. The mouthpiece used has a designed air flow resistance of $R = 0.067\text{sqrt(Pa)}\,\text{m}^3\,\text{s}^{-1}$ to give an air flow of 40 L/min at a pressure drop of 2 kPa. This is slightly higher than the air flow resistance of the Diskus DPI.

The design of the Medspray inhaler was optimized to achieve a look-and-feel similar to a pMDI (Fig. 9.8). The latest design is shown in Fig. 9.9.

9.3.2 *Respimat® Soft Mist™ Inhaler*

The Respimat® Soft Mist™ inhaler is the first internationally marketed non-pressurized inhaler. It addresses the requirements which have been named by Ganderton [13]:

- Generate an aerosol cloud independent of the patient's inspiration
- Spray duration should cover a substantial part of a slow inhalation ($>= 1$ s)
- High fine particle fraction (<5 μm)
- Low velocity of the generated aerosol cloud
- Simple to use inhaler
- Small size (similar to that of a pMDI)
- Multidose capability (>50 doses)
- Dose counter should be included
- Easy to manufacture and reasonably priced
- Dose uniformity throughout life, resistant to contamination, and with a suitable shelf life
- Environmentally friendly

Fig. 9.9 Latest design of the Medspray inhaler. Image used with kind permission from URSATEC Verpackung-GmbH

In order to meet these design criteria, Respimat was optimized step by step in several generations of prototypes and clinical samples. Respimat relies on a well-defined particle size distribution in contrast to monodisperse particles only. The first clinical studies indicated a high efficiency of the device and for that reason, for example, the metered dose of Spiriva (Boehringer Ingelheim) was 18 μg in the capsule-based HandiHaler while Respimat was registered with a therapeutic dose of 5 μg (2 puffs with 2.5 μg each).

Key component responsible for the generation of the soft mist is the uniblock (Fig. 9.10). It comprises two nozzle outlets which create an impinging jet atomizer. Because of the small geometric dimensions (5.6 μm × 8 μm) of the exit channels, a filter unit is integrated in the uniblock. This design prevents the nozzle from clogging and thus guarantees a long operating life [7]. The production process relies on the experience about lateral microstructures gained in semiconductor industry and is highly reproducible because the nozzle structure is transferred optically. A photolithographic process is applied.

The liquid flow through the uniblock and the subsequent atomization can be characterized by two nondimensional parameters: the Weber and the Reynolds numbers. They are defined as follows [4]:

$$We = \rho u_j^2 D/\sigma \text{ and } Re = \rho u_j D/\mu$$

where ρ is the liquid density, D the jet diameter, u_j the mean jet velocity, σ the surface tension, and μ the viscosity of the liquid. Table 9.2 gives the operating data for Respimat with the characteristic length being the hydraulic diameter:

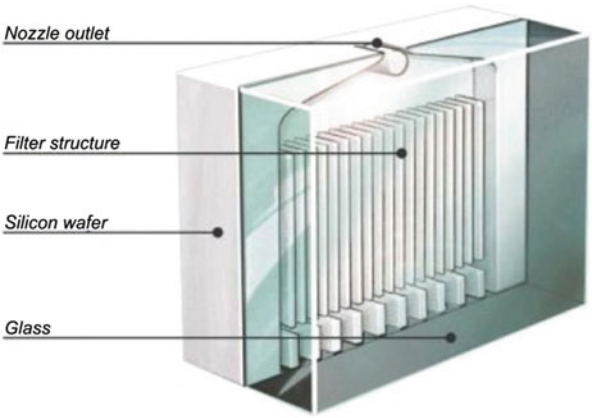

Fig. 9.10 Schematic view of the uniblock. The channel structure is etched into silicon and the open structure is closed by a glass plate bonded on top of the silicon [26]

Table 9.2 Operating regime of Respimat in the field of impinging jet atomizers

Case	Hydraulic diameter (m)	Reynolds number (–)	Weber number (–)	Assessment
Respimat	6.6E−06	738	1840	Impact wave (*We*)
(a)	4.0E−4	1000	27.5	Liquid chain
(b)	4.0E−4	40.4	58.8	Closed rim
(c)	4.0E−4	294	152	Open rim
(d)	4.0E−4	3536	343.5	Unstable rim
(e)	4.0E−4	5000	687	Impact wave

Assessment of cases (a) to (e) according to Chen [4]. Based on the Weber number Respimat generates impact waves. Respimat's micro-jets are responsible for the low *Re* number, indicating highly laminar flow
(The *Re* and *We* numbers are quoted from the publication Chen et al. [4]. =>diameter-related *Re* and *We* numbers)

Figure 9.11 gives a graphical representation of the different flow regimes which are mainly distinguished by their different Weber numbers. At very low flow rates, in front of the nozzle exits large surface drops grow. They prohibit the generation of jets and droplets (not shown). Increasing the flow results in a liquid chain structure (a). Increasing further the jet velocity, a liquid sheet is formed which is enclosed by a thicker closed rim (b). This rim opens (c) at further increase of velocity and when the surface tension of the liquid is reduced. Both variables contribute to an increase of the Weber number. The unstable rim (d) regime is already suitable for droplet generation, however for optimum generation the impact wave (e) regime is preferred.

The repeatable operation of the uniblock nozzle arrangement relies on the precisely metered volume of 15 µL per actuation. From the cartridge the drug solution is pumped through a capillary. It passes a non-return valve and is metered inside a central assembly unit. Upon release of the dose, the capillary acts like a

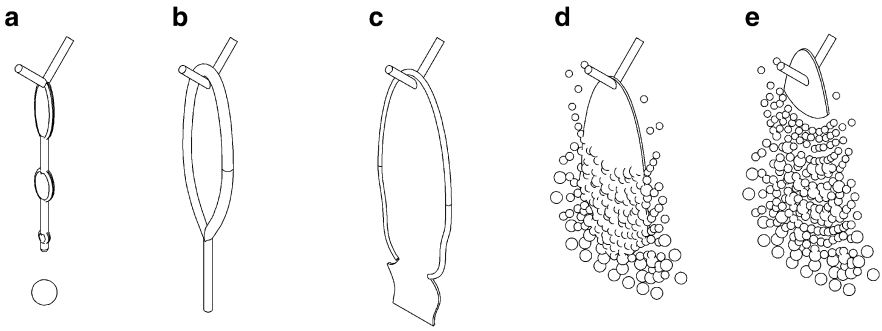

Fig. 9.11 Illustration of the different flow regimes encountered when increasing the Weber number of the impinging jet atomization

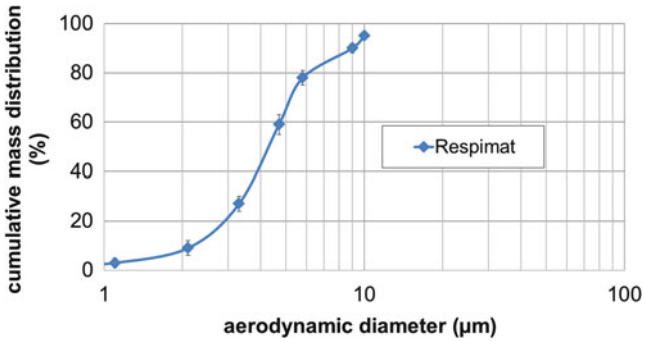

Fig. 9.12 Typical aerodynamic particle size distribution for the aerosol generated by Respimat® Soft Mist™ Inhaler, using an aqueous drug solution and an Andersen cascade impactor (relative humidity > 90 %) (cumulative mass fraction; % ± S.D.) [26]

piston and pushes the liquid through a filter into the uniblock. A pressure of up to 250 bar is built up and the liquid is pushed through the two nozzle channels. The atomization is based on the impinging jet principle. According to the nomenclature by Chen, Respimat operates in "the impact wave" regime (e). The high Weber number predicts that the Respimat reliably stays in this "impact wave" regime.

The particle size distribution of typical aqueous Respimat products is given in Fig. 9.12. The measurement was performed using the Andersen cascade impactor and feeding Respimat at 28.3 L/min with humidified air (>90 % RH). In addition to a large fine particle fraction which may penetrate into the peripheral lung, it seems also important to treat the bronchial region; therefore, a compromise between peripheral treatment and the bronchial airways must be made. Simulations show that Respimat seems to generate droplets fine enough to minimize mouth–throat deposition on the one hand but also large enough to deposit in part in the upper airways on the other hand, thus giving an example for a tuned particle size distribution where the designed-in width of the distribution may be helpful. The aqueous particle size distribution generated by Respimat may be influenced by

drying of the individual droplets. Therefore, care must be taken to select proper environmental conditions. In order to predict the particle size distribution present in the human airways, humidified air was used for the measurements, simulating the humidity inside the human body.

Currently, the manufacturing process of Respimat is scaled-up to a yearly capacity of >40 million units. While casing and mechanical parts of the driving mechanism can be manufactured by external suppliers, the core (e.g., the uniblock) and some critical parts as well as the final assembly with 100 % testing of all devices are handled by Boehringer Ingelheim microParts at Dortmund (Germany). Figure 9.13 gives a view on the processed wafer from which individual uniblocks are picked.

Figure 9.14 shows a section through Respimat in order to visualize the mechanical design of the inhaler.

The mechanical design for robustness of the high-pressure components required a relatively large nozzle holder with its corresponding union nut dimensions. Nevertheless, it was possible to keep the flow resistance of the device as low as the one of previous pMDIs.

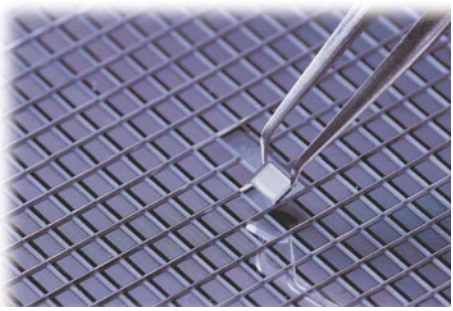

Fig. 9.13 Mass production of uniblocks for the Respimat® Soft Mist™ Inhaler

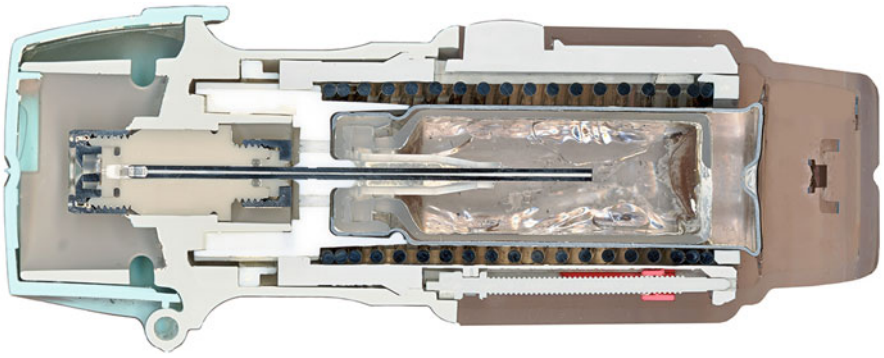

Fig. 9.14 Section through the Respimat (cap closed)

Table 9.3 Comparison of the Medspray inhaler and the Respimat Soft Mist inhaler

	Spray duration (s)	Number of nozzles (–)	Volume (μL)	Nozzle dimension, diameter (μm)	Average jet exit velocity u, [cloud velocity @ 10 cm] (m/s)	Total liquid flow (mL/min)
Medspray	2	~100	30	2.5	31 [–]	0.9
Respimat	1.5	2	15	5.6 × 8	112 [0.8]	0.6

9.3.2.1 Comparison of the Medspray Inhaler and the Respimat Soft Mist Inhaler

The two non-pressurized inhalers described in this chapter rely on microtechnology for the manufacturing process of their nozzle systems. They use mechanical pumps for the generation of the required pressure. However, for the patient the different flow resistances and the different spray durations are obvious differences. On the technical side, two completely different atomizing principles have been applied, resulting in alternative nozzle orifice geometries and the corresponding manufacturing approaches. Table 9.3 summarizes the publicly available key features of the two systems.

After exit from the nozzle structure the droplets are generated by the different mechanisms. However, the initial jet exit velocity is dramatically reduced when the small droplets (approx. 3–8 μm) are released into the slowly moving air. Similar cloud velocities are expected for both inhalers; however, only for Respimat the aerosol cloud velocity (e.g., at a distance of 10 cm from the nozzle outlet) has been published [15].

9.4 Conclusion

Respiratory drug delivery itself is a microfluidic process which consists of generating, transporting, and depositing micron-sized particles or droplets in the lungs. While the lung geometry is individually determined and its variability is out of the engineer's scope, aerodynamic particle size distribution and air flow are viable parameters for influencing deposition of drugs in the lungs. All inhalers depend on the patients' cooperation, and therefore training is a key element to successful therapy. The sheer multitude of inhalers creates the need for standardization of handling in the future.

In addition to the technical view presented here, the regulatory aspects of medicinal products [11], combination products (US wording), and medical devices must be considered when dealing with respiratory drug delivery.

References

1. Abdel Salam H (1947) Kitab Zakhirat El Attar (in Arabic). Dar El Ma-aref Press, Cairo, p 24
2. Boëthius A, Ward-Perkins JB (1970) Etruscan and Roman architecture. Penguin, Harmondsworth
3. Byron P, Delvadia RR, Longest PW, Hindle M (2010) Stepping into the trachea with realistic physical models: uncertainties in regional drug deposition from powder inhalers. Respir Drug Deliv 1:215–224
4. Chen X et al (2013) High-fidelity simulations of impinging jet atomization. Atomization Sprays 23(12):1079–1101
5. Ciciliani AM, Wachtel H, Heussel C, Langguth P (2015) Evaluation of Respimat® Soft Mist™ inhaler based on in vitro measurements and CFD simulations. Respir Drug Deliv Europe 2:357–362
6. Ciciliani AM (2016) Thesis, Department of Department of Biopharmaceutics and Pharmaceutical Technology. University of Mainz, Germany
7. Dalby R, Spallek M, Voshaar T (2004) A review of the development of Respimat® Soft Mist™ inhaler. Int J Pharm 283:1–9
8. de Boer AH, Wissink J, Hagedoorn P et al (2007) In vitro performance testing of the novel Medspray wet aerosol inhaler based on the principle of Rayleigh breakup. Pharm Res 25:1186–1192
9. DeHaan WH, Finlay WH (2001) In vitro monodisperse aerosol deposition in a mouth and throat with six different inhalation devices. J Aerosol Med 14(3):361–367
10. Dolovich M, Bailey DL (2012) Positron emission tomography (PET) for assessing aerosol deposition of orally inhaled drug products. J Aerosol Med Pulm Drug Deliv 25(Suppl 1): S52–S71
11. EMA (2006) Guideline on the pharmaceutical quality of inhalation and nasal products. Document EMEA/CHMP/QWP/49313/2005 Corr
12. Finlay WH (2001) The mechanics of inhaled pharmaceutical aerosols. Academic, London
13. Ganderton D (1999) Targeted delivery of inhaled drugs: current challenges and future goals. J Aerosol Med 12(Suppl 1):S3–S8
14. Haefeli-Bleuer B, Weibel ER (1988) Morphometry of the human pulmonary acinus. Anat Rec 220:401–414
15. Hochrainer D et al (2005) Comparison of the aerosol velocity and spray duration of Respimat® Soft Mist™ inhaler and pressurized metered dose inhalers. J Aerosol Med 18:273–282
16. ICRP-66 (1994) The international commission on radiological protection. Elsevier Science Ltd, Oxford
17. Ling XY, Phang IY, Vancso GJ et al (2009) Stable and transparent superhydrophobic nanoparticle films. Langmuir 25:3260–3263
18. Lyra M (2009) Single photon emission tomography (SPECT) and 3D images evaluation in nuclear medicine. In: Chen Y-S (ed) Image processing. InTech. http://www.intechopen.com/books/image-processing/single-photon-emission-tomography-spect-and-3dimages-evaluation-in-nuclear-medicine
19. Möller W, Schuschnig U, Khadem Saba G et al (2010) Sinus drug delivery by pulsating aerosol: clinical proof of concept studies. Respir Drug Deliv 1:111–120
20. Munnik P, de Boer AH, Wissink J et al (2009) In vivo performance testing of the novel medspray wet aerosol inhaler. J Aerosol Med Pulm Drug Deliv 22(4):317–321
21. Netter FH (1982) Farbatlanten der Medizin, The ciba collection of medical illustrations, Band 4, Atmungsorgane. Georg Thieme Verlag, Stuttgart, p 25
22. Olsson B, Borgström L, Lundbäck H, Svensson M (2013) Validation of a general in vitro approach for prediction of total lung deposition in healthy adults for pharmaceutical inhalation products. J Aerosol Med Pulm Drug Deliv 26(6):355–369
23. Raabe OG, Yeh H, Schum GM, Phalen RF (1976) Tracheobronchial geometry: human, dog, rat, hamster—a compilation of selected data from the project respiratory tract deposition

models. U.S. Energy Research and Development Administration, Division of Biomedical and Environmental Research/Inhalation Toxicology Research Institute, Lovelace Foundation for Medical Education and Research, Albuquerque
24. Schoenbrodt T, Egen M, Heyder K et al (2010) Method development for deposition studies in a nasal cast. Respir Drug Deliv 2:445–450
25. Smutney et al (2014) Dry powder inhaler and system for drug delivery. Applicant Mannkind Corp., CA, USA. Patent no.: US 2014/0007873A1
26. Spallek M, Hochrainer D, Wachtel H (2002) Optimizing nozzles for soft mist inhalers. Respir Drug Deliv VIII(2):375–378
27. Van Hoeve et al (2010) Breakup of diminutive Rayleigh jets. Phys Fluids 22:122003
28. Williams G (2010) EPAG perspective—regulatory advances related to nasal spray pumps. In: Nasal drug delivery, management forum, London, 15 Apr 2010

Chapter 10
Drug Delivery Through Microneedles

R. Luttge

Abstract Drug delivery through microneedles is a new form of a pharmaceutical dosage system. While single microneedles have been clinically applied already, the out-of-plane integration of a multitude of microneedles in a pharmaceutical patch is a disruptive technology. To take advantage of micro- and nanofluidics, such active patches utilize microneedle array (MNA) technology. MNAs are microsystems that adopt their technical uniqueness by the choice of a fabrication technology. MNAs can be made of solid, hollow, porous, or dissolvable materials in a cost-effective manner by the so-called MEMS technology. However, key to their success will be a proof-of-concept in the clinic, which must demonstrate that the intradermal (nano) release of drugs and vaccines serve an unmet medical need. In this chapter, we discuss recently established MNA platform technologies and by means of a case study we assess novel opportunities for MNAs in drug and vaccine delivery arising from this novel skin interface.

10.1 Introduction

10.1.1 Medical Need for Microneedle-Assisted Drug Delivery

Best practices in medicine require well-trained healthcare personal and top medical products to reach market fitness. Today, continuous efforts in technological innovation enable us to offer the best possible care and cure to be customized to a patient's needs. The initial purpose of medicine is to diagnose a patient in case of physiological or mental signs of disease and subsequently provide a medical prescription to avoid or at least minimize long-term failure in vital body functions.

R. Luttge (✉)
Department of Mechanical Engineering, Microsystems Group and ICMS Institute for Complex Molecular Systems, Eindhoven University of Technology, Den Dolech 2, Eindhoven 5612 AZ, The Netherlands

MESA+ Institute for Nanotechnology, University of Twente and MyLife Technologies BV, Enschede 7500 AE, The Netherlands
e-mail: r.luttge@tue.nl

A. Dietzel (ed.), *Microsystems for Pharmatechnology*,
DOI 10.1007/978-3-319-26920-7_10

Often such therapies benefit from the administration of active pharmaceutical ingredients (API).

Generally, developments in the pharmaceutical industry aim for novel drug compounds based on existing and new classes of molecular formulations to combat life-threatening diseases. However, due to higher and higher expectations of healthcare systems in modern societies, it is evident that the costs for drug development and their trials for approval and acceptance have grown to a level that it has become a clear bottleneck. Nevertheless, we aim to extend research efforts further to be able to provide medicine also to the poorest members of society. Therefore, it is important to evaluate how novel technological concepts may help in reducing such costs. New technologies must create new opportunities to assist in saving resources including human capital worldwide and any advances in drug delivery technology is one such opportunity. From this point of view, the challenges may not actually lie in finding yet another interesting new drug compound but in administering it to a patient in the most effective way everywhere and for all.

In contemporary medicine, a wide range of drugs are formulated to be given orally, which can restrict bioavailability of a compound and therefore its use may be suboptimal. On the other hand, many recently developed drugs, the so-called biologics, which are based on the better understanding of the molecular working mechanisms of proteins and peptides, are actually broken down in the gastrointestinal tract and are difficult to formulate in a stable form.

Consequently, this category of drugs must be presented to the body in a different manner. While other routes of delivery may exist, in most cases that a pill does not suffice, the drug is presented to the body by injection using a needle and a syringe. In some cases, a patient may need to receive prolonged medication via intravenous therapy. The medicine may then only be given in a hospital setting, which again elevates healthcare cost compared to a delivery setting at home.

An attractive alternative route of delivery for such novel APIs is the delivery via the skin either by a topical application of a cream or by the administration of a pharmaceutical patch. Currently, there are about 25 drugs approved to be administrated in the dosage form of a patch. To broaden the utility of patch technology towards a larger scope of drugs and particular for large molecular weight drugs and vaccines, a way to circumvent the barrier function of the skin must be found. Compromising the skin's barrier function may have wide-scale implications and should only be considered in a very mild and controlled manner. Nonetheless, we commonly accept the use of the so-called hypodermic needle for breaking through the skin and releasing the drug cargo of a syringe or drip into the body, which can actually be considered quite a harsh way because it comes with a number of side effects. Many people feel discomfort by the inflicted pain, suffer from needle phobia and, most importantly, may experience other adverse reactions by the drug or vaccine being given by such type of bolus injection. Additionally, a large part of the drug may actually not reach its specific target.

One solution for the optimization of drug delivery and vaccination is to control release parameters more stringently and target a drug more specifically. Other means to bypass the barrier function than the hypodermic needle can provide

additional solutions to better drug delivery. Such alternative technologies may be found, for example, in electrical discharge, laser ablation, and the application of ultrasound. However, a more straightforward way to deliver drugs and vaccines into the skin could be found in the simple miniaturization of the hypodermic needle, whereby the insertion depth is highly controlled by the device itself. Assemblies of highly miniaturized needles, the so-called microneedle arrays (MNAs), may just provide an answer to many of the current needs for drug and vaccine delivery being faced in advanced medicine.

10.1.2 Microneedle Development in Pharmaceutical Technology

To tackle the above-stated unmet clinical need, the study of controlled nanorelease mechanism including microneedle-assisted skin patches is a new field of research. Charged with the tasks to boost patient compliance, overcome issues such as API stability, bioavailability, and toxicity and to improve efficacy in drug delivery, pharmaceutical researchers pick up MNAs as a good candidate for the development of novel dosage forms. Such novel technologies can encompass the release of drugs or vaccines simple by applying solid microneedles to the skin as a pretreatment. Subsequently, a well-established patch can be applied either in the form of a simple adhesive liner that contains the API dissolved in the polymer matrix of which it is made of or in the form of a chamber-like patch consisting of an adhesive and an extended drug reservoir containing the liquid formulation. Unfortunately, while being used already quite extensively in the cosmetic market, a pretreatment method is experienced as less reliable and cumbersome and has not found widespread clinical acceptance. The preferred microneedle-assisted drug delivery technology is envisaged by microneedles seamlessly integrated with the drug-containing patch to be applied in one touch. Often such an embodiment is called an active patch.

This requirement leads to a completely new patch design: the MNA, which contains a defined number of tiny microneedles projecting out-of-plane from a base plate. MNA patches are nowadays clearly recognized as a possible route of delivery via the skin by the experts. A variety of different configuration of such MNAs exist in research and development. Whereas all MNAs should combine two basic functions: (1) to provide the means of bypassing the skin barrier and (2) to act as a controlled release interface during the administration of a drug or vaccine via the skin. Pharmacokinetics of the technical varieties of such patch-type release mechanisms can be studied in vitro using either a piece of sliced animal or human skin in the so-called Franz-Cell, which is a well-defined diffusion setup used for these type of studies [28]. The Franz-Cell emulates the basic function of the blood circulation in keeping the skin moist and functional over an extended period of time after retrieval from the body. On the other hand, this setup is limited to the physicochemical investigation of an API's likelihood to pass the upper part of the skin only.

Of course, this is a very valuable model to categorize an API's transport efficiency against other compounds, which is an important aspect in formulation design.

More sophisticated pharmacokinetic studies include full-thickness ex vivo skin and animal models, which can take the complex interplay of biology at least partially into account during the process of an API reaching its target [2]. A suitable extent of such preclinical studies must be performed prior to being allowed to start first-in-man, i.e., experiments in the clinical phase.

10.1.3 Routes to Broaden MNA Applications

Governmentally funded research projects in technology are often initiated to better understand the novel scientific background and eventually assess the possible benefits and risks that a novel technology may have for society. This is also the case for drug delivery through microneedles. MNAs in their various customized forms may offer great potential in revolutionizing pharmaceutical markets, including their novel business models. Henceforth, a variety of projects throughout the world were started to investigate this conceptually totally new way of interfacing with the human body. Since MNAs are self-limiting medical devices being applied to the skin, these devices are most suitable for ease-of-use and self-administration applications and can become the ultimate drug delivery technology in the future.

Besides, MNAs may also be useful devices for novel approaches in diagnostic challenges such as the measurements of vital biosignals, e.g., electrical signals in conjunction with wearable electronics or the monitoring of biomarkers contained in body fluids such as capillary blood similar to the solutions found already in diabetes disease management. Either of these application ideas may provide its own business case and must be evaluated against the challenges and limitations of the current state-of-the-art in these various care and cure market sectors.

In the context of MNA research and development, however, it is important to realize that players in the pharmaceutical and health technology industries may have each very different interests. It is not easy to decide if further governmental investments in MNA technology really add to their market acceptance. It may be more likely a matter of regulations. Conferring, we already know about the side effects of drug delivery by hypodermic needle injections, one may question if it is still ethically accepted to administer drugs and vaccines by this route of administration even if alternative technology is available? Boldly summarized, MNA fabrication technologies are ample investigated since the 1990s. So, is it a technical challenge that we need to combat or the limitations of today's business models in these markets?

In this contribution, we will further focus on the technological aspects of microneedle arrays. Particularly, we will pay attention to MNA technology for its application in drug delivery and leaving microneedles for their application as a biosignal electrode aside. Microneedle-based diagnostics, e.g., by sampling interstitial fluid (or in some cases even blood) has also been vividly discussed in the

scientific literature [20, 36]. We will only briefly touch upon microneedle applications for diagnostic sampling in the context of closed-loop drug delivery systems in the next section.

In conclusion, first, we give an overview of what MNAs are and what they are good for. Secondly, we will provide a general insight in their fabrication methods and subsequently, we will discuss technical requirements for MNAs in transdermal drug delivery and vaccination technology and present the challenges of their development in perspective of a specific application case.

10.2 MNAs: A New Dosage Form

10.2.1 MNAs: What Are They?

Diverse types of microneedles exist consisting of either ordered or randomly distributed micro- or even nano needles across a base plate. Additionally, some microfabricated arrays are configured in an in-plane arrangement, lining up a set of microneedles being inserted similar to the hypodermic needle but at slightly different positions all at once. Generally, an MNA is defined as a number of microneedles arranged in a highly ordered and out-of-plan fashion with a base plate [21]. Here, we will focus on this out-of-plane class of microneedles with their technical varieties of their release approaches established in pharmaceutical technology (Fig. 10.1).

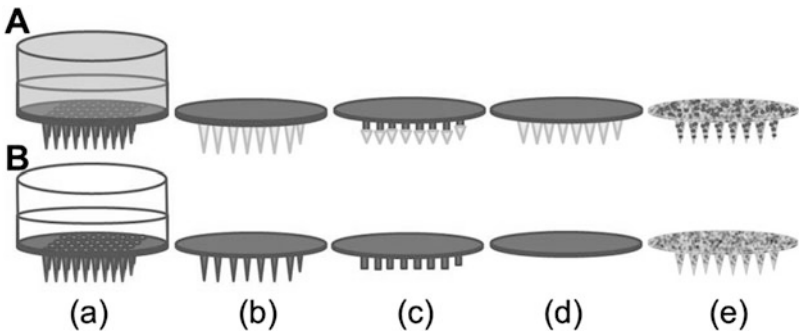

Fig. 10.1 Pharmaceutically established MNA concepts. The technical platforms are shown prior to attachment to the skin (**A**) and after (**B**). The main technical varieties are: MNA add-on with hollow microneedles serving as flow-through channels connecting a syringe or drug reservoir to the dermis (*a*); MNA with solid microneedles coated with a drug-laden layer (*b*); MNA with drug-laden dissolvable tips (*c*); MNA with fully dissolvable drug-laden microneedles (*d*); MNA with a nanopore structure in the microneedles being seamlessly connected to the nanopore structure in the MNA's base plate all made from the same material, whereas the nanopore structure acts as an intrinsic reservoir like a sponge (*e*)

All types of MNAs shown in Fig. 10.1 are microsystems that incorporate three main functions: (1) presenting a drug cargo to the skin, (2) penetrating the upper layer of the skin by the generation of micro-sized incisions, and (3) controlling release of the cargo by forming an intimate interface with the skin by means of exploiting the idea of a patch. Besides precision engineering technologies, MNAs have been demonstrated to be fabricated by a variety of MicroSystems Technologies (MST) often also called Micro-ElectroMechanical Systems (MEMS) technology. They are either made from metal, silicon, glass, polymers, or ceramics. Some of these systems may also explore on two types of materials, e.g., drug-laden microneedle tips from a dissolvable material and the non-dissolvable patch or an assembly of metal microneedles in a polymer base plate. Either of these technical solutions may be selected for their specific properties in defining a patch composition potentially fulfilling a particular clinical need.

MNAs that only pass the drug through the skin via the microneedles have been shown to serve as an add-on to a standard syringe. Nanopass Technologies Ltd. [16], Israel, and Debiotech SA [13], Switzerland, are commercial players in this field. A more compact approach of this concept may be based on integrated MEMS pumps as it has been also demonstrated, for example, by Debiotech. These systems lean on microfluidic inkjet technology as previously developed in the printing industry.

The two most promising configurations of MNAs in current pharmaceutical technology are the solid MNA utilizing a drug-laden coating on the microneedles' surface and MNAs with fully or partially dissolvable microneedles containing the drug in the matrix of the material they are made of. These types of MNAs are marketed, for example, by Corium International Inc., USA [12]. Alternatively, an MNA, which enables a drug cargo to be stored inside of its material in a more generic way, is the concept of a ceramic nanoporous (np)MNA, which is under development at MyLife Technologies BV, The Netherlands [15], and has been just recently confirmed in more detail for its utility in pharmaceutical patch technology [38].

10.2.2 MNAs: What Are They Good for?

ALZA Corporation (Palo Alto, USA), an enterprise in biomedical innovation acquired by Johnson and Johnson in 2001, has been describing as early as the year 1981 that there is a need for a new approach to pharmaceutical developments [44]. While the chemical approach to the invention and improvement of drug products are one mean to advance drug delivery, ALZA Corporation had been working on disruptive technology by implementing new dosage forms for administering medication. One such novel dosage form has been the administration of medication via the skin using an adhesive patch without any additional physical means for enhanced drug transport through the skin. Such a patch is generally applied by the patient once a day. With an eye on allowing to discretely and

comfortably wear such a patch underneath of one's clothing, it has a restricted reservoir function limited by the thickness of the patch and its surface area. Additionally, this passive dosage form via the skin is limited to small molecular and highly potent drugs due to the skin's function to act as a barrier. Introducing an active form of delivery via the skin by MNAs integrated into patch technology, however, was not considered for this purpose prior to the mid-1990s.

Despite microsystems technology being explored heavily throughout this period for microfluidics applications, there was a lack of precise and cost-effective MNA fabrication technology that could enable the integration of microneedles within a base plate in a robust and practical manner. For a relatively low density MNA, assembly of shortened high-precision hypodermic microneedles or glass pipettes into a base plate may have been performed instead by pick and place processing either manually or automatically [39]. Alternatively, laser ablation into a metal sheet and punching-through was also successfully realized as a method to fabricate MNAs [4, 5]. While these more traditional technical concepts for the fabrication of MNAs allowed for research and development of this specific dosage form, its present-day utility is yet a niche in pharmaceutical industry.

10.3 MNA Microfabrication Technologies

10.3.1 History

The development pipeline for microelectronic systems in healthcare may be manifold. These systems may be used to program and monitor the delivery need of a patient. One such solution in advanced disease management involving drug interventions in a personalized manner is a pre-programmable dose release schedule. While examples of such pre-programmable microprocessing units for transdermal delivery are known in the scientific literature for some time now [35], their current status in industry remains under development and studies mainly focus on one clinical parameter, i.e., the measurement of glucose [11, 17].

In this context of "smart" technologies, intelligent devices could also incorporate feedback monitoring of the concentration of specific metabolites in the skin. In this configuration, MNAs may not only work as a one-way device but as a two-way intelligent drug delivery and diagnostic system in one and the same patch. While this field of research has been overhyped since the year 2000, often referred to as micro total analysis systems or lab-on-a-chip devices, various microelectronic technologies are nowadays used in diabetes management though not necessarily in conjunctions with MNAs. There, frequent monitoring of blood glucose levels and pump calibration is required to maintain an appropriate delivery schedule. Unfortunately, due to sensor drift fully closed-loop feedback systems for prolonged periods of time may have to stay a dream. The investigation of microneedles as a microfluidic nanoportal to the body may be a first step towards the development of

such advanced medical systems. Fully integrated working prototypes of these systems, however, have not been demonstrated in clinical practice. Microneedle fabrication technologies as discussed in this chapter are highly compatible with production standards in microelectronics and should foster their applications in sensor-augmented drug delivery systems, too. Learning from the knowledge acquired at a device–skin interface based on the unique concept of MNAs can bridge the technology gap to closed-loop systems in the future.

10.3.2 Many Microneedles at Once: Utilizing Lithographic Masks

Photolithography, employing the exposure of many multiples of the same tiny features through a mask at once in a batch process, has been originally developed for the fabrication of the most successful microproduct so far: the integrated microcomputer chip [18]. Adopting microelectronic technologies, the generation of MNAs is also based on the faithful repetition of many of the same out-of-plane features all-over the wafer surface. In advanced MNA technologies, photolithography is applied in a variety of process steps to yield a 3D-structure that can either be used directly as an MNA or it will be adopted as a master for replication of the MNAs. MNAs present a class of devices related to the research field of microfluidics, which also capitalize on the development in the established microelectronics industry, and is described in its different facets in this book.

This new class of microfluidic devices sets its landmark in the entire Life Sciences with the introduction of the so-called Laboratory-on-a-Chip (LoC). These devices allow for a plethora of applications. Some are concerned directly with clinical applications, like the MNA, others being more in the area of the fundamental sciences such as cell biology. MNAs are either developed as a standalone device or integrated with sensors and actuators [27].

Lithographic techniques result in a tip radius of <1 μm, typical outer diameters below the 300 μm and very well-defined length in the range of a few micrometers to about 1 mm. Additionally, different needle densities from a few 1000 to as little as four single needles in a cm^2 were demonstrated with different technologies. The array layout may be circular or squared and even different lengths of microneedles may be incorporated in the same MNA by well-defined lithographic techniques. The ability of batch processing allows some means of cost reduction in the manufacturing process; however, material costs in the case of silicon may still be too high for applications of MNAs in medicine on the short-term perspective. It has been shown, for example, that hollow MNAs allow for a flow-through delivery of vaccines by connecting a syringe to the MNA (Fig. 10.1a), but it is a more logical aim to utilize MNAs in the form of a self-administered transdermal patch. Recent publications provide comprehensively reviews on microfabricated microneedles and evaluate their performance against other delivery techniques, for example, by McAllister et al. just to name one of the most prominent works [26].

With respect to high-tech means of fabricating MNAs, their benefits in pharmaceutical developments in drug delivery and vaccination technology, the different types of lithographic-based microneedle devices must be technically and economically compared to the more traditional means of fabrication such as precision engineering and assembly or laser ablation and punching. It will depend on the specific niche that a particular type of MNA will be utilized. Successful introduction of this active patch incorporating microneedles will also depend on the evaluation of technology safety and efficiency dependent on the MNA's release mechanism, which will to a certain extent be influenced by the selected microfabrication methods. In the following section, we will discuss some of the key microfabrication principles that are extensively discussed for the microfabrication of MNAs.

10.3.3 Microfabrication Principles

As mentioned previously many good scientific reviews have been published on microneedles including their fabrication methods and applications, the list of over 100 review papers in the years from 2001 to 2015 is too extensive to be fully addressed here. Therefore, we have selected a variety of key processes being used to explain and review the main microfabrication principles for microneedles in drug delivery and vaccination.

10.3.3.1 Photolithography

This is a technique that illuminates photosensitive polymeric material, called a resist, through a mask. Photolithography is amble utilized in microelectronics with thin layers of resist [24]. In this context of MNA fabrication, it may be applied either to pattern a silicon substrate for subsequent additional steps of etching of dedicated masking layers or it is directly employed in the fabrication process of an MNA by applying the so-called thick photoresist, specifically SU-8, which may be given a specific shape, e.g., by a combination of lithography and micromolding [22].

10.3.3.2 Laser-Assisted Microfabrication

Laser ablation, stereolithography, and two-photon polymerization are varieties of laser-assisted microfabrication methods often used in rapid prototyping of microdevices. Two-photon polymerization is a unique three-dimensional laser-assisted microfabrication technique being used for the fabrication of microneedles [7]. In some other text, this technique may even be called 3D printing and is performed in a polymeric resin. Stereolithography may explore also more complex

polymeric system containing micro- and nanoparticles such as silicon, silica, metal, or ceramic particles, often called filler materials. Such materials may be used in fine-tuning strength and other material properties such as surface charge and wettability, wear, and conductivity. In some of these cases, the polymer-based material may be fully converted to another material system, e.g., ceramics or metals. While resolution of stereolithography is restricted to about 5 μm, the resolution of two-photo polymerization maybe at the nanometer scale; however, then this fabrication method is very slow. Even with a micrometer resolution the technique is still slow for production standards of medical mass products, like needles and syringes. Laser ablation (cutting) directly into titanium or stainless steel sheets [26, 29] can be a feasible route to produce a medical product [19]; however, upscaling of these direct-write methods for MNA production is difficult and most of the MNAs being fabricated by this way are limited to research only. Nevertheless, when access to such techniques is available, they are great methods to allow for the study of a number of MNA variables such as microneedle length, needle array arrangement including density and total number of needles in a patch of different sizes. Additionally, conceptual design studies of specific tip shapes may be conducted and can help to investigate the influence of such parameters on the delivery performance. Finally, the technology may be used to fabricate a master structure for subsequent MNA production by micromolding.

10.3.3.3 Isotropic Wet Etching

This type of etching in silicon and thin films may be performed in MNA technology either for the patterning of masking layers or specifically to sharpen pillar structures to form a microneedle tip. In the latter, MNA devices may be designed as a combination of a needle shaft with a defined tip. For an MNA in a flow-through configuration, such structure was created, for example, by dry etching and saw dicing of a cross-bar pattern in silicon. This combination of process steps resulted in a highly ordered array of blunt squared columns, which are subsequently converted into sharp microneedles by isotopic wet etching in HNA [27]. This technique of isotropic wet etching in HNA (a mixture of nitric, fluoric, and acetic acid) can also be used to sharpen pillars made directly by reactive dry etching [43].

10.3.3.4 Silicon Bulk Micromachining

This technique exploits directional (anisotropic) forms of wet and dry etching in a single-crystalline silicon substrate [32] and may be performed in MNA technology to exploit the sharp transition of different etch-rates between crystal planes by etching through a mask opening. This opening results in an inverted pyramidal shape. Subsequently, these master shapes uniformly covering the substrate surface can be repetitive filled and exploited by cost-effective micromolding [1]. Anisotropic silicon wet etching can be combined with other process steps, such

as thick-resist photolithography and anisotropic deep dry-etching of silicon for the micromachining of unique, e.g., knife-like or very pointy, microneedle tips [6, 9, 22, 33].

10.3.3.5 Deep Dry-Etching

This dry-etching technique refers to the deep etching of a substrate through a mask opening, yielding either highly vertical sidewalls, e.g., high aspect ratios, as a result of the directional physical bombardment with highly energetic particles and ions alternated with deposition processes from the gas phase to protect the sidewall or by controlled plasma composition in the so-called black silicon method [10]. As mentioned above, this technique can assist in generating a knife-like feature in combination with wet etching in silicon. On the other hand, it has also been utilized for the deep-dry etch of pillars to act directly as an MNA. Some examples for MNAs are described that demonstrate that simply shrinkage of the pillar's diameter below a critical value may suffice the criteria to penetrate the skin [37]. Often also this technique is then combined with isotropic etching to sharpen the pillar tip or with metal deposition techniques. In the latter, the silicon can be selectively etched against the metal film, e.g., a metal such as nickel-iron, and a thin-walled microneedle feature can be realized [26].

10.3.3.6 Electroplating

This electro-assisted microfabrication technique, like the deposition of a thin-film, is an additive manufacturing technique. Particularly, when the goal is to achieve a metal MNA, electroplating may be used. Microstructure electroplating requires an inverted master structure, which first is made by either photolithography or other advanced lithographic illumination techniques. The electroplated microstructure is realized by exposing the inverted microstructured mold (often called a template in this field of work) formed atop of a conductive seed-layer into a bath with a metal-ion solution and subsequently applying a homogenous electric field between the seed-layer and a counter electrode. Next, the mold will be filled over time by the electro-deposited metal-ions from the bath in dependence of the applied current density. Hence, this process is also referred to as electroforming and in combination with advanced X-ray lithography may yield particularly long and mechanically strong microneedles. Furthermore, high-precision electroforming may be performed with templates realized by micromolding to allow for an economically feasible route of manufacture [31].

10.3.3.7 Soft-Lithography

Soft-lithography [42] is a technique that is a technical variant of micromolding. Since it is utilized in this context of MNAs specifically in the field of dissolvable microneedles and the manufacture of ceramic nanoporous microneedles, which we will introduce also in the case study later below, we briefly introduce it here as one of the MNA microfabrication principles. An MNA structure is made by any of the techniques mentioned above, and consequently this shape is transferred into poly (dimethylsiloxane), PDMS, to present after replication the inverted shape of the microneedle features [30]. It is this soft-mold which can be copied in a diversity of materials, including ceramic slurry or dissolvable polymers and sugars [3].

10.3.4 Upscaling Production Capacity

Ultimate obstacles in the development of MNAs for pharmaceutical technology are twofold: (1) the lack of technologies that can be up-scaled to mass production at an appropriate quality and expenses level; (2) the lack of characterization methods that facilitate the approval of the MNAs by regulatory affairs. While it is one challenge to demonstrate even a relatively low number of devices made by any of the fabrication principles described above in an academic laboratory, the production of a sufficient number of devices to test the fundamental working principle of these devices for drug delivery is another.

Although silicon micromachining techniques now exists, which capitalizing on the industrial standards in microelectronics or the so-called MEMS technology, investments into a new production line is still very high. Besides general concerns of using silicon as a biomaterial, additionally, material costs with a value of 1€ per cm^2 for plain silicon is also keeping the decision-making process for MNA technology in pharmaceutical industry at a low pace. Henceforth, replication techniques by micromolding have been introduced as a feasible route for the cost-effective fabrication of a multitude of MNAs from a high-precision master, which can be formed by the aforementioned MEMS technologies. These replication technologies also open new routes to carry out experiments with other types of materials than classically known to be patterned at high precision. For example, replication allows the generation of MNAs with (bio)dissolvable microneedles (Fig. 10.1d). The latter has led to the introduction of MNAs in extensive preclinical and clinical pharmaceutical research and product development projects during the course of the last 10 years. An overview of MNAs in medicine will be given in the following section.

10.4 MNAs in Medicine: An Overview

Transdermal MNA devices are ranked by the Food and Drug Administration as an invasive device, since the skin barrier is bypassed and probably also ruptured at deeper layers than the stratum granulosum. The latter may have as a side effect that also other substances than the intended drug may intrude the body. Parts of an MNA patch, which are in direct contact with tissue or risking contact through the handling of the device have to fulfill stringent rules prior to medical approval. Microbial load must be characterized as one factor in the failure analysis per technology since devices that may interfere with the body's immune system can generate adverse reactions such as skin rash or even more unfavorable systemic effects such as infections or poisoning.

The definition of material properties for MNAs is defined mainly by its surface charge and fracture force. Both values are not yet fully understood for microstructures of the size of the microneedles in an MNA since measurement values must be generated under nonideal circumstances compared to measurements performed in the bulk material and may deviate from the values in the bulk anyway because of a size effect. Besides, the characterization must be performed with and without the drug cargo as well as after packaging and storing the medical product in its final dosage form. Toxicity of the materials and their combinations with the drugs may be another issue. These validation studies are labor intensive and time consuming and cannot be transferred in general terms from one type of MNA technology to another. Despite MNAs' general potential being widely accepted in the community of drug delivery technology experts, the benefits received from using an MNA versus the use of a hyperdermic needle and syringe is not yet fully proven. The performance of a specific material in the case of drug interference, adsorption, etc. during storage and delivery also has to be addressed for the different novel MNA platform technologies and will have to be studied per medical indication prior to being able to draw general conclusions.

All in all, for these medical developments one has to bear in mind that MNAs are in competition with other standardized, ultra-fine needle systems either integrated in a patient friendly pen-like delivery system or as a classical hypodermic needle mounted on a syringe [14, 18] as well as other means of techniques to penetrate the skin [34]. A traditional needle and syringe delivery system has over the counter cost for a disposable needle in between $0.05 and $0.20. Micromolded MNAs probably can compete with such a low pricing regime. On the other hand, MNAs are a disruptive drug delivery method within the patch technology industry and enables compound uptake by the epidermal layer even of large molecules at more comfortable conditions, which may allow for a higher pricing regime compared to needle and syringe. The study of the pharmacokinetics and pharmacodynamics in these new interfaces needs more research prior to its widespread utilization for the delivery of large molecules and vaccines. Small molecule release into the skin are already far better understood and have been marketed at a large volume in industrial pharmacy in the form of passive patches about 30 years ago. The further

study of similar mechanism for the release of insulin and vaccines utilizing a single microneedle at a controlled insertion depth can accelerate the knowledge of new delivery solutions by MNAs, too [14, 25].

Alternatively, early investor strategies already led to a new MNA drug delivery technology sector by start-ups of which Zosano is one of the key players [19]. Zosano's Macroflux® MNAs (former ALZA) have been described in the scientific literature for more than 10 years. Currently, they maintain for a number of indications a product pipeline with one lead candidate in clinical phase 2. To upgrade MNA technology from a device that purely creates microscale aqueous conduits in the skin for a subsequent application of an occlusive patch into a fully packaged and safe drug delivery system comparable to the Macroflux® will clearly require more than just engineering ingenuity.

Any platform technology must be designed and manufactured as such that it will not only allow testing for a small number of demonstrators for transport studies of a few drug compounds in research but ideally serve as a screening instrument utilizing harvested skin or other suitable models to be able to reach clinical phase. To evaluate the most promising technology-product combinations of an API with an MNA technology prior to elevating the experimental level to an animal model is another challenge for medical engineering. Ideally, the business model for a specific combination should be evaluated not just based on technology match (feasibility), but it must also present a better healthcare solution for disease management, which will subsequently justify investments into clinical trials and even more investments into the entire development chain. The state-of-the-art of MNA applications in medicine for vaccination is further illustrated by selected scientific literature and is highlighted by a specific case study in the next section.

With respect to research in drug delivery technology, devices from the three well-known technology categories: silicon bulk micromachining, soft-lithography, and precision engineering have shown enhanced transdermal delivery rates by circumventing the skin's barrier function. Exact data of efficacy/bioavailability, however, are currently still researched. Further, the devices show no or very little side effects and are considered to be safe with negligible discomfort for the patient during application. Besides the reduction of pain and a higher likelihood to target specific biological processes, other clear advantages compared to the hypodermic needle/syringe concept cannot yet be confirmed. Clinical data on pharmacodynamics for systemic human uptake have not been completed for MNAs. Nevertheless, there is no doubt that MNA-integrated patches can be manufactured and commercialized as an affordable solution for the painless intradermal delivery of APIs such as insulin, biologics, or their analogues and vaccines in the near future.

In conclusion, a sufficiently high technology readiness level of a variety of MNAs has been proven [19]. However, none of the MNA systems discussed are ready for application in clinical practice. To address the urgency of the topic publically, great efforts by MNA researchers are made by moving also into the investigation of factors for MNA acceptance [29].

10.5 Applying MNAs for Vaccination

10.5.1 Transcutaneous Immunization

With respect to drug delivery technology, the realization of multitudes of many microneedles in the form of an ordered array attached to the skin may offer advantages over the traditional approaches using hypodermic needles or chemical penetration enhancers. For certain applications, for example, whereby the target is actually in the skin, the insertion of active compounds into the viable epidermis across a much larger skin area compared to the insertion of compound by needle and syringe will probably further increase efficacy of the therapy. This is especially beneficial in the cases of the delivery of a vaccine. The viable epidermis is crowded with antigen-presenting cells, and these can be perfectly addressed by transcutaneous immunization by using a patch [8].

Based on the vast amount of scientific literature on microneedles, it can be concluded that they are virtually pain-free compared to the hypodermic needle and potentially reduce side effects by cell targeting. In this respect, MNA patches are perceived to be particularly valuable for the delivery of childhood vaccines, conversely, it seems, there is no concise business model to innovate drug delivery technology in this industry, so far. In the case study below, we will address a specific type of MNAs, the ceramic npMNA [3] already introduced in the sections above. Additional scientific experiments may lead to understand the clinical advantage of this unique technology better and assist in its implementation.

10.5.2 Case Study: npMNAs in Immunotherapy

The realization of multitudes of microneedles in the form of a patch attached to the skin offers advantages over the traditional approaches using hypodermic needles in vaccination. Despite the highly promising nature of such type of devices, their introduction to the market is hampered by high costs in development. One such cost factor is testing of MNAs for their penetration efficiency, for their release mechanism and for their compatibility with the appropriate drug dosage. Scientific research in drug delivery technology and specifically immunology has demonstrated that MNAs are generally fit for this application. Also in the case of ceramic nanoporous (np)MNAs (Fig. 10.2), a similar reality check was performed [2, 38, 40] and we can conclude that this specific technology is generally feasible to deliver vaccines into the skin.

For this specific ceramic npMNA platform technology, the question remains if this unique way of release can be implemented in the clinic in competition with any of the other MNA or vaccine delivery technologies. In other words, when is such a new platform technology ready for investments by big pharma to take a lead into advanced clinical phases?

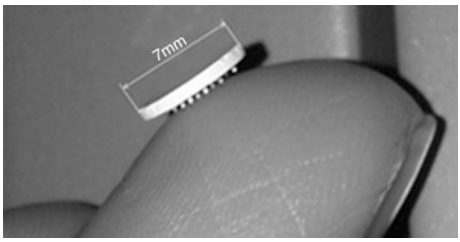

Fig. 10.2 Example of an npMNA configuration atop of a finger for comparison

We started our research on this specific MNA technology at University of Twente, The Netherlands, in 2004 in the framework of an ongoing nationally funded academic research project by the Dutch Technology Foundation STW, applied science division of NWO and the Technology Program of the Ministry of Economic Affairs. Firstly, we invented a soft-lithography technology for replication of microneedles into polymers with a unique tip shape [6] following our aim for an optimized flow-through MNA based on our previous research results in this field. However, in due course of the project we found that we were able to create a totally new class of MNA devices by performing micromolding of this unique shape of microneedles into a ceramic nanoporous material by means of filling the mold with a well-defined ceramic nanopowder slurry [23]. The soft-lithographic process provides for a flexible production mold, which facilitates highly conformal replication of the MEMS microstructure into a ceramic green body. The latter is converted into a nanoporous ceramic by high temperature binder decomposition [3]. This MNA technology can lead to a variety of different tip shapes with a sharpness of a tip radius of below 10 μm, which is capable of penetrating human skin [2] by the application of loads as low as 300 g of a weight. Most likely this is possible due to its very specific tip geometry being inspired by the knife-like tip of a classical hypodermic needle. These types of geometries were previously investigated by direct silicon etching [6]. Based on the ceramics open pore structure at the nanoscale, the MNA can be filled directly with a vaccine from solution by capillary forces (Fig. 10.3) and released upon insertion into the skin by diffusion [2].

One may expect this MNA technology is now ready for licensing and probably it is, but still such an investor must be found. To enable this commercialization path, University of Twente's Holding Technopolis Twente BV created a spin-off and together with STW granted the exclusive commercial rights of her npMNA technology to MyLife Technology BV, The Netherlands [15]. A set of business activities have been started since the start-up's inauguration in February 2012.

The company's activities now focus on product and business development of its MNA platform for patch technology in drug and vaccine delivery. In this contribution, we wish to illustrate just a few considerations that may be relevant to the use of an npMNA for its inventive uniqueness in the clinic someday and move forward on the value creation curve. The npMNA platform technology is selected here just by means of an example. Of course, the aspects given below may also apply to other types of MNA patches being investigated and developed throughout the world.

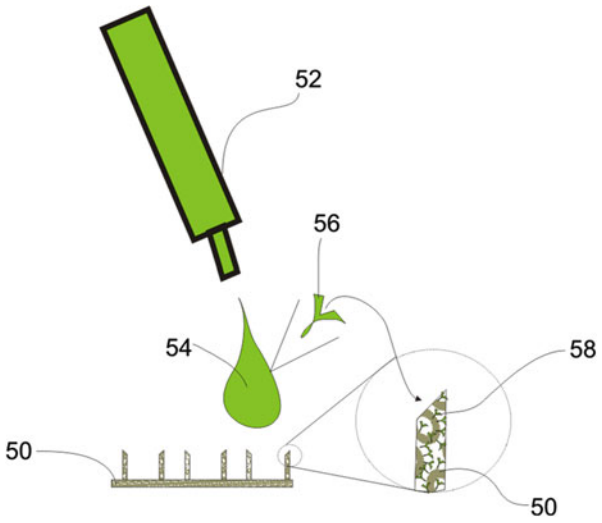

Fig. 10.3 Conceptual representation of the filling process for npMNAs [23]

10.5.2.1 Validating for Technology Uniqueness

In contemporary medicine, drug therapies exist that can be further improved simply by controlling the rate at which the drug enters the bloodstream. For these specific medical indications, it can be particularly beneficial to use a ceramic npMNA patch instead. Here, the microneedles and their base plate are nanoporous and seamlessly connected. One route to find the best technology-product match could be related to the scientific validation of the influence of using a nanoporous material at the skin interface. The materials' extremely high surface-to-volume ratio due to its porosity (Fig. 10.4) should be explored thoroughly to understand the release mechanism found in such a nanofluidic system. In the creation of an intimate contact of the upper skin layer with the very unique nanoporous aluminum oxide surface transport of molecular compounds is not solely diffusion-based anymore. To investigate this multiscale transport problem in depth may open new opportunities to fine-tune release being characterized rather by a multistep profile then just a tiny bolus injection per microneedle in an array. This effect may be similar to the early developments of a slow release pill, and we may be also able to incorporate osmotic agents in the open pore structure of an npMNAs.

In case of vaccination, its efficacy pivots on ease of access of the vaccine to the dendritic cells in the skin [8]. Delivery of a vaccine through conventional intradermal (i.d.) injection is technically challenging, and often fails due to ineffective vaccine depot formation in the subcutaneous fatty tissue, hindering its widespread implementation. We envisage that immune adjuvant delivery through a nanoporous oxide/skin interface can lead to novel routes of vaccination. A nanoporous oxide

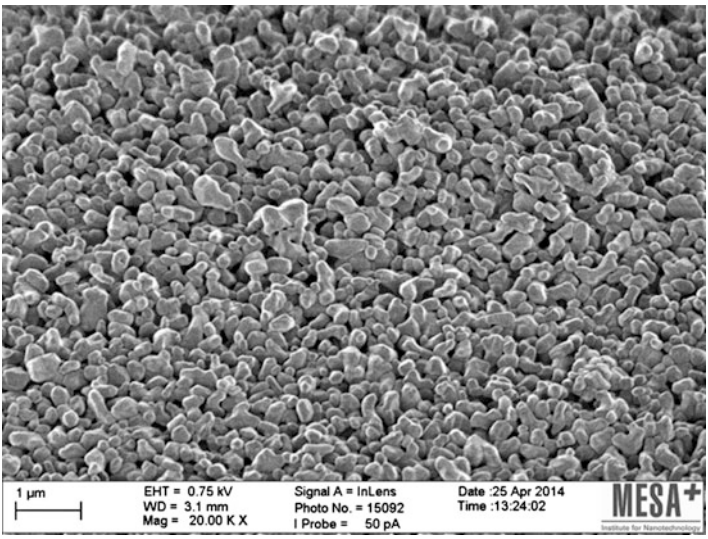

Fig. 10.4 Scanning electron micrograph of the nanoporosity of an npMNA (Image courtesy: M. Smithers, MESA+, 2014)

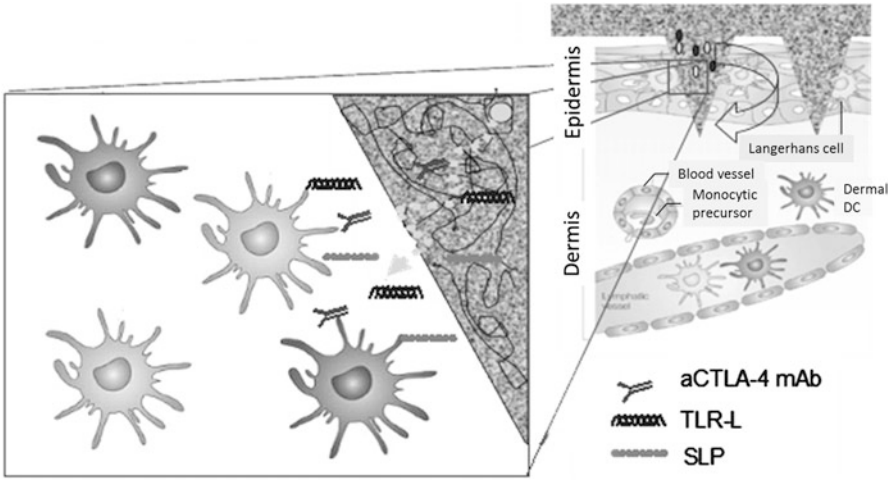

Fig. 10.5 Schematic representation of microneedle/nanoporous oxide interface at the skin for one example of a transcutaneous immunization application (Image courtesy: T.D. de Gruijl, VUmc, 2010)

microneedle patch technology forms a chemically and environmentally very stable platform. Such stable platform is needed to enable reliable self-administration and thus facilitate logistically simplified repeated booster vaccination schemes as required, for example, to induce an optimal antitumor immune response (Fig. 10.5).

10.5.2.2 Characterization of Release Profiles

It is suggested that the particular temporal and positional controlled slow release of minute amounts of drugs or vaccines from an npMNA patch over up to 8 h (or roughly 1 day) can offer totally new pathways of compound targeting not possible to be studied by traditional means of intradermal release of API into the skin. In an initial release study with the cancer vaccine candidate gp100 [41] (performed by our partners at VU University Medical Center, Amsterdam, The Netherlands), we were able to demonstrate this slow release effect by using gp100-laden npMNAs on a human ex viv*o* skin model, previously introduced [2], receiving a biopsy at two time points (Fig. 10.6).

Considering the above uniqueness, the ceramic npMNA release mechanisms may be optimized further. To be able to utilize this specific reservoir function of the device, an enforced attachment of the npMNA with the skin is needed, e.g., applying an adhesive atop of the MNA patch. This attachment will allow for an intimate contact between the MNA patch and the skin throughout the immunization procedure. Generally speaking, such npMNA release profile yields a relatively low end-point dosage and may be narrowed in its utility to a particular niche of compounds and medical indications.

10.5.2.3 Validating Geometric Features of the npMNA for Their Function

The design tested in the gp100 release study above is a specific npMNA with a relatively high density of microneedles across its surface (Fig. 10.7). The current production relies on reliably punching of round npMNA patches from the green body prior to sintering with diameters of about 5–12 mm. Based on this size an

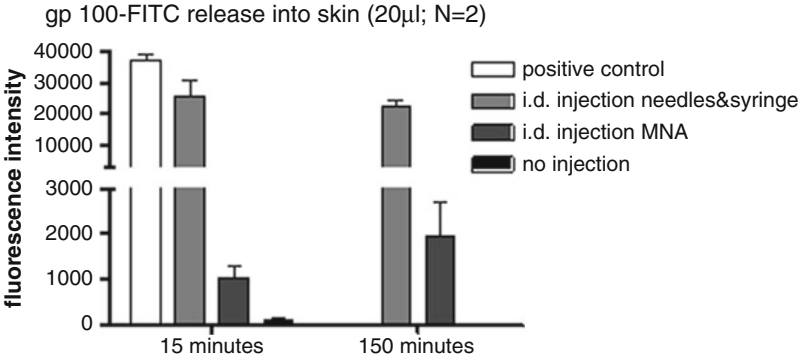

Fig. 10.6 gp100-FITC fluorescence signals collected from digested biopsies and quantified on a Fluostar spectrofluorimeter (BMG Labtech) at 485/520 nm comparing the release of a hypodermic needle versus npMNA (Image courtesy: M. Boks, VUmc, 2014)

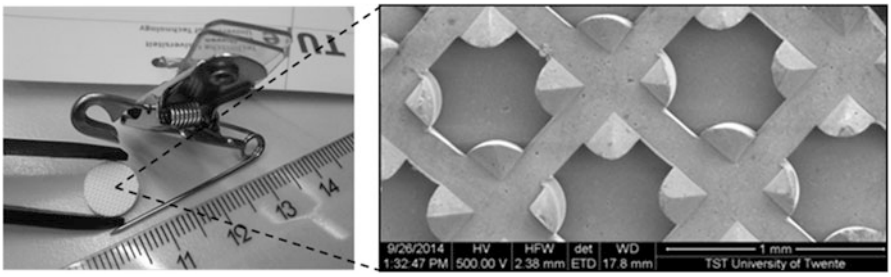

Fig. 10.7 Example of an npMNA patch (Right image courtesy: P. van der Linde, University of Twente, 2014)

applicator should be designed and marketed as a complementary product with an MNA patch and an adhesive.

The overall usable area of the mold covers a surface of a circle of a diameter of about 60–70 mm, which would define also the maximal size of a patch in this stage of development. Due to the stiffness of a ceramic npMNA, however, there are only few places on the body that such a large (non-flexible) patch could be placed without patient discomfort. Of course, this would also depend on the time interval the patch needs to be pressed tight to the skin for the specific purpose of administration. However, considering relatively long application times and keeping the current status of development in mind, we anticipate that this particular npMNA technology may be limited to quite low end-point dosage regime, probably in the microgram range. This dosage is perfectly fine for vaccination. However, bearing this in mind also analytical challenges probably need to be overcome to fully evaluate the platform technology's clinical potential.

Scientific aspects to be determined are whether (epi)dermal nanorelease-mediated delivery of vaccine from the nanopores in the microneedles acts as a reservoir, which is superior over conventional i.d. delivery. Dependent on the various geometric designs, the ex vivo delivery efficacy of npMNA vaccine formulations may be directly compared to conventional i.d. injection of vaccines in a human skin explant model [2].

The ultimate goal of skin-targeted vaccines is the specific activation of effector T cells. The subcutaneous C57BL/6 mouse model should be further employed, since it provides a basis for screening of experimental therapies for both in the prophylactic and therapeutic setting [2]. Vaccinations may be given in a prime/boost regimen at an appropriate time interval of several days.

Much more simplified models, e.g., an eggplant [40], could be useful to characterize the geometrical features of an npMNA patch and its delivery performance (Fig. 10.8).

For a more thorough mechanical evaluation, we suggest to work in such benchmark experiments with a ballistic gel model of the skin, which can guarantee mechanically robust boundary conditions to test different design features of the microneedles, which could be made also ready for detailed nanofluidic investigations in conjunction with appropriate confocal microscopy techniques.

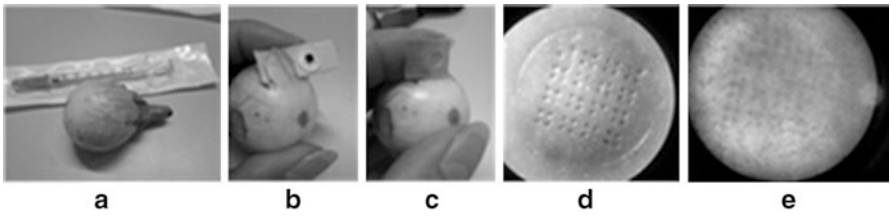

Fig. 10.8 Oversimplified model for the design of a delivery experiment with npMNAs. Eggplant and syringe (**a**); Dissected eggplant and npMNA applied by a plaster and a dye readily dispensed onto the npMNA (**b**); npMNA is pressed onto the outside skin of the eggplant (**c**); insertion marks on the outside of the eggplant (**d**); diffused dye on the inner side of the eggplant skin (**e**)

10.6 Conclusion

In this chapter, we introduced the mechanisms of drug and vaccine release via the skin by means of microneedles. Like an electronic switch in the micro-integrated circuit, microneedles arranged in an array are multitudes of the same feature across a relatively large surface area; hence, these can be realized by lithography. Access to microelectronics technology through foundry services inspired many other industries to utilize it for their innovative products including the fabrication of microneedle arrays.

A great many new microfabrication technologies serve now the pharmaceutical sciences and feasibility for upscaling manufacture of MNAs has been evaluated, too. Exploiting MEMS technology for the fabrication of high-precision molds is also available and offers various routes for the fabrication of MNAs by replication exploring detailed material choices. The abundant, robust production of MNAs by these different ways of manufacture should pave their way into the pharmaceutical industry and later into the clinic to be fully explored as a new dosage form of choice.

Obviously, this solution by utilizing microneedles does not come without challenges. To guarantee reliable penetration of the skin and the possible limitations in drug dosage are amongst the biggest issues of this new form of delivery and must be addressed by engineering design of such devices using suitable models. Additionally, the study of pharmacokinetics as well as pharmacodynamics in drug delivery technology via an active device on the skin is a fairly new field of pharmaceutics. Nevertheless, verification of the device quality and pharmacokinetics and—dynamics are currently carefully benchmarked in preclinical and clinical studies and future research and development should focus on the issues remaining in relation to regulatory approval and clinical acceptance of such devices. All in all, the use of MNAs in pharmaceutical technology is still in need for appropriate method development in characterizing MNAs against established standards in drug and vaccine delivery.

In summary, we contemplated the utility of MNAs for (trans)dermal drug release and vaccination in this contribution. We discussed the variety of configurations and

properties of these specific microsystems and gave some guidelines for their further technical assessment and development based on a case study applying ceramic nanoporous MNAs for their unique nanofluidic release mode in transcutaneous immunization therapy.

References

1. 3M's solid microstructured transdermal system (sMTS). www.3M.com/dds. Accessed 20 Aug 2015
2. Boks MA, Unger WWJ, Engels S, Ambrosini M, van Kooyk Y, Luttge R (2015) Controlled release of a model vaccine by nanoporous ceramic microneedle arrays. Int J Pharm 491 (1–2):375–383. doi:10.1016/j.ijpharm.2015.06.025
3. Bystrova SN, Luttge R (2011) Micromolding for ceramic microneedle arrays. Microelectron Eng 88(8):1681–1684
4. Cormier M, Johnson B, Ameri M, Nyam K, Libiran L, Zhang DD, Daddona P (2004) Transdermal delivery of desmopressin using a coated microneedle array patch system. J Control Release 9(3):503–511. http://dx.doi.org/10.1016/j.jconrel.2004.04.003
5. Cormier M, Neukermans AP, Block B, Theeuwes FT, Amkraut AA (1999) Device for enhancing transdermal agent delivery or sampling. European Patent 0914178
6. Gardeniers HJGE, Luttge R, Berenschot EJW et al (2003) Silicon micromachined hollow microneedles for transdermal liquid transport. J Microelectromech Syst 12:855–862
7. Gittard SD, Ovsianikov A, Chichkov BN, Doraiswamy A, Narayan RJ (2010) Two photon polymerization of microneedles for transdermal drug delivery. Expert Opin Drug Deliv 7 (4):513–533. doi:10.1517/17425241003628171
8. Glenn GM, Taylor DN, Li X, Frankel S, Montemarano A, Alving CR (2000) Transcutaneous immunization: a human vaccine delivery strategy using a patch. Nat Med 6:1403–1406. doi:10.1038/82225
9. Griss P, Stemme G (2003) Side-opened out-of-plane microneedles for microfluidic transdermal liquid transfer. J Microelectromech Syst 12:296–301
10. Henry S, McAllister DV, Allen MG, Prausnitz MR (1998) Microfabricated microneedles: a novel approach to transdermal drug delivery. J Pharm Sci 87:922–925. doi:10.1021/js980042+
11. http://echotx.com/technology/. Accessed 20 Aug 2015
12. http://www.coriumgroup.com/. Accessed 20 Aug 2015
13. http://www.debiotech.com. Accessed 20 Aug 2015
14. http://www.fluzone.com/health-care-professionals/fluzone-intradermal-vaccine.cfm. Accessed 20 Aug 2015
15. http://www.mylifetechnologies.nl/. Accessed 20 Aug 2015
16. http://www.nanopass.com/. Accessed 20 Aug 2015
17. http://www.nemauramedical.com/. Accessed 20 Aug 2015
18. http://www.uneedle.com/. Accessed 20 Aug 2015
19. http://www.zosanopharma.com/. Accessed 20 Aug 2015
20. Jina A, Tierney MJ, Tamada JA, McGill S, Desai S, Chua B, Chang A, Christiansen M (2014) Design, development, and evaluation of a novel microneedle array-based continuous glucose monitor. J Diabetes Sci Technol 8(3):483–487. doi:10.1177/1932296814526191
21. Kim Y-C, Park J-H, Prausnitz MR (2012) Microneedles for drug and vaccine delivery. Adv Drug Deliv Rev 64(14):1547–1568. doi:10.1016/j.addr.2012.04.005
22. Luttge R, Berenschot EJW, de Boer MJ, Altpeter DM, Vrouwe EX, van den Berg A, Elwenspoek M (2007) Integrated lithographic molding for microneedle-based devices. J Microelectromech Syst 16:872–884

23. Lüttge R, Bystrova SN, Van Bennekom JG, Domanski M, Loeters PWH, Lammertink RGH, Winnubst AJA (2008) Integrated microneedle array and a method for manufacturing thereof. European Patent Application No. 08152571.9
24. Mack CA (2007) Fundamental principles of optical lithography. The science of microfabrication. Wiley, Chichester
25. Martanto W, Moore JS, Kashlan O et al (2006) Microinfusion using hollow microneedles. Pharm Res 23:104–113
26. McAllister DV, Wang PM, Davis SP, Park J-H, Canatella PJ, Allen MG, Prausnitz MR (2003) Microfabricated needles for transdermal delivery of macromolecules and nanoparticles: fabrication methods and transport studies. Proc Natl Acad Sci USA 100(24):13755–13760. doi:10.1073/pnas.2331316100
27. Mukerjee EV, Collins SD, Isseroff RR, Smith RL (2004) Microneedle array for transdermal biological fluid extraction and in situ analysis. Sens Actuators A Phys 114:267–275
28. Ng S-F, Rouse JJ, Sanderson FD, Meidan V, Eccleston GM (2010) Validation of a static Franz diffusion cell system for in vitro permeation studies. AAPS PharmSciTech 11(3):1432–1441. doi:10.1208/s12249-010-9522-9
29. Norman JJ, Arya JM, McClain MA, Frew PM, Meltzer MI, Prausnitz MR (2014) Microneedle patches: usability and acceptability for self-vaccination against influenza. Vaccine 32 (16):1856–1862. http://dx.doi.org/10.1016/j.vaccine.2014.01.076
30. Park J-H, Allen MG, Prausnitz MR (2005) Biodegradable polymer microneedles: fabrication, mechanics and transdermal drug delivery. J Control Release 104(1):51–66. http://dx.doi.org/10.1016/j.jconrel.2005.02.002
31. Perennes F, Marmiroli B, Matteucci M, Tormen M, Vaccari L, Fabrizio ED (2006) Sharp beveled tip hollow microneedle arrays fabricated by LIGA and 3D soft lithography with polyvinyl alcohol. J Micromech Microeng 16:473–479
32. Petersen KE (1982) Silicon as a mechanical material. Proc IEEE 70:420–457
33. Roxhed N, Gasser TC, Griss P et al (2007) Penetration-enhanced ultrasharp microneedles and prediction on skin interaction for efficient transdermal drug delivery. J Microelectromech Syst 16:1429–1440
34. Schoellhammer CM, Blankschtein D, Langer R (2014) Skin permeabilization for transdermal drug delivery: recent advances and future prospects. Expert Opin Drug Deliv 11(3):393–407. doi:10.1517/17425247.2014.875528
35. Smart WH, Subramanian K (2000) Diabetes Technol Ther 2(4):549–559. doi:10.1089/15209150050501961
36. Suzuki H, Tokuda T, Kobayashi K (2002) A disposable "intelligent mosquito" with a reversible sampling mechanism using the volume-phase transition of a gel. Sens Actuator B Chem 83:53–59
37. Teo MAL, Shearwood C, Ng KC, Lu J, Moochhala S (2005) In vitro and in vivo characterization of MEMS microneedles. Biomed Microdevices 7:47–52
38. van der Maaden K, Luttge R, Vos PJ, Bouwstra J, Kersten G, Ploemen I (2015) Microneedle-based drug and vaccine delivery via nanoporous microneedle arrays. Drug Deliv Transl Res 5 (4):97–406. doi:10.1007/s13346-015-0238-y
39. Verbaan FJ, Bal SM, van den Berg DJ, Groenink WH, Verpoorten H, Lüttge R, Bouwstra JA (2007) Assembled microneedle arrays enhance the transport of compounds varying over a large range of molecular weight across human dermatomed skin. J Control Release 117:238–245
40. Verhoeven M, Bystrova S, Winnubst L, Qureshi H, de Gruijl TD, Scheper RJ, Luttge R (2012) Applying ceramic nanoporous microneedle arrays as a transport interface in egg plants and an ex-vivo human skin model. Microelectron Eng 98:659–662. http://dx.doi.org/10.1016/j.mee.2012.07.022
41. Weidle UH, Georges G, Tiefenthaler G (2014) TCR-MHC/peptide interaction: prospects for new anti-tumoral agents. Cancer Genomics Proteomics 11:267–278
42. Xia Y, Whitesides GM (1998) Soft lithography. Annu Rev Mater Sci 28:153–184

43. Xie Y, Xu B, Gao Y (2005) Controlled transdermal delivery of model drug compounds by MEMS microneedle array. Nanomedicine 1(2):184–190. http://dx.doi.org/10.1016/j.nano.2005.03.001
44. Zaffaroni A (1981) ALZA: an enterprise in biomedical innovation. Technovation 1:135–146

Chapter 11
Organ on Chip

N. Beißner, T. Lorenz, and S. Reichl

Abstract The process of new drug development is both time and cost intensive. Therefore, all test systems, in particular during the pre-clinical phase, have to provide reliable results to minimize the risk of failure at a later stage of drug development. However, current pre-clinical studies are mainly performed using experimental animals and in vitro cell culture models, which both are not able to reliably emulate human physiology. As a consequence, the common test procedures may be one reason for late-stage drug failures. Hence, improved test systems are needed, which mimic the diverse and dynamic human physiology and are well controllable and suitable for high-throughput screening.

High expectations have been raised by the development of organ on chip (OOC) systems. These novel microdevices combine the benefits of an engineered, physiological-like microenvironment with the advantages of well-characterized human cells. Furthermore, due to the small dimensions of OOCs, it is possible to work with small amounts of drugs, so OOCs are suitable for high-throughput screening. Moreover, OOCs can include biosensors that allow online measurements of the viability and functionality of the cells in real time. Additionally, OOCs containing tissues from different origins can be connected by microfluidic techniques to form multiple OOCs.

This chapter takes a closer look at the technical as well as the cellular aspects of OOC technology. Subsequently, the presentation of various already developed OOCs and promising future applications in pharmaceutical research and development shall underline the enormous potential of OOCs in the reduction of animal experiments and the precise emulation of human physiology.

N. Beißner • S. Reichl (✉)
Institut für Pharmazeutische Technologie, Technische Universität Braunschweig, Mendelssohnstr. 1, Braunschweig 38106, Germany

PVZ—Center of Pharmaceutical Engineering, Technische Universität Braunschweig, Franz-Liszt-Str. 35 A, Braunschweig 38106, Germany
e-mail: s.reichl@tu-braunschweig.de

T. Lorenz
IMT—Institute of Microtechnology, Technische Universität Braunschweig, Alte Salzdahlumer Str. 203, Braunschweig 38124, Germany

A. Dietzel (ed.), *Microsystems for Pharmatechnology*,
DOI 10.1007/978-3-319-26920-7_11

11.1 Introduction

The development of new drugs is complex, scientifically demanding, and economically challenging because such a process is both time and cost intensive. In particular, during the second phase of drug development, or the pre-clinical phase, the right decisions should be made regarding the further development of a new drug substance, given that failure of the substance during the third phase, or the clinical phase, causes high costs and creates a hole in the pipeline of the pharmaceutical company. To minimize the risk of late failure, investigations and tests in the pre-clinical phase, and particularly those regarding the activity, toxicity, and pharmacokinetics of a drug substance, should be as informative as possible. Pre-clinical studies have traditionally been performed using experimental animals, and more recently, whenever possible, two-dimensional (2D) cell culture models are used. Although both test systems yield significant data for drug development and also contribute to drug safety analysis, they exhibit several disadvantages. Animal experiments are always associated with ethical concerns, and the experimental data obtained from animals cannot be uncritically translated to the human situation. Animals, and particularly animals that differ widely from humans in their biology, such as rodents, often respond differently to drugs. In contrast, in certain cases, 2D cell culture models can reduce or replace animal experiments, and thus, the sacrifice of animals can be avoided. Such models are mostly built from cells of human origin and therefore do not feature species-dependent differences. Furthermore, these models are very useful for studying single signaling molecules, such as enzymes, receptors, or ligands. However, in general, 2D cell cultures are not able to reflect the complex cell–cell interactions of the human body or the extracellular environment (matrix and mechanical stimuli). This discrepancy often results in a reduction of the validity of such tests. These disadvantages recently led to the development of three-dimensional (3D) cell culture models with distinctly improved cell–cell and cell–matrix interactions. However, similar to static models, these 3D cell culture constructs mostly did not comprise mechanical stimuli or drug concentration gradients during testing.

Several of the aforementioned drawbacks were addressed using the methods of microtechnology, resulting in the development of so-called organ on chip (OOC) systems. OOC systems are a class of microdevices that allow the cultivation of cells and that support high expression of organotypic properties by creating an in vivo-like microenvironment. The goal is not to reconstruct a whole living organ, but rather to design minimal functional units that reflect tissue- or organ-level functions. The term “chip” was chosen because of the design principle, which is based on microchip technology and is characterized by multiple channels, splitting and merging of channels, pumps, valves, and integrated electrical and biochemical sensors [40]. The term “organ” refers to creating a microenvironmental architecture that is inspired by respective organ-level function. The first studies concerning OOC technology had already been carried out by the end of the last century, but only in the past five years has the number of publications on this topic risen sharply,

indicating the relevance of this emerging field of research. In the field of drug development in particular, OOCs offer significant advantages.

OOCs can reduce or replace animal experiments. Human-based tissue-like structures corresponding to relevant organs can be generated by OOCs, mimicking the natural complexity of tissues. Furthermore, due to the small dimensions of OOCs, it is possible to work with small amounts of drugs, so OOCs are suitable for high-throughput screening. Moreover, OOCs can include biosensors that allow online measurements of the viability and functionality of the cells in real time. Additionally, OOCs containing tissues from different origins can be connected by microfluidic techniques to form multiple OOCs. The response of such multiple OOCs to drug exposure can also be systemically analyzed, as in animal models. The basic concept underlying the establishment of an OOC for drug testing is shown in Fig. 11.1.

This book chapter is divided into three main sections in accordance with Fig. 11.1. Section 11.2 addresses the OOC technology for particular cell types, substrates and structures as well as sensors. In Sect. 11.3, different organ systems on chips are presented, up to the human on chip, whereas Sect. 11.4 is dedicated to the special applications of OOCs, specifically in the pharmaceutical sector.

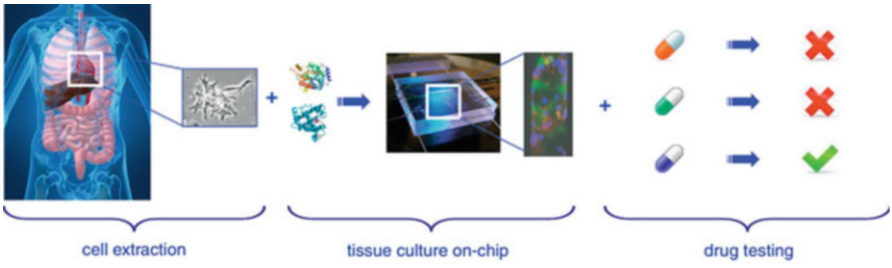

Fig. 11.1 Concept underlying the development and use of an OOC for pharmaceutical applications. The setup begins with the establishment of primary cultures or stem cells from a living organism or the cultivation of cell lines (*left*). The cells are transferred into a microfluidic chip. The specific microenvironment in the chip and the organ-adapted cultivation conditions, consisting of a suitable medium composition containing growth factors as well as matrix and mechanical stimuli, support the expression of organotypic properties. Suitable analytical methods, such as immunostaining (*center*) or biosensor-based testing, are used to investigate the organotypic state of the tissue in terms of quality assurance and are also needed for drug testing. Typically, the tissue is exposed to drug candidates or formulations, and the response of the tissue is measured in various ways, depending on the functionality of the organ. These responses include, for example, cell viability, the toxicity or metabolism of the drug substance, pharmacological effects and drug absorption and transport processes (*right*). Reproduced from Selimović et al. [35] with permission of Elsevier

11.2 Organ on Chip Technology

OOC technology aims to build more realistic in vitro models by integrating cell cultures into microfluidic channels and structures. These systems combine the benefits of an engineered, physiological-like microenvironment with the advantages of well-characterized human cell lines. Furthermore, OOCs offer the potential for parallelization and increased throughput, which are important for drug screening [40]. Due to the complexity of such systems, extensive manufacturing techniques and wisely chosen materials are needed [4]. In the following paragraphs, cellular as well as technical components needed for the construction of OOCs shall be explained in more detail.

11.2.1 Cell Types

Before taking a closer look at the substrates and structures on which cell cultures are immobilized, the different groups of cells commonly used in OOCs shall be introduced. The cells utilized in common chip systems can be divided into three main groups: primary cells, immortalized cells, and stem cells.

Primary cells are cells that have been extracted directly from an organ or a tissue, without further modification. Although they have a morphology and a metabolism similar to their in vivo counterparts, these cells are difficult to obtain and to maintain and can only be cultivated for a limited period of time. Moreover, the cell population and its characteristics can differ from extraction to extraction, complicating standardization.

In contrast, immortalized cells are readily available, standardized, and normally well characterized. These cells can be obtained from clinical tumors or by chemical or viral modification of primary cells. This immortalization ensures continuous cell division for an extended time period. As a consequence, the phenotype of the cells might be altered compared with the original in vivo cell type.

Last but not least, stem cells are the most promising cells because of their enormous, controllable differentiation potential and their physiological phenotype. These cells' limited availability and ethical concerns in the application of embryonic stem cells have led to great popularity for the induction of pluripotent stem cells. With this technique, which was honored with the Nobel Prize in 2012, it is possible to obtain stem cells from biopsies and other adult tissue by reprogramming. Various cell types can then be obtained by subsequent differentiation. Thus, new research fields, such as autologous tissue engineering and personalized drug testing, have become possible (see Sect. 11.4.4).

11.2.2 Materials and Structures for Cell Cultivation

Most human cells, except blood cells, grow on basal membranes or in extracellular matrix (ECM). Therefore, these adherent cells need an adequate substrate during cell cultivation. Common materials for this purpose are, for example, polystyrene and polycarbonate (PC). All of these materials have to ensure proper cell adhesion and biocompatibility, meaning that they should neither affect cell viability nor reduce the concentration of compounds in the medium due to adsorption. The latter effect would also impair the results of in vitro studies by influencing the drug's concentration.

In the growing research field of cell cultivation inside a microfluidic chip, all of these aspects of traditional in vitro models have to be considered as well. To date, only few OOC systems are commercially available due to their novelty and the fact that they are currently not able to replace animal testing completely. However, there are various research approaches in this field. The majority of those OOCs are built using replica molding processes, also known as soft lithography, with polydimethylsiloxane (PDMS) as the main substrate [16, 40]. Soft lithographic fabrication is described in detail in Chap. 2: Fabrication of Microfluidic Devices. The technique allows easy and rapid modeling of new OOC forms and therefore is preferred for the development of new systems. As the most commonly used substrate, PDMS has many desirable properties, such as high biocompatibility, gas permeability, optical transparency, and flexibility. However, certain OOCs use other materials, such as polystyrene and PC (see Sect. 11.3.3.1). Moreover, there are chips that combine PDMS layers with polyester or PC membranes (see Sects. 11.3.3.2 and 11.3.3.7). The commercially available "Multi-Organ-Chip Platform" by TissUse GmbH, Berlin, Germany (see Fig. 11.2), for example, uses PDMS layers for the channel structure. As a result, these parts are easy to produce and are very flexible in the molded geometries. For other rarely changed and geometrically less challenging compounds (see the adapter plate in Fig. 11.2), materials such as PC or glass can be chosen.

Generally, in vitro studies are performed using cell cultures in well plates or insert systems that contain a membrane inlay (e.g., Transwell®, Corning Costar). Consistent with these well-established techniques, membranes or other functional surfaces are often used in OOCs, in contrast to the other microsystems already mentioned in this book. Membranes, for example, ensure the accessibility of both sides of a cell layer, which is important for permeability studies. This analysis of active pharmaceutical ingredient (API) transport through a determined cell layer is one essential task in drug efficacy testing that can be facilitated by OOCs.

Another application for OOCs is safety testing of drugs and chemicals. Therefore, different functional structures with or without membranes can be used. A good example is the heart/muscle on chip generated by Grosberg et al. (see Sects. 11.3.3.5 and 11.3.3.6). Here, muscle cells are cultivated on flexible PDMS films, allowing evaluation of influences on muscular electrophysiology.

Because of their importance for pharmaceutical applications, membranes, microchannels, and PDMS thin films will be described in more detail in this section.

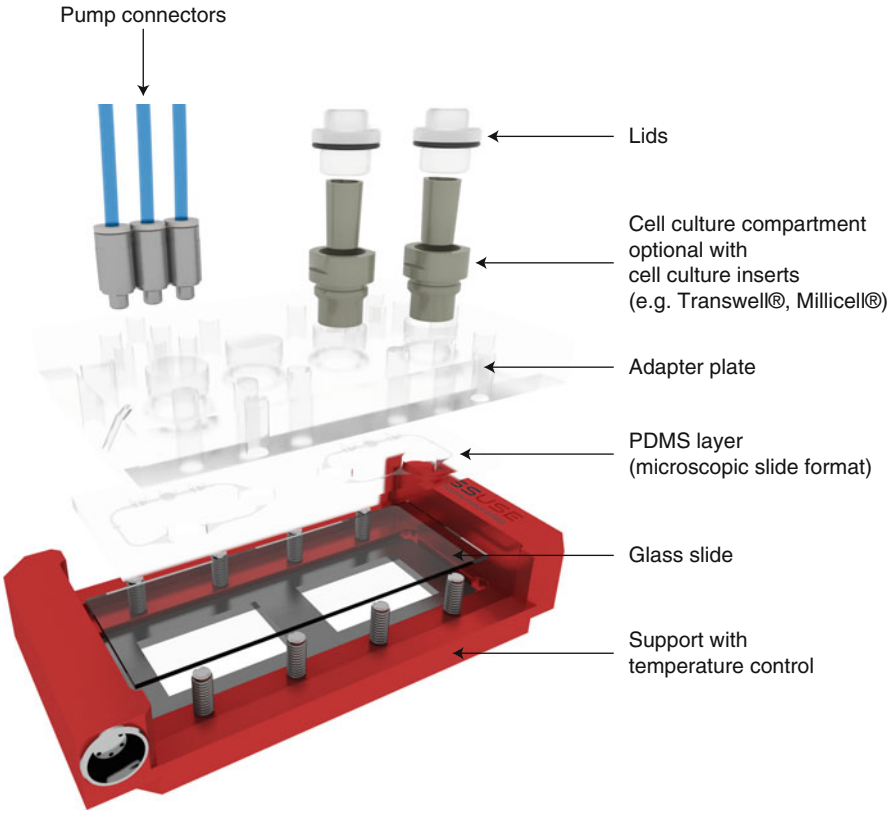

Fig. 11.2 Image of a commercially available OOC system for cell cultivation. Reproduced with permission of TissUse GmbH

11.2.2.1 Membranes

As already mentioned, membrane insert systems (e.g., Transwell®) are widely used in the field of in vitro cell culture. Because of the accessibility of both the apical and the basolateral sides of the cell layer, researchers are now able to study processes such as active or passive transport. The intense demand for insert systems even led to the development of ready-to-use models that can be purchased from various companies (e.g., MatTek®, SkinEthic®). Probably because of this widespread use, Marx and coworkers included cell culture compartments that are compatible with those in vitro models in their "Multi-Organ-Chip Platform" (see Fig. 11.2). This *off-chip* cultivation has to be distinguished from the more frequently used *on-chip* cultivation.

For *on-chip* cultivation, polymer membranes serve as a cell substrate, similar to conventional static well plates and Transwell® systems. The membranes in these

systems are often made of PC or polyester with a thickness of approximately 10 μm and a pore size between 0.4 and 10 μm. Apart from general cell compatibility, the pore size needs to be chosen wisely. Wide pores, on the one hand, allow nutrition and API passage but can result in cell migration. Smaller pores, on the other hand, hinder cell migration but can contribute significantly to the permeation barrier. Therefore, the membrane's permeation coefficient should not be neglected when measuring API transport through a cell layer.

Commercially available membranes are often integrated into OOCs (see Sect. 11.3.3.7). These membranes are similar to those in well plates and can be prepared with a special coating for cell adhesion. For other OOCs, membranes are simply cut out of well plate inserts and transferred to the chip system [10].

Membranes can also be made of PDMS. For their production, a microfabricated silicon wafer with a post array of circular pillars with the desired pore dimensions is prepared as a negative master. PDMS is then poured over the master and cured with a heavy weight on top to extrude excess material. Afterward, the porous membrane can be peeled off (see Sects. 11.3.3.3 and 11.3.3.4). The huge advantages of these membranes are their exactly defined dimensions and their flexibility. Commercially available membranes often contain pores of different sizes and inhomogeneous distribution. Moreover, their rigidity hinders the transfer of strain and motion to the cell layer (see Sects. 11.3.3.3 and 11.3.3.4).

To achieve cell cultivation on the membrane's surface, the membrane first needs to be integrated into the OOC, which is a really challenging step. Usually, bonding of PDMS layers is ensured by oxygen plasma treatment, as described in book Chap. 2: Fabrication of Microfluidic Devices. The same procedure can be employed to bond PDMS membranes and PDMS layers or PDMS and glass surfaces. For other membrane materials, such as PC, it takes more effort to achieve tight and leakage-free bonding. In contrast to PDMS or glass, most polymers do not contain silicon atoms, and therefore, bonding by oxygen treatment is not possible. An effective alternative method for the integration of a polymer membrane between two PDMS layers is the use of PDMS mortar. First, toluene-diluted PDMS prepolymer is applied to both PDMS compounds. Second, the membrane is aligned with one PDMS layer. Finally, the second PDMS layer is attached [5]. An OOC built using this method is shown in Fig. 11.3. Nevertheless, for large membrane areas, supporting structures such as small posts might be necessary to guarantee stability when using the system and applying fluidic pressure [1, 23]. After OOC assembly, the membranes are often pretreated by coating with ECM proteins such as collagen, fibronectin, or laminin to support cell adhesion.

11.2.2.2 Microchannels

Another surface design for drug permeability studies is the use of microchannels, which operate similarly to a membrane. These channels have a height and width of a few micrometers and a much bigger length, of approximately 30–800 μm [26, 28, 37]. These microchannels are normally used in PDMS-based systems, in which they

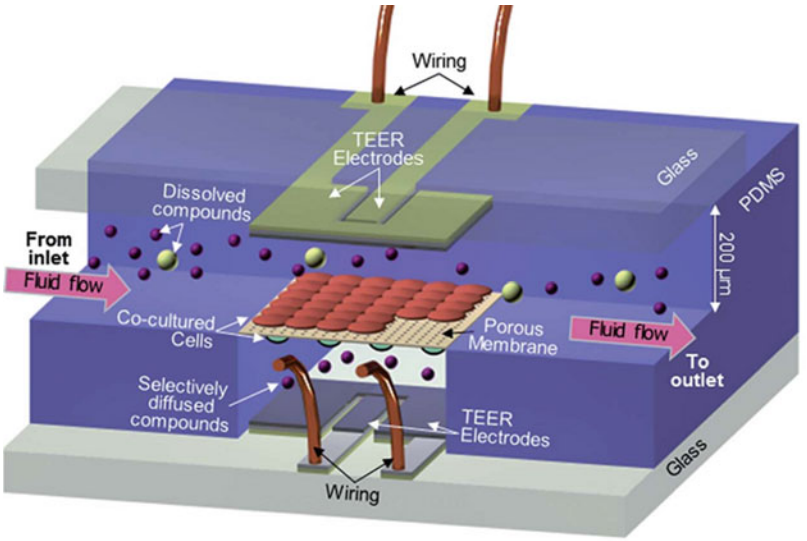

Fig. 11.3 Structure and design of an OOC system for the co-cultivation of endothelial cells and astrocytes to mimic the blood–brain barrier (BBB), as prepared by Booth and Kim [3]. The PC membrane is integrated between two PDMS layers containing fluid channels. Electrodes are deposited and structured on glass slides to allow transepithelial electrical resistance (TEER) measurement. Reproduced from Booth and Kim [3] with permission of The Royal Society of Chemistry

are located between the PDMS layer and the glass substrate. The microchannels can easily be fabricated using a two-step soft lithographic process. Here, SU-8 serves as a negative photoresist, and therefore, only the exposed areas will remain after development (see book Chap. 2: Fabrication of Microfluidic Devices). First, a thin layer of SU-8, with a thickness equal to the microchannel height, is spin coated. Second, exposure is performed using a mask containing small grooves with the microchannels' dimensions. As a result, microridges will remain at the bottom of the master, which will lead to the desired microchannels in the PDMS mold. Third, a second, much thicker layer is spin coated to generate feeding channels and other structures [48]. Finally, the PDMS layer is bonded to a glass substrate to cover the channels.

Another method of obtaining a master is the use of a bulk silicon substrate. The formation of controlled small gaps as well as bigger channels can then be ensured using deep reactive ion etching (DRIE) [28]. Unfortunately, the substrate as well as the process is much more expensive than fabrication using SU-8 masters. The use of such microchannels in an OOC for cell trapping and drug transport is shown in Fig. 11.4, as developed by Park et al. [26].

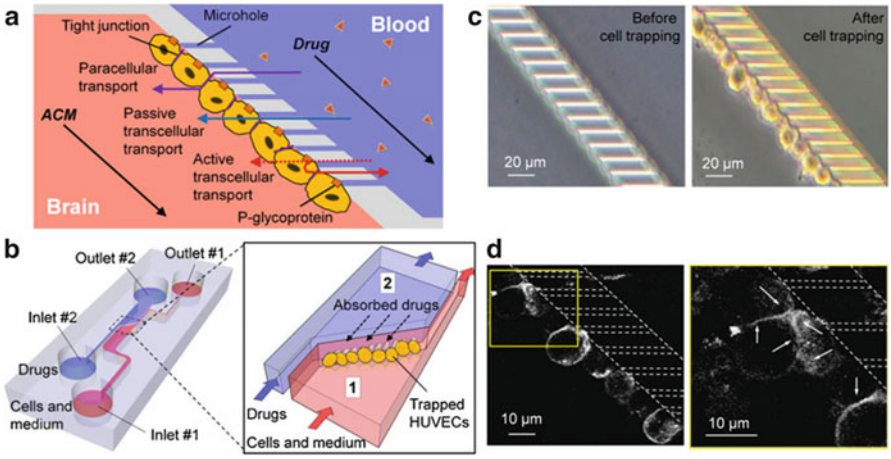

Fig. 11.4 Device concept of the OOC designed by Park et al.; (**a**) Concept of the microfluidic channels for cell trapping and drug transport; (**b**) Schematics of the overall OOC system; (**c**) Pictures of cells trapped at the microholes; (**d**) Tight junctions between cells stained with ZO-1 antibody are visible. Reproduced from Yeon et al. [48] with permission of Springer

11.2.2.3 Polydimethylsiloxane Thin Films

In the development of muscular test systems with vascular or cardiac muscle cells, permeability is a less important characteristic. In contrast, tissue contractility, action potential propagation and cytoskeletal architecture are of interest. The fabrication of muscular thin films (MTFs), which have been enhanced by Grosberg et al. [11], allows the development of reliable anisotropic muscular test systems for safety and efficacy testing (see Sects. 11.3.3.5 and 11.3.3.6). The muscle cells are cultivated on 18.6 μm-thick PDMS films that bend when the attached cells contract. The x-projection of the bent films can then be measured optically and serves as a surrogate for the determination of contractile stress (Fig. 11.5d). The main challenge in MTF fabrication is to ensure movability of the PDMS films. To achieve this aim, first poly(*N*-isopropylacrylamide) (PIPAAm) is spin coated on a glass substrate as a sacrificial layer. This layer is structured by removal of previously attached tape. In the next step, PDMS is spin coated and cured on top of the glass and structured PIPAAm. Subsequently, fibronectin is microcontact printed on the PDMS surface to ensure anisotropic self-organization of the seeded myocytes. The PDMS layer is then cut into the desired form. By exposure to culture media at room temperature, the PIPAAm is dissolved, and the MTF is released for contraction (see Fig. 11.5a–d).

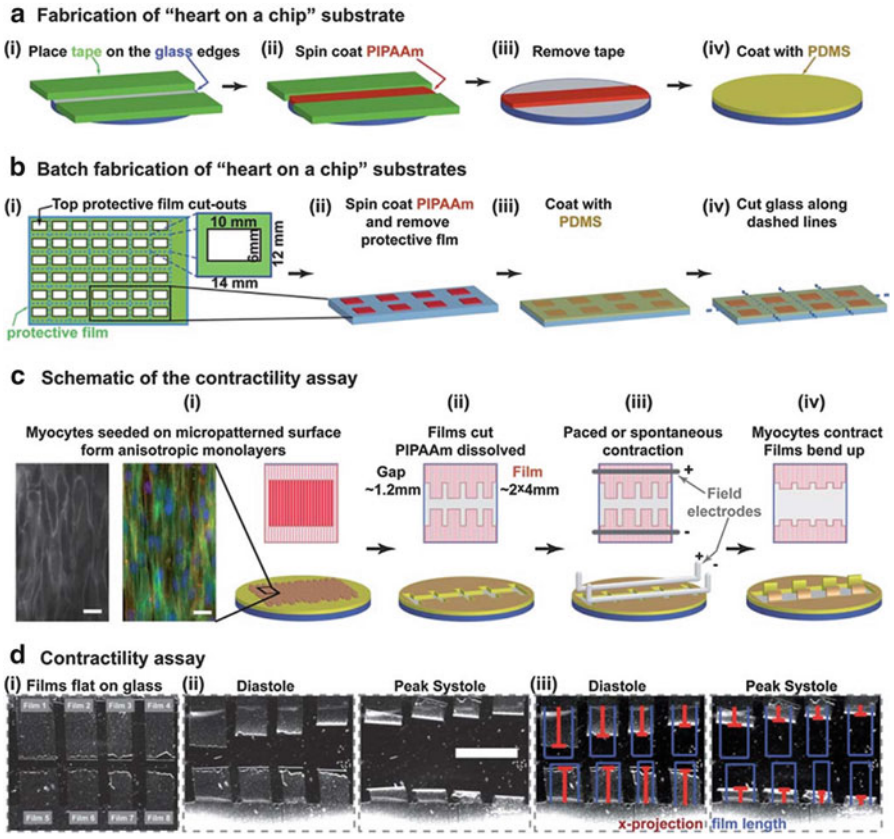

Fig. 11.5 Assembly and use of the heart on a chip developed by Grosberg et al.: (**a**) Fabrication process of the PDMS thin films; (**b**) Batch production for higher throughput; (**c**) Contractility assay; (**d**) Images of the contractility experiment. Reproduced from Grosberg et al. [11] with permission of The Royal Society of Chemistry

11.2.3 Sensors

As the field of OOCs is quite new, the level of sensor integration is only at its beginning. In fact, most tests have to be performed offline, but sooner or later, sensors will be integrated into OOCs for fast and easy online analysis. The first step has already been reached by integration of small sensors for the measurement of transepithelial electrical resistance (TEER) in the current OOC generation (see Sect. 11.3.3.7). In general, methods to control cell morphology and barrier properties are particularly of great interest. Therefore, optical observations, TEER measurements, and quantification of the permeated amount are performed frequently.

11.2.3.1 Optical Observation

One of the huge advantages when using PDMS and glass for building OOCs is their optical transparency. The devices can be placed under an optical microscope during cell cultivation and analysis, so light phase and scanning electron microscopic imaging can easily be used for morphological observations. Moreover, cell viability can be assessed by live/dead staining, and protein expression can be observed by immunostaining (e.g., for tight junctions) [3]. Fluorescence imaging is additionally used in many systems to view, for example, isolated axon cells [37] or cell polarization [17]. The establishment of cell multilayers can also be observed by using confocal microscopy. The obtained morphological information helps in the estimation of cellular function and thus allows comparison of the physiological and the developed phenotypes.

11.2.3.2 Transepithelial Electrical Resistance

Traditionally, TEER measurements are performed in Transwell® systems. The obtained resistance value serves as a surrogate for epithelial integrity, so changes such as the formation of tight junctions can be observed as an increase in TEER. Therefore, resistance values are important for both the estimation of cellular barrier properties and quality control during cultivation.

To perform TEER measurements, electrodes need to be placed on both sides of the membrane. The easiest way to implement this technique is similar to the "macrotechnological" TEER measurements performed using a common voltohmmeter (e.g., EVOM®, WPI). For the transfer of this measuring principle to OOCs, special grooves have to be generated in the PDMS layers. Electrode wires can then be inserted into the system during assembly. The electrode wires on each side of the cell layer have to be in contact with the fluid to ensure a closed circuit [10]. A more integrative approach has been achieved by sputter depositing electrode layers with a thickness of less than 1 μm on glass slides. These slides act simultaneously as a lid for the PDMS fluid channels, whereby the electrodes can be located above and below the membrane [3] (see Fig. 11.3).

11.2.3.3 Permeability Measurement

In the human body, many physiological barriers hinder drugs from reaching their site of action. Therefore, in efficacy testing, the amount of drug that can overcome this barrier is highly important. For this reason, the API concentration on both sides of the cells has to be measured. Unfortunately, the drug's concentration on the donor side is quite low, and on the acceptor side, it is even lower. For offline analysis, fluid from the compartment is collected and measured using a fluorescence microplate reader [3] or high performance liquid chromatography (HPLC) [48], for

example. Future OOCs may also include quantification. However, because of the low concentrations and the small volumes in OOCs, very high sensitivity is necessary to detect and quantify the permeated amount. In fact, in most cases, microsensors cannot provide sufficient sensitivity, so common external methods will have to be used until better sensors are developed.

11.2.4 Outlook

PDMS is an excellent material for fast fabrication and flexible design. Furthermore, it has many desirable properties, such as optical transparency and high biocompatibility. Nevertheless, there are certain characteristics that may lead to problems when PDMS is used in OOCs. PDMS can absorb drugs, proteins, and small hydrophobic molecules, which can significantly change the concentration of nutritional and testing compounds. This phenomenon may alter the results for drug permeability assays, as described above. Surface modifications of PDMS to reduce the absorption can be performed but add significant effort to the manufacturing process [38]. Furthermore, the transient nature of surface modifications can limit the viability of cultured cells inside the system. These issues put significant limitations on OOC models built from PDMS [4]. These problems can be eliminated by using glass as the main material. Glass also has many useful properties for OOCs, such as good cell adhesion, biocompatibility, optical transparency, and suitability for repeated sterilization. However, glass is gas impermeable, which makes an additional supply of gases such as O_2 and CO_2 necessary. Therefore, systems built from a combination of several materials might be a promising approach [50].

Other disadvantages of glass are the time-consuming and expensive traditional fabrication techniques required, such as wet etching or reactive ion etching [50]. Novel fabrication methods, and especially laser machining, can facilitate a much faster glass production process [6]. Furthermore, photosensitive glass has been developed, which allows direct writing of 3D structures. In the laser-irradiated regions, the chemical properties of the material are modified. Afterward, these regions can be removed by successive wet etching [36]. This 3D manufacturing method is highly interesting for the generation of future OOCs with a complex geometry for improved cell cultivation and fluid handling. This method also helps to achieve high levels of integration for different cell cultures as well as for integrated sensors and actuators. Compared with previously used systems built by soft lithography, more complex fluid guidance is possible, different organ layers can be built on top of each other, and several sensors can be integrated into a single OOC device. Furthermore, free-form constructs with 3D microporosity can be produced using two-photon polymerization. With this method, it is even possible to fabricate cell migration constructs inside closed microfluidic chips [25]. This technique allows the creation of an even more realistic microenvironment compared with common 2D membranes.

In summary, the next generations of OOC devices may take advantage of novel materials and fabrication processes. These devices will also feature a high level of integration, containing incorporated sensors, response elements, and peripheral microfluidic components. In this way, even feedback loop mechanisms may be realizable to automatically control, for example, flow, pH, oxygen, glucose, and growth factors during testing [40].

11.3 Organ Systems on Chips

Within our highly engineered and globalized world, modern society is being exposed to an increasing amount of new chemicals. Furthermore, driven by demographic changes and the rising demand for new drugs in the field of pharmaceutical research and development, the number of new substances has risen dramatically [21]. As all of these new substances have to be tested from toxicological, pharmacological, or environmental perspectives before exposure is permitted, there has been increasing demand for reliable testing systems.

In the early stages, those tests were performed only in animals. However, since the postulation of the *3R* principle by Russel and Burch in the 1960s, awareness of the need for *r*eduction, *r*efinement, and *r*eplacement of animal experiments has risen. Even regulatory agencies such as the European Parliament and the Council of the European Union have been advancing the development of alternative methods. The marketing ban of cosmetics with animal-tested ingredients in March 2013 is one of the most important examples of the implementation of the 3R principle in the EU (Directive 2010/63/EU on the protection of animals used for scientific purposes).

Furthermore, industrial companies have noticed the enormous potential of alternative methods not only in drug development, toxicity testing, and environmental research but also in fundamental research. Apart from the reduction in animal use, the companies are interested in suitability for high-throughput screening and parallelization, high data quality, good predictability in clinical trials and especially cost reduction. Unfortunately, common in vitro systems fail to fulfill all of these requirements. As a result, the demand for improved in vitro models and innovative organ systems on chips has risen.

For this reason, this subchapter will take a closer look at the past and present development of different test systems in drug development and will ultimately focus on the latest inventions in the field of organ systems on chips.

11.3.1 Former and Current Test Systems in Drug Development

The development of a novel drug is time consuming and cost intensive. During the 10–15 years of development, over 1.3 billion US dollars have to be invested before the medicinal product is ready for market entry [4].

This development process comprises different phases (see Fig. 11.6). The process starts with the drug discovery phase, in which the substance of interest and similar candidates are discovered. After the group of substances has been reduced to the most promising candidates, those candidates enter the pre-clinical phase. In this second phase, the safety and efficacy of all remaining compounds are tested. The results obtained in this stage strongly influence the selection of the most promising candidates. Thus, this step is extremely important, and therefore, a third of the budget is spent on the tests in the pre-clinical phase [4]. The few substances chosen after this step proceed to further formulation development and are ultimately tested on humans during the following three clinical phases.

Evidently, there is much effort and money invested in the pre-clinical phase. This investment is motivated by the fact that misleading results in this stage may cause failures in the following processes, which may result in time delay, increased costs, harm to patients, or even total failure of the drug itself. In certain cases, the

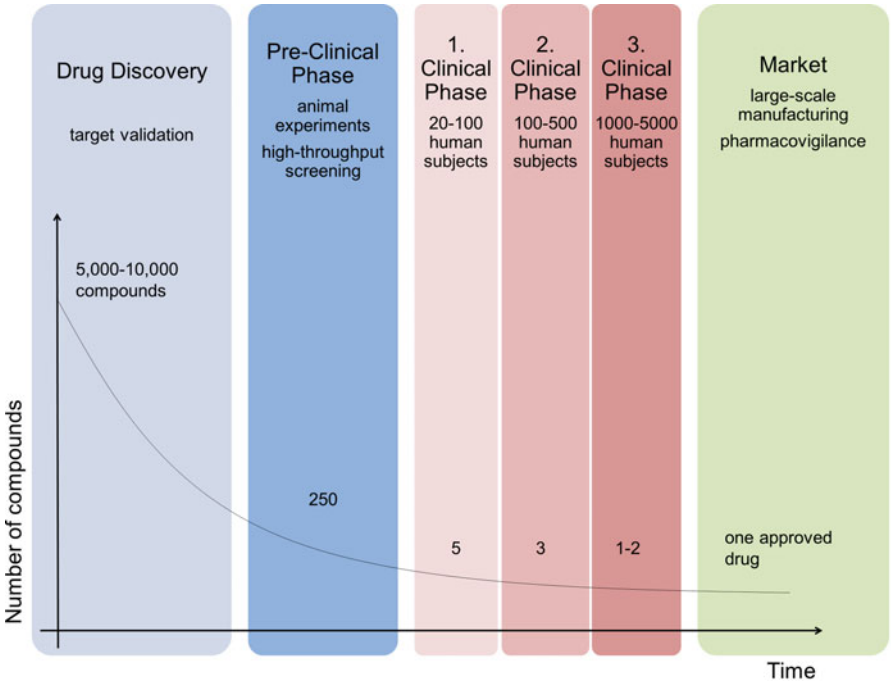

Fig. 11.6 Different phases of drug development

ineffectiveness or hazard of a drug is not observed until market entry. Thus, after adverse effects are noticed in patients, the medicinal product eventually has to be withdrawn from the market.

So, why does the pre-clinical phase often mislead the following phases when so much money and effort are invested? To answer this question, we will take a closer look at the testing methods performed in this particular step of development.

Decades ago, animal tests were broadly performed in pre-clinical studies. In those days, animal tests were very easy to use and had the advantage of a complexity similar to that of humans. Thus, on the one hand, by investigating complete organisms, it was possible to evaluate the *l*iberation, *a*bsorption, *d*istribution, *m*etabolism, and *e*xcretion (*LADME*) of a drug simultaneously. Furthermore, complex interactions with the immune system could be estimated. On the other hand, the use of animals has always complicated the interpretation of results. Because of interspecies differences, the extrapolation of an effect to humans is really challenging. The results of only a third of successful animal studies have been successfully confirmed in human clinical trials [4]. Therefore, results in animal tests may mislead predictions regarding the efficacy of the tested interventions in humans. History has shown that even between closely related species, the unexpected harming potential may be high (e.g., thalidomide, Contergan®). In addition to questionable results, animal experiments are time consuming, not suitable for high-throughput screening, not standardizable because of variation in material [29], and cost intensive in their maintenance. Moreover, the enormous ethical constraints are driving the development of new in vitro methods for the replacement of animal tests.

Alternatives to animal testing have been developed since the early twentieth century [34]. With the establishment of in vitro systems, it was possible to reduce the laboratory equipment needed and the effort required for maintenance. Certain companies have also established shippable, ready-to-use cell culture models (e.g., MatTek®, SkinEthic®), which reduce the user's need for equipment even more and thus support the widespread application of in vitro models. Furthermore, influencing factors such as temperature, the CO_2 concentration, and the medium composition can be more easily controlled in cell culture, improving reproducibility and reducing the variability of results. Moreover, cell culture systems can be built with human cells to eliminate interspecies differences. Additionally, the establishment of cell modifications and diseased cells has facilitated investigation in certain research fields. All in all, in vitro systems are robust, predictable, and repeatable alternatives to animal testing [40].

Unfortunately, current in vitro systems lack certain important physiological conditions, which limits the predictability of clinical results. Most common systems are 2D in vitro systems and thus lack strain, motion, and other mechanical forces, as occur, for example, during breathing and peristaltic gut movement. Additionally, those static systems can simulate neither flow, as in blood vessels, nor nutrition gradients, such as an oxygen supply. Apart from these conditional factors, common in vitro systems comprise only few cell types to minimize the cultivation effort. Missing cell–cell communication is disparate from human complexity, which is

important for the investigation of pharmacokinetic factors. All in all, misleading results in pre-clinical phases may result, on the one hand, from interspecies differences and wide variability in animal testing and, on the other hand, from common in vitro models' lack of complexity [40].

11.3.2 From 2D Cell Culture to Organ Systems on Chips

As cell culture started with the cultivation of tissue slices or cell extracts in Petri dishes, the early in vitro models were 2D [34]. This type of cultivation has always been advantageous because of its simplicity, its straightforward readouts, and its suitability for high-throughput applications. However, the importance of a third dimension quickly became evident [20, 49].

By using ECM materials, such as collagen gels, cultivation in a more physiological 3D pattern became possible. Comparisons of 2D and 3D systems revealed more physiological cell morphology and metabolism in the improved 3D culture [8, 13]. The integration of multiple cell types was another step approaching the natural standard. Unfortunately, the increasing complexity resulted in higher variability, lower robustness of the results, and decreasing applicability to high-throughput screening [40]. All in all, the attempts to improve common in vitro systems were limited and emphasized the need for novel and more different cell culture systems.

An innovative in vitro test system should mimic the simplest and smallest functional unit of an organ or tissue on a small scale under easily controlled physiological conditions [40]. To achieve this aim, researchers took advantage of the latest inventions in the semiconductor industry and the design of bioreactors [35]. The developed microsystems offer the opportunity to run experiments with a lower substance amount. This reduced substance amount is advantageous, especially in the early stages of drug development, when the amount of a novel drug is limited. Furthermore, the reduced volumes are more similar to physiological volume ratios than volumes in static in vitro systems are [27]. By integrating multiple cell types into different compartments in the chip, a cell–cell interface can be established, and the heterogeneous cell demographics of the in vivo counterparts can be recreated. This diversity is highly important for the predictability of the resulting chip system [4].

Furthermore, microsystems enable the operator to fully control the biological microenvironment and to induce physiological forces or gradients. The dynamic flow systems have shown cell morphologies and metabolism similar to the in vivo situation (see Sect. 11.3.3.4) as well as an increased lifespan for primary cells [41, 43]. Moreover, microtechnology can provide surface modifications to induce self-organization of cells (see Sects. 11.3.3.5 and 11.3.3.6). Fortunately, these improvements in the cellular environment increase the complexity and predictability of in vitro systems but do not result in higher variability of findings [40].

Apart from the achievement of improvement in in vitro test systems, the user's need for easy application also has to be considered. For the user in research or development, simple experimentation with reliable and reproducible results and easy transferability to other laboratories is important. Furthermore, parallelization of experiments, automation, and suitability for high-throughput screening, with adequate online analytics and endpoint measurements, are necessary for the regular application of OOC systems in pre-clinical studies. All in all, organ systems on chips have to face the challenge of precisely emulating important characteristics of living tissue while remaining simple and easy to use [40].

11.3.3 Single-Organ Chips

To gradually approach the development of an entire body system on a chip (see Sect. 11.3.5), researchers started by developing single-organ chips that could later be linked to form a body equivalent. Those single-organ chips were developed by taking advantage of efforts in the semiconductor industry and microchip technology. Various microfabricated models have been reported in the literature, but much attention was attracted to the lung on chip, which was the first organ chip reported in Science magazine [15] (see Sect. 11.3.3.3). Since this publication in 2010, many other biomimetic organ systems on chips have been developed. Unfortunately, because of the enormous progress in the field of organ systems on chips, this chapter cannot address all chip systems reported so far. Therefore, only certain interesting representatives will be explained in more detail.

11.3.3.1 Liver on Chip

One of the most important organs in the human body is the liver. This highly metabolizing organ transfers both endogenous and exogenous substances to gain energy or to modify these substances for elimination. As this organ is exposed to a variety of substances, it has always been of great interest in toxicological and pharmacokinetic studies. Moreover, liver toxicity has been one major reason for drug withdrawal, and therefore, pharmaceutical companies have supported the development of reliable test systems for the pre-clinical phase of drug development (see Sect. 11.3.1). As a result, a liver on chip system was one of the first commercially available chip systems. The LiverChip®, which was developed by the Massachusetts Institute of Technology (MIT), can be used for metabolism and toxicity testing, especially in pharmaceutical drug development. The system provides, for example, information concerning substance clearance, metabolite identification, and cytochrome P450 (CYP) interaction.

The dynamic perfusion system comprises two components: a culture plate and a pneumatic dock (see Fig. 11.7a). The culture plate is composed of twelve separate wells. Each well contains a scaffold, a filter, a medium reservoir, and a pneumatic

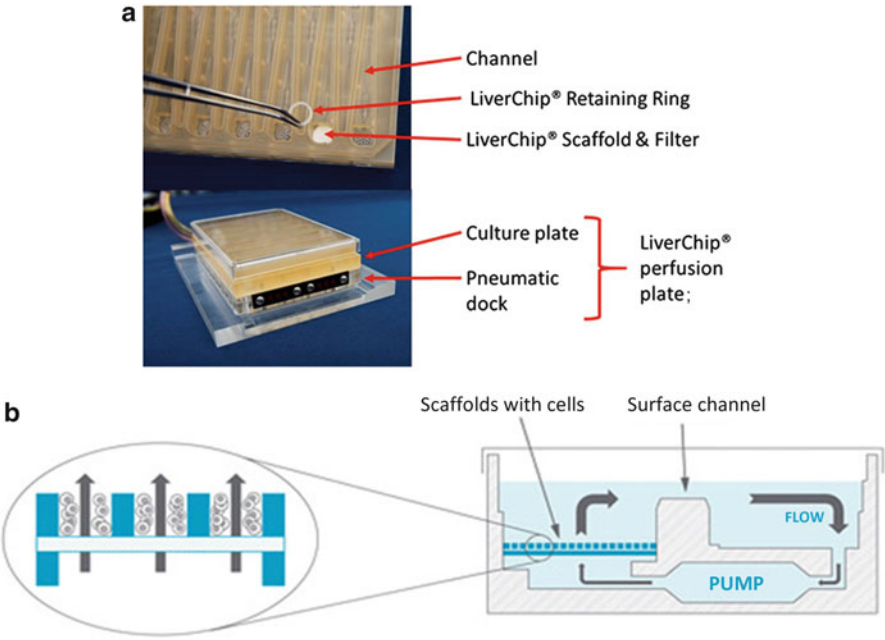

Fig. 11.7 LiverChip® (**a**) *Top picture*: view from above; *bottom picture*: side view; (**b**) Schematic of a single channel in the culture plate, including a scaffold and filter for cells, a medium reservoir and a pneumatic micropump. Reproduced with permission of CN Bio Innovations Limited

diaphragm micropump (see Fig. 11.7b). The scaffold and filter are coated with collagen and bovine serum albumin, respectively. These components help to mimic the capillary bed structure and to induce a 3D in vivo-like phenotype. The micropump pneumatically regulates physiological flow rates and shear forces. A closing lid on top of the cell culture plate can easily be removed for medium changes or sampling.

The pneumatic dock is located at the bottom of the cell culture plate and can be controlled by a computer from outside the incubator. Therefore, all electrical components can be protected from the humidified atmosphere. Furthermore, the culture plate can be disposed of easily, without renewing the pneumatic dock. Most parts of the chip are fabricated by computerized numerical control (CNC) machining. However, the polystyrene and PC scaffolds are formed by microdrilling [9].

A variety of cell types can be seeded onto the scaffold of the LiverChip®. Monocultures of primary human hepatocytes and co-cultures of hepatocytes with non-parenchymal cells of either human or murine origin are available. The co-cultures enable heterotypic cell–cell interaction, which has been shown to have a positive impact on various cell characteristics [7]. Because of this setup, the time period of cell viability can be extended to 14 days. This prolonged lifespan allows the investigation of low-clearance compounds and long-term drug effects. As a result of the substrate structure, flow simulation, and cell–cell interaction,

cultivation in this liver chip leads to in vivo-like sinusoidal cell morphology which supports its improved predictability.

All in all, the dynamic 3D LiverChip® offers the opportunity to conduct standardized and reliable in vivo-like tests for a small number of promising substances in the later stages of pre-clinical selection. Because of the well-conceived design, the system is easy to use, and only little space is required (for further information, see Dash et al. [7], Domansky et al. [9], Van Midwoud et al. [42]; LiverChip® homepage: http://www.liverchip.com/).

The importance of the liver in safety and efficacy testing was also highlighted by integration into the first multi-organ chip systems [22].

11.3.3.2 Kidney on Chip

Beyond the liver being the most metabolically active organ, the kidney is the most important excretory organ of the human body. This organ comprises approximately one million nephrons, which are composed of renal corpuscles and specialized tubules. After filtration in the corpuscle, the urine enters the proximal part of the tubule, where most relevant renal processes, such as active clearance and reabsorption, occur. Those actions are performed at the renal epithelium, which separates the blood from the tubular lumen (see Fig. 11.8a). As a consequence of the renal tasks, the local drug or metabolite concentration can be higher than in other parts of the body. Thus, the kidney is exposed to higher concentrations of diverse chemicals and drugs, which may result in adverse effects. Currently, approximately 20 % of drug failures in clinical phase III and in post-approval

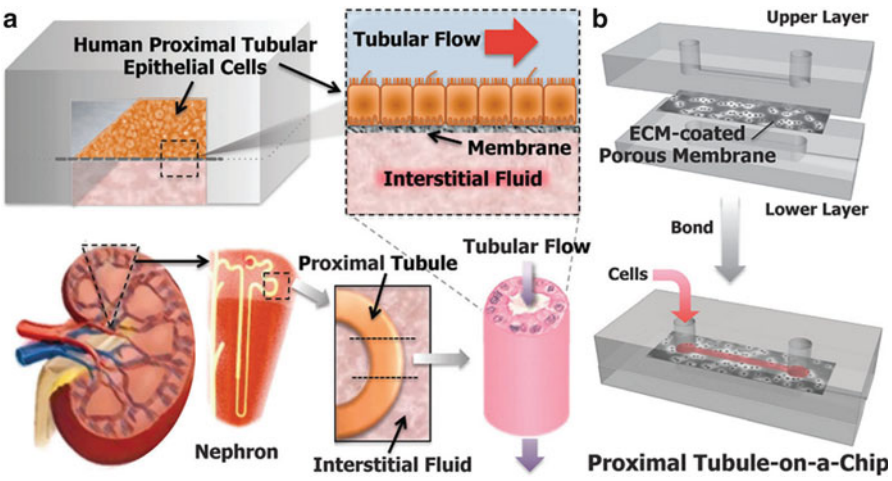

Fig. 11.8 Kidney on chip: (**a**) *Top row*: schematic of the tubular epithelium recreated in the kidney on chip; *bottom row*: physiological hierarchical order in the kidney; (**b**) Assembly of PDMS layers and polyester membrane to form the final chip system. Reproduced from Jang et al. [17] with permission of The Royal Society of Chemistry

stages are due to renal toxicity [17]. As a consequence, more reliable renal in vitro test systems are needed.

In 2013, Jang et al. refined their dynamic microsystem and tested its suitability for renal toxicity evaluation [17, 18]. For their kidney on chip, they focused on the proximal tubule, as the most important and smallest functional unit of the kidney. To mimic the barrier between the tubular and the interstitial fluids, the microsystem comprised two PDMS chambers, which were fabricated by soft lithography and micromolding. Both compartments were separated by a porous polyester membrane that had been precoated with collagen type IV, which is an ECM protein (see Fig. 11.8b). Although a flow similar to the renal blood flow was generated in the top channel, the bottom chamber only served as a reservoir and was not connected to dynamic circulation.

Primary human proximal tubular epithelial cells were seeded on the upper membrane surface after surface modification. Three days of static cultivation to form a confluent monolayer were followed by an additional three days of dynamic cultivation under flow. The applied shear stress, namely, 0.2 dyne/cm^2, was similar to in vivo conditions. Under flow, the cells showed an in vivo-like morphology, with improved polarization, a columnar cell form and increased primary cilia formation, in contrast to static Transwell® cultures. Apart from cell morphology, increased expression of active transporters (Na/K-ATPase), receptor-mediated transporters (albumin transport), and secondary active transporters (glucose reabsorption) could be observed. All advanced characteristics could not be obtained in static Transwell® culture. Therefore, these findings highlight the importance of physiological flow conditions for the achievement of in vivo-like renal cell characteristics and the development of reliable test systems.

Subsequently, Jang et al. tested the suitability of their chip system for drug screening by applying the well-known drug cisplatin. This platinum complex interacts with the DNA and, because of this, is used in cancer therapy. Unfortunately, cisplatin shows nephrotoxicity, mainly because of its accumulation in the renal parenchyma. As the accumulation is assumed to be the result of certain species-specific transporter activities (e.g., the activity of organic cation transporter (OCT 2)), animal models may be inadequate for any predictions. Thus, tests of cisplatin in a chip system with primary human cells and flow-induced cell characteristics were expected to provide more reliable findings. First, Jang et al. found apoptosis and cell damage after the application of cisplatin, but they also noticed that the cells in the chip were able to recover as normal patients do. Second, it was possible to counteract the negative effect of cisplatin to a great extent by applying the OCT 2 inhibitor cimetidine. On the one hand, these observations show that the human proximal tubule on a chip is able to simulate cisplatin toxicity by more closely mimicking the in vivo situation than static cultures can. On the other hand, these observations support the hypothesis of species-specific variation in cisplatin accumulation because of species-specific OCT 2 transportation. As a result, this type of kidney on chip may be suitable for renal pharmacology, renal drug transport, and toxicity testing in pre-clinical studies. The revealed option for cell recovery also provides the opportunity for multiple dose application in this OOC.

The importance of the kidney in safety and efficacy testing was also highlighted by integration into the first multi-organ chip systems to emulate renal excretion [22].

11.3.3.3 Lung on Chip

As the liver and kidney have always been of great interest because of their functions in drug metabolism and drug elimination, the lung was the first organ system on a chip that was reported in Science magazine and thus attracted much attention [15].

In the human lung, the trachea divides into the two lung lobes and continues to divide until the deepest and smallest parts, the alveoli. On the large surface of the alveoli, the gas exchange between air and the blood occurs (see Fig. 11.9b). On the one hand, this exchange is essential for the oxygen supply, but on the other hand, it makes the blood easily accessible to drugs. Therefore, the alveolar membrane is important for the investigation of lung toxicity or pulmonary drug application. For this reason, the alveolar membrane is an important functional unit that was recreated in the lung on chip developed by Huh et al. [15].

The chip, with its three main chambers, was completely built from PDMS by soft lithography (see Sect. 11.2.2). The middle chamber was subdivided by an elastic PDMS membrane to form an alveolar compartment and a vascular compartment (see Fig. 11.9a,c). Furthermore, this separation gave the opportunity to cultivate cells differently in the two compartments. On the upper side of the membrane, cells could be kept under air contact, and in the lower compartment, cells could be submersed. The remaining two adjacent side chambers were obtained by chemical etching of PDMS (see Fig. 11.9d). By cyclic vacuum application in those chambers, a mechanical strain could be transferred to the PDMS membrane, which therefore

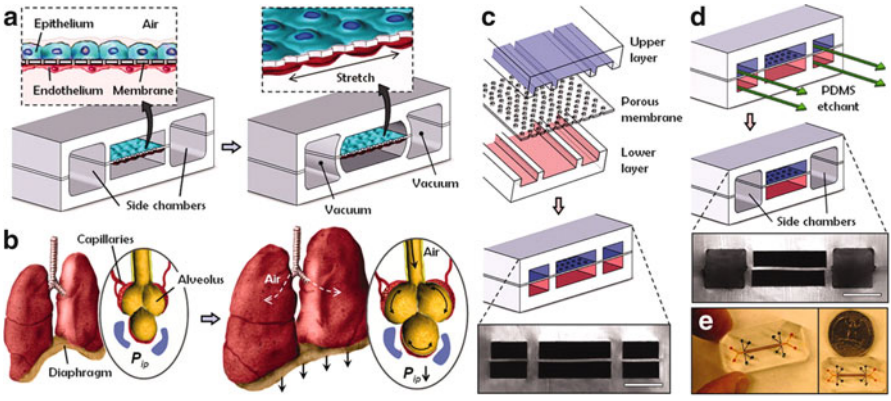

Fig. 11.9 Lung on chip: (**a**) Microfabricated lung with applied cyclic suction; (**b**) Physiological breathing motion; (**c**) Irreversible bonding of the three PDMS layers; (**d**) Chemical etching of side chambers; (**e**) Completed chip system viewed from above (scale bars, 200 μm). Reproduced from Huh et al. [15] with permission of AAAS

relaxed and stretched. This motion was meant to be similar to the influences of in vivo breathing motion and to simulate in vivo-like conditions for the cells (see Fig. 11.9a, b).

In the lung on chip, transformed cell lines were used (see Sect. 11.2.1). Human alveolar epithelial cells, namely, NCI-H441, a tumor cell line, were seeded on the upper side of the membrane, and human pulmonary microvascular endothelial cells were seeded on the bottom side. For better cell adhesion, the membrane was coated with fibronectin and collagen, which are ECM proteins. After cell seeding, both cell lines were first cultivated while submersed in separate media in the alveolar and vascular compartments. After reaching confluence, the alveolar cells were exposed to air, and in the interstitial chamber, a medium mixture with a ratio of 1 to 1 was used for cell nutrition. Due to the dynamic cultivation, the cells were viable for more than two weeks. Additionally, air-induced surfactant production, increased TEER values, and reduced albumin permeability were observed.

For the simulation of pulmonary inflammation, a proinflammatory mediator (tumor necrosis factor-alpha (TNF-α)), which is normally secreted by the lung parenchyma, was added to the cell culture medium. As a result, the expression of the infiltration protein intercellular adhesion molecule 1 (ICAM-1) increased, and thus, applied neutrophils migrated from the vascular compartment to the alveolar surface. Similar observations were obtained after the application of interleukin-8 and *Escherichia coli* bacteria. This application simulated bacterial infection, ending with phagocytosis of the bacteria by the neutrophils.

In additional experiments, the alveolar surface was exposed to silica nanoparticles with a diameter of approximately 12 nm to evaluate their toxicity. Triggered by these nanoparticles, ICAM-1 expression was increased, and thus, neutrophils infiltrated to the alveolar surface. These reactions were intensified when breathing motion was simulated. Other test parameters also showed a remarkable difference between static and biomimetic conditions. Therefore, static test systems may underestimate the toxic effect of an investigated substance. For further improvement of the system, other aspects, such as alveolar clearance, serum-free cultivation, and the use of primary cells or stem cells, may be considered.

In conclusion, the human lung on chip allows simultaneous analysis of barrier properties, permeation, and transport processes. The transparent material facilitates microscopic observation of processes such as cell migration. Thus, the lung on chip may be a suitable device for predicting the alveolar effects of chemicals and drugs. The lung on chip has also been refined into a disease chip for the simulation of pulmonary edema (see Sect. 11.4.3.1).

11.3.3.4 Gut on Chip

The gut is the most important digestive organ in the human body, and it absorbs nutritional elements as well as drugs. For this task, a large surface is needed, which is ensured by the formation of villi and microvilli on the intestinal mucosa. Moreover, the mucosa serves as a barrier between the intestinal lumen and the

blood that regulates the uptake and efflux of substances via a variety of different transporters. Those barrier properties are important for the prediction of drug absorption and thus have to be investigated in the pre-clinical phase via a gut on chip, for example.

In 2012, two years after the lung on chip paper was published (see Sect. 11.3.3.3), the working group of Donald Ingber modified their system to form a gut on chip [19]. For that purpose, they did not have to change the construction (see Fig. 11.9); they only had to adjust the application of the PDMS chip. To emulate the intestinal mucosa, just one cell line was needed, and both compartments had to be filled with fluid.

For the formation of an intestinal epithelium, the common cell line Caco-2BBE, a human colorectal carcinoma line, was used. The cells were seeded on the intestinal side of the ECM-coated membrane. Because of physiological fluid flow, the cells showed a taller and more polarized cell shape. They also displayed three- to fourfold higher TEER values than in static culture. Triggered by cyclic strain, they formed a monolayer with folds and microvilli similar to the natural appearance. This morphology could not be obtained in static Transwell® inserts. Moreover, the cultivation in the chip was less time consuming, lasting only three days, compared with three weeks in Transwell® culture.

The system was also tested with bacterial flora from the intestinal surface to improve the in vivo-like conditions. In contrast to static systems, it was possible to hinder the bacteria from overgrowing and crowding out the cells. Supported by the continuous flow, it was possible to maintain a stable co-culture of *Lactobacillus rhamnosus* GG and Caco-2 cells for more than one week. This symbiosis also improved the cells' barrier function. In the static Transwell® system, it was not possible to maintain the symbiosis. The TEER decreased within 48 h because of cell death and detachment.

All in all, the gut on chip was able to confirm that flow conditions and motion are essential not only for mimicking alveolar physiology; in the presented intestinal device, these influences were also of important interest for the development of in vivo-like barrier properties and physiological morphology. Moreover, the microfluidic system allowed co-cultivation of cells and bacteria. This feature is promising, as the bacterial flora participate in multiple intestinal functions, such as drug metabolism, and support the intestine's barrier function. Therefore, this feature may be essential for future pre-clinical trials. Nevertheless, the gut on chip can be improved by replacing the tumor cell line or the cultivation with serum. Furthermore, physiological gut peristalsis is more diverse than the applied motion in this model. As a consequence, whether the simulation of gut motion in the gut on chip is sufficiently representative of the physiological situation has to be examined.

11.3.3.5 Heart on Chip

The heart is the power unit of the living body. Therefore, cardiac adverse effects can be severely life threatening. For this reason, pre-clinical studies are performed to estimate the potential of cardiac risks, such as QT prolongation. Generally, these

studies are conducted on animals, ex vivo tissue slices, or isotropic cell layers, but these methods entail all of the disadvantages already mentioned in Sect. 11.3.1.

In 2011, Grosberg et al. invented a new in vitro system that was completely different from all common cardiac in vitro systems because of its anisotropic tissue structure [11]. Their heart model used primary neonatal rat ventricular myocytes that had been extracted from the ventricles of two day old neonatal Sprague–Dawley rats. Those cells were seeded on flexible PDMS films (MTFs; for fabrication, see Sect. 11.2.2.3) whose surface had been modified with a microcontact printed ECM pattern. This guidance ensured the development of an anisotropic tissue structure. After four days of cultivation, a monolayer in which the cells aligned perpendicularly to the fixated MTF front had formed. This innovative tissue engineering was able to reproduce the physiological alignment of cardiac cells and the polarization of contractile filaments. An in vivo-like tissue structure was thereby obtained, which ultimately resulted in high diastolic and systolic stresses, similar to those of isolated muscle strips. These high stresses could not be obtained with isotropic cellular alignment.

For the experiments, eight MTFs were transferred to a Petri dish and observed by a video camera (later, this technology was integrated into a chip system (see Sect. 11.3.3.6)). A defined simultaneous contraction with a frequency of 2 Hertz (Hz) was generated by an external field. The resulting film deflection depended on the obtained contractile stress. This stress could be calculated from the x-projection of the MTFs, which correlated with the radius of curvature (see Fig. 11.10d, e). The calculated stress was comparable between the eight films. Grosberg et al. also investigated the effect of cumulative epinephrine dosing. For this experiment, they applied increasing concentrations of epinephrine. At every concentration, the sinusoidal stress profiles were used to calculate the average frequency of contraction. With increasing concentration, the frequency of contraction also rose. Hence, Grosberg et al. were able to confirm the chronotropic effect of epinephrine using their model.

Beyond contractile stress, the researchers also evaluated the electrophysiology of the MTFs. Before recording the action potential wave front, the MTF contraction was hindered with an excitation-contraction decoupler. The action potential morphology and wave front propagation were then visualized with a voltage-sensitive membrane dye (RH 237). This method allowed the assessment of electrophysiological parameters and is, apart from contractility experiments, important for safety and efficacy testing.

Although the anisotropic MTFs were only 2D in vitro models, they were able to show systolic and diastolic stress values similar to those of isolated rat ventricular papillary muscle strip experiments. Moreover, the system applies primary cells, is easy to fabricate and is suitable for high-throughput screening. As a result, the model may be used for contractility and electrophysiology evaluation in fundamental research and drug development processes, especially after integration into an OOC (see Sect. 11.3.3.6).

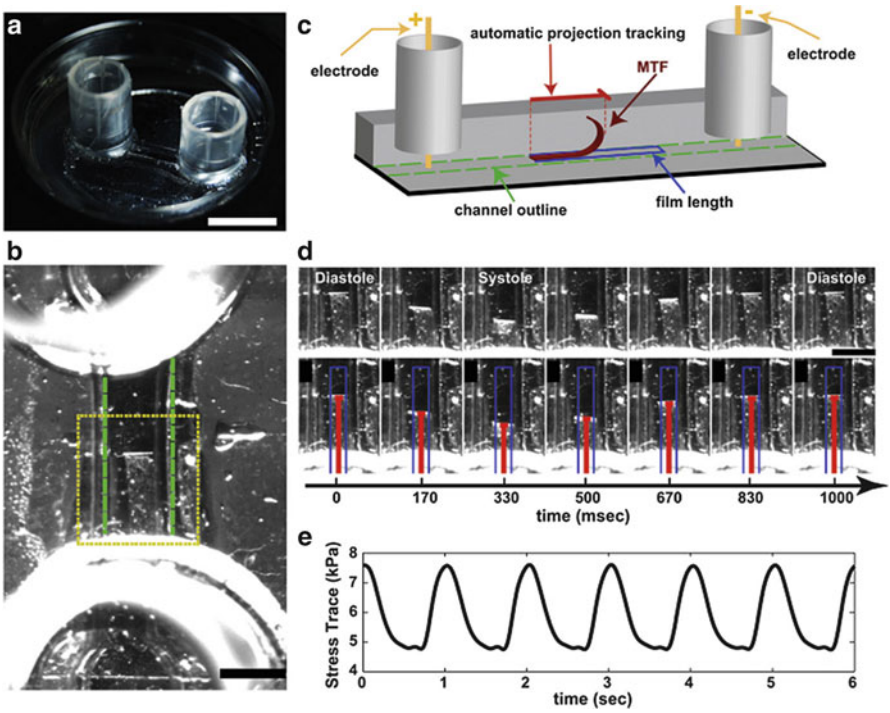

Fig. 11.10 Muscle on chip: (**a**) Photograph of a fluidic channel top, scale bar 10 mm; (**b**) Photograph of a muscle chip from the top, channel marked in *green*, scale bar 2 mm; (**c**) Schematic side view of the chip system; (**d**) *Top row*: bending of the MTF over time; *bottom row*: analysis of the top row (*red*: x-projection of the contracted film, *blue*: original film length); (**e**) An example output of contraction stress data for a film over time (paced at 1 Hz). Reproduced from Grosberg et al. [12] with permission of Elsevier

11.3.3.6 Muscle on Chip

The aforementioned heart on chip was not an actual chip system, but rather served as the preliminary stage for the integration of MTFs (see Sects. 11.2.2.3 and 11.3.3.5) into a microchip. Furthermore, the heart on chip was the first MTF with a tissue design similar to that of human striated muscles. This muscle type can be found in the skeletal muscles and in the cardiac muscle. The striated tissue is composed of repetitive sarcomeres, which result in the tissue's striated structure. Conversely, smooth muscles show spindle-shaped cells without cross-stripes. The smooth muscle type is found mostly in visceral tissue and blood vessels. As their structures as well as their behaviors are highly different, an in vivo test system should differ between those two diverse tissue types.

Therefore, in 2012, an important investigation was performed by Grosberg et al.: they compared different fibronectin patterns for the formation of both smooth and striated anisotropic MTFs [12]. The resulting muscular structures were then

cultivated separately and were afterward linked to each other. This combination was a first step toward multi-organ chips (see Sects. 11.3.4 and 11.3.5). Furthermore, the researchers integrated the MTFs into a chip system for the first time (see Fig. 11.10).

In this study, Grosberg et al. started by producing MTFs as described in Sect. 11.2.2.3. Afterward, different fibronectin patterns were microcontact printed onto the film surface. For the vascular smooth muscle films (vMTFs) and the cardiomyocytes (cMTFs), a pattern of lines with spaces and a "brick-wall" pattern (also used for the heart on chip; see Sect. 11.3.3.5), respectively, were designed to emulate the different physiological tissue structures. Human vascular smooth muscle cells (VSMCs), which were primary cells obtained from human umbilical arteries, were seeded on the vMTFs and cultivated for four days, until the formation of a confluent monolayer. For the cMTFs, neonatal rat ventricular myocytes from two day old Sprague–Dawley rats were used as described before (see Sect. 11.3.3.5). Both generated a tissue-specific anisotropic monolayer. After cultivation, the MTFs were cut and integrated separately into single chips. The chip height was adapted to the length of the MTF to ensure no hindrance in film deflection (see Fig. 11.10b, c).

In contrast to the cMTFs, the novel vMTFs showed no rhythmic contraction. As smooth muscle tissue, they had continuous contraction, similar to their in vivo counterparts. Their muscle tone could be influenced by endothelin-1 (ET-1) and HA-1077. ET-1, as an effective physiological vasoconstrictor, resulted in rising stress and stronger contraction. HA-1077, a Rho-associated protein kinase (ROCK) inhibitor, induced complete relaxation by lowering the muscular stress. Both results met expectations and supported the enormous potential of ROCK inhibitors. The cultivated cMTFs showed similar characteristics, as investigated in previous publications (see Sect. 11.3.3.5).

Before combining the two organ chips, striated and smooth muscle films were cultivated separately. Thus, Grosberg et al. did not have to find an adequate medium for the two-organ chip, and both films were cultivated under optimal conditions. All experiments were performed in a buffer that reduced the potential of substance-medium interactions. The cMTFs were then paced by electrodes with a frequency of 2 Hz. There was no negative effect on the contraction of the vMTFs. The application of ET-1 and HA-1077 showed the same results for the vMTFs as before. Moreover, a decrease in the systolic stress of the cardiomyocytes was observed in response to ET-1 as well as to the ROCK inhibitor. Thus, this early two-organ chip analog was able to simulate differing effects on vascular and cardiac muscles and was able to predict possible cardiac adverse effects.

All in all, by the simple application of different fibronectin patterns, the physiological cellular architecture of smooth as well as striated muscles was successfully recreated. Furthermore, the combination of different tissue chips allowed the simultaneous analysis of diverse tissue behaviors and served as one step toward multi-organ chip systems.

11.3.3.7 Blood–Brain Barrier on Chip

The blood–brain barrier (BBB) is a physiological hurdle, especially for molecules with a molecular weight greater than 500 Dalton (Da). The BBB's special structure consists of multiple different cell layers that build and surround the cerebral blood vessels. Apart from the vascular endothelial cells, with their tight cell–cell connections, the adjacent astrocytes and pericytes contribute significantly to the barrier function. As a consequence, strict control of substance passage from the blood into the brain tissue is obtained, which ensures physiological cerebral homeostasis and protects the brain from harmful compounds.

In pharmaceutical research and development, the BBB is of increasing interest because of the rising prevalence of central nervous diseases (CNDs) such as multiple sclerosis and Alzheimer's disease. In the therapy for those CNDs, the effort of the drug depends highly on passage through the BBB, which physiologically hinders the drug from reaching its site of action. However, there are also APIs that cannot cross the BBB, with the aim of circumventing adverse effects in the central nervous system. All in all, therapeutic as well as adverse effects may be estimated more reliably using a validated BBB chip. Thus, the main objective of Booth et al. in 2012 was to develop a BBB on chip system as a valid alternative for many studies on BBB function and drug delivery. The developed μBBB was intended to address all of the disadvantages of already developed systems [3]. The model, for example, showed a highly controlled microenvironment, decreasing cell distances, physiological shear stress, and influences on the endothelial cell layer and allowing better analysis of test compounds. The chip is also an excellent example of a system allowing easy microscopic observation, despite the integration of electrodes for continuous TEER assessment.

To achieve those aims, Booth et al. developed a multilayered chip system with perpendicular crossing channels, built from four PDMS substrates and two glass layers (see Fig. 11.3). At the crossing, a PC membrane with 400 nm pores was included. The upper channel was meant to mimic the blood vessels. Therefore, the immortalized endothelial cell line b.End3 was seeded onto the membrane, and a high aspect ratio (10:1) was used to promote a uniform shear stress distribution across the cells. The b.End3 cells were chosen because of their good cell characteristics in previous studies. The researchers had achieved, for example, high functionality of P-glycoprotein (P-gp) and other transporters as well as relatively high TEER and permeability values. Adjacent to the endothelial cells, an astrocyte cell line, or C8-D1A, was used on the bottom side of the membrane. Both cell lines were of murine origin.

The bottom channel was significantly wider than the top channel to minimize shear stress influences on the astrocytes. For continuous TEER measurement, two pairs of thin-film AgCl electrodes were included in the glass slides that were embedded in the PDMS layers. As all employed material was clear and the electrodes were designed carefully, microscopic observation was possible and thus facilitated morphological evaluation.

After fibronectin coating of the PC membrane, an astrocyte suspension was injected and left without flow for 2 h. The adhered cells were then cultivated under flow for two days before the endothelial cells were added in the same way. Twelve hours later, the flow was increased to the experimental level. As a result of the co-culture and the influence of the shear stress, the cells expressed cellular markers such as tight junctional proteins. Therefore, the TEER values in the dynamic state were tenfold higher than in the static state. Moreover, the co-cultivation resulted in much higher TEER values than monoculture did. Unfortunately, the co-culture did not reach in vivo-like TEER values (300 Ω cm^2 vs. 1000 Ω cm^2). However, the chip system showed physiological recovery after the TEER values were decreased by histamine application. Thus, the BBB model might be suitable for generating repeatable testing conditions. Additional observations showed that the permeability of different fluorescently marked dextrans was lower in co-cultivation than in monoculture. A tested increase in pH up to 10 resulted in significantly higher permeability and showed that the barrier function could be disturbed.

All in all, this BBB on chip system resulted in TEER values and permeability coefficients higher than in many previous models, even if not as high as in primary cell cultures and under in vivo conditions. Further improvements of the model should also integrate the third BBB cell type, namely, pericytes. All three cell types, together with serum-free cultivation, may lead to better prediction of in vivo drug permeability across the BBB.

A different approach has been proposed by Yeon et al., who developed a BBB chip based on microchannel structures to study drug permeability (see Fig. 11.4). These diverse OOCs for emulation of the BBB show that the challenge of OOC development can be faced with relatively different strategies (for further information, see Wolff et al. [47]).

11.3.3.8 Various Other Organs on Chips

Apart from all of the organ systems on chips mentioned above, various other special organs have been under investigation, such as splenon on chip [30] or bone marrow on chip [39]. Blood vessels on chip are also of particular interest for use as linking units between different OOCs [33]. In summary, all of the latest developments have shown that there will be intense but interesting developments in this field over the coming years, with the objective of emulating human physiology for pre-clinical substance testing.

11.3.4 Multi-Organ Chips

Until the development of a whole human organ system, multi-organ chips will serve as an intermediate step to investigate the interplay of different chip systems. By the combination of a few organ chips, cell–cell signaling and thus communication

between organs can be investigated, for instance. Furthermore, several steps of the LADME principle (see Sect. 11.3.1) can be evaluated. Unfortunately, the combination of multiple cell types and tissues also implies diverse complications, such as finding the optimal culturing conditions and preventing cellular interactions.

For the construction of multi-organ chips as well as a complete human on chip, there are two main strategies: first, the linkage of formerly developed single-organ chips, and, second, the integration of several organs into a single chip device (see Sect. 11.3.5). The latter has been especially supported by the working group of Uwe Marx at the Technische Universität Berlin and TissUse GmbH (see Fig. 11.2) [2, 43]. This group started with a two-organ chip combining a liver compartment and a skin compartment [43]. These two organs are of special interest because of their important physiological functions. The liver, as a metabolizing, detoxifying, and excreting organ, is important for drug metabolism. Furthermore, hepatic adverse effects are often the reason for substance withdrawal during the development process (see Sect. 11.3.3.1). By the combination of liver cells with a biopsy of skin, the researchers were able to estimate the allergic potential in the skin. Those insights are highly important for the cosmetic industry, especially since the marketing ban in 2013 (see Sect. 11.3).

The chip system itself was built to have the size of a standard microscope slide, to minimize space requirements and to obtain more physiological fluid-to-tissue ratios. The size of the single organ compartment had to be small enough to allow the combination of up to ten organs for a human on chip (see Sect. 11.3.5) and to guarantee organ communication. For the crosstalk, a minimum amount of cells is essential, so Wagner et al. decided to recreate 1/100,000 of the human counterpart [43]. As a result, the two-organ system was small enough to include two separated PDMS circuits on one microscope slide. The circular cell culture compartments had the size of a 96-well plate and allowed the integration of common cell culture filter inserts for the cultivation of cell lines, primary cells, tissue biopsies, or ready-to-use models (e.g., MatTek®). Therefore, two different cultivation conditions were possible. The cells could be exposed to shear stress directly in the channel, or they could be protected from shear forces in cell culture inserts. The medium was pumped through the connecting tubing by a peristaltic pump built from three 500 µm-thick PDMS membranes included on the glass slide (see Fig. 11.2). In this way, the medium volume could be reduced to a physiological ratio. Beneficially, the system showed low maintenance under continuous service and thus allowed liver and skin cell cultivation for 28 days. Such long cultivation is, on the one hand, of great interest for examining long-term effects and, on the other hand, an important requirement for the testing of repeated dose exposure.

Lately, a four-organ chip with an integrated small intestine compartment, a liver compartment, renal secretion, and skin biopsies was published [22]. With this stepwise development, researchers are approaching the generation of a human on chip more and more.

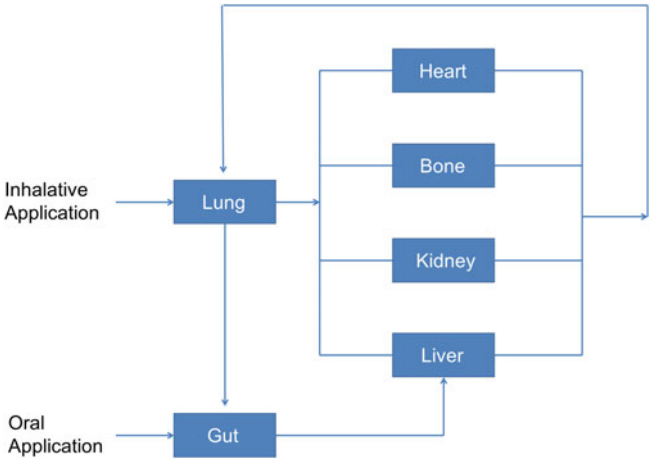

Fig. 11.11 Schematic of a human on chip formed by the linkage of single-organ chips

11.3.5 Human on Chip

The overall aim of the development of a single-organ or multi-organ chip is the establishment of a whole body on chip, also known as a human on chip. There are several governmental projects, such as those funded by the American Defense Advanced Research Projects Agency (DARPA), the National Institutes of Health (NIH), and other institutions, supporting research in the field of OOCs (see Sect. 11.4.1).

For the design of a human on chip, two strategies exist. One faces the problem by linking established single-organ chips (see Fig. 11.11), and the other includes different organ compartments on one chip (see Fig. 11.12). Regardless of the strategy, most approaches focus on approximately ten important organs.

Before a human on chip can be established, various challenges in the engineering as well as in the implementation have to be faced. Apart from challenges also appearing for single-organ chips, for the construction of a human on chip, organ proportions and fluid scales are of great interest. Only in consideration of all of these factors can an exact emulation of physiological circumstances and a reliable prediction of pharmacokinetics and pharmacodynamics be possible [4, 44, 45].

After the choice of cell type or cell combination, the right medium for all cells has to be found. Currently, many working groups are using medium mixtures for multi-organ chips (see Sect. 11.3.4). By the connection of up to ten organs, this strategy will eventually result in severe medium interactions and lower concentrations of individual nutritional factors. Certain researchers therefore plan to use human blood to guarantee optimal conditions for all organs. This strategy may result in lower reproducibility because of natural variability in blood composition. Moreover, by using whole blood and by combining different organs from various

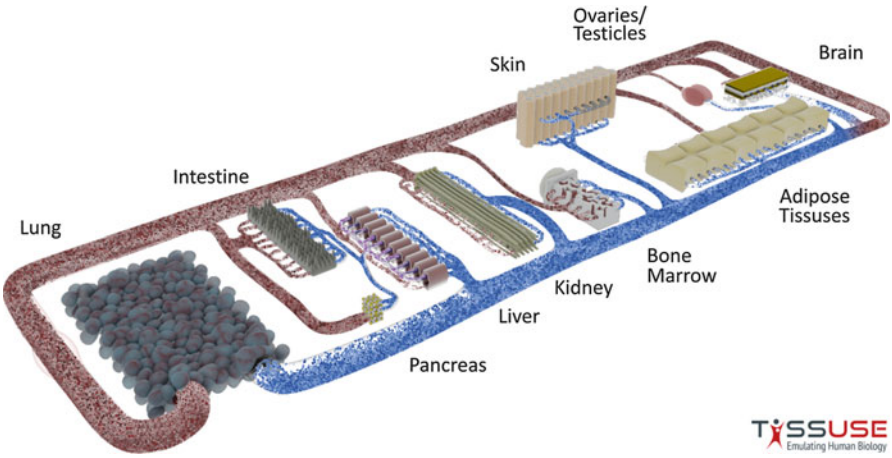

Fig. 11.12 Vision of a human on chip from TissUse GmbH. Reproduced with permission of TissUse GmbH

origins, the risk of immune reactions between those compartments increases. One potential solution for the immune problem and the variation of blood composition may be the generation of organs and blood equivalents from induced pluripotent stem cells (iPSCs; see Sect. 11.4.4).

Problems in the development of human on chip systems have also been addressed by van der Meer and van den Berg. The authors emphasize that complicating the culture conditions and the whole chip construction might result in blurred results. Therefore, the emulation of human physiology should always be as simple as possible. Only highly relevant aspects should be integrated. In certain cases, the use of cells is necessary, but in other cases, they can be substituted by technical compounds. Van der Meer and van den Berg also recommended a dialog between the working groups to develop compatible organ systems for easier combination of all single-organ chips in the future. A modular plug-and-play system may then be used to link compatible chips. Other future visions even consider two-way dynamics between cells and technology to generate, for example, a feedback mechanism between mechanical force units and cellular signaling molecules [40].

Last, but not least, the needs of the industrial users of organ systems on chips must not be forgotten. In pharmaceutical research and development, for example, suitability for high-throughput screening, the reliability of results, the demand for a substance, and costs are important considerations for the implementation of new in vitro models. Hence, the development of organ systems on chips will only be successful if the pharmaceutical industry and regulatory agencies are involved in the development and validation processes.

11.3.6 Outlook

The presented selection of various OOCs highlights the enormous progress that has been made during the last few years. All of these inventions are promising steps toward the implementation of more reliable in vitro test systems and thus might finally be able to replace animal experiments completely.

11.4 Applications

11.4.1 Current Political Development

Organ systems on chips are promising in vitro test systems for many applications. On the one hand, they can be utilized in toxicity testing of cosmetics and chemicals. On the other hand, they can be used in processes for novel and generic drug development or even in special fields such as radiation testing. These examples emphasize the widespread desire to develop reliable organ systems on chips, and they may also be the reason for governmental support for this field. The EU, for example, started a project called "body-on-a-chip" in 2014. In the USA, a similar project, called "Tissue Chip for Drug Screening," is being funded by the NIH, DARPA, and the Food and Drug Administration (FDA). This governmental funding supports the relevance and value of organ chip studies. Therefore, the interest of pharmaceutical companies has also risen. All in all, the resulting chip systems will only be able to meet all of the needs of the participants if governmental institutions, researchers, and the pharmaceutical industry act in concert during the development process. Only this collaboration can result in a significant change in our common pre-clinical test practices.

11.4.2 Organ on Chip in Pharmaceutical Research and Development

After successful development and validation, OOC systems will contribute significantly to pharmaceutical research and development. In the drug development process (see Sect. 11.3.1) and in biowaiver studies for the approval of generic formulations, these systems may reduce the need for animal experiments and provide more reliable results. As a consequence, the prediction of clinical studies will be improved, and late-stage failure may occur more rarely. Apart from the replacement and improvement of common pre-clinical test systems, organ systems on chips will offer many new opportunities in pharmaceutical research and development. For example, these systems will allow the simulation of diseased organisms or the generation of personalized chips.

11.4.3 Disease Chips

In the drug development process, a new drug is first tested in animals and in in vitro test systems. Later, the drug's safety is evaluated in healthy humans, and only in the third clinical phase is the substance tested in diseased people (see Sect. 11.3.1). This approach protects patients from harm but can also result in costly and dangerous late-stage drug failure. Thus, an early evaluation of pharmacokinetic and pharmacodynamic parameters in a diseased OOC test system would be advantageous. In cancer therapy in particular, in which safety and efficacy studies can only be performed with restrictions because of the drug's harmful potential, this approach would be beneficial. Certain examples of already-developed disease states on chips will be introduced in the following paragraphs.

11.4.3.1 Pulmonary Edema on Chip

As one of the first disease chips, Huh et al. developed a pulmonary edema model based on their lung on chip system (see Sect. 11.3.3.3). Pulmonary edema can generally be induced by various diseases or medications. One reason for this condition is the application of interleukin-2 (IL-2), which is used to treat malignant melanoma and metastatic renal cell carcinoma. IL-2 can cause inflammation, extravasation, fluid accumulation, and deposition of fibrin, all of which can be severely life threatening [14].

In the chip system, these effects were simulated by the application of a clinically relevant dose of IL-2 to the previously described lung on chip. This application resulted in leakage of fluid into the air interface, which could be observed as a meniscus at first and as a complete filling of the alveolar channel after four days. A further addition of the plasma proteins prothrombin and fibrinogen to the blood compartment resulted in in vivo-like fibrin clots on the alveolar epithelium. This debris is also present during physiological alveolar inflammation. Huh et al. also investigated the permeability of fluorescently labeled molecules. These experiments showed that mechanical forces dramatically decreased the alveolar barrier function, in contrast to static observations, and therefore are highly important relative to the in vitro results.

After the emulation of critical disease conditions, Huh et al. used the system to identify new and promising therapeutics for the treatment of pulmonary edema. For this reason, angiopoietin-1 (Ang-1) and GSK2193874, a vanilloid 4 (TRPV4) ion channel inhibitor, were applied separately. Ang-1 stabilized endothelial intercellular junctions and, by this mechanism, inhibited the influence of IL-2 both with and without mechanical strain. GSK2193874 also inhibited the effects of IL-2 by hindering the activation of TRPV4 channels, which are generally activated by mechanical strain and support leakage of fluid.

In summary, first, Huh et al. were able to reproduce results from animal experiments and clinical tests using their alveolar inflammation chip system,

without the need for integration of immune cells (see Sect. 11.3.3.3). Second, they verified the inhibition of edema by Ang-1 and GSK2193874. Last, but not least, their work emphasized the importance of physiological motion and strain for organ systems on chips. Therefore, this disease chip might be suitable for the pre-clinical screening of new drug candidates to detect alveolar adverse effects in an early stage of drug development.

11.4.3.2 Allergic Asthma on Chip

Asthma is believed to be a leading cause of emergency department visits and hospitalization in pediatric populations. Allergic asthma is caused by structural remodeling and an increased presence of immune cells in the alveolar tissue. These alterations can result in a dramatic increase in smooth muscle tone because of allergen exposure, which might cause life-threatening airway narrowing (see Fig. 11.13ai, aii). Unfortunately, only two new drug classes for this condition have been released into the US market over the last 30 years, which may be the result of the lack of reliable pre-clinical test systems, such as animal experiments and tests on ex vivo tissue, including muscle strips (see Sect. 11.3.1) [24].

Therefore, the development of reliable OOC systems is a demanding task, as addressed in 2014 by Nesmith et al., who improved MTF technology (see Sects. 11.3.3.5 and 11.3.3.6). For the pre-clinical drug screening of healthy as well as pathologically altered alveolar tissue, an anisotropic, laminar bronchial smooth muscle (BSM) tissue was built. Primary human BSM cells were cultivated on MTFs (see Sect. 11.2.2.3) that had been prepared with a special fibronectin pattern to obtain an anisotropic tissue structure (bMTFs). After cultivation with serum for 48 h, a confluent layer was formed. Subsequently, the serum was left out for 24 h to induce a contractile phenotype, which caused a constant basal tone and an initial curvature after detaching the film from the substrate.

The addition of interleukin-13 (IL-13), which is a cytokine found in asthmatic patients, should induce an inflammatory state. Physiologically, IL-13 increases bronchoconstriction and supports structural remodeling. In IL-13-treated bMTFs, this altered cell morphology was recreated by increasing the cell size and the alignment of contractile fibers. Concerning the tone of the bMTFs, no significant differences in basal values were observed between normal and IL-13-treated bMTFs (see Fig. 11.13bii, cii). However, differences between these groups occurred after application of acetylcholine (ACh), which induces contraction (see Fig. 11.13e). The diseased bMTFs showed hypercontraction, in contrast to healthy films (see Fig. 11.13biii, ciii), which is similar to the altered reaction in the diseased state.

Apart from bronchoconstriction, bronchodilatation was also investigated. Therefore, the beta-agonist isoproterenol was applied with or without previous ACh-induced contraction. As a result, the healthy bMTFs showed no differences in relaxation with or without previous contraction, but the asthmatic bMTFs showed less relaxation after constriction than in the absence of constriction.

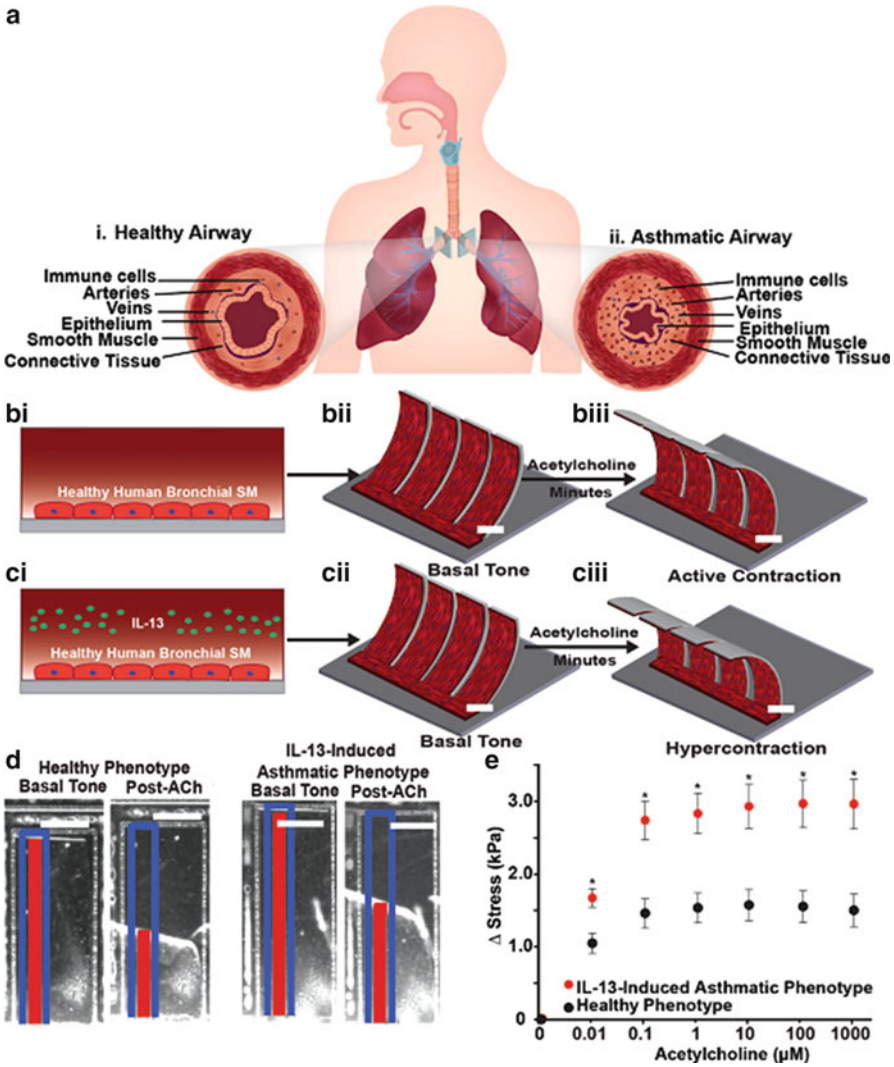

Fig. 11.13 Human airway musculature on chip: (**a**) Schematic of healthy (*i*) and asthmatic (*ii*) airways; (**b**) Schematic depicting ACh-induced contraction of a healthy bMTF chip, scale bar: 2 mm; (**c**) Schematic depicting ACh-induced contraction of an asthmatic bMTF chip, scale bar: 2 mm; (**d**) Representative images of bMTFs at basal tone and after ACh administration, scale bar: 1 mm, *blue*: original length, *red*: horizontal projection; (**e**) Calculated stress of bMTFs plotted against the ACh concentration (* means $p < 0.05$). Reproduced from Nesmith et al. [24] with permission of The Royal Society of Chemistry

These results are similar to the finding of experiments with ex vivo tissue and are comparable to findings obtained in patients. Generally, asthmatic patients also show a weaker response to relaxing drugs after the application of ACh. Hence, the

allergic asthma model managed to successfully recreate this altered reaction. Furthermore, the findings show that when applied alone, cytokines such as IL-13 do not seem to hinder dilatation. However, the combination of IL-13 and ACh was able to impair the effect of isoproterenol. Thus, by this systematic investigation, Nesmith et al. were able to improve the comprehension of cellular signaling pathways.

Because IL-13 is believed to induce RhoA, whose upregulation is assumed to be the cause of hypercontraction, Nesmith et al. applied a RhoA inhibitor known as HA-1077 to prevent hypercontraction. HA-1077 had already been shown to inhibit excessive contraction in animal models. After cultivation, the bMTFs were exposed to HA-1077 in various application regimens. All in all, the HA-1077-treated asthmatic MTFs showed lower stress than the healthy and untreated asthmatic phenotypes did. Relaxation by HA-1077 was more intense than relaxation by isoproterenol was. Additionally, the combination of isoproterenol and HA-1077 caused improved relaxation compared with isoproterenol alone because of their different mechanisms of action. All of these results highlight that HA-1077 may be a promising drug candidate for allergic asthma therapy.

Even though these experiments were performed in a Petri dish, the presented techniques showed results that are comparable to those obtained in animal models and clinical observations. Thus, bMTFs can be advantageous for the identification of promising drug candidates in the pre-clinical phase and for the investigation of cellular mechanisms in fundamental research. Their applicability can further be improved by adaption to chip systems, as has been done for other MTFs (see Sect. 11.3.3.6).

11.4.3.3 Cancer on Chip

Apart from diseases such as pulmonary edema (see Sect. 11.4.3.1) and asthma (see Sect. 11.4.3.2), the application of disease chips is of great interest for fundamental tumor research and therapy. To date, only little is known about the mechanisms of tumor formation and proliferation. Therefore, reasonable therapeutic strategies and anticancer drug development often fail during the development process.

Early in vitro systems for cancer research used ECM proteins and other hydrogels to form a 3D matrix (see Sect. 11.3.2). In this way, the mechanical tumor–matrix interaction as well as cell invasion could be studied, which resulted in the establishment of diverse angiogenesis models. Other, more modern systems are based on spheroids of tumor cells. Those 3D constructs can comprise multiple cell types and thus are better replicates of multicellular tumor nodules. The spheroids can be built from a hanging drop system or roller flasks to ensure non-adherent conditions. After cultivation, the spheroids can be used in 96-well plates, in channel systems or embedded in ECM gels to investigate tumor growth and drug efficacy. Moreover, co-cultivation of differently composed spheroids helps to emulate the physiological heterogeneity of tumor tissue.

Apart from tumor spheroids, well plates and Transwell® systems are used in cancer research. Tumor–stromal interaction may then be built up using two adjacent cell layers. One bottom cell layer comprises feeder cells, and the second layer contains the tumor cells. With this experimental setup, paracrine influences can be evaluated, for example. Unfortunately, these systems lack important physiological factors, such as a small scale and an appropriate medium-tissue ratio. The medium volume is, for example, relatively high, and the diffusion distances are very long. Because of these drawbacks, the establishment of a microfluidic system would improve reliability, facilitate automation, and allow simulation of physiological gradients (e.g., growth factors, oxygen).

Nevertheless, for a better understanding of cancer, in vitro models should model not only tumor development but also tumor–tissue interactions. In the past, most metastasis studies had to be conducted with in vivo mouse models because of a lack of reliable in vitro methods. Microfluidic systems would offer the opportunity to control and test environmental factors more easily. Moreover, the combination of tumor compartments with different tissue beds using a circulating system could help to improve understanding of the role of mechanics in the formation of secondary tumors. Apart from dynamic simulation in an OOC, the combination of multiple tumor compartments will help to recreate physiological tumor heterogeneity, which is important to obtain significant results. All in all, these advantages emphasize the importance of cancer systems on chips to improve and enrich tumor research and therapy (for further information, see Young [49]).

11.4.4 Induced Pluripotent Stem Cells: Patient on Chip?!

Stem cells are generally cells that have not yet differentiated into a specialized cell type. Depending on their origin, these cells can be distinguished as embryonic or adult stem cells. Because of ethical concerns, embryonic stem cells cannot be used easily. Therefore, researchers often refer to iPSCs. These cells can be obtained, for example, by treating adult cells with reprogramming factors. The resulting iPSCs are pluripotent and similar to embryonic stem cells, which means that they can differentiate into nearly every cell type when exposed to certain differentiation factors (see Fig. 11.14). On the one hand, the resulting cell type could be reprogrammed and returned to the same patient for therapeutic tissue engineering. On the other hand, these cells can allow for patient-specific drug testing [32]. Patient-derived iPSCs can, for example, be used for the fabrication of patient on chip systems. This OOC would combine the benefits of microfluidic systems with the characteristics of physiological, human, and untransformed cells differentiated from iPSCs (see Sect. 11.2.1). Moreover, demanding conditions such as genetic polymorphisms as well as disease states can be emulated more easily.

Apart from the vision of personalized chips, iPSC technology offers many advantages for the development of a human on chip (see Sect. 11.3.5). The generation of all organs from one donor may, for example, reduce immune

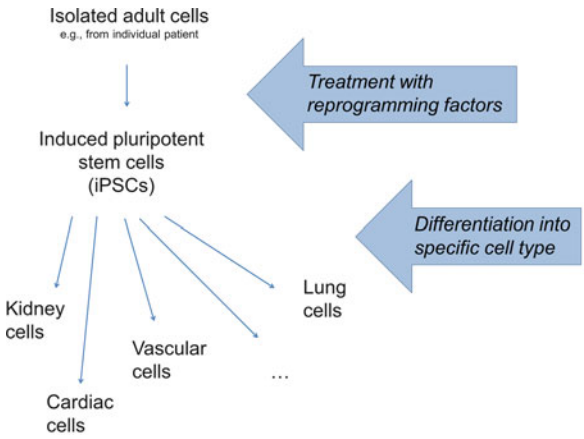

Fig. 11.14 Preparation of iPSCs, with subsequent differentiation into diverse specific cell types

reactions. Moreover, the influence of patient-specific factors, such as genetics, sex, age, and ethnicity, on a drug's efficacy may be investigated more easily. In the future, maybe those tests will be routinely performed and will directly affect the therapeutic regimen.

Currently, the benefits of iPSCs are controversial, but the coming years will show whether this cell type can meet all expectations and whether these cells will offer new opportunities in OOC research and application [31, 46].

11.4.5 Outlook

In contrast to the general field of OOCs, the implementation of disease chips or personalized chips for drug testing is still at its beginning. However, by taking advantage of the rapid development of OOCs, pharmaceutical application will keep up easily. Thus, innovations and processes in this field shall be watched with great interest over the coming years.

11.5 Concluding Remarks

OOC systems are promising new tools for studying physiology and pathogenesis as well as drug discovery. These systems show distinct advantages over traditional animal testing and conventional 2D in vitro cell culture models in many areas of pharmaceutical research. It can therefore be assumed that one day, OOCs will replace a large number of animal experiments, particularly in the pre-clinical development of new drugs. However, this field is still at an early stage, and major challenges still need to be addressed before OOC technology becomes available to

the pharmaceutical industry on a large scale. Numerous OOC systems representing various organs have been described, but these vary in design and approach between working groups. Therefore, the optimization of established OOCs toward a more unified, widespread in vitro test system and characterization and validation of this system so that it will be accepted by the pharmaceutical industry and the regulatory authorities are still a long way off and a major task for the coming years. The focus of future developments should lie in standardization of design principles; improvement of analytics, and particularly integrable biosensors; and identification of new biocompatible materials for OOCs, with improved properties compared with the previously used materials. In addition, future OOC systems for widespread application in drug discovery should be reproducible, user friendly, cost effective, and available in high quantities for high-throughput screening. Another challenge will therefore be the transfer of laboratory-based prototyping to commercial manufacturing of OOCs to bring these OOCs from the laboratory scale to the industrial scale for robust animal replacement for the development of drugs.

References

1. Achyuta AKH, Conway AJ, Crouse RB, Bannister EC, Lee RN, Katnik CP, Behensky AA, Cuevas J, Sundaram SS (2013) A modular approach to create a neurovascular unit-on-a-chip. Lab Chip 13(4):542–553
2. Ataç B, Wagner I, Horland R, Lauster R, Marx U, Tonevitsky AG, Azar RP, Lindner G (2013) Skin and hair on-a-chip: in vitro skin models versus ex vivo tissue maintenance with dynamic perfusion. Lab Chip 13(18):3555–3561
3. Booth R, Kim H (2012) Characterization of a microfluidic in vitro model of the blood-brain barrier (μBBB). Lab Chip 12(10):1784–1792
4. Capulli AK, Tian K, Mehandru N, Bukhta A, Choudhury SF, Suchyta M, Parker KK (2014) Approaching the in vitro clinical trial: engineering organs on chips. Lab Chip 14 (17):3181–3186
5. Chueh B, Huh D, Kyrtsos CR, Houssin T, Futai N, Takayama S (2007) Leakage-free bonding of porous membranes into layered microfluidic array systems. Anal Chem 79(9):3504–3508
6. Darvishi S, Cubaud T, Longtin JP (2012) Ultrafast laser machining of tapered microchannels in glass and PDMS. Opt Lasers Eng 50(2):210–214
7. Dash A, Inman W, Hoffmaster K, Sevidal S, Kelly J, Obach RS, Griffith LG, Tannenbaum SR (2009) Liver tissue engineering in the evaluation of drug safety. Expert Opin Drug Metab Toxicol 5(10):1159–1174
8. Deiss F, Mazzeo A, Hong E, Ingber DE, Derda R, Whitesides G (2013) Platform for high-throughput testing of the effect of soluble compounds on 3D cell cultures. Anal Chem 85 (17):8085–8094
9. Domansky K, Inman W, Serdy J, Dash A, Lim M, Griffith LG (2010) Perfused multiwell plate for 3D liver tissue engineering. Lab Chip 10(1):51–58
10. Griep LM, Wolbers F, de Wagenaar B, Ter Braak PM, Weksler BB, Romero IA, Couraud PO, Vermes I, Van Der Meer AD, Van Den Berg A (2013) BBB on chip: microfluidic platform to mechanically and biochemically modulate blood-brain barrier function. Biomed Microdevices 15(1):145–150
11. Grosberg A, Alford PW, McCain ML, Parker KK (2011) Ensembles of engineered cardiac tissues for physiological and pharmacological study: heart on a chip. Lab Chip 11 (24):4165–4173

12. Grosberg A, Nesmith AP, Goss JA, Brigham MD, McCain ML, Parker KK (2012) Muscle on a chip: in vitro contractility assays for smooth and striated muscle. J Pharmacol Toxicol Methods 65(3):126–135
13. Huh D, Hamilton GA, Ingber DE (2011) From 3D cell culture to organs-on-chips. Trends Cell Biol 21(12):745–754
14. Huh D, Leslie DC, Matthews BD, Fraser JP, Jurek S, Hamilton GA, Thorneloe KS, McAlexander MA, Ingber DE (2012) A human disease model of drug toxicity-induced pulmonary edema in a lung-on-a-chip microdevice. Sci Transl Med 4(159):159ra147
15. Huh D, Matthews BD, Mammoto A, Montoya-Zavala M, Yuan Hsin H, Ingber DE (2010) Reconstituting organ-level lung functions on a chip. Science 328(5986):1662–1668
16. Huh D, Torisawa Y, Hamilton GA, Kim HJ, Ingber DE (2012) Microengineered physiological biomimicry: organs-on-chips. Lab Chip 12(12):2156–2164
17. Jang K, Mehr AP, Hamilton GA, McPartlin LA, Chung S, Suh K, Ingber DE (2013) Human kidney proximal tubule-on-a-chip for drug transport and nephrotoxicity assessment. Integr Biol (Camb) 5(9):1119–1129
18. Jang K, Suh K (2010) A multi-layer microfluidic device for efficient culture and analysis of renal tubular cells. Lab Chip 10(1):36–42
19. Kim HJ, Huh D, Hamilton G, Ingber DE (2012) Human gut-on-a-chip inhabited by microbial flora that experiences intestinal peristalsis-like motions and flow. Lab Chip 12(12):2165–2174
20. Kimlin L, Kassis J, Virador V (2013) 3D in vitro tissue models and their potential for drug screening. Expert Opin Drug Discov 8(12):1455–1466
21. Marx U, Walles H, Hoffmann S, Lindner G, Horland R, Sonntag F, Klotzbach U, Sakharov D, Tonevitsky A, Lauster R (2012) 'Human-on-a-chip' developments: a translational cutting edge alternative to systemic safety assessment and efficiency evaluation of substances in laboratory animals and man? Altern Lab Anim 40(5):235–257
22. Maschmeyer I, Lorenz AK, Schimek K, Hasenberg T, Ramme AP, Hubner J, Lindner M, Drewell C, Bauer S, Thomas A, Sambo NS, Sonntag F, Lauster R, Marx U (2015) A four-organ-chip for interconnected long-term co-culture of human intestine, liver, skin and kidney equivalents. Lab Chip 15(12):2688–2699
23. Mauleon G, Fall CP, Eddington DT (2012) Precise spatial and temporal control of oxygen within in vitro brain slices via microfluidic gas channels. PLoS One 7(8)
24. Nesmith AP, Agarwal A, McCain ML, Parker KK (2014) Human airway musculature on a chip: an in vitro model of allergic asthmatic bronchoconstriction and bronchodilation. Lab Chip 14(20):3925–3936
25. Olsen MH, Hjortø GM, Hansen M, Met Ö, Svane IM, Larsen NB (2013) In-chip fabrication of free-form 3D constructs for directed cell migration analysis. Lab Chip 13(24):4800–4809
26. Park J, Koito H, Li J, Han A (2009) Microfluidic compartmentalized co-culture platform for CNS axon myelination research. Biomed Microdevices 11(6):1145–1153
27. Polini A, Prodanov L, Bhise NS, Manoharan V, Dokmeci MR, Khademhosseini A (2014) Organs-on-a-chip: a new tool for drug discovery. Expert Opin Drug Discov 9(4):335–352
28. Prabhakarpandian B, Shen M, Nichols JB, Mills IR, Sidoryk-Wegrzynowicz M, Aschner M, Pant K (2013) SyM-BBB: a microfluidic blood brain barrier model. Lab Chip 13 (6):1093–1101
29. Reichl S (2008) Cell culture models of the human cornea—a comparative evaluation of their usefulness to determine ocular drug absorption in-vitro. J Pharm Pharmacol 60(3):299–307
30. Rigat-Brugarolas LG, Bernabeu M, Elizalde A, Niz M, Martin-Jaular L, Fernandez-Becerra C, Homs-Corbera A, Del Portillo HA, Samitier J (2014) Human splenon-on-a-chip: design and validation of a microfluidic model resembling the interstitial slits and the close/fast and open/slow microcirculations. In: IFMBE Proceedings, vol 41
31. Robinton DA, Daley GQ (2012) The promise of induced pluripotent stem cells in research and therapy. Nature 481(7381):295–305
32. Rubin LL (2008) Stem cells and drug discovery: the beginning of a new era? Cell 132 (4):549–552

33. Schimek K, Busek M, Brincker S, Groth B, Hoffmann S, Lauster R, Lindner G, Lorenz A, Menzel U, Sonntag F, Marx U, Horland R (2013) Integrating biological vasculature into a multi-organ-chip microsystem. Lab Chip 13(18):3588–3598
34. Schmitz S (2011) Der Experimentator Zellkultur, 3. Aufl. Experimentator. Spektrum Akademischer Verlag, Heidelberg
35. Selimović S, Dokmeci MR, Khademhosseini A (2013) Organs-on-a-chip for drug discovery. Curr Opin Pharmacol 13(5):829–833
36. Sugioka K, Cheng Y (2011) Integrated microchips for biological analysis fabricated by femtosecond laser direct writing. MRS Bull 36(12):1020–1027
37. Taylor AM, Blurton-Jones M, Rhee SW, Cribbs DH, Cotman CW, Jeon NL (2005) A microfluidic culture platform for CNS axonal injury, regeneration and transport. Nat Methods 2(8):599–605
38. Toepke MW, Beebe DJ (2006) PDMS absorption of small molecules and consequences in microfluidic applications. Lab Chip 6(12):1484–1486
39. Torisawa Y, Spina CS, Mammoto T, Mammoto A, Weaver JC, Tat T, Collins JJ, Ingber DE (2014) Bone marrow-on-a-chip replicates hematopoietic niche physiology in vitro. Nat Methods 11(6):663–669
40. Van Der Meer AD, Van Den Berg A (2012) Organs-on-chips: breaking the in vitro impasse. Integr Biol 4(5):461–470
41. Van Midwoud PM, Groothuis G, Merema MT, Verpoorte E (2010) Microfluidic biochip for the perifusion of precision-cut rat liver slices for metabolism and toxicology studies. Biotechnol Bioeng 105(1):184–194
42. Van Midwoud PM, Verpoorte E, Groothuis G (2011) Microfluidic devices for in vitro studies on liver drug metabolism and toxicity. Integr Biol 3(5):509–521
43. Wagner I, Materne E, Brincker S, Süßbier U, Frädrich C, Busek M, Sonntag F, Sakharov DA, Trushkin EV, Tonevitsky AG, Lauster R, Marx U (2013) A dynamic multi-organ-chip for long-term cultivation and substance testing proven by 3D human liver and skin tissue co-culture. Lab Chip 13(18):3538–3547
44. Wikswo JP, Block FE, Cliffel DE, Goodwin CR, Marasco CC, Markov DA, McLean DL, McLean JA, McKenzie JR, Reiserer RS, Samson PC, Schaffer DK, Seale KT, Sherrod SD (2013) Engineering challenges for instrumenting and controlling integrated organ-on-chip systems. IEEE Trans Biomed Eng 60(3):682–690
45. Wikswo JP, Curtis EL, Eagleton ZE, Evans BC, Kole A, Hofmeister LH, Matloff WJ (2013) Scaling and systems biology for integrating multiple organs-on-a-chip. Lab Chip 13 (18):3496–3511
46. Williamson A, Singh S, Fernekorn U, Schober A (2013) The future of the patient-specific Body-on-a-chip. Lab Chip 13(18):3471–3480
47. Wolff A, Antfolk M, Brodin B, Tenje M (2015) In vitro blood-brain barrier models—an overview of established models and new microfluidic approaches. J Pharm Sci 104 (9):2727–2746
48. Yeon JH, Na D, Choi K, Ryu S, Choi C, Park J (2012) Reliable permeability assay system in a microfluidic device mimicking cerebral vasculatures. Biomed Microdevices 14(6):1141–1148
49. Young EWK (2013) Cells, tissues, and organs on chips: challenges and opportunities for the cancer tumor microenvironment. Integr Biol 5(9):1096–1109
50. Ziółkowska K, Kwapiszewski R, Brzózka Z (2011) Microfluidic devices as tools for mimicking the in vivo environment. New J Chem 35(5):979–990

Index

A. Dietzel (ed.), *Microsystems for Pharmatechnology*,
DOI 10.1007/978-3-319-26920-7